

The Structure of the Water Oxidizing Complex of Photosystem II and the Sites of Substrate Binding as Investigated by Pulse EPR Spectroscopy

Inaugural-Dissertation

zur Erlangung des Doktorgrades
der Mathematisch-Naturwissenschaftlichen Fakultät
der Heinrich-Heine-Universität Düsseldorf

vorgelegt von

Leonid Rapatskiy

aus Nowosibirsk, Russland

Düsseldorf, June 2012

aus dem Max Planck Institut für Bioanorganische Chemie

Gedruckt mit der Genehmigung der
Mathematisch-Naturwissenschaftlichen Fakultät der
Heinrich-Heine-Universität Düsseldorf

Referent: Prof. Dr. Lubitz
Korreferent: Prof. Dr. Schierbaum

Tag der mündlichen Prüfung: 12.06.2012

DECLARATION

The work in this thesis is set out in five self-contained chapters. Each of the chapters forms a journal article. A brief introduction into this research field and theoretical approaches, as well as description of main experimental techniques, are presented. The summary section contains a general review on each of the journal articles.

The investigations detailed in this thesis were carried out jointly with other co-authors. Their contributions to this thesis include:

- Biological sample preparation, isolation of the PS II enzyme etc. This was done by Dr. A. Boussac's research group (chapters 1, 2 and 4) and Dr. M. Nowaczyk's research group (chapter 4).
- Model inorganic complex preparation. This was done by Dr. T. Wehymueller's research group (chapters 3, 4 and 5)
- EPR measurements in chapters 1 to 5. I was assisted by Dr. A. Savitsky, Dr. Ji-Hu Su and Dr. N. Cox.
- DFT calculations in chapter 1, 3, 4 and 5 were completed by Dr. D.A. Pantazis and Dr. W.M. Ames.

All other work in thesis is my own

Leonid Rapatskiy

ABSTRACT

The work performed in this thesis aimed to resolve several key functions of the photosystem II (PS II) enzyme, in particular the structure and mechanism of the water oxidizing complex (WOC). Advanced electron paramagnetic resonance (EPR) methodologies were employed to provide detailed atomic level information about the complex and its reaction (S-state) cycle. A strong emphasis was placed on determining the sites of substrate water binding. Topics addressed in this thesis include the following:

- Resolution of the site(s) of substrate binding. A direct probe for water derived ligands via the detection of labeled substrates with the ^{17}O isotope was developed that allowed an assignment of one the substrate sites of the WOC. This substrate site, generally termed ‘the slow substrate’ likely represents a bridging ligand (μ -oxo) ligand throughout most of the reaction cycle.
- The role of the Ca^{2+} ion of the WOC, as probed by replacing the Ca^{2+} ion with Sr^{2+} biosynthetically. Multi-frequency EPR and electron nuclear double resonance (ENDOR) data demonstrate Ca/Sr substitution has little effect on the electronic properties of the WOC. Together with density functional theory (DFT) calculations, these measurements further refine models of the geometric structure of the WOC and assign specific oxidation states the four manganese ions.
- Variation in the structure and coordinating residues of the WOC across different species and the influence of small, substrate analogues such as methanol. It is suggested that the underlying cause of these variations is the flexibility of μ -oxo bridge connecting the dangler Mn ion and Mn_3 cuboidal unit, which leads to distortions of ligand arrangement in the vicinity of the WOC.
- Benchmarking of all experimental data collected in biological systems to inorganic model complexes. Models have well defined geometry in which particular structural features can be examined in depth. Broken symmetry DFT calculations performed in tandem on such model complexes allow further insight to be ascertained as to the parameters which lead to certain molecular arrangements within metallocofactors.

ACKNOWLEDGEMENTS

I would like to express my deepest gratitude to:

- ✧ *Prof. Dr. Wolfgang Lubitz* for the opportunity to work in *Max-Planck-Institute for Bioinorganic Chemistry* and to do my research in his group, for his excellent guidance and discussions, for stimulating my conference travels and for constant support in any issues.
- ✧ *Prof. Dr. Klaus Schierbaum* for outstanding discussions and reviewing my work, providing new ideas and constructive critic comments.
- ✧ *Dr. Nicholas Cox* for inestimable help over all time we work together on this project; for supervising me and keeping me on right direction; and also for his patience during proofreading of this work.
- ✧ *Dr. William Ames* and *Dr. Dimitrios Pantazis*, who performed all DFT calculations, for comprehensive explanations and discussions.
- ✧ *Ethel Hüttel* for outstanding help in any technical and organizational problems, for improving my German-speaking skills, for taking care of our group, for gifts and creating positive working atmosphere.
- ✧ *Thomas Lohmiller* for all help as a coworker and as a friend, for correcting my German all the time.
- ✧ *Montse Pérez Navarro* for supporting me during hard times, she was always there taking care of me, encouraging me. It wouldn't be possible to finish this work in time without her love and support.

I would like to thank all coworkers and collaborators for their help and support.

I am sincerely thankful to the NRW Research School "BioStruct" for financing my research, which was supported by grants from the Ministry of Innovation, Science and Research of the German Federal State North Rhine-Westphalia (NRW) and from the Entrepreneur Foundation at the Heinrich-Heine-Universität Düsseldorf. I personally thank *Cordula Kruse* and *Christian Dumpitak* for coordinating and helping me in organizational issues.

I would also like to thank my family, especially my parents and elder brother *Vladimir*. They were always supporting me and encouraging me with their best wishes.

TABLE OF CONTENTS

ACKNOWLEDGEMENTS	5
ABBREVIATIONS	8
1. INTRODUCTION	11
1.1. Structure and function of the Photosystem II	12
1.2. Structure of the WOC	16
1.3. Substrate (water) binding and the mechanism of O-O bond formation	19
1.4. Model complexes that represent structural motifs of the WOC	22
2. EPR THEORY	23
2.1. The Spin Hamiltonian Formalism	23
2.1.1. Electron and nuclear Zeeman interaction	24
2.1.2. Hyperfine interaction	25
2.1.3. Nuclear quadrupole interaction	25
2.1.4. High-Spin Systems ($S > 1/2$)	26
2.1.5. Spin-Coupling Model. Mixed Valence Mn-Mn Complexes	28
2.1.6. The Spin Hamiltonian of the Mn Cluster of the WOC	31
2.1.7. The Spin Hamiltonian of the ^{17}O -Mn Cluster of the WOC	32
2.1.8. ^{17}O ENDOR spectra simulations	34
2.2. EPR spectroscopy techniques and spectral analysis	34
2.2.1. Continuous-Wave (cw) EPR	35
2.2.2. Continuous-Wave ENDOR	37
2.2.3. Pulse EPR techniques	38
2.2.3.a. Field-swept Echo-detected EPR	40
2.2.3.b. Electron Spin Echo Envelope Modulation (ESEEM)	40
2.2.3.c. Davies and Mims ENDOR	41
2.2.3.d. High field ELDOR-detected NMR as an alternative to ENDOR spectroscopy	43
2.2.3.e. Two dimensional EDNMR	45
3. SUMMARY	47

3.1.	The effect of Ca ²⁺ /Sr ²⁺ substitution on the electronic structure of the oxygen-evolving complex of photosystem II: A combined pulse ⁵⁵ Mn-ENDOR, multi-frequency EPR and DFT study of the S ₂ state.....	49
3.2.	The electronic structures of the S ₂ states of the oxygen evolving complexes of photosystem II in plants and cyanobacteria in the presence and absence of methanol	51
3.3.	Electronic structure of a weakly antiferromagnetically coupled Mn ^{II} Mn ^{III} model relevant to manganese proteins: a combined EPR, ⁵⁵ Mn-ENDOR, and DFT study	53
3.4.	Detection of water binding sites in the oxygen-evolving complex of photosystem II poised in the S ₂ state using high field (94 GHz) ¹⁷ O-ELDOR-detected NMR spectroscopy	55
3.5.	Characterization of μ-oxo bridge of Mn model complexes using high field (94 GHz) ¹⁷ O-HYSCORE and ¹⁷ O-ELDOR detected NMR spectroscopy.....	58
	REFERENCES	59
	JOURNAL ARTICLES.....	65
	APPENDIX	204

ABBREVIATIONS

<i>A</i>	hyperfine coupling
ATP	adenosine-5'-triphosphate
β_e	Bohr magneton
BIPY	Mn ^{III} Mn ^{IV} (μ -O) ₂ bipy ₄]ClO ₄ complex
Chl	chlorophyll
Chl <i>a</i>	chlorophyll <i>a</i>
Chl _{D1}	chlorophyll <i>a</i> bound to the D1 polypeptide
Chl _{D2}	chlorophyll <i>a</i> bound to the D2 polypeptide
Chl _Z	peripheral chlorophyll's associated with the PS II RC
CP43	protein of inner antenna complex
CP47	protein of inner antenna complex
CW	continuous wave
cyt. _{b559}	cytochrome b ₅₅₉ of PS II
DFT	Density Functional Theory
DTNE	Mn ^{III} Mn ^{IV} (μ -O) ₂ (μ -O ₂ CCH ₃)DTNE]BPh ₄ complex
EDNMR	ELDOR Detected Nuclear Magnetic Resonance
ELDOR	Electron-electron Double Resonance
ENDOR	Electron Nuclear Double Resonance
EPR	Electron Paramagnetic Resonance
ESE	electron spin echo
ESSEM	Electron Spin Echo Envelope Modulation

EXAFS	extended X-ray absorption fine-structure
FID	free induction decay
g_e	Lande factor
HYSCORE	Hyperfine Sub-level Correlation
J	Heisenberg exchange coupling constant
k	Boltzmann constant
LHI	light harvesting complex I
LHII	light harvesting complex II
ML	multi-line
mw	microwave
NADPH	nicotinamide adenine dinucleotide phosphate
NMR	nuclear magnetic resonance
OEC	Oxygen Evolving Complex
P680	primary electron donor chlorophyll molecule in PSII
P _{D1} /P _{D2}	‘special pair’ chlorophyll a’s bound to the D1/ D2 polypeptides
Pheo	pheophytin
Pheo a	pheophytin <i>a</i>
Pheo _{D1}	Pheophytin A bound to the D1 polypeptide
Pheo _{D2}	pheophytin a bound to the D2 polypeptide
PivOH	Mn ^{II} Mn ^{III} (μ-OH)-(μ-piv) ₂ (Me ₃ tacn) ₂ [(ClO ₄) ₂] complex
PQ	plastoquinone
PQH ₂	plastoquinol
PSI	photosystem I

PSII	photosystem II
Q	electrical quadrupole moment
Q_A	primary plasto-quinone acceptor of PS II
Q_B	secondary plasto-quinone acceptor of PS II
RC	reaction center
rf	radio frequency
<i>T.elongatus</i>	<i>Thermosynechococcus elongatus</i>
T_1	longitudinal (spin-lattice) relaxation time
T_2	spin-spin relaxation time
W_f	fastly exchanging substrate
WOC	Water Oxidizing Complex
W_s	slowly exchanging substrate
Y_D	tyrosine D or residue 161 of the D2 polypeptide of PS II
Y_Z	tyrosine Z or residue 161 of the D1 polypeptide of PS II
ZFS	Zero Field Splitting

1. INTRODUCTION

Photosynthesis plays a very important biological role on Earth (1). About 2.3 billion years ago, early photosynthetic organisms that had developed water splitting – became the dominant life-form in the world's oceans (2). This led to the formation of the oxygen-rich atmosphere and the protective ozone (O₃) layer in the stratosphere, which was important for the development of aerobic metabolism and the evolution of multicellular life forms on Earth. Photosynthesis, coupled to carbon fixation, which reduces carbon dioxide (CO₂) into energy-rich organic compounds such as carbohydrates, is responsible for the conversion of the solar energy into the best energy storage unit – chemical bonds. Thus, photosynthesis is a source not only for food and biomass, but also for all fossil fuels such as coal, oil and natural gas. The production of fossil fuels takes millions of years. Rapidly increasing consumption has led to a shortage of these fuels and, consequently, to an impending energy crisis. It is therefore necessary to find alternative renewable energy sources. Solar energy seems to be excellent choice, since it is essentially unlimited. The only problem is its efficient conversion and storage into a useful form of energy like electricity, heat or chemical fuels. The technologies for the first two forms are already developed quite well; however, that's not the case for chemical fuels, and this is still a challenging project (3). The invention of an efficient way to store solar energy in chemical fuels on an industrial scale would be a breakthrough in scientific research, solving the energy problem. The potential fuel material would have to be abundant, non-toxic, and inexpensive for storage and usage. One promising material is water, which can be split into molecular oxygen and hydrogen. Hydrogen is considered the ideal primary fuel for the future, since only water is generated as a waste product during its combustion (4). However, this process requires a synthetic light-driven water-splitting catalyst.

The development of such catalyst is the primary target of many scientific centers. A promising starting point is to look at nature's catalyst for inspiration. The water-splitting reaction of oxygenic photosynthesis occurs in a single biological super-complex, Photosystem II (PSII), which is found in plants, algae and cyanobacteria (5).

1.1. Structure and function of the Photosystem II

PSII is a large, pigment-containing protein complex embedded in the thylakoid membrane of chloroplasts and cyanobacteria. Recently, a high-resolution X-ray crystal structure of the super-complex purified from cyanobacteria *Thermosynechococcus vulcanus* (Fig. 1.1) was reported (6). It has a dimer structure, where each monomer contains about 20 protein subunits that harbor 77 cofactors: 35 chlorophylls (Chl *a*); 11 β -carotenes; 2 plastoquinones (PQ); 2 pheophytins (Pheo *a*); 1 Mn_4O_5Ca complex; 2 heme Fe centers; 1 non-heme Fe center; and 1 hydrogencarbonate (HCO_3^- , CO_3) (7).

PSII functions as a water:plastoquinone oxidoreductase, catalysing the following reaction:



The water-splitting reaction occurs using light within the visible range (400-700 nm). The chemical energy produced is temporarily stored as reduced plastoquinol (PQH_2), which is subsequently used by Photosystem I (PSI) to reduce $NADP^+$ to NADPH (Nicotinamide adenine dinucleotide phosphate) – one of the two major energy carriers in biology. During this process a proton (H^+) gradient builds up across the thylakoid membrane, driving the synthesis of ATP (Adenosine-5'-triphosphate) – the second primary biological energy carrier. Both ATP and NADPH are used in carbon fixation processes, and therefore, PSII and PSI are responsible for the majority of biological energy storage that is derived from sunlight.

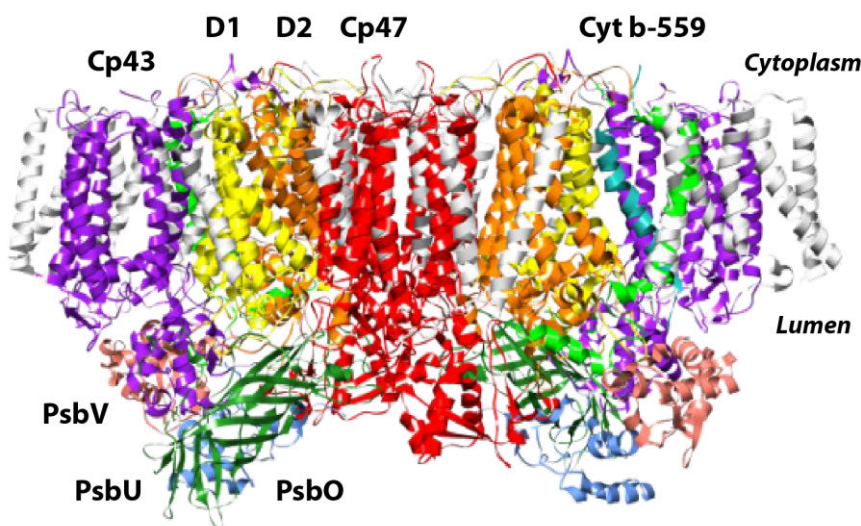


Figure 1.1 The X-ray crystal structure of the PSII dimer, view from the direction perpendicular to the thylakoid membrane normal. The most important subunits are shown in color.

preventing recombination of the radical pair. The $\text{Pheo}_{\text{D1}}^{\bullet-}$ passes its electron to the neighboring plastoquinone Q_A (within 100-200 ps), whereas $\text{P680}^{\bullet+}$ is reduced by a redox-active tyrosine residue Tyr_Z (Y_Z). This leads to a very high quantum efficiency for the PSII complex (over 90%). However, the multiple electron transfer reactions decrease ΔG , reducing the overall energy efficiency of photosynthesis (11).

The next step is the reduction of plastoquinone Q_B by $\text{Q}_\text{A}^{\bullet-}$ (~200-600 μs) and protonation at the acceptor side of PSII (~1 ms). The tightly-bound $\text{Q}_\text{A}^{\bullet-}$ passes one electron to a second plastoquinone Q_B , which is much less strongly associated within the protein. Overall, Q_B can accept two electrons and two protons from $\text{Q}_\text{A}^{\bullet-}$, and thus is fully reduced after two photon absorptions/charge separation events. At this point, it is exchanged with an oxidized quinone from the pool in the membrane (~5 ms). The reduced plastoquinol $\text{Q}_\text{B}\text{H}_2$ therefore acts as a mobile electron carrier, transferring electrons to the next protein complex of the photosynthetic apparatus, the cytochrome b_6f complex.

On the donor side of PSII, the water-splitting reaction takes place:



This reaction is catalysed by the oxygen-evolving complex (OEC) or water-oxidizing complex (WOC) of PSII. The WOC consists of an inorganic $\text{Mn}_4\text{O}_5\text{Ca}$ cluster and its surrounding protein matrix (12,13). To drive this reaction, four electrons must be removed from two water molecules, and since only one electron-hole pair is generated per photon absorbed, the PSII must temporarily store four oxidizing equivalents. The tetra-nuclear Mn cluster allows such complicated chemistry. The functionally important protein matrix includes the redox-active tyrosine residue Y_Z ($\text{D}_1\text{-Y}_{161}$), which couples the electron transfer from the primary donor $\text{P680}^{\bullet+}$ to the manganese cluster and is involved in proton transfer reactions (14). During water-splitting, the $\text{Mn}_4\text{O}_5\text{Ca}$ cluster goes through a reaction cycle proposed by Kok et al. (15). The catalytic cycle comprises five distinct redox intermediates known as the S_i states (Fig. 1.3), where the index indicates the number of stored oxidizing equivalents ($i = 0-4$). Once formed, the $\text{S}_3\text{Y}_\text{Z}^\bullet$ state rapidly decays to the S_0 state under the release of molecular triplet oxygen and the rebinding of at least one substrate water molecule (11,16). The S_4 state, which is different from the $\text{S}_3\text{Y}_\text{Z}^\bullet$ state, has not yet been spectroscopically identified.

The dark stable state of the enzyme is S_1 . Higher S-states, S_2 - S_3 , decay back to this state on a timescale of seconds at room temperature. The S_0 state is of sufficient reduction potential that it can be oxidized by a second redox-active tyrosine residue Y_D (D2-161) (17). Y_D (D2-161) does not participate further in the S-state cycle.

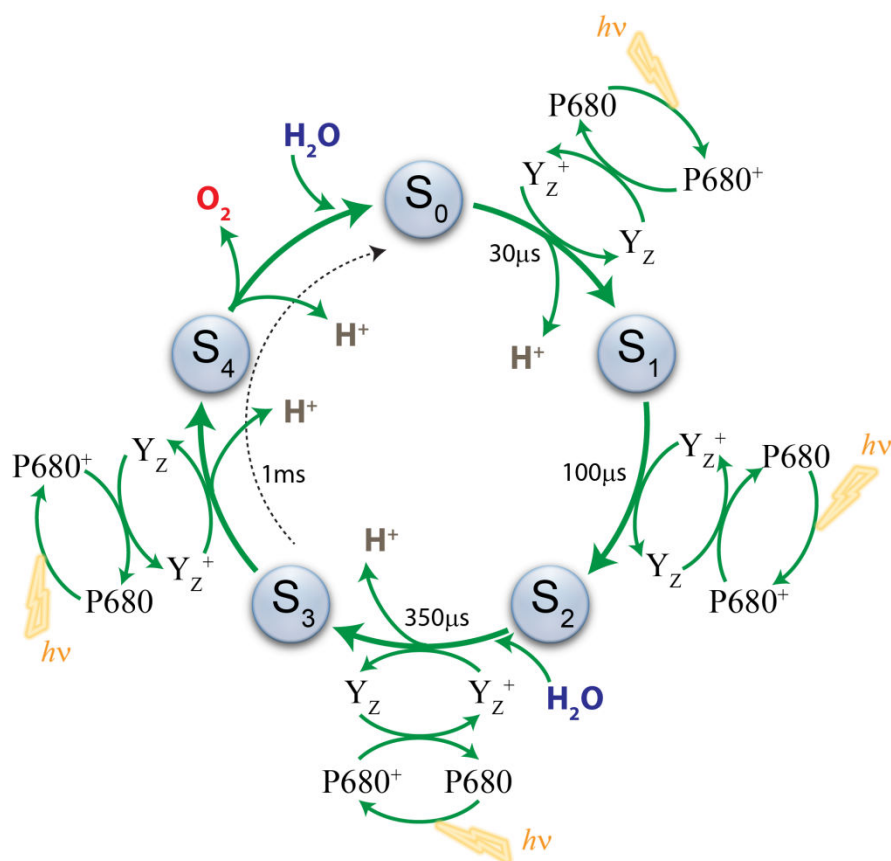


Figure 1.3 The S-state cycle of the WOC. The rates of corresponding S-state transitions are shown along with the four light absorption and the subsequent four electron “hole” transfer events. The binding of the two water molecules and as the release of molecular oxygen and protons is also indicated.

Water oxidation chemistry is relatively slow, requiring substrate binding, proton translocation and ultimately O-O bond formation. Early S-state transitions, $S_0 \rightarrow S_1 \rightarrow S_2 \rightarrow S_3$, which involve oxidation of the Mn ions, occur on a timescale of $\sim 100 \mu\text{s}$, whereas the transitions $S_3 \rightarrow S_4 \rightarrow S_0$, in which O-O bond is formed, occur on a timescale of about 1-2 ms (18). The timescales involved in the water-splitting chemistry are more than nine orders of magnitude slower than the reaction center photochemistry. Thus, the secondary and tertiary electron transfer events described above, which stabilize an oxidized state of the complex are critical, as they lengthen the lifetime of the chemical oxidant.

1.2. Structure of the WOC

The WOC is made up of four Mn ions and one Ca ion. The five metal centres are connected via a network of five bridging oxygen (μ -oxo) atoms(6). The proposed structure from X-ray crystallography bears similarities to earlier literature models, including those derived from (polarized) extended X-ray absorption fine-structure (EXAFS) measurements (19,20) and to the computational models of Kusunoki (21), Siegbahn (22) and Dau (23,24). The metals are arranged in a ‘distorted chair-like’ arrangement where the base is formed by a μ -oxo-bridged cuboidal Mn_3O_4Ca unit (Fig. 1.4). The fourth ‘outer’ Mn_{A4} is attached to this core structure via a μ -oxo-bridged ligation (O4) and presumably hydroxo bridge (O5) to the central Mn_{B3} . In addition to the μ -oxo-bridged network, the Mn_4O_5Ca is held together by six carboxylate ligands, four of which (Asp342, Asp170, Glu333, CP47-Glu354) forming μ -carboxylato bridges between Mn sites (25). The cluster has only one nitrogen ligand, the His332.

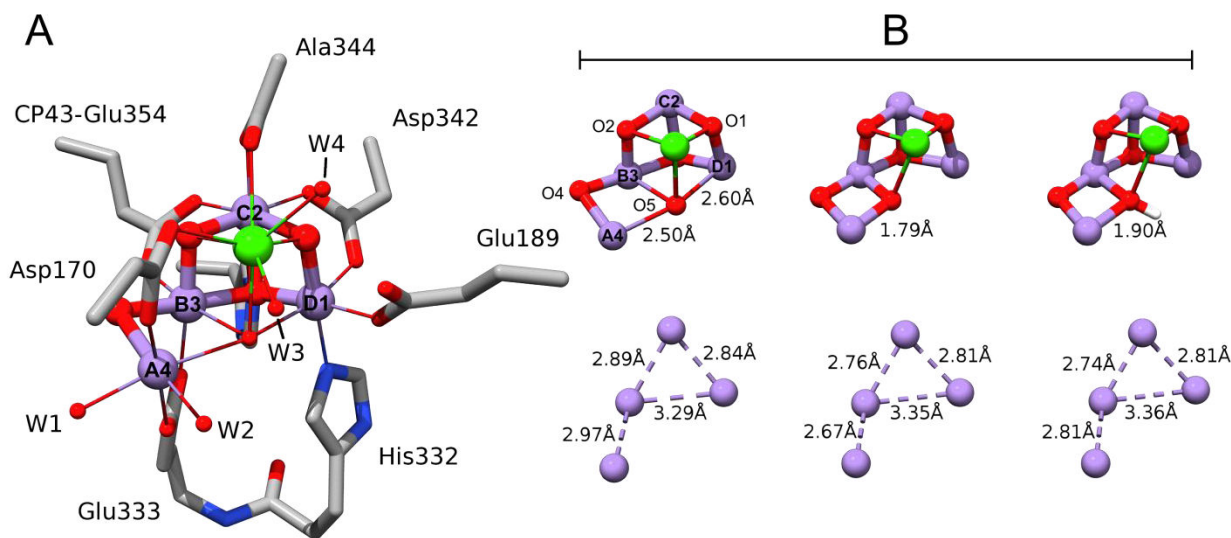


Figure 1.4 (A) The crystal structure Mn_4O_5Ca cluster(6); **(B)** Modeled geometric structures of the WOC poised in the S_2 state as derived from DFT calculations based on the crystal structure coordinates, from left to right: Mn_4O_5Ca inorganic core seen in the crystal structure of Umena et al.(6); the ‘best’ geometry optimized DFT structure of Ames et al. (26); optimized DFT structure which contains a protonated O5 bridge.

When compared to the experimental EXAFS data, the Mn-Mn, Mn-Ca and Mn-O/N distances determined from the crystal structure are all elongated, suggesting that the cluster underwent some degree of

radiation-induced reduction during data collection. Thus, the crystal structure of the Mn-cluster may not represent a physiological S-state, but rather a ‘super-reduced’ state (S_{-1} , S_{-2}). These reduced states are typically formed using chemical reagents such as NH_2OH , NH_2NH_2 and NO (27,28). Nevertheless, the X-ray structure has the general pattern of three short and one long Mn-Mn distances and four distinct Mn-Ca distances as observed earlier in EXAFS measurements.

It should also be noted that in the different S-states the $\text{Mn}_4\text{O}_5\text{Ca}$ cluster undergoes structural changes during the catalytic cycle (29-31), particularly during the $S_2 \rightarrow S_3$ transition. Thus, the structures of the $\text{Mn}_4\text{O}_5\text{Ca}$ cluster in the lower oxidation states, S_1 and S_2 states, are expected to be different from those in the S_3 and/or the S_4 states in which the O-O bond is formed. In other words, the catalyst is not a static entity but rather a dynamic structure undergoing geometric changes that are necessary for proper function.

The presence of both the coordinated Ca^{2+} and more distant Cl^- ions is crucial for water splitting activity. Removal of either the Ca^{2+} or Cl^- ions inhibits the water-splitting process by blocking the S-state cycle at the $S_2 \rightarrow S_3$ transition (32,33). Interestingly, surrogates of these ions (Sr^{2+} instead of Ca^{2+} , Br^- and I^- for Cl^- substitution) are able to restore water-splitting, however, at slower turnover rates. The replacement of both Ca^{2+} and Cl^- by surrogate ions, leads to an additive effect on the turnover frequency, slowing the $S_3 \rightarrow S_4 \rightarrow S_0$ transitions by 30-fold (34). Both chloride and calcium ions have been proposed to influence proton transfer away from the WOC. Ca^{2+} may also play a role for substrate water binding.

For understanding of the mechanism of water oxidation it is important to not simply look at the geometric structure, but the electronic structure as well, in all S-states. These measurements provide information of the net oxidation state of the cluster, the order in which the four Mn are oxidized and the level to which the Mn ions interact (via spin exchange, J). These three features will all influence the redox properties of the cluster, binding of the substrates, and O_2 and H^+ release.

Since the S_i state cycle consists of four single oxidation events of the $\text{Mn}_4\text{O}_5\text{Ca}$ cluster, it is possible to probe the electronic structure by electron paramagnetic resonance (EPR) spectroscopy, which is well suited for detection of chemical systems with unpaired electrons. All the S-states are paramagnetic (35,36), and two of them have a half-integer ground spin, S_0 and S_2 . It is these two states that are easily probed by standard perpendicular mode continuous-wave (cw) EPR and pulse EPR techniques, and thus most studies on the

The arrangement of all redox cofactors required for photochemical charge separation and water oxidation is shown in Fig. 1.2. Initially, light is absorbed by the chlorophyll molecules of the outer antenna (LHI, LHII) and inner antenna complexes (CP43 and CP47), and subsequently the energy is transferred to the reaction center (RC) of the PSII. The RC is a multi-pigment assembly of four Chl *a* and two Pheo *a* molecules (Fig. 1.2), which are bound by the D1 and D2 proteins. The cytochrome Cyt b-559 and carotene pigments play a role in preventing photodamage of the RC.

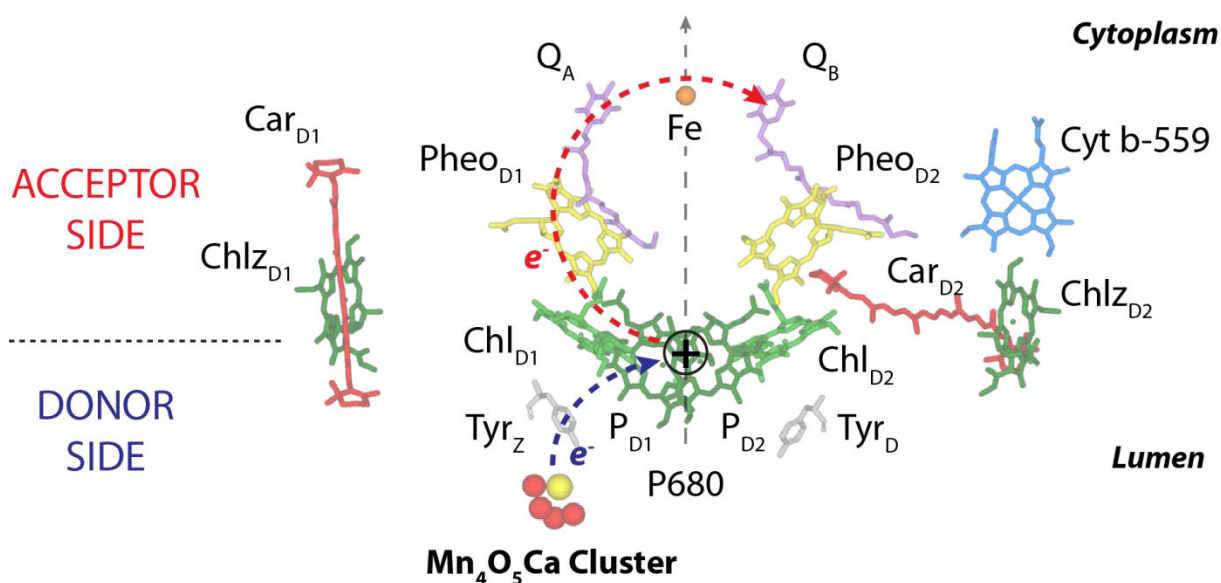


Figure 1.2 The arrangement of main cofactors in PSII and the electron transfer pathways on acceptor and donor sides.

In the RC, the next process occurs – charge separation, initiated by the photo-excited state, P680*. The transfer of a single electron within the multi-pigment assembly results in a charge-separated (radical pair) state (8), which forms on a timescale of about 3 ps (9). The positive charge (“hole”) is predominantly localized at a single Chl *a* pigment (P_{D1}), forming the cation radical (primary donor), which is commonly referred to as P680*⁺ because of the position of its optical absorption maximum. The estimated oxidizing potential of P680*⁺ is +1.2 to +1.3 V – one of the highest known in biology (10). The electron is transferred to the primary acceptor, the anion radical Pheo_{D1}*⁻ on a time scale of 3-20 ps. The fast subsequent electron/hole transfer from both primary donor and acceptor further separates the two charges in space,

electronic structure of the Mn-cluster have been performed on these two intermediates. The characteristic EPR signals seen in both the S_0 and S_2 states are the so-called “multiline (ML) signals” of the OEC (Figure 1.5). These spectra are centred at $g \sim 2$ and contain a large number of spectral lines (S_0 26 lines, S_2 18-20 lines). These lines arise from the hyperfine interaction of the unpaired electron spin (effective spin of the ground spin-state $S_{\text{eff}} = 1/2$) with the four ^{55}Mn nuclei (nuclear spin $I = 5/2$). Unfortunately, as the resonance lines overlap, there is no unique interpretation of the experimental data. As a consequence, advanced NMR-related techniques such as ^{55}Mn -electron nuclear double resonance (ENDOR), that probe the ^{55}Mn nuclei directly, have been developed to more accurately probe the electronic structure (37-39).

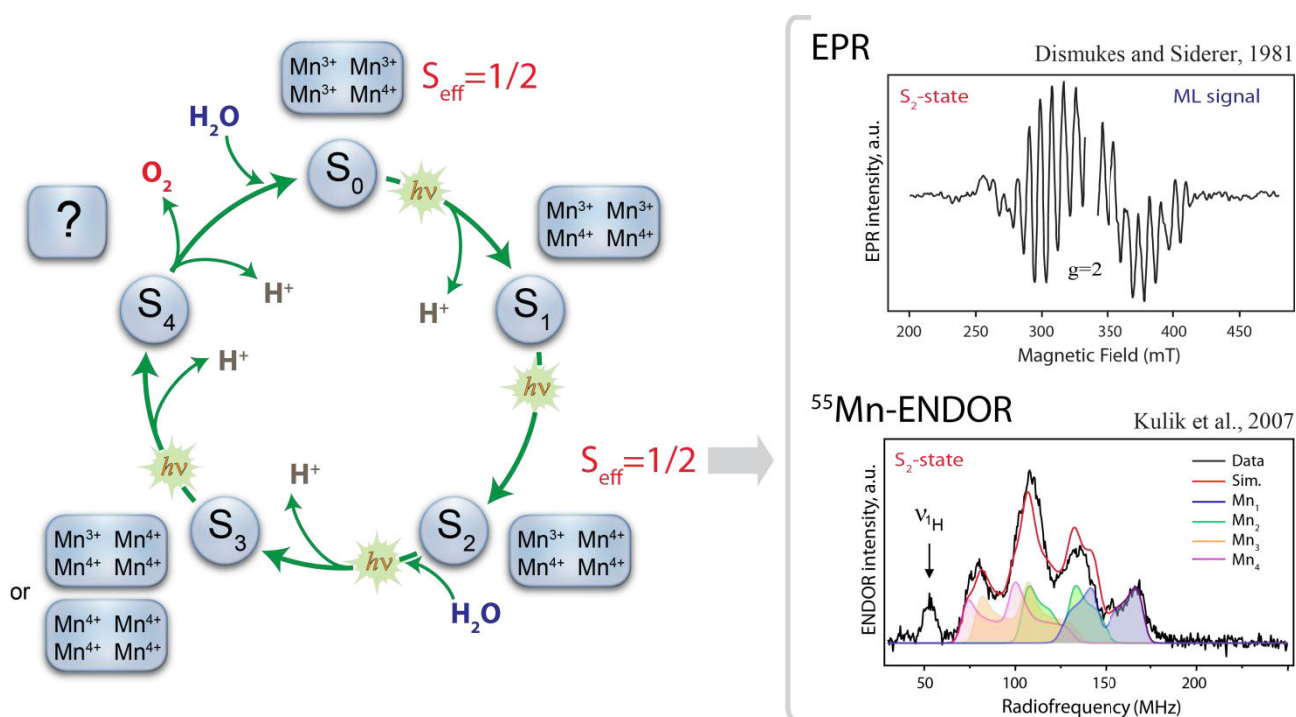


Figure 1.5 The S-state catalytic cycle of the WOC. The typical EPR/ENDOR spectra for the S_2 -state are shown, EPR/ENDOR data adapted from works of Dismukes (35) and Kulik (37).

^{55}Mn -ENDOR data for the OEC are shown in Figure 1.5, where contributions from individual Mn ions are additive and sum in the spectrum. The key observation that can be made from this data set is that all four Mn of the WOC must carry significant electron spin density, that is to say all four Mn contribute (almost) equally to the electronic ground state of the complex. This result along with comparison to model compounds strongly suggests that the OEC does not contain a Mn^{II} ion in any S-state during its reaction

cycle. Thus, the net oxidation states of the S_0 and S_2 states are determined to be: $Mn_4(III,III,III,IV)$ and $Mn_4(III,IV,IV,IV)$ respectively to yield the experimentally observed spin multiplicity (37).

1.3. Substrate (water) binding and the mechanism of O-O bond formation

One outstanding problem in this research field is identification of the water-derived ligands of the WOC that represent the two substrate molecules. The best data on substrate binding currently come from time-resolved $H_2^{16}O/H_2^{18}O$ exchange membrane-inlet mass spectrometry experiments, which demonstrate that at least one substrate water (the slowly exchanging substrate, W_s) is bound in all S-states, and that its exchange kinetics are significantly affected by replacement of the Ca^{2+} ion with Sr^{2+} (40,41). In contrast, the second, faster exchanging substrate water (W_f) is thought to bind late in the S-state cycle, possibly in the S_3 state or during the $S_2 \rightarrow S_3$ transition (29,30,42-46). These observations can be used as constraints for the sites of the substrates. The positions of all ‘water’ (including Mn ligands, bridges, etc) molecules according to the Umena et al. crystal structure within a 5 Å radius of the WOC are shown in Fig. 1.6. Waters ligated to the Ca ion (W3 or W4) or the Mn-oxo bridges (O1, O3 and O5) are probably the best candidates for W_s , the water bound in the early S –states (S_0 - S_2). In contrast, it is more difficult to determine the position of W_f as it may not be bound or occupy the position required for O-O bond formation to occur (the crystal structure is representative of the earlier S-states). It is noted that the site still needs to be close to the position of the first substrate W_s , and may include the Mn_{A4} terminal ligand H_2O/OH (W1 or W2), among others.

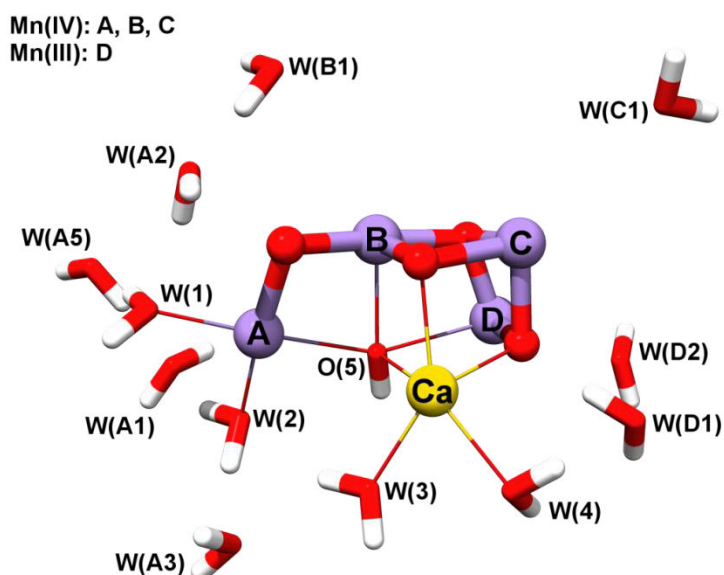


Figure 1.6 The positions of water molecules within a 5 Å radius of the WOC with proposed hydroxo bridge (O5).

From the considerations above, a large number of mechanisms have been proposed for O-O bond formation by the WOC (for reviews see (47,48)). These can be grouped into two basic classes: a nucleophilic attack mechanism and an oxo/oxyl radical coupling mechanism (Figure 1.7). For the nucleophilic attack mechanism, the O-O bond is formed between two adjacent substrate oxygen atoms, with one deriving from a water molecule bound to either Ca or Mn (the nucleophile) and the second as an oxygen ligand of high-valent Mn (the electrophile). Two pathways for nucleophilic attack are shown in Fig. 1.7A and B. In A, the nucleophile is bound to the Ca^{2+} which attacks a terminal or bridging oxygen ligand on Mn_{A4} , i.e. W3 and W2/O5 (49,50). Alternatively, the same reaction could occur between a water bound to Mn_{A4} , i.e. W1 and W2/O5 (21,51), see Figure 1.7B. In both of these reactions, the substrate bound to the Mn is progressively deprotonated during the S-state cycle such that in S_4 it is a strong electrophile. In the simplest case for a terminal ligand, this species can be considered to be a Mn(V)=O species; however, it may equivalently be described as a $\text{Mn(IV)}\equiv\text{O}^+$ or $\text{Mn(IV)-O}^{\bullet}$ species. Nucleophilic attack mechanisms have been previously observed in Mn model systems that perform O-O bond formation. However, these systems display turnover rates that are orders of magnitude slower than that of the WOC (52).

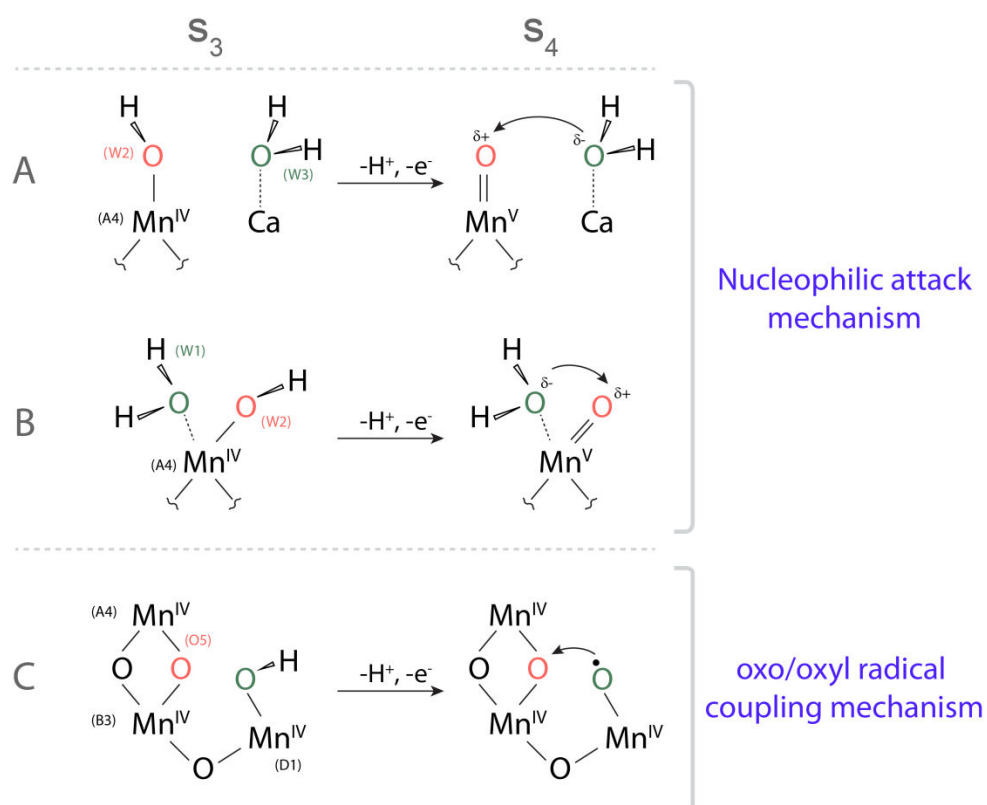


Figure 1.7 The proposed mechanism for O-O bond formation via a nucleophilic attack mechanism and radical attack as described in the text.

In the proposed oxo/oxyl coupling mechanisms, the O-O bond is formed between two adjacent substrate oxygen atoms which are already fully deprotonated. The most detailed and rigorous mechanism to this date is the mechanism proposed by Siegbahn (22). In this catalytic cycle, the slowly-exchanging substrate is considered to be the O5 μ -oxo bridge between Mn_{A4} and Mn_{B3} . The fast substrate water binds then at the open coordination site on the Mn_{D1} as water/hydroxo in S_2/S_3 , forming an oxyl radical in S_4 (see Figure 1.7C). This type of mechanism allows for the possibility that O-O bond formation can occur in the S_3 state (53), i.e., the WOC contains a complexed peroxide in the S_3 state which presumably is in redox equilibrium with other forms of S_3 that may include an oxygen radical and/or a formal $Mn_4(IV,IV,IV,IV)$ state. Upon formation of the $S_3 Y_Z^\bullet$ state, only centers which contain the complexed peroxide configuration are able to donate an electron to Y_Z^\bullet and liberate O_2 . Thus the rate of the $S_3 \rightarrow S_4$ transition reflects the equilibrium constants between the different S_3 redox states, and would directly follow the time course of Y_Z^\bullet reduction, as is observed experimentally. In contrast to the nucleophilic attack mechanism, the radical coupling

mechanism has no precedence in manganese chemistry. However, it is the energetically favorable pathway for efficient O-O bond formation in rare earth catalysts such as the ruthenium “blue dimer” (54).

1.4. Model complexes that represent structural motifs of the WOC

Mixed-valence Mn dimer complexes have been historically used to calibrate measurements performed on the WOC of PSII. These complexes are considered ‘good’ models for the WOC as they typically display the same electronic ground state ($S = 1/2$) and thus their multiline EPR spectrum is similar to that seen for the half-integer paramagnetic states of the WOC, S_0 and S_2 (35,37,38,55-61). In this way, a magnetic fingerprint for different ligand motifs can be resolved and an understanding of the factors that affect the electronic environment can be developed. This approach of using Mn dimer complexes as electronic structure mimics has been previously used to benchmark ^{55}Mn -ENDOR (37,38,58,61,62) and ^{13}C ENDOR (63) studies on the WOC. Three such models are shown in Fig. 1.8.

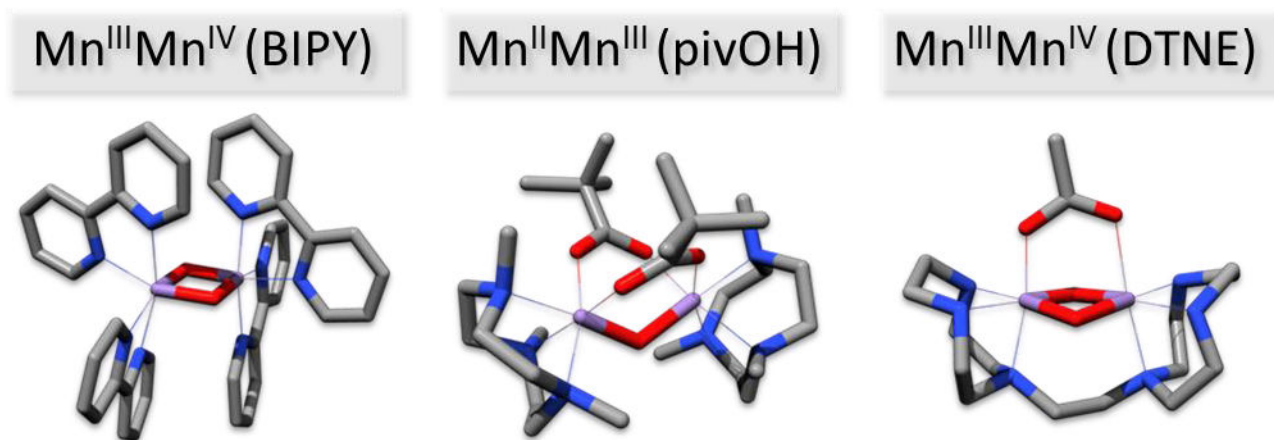


Figure 1.8 Manganese dimer model complexes used to calibrate ^{17}O -EDNMR results for the OEC. **Left:** planer $\text{Mn}^{\text{III}}-\mu\text{O}_2-\text{Mn}^{\text{IV}}$ BIPY complex (64-66), $[\text{Mn}^{\text{III}}\text{Mn}^{\text{IV}}(\mu\text{-O})_2\text{bipy}_4]\text{ClO}_4$, BIPY = bipyridine. **Center:** mono- μ -hydroxo bridged $[\text{Mn}^{\text{II}}\text{Mn}^{\text{III}}(\mu\text{-OH})(\mu\text{-piv})_2(\text{Me}_3\text{tacn})_2](\text{ClO}_4)_2$ complex (PivOH). **Right:** bent $\text{Mn}^{\text{III}}-\mu\text{O}_2-\text{Mn}^{\text{IV}}$ DTNE complex, $[\text{Mn}^{\text{III}}\text{Mn}^{\text{IV}}(\mu\text{-O})_2(\mu\text{-O}_2\text{CCH}_3)\text{DTNE}]\text{BPh}_4$, DTNE = 1,2-di-(1,4,7-triazacyclononyl)-ethane (60,67). The bridging oxygens of the BIPY complex have an identical chemical environment. In contrast, the bridging oxygens of the DTNE complex are not strictly identical due to the additional bridge ($-\text{N}(\text{CH}_2)_2\text{N}-$) that connects the two ligand adducts.

2. EPR THEORY

The aim of this chapter is to provide an overview of the theoretical principles of EPR spectroscopy and its application to exchange-coupled transition metal complexes, i.e. the tetra-manganese cluster of PSII or synthetic Mn complexes. For a full treatment of the principles of EPR theory, see (68-70).

2.1. The Spin Hamiltonian Formalism

The spin Hamiltonian formalism was first described in the work of Abraham and Pryce (25). The complete static spin Hamiltonian that operates on the wavefunction of bound electrons using the perturbation theory approximation includes the following terms:

$$\begin{aligned}
 H &= H_{EZ} + H_{ZFS} + H_{HF} + H_{NZ} + H_{NQ} + H_{EX} & \text{(Eq. 2.1)} \\
 &= \sum_i \beta_e \vec{B}_0 \cdot \hat{g}_i \cdot \vec{S}_i + \sum_i \vec{S}_i \cdot \hat{D}_i \cdot \vec{S}_i + \sum_i \vec{S}_i \cdot \hat{A}_i \cdot \vec{I}_i - \sum_i g_n \beta_n \vec{B}_0 \cdot \vec{I}_i + \sum_i \vec{I}_i \cdot \hat{P}_i \cdot \vec{I}_i - \sum_{i < j} \vec{S}_i \cdot \hat{J}_{ij} \cdot \vec{S}_j
 \end{aligned}$$

where H_{EZ} : the electron Zeeman interaction; H_{ZFS} : the zero field splitting term; H_{HF} : the hyperfine interaction between bound electrons spins and nuclear spins; H_{NZ} : the nuclear Zeeman interaction; H_{NQ} : the nuclear quadrupole interactions for spins with nuclear quantum numbers $I > 1/2$; and H_{EX} : the spin-spin exchange interaction. This spin Hamiltonian describes the energy states of any paramagnetic species with several bound electrons and nuclei.

For the system of n electron spins and k nuclear spins the initial (uncoupled) wavefunctions have the following form:

$$|S_1 \dots S_n M_1 \dots M_n I_1 \dots I_k m_1 \dots m_k \rangle, \quad \text{(Eq. 2.2)}$$

where S_i : electron spin of unpaired electron(s); M_i : its magnetic sub-level (projection on magnetic field axis); I_j : nuclear spin of certain nuclei; m_j : its magnetic sub-level. The basis set of eigenfunctions and eigenstates for the coupled system can be built via diagonalization of the spin Hamiltonian.

2.1.1. *Electron and nuclear Zeeman interaction*

The electron Zeeman interaction describes the interaction between electron spin and the external magnetic field \vec{B}_0 :

$$H_{EZ} = \beta_e \vec{B}_0 \cdot \hat{g} \cdot \vec{S} = \beta_e \vec{B}_0 (\vec{L} + g_e \vec{S}), \quad (\text{Eq. 2.3})$$

where β_e : the Bohr magneton; $g_e = 2.0023193043737$: the Lande factor of the free electron. The \hat{g} tensor is represented by a symmetric matrix 3x3 in the laboratory coordinate system and can be transformed to a diagonal form in the principal axes frame via rotation. The diagonal elements of the \hat{g} tensor are called principal values (g_x, g_y, g_z) . The three Euler angles describe the orientation of principal axes in the laboratory frame. Typically, the principal axes frame is considered as the molecular frame, and all interaction tensors are referred to within this frame.

In most cases, the ground spin state of molecules is non-degenerate and the orbital angular momentum \vec{L} is quenched. This leads to a deviation of the principal values from the free electron g_e value, which is caused by the interaction of the ground spin state with excited states. Due to spin-orbit coupling, for which the Hamiltonian can be written in the form:

$$H_{SO} = \lambda \vec{L} \vec{S}, \quad (\text{Eq. 2.4})$$

the orbital angular momentum mixes with the spin, introducing a second-order contribution to the g values. Here, λ is the effective spin-orbit coupling constant. Since these second-order contributions are inversely proportional to the energy difference between the ground state and excited states, the deviation from g_e can be significant if the energy levels are close to each other.

The nuclear Zeeman interaction describes the coupling between the nuclear spin \vec{I} and the external magnetic field \vec{B}_0 :

$$H_{NZ} = -g_n \beta_n \vec{B}_0 \cdot \vec{I}. \quad (\text{Eq. 2.5})$$

The nuclear spin quantum number and the nuclear g_n factor are intrinsic properties of a particular nucleus. In most EPR experiments, the nuclear Zeeman interaction can be considered isotropic, and this approximation will be used throughout this work.

2.1.2. *Hyperfine interaction*

The spin Hamiltonian of the hyperfine interaction between an electron and a nuclear spin have the following form:

$$H_{HF} = \vec{S} \cdot \hat{A} \cdot \vec{I}, \quad (\text{Eq. 2.6})$$

Where \hat{A} is defined as the hyperfine tensor. This Hamiltonian consists of an isotropic and an anisotropic term. The isotropic term is described by the Fermi contact interaction:

$$H_F = A_{iso} \vec{S} \cdot \vec{I} = \frac{8\pi}{3} g_e \beta_e g_n \beta_n \delta(r) \cdot \vec{S} \cdot \vec{I}, \quad (\text{Eq. 2.7})$$

with the isotropic hyperfine constant A_{iso} . The anisotropic part represents the electron-nuclear dipole-dipole coupling

$$H_{DD} = \vec{S} \cdot \hat{A}_{aniso} \cdot \vec{I} = g_e \beta_e g_n \beta_n \left[\frac{3(\vec{S} \cdot \vec{r})(\vec{r} \cdot \vec{I})}{r^5} - \frac{\vec{S} \cdot \vec{I}}{r^3} \right], \quad (\text{Eq. 2.8})$$

with a dipolar coupling tensor \hat{A}_{aniso} , which is typically traceless and symmetric.

The Fermi contact interaction describes the interaction of the nuclear spin with the electron spin from atomic s-orbitals.

2.1.3. *Nuclear quadrupole interaction*

Nuclei with nuclear spin quantum number $I \geq 1$ have a non-spherical charge distribution due to a nuclear electrical quadrupole moment Q . The nuclear quadrupole interaction is the interaction of this charge

distribution with the electric field gradient caused by the surrounding electrons and nuclei. The corresponding spin Hamiltonian is:

$$H_{NQ} = \vec{I} \cdot \hat{P} \cdot \vec{I}, \quad (\text{Eq. 2.9})$$

where \hat{P} is the nuclear quadrupole tensor – a diagonal traceless tensor in its principal axes system. The Hamiltonian can be expanded as

$$H_{NQ} = P_x I_x^2 + P_y I_y^2 + P_z I_z^2 = \frac{3}{2} P_z \left[\left(I_z^2 - \frac{1}{3} I(I+1) \right) + \frac{1}{3} \eta (I_x^2 - I_y^2) \right], \quad (\text{Eq. 2.10})$$

where $|P_z| \geq |P_y| \geq |P_x|$; η : the asymmetry parameter, which is defined by

$$\eta = \frac{P_x - P_y}{P_z}. \quad (\text{Eq. 2.11})$$

The largest principal value of the quadrupole tensor is given by

$$P_z = \frac{e^2 q Q}{h \cdot 2I(2I-1)}, \quad (\text{Eq. 2.12})$$

where eq is the electric field gradient. The quadrupole tensor is usually expressed in terms of the two parameters $e^2 q Q/h$ and η .

2.1.4. High-Spin Systems ($S > 1/2$)

For spin systems with more than two unpaired electrons, i.e. systems with an effective spin $S > 1/2$, the “fine-structure” and exchange terms have to be included in the spin Hamiltonian:

$$H_{ZFS} + H_{EX} = \sum_i \vec{S}_i \cdot \hat{D}_i \cdot \vec{S}_i - \sum_{i < j} \vec{S}_i \cdot \hat{J}_{ij} \cdot \vec{S}_j, \quad (\text{Eq. 2.13})$$

where \hat{D}_i is the traceless zero-field splitting (ZFS) tensor and \hat{J}_{ij} is the exchange coupling tensor.

For the effective electron spin S the ZFS term can be written as:

$$H_{ZFS} = \vec{S} \cdot \hat{D} \cdot \vec{S}, \quad (\text{Eq. 2.14})$$

with the ZFS tensor \hat{D} , which is diagonal in the principal axes system. Then the spin Hamiltonian can be rewritten as

$$H_{ZFS} = D_{xx}S_x^2 + D_{yy}S_y^2 + D_{zz}S_z^2 = D \left[S_z^2 - \frac{1}{3}S(S+1) \right] + E(S_x^2 - S_y^2), \quad (\text{Eq. 2.15})$$

where $D = 3D_{zz}/2$ and $E = (D_{xx} - D_{yy})/2$ – axial and rhombic ZFS parameters.

In systems with high local symmetry, e.g. octahedral or tetrahedral, the ZFS contribution is constant in all Zeeman energy levels and thus is not observed using EPR. However, for systems with $S > 2$, ZFS can also be detected for these symmetric systems. The effect of crystal fields with cubic symmetry makes it obligatory to include higher order terms in S_i , and the spin Hamiltonian for the ZFS is given by

$$H_{ZFS} = \frac{a_{ZFS}}{6} \left[S_x^4 + S_y^4 + S_z^4 - \frac{1}{5}S(S+1)(3S(S+1)-1) \right]. \quad (\text{Eq. 2.16})$$

The exchange coupling spin Hamiltonian describes weakly interacting unpaired electrons or group spins \vec{S}_i and \vec{S}_j with an exchange coupling tensor \hat{J}_{ij} , which consists of isotropic part and anisotropic part. The anisotropic part of the exchange interaction tensor is caused by spin-orbit coupling and can be usually neglected.

The isotropic part of the exchange interaction consists of two components: Heisenberg (direct) exchange and super-exchange (indirect). Heisenberg exchange becomes relevant when the orbitals of two spins overlap significantly, and therefore unpaired electrons strongly interact. There are many definitions of the exchange interaction spin Hamiltonian, i.e. $\hat{H} = -2J\vec{S}_1\vec{S}_2$, $\hat{H} = -J\vec{S}_1\vec{S}_2$ and $\hat{H} = J\vec{S}_1\vec{S}_2$; however, the most frequently used is

$$\hat{H} = -2J\vec{S}_1\vec{S}_2. \quad (\text{Eq. 2.17})$$

Here, $J < 0$ corresponds to an antiferromagnetic exchange interaction (a weak bonding situation) and $J > 0$ to a ferromagnetic interaction (a weak anti-bonding situation).

Indirect exchange appears from overlap between orbitals of a bridging ligand across two centers, with each of these centers (71,72). The same spin Hamiltonian (Eq. 2.17) can also be used to describe super-exchange interaction.

In most cases, direct exchange is antiferromagnetic, since the electronic configuration with the highest number of paired electrons is lower in energy. Depending on the specific bridging environment, the super-exchange interaction can be ferromagnetic or antiferromagnetic. Overall, antiferromagnetic contributions are usually dominant.

2.1.5. *Spin-Coupling Model. Mixed Valence Mn-Mn Complexes*

In cases where the electron exchange interaction is significantly larger than any other term of the total spin Hamiltonian, the spin manifold can be described in terms of coupled or effective electronic spin states(73). For example, a two spin system containing S_1 and S_2 can be expressed in term of a single quantum number S , which takes values

$$S = |S_1 - S_2|, |S_1 - S_2 + 1|, \dots, S_1 + S_2 . \quad (\text{Eq. 2.18})$$

The energy levels and differences between neighboring energy levels are

$$E_S = -J[S(S+1) - S_1(S_1+1) - S_2(S_2+1)], \quad (\text{Eq. 2.19})$$

$$E_S - E_{S-1} = 2JS . \quad (\text{Eq. 2.20})$$

The spin Hamiltonian for two electron spins can be written as

$$\begin{aligned} \hat{H} = & -2J\vec{S}_1\vec{S}_2 + \sum_i \vec{S}_i \cdot \hat{d}_i \cdot \vec{S}_i + \sum_i \beta_e \vec{B}_0 \cdot \hat{g}_i \cdot \vec{S}_i + \sum_i \vec{S}_i \cdot \hat{a}_i \cdot \vec{I}_i \\ & - \sum_i g_n \beta_n \vec{B}_0 \cdot \vec{I}_i + \sum_i \vec{I}_i \cdot \hat{P}_i \cdot \vec{I}_i \end{aligned} \quad (\text{Eq. 2.21})$$

Depending on the manifold of S , the coupled representation of the spin Hamiltonian is given by

$$\begin{aligned} \hat{H}_S = & -J[S(S+1) - S_1(S_1+1) - S_2(S_2+1)] + \vec{S} \cdot \hat{D} \cdot \vec{S} + \beta_e \vec{B}_0 \cdot \hat{G} \cdot \vec{S} + \sum_i \vec{S} \cdot \hat{A}_i \cdot \vec{I}_i \\ & - \sum_i g_n \beta_n \vec{B}_0 \cdot \vec{I}_i + \sum_i \vec{I}_i \cdot \hat{P}_i \cdot \vec{I}_i \end{aligned} \quad (\text{Eq. 2.22})$$

It should be noted that \hat{G} , \hat{D} and \hat{A}_i no longer represent onsite values, i.e., intrinsic to a specific spin center, but instead now reflect a property of the coupled system. The uncoupled spin basis is transformed to the coupled basis using Wigner-Eckardt theorem. This allows the effective tensors \hat{G} and \hat{A}_i to be expressed in terms of intrinsic (uncoupled) tensors via spin projection factors ρ_j . The relation between the effective and intrinsic tensors can be analytically solved for the system with two centers and is given below for a total spin of $S = 1/2$. This was first described by Sage et al. (74) in relation to the dimeric iron cofactor of purple acid phosphatase and extended to mixed valence manganese complexes by Zheng et al. (75) and Peloquin et al. (62). The isotropic spin projection factors are given by

$$\rho_1 = \frac{S(S+1) + S_1(S_1+1) - S_2(S_2+1)}{2S(S+1)}, \quad (\text{Eq. 2.23})$$

$$\rho_2 = \frac{S(S+1) - S_1(S_1+1) + S_2(S_2+1)}{2S(S+1)}, \quad (\text{Eq. 2.24})$$

and, assuming g_i and a_i are isotropic, effective \hat{G} and hyperfine \hat{A}_i tensors are

$$G = \rho_1 g_1 + \rho_2 g_2 + \frac{\rho_1 \rho_2}{5J} (g_1 - g_2) [(3\rho_1 + 1)d_1 - (3\rho_2 + 1)d_2], \quad (\text{Eq. 2.25})$$

$$A_1 = \rho_1 a_1 - \frac{a_1}{5J} \rho_1 \rho_2 [(3\rho_1 + 1)d_1 - (3\rho_2 + 1)d_2], \quad (\text{Eq. 2.26})$$

$$A_2 = \rho_2 a_2 + \frac{a_2}{5J} \rho_1 \rho_2 [(3\rho_1 + 1)d_1 - (3\rho_2 + 1)d_2]. \quad (\text{Eq. 2.27})$$

For a $\text{Mn}^{\text{II}}\text{Mn}^{\text{III}}$ dimer, $S_{1(\text{MnII})} = 5/2$ and $S_{2(\text{MnIII})} = 2$ which gives isotropic spin projection values of $\rho_1 = 7/3$ and $\rho_2 = -4/3$ respectively. In the limit where exchange coupling J is large ($J \gg d_i$), the above relations are approximately: $G = \frac{7}{3}g^{\text{II}} - \frac{4}{3}g^{\text{III}}$, $A^{\text{II}} = \frac{7}{3}a^{\text{II}}$ and $A^{\text{III}} = -\frac{4}{3}a^{\text{III}}$ (74).

It is important to note that the expressions above are derived from first order perturbation theory, which breaks down in systems where J is not large. In systems that have a pseudo-well-isolated ground state, it is often more convenient to describe the spin projections ρ_j as a tensor as opposed to a scalar quantity, that is,

the correction to the projected g /hyperfine tensor (second/third terms of eqs. 2.25 – 2.27) is subsumed into the spin projection coefficient itself. This formalism can also be readily generalized to the large spin systems. Here, the Mn ion fine structure terms are included in the spin Hamiltonian that describes the spin manifold (total zero-field splitting) of the complex:

$$\hat{H} = -2J\vec{S}_1\vec{S}_2 + \vec{S}_1 \cdot \hat{d}_1 \cdot \vec{S}_1 + \vec{S}_2 \cdot \hat{d}_2 \cdot \vec{S}_2, \quad (\text{Eq. 2.28})$$

where the ZFS tensors for two centers are traceless and can be represented as

$$\hat{d}_j = \begin{bmatrix} -\frac{1}{3}(d_i - 3e_i) & 0 & 0 \\ 0 & -\frac{1}{3}(d_i + 3e_i) & 0 \\ 0 & 0 & \frac{2}{3}d_i \end{bmatrix}. \quad (\text{Eq. 2.29})$$

The projection of the total spin onto the individual Mn centers is defined as the ratio of the on-site spin expectation value $\langle S_Z^i \rangle$ of the i -th Mn to the ‘total spin’ S or $\langle S_Z \rangle$ (76,77):

$$\rho_i = \frac{\langle S_Z^i \rangle}{\langle S_Z \rangle}. \quad (\text{Eq. 2.30})$$

For the $S = 1/2$ electronic spin manifold, the expectation value of the spin operator $\langle S_Z \rangle$ is $1/2$ and thus (Eq. 2.30) can be rewritten as:

$$\rho_i = 2\langle S_Z^i \rangle.$$

The effective \hat{G} and hyperfine \hat{A}_i tensors are weighted linear sums of the intrinsic tensors of individual Mn ions:

$$\hat{G} = \hat{\rho}_1\hat{g} + \hat{\rho}_2\hat{g}, \quad (\text{Eq. 2.31})$$

$$\hat{A}_i = \hat{\rho}_i\hat{a}_i. \quad (\text{Eq. 2.32})$$

2.1.6. The Spin Hamiltonian of the Mn Cluster of the WOC

Here, an exchange-coupled Mn tetramer is considered. The current assignment for the oxidation states of the four Mn ions when poised in the S_2 state is $\text{Mn}^{\text{III}}\text{Mn}^{\text{IV}}\text{Mn}^{\text{IV}}\text{Mn}^{\text{IV}}$ (37,78,79). This net oxidation state is assumed throughout the text. A basis set that describes the Mn-tetramer spin manifold can be built from the product of the eigenstates of the four interacting spins:

$$|S_1 S_2 S_3 S_4 M_1 M_2 M_3 M_4 I_1 I_2 I_3 I_4 m_1 m_2 m_3 m_4\rangle, \quad (\text{Eq. 2.33})$$

Here S_i refers to the electronic spin state of Mn_i , M_i refers to the electronic magnetic sub-level of Mn_i , I_i refers to the nuclear spin state of Mn_i , and m_i refers to the nuclear magnetic sub-level of Mn_i . S_i takes the value 2 for Mn^{III} and 3/2 for Mn^{IV} ; $M_i = -S_i, -S_i + 1, \dots, S_i$; I_i takes the value 5/2 for ^{55}Mn (100% natural abundance); $m_i = -I_i, -I_i + 1, \dots, I_i$.

The Spin Hamiltonian that describes the spin manifold of the Mn tetramer is:

$$H = \sum_i \beta_e \vec{B}_0 \cdot \hat{g}_i \cdot \vec{S}_i - \sum_i g_n \beta_n \vec{B}_0 \cdot \vec{I}_i + \sum_i \vec{S}_i \cdot \hat{a}_i \cdot \vec{I}_i + \sum_i \vec{I}_i \cdot \hat{p}_i \cdot \vec{I}_i + \sum_i \vec{S}_i \cdot \hat{d}_i \cdot \vec{S}_i - \sum_{i<j} \vec{S}_i \cdot \hat{J}_{ij} \cdot \vec{S}_j \quad (\text{Eq. 2.34})$$

It contains: i) an electronic Zeeman term for each Mn (g_i) ion ; ii) a nuclear Zeeman term for each ^{55}Mn (g_n); iii) an electron-nuclear hyperfine term for each ^{55}Mn (a_i); iv) a nuclear quadrupole term for each ^{55}Mn (p_i); v) a fine structure term for each Mn (d_i) ion and vi) pair-wise exchange terms for each Mn-Mn (J_{ij}) interaction.

The tetra-nuclear manganese cluster of the WOC ($\text{Mn}_4\text{O}_5\text{Ca}$), already presents a daunting theoretical exercise. A basis set that describes the entire spin manifold of the coupled four Mn ions requires 414720 vectors, too many to be readily handled by current numerical techniques. The problem can be greatly simplified by assuming all Mn-Mn couplings are large, i.e. within the strong exchange limit. In this case, the exchange interactions between the Mn ions have to be significantly larger than any other term of the spin Hamiltonian. The resultant electronic spin states of the manifold are then adequately described by a single quantum number, the total spin S_T . The ‘multiline’ EPR signal observed for the S_2 state of the WOC is

derived from only one total spin state, the ground state of the spin manifold with total spin $S_T = 1/2$. The basis set that describes this subspace requires only 2592 vectors which represent the coupling of the effective electronic spin $S_T = 1/2$ to the nuclear spin of each ^{55}Mn ($I = 5/2$) nucleus.

The wavefunctions of this basis are given by

$$\left| \frac{1}{2} \quad M \quad m_1 \quad m_2 \quad m_3 \quad m_4 \right\rangle, \quad (\text{Eq. 2.35})$$

where $M = \pm \frac{1}{2}$ and $m_i = -\frac{5}{2}, -\frac{3}{2}, \dots, \frac{5}{2}$.

The effective spin Hamiltonian that describes the ground state of the spin manifold ($S_T = 1/2$) is:

$$H = \beta_e \vec{B}_0 \cdot \hat{G} \cdot \vec{S} + \sum_i \left(g_n \beta_n \vec{B}_0 \cdot \vec{I}_i + \vec{S} \cdot \hat{A}_i \cdot \vec{I}_i \right). \quad (\text{Eq. 2.36})$$

It contains: i) the Zeeman term for the total electronic spin; ii) Zeeman terms for each ^{55}Mn nucleus; iii) hyperfine terms for each ^{55}Mn nucleus. Quadrupole terms are neglected for the ^{55}Mn nuclei since they are considered to only have a small contribution to the energy levels (eigenstates) of the system.

2.1.7. The Spin Hamiltonian of the ^{17}O -Mn Cluster of the WOC

To study water binding modes and sites we need to address a more general case, when a single ^{17}O nucleus is magnetically interacting with an exchange coupled Mn tetramer. Similar to as described before, the uncoupled extended basis set can be written as:

$$\left| S_1 S_2 S_3 S_4 M_1 M_2 M_3 M_4 I_1 I_2 I_3 I_4 m_1 m_2 m_3 m_4 L k \right\rangle \quad (\text{Eq. 2.37})$$

Here S_i refers to the electronic spin state of Mn_i , M_i refers to the electronic magnetic sub-level of Mn_i , I_i refers to the nuclear spin state of Mn_i , and m_i refers to the nuclear magnetic sub-level of Mn_i . S_i takes the value 2 for Mn^{III} and $3/2$ for Mn^{IV} ; $M_i = -S_i, -S_i + 1, \dots, S_i$; I_i takes the value $5/2$ for ^{55}Mn (100% natural abundance); $m_i = -I_i, -I_i + 1, \dots, I_i$; $L = 5/2$ for ^{17}O (0.038% natural abundance); and $k = -L, -L + 1, \dots, L$.

The Spin Hamiltonian that describes the spin manifold of the ^{17}O -Mn cluster is:

$$H = \sum_i \beta_e \vec{B}_0 \cdot \hat{g}_i \cdot \vec{S}_i - \sum_i g_n \beta_n \vec{B}_0 \cdot \vec{I}_i + \sum_i \vec{S}_i \cdot \hat{a}_i \cdot \vec{I}_i + \sum_i \vec{I}_i \cdot \hat{p}_i \cdot \vec{I}_i + \sum_i \vec{S}_i \cdot \hat{d}_i \cdot \vec{S}_i - \sum_{i < j} \vec{S}_i \cdot \hat{J}_{ij} \cdot \vec{S}_j + g_o \beta_n \vec{B}_0 \cdot \vec{L} + \sum_i \vec{S}_i \cdot \hat{c}_i \cdot \vec{L} + \vec{L} \cdot \hat{f} \cdot \vec{L} \quad (\text{Eq. 2.38})$$

It contains: i) an electronic Zeeman term for each Mn (g_i) ion ; ii) a nuclear Zeeman term for each ^{55}Mn (g_n) and ^{17}O (g_o) nucleus; iii) an electron-nuclear hyperfine term for each ^{55}Mn (a_i) and ^{17}O (c_i) nucleus; iv) an nuclear quadrupole term for each ^{55}Mn (p_i) and ^{17}O (f) nucleus; v) a fine structure term for each Mn (d_i) ion and vi) pair-wise exchange terms for each Mn-Mn (J_{ij}) interaction.

Again, we can simplify the task using the strong exchange limit for the Mn ions. The basis set that describes the ground state of the spin manifold with total spin $S_T = 1/2$ requires only 15552 vectors, which represent the coupling of the effective electronic spin $S_T = 1/2$ to the nuclear spin of each ^{55}Mn ($I = 5/2$) and ^{17}O ($I = 5/2$) nucleus.

The wavefunctions of this basis are given by

$$\left| \frac{1}{2} \ M \ m_1 \ m_2 \ m_3 \ m_4 \ L \ k \right\rangle, \quad (\text{Eq. 2.39})$$

where $M = \pm \frac{1}{2}$; $m_i = -\frac{5}{2}, -\frac{3}{2}, \dots, \frac{5}{2}$ and $k = -\frac{5}{2}, -\frac{3}{2}, \dots, \frac{5}{2}$.

The effective spin Hamiltonian that describes the ground state of the spin manifold ($S_T = 1/2$) is:

$$H = \beta_e \vec{B}_0 \cdot \hat{G} \cdot \vec{S} + \sum_i \left(g_n \beta_n \vec{B}_0 \cdot \vec{I}_i + \vec{S} \cdot \hat{A}_i \cdot \vec{I}_i \right) + g_o \beta_n \vec{B}_0 \cdot \vec{L} + \vec{S} \cdot \hat{C} \cdot \vec{L} + \vec{L} \cdot \hat{F} \cdot \vec{L} \quad (\text{Eq. 2.40})$$

It contains: i) the Zeeman term for the total electronic spin; ii) Zeeman terms for each ^{55}Mn nucleus and the ^{17}O nucleus; iii) hyperfine terms for each ^{55}Mn nucleus and the ^{17}O nucleus and iv) a quadrupole term for the ^{17}O nucleus. Quadrupole terms are neglected for the ^{55}Mn nuclei since they are considered to only have a small contribution to the energy levels (eigenstates) of the system.

2.1.8. ^{17}O ENDOR spectra simulations

The simulation of ^{17}O EPR/ENDOR spectra of the WOC can be further simplified. Because the ^{17}O couplings are small, they do not contribute significantly to the inhomogeneous linewidth of the S_2 EPR spectrum. Thus, for simulation of the EPR spectrum, the terms in Eq. 2.40 relating to the ^{17}O nucleus can be excluded as given below:

$$H_{EPR} = \beta_e \vec{B}_0 \cdot \hat{G} \cdot \vec{S} + \sum_i \left(g_n \beta_n \vec{B}_0 \cdot \vec{I}_i + \vec{S} \cdot \hat{A}_i \cdot \vec{I}_i \right) \quad (\text{Eq. 2.41})$$

Similarly, a simplified effective Spin Hamiltonian can be used for the simulation of ENDOR spectra associated with the ^{17}O nucleus. As the ^{17}O nucleus does not significantly couple to the four ^{55}Mn nuclei, the terms in Eq. 2.40 associated with the ^{55}Mn nuclei can be excluded:

$$H_{ENDOR} = \beta_e \vec{B}_0 \cdot \hat{G} \cdot \vec{S} + g_o \beta_o \vec{B}_0 \cdot \vec{L} + \vec{S} \cdot \hat{C} \cdot \vec{L} + \vec{L} \cdot \hat{F} \cdot \vec{L} \quad (\text{Eq. 2.42})$$

In practice, however, the above Spin Hamiltonian (Eq. 2.42) is only valid when the ^{17}O ENDOR spectrum is collected at the center field of the S_2 multiline spectrum, for this position, all powder-pattern orientations are sampled uniformly. ^{17}O ENDOR spectra that are collected on the high and low field edges of the multiline spectrum must also take into account the sampling of the powder-pattern orientations.

2.2. EPR spectroscopy techniques and spectral analysis

Electron and nuclear spin transitions can be induced in spin system within an external magnetic field by application of a second electromagnetic field at the condition of resonance, i.e. when the frequency of the field is close to the corresponding transition frequency. For a spin system with $S = 1/2$, the electron Zeeman term is dominant at commonly used in EPR magnetic fields, and energy levels are split into two levels. Then the resonance condition is described by:

$$h\nu = \Delta E = g_e \beta_e B_0. \quad (\text{Eq. 2.43})$$

To induce these spin transitions, linearly polarized monochromatic microwave (mw) or radio frequency (rf) fields are used in EPR spectroscopy. Detection of an electronic transition essentially amounts to searching for the resonance condition. This search can be performed in two ways: i) the frequency of the

incident mw frequency can be scanned while the external (static) magnetic field is kept fixed or ii) the external magnetic field is scanned while the incident mw frequency is kept fixed. Due to technical reasons, latter option is typically used. There are different fixed mw bands used in EPR. Historically, the most widely used EPR wavebands are X-, Q- and, since end of 1970s, W-bands, with working frequencies of 9.5, 34 and 95 GHz, respectively. The most frequently used EPR techniques and their application to particular systems of interest are described below.

2.2.1. Continuous-Wave (cw) EPR

Observation of a cw EPR signal is based on detection of the energy absorbed by the system at a resonant frequency. The absorption of energy by the spin ensemble is possible since there is a difference in population of upper and lower energy levels. The populations of energy levels are described by the Maxwell-Boltzmann distribution, and the ratio of populations can be written as

$$\frac{n_{+1/2}}{n_{-1/2}} = \exp\left(-\frac{\Delta E}{kT}\right), \quad (\text{Eq. 2.44})$$

where k is the Boltzmann constant and T the temperature in kelvin. For example, this ratio is ~ 0.998 at X-band resonance frequency (9.5 GHz) and at temperature 300 K. Small difference in populations leads to a sensitivity problem. Therefore, magnetic field modulation is used to record cw EPR spectra, and thus cw EPR spectra are usually represented as the first derivative.

The sensitivity of EPR technique is defined as the minimum number of detectable spins, which is dependent on microwave power P , resonance frequency ν , sample volume V and the unloaded quality factor of resonator Q in the following way

$$N_{\min} \propto VQ^{-1}\nu^{-2}P^{-1/2}. \quad (\text{Eq. 2.45})$$

Thus, high microwave power is preferable for higher sensitivity; however, this may saturate the spin ensemble. At low power, the EPR signal should increase proportionally to the square root of mw power. Saturation occurs at higher power, where the signal intensity grows most slowly and may actually diminish due to local heating of the measured sample. Increased temperatures prevent saturation problems, since

relaxation processes slow down at low temperatures. At lower temperatures, though, the population difference between the spin levels is enhanced, increasing signal intensity. The two effects have to be balanced to achieve the best performance.

For the spin system $S = 1/2$, $I = 1/2$, with a positive isotropic hyperfine coupling constant, and assuming that external magnetic field is directed along z axis and linearly polarized magnetic field – along x axis, the non-perturbed spin Hamiltonian can be written as

$$H_0 = \beta_e B_0 g S_z + a S_z I_z - g_n \beta_n B_0 I_z. \quad (\text{Eq. 2.46})$$

The corresponding energy level diagram is shown in Fig. 2.1 (panel A). Here the following interactions are shown: the electron Zeeman splitting, the hyperfine splitting, and the nuclear Zeeman interaction. There are six possible transitions in this scheme that can be induced by an oscillating electromagnetic field.

The interaction of a given spin system with oscillating electromagnetic field B_1 can be described by the following spin Hamiltonian.

$$H_1 = 2B_1 \cos(\omega_{m.w.} t) (g\beta_e S_x - g_n \beta_n I_x). \quad (\text{Eq. 2.47})$$

Its matrix elements partitioned against the eigenstates of the system gives transitions amplitudes:

$$V_{if} = \left| \langle \psi_i | \hat{H}_1 | \psi_f \rangle \right|^2, \quad (\text{Eq. 2.48})$$

where ψ_i, ψ_f represent initial and final wavefunctions of the eigenstates and can be defined for a given system by two spin quantum numbers of electron ($m_s = \alpha, \beta$) and nucleus ($m_I = \alpha_n, \beta_n$).

For the first term, there are only two non-zero matrix elements, which represent transitions without changing the projection of nuclear spin, i.e. $\alpha\alpha_n \leftrightarrow \beta\alpha_n$ and $\alpha\beta_n \leftrightarrow \beta\beta_n$ transitions (solid line arrows in panel A, Fig. 2.1.). Only transitions of this type ($\alpha \leftrightarrow \beta$) are relevant for EPR detection, since an applied mw frequency cannot flip the nuclear spin (this process requires an additional oscillating rf field). Thus the second term in Eq. 2.45 is irrelevant for the EPR transitions, since matrix elements for those transitions are equal zero. In total, there are two EPR transitions with frequencies $\nu_{1,2} = g_e \beta_e B_0 / h \pm a/2$ that appear in the cw EPR spectrum shown in Fig. 2.1 (Panel B).

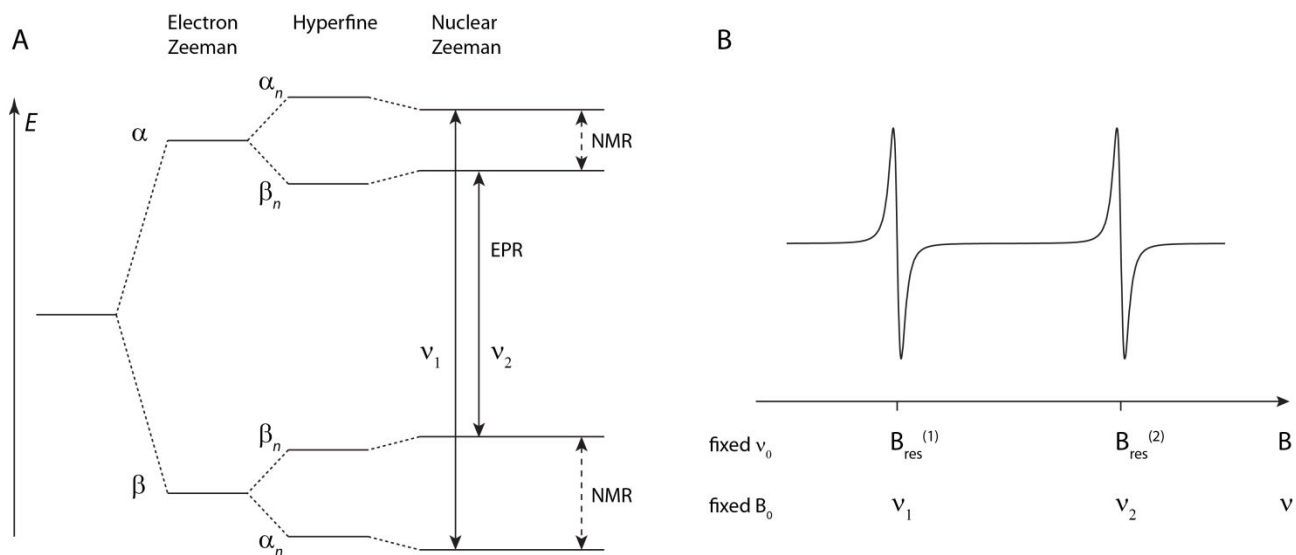


Figure 2.1 (A) The energy level scheme for the $S = 1/2$, $I = 1/2$ spin system with isotropic g and $a > 0$; (B) Corresponding cw EPR spectrum in different representation form.

Transitions of type $\alpha_n \leftrightarrow \beta_n$ can be detected by applying special techniques such as Electron Nuclear Double Resonance (ENDOR), where an additional rf source is used to induce NMR transitions.

2.2.2. Continuous-Wave ENDOR

The cw ENDOR is a double resonance technique that was developed by Feher for his studies of phosphorus-doped silicon (80). NMR transitions are detected by monitoring the intensity of the EPR transition.

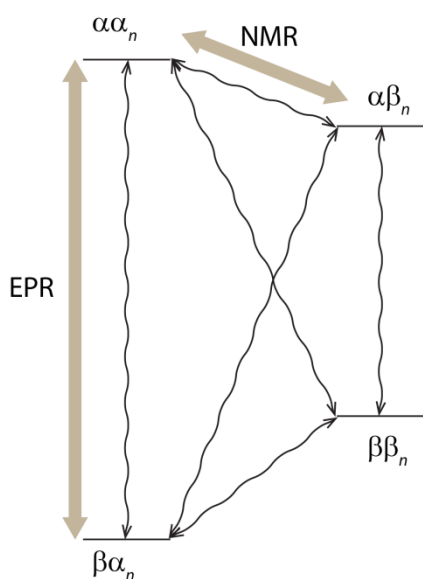


Figure 2.2 The scheme of induced transitions and possible relaxation pathways in the cw ENDOR experiment for the $S = 1/2$, $I = 1/2$ spin system with isotropic g and $a > 0$.

The first step in performing a cw ENDOR experiment is to record an EPR spectrum to determine the resonance magnetic fields. Then, the chosen resonance magnetic field is fixed, and the corresponding EPR transition is saturated with a high power mw field. Finally, the rf frequency is swept while monitoring the EPR absorption signal. If the swept rf induces a nuclear transition, connected to the pumped EPR transition, desaturation of the EPR transition takes place. Analogous to cw EPR, modulation of the rf is used to increase sensitivity of the cw ENDOR technique, and as such, the spectrum typically is presented with a derivative line shape.

Double resonance experiments such as cw ENDOR require more effort than common EPR or NMR experiments, but they combine the high sensitivity of EPR with the high resolution of NMR techniques and can provide information about a molecular system not accessible with a single technique.

2.2.3. Pulse EPR techniques

In contrast to cw methods, where mw or rf radiation is continuously applied, in pulse EPR techniques transitions are induced by pulses of a certain frequency. The quantum mechanical explanation of the effect is rather complex and discussed in many fundamental works, e.g. (68). Here, the formation of the signal in pulsed experiments is discussed using the vector model, which describes the evolution of the magnetization

vector in time. The scheme of the electron spin echo (ESE) signal formation is presented in Fig. 2.3. This was first developed by Hahn (81) for detection of NMR signals using rf pulses.

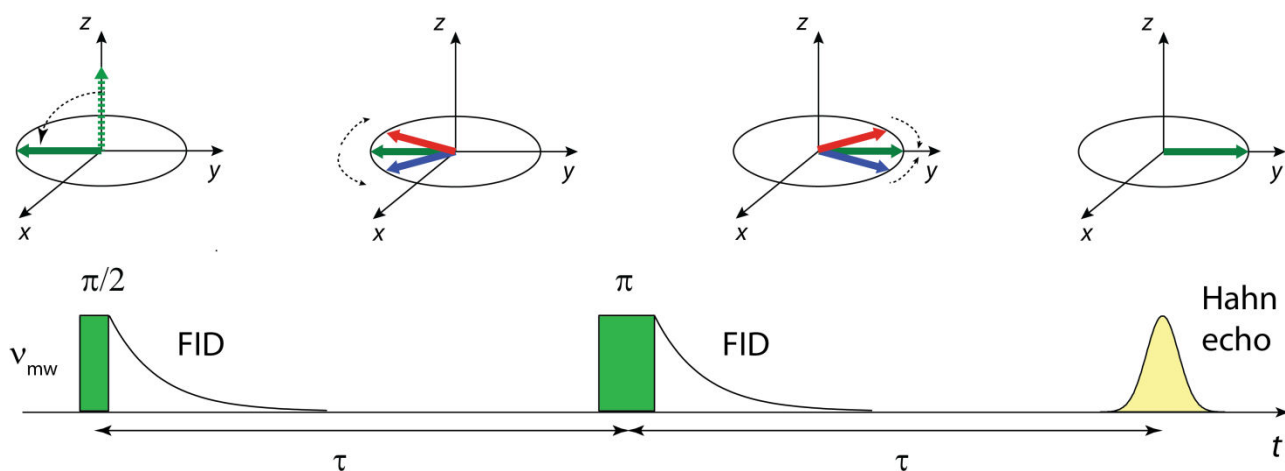


Figure 2.3 The vector model of Hahn echo signal formation.

In a system where the external (static) magnetic field is applied along z -axis, all spins precess around the z -axis, and therefore the net magnetization can be considered to be aligned along z -axis. A pulse of resonance frequency applied along the x -axis leads to a rotation of the total magnetization vector around the x -axis. The length of the pulse is chosen such that magnetization vector is turned by 90° ($\pi/2$ pulse). Immediately after the pulse, the net magnetization of the system is aligned along y -axis, and spins start to precess in the xy plane. Detection of magnetization occurs in the y direction via one of two possible techniques. The decay of magnetization in the xy plane can be monitored immediately after the $\pi/2$ pulse, which results in the so-called free induction decay (FID) signal. Alternatively, a second pulse can be used to refocus the magnetization at a later time (τ). This second 180° (π pulse) is also along the x -axis, which reverses the precession of spins. At twice the time difference between the two pulses ($t = 2\tau$), the spins refocus, and the electron spin echo (ESE) signal is observed. The dephasing of the magnetization in the xy plane derives from inhomogeneity of local fields or spin-spin interactions, which engender slightly different Larmor frequencies for the ensemble of spin packets. The decay of magnetization due to spin-spin interaction is irreversible and cannot be restored by the second pulse. This is called spin-spin relaxation and is associated with the time constant T_2 , or phase memory time. The ESE amplitude decays exponentially with correlation time T_2 .

2.2.3.a. Field-swept Echo-detected EPR

Field-swept echo detected EPR is one of the simplest pulse EPR techniques, where the $\pi/2$ - τ - π pulse sequence is used to generate a spin echo signal which is integrated while magnetic field is swept. This pulse experiment has some advantages over conventional cw EPR, such as the absence of mw irradiation during signal detection, and that the measured EPR response is proportional to the magnetization vector amplitude at the moment of mw excitation. Thus, the noise level is defined by only spectrometer limits, without additional noise from the mw source, and spectral analysis is simplified due to the absence of mw excitation in the detected signal. In particular, cw EPR is insensitive to very broad spectra due to the field modulation when collecting data. Echo detected EPR does not suffer from this problem. However, echo detected EPR does suffer from some serious limitations, including time resolution and sensitivity. The time resolution is limited by two factors: the length of the pulse sequence and the deadtime of the spectrometer. Deadtime is defined as the time between switching off the mw power and when the ringing intensity in the cavity decreases to the same order of magnitude as the echo intensity, which is when it becomes possible to measure the response signal.

2.2.3.b. Electron Spin Echo Envelope Modulation (ESEEM)

A very important class of ESE experiments is the Electron Spin Echo Envelope Modulation (ESEEM) experiment (82). The simplest experiment is the two-pulse ESEEM technique with the Hahn echo pulse sequence, where the echo intensity is monitored while sweeping τ (Fig. 2.4). The interaction of electron spins with nearby nuclei causes a modulation in the decay of the electron spin echo. In order to obtain the hyperfine coupling constants of those nuclei, the decay of the spin echo is subtracted, and a Fourier transformation is applied to the oscillations. This Fourier transform of the time domain spectrum yields a frequency domain spectrum that contain information about all of the nuclei that are coupled to the electron, such as hyperfine interactions, nuclear quadrupolar interactions for $I \geq 1$, as well as a measure of unpaired electron spin density on a given nucleus or the distance between the coupled nucleus and the electron.

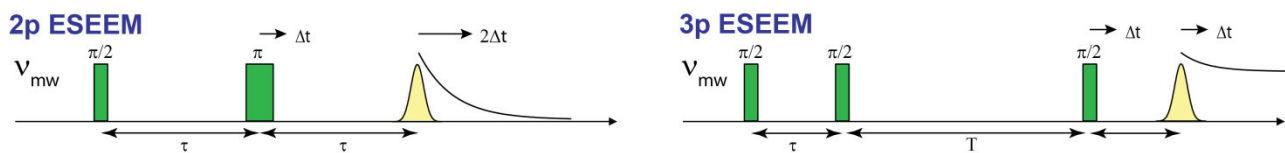


Figure 2.4 Pulse sequences of two-pulse and three-pulse ESEEM techniques.

The linewidth in two-pulse ESEEM is related to the phase memory time of the electron spins and is twice as large as the homogeneous EPR linewidth. The natural linewidths of nuclear transition spectra are related to the phase memory time of nuclear spins, which is usually much longer than that of the electron spins, and hence the nuclear linewidth can be much smaller. As a consequence, the resolution of the 2p ESEEM spectra may be lower than ENDOR spectra. To avoid this limitation, the three-pulse ESEEM method is used with a pulse sequence based on detection of a stimulated echo (Fig. 2.4).

The three-pulse ESEEM is the one of the most commonly used techniques, where the echo modulation is recorded as the time delay T between second and third pulses is incremented. As a result, the echo intensity decays with the time constant of the phase memory time of nuclear spins, allowing echo detection for systems with short spin-spin relaxation times (T_2). The advantage of this technique over the two pulse method is increased spectral resolution, since the linewidths are determined by the phase memory time of the nuclear spins, which is usually of the same order of magnitude as the longitudinal relaxation time T_1 of the electron spins. However, due to the nature of the experiment, 3p ESEEM suffers from blind spots at nuclear frequencies with a period of $1/\tau$. Because of this, 3p ESEEM experiments are typically conducted at several values of τ to identify and minimize artifacts from blind spots. However, this effect can also be used advantageously to suppress effects from unnecessary background signals such as large matrix proton peaks coming from water.

2.2.3.c. *Davies and Mims ENDOR*

Davies and Mims ENDOR are additional commonly-used pulse techniques, first described by Davies (83) and Mims (84). Both techniques rely on transfer of spin polarization. Pulsed techniques have several

advantages over continuous wave ENDOR. Though cw ENDOR is a more sensitive technique in comparison with pulsed ENDOR, pulsed ENDOR allows the observation of weakly coupled nuclei.

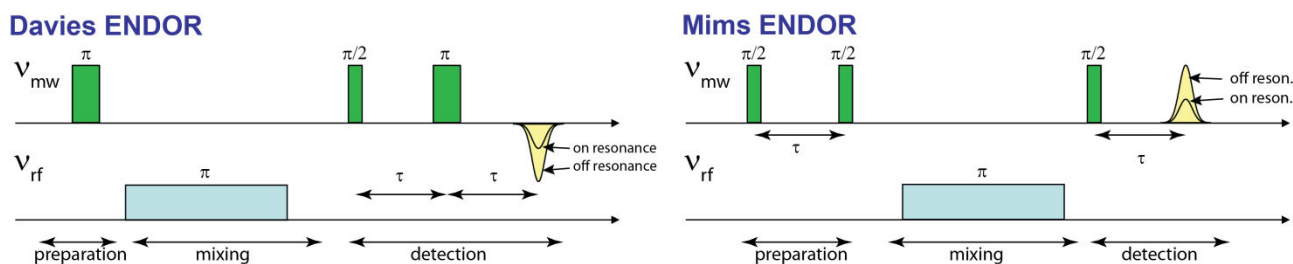


Figure 2.5 Pulse sequences of Davies and Mims ENDOR techniques.

The corresponding sequences are shown in Fig. 2.5. In the Davies ENDOR sequence, the first selective mw π -pulse inverts the spin population of a single EPR transition (preparation period). This essentially creates a hole in the EPR spectrum. The width and depth of this “burned” hole depend on the length of the applied pulse, with long pulse producing narrow holes and vice versa. Then, during the mixing period, a selective rf pulse is applied to induce NMR transitions. When the swept rf is in resonance with an NMR transition, magnetization is transferred to the other spin manifold, otherwise no mixing occurs to fill in the hole created by the inversion pulse. During the detection period, the z -component of the magnetization is measured using a two pulse echo sequence. In short, the EPR signal that is restored during the mixing period is observed. This technique is most suited to nuclei with large hyperfine coupling values.

The Mims ENDOR technique is based on a stimulated echo sequence. It consists of a preparation pulse sequence of two $\pi/2$ pulses to invert the electron spin population, and a final $\pi/2$ pulse after the mixing period to stimulate the ESE for signal detection. During the mixing period, an rf π pulse is used to invert the nuclear spin population, resulting in polarization transfer between the nuclear and electronic transitions. This results in changing the intensity of the EPR transition when the rf frequency is in resonance with specific NMR transitions. The echo intensity is subsequently measured as a function of the radio frequency to give the characteristic ENDOR spectrum shown in Fig. 2.6.

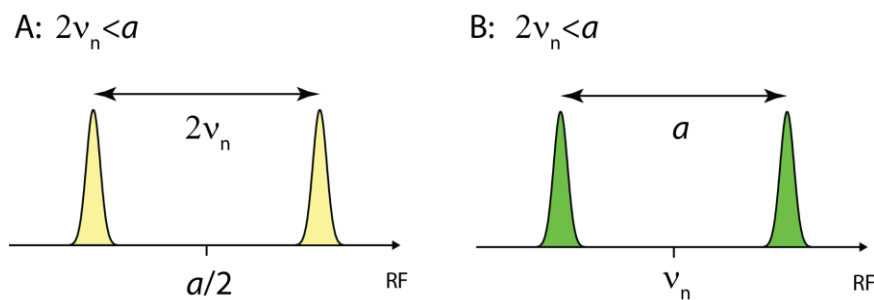


Figure 2.6 The ENDOR spectra of the spin system $S = 1/2$, $I = 1/2$ with isotropic g at different conditions. A) low field limit; B) high field limit.

Here the resonance frequencies are given by:

$$\nu_{ENDOR} = \left| \nu_n \pm \frac{a}{2} \right| \quad (\text{Eq. 2.49})$$

In the low field limit, the nuclear Larmor frequency is less than half of the hyperfine coupling, and resonance lines are split by $2\nu_n$ around a frequency equal to $a/2$. The opposite situation occurs in the high field limit $2\nu_n > a$, where the ENDOR lines are split around the nuclear Larmor frequency by the hyperfine coupling a (see Fig. 2.6).

2.2.3.d. High field ELDOR-detected NMR as an alternative to ENDOR spectroscopy

Electron-electron Double Resonance (ELDOR) detected NMR (EDNMR) (85) is an example of a polarization transfer experiment and as such is similar to Davies ENDOR. In the EDNMR experiment, nuclear transitions of the spin manifold are probed indirectly using a second microwave pulse, which pumps spin forbidden electronic transitions (gray solid arrows in Fig. 2.7A) i.e. transitions where both the electron and nuclear spin states change. The pump pulse is swept around the resonance frequency ($\nu_{mw}^{(0)}$). At microwave frequencies where the pump pulse coincides with the forbidden electron transitions of the spin manifold ($\nu_i = \nu_{ELD}^{(i)} - \nu_{mw}^{(0)}$), the observed echo signal decreases, leading to apparent side-holes, which correspond to the nuclear transitions of the spin manifold. In addition, the pump pulse excites the allowed transitions of the spin manifold. These results in a decrease in the observed primary echo across the entire

region swept. This response profile is Lorentzian, and centered at the resonance frequency ($\nu_{\text{mw}}^{(0)}$). This profile is termed here the central hole. Side holes appear symmetrically about the resonance frequency ($\nu_{\text{mw}}^{(0)}$), for an inhomogeneously broadened EPR line i.e. where the EPR linewidth is larger than that of the nuclear coupling of interest.

EDNMR has been used for the detection of strongly coupled nuclei at low microwave frequencies (X, Q band). At high field (W-band) though, the Larmor frequency of many more low γ nuclei (^{14}N , ^{17}O) is now sufficiently large that signals from these nuclei can be resolved from the central hole even for the circumstance where the coupling of the nuclei to the electronic spin is weak (i.e. less than twice the Larmor frequency). The W-band EDNMR of a complex containing both ^{14}N and ^{17}O ligands in the weak coupling limit is shown diagrammatically in Figure 2.7. The lines associated with a particular nucleus are centered at the Larmor frequency of the nucleus of interest, split by the hyperfine (and quadrupole) coupling. Importantly, at high field, the Larmor frequency of ^{17}O [$\nu(^{17}\text{O})=19.63$ MHz at $B_0=3.4$ T] is significantly different from that of ^{14}N [$\nu(^{14}\text{N})=10.46$ MHz at $B_0=3.4$ T], thus allowing both components to be readily identified.

For nuclei with $I > 1/2$, multiple quantum transitions are observed. These are centered about scalar multiples of the Larmor frequency split by the same scalar multiple, i.e. in double quantum transitions are centered about twice the Larmor frequency split by twice the hyperfine coupling. It is important to note that high field (W-band) detection of ^{17}O signals arising from oxygen ligands of metallocofactors is the preferred as compared to X- or Q-band frequencies. In previous literature studies, hyperfine couplings of the order of ~ 10 MHz have been observed for ^{17}O ligands. At both X- and Q-band frequencies, couplings of this magnitude result in one of the branches of the signal envelope appearing at ~ 0 MHz, which is generally strongly suppressed or technically difficult to measure, thus only half of the signal envelope is resolved. In contrast, at W-band, both branches are shifted at least 10 MHz from the origin, allowing resolution of the whole signal envelope.

EDNMR has several advantages over ENDOR and ESEEM for the detection of ^{17}O ligands to metallocomplexes. For metallocomplexes, EDNMR is often more sensitive than Davies ENDOR, especially for systems for which the T_1 relaxation is short, since the detection sequence can be placed directly after the

pump pulse. EDNMR also allows the simultaneous detection of multiple overlapping nuclei (i.e. ^{14}N , ^{17}O). In the corresponding Davies ENDOR experiment, the two nuclei of interest may have very different optimal π_{RF} pulses leading to suppression of one species relative to the other. Similarly, ESEEM and Mims ENDOR are both limited by T_1 relaxation and thus large, highly anisotropic coupling can be often lost or distorted due to the deadtime of the spectrometer. Because the profile of the EDNMR spectrum is not dependent on T_1 time, EDNMR does not suffer from this disadvantage.

2.2.3.e. Two dimensional EDNMR

Further information on the spin system can be obtained using 2D EDNMR. In the 2D experiment, an EDNMR spectrum is taken at a series of magnetic field positions across the EPR spectrum. Pictorial 2D EDNMR surfaces representing two limiting cases are shown in Figures 2.7D. As stated previously, the peak positions of the side-holes associated with a particular nucleus are centered at the Larmor frequency of the nucleus of interest, split by the hyperfine (and quadrupole) coupling. As the Larmor frequency is linearly field dependent, the mean peak position linearly increases with respect to the central hole ($\nu_{\text{mw}}^{(0)}$) as the magnetic field increases. As a consequence, not only the position but also the rate of change of the peak shift is characteristic of a particular nucleus. It is noted that double quantum transitions must have twice the field dependence of the corresponding single quantum transitions.

In Figure 2.7, the hyperfine coupling of all detected nuclei (^{14}N , ^{17}O) is significantly anisotropic. In this circumstance, the splitting of the two peaks is also dependent on the magnetic field because the sampling of the powder pattern orientation is field dependent. Therefore, non-linear dependence of peak positions are observed. However, the average peak position still linearly increases with respect to the central hole ($\nu_{\text{mw}}^{(0)}$) as the magnetic field increases, and as such can be used as a marker for the nucleus identity.

The 2D EDNMR spectrum should nominally reproduce the corresponding 2D Davies ENDOR spectrum, accounting for artifacts systematic to this technique. This requires two conditions: (i) the nucleus of interest does not contribute to the inhomogeneous linewidth of the EPR spectrum, and (ii) the signal envelope is relatively narrow such that the side-holes are placed on the “wings” of the Lorentzian signal envelope. It is

noted though that the relative intensities of multiple quantum transitions to a single quantum transition differ between the ENDOR and EDNMR experiments.

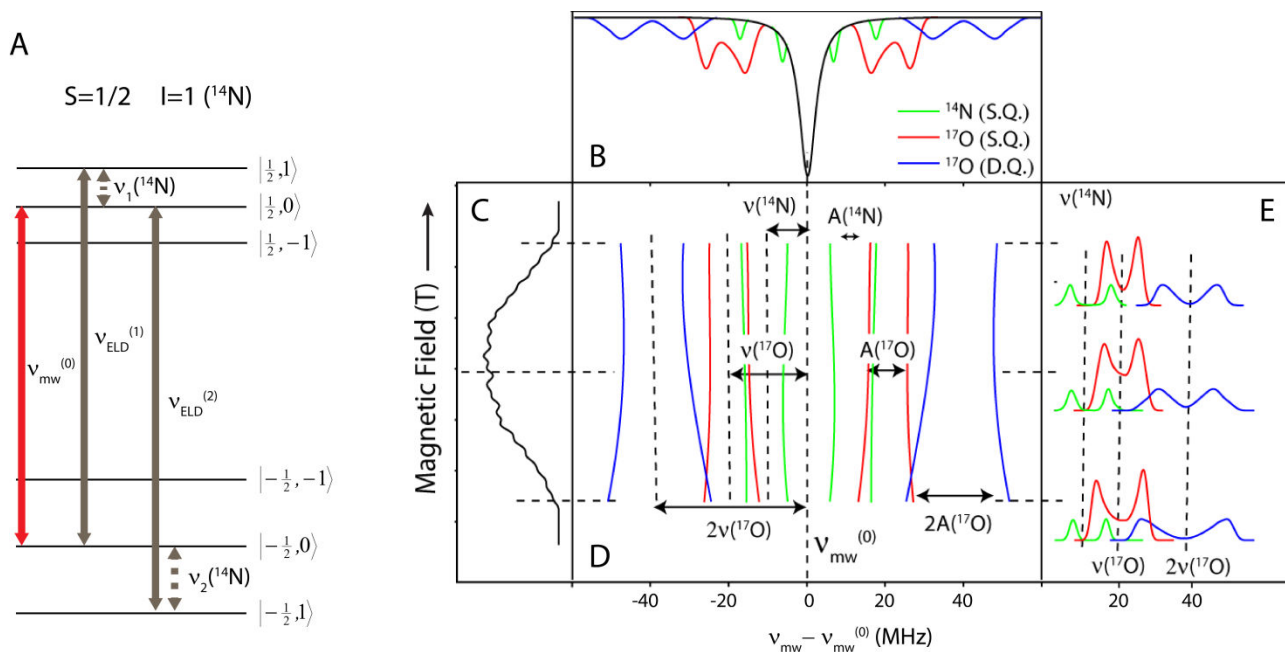


Figure 2.7 High field ELDOR detected NMR (EDNMR) of a mixed valence Mn dimer complex ($S = 1/2$) containing weakly anisotropically coupled low γ nuclei (^{17}O , ^{14}N). **(A)** Energy level diagram and EPR/EDNMR transitions for the $S = 1/2$, $I = 1$ (^{14}N) system. **(B)** The EDNMR spectrum measured at the center of the multiline spectrum. **(C)** The EPR multiline spectrum of the complex. **(D)** The 2D EDNMR representation of B. Here a series of EDNMR spectra have been collected across the EPR spectrum (i.e. C) of the complex. The lines represent the peak positions of the side-holes observed in B. The field dependence of the side-holes for each nuclei are non-linear, however the mean peak position does shift linearly away from the central hole ($\nu_{\text{mw}}^{(0)}$) with increasing magnetic field. **(E)** The baseline corrected EDNMR spectrum at three selected field positions within C: the centre field and the low and high field edge. Only half of the EDNMR spectrum is shown and inverted for clarity of presentation.

3. *SUMMARY*

This chapter has an overview of the academic work produced during my PhD project. This work includes five journal articles, three of which are already published, one is submitted, and the remaining is still in preparation. My contribution to each study is described below:

3.1 The effect of Ca²⁺/Sr²⁺ substitution on the oxygen evolving complex of PSII

- I collected most of the EPR experimental data;
- I performed most of the data simulations and modeling
- I was involved in the production of the manuscript

A. Boussac provided all biological samples. D. Pantazis performed all the DFT calculations.

3.2 The electronic structures of the oxygen evolving complexes in plants and cyanobacteria

- I was involved in the collection of the EPR experimental data;
- I performed part of the data simulations and modeling

A. Boussac provided the biological samples.

3.3 Electronic structure of a weakly antiferromagnetically coupled Mn^{II}Mn^{III} model complex

- I performed part of the data simulations and modeling

T. Wehyermueller provided the chemical samples. W. Ames performed all DFT calculations.

3.4 Detection of water binding sites in the oxygen-evolving complex of photosystem II (major work of my thesis)

- I performed all the EPR measurements
- I performed most of the data simulations and modeling
- I was involved in the production of the manuscript

T. Wehyermueller provided the chemical samples. A. Boussac/M. Nowaczyk provided the biological samples. W. Ames performed all the DFT calculations.

3.5 Characterization of μ -oxo bridge of Mn model complexes using high field EPR spectroscopy

(second major work of my thesis)

- I performed all the EPR measurements
- I performed most of the data simulations and modeling
- I was involved in the production of the manuscript

T. Wehyermueller provided the chemical samples. W. Ames performed all the DFT calculations.

3.1. The effect of Ca²⁺/Sr²⁺ substitution on the electronic structure of the oxygen-evolving complex of photosystem II: A combined pulse ⁵⁵Mn-ENDOR, multi-frequency EPR and DFT study of the S₂ state

Published in the Journal of the American Chemical Society, 2011 Vol. 133 (10), pp 3635–3648.

Under normal conditions, photosynthetic organisms typically take up Ca²⁺ ions when assembling the WOC (see section 1.2). However, in cyanobacterial cultures (*T. elongatus*) grown in a medium devoid of Ca²⁺ salts, but enriched in Sr²⁺ salts, a Sr²⁺ ion can be used instead (86). No other metals can be naturally used by living organisms for driving water-splitting chemistry. The modified, Sr²⁺-containing WOC (Mn₄O₅Sr), shows a slower rate of molecular oxygen formation, as the S₃→S₄→S₀ transition time is significantly longer. In contrast, the yield of oxygen evolution remains the same as for Mn₄O₅Ca cluster. We investigated the change in the electronic structure induced by the replacement of Ca with Sr using multi-frequency EPR spectroscopy. EPR spectra of the Mn₄O₅Sr cluster poised in the S₂ state exhibited the characteristic differences in the hyperfine pattern of the multiline EPR signal seen in earlier literature (see Fig. 3.1A and B). In contrast, the manganese (⁵⁵Mn) ENDOR spectra of the Ca and Sr forms of the WOC were very similar (Fig. 3.1 C). Simultaneous simulation of all multi-frequency EPR/ENDOR data allowed a unique solution for magnetic parameters to be determined. We found that the change in these parameters upon Ca/Sr substitution is relatively small. Density Functional Theory calculations supported simulated experimental values.

In addition, these results allowed a further analysis of the geometric structure of the WOC, particularly the site and ligand environment of the unique Mn_D (Mn^{III}) of the S₂-state. This Mn^{III} is a potential site for substrate ‘water’ (H₂O, OH⁻) binding (see section 1.3, Figure 1.7C). Its location within the cuboidal structural unit, as opposed to the external ‘dangler’ position, may have important consequences for the mechanism of O–O bond formation.

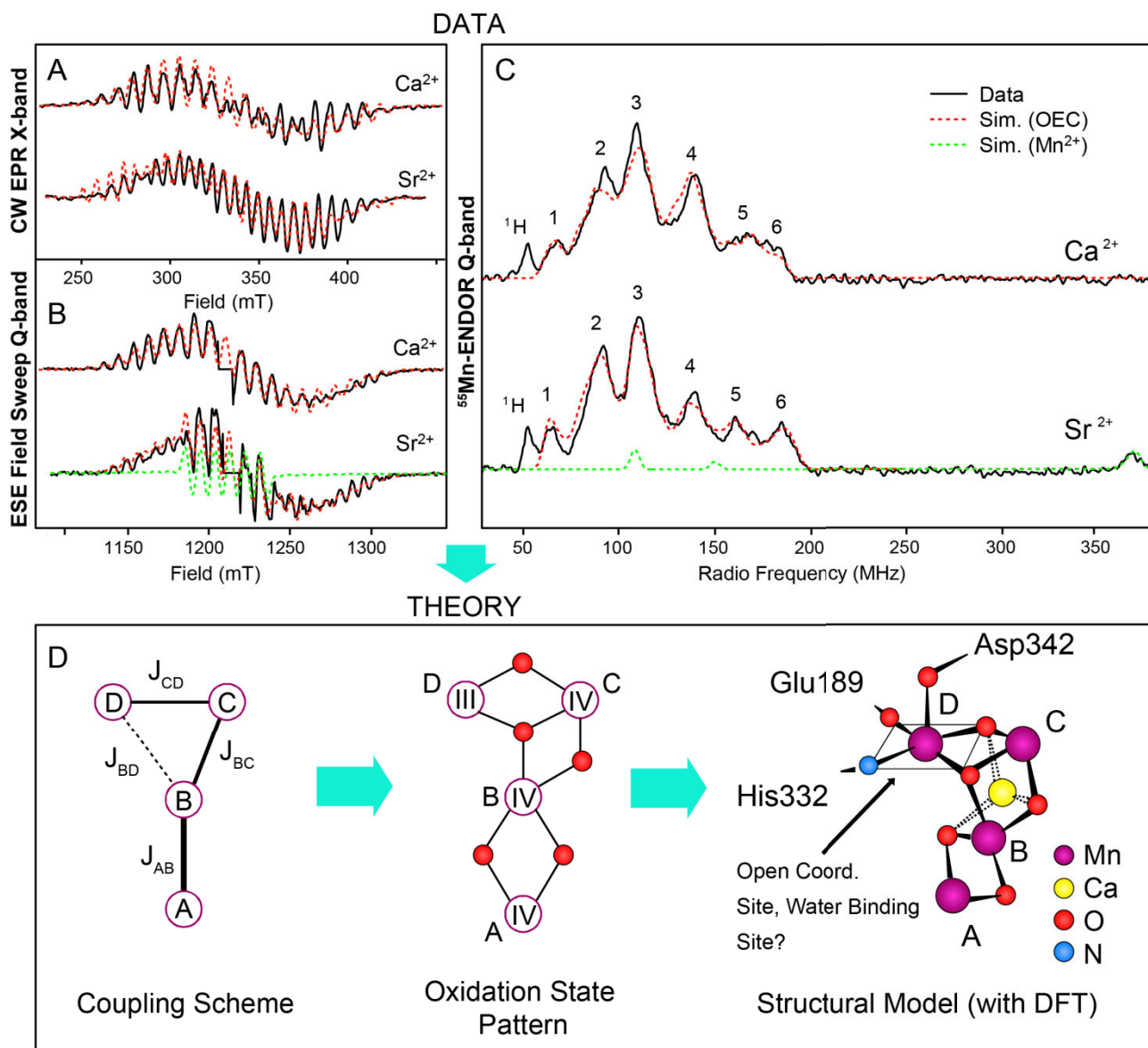


Figure 3.1 Summary scheme of work: coupling EPR/ENDOR spectroscopy with theoretical approaches. **(A)** X-band cw EPR spectra. **(B)** Q-band pulse echo-detected field sweep EPR spectra. **(C)** Q-band pulse ^{55}Mn -Davies ENDOR spectra. **(D)** Theory: from a coupling scheme to a structural model constrained by experimentally-determined parameters.

3.2. The electronic structures of the S_2 states of the oxygen evolving complexes of photosystem II in plants and cyanobacteria in the presence and absence of methanol

Published in Biochimica Biophysica Acta, 2011 Vol. 1807 (7), pp 829–840.

The variations are seen in the WOC across different species, in particular, differences in the electronic structure of the WOC in plants and cyanobacterial PSII. The possible reason for that is distortion of geometric structure of the WOC. Currently, the only existing crystallographic data on PSII thus far comes from cyanobacterial membranes. However, much of the spectroscopic data in the literature were obtained using PS II from plants rather than *T. elongatus*. Thus, it is important to identify possible differences between the different species to aid the collective interpretation of all PSII data. EPR spectroscopy techniques are well-suited for comparison studies of different species, particularly because it can be used to probe the electronic structure of the paramagnetic S-states of the WOC in detail.

As described in the introduction, the S_2 state of the WOC in plants and cyanobacteria displays a structured EPR signal centered at $g \sim 2$ called the multi-line (ML) signal. It comes from a $S_T = 1/2$ ground state configuration of the manganese cluster. However, under certain preparatory procedures, other EPR signals are observed for the S_2 state, including signals above $g \sim 4.1$, which arise from ground state configurations of higher spin i.e. $S \geq 5/2$. One of the most well-characterized effects is the addition of methanol. This organic solvent prevents the formation of signals at high g -values and modifies the ML signal through the narrowing of the EPR lines. However, the methanol effect occurs only in plant PSII; cyanobacterial PSII spectroscopic signals are not modified by methanol. Small changes such as these suggest the WOC from plants and cyanobacteria are similar but not identical in terms of their electronic structure.

A detailed analysis of the obtained EPR/ENDOR data identified possible differences between the two species. Only small changes are seen in hyperfine couplings measured on the plant and cyanobacterial WOC, suggesting the overall spin distribution and the coordination environment of the Mn is the same for both species and only the contribution of the on-site ZFS of the Mn^{III} to the total ZFS of the cluster changes. The

small changes that are observed are rationalized within a model in which the connectivity of the Mn cluster is slightly different between the two species. The effect of small organic solvents on the electronic structure of the cluster is to change the coupling between the outer Mn (Mn_A) and the other three Mn ions that form the trimeric part of the cluster (Mn_B , Mn_C , Mn_D) by perturbing the linking bis- μ -oxo bridge. The flexibility of this bridging unit is discussed with regard to the mechanism of O-O bond formation.

3.3. Electronic structure of a weakly antiferromagnetically coupled Mn^{II}Mn^{III} model relevant to manganese proteins: a combined EPR, ⁵⁵Mn-ENDOR, and DFT study

Published in *Inorganic Chemistry*, 2011 Vol. 50 (17), pp 8238–8251.

An analysis of the electronic structure of the [Mn^{II}Mn^{III}(μ -OH)-(μ -piv)₂(Me₃tacn)₂](ClO₄)₂, (PivOH), complex is reported in this work. PivOH is a mixed-valence compound which exhibits antiferromagnetic coupling leading to a ground state configuration with total electron spin (S_T) of 1/2 and a large on-site zero field splitting (ZFS) for Mn^{III}. The $S_T = 1/2$ state manifests the characteristic multiline signal centered at $g \sim 2$ which arises from the coupling of the two ⁵⁵Mn nuclei to the total unpaired electronic spin. Mn^{II}Mn^{III} systems are structural model complexes of the oxygen evolving complex (WOC) due to the presence of same properties: (i) a ground 1/2 spin state; (ii) a small exchange (J) coupling between the two Mn ions; (iii) a mono- μ -hydroxo bridge, bis- μ -carboxylato motif; and (iv) a strongly coupled, terminally bound N ligand to the Mn^{III}.

The electronic structure and properties of these complexes can be elucidated by EPR spectroscopy, although the analysis of this type of exchange-coupled systems is complicated by the presence of multiple terms of similar energetic importance in the spin Hamiltonian. This problem can be solved by measuring EPR spectra at multiple frequencies and using ENDOR spectroscopy. ⁵⁵Mn-ENDOR spectroscopy is a powerful tool in this study because of the lower number of overlapping transitions. The ⁵⁵Mn-ENDOR spectra provide information not only about the hyperfine couplings but also about nuclear quadrupole couplings of the ⁵⁵Mn ($I = 5/2$) ions, allowing determination of the effective G and hyperfine tensors and their relative orientation. The strong magnetic field dependence of these spectra allowed us to obtain a unique solution for the electronic structure parameters by simultaneous simulation of all experimental EPR/ENDOR data.

Multi-frequency EPR/ENDOR simulations showed that unusually large anisotropy of the effective hyperfine tensors for both the Mn^{II} and Mn^{III} ions is required to reproduce the experimental spectra. The

large effective hyperfine tensor anisotropy of the Mn^{II} ion, which is a d^5 ion and usually exhibits small anisotropy, is interpreted within a formalism in which the fine structure tensor of the Mn^{III} ion strongly perturbs the zero-field energy levels of the $\text{Mn}^{\text{II}}\text{Mn}^{\text{III}}$ complex. The magnitude of the fine structure and intrinsic (onsite) hyperfine tensor of the Mn^{III} is consistent with the known coordination environment of the Mn^{III} ion, as seen from its crystal structure.

This work also demonstrates that broken symmetry density functional theory (BS-DFT) calculations provide accurate estimates for all Spin Hamiltonian parameters, including tensor anisotropy. The isotropic and anisotropic components of the calculated hyperfine tensors match those obtained from EPR/ENDOR data within an error of 10%. It is possible to conclude from this study that BS-DFT is a very useful tool for examining complicated exchange coupled systems, and the combination of experimental and theoretical methodologies developed in this work should be directly applicable to biological systems.

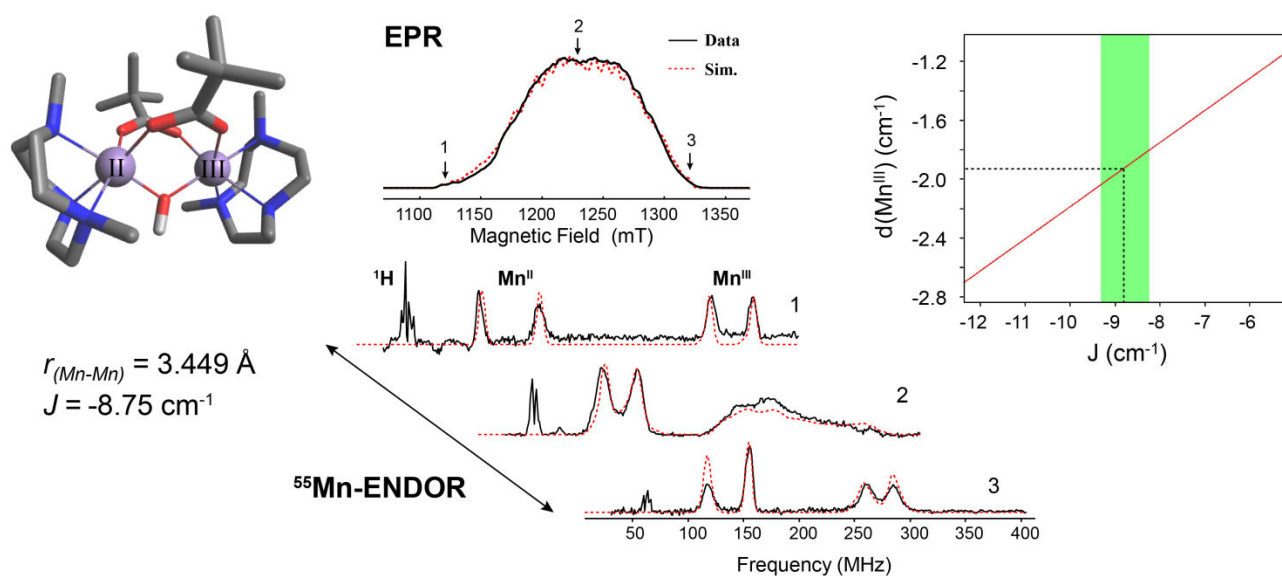


Figure 3.2 Summary scheme of work: crystal structure of PivOH complex; EPR/ENDOR spectra and corresponding simulations; estimation of the on-site fine-structure parameter for the Mn^{III} ion.

3.4. Detection of water binding sites in the oxygen-evolving complex of photosystem II poised in the S_2 state using high field (94 GHz) ^{17}O -ELDOR-detected NMR spectroscopy

Submitted to the Journal of the American Chemical Society.

The light-driven water-splitting reaction that plays a crucial role in photosynthesis is catalyzed by the oxygen-evolving complex (WOC). In order to elucidate the mechanism of oxidation of water to molecular oxygen, it is necessary to identify the water-derived ligands which represent the two substrate molecules. EPR spectroscopy is a powerful tool for determining the identity, including protonation state ($\text{H}_2\text{O}/\text{OH}/\text{O}^{2-}$), and location of water-derived species bound in the vicinity of the $\text{Mn}_4\text{O}_5\text{Ca}$ cluster. In the paramagnetic S_2 and S_0 states, exchangeable protons can be identified via the disappearance of signals originating from coupling of the ^1H nucleus ($I = 1/2$) to the net electronic spin ($S_T = 1/2$) of the $\text{Mn}_4\text{O}_5\text{Ca}$ cluster after $^1\text{H}_2\text{O}/^2\text{H}_2\text{O}$ exchange. A more direct probe for water-derived ligands is via the detection of oxygen using ^{17}O labeling. One particular advantage of this approach is that the fully deprotonated substrate, which is likely to be a critical intermediate in the O-O bond formation mechanism, is observable. Thus, it is possible to identify the incorporation of water into a Mn- μ -oxo bridge. Only a small number of publications describing ^{17}O couplings of metallocofactors and related model complexes have been published to date (87); (88); (89); (90); (91). This is due to a combination of factors, including the low natural abundance (0.038%) of ^{17}O and as a consequence the high costs for enrichment, the large nuclear spin ($I = 5/2$) and small nuclear g-factor (-0.7575) of ^{17}O , and its typically large quadrupole splitting.

Multi-frequency EPR, ENDOR and EDNMR techniques were used in this work in combination with isotopic labeling. The utilization of ^{17}O labeling helps to determine the hyperfine coupling of ^{17}O ($I = 5/2$) nuclei to the spin system, which can be detected using 94 GHz (W-band) EDNMR. PSII preparations were suspended in $^1\text{H}_2^{17}\text{O}$ and $^2\text{H}_2^{16}\text{O}$. ^{15}N ($I = 1/2$) labeling was necessary to uniquely identify the ^{17}O couplings which overlap with the His332 ^{14}N ($I = 1$) background signals. BIPY and DTNE complexes were used as model compounds in ^{17}O labeling experiments in order to recognize signals deriving from the ^{17}O oxo bridge

in the PSII sample. ^{17}O signals were seen even after very short, 15 second-incubation of PSII poised in the S_1 state suggesting that detected signals represent the slowly-exchanging substrate in S_1 . Multi-frequency $^1\text{H}/^2\text{H}$ ($I = 1/2, 1$) ENDOR data complement the above findings. The relatively small $^1\text{H}/^2\text{H}$ couplings observed implies that the μ -oxo bridges of the $\text{Mn}_4\text{O}_5\text{Ca}$ cluster are deprotonated in the S_2 state.

Consideration of the calibration data from the model compounds and experimental results which constrain the system enabled a detailed analysis of the observed ^{17}O signals. At least three type of signals were identified: (i) strongly coupled species with hyperfine couplings of ~ 10 MHz representing a ^{17}O - μ -oxo bridge; (ii) intermediate coupled species with ^{17}O hyperfine coupling of ~ 5 MHz representing terminal ligation of water/hydroxo to Mn, and (iii) unresolved hyperfine couplings of non-manganese bound ^{17}O signals corresponding to ligation of a water/hydroxo species to Ca or water in the second coordination shell. The hyperfine tensor anisotropy and orientation observed for the exchangeable μ -oxo bridge of the WOC constrains its position to either O4 or O5. Together, these results further refine the reaction pathway of O-O bond formation, supporting an oxo/oxyl coupling mechanism in S_4 .

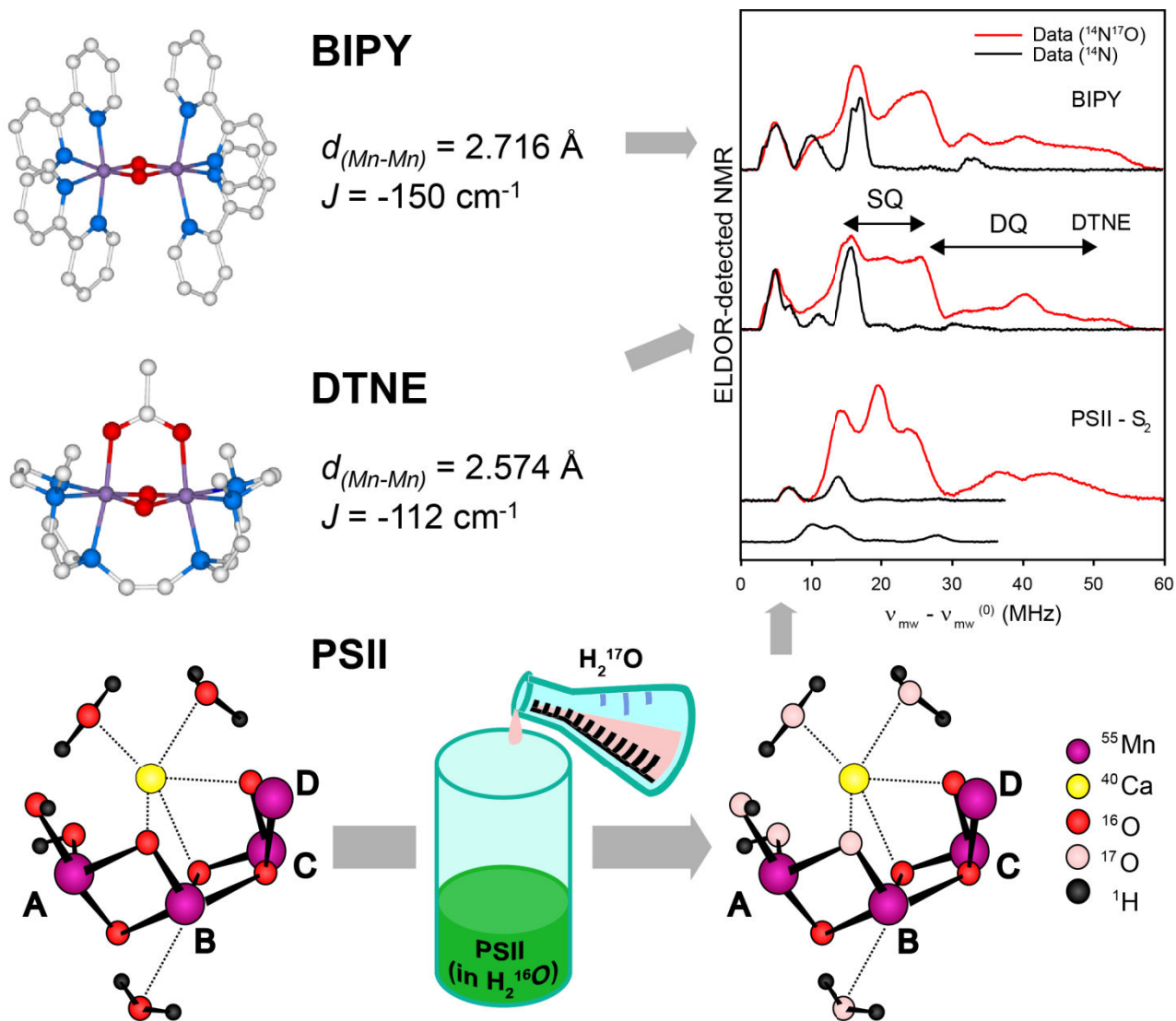


Figure 3.3. Summary scheme of work.

3.5. Characterization of μ -oxo bridge of Mn model complexes using high field (94 GHz) ^{17}O -HYSCORE and ^{17}O -ELDOR detected NMR spectroscopy

Manuscript is in preparation.

The μ -oxo bridge forms a key structural unit of many biological homo and heteronuclear metal clusters, governing the electronic (exchange) interaction between the metal ions. Important examples of Mn-metallocofactors include: (i) the di-manganese catalase, which catalyses the dismutation of H_2O_2 to H_2O and O_2 ; (ii) the recently identified di-manganese cofactor of class Ib ribonucleotide reductase; and (iii) the tetra-manganese oxygen evolving complex (OEC) of Photosystem II, which performs the multi-step oxidation of H_2O to O_2 . As such it is of importance to understand the electronic structure of this unit and the parameters that influence it. To this end, a detailed analysis of the electronic structure of two mixed-valence Mn dimer complexes was performed. The two compounds examined were the planer $\text{Mn}^{\text{III}}-\mu\text{O}_2-\text{Mn}^{\text{IV}}$ BIPY and the bent $\text{Mn}^{\text{III}}-\mu\text{O}_2-\text{Mn}^{\text{IV}}$ DTNE complexes. They both have bis- μ -oxo bridge connecting Mn ions, similar to that seen in many biological catalytic sites listed above.

The electronic structure of the μ -oxo bridge was examined by labelling with the magnetic isotope ^{17}O . In addition, high field EPR techniques were used to allow an accurate characterization of the magnetic properties of the bridge, including the hyperfine and quadrupole coupling. From these parameters a spectroscopic ‘fingerprint’ for the μ -oxo bridge could be developed, to allow easy identification in metallocofactors. This fingerprint provides a means of monitoring the μ -oxo bridges of a metallocofactor throughout its catalytic cycle. This is critical for understanding the chemistry that Mn metallocofactors perform, as they often locate substrates for the reaction they catalyze as bridging species, e.g. the Mn catalase takes up a HOOH as a μ -oxo during the dismutation reaction.

REFERENCES

- (1) Govindjee. Discoveries in photosynthesis. : Kluwer Academic Pub; 2005.
- (2) Bekker A, Holland H, Wang PL, Rumble D, Stein H, Hannah J, et al. Dating the rise of atmospheric oxygen. *Nature* 2004;427(6970):117-120.
- (3) Wydrzynski TJ, Hillier W, Peter L, Schüth F, Zhao TS. *Molecular Solar Fuels*. : Royal Society of Chemistry; 2011.
- (4) Rand DAJ, Dell R. *Hydrogen energy: challenges and prospects*. : Royal Society of Chemistry; 2008.
- (5) Lubitz W, Reijerse EJ, Messinger J. Solar water-splitting into H₂ and O₂: design principles of photosystem II and hydrogenases. *Energy Environ.Sci.* 2008;1(1):15-31.
- (6) Umena Y, Kawakami K, Shen JR, Kamiya N. Crystal structure of oxygen-evolving photosystem II at a resolution of 1.9 [thinsp] Å. *Nature* 2011;473(7345):55-60.
- (7) Cox N, Jin L, Jaszewski A, Smith PJ, Krausz E, Rutherford AW, et al. The Semiquinone-Iron Complex of Photosystem II: Structural Insights from ESR and Theoretical Simulation; Evidence that the Native Ligand to the Non-Heme Iron Is Carbonate. *Biophys J* 2009 10/07;97(7):2024-2033.
- (8) Holzwarth A, Müller M, Reus M, Nowaczyk M, Sander J, Rögner M. Kinetics and mechanism of electron transfer in intact photosystem II and in the isolated reaction center: pheophytin is the primary electron acceptor. *Proceedings of the National Academy of Sciences* 2006;103(18):6895-6900.
- (9) Renger G, Holzwarth A. Primary Electron Transfer. 2005;22:139-175.
- (10) Rappaport F, Guergova-Kuras M, Nixon PJ, Diner BA, Lavergne J. Kinetics and pathways of charge recombination in photosystem II. *Biochemistry (N Y)* 2002;41(26):8518-8527.
- (11) Nöring B, Shevela D, Renger G, Messinger J. Effects of methanol on the S_i-state transitions in photosynthetic water-splitting. *Photosynthesis Research* 2008;98(1):251-260.
- (12) Åhrling K, Pace R, Evans M. The catalytic manganese cluster: Implications from spectroscopy. *Photosystem II* 2005:285-305.
- (13) Nelson N, Yocum CF. Structure and function of photosystems I and II. *Annu.Rev.Plant Biol.* 2006;57:521-565.
- (14) Tommos C, Babcock G. Oxygen production in nature: A light-driven metalloradical enzyme process. *Acc Chem Res* 1998 JAN;31(1):18-25.
- (15) Kok B, Forbush B, McGLOIN M. Cooperation of charges in photosynthetic O₂ evolution—I. A linear four step mechanism. *Photochem Photobiol* 1970;11(6):457-475.
- (16) Hillier W, Messinger J. Mechanism of Photosynthetic Oxygen Production. 2005;22:567-608.
- (17) Styring S, Rutherford AW. In the oxygen-evolving complex of photosystem II the S₀ state is oxidized to the S₁ state by D (signal IIslow). *Biochemistry (N Y)* 1987;26(9):2401-2405.

- (18) Dau H, Haumann M. The manganese complex of photosystem II in its reaction cycle—basic framework and possible realization at the atomic level. *Coord Chem Rev* 2008;252(3):273-295.
- (19) Yano J, Kern J, Sauer K, Latimer MJ, Pushkar Y, Biesiadka J, et al. Where water is oxidized to dioxygen: structure of the photosynthetic Mn₄Ca cluster. *Science* 2006;314(5800):821-825.
- (20) Yano J, Yachandra VK. Where water is oxidized to dioxygen: Structure of the photosynthetic Mn₄Ca cluster from X-ray spectroscopy. *Inorg Chem* 2008;47(6):1711-1726.
- (21) Kusunoki M. Mono-manganese mechanism of the photosystem II water splitting reaction by a unique Mn₄Ca cluster. *Biochimica et Biophysica Acta (BBA)-Bioenergetics* 2007;1767(6):484-492.
- (22) Siegbahn PEM. Structures and energetics for O₂ formation in photosystem II. *Acc Chem Res* 2009;42(12):1871-1880.
- (23) Dau H, Zaharieva I. Principles, efficiency, and blueprint character of solar-energy conversion in photosynthetic water oxidation. *Acc Chem Res* 2009;42(12):1861-1870.
- (24) Dau H, Grundmeier A, Loja P, Haumann M. On the structure of the manganese complex of photosystem II: extended-range EXAFS data and specific atomic-resolution models for four S-states. *Philosophical Transactions of the Royal Society B: Biological Sciences* 2008;363(1494):1237-1244.
- (25) Abragam A, Pryce MHL. Theory of the nuclear hyperfine structure of paramagnetic resonance spectra in crystals. *Proceedings of the Royal Society of London. Series A. Mathematical and Physical Sciences* 1951;205(1080):135-153.
- (26) Ames W, Pantazis DA, Krewald V, Cox N, Messinger J, Lubitz W, et al. Theoretical Evaluation of Structural Models of the S₂ State in the Oxygen Evolving Complex of Photosystem II: Protonation States and Magnetic Interactions. *J Am Chem Soc* 2011.
- (27) Messinger J, Pauly S, Witt H. The flash pattern of photosynthetic oxygen evolution after treatment with low concentrations of hydroxylamine as a function of the previous Si/So ratio: Further evidence that NH₂OH reduces the water oxidizing complex in the dark. *Z Naturforsch., 46c* 1991:1033-1038.
- (28) Schansker G, Goussias C, Petrouleas V, Rutherford A. Reduction of the Mn cluster of the water-oxidizing enzyme by nitric oxide: Formation of an S₂ state. *Biochemistry (N Y)* 2002 MAR 5;41(9):3057-3064.
- (29) Noguchi T, Sugiura M. FTIR detection of water reactions during the flash-induced S-state cycle of the photosynthetic water-oxidizing complex. *Biochemistry (N Y)* 2002;41(52):15706-15712.
- (30) Noguchi T, Sugiura M. Flash-induced FTIR difference spectra of the water oxidizing complex in moderately hydrated photosystem II core films: Effect of hydration extent on S-state transitions. *Biochemistry (N Y)* 2002 FEB 19;41(7):2322-2330.
- (31) Siegbahn PEM. A Structure-Consistent Mechanism for Dioxygen Formation in Photosystem II. *Chemistry-A European Journal* 2008;14(27):8290-8302.
- (32) Boussac A, Rutherford A. Nature of the inhibition of the oxygen-evolving enzyme of photosystem II induced by sodium chloride washing and reversed by the addition of calcium (2) or strontium (2). *Biochemistry (N Y)* 1988;27(9):3476-3483.
- (33) Boussac A, Setif P, Rutherford AW. Inhibition of tyrosine Z photooxidation after formation of the S₃-state in calcium-depleted and chloride-depleted photosystem-II. *Biochemistry (N Y)* 1992;31(4):1224-1234.

- (34) Ishida N, Sugiura M, Rappaport F, Lai TL, Rutherford AW, Boussac A. Biosynthetic exchange of bromide for chloride and strontium for calcium in the photosystem II oxygen-evolving enzymes. *J Biol Chem* 2008;283(19):13330-13340.
- (35) Dismukes GC, Siderer Y. Intermediates of a polynuclear manganese center involved in photosynthetic oxidation of water. *Proceedings of the National Academy of Sciences* 1981;78(1):274.
- (36) Haddy A. EPR spectroscopy of the manganese cluster of photosystem II. *Photosynthesis Res* 2007;92(3):357-368.
- (37) Kulik LV, Epel B, Lubitz W, Messinger J. Electronic structure of the Mn₄O_xCa cluster in the S-0 and S-2 states of the oxygen-evolving complex of photosystem II based on pulse Mn-55-ENDOR and EPR Spectroscopy. *J Am Chem Soc* 2007 NOV 7;129(44):13421-13435.
- (38) Randall D, Chan M, Armstrong W, Britt R. Pulsed H-1 and Mn-55 ENDOR studies of dinuclear Mn(III)Mn(IV) model complexes. *Mol Phys* 1998 DEC 20;95(6):1283-1294.
- (39) Kulik L, Lubitz W. Electron-nuclear double resonance. *Photosynthesis Res* 2009;102(2):391-401.
- (40) Hendry G, Wydrzynski T. O-18 isotope exchange measurements reveal that calcium is involved in the binding of one substrate-water molecule to the oxygen-evolving complex in photosystem II. *Biochemistry (N Y)* 2003 MAY 27;42(20):6209-6217.
- (41) Hillier W, Wydrzynski T. ¹⁸O-Water exchange in photosystem II: Substrate binding and intermediates of the water splitting cycle. *Coord Chem Rev* 2008 2;252(3-4):306-317.
- (42) Messinger J, Badger M, Wydrzynski T. Detection of one slowly exchanging substrate water molecule in the S₃ state of photosystem II. *Proceedings of the National Academy of Sciences* 1995;92(8):3209.
- (43) Hillier W, McConnell I, Singh S, Debus R, Boussac A, Wydrzynski T. Substrate Water Oxygen Exchange in Photosystem II: Insights from Mutants and Ca vs. Sr Substitution. *Photosynthesis. Energy from the Sun* 2008:427-430.
- (44) Hillier W, Messinger J, Wydrzynski T. Kinetic determination of the fast exchanging substrate water molecule in the S₃ state of photosystem II. *Biochemistry (N Y)* 1998;37(48):16908-16914.
- (45) Noguchi T. FTIR detection of water reactions in the oxygen-evolving centre of photosystem II. *Philosophical Transactions of the Royal Society B: Biological Sciences* 2008;363(1494):1189-1195.
- (46) Noguchi T, Sugiura M. Structure of an active water molecule in the water-oxidizing complex of photosystem II as studied by FTIR spectroscopy. *Biochemistry (N Y)* 2000 SEP 12;39(36):10943-10949.
- (47) Messinger J. Evaluation of different mechanistic proposals for water oxidation in photosynthesis on the basis of Mn₄O_xCa structures for the catalytic site and spectroscopic data. *Phys.Chem.Chem.Phys.* 2004;6(20):4764-4771.
- (48) McEvoy JP, Brudvig GW. Water-splitting chemistry of photosystem II. *Chem Rev* 2006;106(11):4455-4483.
- (49) Barber J, Ferreira K, Maghlaoui K, Iwata S. Structural model of the oxygen-evolving centre of photosystem II with mechanistic implications. *Physical Chemistry Chemical Physics* 2004;6(20):4737-4742.

- (50) Sproviero EM, Gascón JA, McEvoy JP, Brudvig GW, Batista VS. Quantum mechanics/molecular mechanics study of the catalytic cycle of water splitting in photosystem II. *J Am Chem Soc* 2008;130(11):3428-3442.
- (51) Yamanaka S, Isobe H, Kanda K, Saito T, Umena Y, Kawakami K, et al. Possible mechanisms for the OO bond formation in oxygen evolution reaction at the CaMn₄O₅ (H₂O)₄ cluster of PSII refined to 1.9 Å resolution. *Chemical Physics Letters* 2011.
- (52) Gao Y, Åkermark T, Liu J, Sun L, Åkermark B. Nucleophilic Attack of Hydroxide on a MnV Oxo Complex: A Model of the O–O Bond Formation in the Oxygen Evolving Complex of Photosystem II. *J Am Chem Soc* 2009;131(25):8726-8727.
- (53) Renger G. Oxidative photosynthetic water splitting: energetics, kinetics and mechanism. *Photosynthesis Res* 2007;92(3):407-425.
- (54) Liu F, Concepcion JJ, Jurss JW, Cardolaccia T, Templeton JL, Meyer TJ. Mechanisms of water oxidation from the blue dimer to photosystem II. *Inorg Chem* 2008;47(6):1727-1752.
- (55) Cooper SR, Dismukes GC, Klein MP, Calvin M. Mixed valence interactions in di- μ -oxo bridged manganese complexes. Electron paramagnetic resonance and magnetic susceptibility studies. *J Am Chem Soc* 1978;100(23):7248-7252.
- (56) Åhrling KA, Peterson S, Styring S. An oscillating manganese electron paramagnetic resonance signal from the S₀ state of the oxygen evolving complex in photosystem II. *Biochemistry (N Y)* 1997;36(43):13148-13152.
- (57) Messinger J, Robblee JH, Yu WO, Sauer K, Yachandra VK, Klein MP. The S₀ state of the oxygen-evolving complex in photosystem II is paramagnetic: detection of an EPR multiline signal. *J Am Chem Soc* 1997;119(46):11349-11350.
- (58) Randall DW, Sturgeon BE, Ball JA, Lorigan GA, Chan MK, Klein MP, et al. ⁵⁵Mn ESE-ENDOR of a mixed valence Mn(III)Mn(IV) complex: comparison with the Mn cluster of the photosynthetic oxygen-evolving complex. *J Am Chem Soc* 1995;117(47):11780-11789.
- (59) Schafer K, Bittl R, Lenzian F, Barynin V, Weyhermuller T, Wieghardt K, et al. Multifrequency EPR investigation of dimanganese catalase and related Mn(III)Mn(IV) complexes. *J Phys Chem B* 2003 FEB 6;107(5):1242-1250.
- (60) Schafer K, Bittl R, Zwegart W, Lenzian F, Haselhorst G, Weyhermuller T, et al. Electronic structure of antiferromagnetically coupled dinuclear manganese ((MnMnIV)-Mn-III) complexes studied by magnetic resonance techniques. *J Am Chem Soc* 1998 DEC 23;120(50):13104-13120.
- (61) Kulik LV, Epel B, Lubitz W, Messinger J. ⁵⁵Mn pulse ENDOR at 34 GHz of the S₀ and S₂ states of the oxygen-evolving complex in photosystem II. *J Am Chem Soc* 2005;127(8):2392-2393.
- (62) Peloquin JM, Campbell KA, Randall DW, Evanchik MA, Pecoraro VL, Armstrong WH, et al. ⁵⁵Mn ENDOR of the S₂-state multiline EPR signal of photosystem II: implications on the structure of the tetranuclear Mn cluster. *J Am Chem Soc* 2000;122(44):10926-10942.
- (63) Stull JA, Stich TA, Service RJ, Debus RJ, Mandal SK, Armstrong WH, et al. ¹³C ENDOR Reveals That the D1 Polypeptide C-Terminus Is Directly Bound to Mn in the Photosystem II Oxygen Evolving Complex. *J Am Chem Soc* 2009;132(2):446-447.

- (64) Plaksin P, Stoufer R, Mathew M, Palenik G. Novel antiferromagnetic oxo-bridged manganese complex. *J Am Chem Soc* 1972;94(6):2121-2122.
- (65) Cooper SR, Calvin M. Mixed valence interactions in di- μ -oxo bridged manganese complexes. *J Am Chem Soc* 1977;99(20):6623-6630.
- (66) Jensen AF, Su Z, Hansen NK, Larsen FK. X-Ray Diffraction Study of the Correlation between Electrostatic Potential and K-Absorption Edge Energy in a Bis (μ -oxo) Mn (III)-Mn (IV) Dimer. *Inorg Chem* 1995;34(16):4244-4252.
- (67) Thomas Weyhermüller. Synthese und Charakterisierung oxo-verbrückter Mangankomplexe mit Azamakrozyklen Bochum, Univ., Diss., 1995; 1994.
- (68) Schweiger A, Jeschke G. Principles of pulse electron paramagnetic resonance. 2001.
- (69) Weil JA, Bolton JR. Electron paramagnetic resonance: elementary theory and practical applications. : Wiley; 2007.
- (70) Atherton NM, Gilbert B, Davies M. Electron spin resonance. : Royal Society of Chemistry; 1994.
- (71) Anderson P. Antiferromagnetism. Theory of superexchange interaction. *Physical Review* 1950;79(2):350.
- (72) Yafet Y. $\langle g \rangle$ Factors and Spin-Lattice Relaxation of Conduction Electrons. *Solid State Physics* 1963;14:1-98.
- (73) Weltner W. EPR of exchange-coupled systems:: Alessandro Bencini and Dante Gatteschi. Springer-Verlag, Berlin, 1989. 287 pages. \$79.00. ISBN: 0-387-50944-5. *Journal of Magnetic Resonance* (1969) 1990;90(3):618-619.
- (74) Sage J, Xia Y, Debrunner P, Keough D, De Jersey J, Zerner B. Mössbauer analysis of the binuclear iron site in purple acid phosphatase from pig allantoinic fluid. *J Am Chem Soc* 1989;111(18):7239-7247.
- (75) Zheng M, Khangulov S, Dismukes G, Barynin V. Electronic structure of dimanganese (II, III) and dimanganese (III, IV) complexes and dimanganese catalase enzyme: a general EPR spectral simulation approach. *Inorg Chem* 1994;33(2):382-387.
- (76) Pantazis DA, Orio M, Petrenko T, Zein S, Lubitz W, Messinger J, et al. Structure of the oxygen-evolving complex of photosystem II: information on the S₂ state through quantum chemical calculation of its magnetic properties. *Phys.Chem.Chem.Phys.* 2009;11(31):6788-6798.
- (77) Charlot MF, Boussac A, Blondin G. Towards a spin coupling model for the Mn₄ cluster in Photosystem II. *Biochimica et Biophysica Acta (BBA)-Bioenergetics* 2005;1708(1):120-132.
- (78) Messinger J, Robblee JH, Bergmann U, Fernandez C, Glatzel P, Visser H, et al. Absence of Mn-Centered oxidation in the S₂→ S₃ transition: implications for the mechanism of photosynthetic water oxidation. *J Am Chem Soc* 2001;123(32):7804-7820.
- (79) Haumann M, Müller C, Liebisch P, Iuzzolino L, Dittmer J, Grabolle M, et al. Structural and oxidation state changes of the photosystem II manganese complex in four transitions of the water oxidation cycle (S₀→ S₁, S₁→ S₂, S₂→ S₃, and S₃, 4→ S₀) characterized by X-ray absorption spectroscopy at 20 K and room temperature. *Biochemistry (N Y)* 2005;44(6):1894-1908.
- (80) Feher G, Gere E. Polarization of phosphorus nuclei in silicon. *Physical Review* 1956;103(2):501.

- (81) Hahn EL. Spin echoes. *Physical Review* 1950;80(4):580.
- (82) Rowan L, Hahn E, Mims W. Electron-spin-echo envelope modulation. *Physical Review* 1965;137(1A):A61.
- (83) Davies E. A new pulse ENDOR technique. *Physics Letters A* 1974;47(1):1-2.
- (84) Mims W. Pulsed ENDOR experiments. *Proceedings of the Royal Society of London. Series A. Mathematical and Physical Sciences* 1965;283(1395):452-457.
- (85) Schosseler P, Wacker T, Schweiger A. Pulsed ELDOR detected NMR. *Chemical Physics Letters* 1994 7/15;224(3-4):319-324.
- (86) Boussac A, Rappaport F, Carrier P, Verbavatz JM, Gobin R, Kirilovsky D, et al. Biosynthetic Ca² /Sr² exchange in the photosystem II oxygen-evolving enzyme of *Thermosynechococcus elongatus*. *J Biol Chem* 2004;279(22):22809.
- (87) Thomann H, Bernardo M, Goldfarb D, Kroneck P, Ullrich V. Evidence for Water Binding to the Fe Center in Cytochrome P450cam Obtained by ¹⁷O Electron Spin-Echo Envelope Modulation Spectroscopy. *J Am Chem Soc* 1995;117(31):8243-8251.
- (88) Burdi D, Willems JP, Riggs-Gelasco P, Antholine WE, Stubbe JA, Hoffman BM. The core structure of X generated in the assembly of the diiron cluster of ribonucleotide reductase: ¹⁷O₂ and H₂¹⁷O ENDOR. *J Am Chem Soc* 1998;120(49):12910-12919.
- (89) Carepo M, Tierney DL, Brondino CD, Yang TC, Pamplona A, Telser J, et al. ¹⁷O ENDOR Detection of a Solvent-Derived Ni-(OH_x)-Fe Bridge That Is Lost upon Activation of the Hydrogenase from *Desulfovibrio gigas*. *J Am Chem Soc* 2002;124(2):281-286.
- (90) Astashkin AV, Feng C, Raitsimring AM, Enemark JH. ¹⁷O ESEEM evidence for exchange of the axial oxo ligand in the molybdenum center of the high pH form of sulfite oxidase. *J Am Chem Soc* 2005;127(2):502-503.
- (91) Enemark JH, Raitsimring AM, Astashkin AV, Klein EL. Implications for the mechanism of sulfite oxidizing enzymes from pulsed EPR spectroscopy and DFT calculations for “difficult” nuclei. *Faraday Discuss* 2010;148(0):249-267.

JOURNAL ARTICLES

This section consists of five research articles mentioned above in the format as they are accepted or submitted to corresponding scientific journal.

The effect of $\text{Ca}^{2+}/\text{Sr}^{2+}$ substitution on the electronic structure of the oxygen-evolving complex of photosystem II: A combined pulse ^{55}Mn -ENDOR, multi-frequency EPR and DFT study of the S_2 state

Nicholas Cox, Leonid Rapatskiy, Ji-Hu Su, Dimitrios A. Pantazis, Miwa Sugiura, Leonid Kulik, Pierre Dorlet, A. William Rutherford, Frank Neese, Alain Boussac, Wolfgang Lubitz and Johannes Messinger

Effect of $\text{Ca}^{2+}/\text{Sr}^{2+}$ Substitution on the Electronic Structure of the Oxygen-Evolving Complex of Photosystem II: A Combined Multifrequency EPR, ^{55}Mn -ENDOR, and DFT Study of the S_2 State

Nicholas Cox,^{*,†} Leonid Rapatskiy,[†] Ji-Hu Su,[†] Dimitrios A. Pantazis,^{†,‡} Miwa Sugiura,[§] Leonid Kulik,^{||} Pierre Dorlet,[⊥] A. William Rutherford,[⊥] Frank Neese,^{†,‡} Alain Boussac,[⊥] Wolfgang Lubitz,^{*,†} and Johannes Messinger^{*,#}

[†]Max-Planck-Institut für Bioorganische Chemie, Stiftstrasse 34-36, D-45470 Mülheim an der Ruhr, Germany

[‡]Lehrstuhl für Theoretische Chemie, Institut für Physikalische und Theoretische Chemie, Universität Bonn, Wegelerstrasse 12, D-53115 Bonn, Germany

[§]Cell-Free Science and Technology Research Center, Ehime University, Bunkyo-cho, Matsuyama Ehime 790-8577, Japan

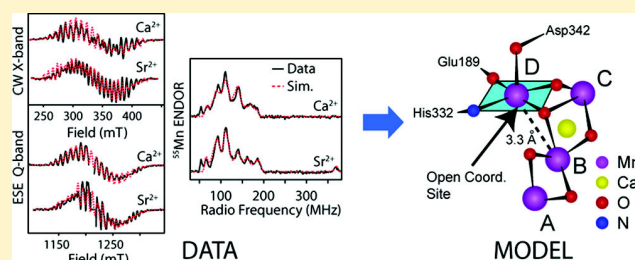
^{||}Institute of Chemical Kinetics and Combustion, Institutskaya 3, 630090 Novosibirsk, Russia

[⊥]iBiTec-S, URA CNRS 2096, CEA Saclay, 91191 Gif-sur-Yvette, France

[#]Department of Chemistry, Chemical Biological Centre (KBC), Umeå University, S-90187 Umeå, Sweden

S Supporting Information

ABSTRACT: The electronic structures of the native $\text{Mn}_4\text{O}_x\text{Ca}$ cluster and the biosynthetically substituted $\text{Mn}_4\text{O}_x\text{Sr}$ cluster of the oxygen evolving complex (OEC) of photosystem II (PSII) core complexes isolated from *Thermosynechococcus elongatus*, poised in the S_2 state, were studied by X- and Q-band CW-EPR and by pulsed Q-band ^{55}Mn -ENDOR spectroscopy. Both wild type and tyrosine D less mutants grown photoautotrophically in either CaCl_2 or SrCl_2 containing media were measured. The obtained CW-EPR spectra of the S_2 state displayed the characteristic, clearly noticeable differences in the hyperfine pattern of the multiline EPR signal [Boussac et al. *J. Biol. Chem.* **2004**, *279*, 22809–22819]. In sharp contrast, the manganese (^{55}Mn) ENDOR spectra of the Ca and Sr forms of the OEC were remarkably similar. Multifrequency simulations of the X- and Q-band CW-EPR and ^{55}Mn -pulsed ENDOR spectra using the Spin Hamiltonian formalism were performed to investigate this surprising result. It is shown that (i) all four manganese ions contribute to the ^{55}Mn -ENDOR spectra; (ii) only small changes are seen in the fitted isotropic hyperfine values for the Ca^{2+} and Sr^{2+} containing OEC, suggesting that there is no change in the overall spin distribution (electronic coupling scheme) upon $\text{Ca}^{2+}/\text{Sr}^{2+}$ substitution; (iii) the changes in the CW-EPR hyperfine pattern can be explained by a small decrease in the anisotropy of at least two hyperfine tensors. It is proposed that modifications at the Ca^{2+} site may modulate the fine structure tensor of the Mn^{III} ion. DFT calculations support the above conclusions. Our data analysis also provides strong support for the notion that in the S_2 state the coordination of the Mn^{III} ion is square-pyramidal (5-coordinate) or octahedral (6-coordinate) with tetragonal elongation. In addition, it is shown that only one of the currently published OEC models, the Siegbahn structure [Siegbahn, P. E. M. *Acc. Chem. Res.* **2009**, *42*, 1871–1880, Pantazis, D. A. et al. *Phys. Chem. Chem. Phys.* **2009**, *11*, 6788–6798], is consistent with all data presented here. These results provide important information for the structure of the OEC and the water-splitting mechanism. In particular, the 5-coordinate Mn^{III} is a potential site for substrate ‘water’ (H_2O , OH^-) binding. Its location within the cuboidal structural unit, as opposed to the external ‘dangler’ position, may have important consequences for the mechanism of O–O bond formation.



1. INTRODUCTION

In oxygenic photosynthesis light-driven water-splitting is catalyzed by the oxygen-evolving complex (OEC) of Photosystem II (PSII). The OEC consists of an inorganic $\text{Mn}_4\text{O}_x\text{Ca}$ cluster (where $4 \leq x \leq 6$ indicates the number of oxygen bridges) and its surrounding protein matrix.^{1–14} The functionally important protein matrix includes the redox-active tyrosine residue Y_Z ($\text{D}_1\text{-Y}_{161}$). Y_Z couples electron transfer from the $\text{Mn}_4\text{O}_x\text{Ca}$

cluster to P_{680} and is involved in proton transfer reactions.¹⁵ $\text{P}_{680}/\text{P}_{680}^{*\cdot+}$ and $\text{Pheo}/\text{Pheo}^{*\cdot-}$ form the primary component of the photoactive reaction center of PSII, which energetically drives water-splitting by four sequential light-induced charge separations, for reviews see refs 8–14, and 16–18. During

Received: November 21, 2010

Published: February 22, 2011

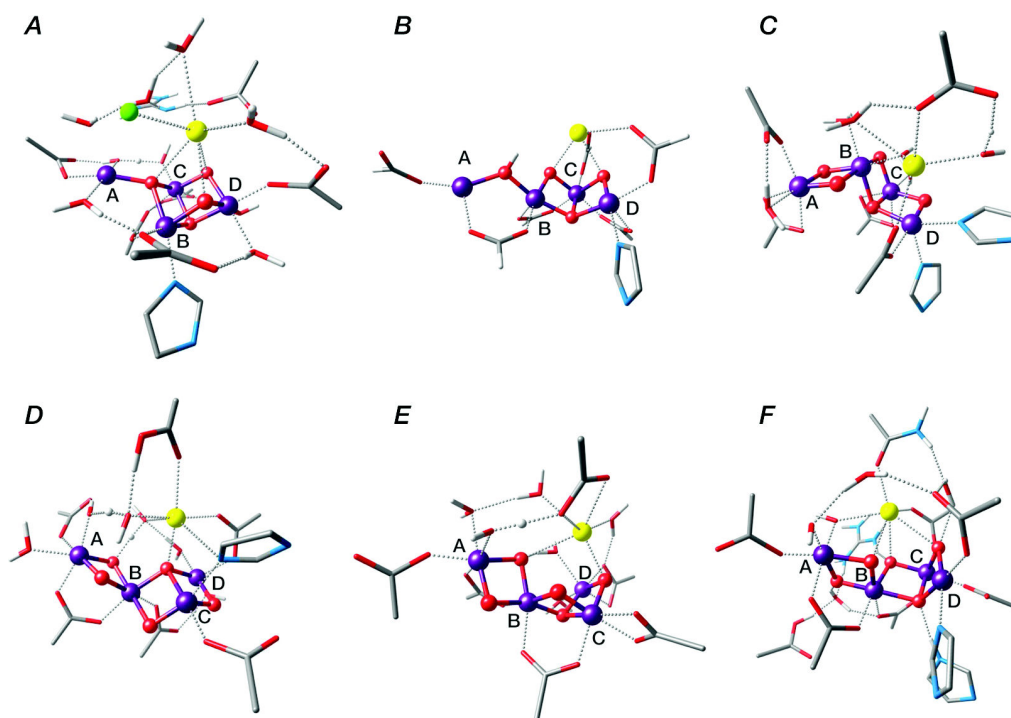
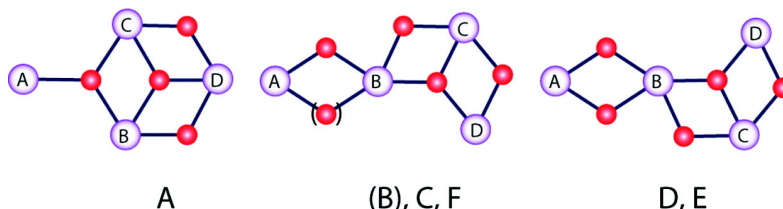


Figure 1. Current QM/MM and DFT literature models for the OEC poised in the S_2 state based on recent X-ray crystallographic^{3–5} and polarized EXAFS^{6,7} data. A) London crystal structure;^{3,43–45} B) Berlin crystal structure;^{4,5,53,54} C) EXAFS core I;^{6,57} D) EXAFS core II;^{6,57} E) EXAFS core III;^{6,57} F) Siegbahn model.^{11,58,59} Purple spheres: manganese; red: oxygens; yellow: calcium; green: chloride; blue: nitrogen; gray: carbon.

Scheme 1



water-splitting, the Mn_4O_xCa cluster steps through a reaction cycle comprising five distinct redox intermediates. These are known as the S_n states, where the index indicates the number of stored oxidizing equivalents ($n = 0–4$).¹⁹ Once formed the $S_3YZ\cdot$ rapidly decays to the S_0 state upon the release of molecular triplet oxygen and the rebinding of at least one substrate water molecule.^{9,10} A S_4 state, which is different from $S_3YZ\cdot$, has not yet been spectroscopically identified.

Ca^{2+} is known to be an essential cofactor for the water-splitting reaction.^{20–25} Removal of Ca^{2+} inhibits water-splitting by blocking the $S_2 \rightarrow S_3$ transition.²⁶ It was demonstrated that Sr^{2+} is the only surrogate that is able of restoring water-splitting after Ca^{2+} removal, albeit at a slower turnover rate.^{23,26,27} It has been speculated that this may be due to a combination of two important factors. The surrogate must match: (i) the approximate size and (ii) the Lewis acidity²⁸ of Ca^{2+} . This suggests a role for Ca/Sr in substrate water binding. Time-resolved $H_2^{16}O/H_2^{18}O$ exchange measurements performed by membrane-inlet mass spectrometry^{29,30} demonstrate that the exchange kinetics of the slowly exchanging substrate water molecule are strongly affected by Ca/Sr exchange.^{31,32}

It has been recently shown that the thermophilic cyanobacterium *Thermosynechococcus elongatus* (*T. elongatus*) can be photoautotrophically grown in either Ca^{2+} or Sr^{2+} containing media. It is thus possible to obtain PSII complexes with intact Mn_4O_xCa or Mn_4O_xSr clusters that display high oxygen-evolving activities.^{27,33,34} Consistent with these high activities, only minor structural differences – mainly in $Mn–Ca^{2+}/Sr^{2+}$ distances – are observed in the S_1 and S_2 states between these two sample types by EXAFS spectroscopy.³⁵ The physical proximity of the Ca^{2+} to the Mn cluster was first demonstrated by Mn K-edge EXAFS measurements on isotropic PSII samples^{35–40} and then refined by X-ray crystallographic data^{3–5,33} and polarized EXAFS.^{6,7,41} Figure 1 summarizes current structural models of the Mn_4O_xCa cluster that are based on these approaches.⁴² The manganese connectivity and labeling for the models of Figure 1 is depicted in Scheme 1 in which it can be seen that apart from model A, all other models share the same basic topology. It is noted however that model B lacks one μ -oxo linkage between Mn_A and Mn_B .

Model A is based on the London crystal structure and QM/MM and DFT based refinements.^{3,43–45} Here the Ca^{2+} was

assigned as a vertex of a μ -oxo-bridged cubane-like structure, with three Mn defining the other three vertices. They form the three short (about 2.7 Å) Mn–Mn distances known from EXAFS spectroscopy.^{46–48} Ca^{2+} is suggested to bind the slowly exchanging substrate water and a Cl^- ion. This is in conflict with recent crystallographic and spectroscopic data, which both demonstrate that the shortest Cl^- to metal distance is >5 Å in dark-adapted samples.^{54,49–52} The fourth ‘dangler’ or outer Mn is attached to this core structure via a μ_4 -oxo-bridged ligation to one of the oxygen corners of the cube and thereby forms the long (3.3 Å) Mn–Mn distance known from EXAFS spectroscopy.^{46–48} Water-oxidation chemistry in these models was suggested to occur between one water bound to Ca and one that is bound as a terminal oxo to the outer Mn ion (Mn_A). Model B is based on the Berlin crystal structure⁴ and was also refined by DFT calculations. In contrast to model A it has an open and flattened cube structure (one corner oxygen is missing), and the outer Mn is attached via one mono μ_2 -oxo bridge. Ca^{2+} is suggested to coordinate to two μ_2 -oxo bridges of the open cube; required protein ligands are not completely included in this minimal model^{53,54} but see Kusunoki for a similar, more complete model.⁵⁵ Water-oxidation chemistry may occur in such models for example between two water molecules bound to the outer Mn (Mn_A).⁵⁵ Models C, D, and E of Figure 1 are based on structures (models I, II, and III, respectively) derived from polarized EXAFS measurements on PSII single crystals⁶ that were further refined based on crystallographic information on possible ligands and DFT calculations.^{56,57} These models also have a more planar geometry and are somewhat reminiscent of the original Berkeley ‘dimer of dimers’ model.⁴⁷ However, they are more interconnected than this original suggestion and have one additional 2.7 Å Mn–Mn distance⁴⁸ that is formed by connecting the di- μ -oxo bridge of one ‘dimer’ to a Mn of the other ‘dimer’. Importantly, the symmetry of the cuboidal Mn_3O_3 -Ca part is broken by the absence of one corner oxygen, which leads to a longer Mn–Mn distance of 3.3 Å inside this segment.⁶ In model C, the Ca^{2+} is ligated in a similar fashion to the Mn_4O_x core as in model B, while in model D, the Ca^{2+} only has contact with the rest of the Mn cluster via its binding to the μ_3 -oxo bridge connecting the Mn ions of the trimeric part. In model E the Ca^{2+} connects to two μ_2 -oxo bridges: to one of the oxo’s of the trimeric unit and to one of the bridges to the outer Mn ion. The most detailed and rigorous proposal at present is shown in Figure 1F.^{11,58,59} The model of Siegbahn combines many crystallographic and spectroscopic data. It was designed to be of the lowest possible total energy and to allow low energy barrier O–O bond formation to occur between a hydroxo that binds to Mn_C in the S_3 state (which is 5 coordinated in the S_0 to S_2 states) and the μ_3 -oxo bridge connecting Mn_A , Mn_B , and Ca. This model has strong similarities to models C and E but is more compact. In this model Ca is connected to all four Mn ions via three μ_2 -oxo bridges. Recently a model related to models C, E, and F was proposed based on molecular mechanics modeling of the Berlin crystal structure⁴ and comparison to polarized EXAFS data. Here two long (3.2 Å) Mn–Mn distances are assumed to be within the cuboidal part in the S_0 , S_1 , and S_2 states (between Mn_C – Mn_D and Mn_C – Mn_B), that shorten (to about 2.7 Å) during the $S_2 \rightarrow S_3$ transition due to the oxidation of Mn_C^{III} and concomitant formation of another oxo bridge. As a consequence, water-oxidation is expected to occur between waters bound at the Mn_A and to Ca since all other manganese are coordinatively saturated in S_3 and S_4 .^{60,61}

As water oxidation involves four single oxidation events of the $\text{Mn}_4\text{O}_x\text{Ca}$ cluster during the S_n state cycle, it is particularly well suited for study by EPR. By using standard perpendicular mode CW-EPR the OEC in the S_2 state exhibits a characteristic multiline signal ($S = 1/2$, see below) as well as a broad signal at $g = 4.1$ ($S = 5/2$)⁶² under certain sample conditions. Pulse EPR techniques have further advanced our understanding of the S_2 multiline state in higher plant (spinach).^{63–67} In particular, ⁵⁵Mn-ENDOR has allowed the unambiguous determination of all four ⁵⁵Mn-hyperfine tensors and has thus made it possible to probe Mn-coupling schemes, which necessarily reflect the structure of the OEC, demonstrating that (i) all four Mn are strongly coupled ($|J| > 10 \text{ cm}^{-1}$) and (ii) the most likely oxidation state of the Mn cluster in the S_2 state is $\text{Mn}^{\text{III}}(\text{Mn}^{\text{IV}})_3$,⁶⁵ consistent with XANES data (for review see ref 47).

The Sr^{2+} containing OEC, poised in the S_2 state, has been first studied in higher plant (spinach) BBY type preparations.²⁶ In these samples the Ca^{2+} is chemically removed by a low pH treatment, citric acid at pH 3,^{20,68} or by NaCl/EDTA washing.^{21,22} Supplemented Sr^{2+} then binds at the Ca^{2+} site, restoring the catalytic activity of the OEC albeit at a slower turnover rate.²⁶ The removal of Ca^{2+} and the subsequent introduction of Sr^{2+} into the Ca^{2+} site leads to a significant modification of the S_2 multiline EPR signal.²⁶ Here we use photoautotrophically grown Ca^{2+} - and Sr^{2+} - from *T. elongatus* to further refine current models of the electronic structure of the paramagnetic S_2 -state of the OEC.

2. MATERIALS AND METHODS

2.1. PSII Sample Preparation. $\text{Ca}^{2+}/\text{Sr}^{2+}$ PSII core complex preparations from WT* *T. elongatus*⁶⁹ and from a TyrD less mutant⁷⁰ were isolated as described earlier.^{27,34} Dark-adapted samples ($\sim 10 \text{ mg}$ chlorophyll/mL) containing $\sim 0.5 \text{ mM}$ phenyl-para benzoquinone (PPBQ) and $\sim 3\%$ methanol were placed in Q-band quartz tubes with 3 mm outer diameter. The S_2 -state was generated by short, white light illumination (5 s) at 200 K (dry ice/ethanol bath).

2.2. EPR Measurements. X-band CW-EPR spectra were recorded at 8.5 K using a Bruker ELEXSYS E500 X-band spectrometer equipped with an Oxford Instruments cryostat. For these measurements the Q-band tube was inserted into a X-band tube. Q-band pulse EPR and ⁵⁵Mn-Davies ENDOR measurements were performed at 4.2 K using a Bruker ELEXSYS E580 Q-band pulse EPR spectrometer equipped with an Oxford-CF935 liquid helium cryostat and an ITC-503 temperature controller. Electron spin echo-detected (ESE) field-swept spectra were measured using the pulse sequence: $\pi/2 - \tau - \pi - \tau - \text{echo}$, where $\pi = 80 \text{ ns}$ and $\tau = 440 \text{ ns}$. ⁵⁵Mn-Davies ENDOR spectra were collected using the pulse sequence: $\pi - \pi_{\text{RF}} - T - \pi/2 - \tau - \pi - \tau - \text{echo}$, where $\pi = 80 \text{ ns}$, $\tau = 440 \text{ ns}$, π_{RF} (RF pulse, radio frequency) = $3.5 \mu\text{s}$, and a delay $T = 600 \text{ ns}$. To measure hyperfine couplings in excess of 150 MHz, a home-built computer console (SpecMan control software^{63,64,71}) was used coupled to an external RF generator (SMT02 signal generator) and RF amplifier (ENI 5100 L). A shot repetition rate of $\sim 300 \text{ Hz}$ was used for all measurements.

2.3. CW-EPR/⁵⁵Mn-ENDOR Simulations. CW-EPR/⁵⁵Mn-ENDOR spectra were simultaneously fit assuming an effective spin $S = 1/2$ ground state (see Theory (section 3.2)). Calculations assumed that all tensors were colinear. The same Spin Hamiltonian was used for both CW-EPR and ⁵⁵Mn-ENDOR spectra. The electron Zeeman term was treated exactly. The nuclear Zeeman and hyperfine terms were treated using second order perturbation theory. Spectral simulations were performed numerically using Scilab-4.4.1, an open source vector-based linear algebra package (www.scilab.org) and the easyspin

package⁷² in MATLAB. A Gaussian profile was used to describe the excitation line width, with a fwhm (full width at half maximum) of 20 MHz.

2.4. Computational Details. All models considered in the present study were optimized without restrictions, both with Ca²⁺ and with Sr²⁺, using the previously benchmarked BP86 density functional^{73,74} and TZVP basis sets for all atoms.⁷⁵ The optimizations took advantage of the RI approximation with the auxiliary def2-TZV/J Coulomb fitting basis sets⁷⁶ as implemented in ORCA.⁷⁷ Increased integration grids (Grid4 in ORCA convention) and tight SCF convergence criteria were used throughout. Exchange coupling constants (J_{ij}) for all pairs of Mn centers were subsequently computed for each optimized model using the broken-symmetry DFT methodology (BS-DFT),^{78–81} assuming the isotropic Heisenberg Hamiltonian (Supporting Information eq S1). The hybrid meta-GGA TPSSH functional⁸² was used in this case, and the calculations employed the chain-of-spheres (RIJCOSX) approximation to exact exchange.⁸³ Additionally, the effect of scalar relativistic effects was tested for selected systems using the zero-order regular approximation (ZORA) in conjunction with appropriately contracted all-electron scalar relativistic (SARC) basis sets.^{84–86} Inclusion of scalar relativistic effects was not found to alter the results to any significant extent and thus was not considered further in the present study. The application of the BS-DFT approach and the performance of the TPSSH functional for the calculation of exchange coupling constants in oligonuclear manganese systems has been extensively discussed, benchmarked, and calibrated in previous studies of manganese dimers,^{87–89} trimers,⁹⁰ and tetramers.^{57,91}

3. THEORY

3.1. The Spin Hamiltonian Formalism. Here we consider an exchange coupled Mn tetramer. The current assignment for the oxidation states of the four Mn ion when poised in the S₂ state is Mn^{III}Mn^{IV}Mn^{IV}Mn^{IV}.^{47,65,92,93} This net oxidation state is assumed throughout the text. A basis set that describes the Mn-tetramer spin manifold can be built from the product of the eigenstates of the four interacting spins

$$|S_1 S_2 S_3 S_4 M_1 M_2 M_3 M_4 I_1 I_2 I_3 I_4 m_1 m_2 m_3 m_4\rangle \quad (1)$$

Here S_i refers to the electronic spin state of Mn_{*i*}, M_i refers to the electronic magnetic sublevel of Mn_{*i*}, I_i refers to the nuclear spin state of Mn_{*i*}, and m_i refers to the nuclear magnetic sublevel of Mn_{*i*}. S_i takes the value 2 for Mn^{III} and 3/2 for Mn^{IV}; M_i takes the values $S_i, S_i-1, \dots, 1-S_i, -S_i$; I_i takes the value 5/2 for ⁵⁵Mn; and m_i takes the values $-I_i, 1-I_i, \dots, I_i-1, I_i$.

The Spin Hamiltonian that describes the spin manifold of the Mn tetramer is

$$H = \sum_i \beta_e B_0 \cdot g_i \cdot S_i - \sum_i g_n \beta_n B_0 \cdot I_i + \sum_i S_i \cdot a_i \cdot I_i + \sum_i I_i \cdot q_i \cdot I_i + \sum_i S_i \cdot d_i \cdot S_i - \sum_{i < j} S_i \cdot J_{ij} \cdot S_j \quad (2)$$

It contains the following: i) an electronic Zeeman term for each Mn ion; ii) a nuclear Zeeman term for each ⁵⁵Mn nucleus; iii) a hyperfine term for each ⁵⁵Mn nucleus; iv) a quadrupole term for each ⁵⁵Mn nucleus; v) a fine structure term for each Mn ion; and vi) pairwise exchange terms for each Mn–Mn interaction.

3.2. An Effective Spin 1/2 Ground State. The tetranuclear-manganese cluster of the OEC Mn₄O_xCa(Sr), presents a daunting theoretical exercise. A basis set that describes the entire spin manifold of the coupled four Mn ions requires 414720 vectors, too many to be readily handled by current numerical techniques. The problem can be greatly simplified by assuming all Mn–Mn couplings are large, i.e. within the strong exchange

limit. For this, the exchange interactions between the Mn ions have to be significantly larger than any other term of the Spin Hamiltonian. The resultant electronic spin states of the manifold are then adequately described by a single quantum number, the total spin (S_T). The ‘multiline’ EPR signal observed for the S₂ state of the OEC is derived from only one total spin state, the ground state of the spin manifold with total spin $S_T = 1/2$. The basis set that describes this subspace requires only 2592 vectors which represent the coupling of the effective electronic spin ($S_T = 1/2$) to the nuclear spin of each Mn ($I = 5/2$) nucleus

$$\left| \frac{1}{2} M m_1 m_2 m_3 m_4 \right\rangle \quad (3)$$

Where M takes all half-integer values: $-1/2 \leq M \leq 1/2$; and m_i (where $i = 1-4$) takes all half integer values: $-5/2 \leq m_i \leq 5/2$.

The effective Spin Hamiltonian that describes the ground state of the spin manifold ($S_T = 1/2$) is

$$H = \beta_e B_0 \cdot G \cdot S + \sum_i (g_n \beta_n B_0 \cdot I_i + S \cdot A_i \cdot I_i) \quad (4)$$

It contains the following: i) the Zeeman term for the total electronic spin; ii) Zeeman terms for each ⁵⁵Mn nucleus; and iii) hyperfine terms for each ⁵⁵Mn nucleus. Quadrupole terms are neglected as they are considered to only have a small contribution to the energy levels/eigenstates of the system. A description of the connection between the two Spin Hamiltonians given above is outlined in the Supporting Information S1 and S2.

4. RESULTS

4.1. CW-EPR/ESE-Detected Field Sweep Pulse EPR. CW-EPR spectra of the Mn₄O_xCa and Mn₄O_xSr OEC poised in the S₂ state are shown in Figure 2A. In both samples a point mutation was made to replace the tyrosine Y_D (D₂-Y₁₆₀) with a phenylalanine.⁷⁰ This mutation removed from the spectrum the Y_D[•] (oxidized, radical form of Y_D) signal, which in *wild type* (*wt*) samples appears as a strong, narrow (fwhm ~3 mT) signal centered at $g \sim 2$ superimposing the central hyperfine lines of the S₂ state multiline signal.

The Mn₄O_xCa S₂ multiline signal reported here is very similar to previous literature reports.^{67,68,94–98} The signal is centered about $g \sim 2.0$, and its hyperfine pattern contains at least 22 peaks, spread over the 250–430 mT field range.⁹⁹ A ‘modified multiline’ signal is observed for the Mn₄O_xSr OEC, poised in the S₂ state. The ‘modified multiline’ is also centered at about $g \sim 2.0$, and its hyperfine pattern is spread over the same field range (250–430 mT). The hyperfine pattern of the modified multiline resolves additional peaks compared to the Ca-multiline signal, so that a total of at least 24 peaks are observed with a markedly different line-intensity distribution. The modified multiline signal reported here is very similar to the Mn₄O_xSr multiline signal seen in higher plant (spinach) BBY type preparations obtained by chemical Ca²⁺/Sr²⁺ exchange²⁶ and to an earlier study performed with *T. elongatus* grown photoautotrophically in Sr²⁺-containing medium.⁹⁴

Similar observations are seen for the pseudomodulated field sweep Q-band measurements obtained with *T. elongatus* samples containing Y_D[•] (Figure 2B). The multiline signals are both centered at approximately $g \sim 2.0$ and are spread over the same spectral range (1130–1320 mT). As at X-band, the Mn₄O_xSr OEC multiline does show more resolved hyperfine structure.

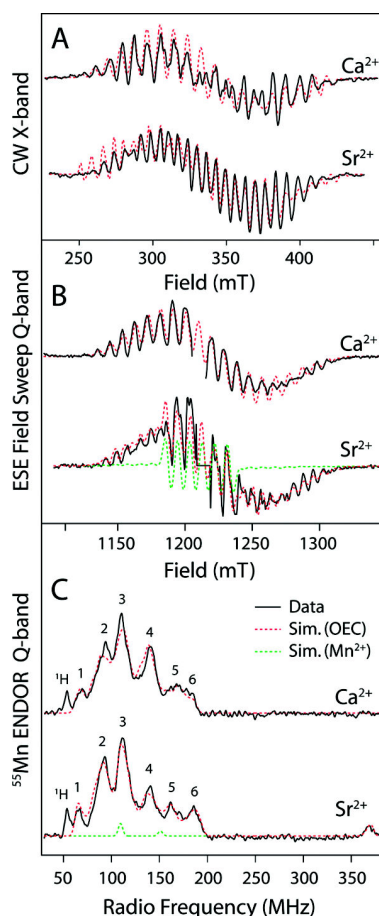


Figure 2. EPR/ENDOR spectra of the Ca^{2+} and Sr^{2+} containing OEC, poised in the S_2 state, of PS II derived from *T. elongatus* (solid black lines). **A**) CW X-band. In these samples a point mutation was made to replace the tyrosine Y_D with a phenylalanine (Y160F). Y_D^\bullet (oxidized, radical form) appears in wild type samples as a strong, narrow (fwhm ~ 3 mT) signal centered at $g \sim 2$. Experimental parameters: microwave frequencies: 9.4097 GHz (Ca), 9.4213 GHz (Sr); microwave power: 20 mW; modulation amplitude: 25 G; time constant: 80 ms, temperature: 8.6 K. **B**) Q-band pulse EPR, ESE-detected field sweep. The derivative spectra represent the pseudo modulated (2 mT) raw data. The Y_D^\bullet , centered at about $g \sim 2$, was removed for clarity of presentation. Experimental parameters: microwave frequencies: 33.6870 GHz (Ca), 33.8160 GHz (Sr); shot repetition rate: 5 μs ; microwave pulse length (τ): 80 ns, τ : 440 ns, temperature: 4.2 K. **C**) Q-band pulse ^{55}Mn -Davies ENDOR. Spectra presented were smoothed using a 5 point moving average. Experimental parameters: microwave frequencies: 34.0450 GHz (Ca), 34.0286 GHz (Sr); magnetic field: $B_0 = 1260$ mT; shot repetition rate: 5 ms; microwave pulse length (τ): 80 ns, τ : 440 ns, RF pulse (τ_{RF}): 3.5 μs . The red dashed lines superimposing each trace represent a least-squares fitting to the whole data set using a model based on the Spin Hamiltonian formalism (see Theory eq 4). The optimized parameter sets are given in Table 1. It is noted that the Sr-OEC sample contains a small contribution of free Mn^{2+} . Mn^{2+} in protein environments and in solution appears as a narrow EPR signal centered at $g \sim 2$, with 6 sharp peaks with peak-to-peak separation of 8–10 mT. In the corresponding ^{55}Mn -ENDOR experiment, three peaks are observed using the experimental conditions described above. These peaks are centered at the positions: 114, 158, and 375 MHz. The contribution of the Mn^{2+} signal is shown by the green dashed traces and is included in the OEC simulation profile shown by the red dashed traces. Simulation parameters for the Mn^{2+} artifact are given in the Supporting Information S3.

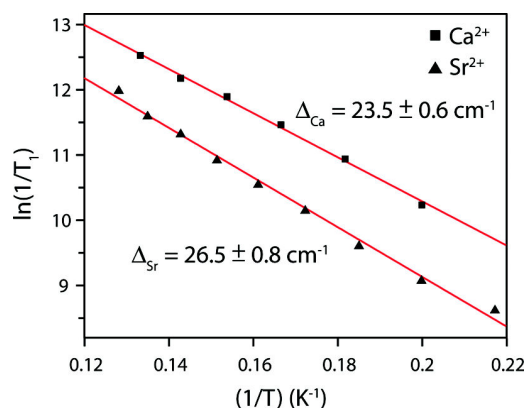


Figure 3. The temperature dependence of the T_1 relaxation time of the Ca^{2+} (■) and Sr^{2+} (▲) containing OEC in *T. elongatus*. The data are shown as the natural logarithm of the inverse of the T_1 time versus the inverse of the temperature. Electron spin echo-detected T_1 relaxation data were measured using a 3 pulse sequence: $\pi - \Delta T - \pi/2 - \tau - \pi - \tau - \text{echo}$, where $\pi = 80$ ns, $\tau = 440$ ns, and ΔT was swept over the range 0.1–10 ms. An estimate of the T_1 time was made by fitting the raw data to a biexponential decay collected at each temperature (see the Supporting Information). The superimposed red lines correspond to a linear fit of the data. The slope of each line is given in cm^{-1} . Both experiments were performed at $B_0 = 1260$ mT.

Q-band pulse spectroscopy is particularly sensitive to Mn^{2+} , and consequently a weak six-line Mn^{2+} signal is seen in the Q-band EPR spectrum of the Sr-PSII sample, which was not detectable in the corresponding X-band spectrum. The Mn^{2+} signal represents only a small fraction (<5%) of the PSII centers. It is not observed in the respective Ca^{2+} sample.

4.2. T_1 Relaxation of the $\text{Ca}^{2+}/\text{Sr}^{2+}$ Containing OEC. Previous studies of higher plant *spinach* PS II^{66,100} demonstrated that the OEC cluster in both the S_2 and S_0 oxidation states dominantly displays Orbach relaxation over the 5–10 K temperature range. As the relaxation rate of an Orbach process is dependent on the ground to first excited state energy separation, an estimate could be made for the energy ladder. Lorigan et al.⁶⁶ reported a ground to first excited state energy difference (Δ) of 35 cm^{-1} for the S_2 state, and Kulik et al.¹⁰⁰ reported $\Delta = 21.7 \text{ cm}^{-1}$ for the S_0 state. Our measurements for S_2 in the cyanobacterium *T. elongatus* yielded very similar results (Figure 3). The $\text{Mn}_4\text{O}_x\text{Ca}$ and $\text{Mn}_4\text{O}_x\text{Sr}$ OEC poised in the S_2 state show $\Delta = 23.5 \pm 0.6 \text{ cm}^{-1}$ (31.0 K^{-1}) and $\Delta = 26.5 \pm 0.8 \text{ cm}^{-1}$ (35.8 K^{-1}), respectively. These results suggest that the energy ladder and thus the Mn electronic structure of the OEC with either Ca^{2+} or Sr^{2+} present are likely to be very similar in *T. elongatus*. The relatively large energy separation between the ground and first excited state allows us to consider the system as an effective spin 1/2 state, well removed from spin states of higher spin multiplicity (see Theory 3.2). Mn^{III} and Mn^{IV} typically have zero-field splittings (ZFS) of the order of $|\sim 2 \text{ cm}^{-1}|$ and $|\sim 0.1 \text{ cm}^{-1}|$, respectively (see Supporting Information S4). Similarly, the Zeeman term at Q-band is of the order of 1 cm^{-1} . Thus the exchange terms (J_{ij}) of the Spin Hamiltonian (eq 2) dominate the total zero-field splitting of the cluster. This allows us to treat the system in the strong exchange limit. It is noted though that this is only an approximation. The onsite ZFS of the individual Mn ions will affect the electronic structure, see Discussion.

4.3. ^{55}Mn -ENDOR. Figure 2C displays Q-band ^{55}Mn -Davies ENDOR spectra of the $\text{Mn}_4\text{O}_x\text{Ca}$ and $\text{Mn}_4\text{O}_x\text{Sr}$ OEC, poised in

the S_2 -state measured at $B_0 = 1260$ mT. The line shape of the ^{55}Mn -ENDOR signal shows only a small field dependence over the 1190–1260 mT range, consistent with its assignment to the tetramanganese cluster^{64,65} (see above). The $\text{Mn}_4\text{O}_x\text{Ca}$ spectrum shown in Figure 2C is similar but not identical to that reported in the previous study of Pudollek et al.;¹⁰¹ the total ENDOR signal spans approximately the same width, but there are differences in the intensities of the individual lines. The spectra reported in Figure 2C were measured at a field position where the contribution from free or nonspecifically bound Mn^{2+} is small. Mn^{2+} signals of this type usually yield two relatively sharp lines at ~ 115 MHz and ~ 155 MHz and a third broader line at 375 MHz at all field positions across the 1190–1220 mT range. Control experiments on purposely denatured PSII samples clearly show these signals (see Figure S3 in the Supporting Information).

In contrast to the CW-X-band and field sweep ESE Q-band spectra (see Figures 2 and 3), the $\text{Mn}_4\text{O}_x\text{Ca}$ and $\text{Mn}_4\text{O}_x\text{Sr}$ OEC give rise to surprisingly similar ^{55}Mn -ENDOR spectra. No large difference is seen with regard to the total spectral breadth of the signal (60–200 MHz). The low field peak centered at ~ 52 MHz originates from the magnetic coupling of protons with the Mn cluster. Approximately six peaks are resolved for both the Ca^{2+} and Sr^{2+} containing OEC. Small changes in the line-intensity of the six peaks are observed upon $\text{Ca}^{2+}/\text{Sr}^{2+}$ replacement. It also appears that the maxima of peaks 1 and 2 downshift by approximately 10 MHz. The high frequency region clearly resolves two peaks in the Sr-containing OEC and peak 6 may upshift by ~ 5 MHz as compared to Ca^{2+} . A comparison of the ^{55}Mn -ENDOR *T. elongatus* data reported here with earlier higher plant spinach data^{63,64,67} suggests that intrinsic differences between the two species are significantly larger than the effect of $\text{Ca}^{2+}/\text{Sr}^{2+}$ replacement. The total spectral breadth of the ^{55}Mn -ENDOR spectrum is significantly larger in *T. elongatus* as compared to spinach.^{64,65} The high frequency edge is approximately 20 MHz up-shifted, and the low frequency edge decreases by approximately the same degree.

4.4. Spectral Simulations of the EPR/ENDOR data. Spectral simulations of the EPR and ENDOR spectra of the $\text{Mn}_4\text{O}_x\text{Ca}$ and $\text{Mn}_4\text{O}_x\text{Sr}$ OEC poised in the S_2 state are described in the Materials and Methods and Theory section. CW X-band EPR (9 GHz), pulse Q-band EPR (34 GHz), and Q-band ^{55}Mn -ENDOR data were simultaneously fit using a least-squares routine. Powder pattern simulations are shown in Figure 2 as red dashed lines. The simulations reported here reproduce the total spectral breadth of the X- and Q-band multiline EPR signals for both the $\text{Mn}_4\text{O}_x\text{Ca}$ and $\text{Mn}_4\text{O}_x\text{Sr}$ and all the major spectral lines.

The fitted G and hyperfine tensors (A_i) are given in Table 1. Four hyperfine tensors are required to fit the EPR absorption and first derivative lineshapes at X- and Q-band (Figure 2A, B). Near axial symmetry was obtained for the fitted hyperfine tensors in the $\text{Mn}_4\text{O}_x\text{Ca}$ simulation. With the exception of A_1 , the z component of all hyperfine tensors was the largest. The geometry and magnitude of the four hyperfine tensors are approximately the same as those determined in previous higher plant ^{55}Mn -ENDOR studies.^{65,67} Comparison of the fitted parameters obtained for the $\text{Mn}_4\text{O}_x\text{Ca}$ and $\text{Mn}_4\text{O}_x\text{Sr}$ demonstrate that only small changes occur upon $\text{Ca}^{2+}/\text{Sr}^{2+}$ replacement. Importantly, the four isotropic values ($A_{i,\text{iso}}$) of the fitted hyperfine tensors (Table 1) all approximately match for both OECs (<10% deviation) suggesting that there is no significant change in the electronic structure/coupling scheme of the $\text{Mn}_4\text{O}_x\text{Ca}/\text{Sr}$

Table 1. Principal Values of the Effective G and ^{55}Mn HFI Tensors for the Simulations of the S_2 Spectra of $\text{Mn}_4\text{O}_x\text{Ca}$ and $\text{Mn}_4\text{O}_x\text{Sr}$ OEC from *T. elongatus*^a

		G	A_i (MHz)			
			A_1	A_2	A_3	A_4
Ca^{2+}	x	1.971	350	249	202	148
	y	1.948	310	227	182	162
	\perp	1.960	330	238	192	155
	z ()	1.985	275	278	240	263
	iso	1.968	312	251	208	191
	aniso	0.025	55	−40	−48	−108
Sr^{2+}	x	1.995	343	244	200	156
	y	1.968	361	217	185	152
	\perp	1.982	352	231	193	154
	z ()	1.957	293	268	223	210
	iso	1.973	332	243	203	173
	aniso	−0.025	59	−37	−30	−56

^a The G -tensor principal values for the simulation of the S_2 spectra from $\text{Mn}_4\text{O}_x\text{Ca}$ OEC and $\text{Mn}_4\text{O}_x\text{Sr}$ were only allowed to vary by <0.05 compared to the values reported in ref 102. The isotropic G and A_i ($i = 1-4$) values are the average of the individual values: $G_{\text{iso}} = (G_x + G_y + G_z)/3$ and $A_{i,\text{iso}} = (A_{i,x} + A_{i,y} + A_{i,z})/3$. The equatorial and axial G and A_i values are defined as $G_{\perp} = (G_x + G_y)/3$, $G_{\parallel} = G_z$ and $A_{i\perp} = (A_{i,x} + A_{i,y})/2$, $A_{i\parallel} = A_{i,z}$. The anisotropy in the G and A_i values is expressed as the difference between the axial and equatorial component of the tensor.

Table 2. Experimental Spin Projections (ρ_i) for the Four Mn Centers As Estimated from the Fitted $A_{i,\text{iso}}$ Values Listed in Table 1^a

	Mn_1 ($\rho_{\text{iso}1} \text{Mn}^{\text{III}}$)	Mn_2 ($\rho_{\text{iso}2} \text{Mn}^{\text{IV}}$)	Mn_3 ($\rho_{\text{iso}3} \text{Mn}^{\text{IV}}$)	Mn_4 ($\rho_{\text{iso}4} \text{Mn}^{\text{IV}}$)
Ca^{2+}	1.39–1.89	0.99–1.34	0.82–1.11	0.75–1.02
Sr^{2+}	1.48–2.01	0.96–1.30	0.80–1.09	0.68–0.93

^a The ranges given result from the spread of the intrinsic isotropic hyperfine values reported in the literature for Mn^{III} and Mn^{IV} ions (Mn^{III} : $|a_{\text{iso}}| = 165\text{--}225$ MHz; Mn^{IV} : $|a_{\text{iso}}| = 187\text{--}253$ MHz; see Table S3 in the SI).

cluster. Instead, the change that occurs upon $\text{Ca}^{2+}/\text{Sr}^{2+}$ substitution seems to manifest itself in a decrease in hyperfine tensor anisotropy e.g. see A_3 and A_4 .

The principal values of the G -tensor were allowed to vary slightly ($< \pm 0.05$) from that reported by Teutloff et al.,¹⁰² as deduced from high field measurements (W-band) on PSII crystals. As seen for the fitted hyperfine tensors, the isotropic G_{iso} value for the $\text{Mn}_4\text{O}_x\text{Ca}$ and $\text{Mn}_4\text{O}_x\text{Sr}$ OEC is approximately the same. It is again the anisotropy of the two clusters that is perturbed when Ca^{2+} is replaced by Sr^{2+} .

4.5. Experimental Spin Projections. The projection of the total spin onto each individual Mn ion was calculated as described in the Supporting Information S1 and S2. The obtained spin projection coefficients can be considered as a measure of the contribution of each Mn to the electronic structure; a measure of the electron density on each Mn ion. Spin projections (ρ_i) for each Mn were calculated by assuming: (i) the net oxidation state of S_2 was $\text{Mn}^{\text{III}}(\text{Mn}^{\text{IV}})_3$,^{47,65,92,93,103,104} and (ii) that the effective hyperfine tensor with the largest isotropic component was associated with the only Mn^{III} in the

Table 3. Comparison of Ca²⁺/Sr²⁺–Mn and Mn–Mn Distances (Å) for the Optimized Calcium- and Strontium-Containing OEC Models (See Figure 1A–F), in the S₂ State (IV, IV, IV, III)^b

model	Ca/Sr–Mn _A	Ca/Sr–Mn _B	Ca/Sr–Mn _C	Ca/Sr–Mn _D	Mn _A –Mn _B	Mn _B –Mn _C	Mn _C –Mn _D	Mn _B –Mn _D
A-Ca ^a	3.577	3.766	3.755	3.366	3.857	2.796	2.805	2.819
A-Sr	3.610	3.802	3.796	3.400	3.862	2.798	2.805	2.820
C-Ca	4.307	3.456	5.614	4.164	2.729	2.760	2.793	3.239
C-Sr	4.397	3.531	5.691	4.231	2.728	2.763	2.792	3.231
D-Ca	3.690	3.676	4.117	3.780	2.739	2.835	2.820	3.330
D-Sr	3.748	3.743	4.108	3.868	2.724	2.833	2.817	3.334
E-Ca	4.095	3.647	3.548	3.494	2.744	2.780	2.752	3.513
E-Sr	4.152	3.685	3.564	3.580	2.746	2.785	2.756	3.510
F-Ca	3.462	3.569	3.482	3.842	2.708	2.782	2.786	3.293
F-Sr	3.518	3.611	3.535	3.902	2.713	2.786	2.787	3.303

^aMn_A–Mn_C distances for model A are 3.680 Å and 3.683 Å for Ca and Sr, respectively. ^bThe labels of the Mn atoms follow Figure 1, i.e. Mn_A, Mn_B etc.

complex. The spin center of highest multiplicity (most unpaired electrons) is expected to carry the largest spin projection. This was indirectly tested for tetranuclear Mn complexes in the recent DFT study of Pantazis et al.⁵⁷ The experimental spin projections could then be calculated by simply taking the ratio of the isotropic component of the effective hyperfine tensors (A_1 to A_4) and literature values for the intrinsic isotropic hyperfine coupling seen in monomeric Mn^{III} and Mn^{IV} complexes^{67,96,105–107} (see eq S4 in the Supporting Information S1 and S4). It is readily seen that the experimental spin projections for the Mn₄O_xCa and Mn₄O_xSr in *T. elongatus* for all four Mn ions are very similar. Only subtle changes are observed; the range of spin projection values of the Mn^{III} (associated with the hyperfine tensor A_1) upshift and one Mn^{IV} (associated with the hyperfine tensor A_4) downshift for the Mn₄O_xSr OEC relative to the Mn₄O_xCa.

4.6. DFT Calculations. DFT calculations were performed on all OEC models (S₂ state) with published coordinates (see Figure 1) to assess the effect of Ca/Sr substitution on the electronic structure of the OEC. It must be stressed from the outset that our purpose here is not to evaluate these models as candidates for the OEC or to propose improvements based on their computed structural or spectroscopic properties but strictly to identify the differences—if any—between calcium-containing and strontium-containing systems. The respective Ca²⁺ and Sr²⁺ models were fully geometry optimized, i.e. without any constraints to the inorganic core or the movement of ligating amino acids, and subsequently their electronic structure was determined employing the methods described previously.^{56,57} Accordingly, the differences observed between Ca²⁺-containing and Sr²⁺-containing structures of each model should be treated as upper-bound limits, in the sense that the protein backbone in the actual system can only be more restricted in its ability to adjust to ions of different size.

The structural variations observed upon substitution of Sr²⁺ for Ca²⁺ are uniform across all the various models considered, with differences in the optimized parameters being of the same nature and magnitude. Specifically, compared to the Ca²⁺ models, all optimized Sr–Mn distances are of the order of 0.06 Å longer compared to the corresponding Ca–Mn distances, giving the impression that the larger Sr²⁺ ion moves marginally “away” from the Mn₄O_x cluster (Table 3). These uniform changes are readily attributed to the difference in ionic radius between calcium (0.99 Å) and strontium (1.12 Å).¹⁰⁸ The same observation was made in the polarized EXAFS study of Pushkar et al.³⁵ Most significant for the present study is that in the

Table 4. Comparison of Exchange Coupling Constants (cm⁻¹) between the Mn Sites (Mn_A, Mn_B, Mn_C, Mn_D) for Ca²⁺ and Sr²⁺-Containing Models (See Figure 1A–F)

J	Mn _A - Mn _B	Mn _A - Mn _C	Mn _A - Mn _D	Mn _B - Mn _C	Mn _B - Mn _D	Mn _C - Mn _D
A-Ca	12	-13	0	57	20	46
A-Sr	11	-14	0	53	15	40
C-Ca	-90	8	0	-52	32	-81
C-Sr	-91	8	0	-55	31	-85
D-Ca	2	3	-4	-17	28	10
D-Sr	-1	3	-4	-17	28	9
E-Ca	1	4	-1	47	11	-80
E-Sr	-2	4	-1	39	12	-83
F-Ca	22	5	16	45	11	-43
F-Sr	16	6	15	37	11	-44

strontium-containing models the Mn–Mn and Mn–O distances remain essentially identical to those of the respective calcium-containing ones. Therefore, the present calculations confirm that the substitution of Ca²⁺ for Sr²⁺ does not affect the overall geometry of the Mn₄O_x cluster, regardless of the particular topology assumed.

The above observations also imply that the exchange pathways regulating the magnetic coupling between the metal centers should not be very sensitive to the substitution, and this is indeed confirmed by the computed exchange coupling constants. From the results presented in Table 4 it is readily seen that there are practically no changes in most pairwise exchange interactions, consistent with the EPR/ENDOR results presented above. Regardless of the specific core topology, only minimal shifts are to be expected in the energy levels of the spin ladder.

According to the computed exchange coupling constants (see Table 4) two of the models (C and D) yield an S = 1/2 ground state; an S = 5/2 ground state is obtained for model E, whereas models A and F are predicted to have S = 7/2 ground spin states. Note however, that very small structural perturbations to model F can confer this model a S = 1/2 ground state, as shown for a backbone constrained version of the model used in ref 57, model 11 in that study.

A final note concerns the ^{55}Mn isotropic hyperfine coupling constants (A_{iso}), which can be computed for the present OEC models that display an $S = 1/2$ ground state after unconstrained optimization (models C and D). In line with the minimal perturbations on the exchange coupling interactions, the strontium-containing systems exhibit ^{55}Mn A_{iso} values that are almost identical with those of the calcium-containing systems. Specifically, for model C the computed A_{iso} values for centers Mn_A to Mn_D change from -212 , -286 , -262 , and -413 MHz for the calcium system to -211 , -284 , -261 , and -415 MHz for the strontium system. Similarly, the corresponding A_{iso} values for model D change from -227 , -288 , -191 , and -449 MHz for the calcium system to -227 , -287 , -190 , and -451 MHz for the strontium system, respectively. We consider these minute differences to be at the limit or beyond the expected accuracy of the present theoretical methodology. These results lend additional support to the hypothesis that strontium substitution does not lead to any significant change in the electronic structure of the OEC and to the overall spin density distribution.

5. DISCUSSION

5.1. General Considerations. Historically the ‘modified multiline’ observed upon Ca^{2+} substitution with Sr^{2+} has been thought to indicate a significant change of the electronic structure of the OEC. The data presented here requires a reappraisal of this hypothesis. The $\text{Mn}_4\text{O}_x\text{Sr}$ OEC of *T. elongatus*, which exhibits the same ‘modified multiline spectra’ seen in earlier studies performed on spinach preparations, displays very similar relaxation behavior and ^{55}Mn -ENDOR data as compared to the native $\text{Mn}_4\text{O}_x\text{Ca}$ OEC. This suggests a near equivalence of the electronic structures of the OEC when either Ca^{2+} or Sr^{2+} is present and thus supports the assignment of a functional instead of a structural role for Ca^{2+} in water splitting catalysis, such as substrate water binding/delivery, for reviews see ref 109.

5.2. Fitted Spin Hamiltonian Parameters. The reasonably good simulation quality observed for the fitting of the CW EPR X-band, pulse EPR Q-band, and Q-band ^{55}Mn -ENDOR spectra for both the $\text{Mn}_4\text{O}_x\text{Ca}$ and $\text{Mn}_4\text{O}_x\text{Sr}$ poised in the S_2 state demonstrates that the effective spin Hamiltonian approach outlined in the Theory section is sound. This result is consistent with the proposed energy-level scheme as determined by T_1 relaxation data. It supports the notion that the ground (doublet) state is well resolved (separated) from states of higher spin multiplicity. The inclusion of two microwave frequencies demonstrates that the correct estimates are made for both the field dependent (Zeeman) and field independent (Hyperfine) terms and shows that the zero-field splitting of each of the Mn ions needs not to be explicitly considered in order to simulate the EPR spectra. Similarly, the approximation that collinear tensors can be assumed for all Mn ions appears reasonable. In Mn dimer complexes, the same approximation holds due to the enforced symmetry of the μ -oxo-bridge motif.^{96,105} As this is a key structural feature of the OEC,^{6,7,47} it is not surprising that the same simplification can be applied. These general results are in line with previous simulation studies of Peloquin et al.,⁶⁷ Charlot et al.,¹¹⁰ Kulik et al.,⁶⁵ Kusunoki and co-workers,^{55,111} and Zheng et al.¹⁰⁶

The changes that occur to the CW EPR and ^{55}Mn -ENDOR spectra upon Ca^{2+} replacement with Sr^{2+} can be rationalized by relatively small alterations in the effective hyperfine tensors. Only small changes are observed in the isotropic components of the

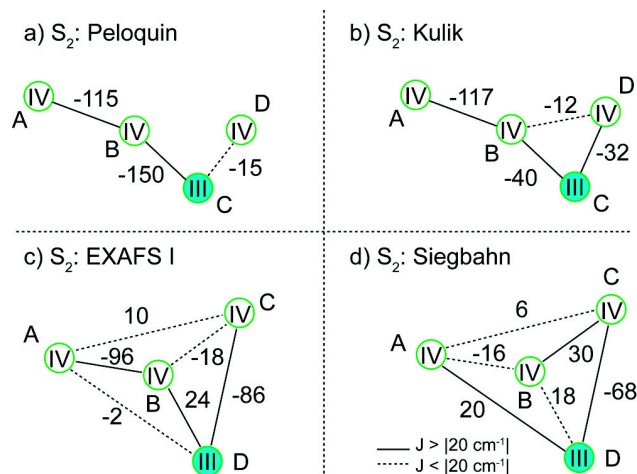


Figure 4. Current models for the electronic structure of the OEC in the S_2 state. a) The original model of Peloquin et al.;⁶⁷ b) Kulik model (Mn_C is the only Mn^{III} ion);⁶⁵ c) Pantazis model 1,⁵⁷ based on EXAFS core I;^{6,57} and d) Pantazis model 11,⁵⁷ based on the Siegbahn structure.^{11,58,59} The Peloquin, Kulik, and EXAFS I models require Mn_A to be strongly coupled to Mn_B . The Kulik, EXAFS I, and Siegbahn models require Mn_C to be strongly coupled to Mn_D . The EXAFS I and Siegbahn models differ by their connectivity of Mn_A to the trimer unit.

four hyperfine tensors. As, a consequence no significant change is seen for the onsite spin projection values, suggesting the electronic structure of the OEC (exchange pathways, distribution of oxidation states, etc.) is unaltered by $\text{Ca}^{2+}/\text{Sr}^{2+}$ exchange. The same result is seen in our DFT calculations. Instead, the change that occurs upon Ca^{2+} substitution with Sr^{2+} appears to manifest itself in the fitted hyperfine tensor anisotropy.

5.3. Current Electronic Models of the OEC. Current models of the electronic structure of the OEC, which are developed from EPR/ENDOR studies, are all based on the ‘3 + 1’ Mn tetramer topology, first proposed as possible geometric arrangement among other models by DeRose et al.¹¹² and as electronic models by Hasegawa et al.^{111,113} and subsequently by Peloquin et al.⁶⁷ (Figure 4a). The Peloquin model was further refined by Charlot et al.,¹¹⁰ Kulik et al.,⁶⁵ Britt et al.,¹¹⁴ and Carrell et al.¹¹⁵ A Y-shaped core was considered the most likely arrangement of the four Mn ions, where three of the Mn ions form a triangle unit (trimer), with the fourth Mn ion strongly coupled to one Mn ion of the triangle (Figure 4b). The position of the only Mn^{III} of the S_2 within the Y shaped core is ambiguous. Two consistent coupling schemes were developed by Kulik et al. where the Mn^{III} is assigned to either Mn_A or Mn_C . As stated in Kulik et al.,⁶⁵ Mn_A was considered the most likely candidate for the Mn^{III} ion. This preference was based on the inferred changes in the exchange coupling scheme between the S_0 and S_2 oxidation states^{65,116} and S_n state dependent changes in FTIR data.^{117–119} This is in contrast to Charlot et al.¹¹⁰ who instead favored assigning the Mn^{III} to one of the corners of the trimer (Mn_C or Mn_D). It is noted that in all models the Mn^{III} cannot be assigned to the connecting Mn_B , the corner of the triangle unit that makes the connection to the fourth outer Mn (Mn_A).

In our recent DFT study⁵⁷ we used the experimental electronic scheme discussed above, developed from higher plant EPR/ENDOR data, to screen all possible models for the state S_2 of the OEC (see Introduction) two coupling schemes based on the EXAFS core I⁶ (Figure 1C) topology and the Siegbahn

core^{11,58,59} (Figure 1 F) were identified as promising candidates for the OEC. It is noted that the Siegbahn structure was slightly modified (as compared to the structure reported in ref¹¹) to confer it a ground state of spin 1/2, see Pantazis et al.⁵⁷ The electronic coupling schemes for both models are shown in Figure 4 (c and d). These two models were selected as they (i) reproduce the correct ground state spin multiplicity ($S = 1/2$); (ii) the correct ground to first excited state energy difference (to within a factor of 2–3); and (iii) yield a spin projection coefficient of ~ 1 on all four Mn ions, consistent with the EPR/ENDOR data discussed in detail above. This is in contrast to the other models shown in Figure 1. DFT calculations for model A, based on the London structure, never reproduce a ground state $S = 1/2$, as seen for the S_2 multiline signal. Similarly, EXAFS models II and III (Figure 1 D, E), do not reproduce the correct ground to first excited state energy difference or spin projection coefficients. Model B has yet to be tested as coordinates for this model are not published.

The two preferred DFT developed exchange coupling schemes, denoted EXAFS I (Figure 1C) and Siegbahn (Figure 1F), broadly match the experimentally derived coupling scheme of Kulik et al., where Mn_C is the Mn^{III} . It is noted though that these two new models are more sophisticated, due to the inclusion of additional exchange pathways. As such, the three schemes: Kulik, EXAFS I, and Siegbahn (Figure 4 b, c, d) differ mainly in the electronic coupling of the outer Mn_A to the trimer (Mn_B, Mn_C, Mn_D) unit. The two DFT models (EXAFS I and Siegbahn) have the same Mn–O bridging pattern (see Scheme 1) but differ in the geometry around Mn_B and the ligation by amino acids. Nevertheless, they both require Mn_D to be the Mn^{III} ion, and that it has a square-pyramidal ligand field.¹²⁰ In the subsequent section we will show that the above Ca^{2+}/Sr^{2+} data obtained with *T. elongatus* core preparations provide a robust experimental test for these two models.

5.4. Ca^{2+}/Sr^{2+} Substitution – An Experimental Test of the Current Electronic Models of the OEC. The large anisotropy seen for the fitted hyperfine tensors (A_2 – A_4 ; Table 1) of both the Ca^{2+} and the Sr^{2+} OEC is outside the range seen for monomeric Mn^{IV} complexes (see Supporting Information S4). A similar observation was previously made for dimeric mixed valence $Mn^{III}Mn^{IV}$ model complexes.^{67,105,107,121} This phenomenon was interpreted as the ‘transfer of anisotropy’ from the Mn^{III} to the Mn^{IV} . More accurately though it represents a partial breakdown of the simple description of the spin system in terms of an effective spin 1/2 ground state. As outlined above (see Theory and Supporting Information S1) this description requires the ZFS of the whole cluster (i.e., exchange couplings between the four Mn) to be significantly larger than any other term of the Spin Hamiltonian. As can be seen from the coupling schemes displayed in Figure 4 this is, despite the overall good fit quality achieved with this approach, not strictly the case, as the onsite ZFS of the Mn^{III} , typically ~ 1 – 3 cm^{-1} , is of the similar order as some Mn–Mn exchange couplings (i.e., $\sim 10\text{ cm}^{-1}$). It is noted that in octahedral ligand environments the inherent symmetry of the Mn^{IV} ’s half filled $^3T_{2g}$ levels usually leads to small zero-field splittings ($|d| < 0.1\text{ cm}^{-1}$).¹⁰⁷

The effect of the onsite ZFS of the Mn^{III} ion can be taken into account in the calculation of the spin projections (see Supporting Information S1). Here, the spin projections for all four Mn ions have to be considered as tensors as opposed to scalar quantities; their magnitude is now orientationally dependent. As the Mn^{III} ion is strongly exchange coupled to the three Mn^{IV} ions, the inclusion of the intrinsic ZFS of the Mn^{III} does not only influence

the spin projection of Mn^{III} but of all four Mn ions. Thus the fitted hyperfine tensor anisotropy for the three Mn^{IV} ions in Table 1 is a measure of the onsite ZFS of the Mn^{III} . Based on this interpretation, a change in the tensor anisotropy of the hyperfine tensors between the Ca^{2+} and Sr^{2+} OECs indicates that Ca^{2+}/Sr^{2+} exchange alters the onsite ZFS of the only Mn^{III} of the OEC in the S_2 state. That is to say, Ca^{2+}/Sr^{2+} exchange perturbs the ligand environment of the Mn^{III} ion.

It is suggested that this provides a means to test the current electronic models of the OEC. From the previous sections it was shown that (i) there is virtually no change in the electronic coupling pathways (J_{ij}) when Ca^{2+} is replaced by Sr^{2+} , as the isotropic spin projections on all four Mn are very similar and (ii) there is no large structural change that occurs when Ca^{2+} is replaced by Sr^{2+} , i.e. the coordination of the Mn^{III} does not change. Within this framework we would expect that for an electronic model to be consistent it should give (i) sensible onsite ZFS values for both the Ca^{2+} and Sr^{2+} OECs. Here we will define ‘sensible’ as within the range of ZFS measured in monomeric Mn^{III} model complexes i.e. $1 < |d| < 5\text{ cm}^{-1}$ (see Supporting Information S4); and (ii) we would expect that the change of the onsite ZFS of the Mn^{III} that occurs when Ca^{2+} is replaced with Sr^{2+} would be small ($< |1|\text{ cm}^{-1}$). Typically, Mn^{III} complexes of the same type/coordination environment (e.g., porphyrins, corroles, etc.) give similar ZFS values ($\ll |1|\text{ cm}^{-1}$). A quantitative assessment of the EXAFS I and Siegbahn model is presented in section 5.4.2.

Finally it is noted that the onsite ZFS of the Mn^{III} ion, in addition to changing the effective hyperfine tensors (A_i), will also perturb the effective G tensor of the system in an analogous way. Thus it is not surprising that in the fittings of the Mn_4O_xCa and Mn_4O_xSr EPR/ENDOR data, the isotropic G tensor component is approximately the same for the two systems while the anisotropic component changes. Furthermore, the contribution of the ZFS of the Mn^{III} to the G anisotropy will depend on the frequency at which the EPR measurement is performed. This leads to, in our simplified $S = 1/2$ fit approach, an apparent frequency dependence of the G anisotropy, which may explain why we observe good agreement in terms of the frequency independent isotropic component of the G tensor in our X- and Q-band simulations as compared to the high field measurements of Teuloff et al.,¹⁰² but by contrast infer a different G anisotropy.

5.4.1. The Onsite Zero-Field Splitting (ZFS) of the Mn^{III} . The sign of the onsite ZFS of the Mn^{III} provides important information of its ligand environment. Mn^{III} ($S = 2$) is a d^4 ion, which does not usually exhibit Kramers degeneracy at zero-field.^{107,122–124} The inherent asymmetry of the valence electron configuration leads to a large Jahn–Teller distortion, due to a coupling of the electronic and nuclear motion. Spin–orbit coupling removes the degeneracy of the 5E_g energy-levels giving rise to either an $^5A_{1g}$ or $^5B_{1g}$ ground state.^{122,125} It was demonstrated in refs 125 and 126 that

i) a $^5A_{1g}$ ground state is obtained for a trigonal bipyramidal (5-coordinate) or a tetragonally compressed octahedral (6-coordinate) ligand geometry (see Figure 5). The vacant electron orbital is the d_{z^2} orbital. Spectroscopically this manifests itself as both a positive ZFS parameter (d) and yields a positive hyperfine tensor anisotropy, where the anisotropy of the hyperfine tensor is defined as the difference between the absolute values of the axial and equatorial hyperfine components ($a_{\Delta} = |a_{\parallel}| - |a_{\perp}|$), for a complete discussion see Campbell et al.¹²⁶

ii) a $^5B_{1g}$ ground state is obtained for a square-pyramidal (5-coordinate) or tetragonally elongated (6-coordinate) ligand geometry (see Figure 5). The vacant electron orbital is now

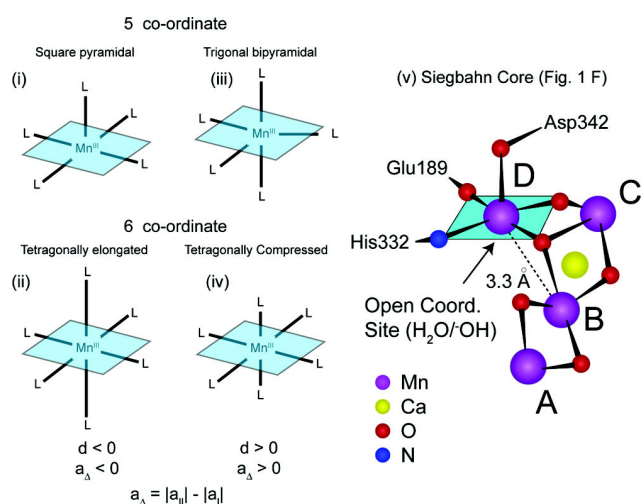


Figure 5. The coordination environment of Mn^{III} and its correlation with the sign of d , the ZFS parameter. Mn^{III} complexes that exhibit a ${}^5\text{B}_{1g}$ ground state (left side, models i, ii) display a negative d value; the vacant d-orbital is $d_{x^2-y^2}$; and the ligand environment of the Mn^{III} is either: (i) 5-coordinate square planar or (ii) 6-coordinate tetragonally elongated. Mn^{III} complexes that exhibit a ${}^5\text{A}_{1g}$ ground state (center, models iii, iv) display a positive d value; the vacant d-orbital is d_{z^2} ; and the ligand environment of the Mn^{III} is either: (iii) 5-coordinate trigonal bipyramidal or (iv) 6-coordinate tetragonally compressed. Right side (v): The ligand environment of the Mn^{III} in the Siegbahn core (Figure 1F).

the $d_{x^2-y^2}$ orbital. Spectroscopically this manifests itself as both a negative ZFS parameter (d) and yields a negative hyperfine tensor anisotropy as defined above.

This behavior was observed for monomeric Mn^{III} model complexes and mixed valence $\text{Mn}^{\text{II}}\text{Mn}^{\text{III}}$ and $\text{Mn}^{\text{III}}\text{Mn}^{\text{IV}}$ dimers (see Supporting Information S4). The only exception known is the complex *trans*- $[\text{Mn}(\text{cyclam})_2]\text{I}$,¹²⁷ which is thought to have unique, low-lying charge transfer states which strongly perturbs the ground state multiplet. Thus the sign of the onsite ZFS of the Mn^{III} (d) provides another criterion that we can use to test current OEC models. As both the EXAFS I and Siegbahn model contain a Mn^{III} that has 5 coordination, a square-pyramidal ligand field, the Mn^{III} onsite ZFS (d) value has to be negative for these models to be consistent.

5.4.2. The Onsite ZFS (d) of the Mn^{III} for the Two Selected DFT Models: EXAFS I and Siegbahn. Figure 6 displays a graphical analysis of the dependence of the spin projections and consequently the inferred onsite/intrinsic hyperfine tensors (a_i) of the individual Mn ions as a function of the Mn zero-field splitting of the Mn^{III} ion (d). The analysis presented in Figure 6 is based on the Siegbahn core exchange coupling scheme (Figure 1F and Figure 4d). A similar figure for EXAFS I model is given in the Supporting Information S5. Panel A displays the dependence of the axial and equatorial components of the spin projection tensor of each of the four Mn (A, B, C, D) ions as a function of the ZFS of the Mn^{III} . When $d = 0$, the two components are necessarily equal. It can be readily observed that the correct anisotropy of the effective hyperfine tensors of the Mn^{IV} ions can only be reproduced if the d value is negative. This yields a larger axial as opposed to equatorial spin projection component, as seen for the effective Mn^{IV} hyperfine tensors (A_2 - A_4). It is noted that while the spin projections are signed quantities, the sign cannot be extracted from the effective hyperfine tensors. As such we are only interested in the absolute magnitude of the spin projection

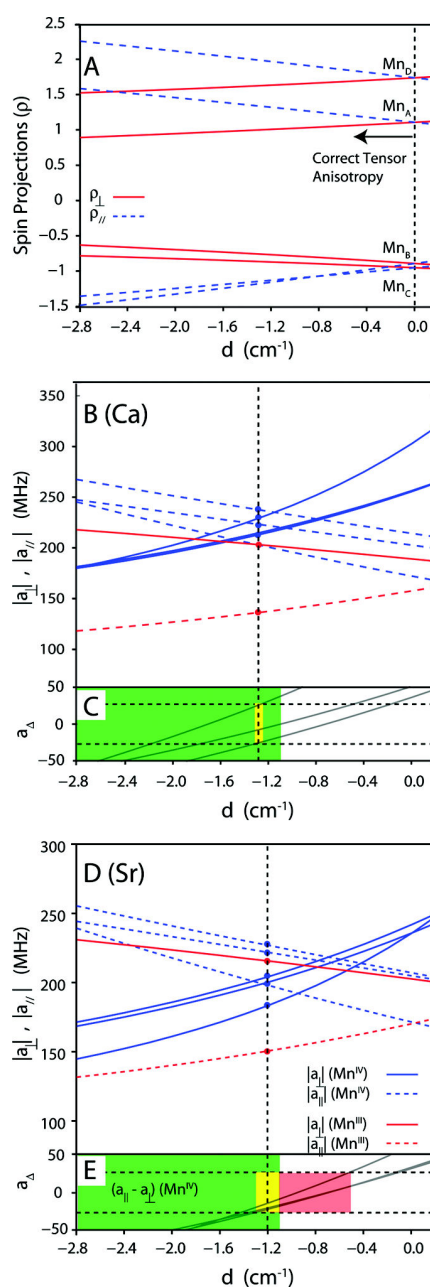


Figure 6. Panel A: The dependence of the spin projection factors (ρ_{\perp} , ρ_{\parallel}) on the zero-field splitting parameter (d) of the Mn^{III} ion assuming the exchange coupling model for the Siegbahn core (scheme Figure 1F). Panel B: The dependence of the on-site hyperfine tensor components (a_{\perp} , a_{\parallel}) of the $\text{Mn}_4\text{O}_x\text{Ca}$ cluster for each of the four manganese ions on the zero-field splitting parameter (d) of the Mn^{III} ion (see text). The bottom panel (C) shows the difference (a_{Δ}) between the parallel (a_{\parallel} or a_z) and perpendicular (a_{\perp} or a_x, a_y) hyperfine components of the three Mn^{IV} ions. The green shaded region represents the range of ZFS values for the Mn^{III} seen in model complexes (when $d < 0$). The red shaded region represents the range of acceptable ZFS values for the Mn^{III} which are consistent with the electronic model, i.e. the range over which the intrinsic hyperfine anisotropy of the Mn^{IV} ions are within the range seen for model complexes. Their intersection is shown by the yellow shaded region. Panels D and E are exactly the same as panels B and C, except that here the Sr-containing OEC was examined. Table 5 lists the intrinsic hyperfine tensor components for all four Mn ions calculated at the midpoint of the range of consistent d values i.e. the yellow shaded region.

Table 5. Calculated Spin Projection Tensor Components (ρ_{\perp} , ρ_{\parallel}) and Isotropic Hyperfine Tensor Components (a_{\perp} , a_{\parallel}) for the 4 Mn Ions of the OEC^a

(i) Siegbahn core		ρ_{\perp}	ρ_{\parallel}	a_{\perp}	a_{\parallel}	a_{iso}	a_{aniso}
Ca ²⁺	Mn _A (Mn ^{IV})	1.01	1.33	235.2	209.6	226.6	-25.6 (-8.5)
d (Mn ^{III}) = -1.32 to -1.26 cm ⁻¹	Mn _B (Mn ^{IV})	-0.77	-1.16	201.7	226.7	210.0	25.0 (8.3)
d_{midpt} = -1.29 cm ⁻¹	Mn _C (Mn ^{IV})	-0.87	-1.12	221.6	213.5	218.9	-8.0 (-2.7)
	Mn _D (Mn ^{III})	1.62	1.96	203.3	140.5	182.4	-62.8 (-20.9)
Sr ²⁺	Mn _A (Mn ^{IV})	1.02	1.31	226.9	204.0	219.3	-22.9 (-7.6)
d (Mn ^{III}) = -1.31 to -1.1 cm ⁻¹	Mn _B (Mn ^{IV})	-0.78	-1.14	198.5	183.6	193.5	-15.0 (-5.0)
d_{midpt} = -1.21 cm ⁻¹	Mn _C (Mn ^{IV})	-0.87	-1.11	221.5	200.4	214.5	-21.2 (-7.1)
	Mn _D (Mn ^{III})	1.63	1.94	216.1	150.7	194.3	-65.3 (-21.8)
(ii) EXAFS I		ρ_{\perp}	ρ_{\parallel}	a_{\perp}	a_{\parallel}	a_{iso}	a_{aniso}
Ca ²⁺	Mn _A (Mn ^{IV})	-0.75	-1.10	205.4	238.5	216.4	33.2 (11.1)
d (Mn ^{III}) = -6.8 to -5.6 cm ⁻¹	Mn _B (Mn ^{IV})	0.93	1.22	255.2	227.5	246.0	-27.7 (-9.2)
d_{midpt} = -6.2 cm ⁻¹	Mn _C (Mn ^{IV})	-0.86	-1.27	222.7	189.2	211.5	-33.4 (-11.1)
	Mn _D (Mn ^{III})	1.68	2.15	195.9	128.0	173.3	-67.9 (-22.6)
Sr ²⁺	Mn _A (Mn ^{IV})	-0.80	-1.00	193.0	209.3	198.4	16.3 (5.4)
d (Mn ^{III}) = -4.4 to -2.8 cm ⁻¹	Mn _B (Mn ^{IV})	0.97	1.14	238.5	235.2	237.4	-3.3 (-1.1)
d_{midpt} = -3.6 cm ⁻¹	Mn _C (Mn ^{IV})	-0.91	-1.15	211.4	193.7	205.5	-17.8 (-5.9)
	Mn _D (Mn ^{III})	1.74	2.01	202.0	145.4	183.1	-56.7 (-18.9)

^a The isotropic a_i values are defined as $a_{i,\text{iso}} = (2a_{i\perp} + a_{i\parallel})/3$. The anisotropy $a_{i,\text{aniso}}$ is expressed as the difference between the axial and equatorial component of the tensor. For direct comparison to the work of Peloquin et al.⁶⁷ the anisotropy is also expressed in terms of a_{aniso} described above, divided by three (see value in brackets).

components and not their signed magnitude. The onsite/intrinsic axial and equatorial hyperfine tensor components (a_{\parallel} , a_{\perp}) can be calculated from the spin projection components seen in panel A (ρ_{\parallel} , ρ_{\perp}), and the fitted effective hyperfine tensor components (A_{\parallel} , A_{\perp}) based on eq S4. Their dependence on the choice of the ZFS of the Mn^{III} ion is shown in Figure 6 panels B, C (Mn₄O_xCa) and panels D, E (Mn₄O_xSr).

(i) *Siegbahn Core*. The inferred ZFS of the Mn^{III} ion for the Siegbahn core is ~ -1.3 cm⁻¹, for the Ca²⁺ containing OEC. This value is small for a Mn^{III} ion, falling just inside the range of d values seen in model complexes i.e. $1 < |d| < 5$ cm⁻¹ (see Supporting Information S4). The range of consistent ZFS values for the Mn^{III} in the Sr²⁺ containing OEC is broader and shifting to lower $|d|$. Intrinsic hyperfine parameters were calculated at the midpoint of the range of consistent d values, i.e. the yellow shaded region shown in Figure 6 (see figure caption) for both the Ca²⁺ and Sr²⁺ containing OEC (see Table 5). It is readily observed that only a small change in the d value (<0.1 cm⁻¹) of the Mn^{III} results in very similar intrinsic hyperfine tensors for all four Mn, i.e. the same intrinsic hyperfine parameters can be generated from the Ca²⁺ and Sr²⁺ EPR/ENDOR parameter sets by adjusting the ZFS of the Mn^{III} by <0.1 cm⁻¹. Thus the Siegbahn core is consistent with the two criteria described at the end of section 5.4: (i) the model gives sensible onsite ZFS values for both the Ca²⁺ and Sr²⁺ OECs and (ii) the change of the onsite ZFS of the Mn^{III} that occurs when Ca²⁺ is replaced with Sr²⁺ must be small.

It is also noted that the d value is negative and the intrinsic parameters for the Mn^{III} are as follows: $a_{\text{iso}} \sim 182$ MHz, $a_{\perp} \sim 203$ MHz, $a_{\parallel} \sim 1491$ MHz, $a_{\text{aniso}} \sim 63$ MHz. These values are consistent with a Mn^{III} with a square-pyramidal ligand field (see section 5.4.1), that is to say, with the co-ordination sphere seen for the Mn^{III} in the Siegbahn core (Figure 5v).

(ii) *EXAFS Core I*. Unlike the Siegbahn model, there is no consistent range for the ZFS for the Mn^{III} ion for the Ca²⁺

containing OEC, i.e. there is no range of ZFS values for the Mn^{III} where the intrinsic hyperfine tensor anisotropy for all three Mn^{IV} hyperfine tensors are simultaneously within the range seen for model Mn^{IV} complexes, (see Supporting Information S4 and S5). Furthermore, if we consider the solution space just outside the range seen for model complexes, we find that the predicted range of ZFS for the Mn^{III} is very large, -6.8 cm⁻¹ to -5.6 cm⁻¹. These values are outside the range seen for Mn^{III} model complexes. We also note that the inferred change in the ZFS of the Mn^{III} when Ca²⁺ is replaced by Sr²⁺ is also large, $\sim |2|$ cm⁻¹ range. These observations do not fulfill the two criteria introduced in section 5.4 and thus suggest the EXAFS I model is inconsistent with the EPR/ENDOR data presented here, in its current construction.

Thus from the currently available DFT models with published coordinates only the Siegbahn model is found in our EPR/ENDOR analysis to be consistent with model complex data (see Supporting Information S4). This consistency between proposed structure and calculated and measured EPR/ENDOR parameters further supports the oxidation state model used in the above analysis, i.e. S₂ contains three Mn^{IV} and one Mn^{III} and that the assignment that Mn_D is the only Mn^{III} ion in the S₂ state. The above conclusions about the geometry of the Mn^{III} site also agrees with i) the original ⁵⁵Mn-ENDOR analysis of Peloquin et al., which was performed on higher plant spinach data employing the simpler coupling topology shown in Figure 4a, and ii) recent DFT calculations by Schinzel et al.¹²⁸

5.5. The Physical Nature of the Ca/Sr Effect – The Near-Infrared Absorption Band. The Siegbahn core assigns the position of the only Mn^{III} in the S₂ state to within the distorted cuboidal Mn₃O₃Ca element; the Mn^{III} has a μ -oxo linkage to the Ca²⁺/Sr²⁺ site. Experimental evidence from EXAFS suggests the Ca²⁺/Sr²⁺ substitution leads to a small elongation of the Mn–Sr distance of the order of ~ 0.1 Å.³⁵ DFT calculations on the Siegbahn structure above, where the Ca was replaced by the Sr,

reproduced the same result; the Mn–Ca/Sr distance lengthens by 0.03–0.09 Å when Ca^{2+} is replaced by Sr^{2+} . Thus Sr substitution in this model should indeed modify the co-ordination sphere of the Mn^{III} ion. It is this change that could presumably lead to a decrease in the Mn^{III} zero-field splitting parameter d and, as shown above, consequently to the ‘modified multiline’ EPR signal.

Consistent with this interpretation is the known effect of Ca/Sr substitution on the sensitivity of the OEC to near-infrared (NIR) light. The native OEC poised in the S_2 state is sensitive to NIR light under certain conditions.^{94,129} NIR can induce a conformational change that converts the $S_T = 1/2$ multiline state into a high spin species ($S_T \geq 5/2$), with a broad EPR resonance at $g = 4.1$ in spinach¹²⁹ and higher g -values in cyanobacteria preparations.⁹⁴ It is interesting to note that the spin state of the natural $\text{Mn}_4\text{O}_x\text{Ca}$ cluster is quite sensitive, and signals with $S_T = 1/2$, $5/2$ and $7/2$ have been observed depending on species, alcohol additions, and cryoprotectant conditions.^{94,130–134} It is expected that the absorption characteristics of the NIR bands of the OEC in the S_2 state will be strongly dependent on the Mn^{III} ion; as Mn^{III} model complexes can exhibit strong d-d transitions in this wavelength region. Ca^{2+} substitution with Sr^{2+} enhances the sensitivity of the OEC toward NIR light, suggesting the Mn^{III} NIR absorption profile has been in some way perturbed. Changes of the ZFS of the Mn^{III} of the order of $\sim 0.1 \text{ cm}^{-1}$, as inferred from our above EPR/ENDOR analysis could sufficiently shift the absorption(s) or change the extinction coefficient(s) of the Mn^{III} ion and thus explain the enhancement of the conversion of the multiline signal to the $g = 4.1$ signal in the S_2 state.

CONCLUSIONS

The multifrequency EPR and ENDOR analysis presented above demonstrates that Ca^{2+} replacement with Sr^{2+} does not significantly alter the overall electronic structure of the OEC. The spin density distribution across the tetramanganese cluster does not change significantly as estimated from the isotropic component of the four fitted hyperfine tensors. This result is consistent with structural data (EXAFS) which demonstrated that only small elongations in Mn–Ca/Sr distances are observed in the $\text{Mn}_4\text{O}_x\text{Sr}$ cluster, and with DFT calculations presented here that show that Sr does not significantly alter Mn–Mn distances and the exchange coupling pathways of the Mn_4O_x complex. The effect of Ca/Sr substitution on the electronic structure of the OEC is interpreted as a small modification to the ZFS of the Mn^{III} ion, which is shown to have a 5-coordinate square-bipyramidal or 6-coordinate tetragonally elongated ligand field. The presented EPR/ENDOR data are consistent with only one current structural model of the OEC, namely the Siegbahn core. Within this model the only Mn^{III} of the S_2 state is structurally coupled to the Ca/Sr ion via a μ -oxo or μ -hydroxo bridge.

The $\text{Mn}_4\text{O}_x\text{Ca}$ core topology of the Siegbahn model is such that it contains, like EXAFS models I–III (Figure 1 C–E), three short Mn–Mn distances, and one long (3.3 Å) Mn–Mn distance. The long Mn–Mn distance is inside a distorted cuboidal structure and forms its open site. The missing ‘corner oxygen’ leads to a 5-coordinate, square-pyramidal ligation for the Mn_D^{III} ion in the S_2 state. Assuming that a substrate ‘water’ (H_2O , OH^-) binds to this open coordination site of Mn_D during the $S_2 \rightarrow S_3$ transition (either from bulk water or water bound to Ca^{2+}) or that it is already very weakly bound in the S_2 state (tetragonally elongated coordination site), the 3.3 Å

Mn–Mn distance could provide an ideal geometry for low energy barrier O–O bond formation during the $S_3 \rightarrow S_4 \rightarrow S_0$ transition.^{11,56,65,135,136}

ASSOCIATED CONTENT

S Supporting Information. Additional material detailing spin projection calculations, collated data on model Mn^{III} and Mn^{IV} complexes, and additional graphs that show the effect of the ZFS of the Mn^{III} for all literature models with a spin 1/2 ground state. This material is available free of charge via the Internet at <http://pubs.acs.org>.

AUTHOR INFORMATION

Corresponding Author

*Phone: +49-208-306-3865. E-mail: cox@mpi-muelheim.mpg.de (N.C.). Phone: +46-90-7865933. E-mail: johannes.messinger@chem.umu.se (J.M.). Phone: +49-208-306-3614. E-mail: lubit@mpi-muelheim.mpg.de (W.L.).

ACKNOWLEDGMENT

Financial support was provided by the DFG (Me1629/2-4), the Max Planck Gesellschaft, the JSPS and CNRS under the Japan-France Research Cooperative Program, the EU/Energy Network project SOLAR-H2 (FP7 contract 212508), Vetenskapsrådet, the Wallenberg and Kempe foundations (J.M.). J.S. acknowledges the support of Dept. of Modern Physics, University of Science and Technology of China. L.R. is a fellow of North Rhine-Westphalia (NRW) Research School BioStruct program.

REFERENCES

- (1) Zouni, A.; Witt, H.-T.; Kern, J.; Fromme, P.; Krauss, N.; Saenger, W.; Orth, P. *Nature* **2001**, *409*, 739–743.
- (2) Kamiya, N.; Shen, J.-R. *Proc. Natl. Acad. Sci. U.S.A.* **2003**, *100*, 98–103.
- (3) Ferreira, K. N.; Iverson, T. M.; Maghlaoui, K.; Barber, J.; Iwata, S. *Science* **2004**, *303*, 1831–1838.
- (4) Loll, B.; Kern, J.; Saenger, W.; Zouni, A.; Biesiadka, J. *Nature* **2005**, *438*, 1040–1044.
- (5) Guskov, A.; Kern, J.; Gabdulkhakov, A.; Broser, M.; Zouni, A.; Saenger, W. *Nat. Struct. Mol. Biol.* **2009**, *16*, 334–342.
- (6) Yano, J.; Kern, J.; Sauer, K.; Latimer, M. J.; Pushkar, Y.; Biesiadka, J.; Loll, B.; Saenger, W.; Messinger, J.; Zouni, A.; Yachandra, V. K. *Science* **2006**, *314*, 821–825.
- (7) Pushkar, Y.; Yano, J.; Glatzel, P.; Messinger, J.; Lewis, A.; Sauer, K.; Bergmann, U.; Yachandra, V. K. *J. Biol. Chem.* **2007**, *282*, 7198–7208.
- (8) Lubitz, W.; Reijerse, E. J.; Messinger, J. *Energy Environ. Sci.* **2008**, *1*, 15–31.
- (9) Messinger, J.; Renger, G. In *Primary Processes of Photosynthesis - Part 2: Basic Principles and Apparatus*; Renger, G., Ed.; Royal Society of Chemistry: Cambridge, 2008; pp 291–349.
- (10) Hillier, W.; Messinger, J. *Mechanism of photosynthetic oxygen production*; Springer, 2005; Vol. 1.
- (11) Siegbahn, P. E. M. *Acc. Chem. Res.* **2009**, *42*, 1871–1880.
- (12) Dasgupta, J.; van Willigen, R. T.; Dismukes, G. C. *Phys. Chem. Chem. Phys.* **2004**, *6*, 4793–4802.
- (13) Dau, H.; Zaharieva, I. *Acc. Chem. Res.* **2009**, *42*, 1861–1870.
- (14) McEvoy, J. P.; Brudvig, G. W. *Chem. Rev.* **2006**, *106*, 4455–4483.
- (15) Tommos, C.; Babcock, G. T. *Acc. Chem. Res.* **1998**, *31*, 18–25.
- (16) Åhrling, K.; Pace, R. J.; Evans, M. C. W. *The catalytic Manganese Cluster: Implications from Spectroscopy*; Springer, 2005; Vol. 1.

- (17) Nelson, N.; Yocum, C. F. *Annu. Rev. Plant Biol.* **2006**, *57*, 521–565.
- (18) Renger, G.; Renger, T. *Photosynth. Res.* **2008**, *98*, 53–80.
- (19) Kok, B.; Forbush, B.; McGloin, M. *Photochem. Photobiol.* **1970**, *11*, 457–475.
- (20) Ono, T.-A.; Inoue, Y. *FEBS Lett.* **1988**, *227*, 147–152.
- (21) Boussac, A.; Zimmermann, J.-L.; Rutherford, A. W. *Biochemistry* **1989**, *28*, 8984–8989.
- (22) Boussac, A.; Zimmermann, J.-L.; Rutherford, A. W. *FEBS Lett.* **1990**, *277*, 69–74.
- (23) Ghanotakis, D. F.; Babcock, G. T.; Yocum, C. F. *FEBS Lett.* **1984**, *167*, 127–130.
- (24) Sandusky, P. O.; Yocum, C. F. *Biochim. Biophys. Acta* **1984**, *766*, 603–611.
- (25) Sandusky, P. O.; Yocum, C. F. *Biochim. Biophys. Acta* **1986**, *849*, 85–93.
- (26) Boussac, A.; Rutherford, A. W. *Biochemistry* **1988**, *27*, 3476–3483.
- (27) Boussac, A.; Rappaport, F.; Carrier, P.; Verbavatz, J. M.; Gobin, R.; Kirilovsky, D.; Rutherford, A. W.; Sugiura, M. *J. Biol. Chem.* **2004**, *279*, 22809–22819.
- (28) Vrettos, J. S.; Stone, D. A.; Brudvig, G. W. *Biochemistry* **2001**, *40*, 7937–7945.
- (29) Messinger, J.; Badger, M.; Wydrzynski, T. *Proc. Natl. Acad. Sci. U.S.A.* **1995**, *92*, 3209–3213.
- (30) Beckmann, K.; Messinger, J.; Badger, M. R.; Wydrzynski, T.; Hillier, W. *Photosynth. Res.* **2009**, *102*, 511–522.
- (31) Hendry, G.; Wydrzynski, T. *Biochemistry* **2003**, *42*, 6209–6217.
- (32) Hillier, W.; McConnell, I.; Singh, S.; Debus, R.; Boussac, A.; Wydrzynski, T. *Photosynthesis. Energy from the Sun* **2008**, 427–430.
- (33) Kargul, J.; Maghlaoui, K.; Murray, J. W.; Deak, Z.; Boussac, A.; Rutherford, A. W.; Vass, I.; Barber, J. *Biochim. Biophys. Acta* **2007**, *1767*, 404–413.
- (34) Ishida, N.; Sugiura, M.; Rappaport, F.; Lai, T. L.; Rutherford, A. W.; Boussac, A. *J. Biol. Chem.* **2008**, *283*, 13330–13340.
- (35) Pushkar, Y. L.; Yano, J.; Sauer, K.; Boussac, A.; Yachandra, V. K. *Proc. Natl. Acad. Sci.* **2008**, *105*, 1879–1884.
- (36) Latimer, M. J.; DeRose, V. J.; Mukerji, I.; Yachandra, V. K.; Sauer, K.; Klein, M. P. *Biochemistry* **1995**, *34*, 10898–10909.
- (37) Latimer, M. J.; DeRose, V. J.; Yachandra, V. K.; Sauer, K.; Klein, M. P. *J. Phys. Chem. B* **1998**, *102*, 8257–8265.
- (38) Cinco, R. M.; McFarlane Holman, K. L.; Robblee, J. H.; Yano, J.; Pizarro, S. A.; Bellacchio, E.; Sauer, K.; Yachandra, V. K. *Biochemistry* **2002**, *41*, 12928–12933.
- (39) Cinco, R. M.; Robblee, J. H.; Rompel, A.; Fernandez, C.; Yachandra, V. K.; Sauer, K.; Klein, M. P. *J. Phys. Chem. B* **1998**, *102*, 8248–8256.
- (40) Robblee, J. H.; Cinco, R. M.; Yachandra, V. K. *Biochim. Biophys. Acta* **2001**, *1503*, 7–23.
- (41) Cinco, R. M.; Robblee, J. H.; Messinger, J.; Fernandez, C.; McFarlane Holman, K. L. M.; Sauer, K.; Yachandra, V. K. *Biochemistry* **2004**, *43*, 13271–13282.
- (42) A new crystal structure was recently disclosed by Jian-Ren Shen (Okayama University, Japan) at the 15th International Congress of Photosynthesis. This new structure has yet to be published and, as such, is not explicitly considered in this manuscript. It is noted that the structure of the OEC reported is most similar to the Siegbahn structure (Figure 1 F).
- (43) Sproviero, E. M.; Gascón, J. A.; McEvoy, J. P.; Brudvig, G. W.; Batista, V. S. *J. Chem. Theory Comput.* **2006**, *2*, 1119–1134.
- (44) Sproviero, E. M.; Gascón, J. A.; McEvoy, J. P.; Brudvig, G. W.; Batista, V. S. *J. Am. Chem. Soc.* **2008**, *130*, 6728–6730.
- (45) Sproviero, E. M.; Gascón, J. A.; McEvoy, J. P.; Brudvig, G. W.; Batista, V. S. *Curr. Opin. Struct. Biol.* **2007**, *17*, 173–180.
- (46) Yachandra, V.; DeRose, V.; Latimer, M.; Mukerji, I.; Sauer, K.; Klein, M. *Science* **1993**, *260*, 675–679.
- (47) Yachandra, V. K.; Sauer, K.; Klein, M. P. *Chem. Rev.* **1996**, *96*, 2927–2950.
- (48) Robblee, J. H.; Messinger, J.; Cinco, R. M.; McFarlane, K. L.; Fernandez, C.; Pizarro, S. A.; Sauer, K.; Yachandra, V. K. *J. Am. Chem. Soc.* **2002**, *124*, 7459–7471.
- (49) Murray, J. W.; Maghlaoui, K.; Kargul, J.; Ishida, N.; Lai, T.-L.; Rutherford, A. W.; Sugiura, M.; Boussac, A.; Barber, J. *Energy Environ. Sci.* **2008**, *1*, 161–166.
- (50) van Gorkom, H. J.; Yocum, C. F. *The calcium and chloride cofactors*; Springer, 2005; Vol. 1.
- (51) Kawakami, K.; Umena, Y.; Kamiya, N.; Shen, J. R. *Proc. Natl. Acad. Sci. U.S.A.* **2009**, *106*, 8567–8572.
- (52) Haumann, M.; Barra, M.; Loja, P.; Löscher, S.; Krivanek, R.; Grundmeier, A.; Andreassen, L. E.; Dau, H. *Biochemistry* **2006**, *45*, 13101–13107.
- (53) Petrie, S.; Stranger, R.; Gatt, P.; Pace, R. J. *Chem.—Eur. J.* **2007**, *13*, 5082–5089.
- (54) Petrie, S.; Stranger, R.; Pace, R. J. *Chem.—Eur. J.* **2008**, *14*, 5482–5494.
- (55) Kusunoki, M. *Biochim. Biophys. Acta* **2007**, *1767*, 484–492.
- (56) Zein, S.; Kulik, L. V.; Yano, J.; Kern, J.; Pushkar, Y.; Zouni, A.; Yachandra, V. K.; Lubitz, W.; Neese, F.; Messinger, J. *Philos. Trans. R. Soc.* **2008**, *363*, 1167–1177.
- (57) Pantazis, D. A.; Orio, M.; Petrenko, T.; Zein, S.; Lubitz, W.; Messinger, J.; Neese, F. *Phys. Chem. Chem. Phys.* **2009**, *11*, 6788–6798.
- (58) Siegbahn, P. E. M. *Chem.—Eur. J.* **2008**, *14*, 8290–8302.
- (59) Siegbahn, P. E. M. *J. Am. Chem. Soc.* **2009**, *131*, 18238–18239.
- (60) Dau, H.; Grundmeier, A.; Loja, P.; Haumann, M. *Philos. Trans. R. Soc., B* **2008**, *363*, 1237–1244.
- (61) Dau, H.; Haumann, M. *Coord. Chem. Rev.* **2008**, *252*, 273–295.
- (62) Horner, O.; Rivière, E.; Blondin, G.; Un, S.; Rutherford, A. W.; Girerd, J.-J.; Boussac, A. *J. Am. Chem. Soc.* **1998**, *120*, 7924–7928.
- (63) Kulik, L.; Epel, B.; Messinger, J.; Lubitz, W. *Photosynth. Res.* **2005**, *84*, 347–353.
- (64) Kulik, L. V.; Epel, B.; Lubitz, W.; Messinger, J. *J. Am. Chem. Soc.* **2005**, *127*, 2392–2393.
- (65) Kulik, L. V.; Epel, B.; Lubitz, W.; Messinger, J. *J. Am. Chem. Soc.* **2007**, *129*, 13421–13435.
- (66) Lorigan, G. A.; Britt, R. D. *Biochemistry* **1994**, *33*, 12072–12076.
- (67) Peloquin, J. M.; Campbell, K. A.; Randall, D. W.; Evanchik, M. A.; Pecoraro, V. L.; Armstrong, W. H.; Britt, R. D. *J. Am. Chem. Soc.* **2000**, *122*, 10926–10942.
- (68) Sivaraja, M.; Tso, J.; Dismukes, G. C. *Biochemistry* **1989**, *28*, 9459–9464.
- (69) Sugiura, M.; Boussac, A.; Noguchi, T.; Rappaport, F. *Biochim. Biophys. Acta* **2008**, *1777*, 331–342.
- (70) Sugiura, M.; Rappaport, F.; Brettel, K.; Noguchi, T.; Rutherford, A. W.; Boussac, A. *Biochemistry* **2004**, *43*, 13549–13563.
- (71) Epel, B.; Gromov, I.; Stoll, S.; Schweiger, A.; Goldfarb, D. *Concepts Magn. Reson., Part B* **2005**, *26B*, 36–45.
- (72) Stoll, S.; Schweiger, A. *J. Magn. Reson.* **2006**, *178*, 42–55.
- (73) Becke, A. D. *Phys. Rev. A* **1988**, *38*, 3098–3100.
- (74) Perdew, J. P. *Phys. Rev. B* **1986**, *33*, 8822–8824.
- (75) Schäfer, A.; Huber, C.; Ahlrichs, R. *J. Chem. Phys.* **1994**, *100*, 5829–5835.
- (76) Weigend, F. *Phys. Chem. Chem. Phys.* **2006**, *8*, 1057–1065.
- (77) Neese, F. Universität Bonn: Bonn, Germany, 2007.
- (78) Noodleman, L. *J. Chem. Phys.* **1981**, *74*, 5737–5743.
- (79) Noodleman, L.; Case, D. A. *Adv. Inorg. Chem.* **1992**, *38*, 423–470.
- (80) Noodleman, L.; Davidson, E. R. *Chem. Phys.* **1986**, *109*, 131–143.
- (81) Neese, F. *Coord. Chem. Rev.* **2009**, *253*, 526–563.
- (82) Staroverov, V. N.; Scuseria, G. E.; Tao, J.; Perdew, J. P. *J. Chem. Phys.* **2003**, *119*, 12129–12137.
- (83) Neese, F.; Wennmohs, F.; Hansen, A.; Becker, U. *Chem. Phys.* **2009**, *356*, 98–109.
- (84) van Wüllen, C. *J. Chem. Phys.* **1998**, *109*, 392–399.
- (85) van Lenthe, E.; Snijders, J. G.; Baerends, E. J. *J. Chem. Phys.* **1996**, *105*, 6505–6516.

- (86) Pantazis, D. A.; Chen, X. Y.; Landis, C. R.; Neese, F. *J. Chem. Theory Comput.* **2008**, *4*, 908–919.
- (87) Sinnecker, S.; Neese, F.; Noodleman, L.; Lubitz, W. *J. Am. Chem. Soc.* **2004**, *126*, 2613–2622.
- (88) Orio, M.; Pantazis, D. A.; Petrenko, T.; Neese, F. *Inorg. Chem.* **2009**, *48*, 7251–7260.
- (89) Pantazis, D. A.; Krewald, V.; Orio, M.; Neese, F. *Dalton Trans.* **2010**, *39*, 4959–4967.
- (90) Baffert, C.; Orio, M.; Pantazis, D. A.; Duboc, C.; Blackman, A. G.; Blondin, G.; Neese, F.; Deronzier, A.; Collomb, M.-N. *Inorg. Chem.* **2009**, *48*, 10281–10288.
- (91) Pantazis, D. A.; Orio, M.; Petrenko, T.; Zein, S.; Bill, E.; Lubitz, W.; Messinger, J.; Neese, F. *Chem.—Eur. J.* **2009**, *15*, 5108–5123.
- (92) Messinger, J.; Robblee, J. H.; Bergmann, U.; Fernandez, C.; Glatzel, P.; Visser, H.; Cinco, R. M.; McFarlane, K. L.; Bellacchio, E.; Pizarro, S. A.; Cramer, S. P.; Sauer, K.; Klein, M. P.; Yachandra, V. K. *J. Am. Chem. Soc.* **2001**, *123*, 7804–7820.
- (93) Haumann, M.; Müller, C.; Liebisch, P.; Iuzzolino, L.; Dittmer, J.; Grabolle, M.; Neisius, T.; Meyer-Klaucke, W.; Dau, H. *Biochemistry* **2005**, *44*, 1894–1908.
- (94) Boussac, A.; Sugiura, M.; Inoue, Y.; Rutherford, A. W. *Biochemistry* **2000**, *39*, 13788–13799.
- (95) Beck, W. F.; de Paula, J. C.; Brudvig, G. W. *J. Am. Chem. Soc.* **1986**, *108*, 4018–4022.
- (96) Randall, D. W.; Sturgeon, B. E.; Ball, J. A.; Lorigan, G. A.; Chan, M. K.; Klein, M. P.; Armstrong, W. H.; Britt, R. D. *J. Am. Chem. Soc.* **1995**, *117*, 11780–11789.
- (97) Tso, J.; Sivaraja, M.; Dismukes, G. C. *Biochemistry* **1991**, *30*, 4734–4739.
- (98) Boussac, A.; Rutherford, A. W.; Styring, S. *Biochemistry* **1990**, *29*, 24–32.
- (99) Boussac, A.; Kuhl, H.; Ghibaudi, E.; Rögner, M.; Rutherford, A. W. *Biochemistry* **1999**, *38*, 11942–11948.
- (100) Kulik, L. V.; Lubitz, W.; Messinger, J. *Biochemistry* **2005**, *44*, 9368–9374.
- (101) Pudollek, S.; Lenzian, F.; Bittl, R. *Biochem. Soc. Trans.* **2008**, *36*, 1001–1004.
- (102) Teutloff, C.; Kessen, S.; Kern, J.; Zouni, A.; Bittl, R. *FEBS Lett.* **2006**, *580*, 3605–3609.
- (103) Bergmann, U.; Grush, M. M.; Horne, C. R.; DeMarois, P.; Penner-Hahn, J. E.; Yocum, C. F.; Wright, D. W.; Dubé, Armstrong, W. H.; Christou, G.; Eppley, H. J.; Cramer, S. P. *J. Phys. Chem. B* **1998**, *102*, 8350–8352.
- (104) Roelofs, T. A.; Liang, W.; Latimer, M. J.; Cinco, R. M.; Rompel, A.; Andrews, J. C.; Sauer, K.; Yachandra, V. K.; Klein, M. P. *Proc. Natl. Acad. Sci. U.S.A.* **1996**, *93*, 3335–3340.
- (105) Schäfer, K. O.; Bittl, R.; Zweggart, W.; Lenzian, F.; Haselhorst, G.; Weyhermüller, T.; Wieghardt, K.; Lubitz, W. *J. Am. Chem. Soc.* **1998**, *120*, 13104–13120.
- (106) Zheng, M.; Dismukes, G. C. *Inorg. Chem.* **1996**, *35*, 3307–3319.
- (107) Zheng, M.; Khangulov, S. V.; Dismukes, G. C.; Barynin, V. V. *Inorg. Chem.* **1994**, *33*, 382–387.
- (108) Wiberg, E.; Hollerman, A. F.; Wiberg, N. *Lehrbuch der Anorganischen Chemie*; Walter de Gruyter GmbH & Co: Berlin, 2009.
- (109) Yocum, C. F. *Coord. Chem. Rev.* **2008**, *252*, 296–305.
- (110) Charlot, M.-F.; Boussac, A.; Blondin, G. *Biochim. Biophys. Acta* **2005**, *1708*, 120–132.
- (111) Hasegawa, K.; Ono, T. A.; Kusunoki, M. *Bull. Chem. Soc. Jpn.* **1999**, *72*, 1013–1023.
- (112) DeRose, V. J.; Mukerji, I.; Latimer, M. J.; Yachandra, V. K.; Sauer, K.; Klein, M. P. *J. Am. Chem. Soc.* **1994**, *116*, 5239–5249.
- (113) Hasegawa, K.; Ono, T.-A.; Inoue, Y.; Kusunoki, M. *Chem. Phys. Lett.* **1999**, *300*, 9–19.
- (114) Britt, R. D.; Campbell, K. A.; Peloquin, J. M.; Gilchrist, M. L.; Aznar, C. P.; Dicus, M. M.; Robblee, J.; Messinger, J. *Biochim. Biophys. Acta* **2004**, *1655*, 158–171.
- (115) Carrell, T. G.; Tyryshkin, A.; Dismukes, G. C. *J. Biol. Inorg. Chem.* **2002**, *7*, 2–22.
- (116) Baldwin, M. J.; Stemmler, T. L.; Riggs-Gelasco, P. J.; Kirk, M. L.; Penner-Hahn, J. E.; Pecoraro, V. L. *J. Am. Chem. Soc.* **1994**, *116*, 11349–11356.
- (117) Debus, R. J.; Strickler, M. A.; Walker, L. M.; Hillier, W. *Biochemistry* **2005**, *44*, 1367–1374.
- (118) Chu, H.-A.; Hillier, W.; Debus, R. J. *Biochemistry* **2004**, *43*, 3152–3166.
- (119) Debus, R. J.; Aznar, C.; Campbell, K. A.; Gregor, W.; Diner, B. A.; Britt, R. D. *Biochemistry* **2003**, *42*, 10600–10608.
- (120) *The labels Mn_C and Mn_D are arbitrary from an electronic perspective. They depend on the labeling of the specific exchange pathways within the cluster. They represent the same electronic structural position for the Mn^{III}; a corner of the trimer/triangle unit (Mn_B, Mn_C, Mn_D) that does not link the trimer to the external Mn (Mn_A).*
- (121) Schäfer, K. O. Doctoral Thesis, Technische Universität Berlin, 2002.
- (122) Griffith, J. S. *The theory of Transition-Metal Ions*; Cambridge University Press: London, 1971.
- (123) Abragam, A.; Bleaney, B. *Electron Paramagnetic Resonance of Transition Metal Ions*; Clarendon Press: Oxford, 1970.
- (124) Carrington, A.; McLachlan, A. D. *Introduction to Magnetic Resonance*; 1st ed.; Harper and Row: New York, 1967.
- (125) Gerritsen, H. J.; Sabisky, E. S. *Phys. Rev.* **1963**, *132*.
- (126) Campbell, K. A.; Force, D. A.; Nixon, P. J.; Dole, F.; Diner, B. A.; Britt, R. D. *J. Am. Chem. Soc.* **2000**, *122*, 3754–3761.
- (127) Mossin, S.; Weihe, H.; Barra, A.-L. *J. Am. Chem. Soc.* **2002**, *124*, 8764–8765.
- (128) Schinzel, S.; Schraut, J.; Arbuznikov, A.; Siegbahn, P. E. M.; Kaupp, M. *Chem.—Eur. J.* **2010**, *16*, 10424–10438.
- (129) Boussac, A.; Girerd, J.-J.; Rutherford, A. *Biochemistry* **1996**, *35*, 6984–6989.
- (130) Zimmermann, J. L.; Rutherford, A. W. *Biochemistry* **1986**, *25*, 4609–4615.
- (131) Åhring, K. A.; Evans, M. C. W.; Nugent, J. H. A.; Pace, R. J. *Biochim. Biophys. Acta, Bioenerg.* **2004**, *1656*, 66–77.
- (132) Force, D. A.; Randall, D. W.; Lorigan, G. A.; Clemens, K. L.; Britt, R. D. *J. Am. Chem. Soc.* **1998**, *120*, 13321–13333.
- (133) Åhring, K. A.; Evans, M. C. W.; Nugent, J. H. A.; Ball, R. J.; Pace, R. J. *Biochemistry* **2006**, *45*, 7069–7082.
- (134) Pace, R. J.; Smith, P. J.; Bramley, R.; Stehlik, D. *Biochim. Biophys. Acta* **1991**, *1058*, 161–170.
- (135) Messinger, J. *Phys. Chem. Chem. Phys.* **2004**, *6*, 4764–4771.
- (136) Petrie, S.; Stranger, R.; Pace, R. J. *Angew. Chem.* **2010**, *122*, 4329–4332.

The electronic structures of the S₂ states of the oxygen evolving complexes of photosystem II in plants and cyanobacteria in the presence and absence of methanol

Ji-Hu Su, Nicholas Cox, William Ames, Dimitrios A. Pantazis, Leonid Rapatskiy, Thomas Lohmiller, Leonid Kulik, Pierre Dorlet, A. William Rutherford, Frank Neese, Alain Boussac, Wolfgang Lubitz and Johannes Messinger



The electronic structures of the S_2 states of the oxygen-evolving complexes of photosystem II in plants and cyanobacteria in the presence and absence of methanol

Ji-Hu Su^{a,1}, Nicholas Cox^{a,*}, William Ames^{a,b}, Dimitrios A. Pantazis^{a,b}, Leonid Rapatskiy^a, Thomas Lohmiller^a, Leonid V. Kulik^c, Pierre Dorlet^d, A. William Rutherford^d, Frank Neese^{a,b}, Alain Bousset^d, Wolfgang Lubitz^{a,**}, Johannes Messinger^{e,***}

^a Max-Planck-Institut für Bioorganische Chemie, Stiftstrasse 34–36, D-45470 Mülheim an der Ruhr, Germany

^b Lehrstuhl für Theoretische Chemie, Institut für Physikalische und Theoretische Chemie, Universität Bonn, Wegelerstr. 12, D-53115 Bonn, Germany

^c Institute of Chemical Kinetics and Combustion, Institutskaya 3, 630090 Novosibirsk, Russia

^d iBiTec-S, URA CNRS 2096, CEA Saclay, 91191 Gif-sur-Yvette, France

^e Department of Chemistry, Chemical Biological Centre (KBC), Umeå University, S-90187 Umeå, Sweden

ARTICLE INFO

Article history:

Received 20 January 2011

Received in revised form 2 March 2011

Accepted 4 March 2011

Available online 13 March 2011

Keywords:

EPR

⁵⁵Mn-ENDOR

Photosystem II

OEC

Mn₄O_xCa cluster

Methanol

Orbach process

Raman process

Spin Hamiltonian

ABSTRACT

The electronic properties of the Mn₄O_xCa cluster in the S_2 state of the oxygen-evolving complex (OEC) were studied using X- and Q-band EPR and Q-band ⁵⁵Mn-ENDOR using photosystem II preparations isolated from the thermophilic cyanobacterium *T. elongatus* and higher plants (spinach). The data presented here show that there is very little difference between the two species. Specifically it is shown that: (i) only small changes are seen in the fitted isotropic hyperfine values, suggesting that there is no significant difference in the overall spin distribution (electronic coupling scheme) between the two species; (ii) the inferred fine-structure tensor of the only Mn^{III} ion in the cluster is of the same magnitude and geometry for both species types, suggesting that the Mn^{III} ion has the same coordination sphere in both sample preparations; and (iii) the data from both species are consistent with only one structural model available in the literature, namely the Siegbahn structure [Siegbahn, P. E. M. *Accounts Chem. Res.* **2009**, *42*, 1871–1880, Pantazis, D. A. et al., *Phys. Chem. Chem. Phys.* **2009**, *11*, 6788–6798]. These measurements were made in the presence of methanol because it confers favorable magnetic relaxation properties to the cluster that facilitate pulse-EPR techniques. In the absence of methanol the separation of the ground state and the first excited state of the spin system is smaller. For cyanobacteria this effect is minor but in plant PS II it leads to a break-down of the $S_T = \frac{1}{2}$ spin model of the S_2 state. This suggests that the methanol–OEC interaction is species dependent. It is proposed that the effect of small organic solvents on the electronic structure of the cluster is to change the coupling between the outer Mn (Mn_A) and the other three Mn ions that form the trimeric part of the cluster (Mn_B, Mn_C, Mn_D), by perturbing the linking bis-μ-oxo bridge. The flexibility of this bridging unit is discussed with regard to the mechanism of O–O bond formation.

© 2011 Elsevier B.V. All rights reserved.

Abbreviations: EPR, electron paramagnetic resonance; ENDOR, electron nuclear double resonance; ESEEM, electron spin-echo envelope modulation; PS II, photosystem II; OEC, oxygen-evolving complex; MeOH, methanol; CW, continuous wave; ZFS, zero-field splitting

* Corresponding author. N. Cox: Tel.: +49 208 306 3865.

** Corresponding author. W. Lubitz: Tel.: +49 208 306 3614.

*** Corresponding author. J. Messinger: Tel.: +49 90 7865933.

E-mail addresses: cox@mpi-muelheim.mpg.de (N. Cox),

lubitz@mpi-muelheim.mpg.de (W. Lubitz), johannes.messinger@chem.umu.se

(J. Messinger).

¹ Current address: Department of Modern Physics, University of Science and Technology of China, Hefei, Anhui 230026, China.

1. Introduction

In oxygenic photosynthesis, light-driven water-splitting is catalyzed by the oxygen-evolving complex (OEC) of photosystem II (PS II), a membrane-bound pigment–protein complex embedded in the thylakoid membranes of higher plants, green algae, and cyanobacteria. The OEC also comprises the protein matrix surrounding this inorganic core, and a nearby redox-active tyrosine residue (D₁-Y₁₆₁, Y_Z), for reviews see [1–10]. The latter mediates the proton-coupled electron transfer from the Mn₄O_xCa cluster to the photoactive reaction centre, P₆₈₀, a chlorophyll *a* species, which energetically drives water-splitting by undergoing sequential light-induced charge separation events. During water-oxidation, the Mn₄O_xCa cluster steps through a reaction cycle comprising five distinct redox intermediates [2,3,11].

These are known as the S_n states, where the index gives the number of stored oxidizing equivalents ($n = 0-4$). Molecular oxygen is released during the $S_3 \rightarrow [S_4] \rightarrow S_0$ transition, with the S_4 state being a transient state that could so far not be trapped [12–16]. The S_1 state is stable in the dark. S_2 and S_3 are metastable intermediate states that can be studied after one or two flashes are given to a sample pre-incubated in the dark. S_0 is the most reduced state in the O_2 -evolution cycle and can be produced by subjecting dark-adapted samples to three short flashes. In the dark, S_0 is slowly oxidized to S_1 by the nearby redox-active tyrosine residue Y_D^{ox} (D_2 - Y_{161}) [17,18].

Single crystals of PS II from the thermophilic cyanobacterium *Thermosynechococcus elongatus* (*T. elongatus*) [19–23] have been intensively studied by X-ray diffraction and the geometric structure obtained is widely considered to be a model for PS II in all organisms. In spite of the advances in the X-ray structure analysis [22], the precise geometric structure of the OEC has yet to be determined, especially in the high redox states of the enzyme [24]. The inorganic core of the OEC consists of a Mn_4O_xCa cluster with $4 \leq x \leq 6$ indicating the number of oxygen bridges. As such, the current structural description of the Mn_4O_xCa cluster relies on a variety of spectroscopic techniques including: X-ray crystallographic data [21,23,25,26] and polarized EXAFS [10,27,28]. From this body of work, six types of computational structures have been developed as models for the OEC based on: i) London crystal structure [21,29–31]; ii) Berlin crystal structure [23,25,32–35]; iii) EXAFS core I [10,36]; iv) EXAFS core II [10,36]; v) EXAFS core III [10,36]; vi) Siegbahn model [4,37,38]. An in-depth review of these six structures is given in an earlier article [39].

It is well-established that the four Mn ions that constitute the OEC are magnetically coupled in all S_n states and that each S_n state ($n = 0-3$) of the Mn_4O_xCa cluster has distinct EPR signals [6,40–50]. Of particular interest is the S_2 state which has a ground spin state of total spin $S_T = \frac{1}{2}$. This spin configuration gives rise to the well known S_2 state EPR multiline signal [40]. Depending on the conditions used the S_2 state of higher plant PS II also exhibits another broad EPR signal, centered at $g \sim 4.1$ that has been assigned to an $S_T = 5/2$ [51] spin state (see [52]). The $g \sim 4.1$ signal can also be induced by near-infrared (NIR) illumination of the S_2 multiline state at temperatures ≤ 160 K [53]. In plant PS II, the presence of small alcohols prevents the formation of the $g \sim 4.1$ signal. Amongst all the alcohols, methanol (MeOH) has a specific effect; it modifies the S_2 multiline signal and this signal is no longer sensitive to NIR illumination (discussed in [53–57]). The modified S_2 multiline signal is narrower than that seen for the non-treated plant PS II preparation, resolving fewer spectral lines. MeOH also has effects on the other S_n states. In spinach the S_0 state multiline signal can only be detected in the presence of MeOH [49,50,58]. In contrast, the parallel mode S_1 $g \sim 4.9$ [45,46] and S_3 $g \sim 8$ and $g \sim 12$ EPR signals [59], and the EPR “split” signals, which arise from the weak magnetic interaction between the Mn_4O_xCa cluster and the Y_2 [60,61], are no longer visible when the MeOH concentration is increased to 3–5% (v/v). Curiously, in cyanobacterial PS II the addition of MeOH does not modify the S_2 multiline signal, the addition of MeOH does not prevent the formation of high spin S_2 states under NIR illumination [62] and the S_0 state multiline is observable also in the absence of MeOH [63].

Binding of small alcohols in close proximity to the Mn_4O_xCa cluster in PS II isolated from spinach was first demonstrated for the S_2 state by ESEEM spectroscopy by Force et al. [64,65] and later by Åhrling et al. [66]; however, the precise mode and site of binding was not resolved. In flash-induced oxygen evolution measurements it was recently observed that the miss parameter of PS II increases linearly with the MeOH concentration and that this effect is fully reversible up to 10% (v/v) MeOH [67]. This observation is consistent with MeOH binding at a substrate water binding site; however, other mechanisms may also explain this result.

The precise nature of the differences between the electronic structures of the Mn_4O_xCa cluster in plant and cyanobacterial PS II is

not known to date. This is problematic, since for DFT calculations of the OEC often the geometric structure is derived based on X-ray diffraction measurements or (polarized) X-ray absorption measurements on *T. elongatus* samples, while electronic parameters such as the hyperfine couplings calculated for these structures are then compared to experimental EPR/ENDOR data obtained with PS II membranes from spinach [68–70]. Here we employ multi-frequency EPR and ^{55}Mn -ENDOR spectroscopy to gain detailed information about the species-dependent differences in the electronic structures of the S_2 -states of the Mn_4O_xCa clusters of PS II isolated from higher plants (spinach) and cyanobacteria (*T. elongatus*).

2. Materials and methods

2.1. Sample preparation

PS II-enriched membranes from spinach (plant PS II) were prepared as described in [71]. These samples were concentrated to 20–30 mg Chl/ml in 3-mm Q-band EPR tubes by 30 min centrifugation at 4 °C. PS II core complexes (~ 30 – 40μ l) from *T. elongatus* were prepared as previously described [72–74]. The concentration of the EPR samples used was ~ 10 mg Chl/ml. The dark-adapted PS II samples poised in the S_1 state were illuminated by continuous white light at 200 K (dry ice/ethanol bath) for 3 min for plant PS II and 30 s for *T. elongatus* PS II.

2.2. Q-band pulse-EPR measurements

As in [69,75], Q-band pulse-EPR and ^{55}Mn Davies ENDOR measurements were performed at the indicated temperatures on a Bruker ELEXSYS E-580 Q-band pulse-EPR spectrometer equipped with a laboratory-built ENDOR cylindrical resonator and an Oxford-900 liquid helium cryostat and ITC-503 temperature controller, and with a SMT02 signal generator and an ENI 5100 L RF amplifier. Electron spin-echo (ESE)-detected field-swept spectra were measured with the pulse sequence of $\pi/2$ - τ - π - τ echo, with $\pi = 80$ ns and $\tau = 440$ ns. The spin lattice relaxation time (T_1) was measured with the inversion recovery pulse sequence π - T - $\pi/2$ - τ - π - τ echo, where $\pi = 80$ ns, $\tau = 400$ ns and T varies from 0.1 μ s to 10 ms. ^{55}Mn Davies ENDOR measurements were collected by using SpecMan control software that varies the radiofrequency (RF) randomly in the desired range [75–77]. The employed pulse sequence was π - π_{RF} - T - $\pi/2$ - τ - π - τ echo, where π , π_{RF} , T , and τ were 80 ns, 3.5 μ s, 1.5 μ s and 420 ns, respectively. A shot repetition time of 3 ms was used for all Q-band experiments with the exception of the T_1 measurements, where a shot repetition time of 5 ms was used.

3. Results

3.1. Species comparison

3.1.1. Q-band EPR/ ^{55}Mn -ENDOR experiments

ESE-detected EPR spectra of the Mn_4O_xCa cluster seen in PS II core complexes isolated from the cyanobacterium *T. elongatus* and higher plant spinach membranes, poised in the S_2 state are shown in Fig. 1a (black traces). A multiline signal is observed in both species [39,69,76], centered at approximately $g \sim 2.0$ and spread over the same field range (1130–1320 mT). The signal from the stable tyrosyl radical, Y_D^{\bullet} , which appears as a strong, narrow (FWHM ~ 3 mT) signal centered at $g \sim 2$ and obscures the central hyperfine lines of the S_2 state multiline signal, was removed for clarity of presentation. The hyperfine structure is very similar for both sample types; at least eight low-field lines (relative to the position of the Y_D^{\bullet} radical) and 10 high field lines are observed for both sample types.

Differences between the two species are more readily observed using ^{55}Mn -ENDOR. Fig. 1b shows the ^{55}Mn -ENDOR signals seen for

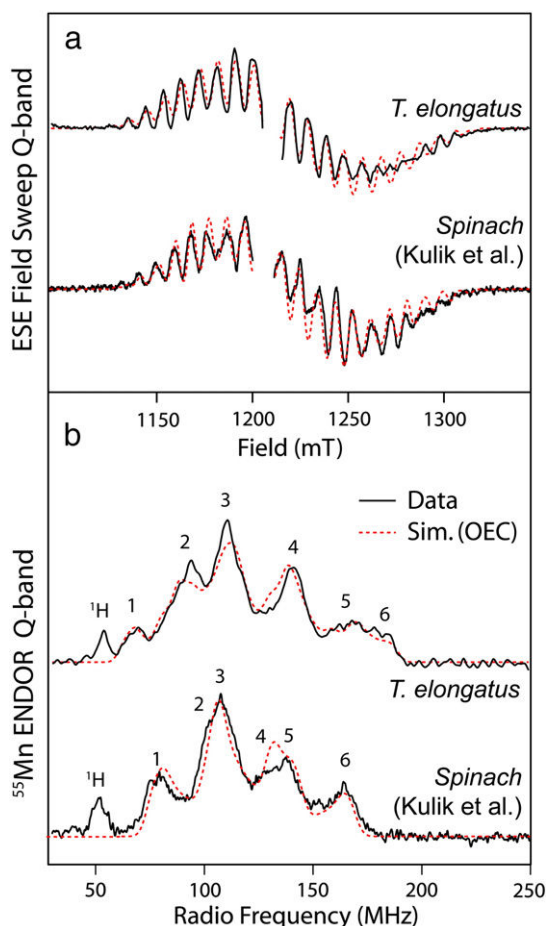


Fig. 1. EPR/ENDOR spectra of PS II core complexes obtained from *T. elongatus* PS II and PS II-enriched membranes from spinach, poised in the S_2 state with 4% MeOH added (solid black lines). (a) Q-band pulse ESE-detected field sweep. The derivative spectra represent the pseudo modulated (2 mT) raw data. The small offset between the two multiline spectra is caused by the fact that each spectrum was recorded at a slightly different microwave frequency. Experimental parameters: microwave frequencies: 33.69 GHz (*T. elongatus*), 33.85 GHz (spinach); shot repetition rate: 5 ms; microwave pulse length (π): 80 ns, τ : 440 ns, temperature: 4.2 K. (b) Q-band pulse ^{55}Mn -Davies ENDOR. The *T. elongatus* spectrum presented was smoothed using a 5 point moving average. Experimental parameters: microwave frequencies: 34.05 GHz (*T. elongatus*), 33.85 GHz (spinach); magnetic field: $B_0 = 1260$ mT; shot repetition rate: 5 ms; microwave pulse length (π): 80 ns, τ : 440 ns, RF pulse (π_{RF}): 3.5 μs . The red dashed lines superimposing each trace represent the least squares fittings to the whole data sets of each species using a model based on the Spin Hamiltonian formalism [39,69]. The optimized parameter sets are given in Table 1.

the *T. elongatus* and spinach PS II preparations described above, poised in the S_2 state, and measured at $B_0 = 1260$ mT. The spinach and *T. elongatus* preparations give rise to comparable but not identical ^{55}Mn -ENDOR spectra. The total spectral breath of the ^{55}Mn -ENDOR spectrum is significantly larger in *T. elongatus* as compared to spinach [69,75]. The high frequency edge shifts 20 MHz to higher frequency and the low frequency edge decreases by approximately the same degree. The lowest field peak, centered at ~ 52 MHz, originates from the magnetic coupling of protons with the $\text{Mn}_4\text{O}_x\text{Ca}$ cluster. Approximately six peaks are observed for the OEC of *T. elongatus*. This is in contrast to spinach PS II, where only four peaks are clearly visible; peaks 2 and 4 appear as shoulders on peak 3 and 5, respectively. It is noted that the above described line shapes of the ^{55}Mn -ENDOR signals of both sample types are essentially invariant over the 1190–1260 mT magnetic field range, consistent with their assignment to the OEC [69,76].

3.1.2. Spectral simulations

The S_2 -state Q-band EPR and Q-band pulse ^{55}Mn ENDOR spectra were simulated using the Spin Hamiltonian formalism described in [69,76,78]. Here, the S_2 multiline signal is considered to arise from an effective $S = 1/2$ ground state, coupled to four ^{55}Mn nuclei. The hyperfine interaction was treated with second-order perturbation theory. The quadrupole interaction was not explicitly considered; it was assumed to contribute to the fitted line-width (for details on the simulation procedure see [39,69]).

The fitted G and hyperfine tensors are given in Table 1. Four hyperfine tensors are required to fit the absorption and 1st derivative line shapes and ENDOR spectra for both sample types (Fig. 1a and b, red dashed line). Near-axial symmetry was seen for the fitted hyperfine tensors for both species. With the exception of A_1 , the z (parallel) component of all hyperfine tensors was the largest. Comparison of the fitted parameters obtained for spectra from spinach and *T. elongatus* demonstrates that there are only subtle differences between the two species. Importantly, the four isotropic values ($A_{i,\text{iso}}$) of the fitted hyperfine tensors (Table 1) all approximately match both OECs suggesting that there is no significant change in the electronic structure/coupling scheme i.e. a difference of less than $<10\%$ is seen between the fitted $A_{i,\text{iso}}$ values. The isotropic components of three of the hyperfine tensors are close to that observed for monomeric $\text{Mn}^{\text{III}}/\text{Mn}^{\text{IV}}$ complexes, while that of the fourth Mn is ~ 1.5 times larger than that reported in the current literature [70,79–82]. This suggests that all four Mn ions equally contribute to the EPR and ENDOR spectra.

The reason for the increase in breadth of the S_2 state ^{55}Mn -ENDOR spectrum of *T. elongatus* as compared to spinach is due to a small increase in hyperfine tensor anisotropy (A_{aniso}). This is seen particularly for hyperfine tensors A_1 and A_4 , which define the high- and low-field edges of the ENDOR spectrum, respectively. The ENDOR signals associated with these two Mn ions are spread over a larger frequency range leading to a broadening of the entire signal envelope. Consistent with this description is the apparent decrease in signal intensity of the edges relative to the intense central line (peak 3) of the ^{55}Mn -ENDOR spectrum of *T. elongatus* as compared to spinach.

3.2. The effect of methanol

3.2.1. T_1 relaxation

Over a 5–10 K temperature range, two phonon relaxation processes usually form the dominant T_1 relaxation pathway for metallofactors seen in enzymes, namely the Raman and Orbach processes

Table 1

The principal values of the effective G and ^{55}Mn hyperfine tensors for the simulations of the S_2 spectra of *T. elongatus* and spinach PS II.

	G	A_i (MHz)				
		A_1	A_2	A_3	A_4	
<i>T. elongatus</i>	x	1.971	350	249	202	148
	y	1.948	310	227	182	162
	\perp	1.960	330	238	192	155
	z (\parallel)	1.985	275	278	240	263
	iso	1.968	312	251	208	191
	aniso	0.025	55	-40	-48	-108
Spinach	x	1.997	310	235	185	170
	y	1.970	310	235	185	170
	\perp	1.984	310	235	185	170
	z (\parallel)	1.965	275	275	245	240
	iso	1.977	298	248	205	193
	aniso	0.019	35	-40	-60	-70

The isotropic G_{iso} and $A_{i,\text{iso}}$ ($i = 1-4$) values are the average of the individual values: $G_{\text{iso}} = (G_x + G_y + G_z)/3$ and $A_{i,\text{iso}} = (A_{i,x} + A_{i,y} + A_{i,z})/3$. The equatorial and axial G and A_i values are defined as: $G_{\perp} = (G_x + G_y)/2$, $G_{\parallel} = G_z$ and $A_{i,\perp} = (A_{i,x} + A_{i,y})/2$, $A_{i,\parallel} = A_{i,z}$. The anisotropy in the G and A_i values is expressed as the difference between the perpendicular and parallel components of the tensor.

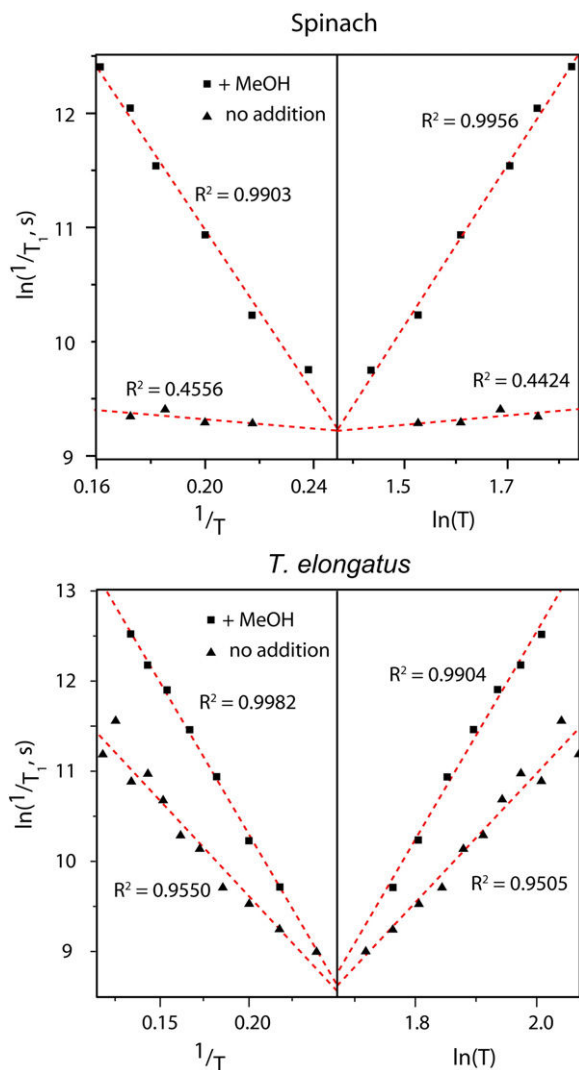


Fig. 2. The temperature dependence of the T_1 relaxation time of the OEC poised in the S_2 multiline state in PS II samples containing 4% MeOH (■) and in the absence of MeOH (no addition) (▲). The left hand side panel data plots the inverse temperature vs. the natural logarithm of the inverse of the T_1 time (Orbach process). The right hand panel plots the natural logarithm of the inverse of the T_1 time (Raman process). Electron spin-echo-detected T_1 relaxation data were measured using a 3 pulse sequence: π - T - $\pi/2$ - τ - π - τ echo, using $\pi = 80$ ns, $\tau = 440$ ns, and T was swept over the range of 0.1–10 ms. An estimate of the T_1 time was made by fitting the raw data to a bi-exponential decay collected at each temperature. The superimposed red lines correspond to a linear fit of the data. Experiments were performed at $B_0 = 1260$ mT.

[83,84]. Both processes rely on the system containing spin levels that are thermally accessible, but each has a slightly different dependence on the measurement temperature (T):

$$\ln\left(\frac{1}{T_1}\right) = \frac{\Delta}{T} \quad (1)$$

$$\ln\left(\frac{1}{T_1}\right) \propto \ln(T) \quad (2)$$

It is noted that the relaxation rate of an Orbach process is dependent on the ground to first excited state energy separation (Δ). As such, an estimate of the energy ladder can be made when this process is the dominant relaxation process [83,84]. Previous studies in spinach PS II [85] in the presence of a small percentage of MeOH, demonstrated that the OEC cluster in the S_2 multiline state displays dominantly

Table 2

The energy separation Δ between the ground and first excited electronic states for the S_2 -state in plant PS II and *T. elongatus* PS II samples assuming an Orbach relaxation process.

		Δ (cm^{-1})	
		No addition	+ MeOH
<i>T. elongatus</i>	T_1 relaxation	13.5 ± 1.2	22.4 ± 0.6
Spinach	T_1 relaxation	2.7 ± 0.5	$24.7 \pm 1.2, 36.5$ [85]
	CW EPR	~ 6 [48,54]	12 [48,54], 30 [48,54]

an Orbach relaxation over the 5–10 K temperature range. This work reported a ground to first excited state energy difference (Δ) of 35 cm^{-1} for the S_2 state [85]. We have repeated this experiment using our plant PS II membrane samples and found that over the 4.6–7.5 K temperature range both the relationships $\ln(1/T_1)$ versus $1/T$ and $\ln(1/T_1)$ vs. $\ln(T)$ are approximately linear ($R^2 = 0.9903$ and $R^2 = 0.9956$, respectively; Fig. 2, upper panel). Thus, under our experimental conditions, we cannot distinguish whether an Orbach or Raman relaxation process dominates. If an Orbach process is assumed, Δ is estimated to $24.7 \pm 1.2 \text{ cm}^{-1}$ (Table 2). This value is lower than that seen in the earlier study of Lorigan and Britt [85], but still of approximately the same magnitude. In the absence of MeOH, the behavior of the T_1 time changes dramatically. The observed spin-echo is more difficult to measure in samples without MeOH (no addition) and as such the data quality is poorer. Nevertheless, a semi-quantitative description of the system can still be made. As before, the data are equally consistent with either an Orbach or a Raman process. If we again assume an Orbach process, the energy difference (Δ) has collapsed to $2.7 \pm 0.5 \text{ cm}^{-1}$ (Table 2). This value is small and should be considered as a lower bound for Δ . A decrease in the observed Δ is consistent with literature CW EPR results. In higher plant spinach a Δ of $\sim 6 \text{ cm}^{-1}$ was measured for the non-MeOH treated OEC S_2 multiline state [48] as opposed to ~ 25 – 35 cm^{-1} when MeOH is present. Similar results have been observed for OEC poised in the S_1 -state. A ground to first excited state energy separation of $\Delta = 1.7 \text{ cm}^{-1}$ was reported for higher plant spinach in the absence of solvents poised in the S_1 state [46]. These results were obtained by examining the temperature dependence of the S_1 parallel polarization CW EPR signal. This signal arises from a low lying excited spin state ($S = 1$). It was observed that the excited state signal was lost by the addition of MeOH. That is to say, the proportion of S_1 in the EPR visible excited state ($S = 1$) decreased and that in the diamagnetic $S = 0$ ground state increased upon MeOH addition which suggests that Δ increased by at least $\sim 7 \text{ cm}^{-1}$, see [46].

Analogous results are observed for *T. elongatus* (Fig. 2, lower panel). Unlike the spinach PS II data presented above, our results for the MeOH treated OEC poised in the S_2 state in *T. elongatus* do slightly favor an Orbach process (R^2 of 0.9982 vs. 0.9904 for Raman process). The Orbach fit gave a Δ of $22.4 \pm 0.6 \text{ cm}^{-1}$ approximately that seen in our spinach measurements. The temperature dependence of T_1 was measured at several field positions yielding values within the error stated. In contrast to spinach samples, similar T_1 times are observed in *T. elongatus* preparations with and without MeOH. The *T. elongatus* preparation without MeOH was consistent with either Orbach (R^2 of 0.9550) or Raman (R^2 of 0.9505) relaxation. If Orbach relaxation is assumed, the energy difference between the ground and first excited state Δ is estimated to be $13.5 \pm 1.2 \text{ cm}^{-1}$ (Table 2).

3.2.2. CW EPR and ^{55}Mn -ENDOR

The effect of small alcohols on the CW EPR line shape of the S_2 multiline signal of higher plants has been well documented [53–57]. A slight narrowing of the S_2 multiline spectrum is observed when MeOH is added (Fig. 3a). The amplitudes of the central lines of the multiline pattern increase to the detriment of the external lines and the super hyperfine structure is lost. The corresponding ^{55}Mn -ENDOR spectrum (Fig. 3b) also changes. In samples to which MeOH is not added the

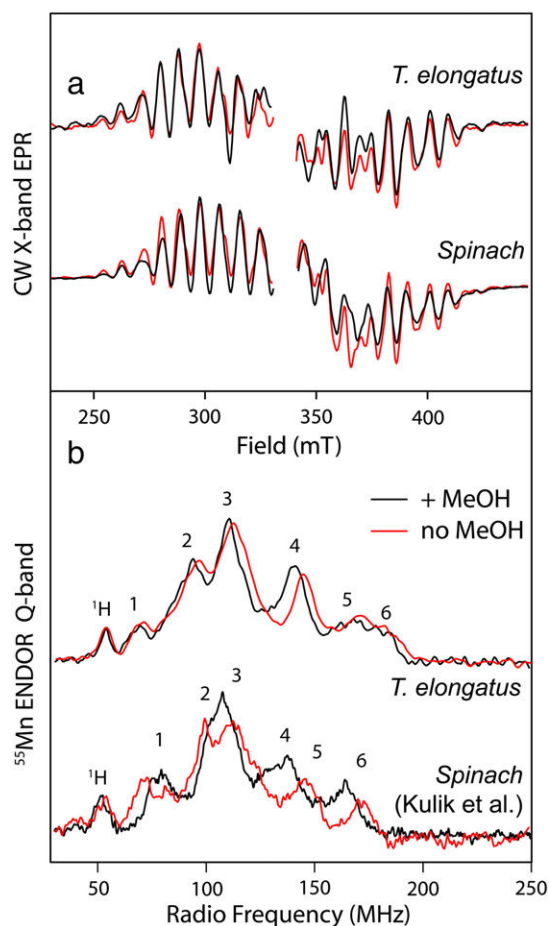


Fig. 3. The effect of MeOH on the EPR/ENDOR spectra of PS II core complexes obtained from *T. elongatus* and spinach BBY membranes, poised in the S_2 state. Solid black lines: 4% MeOH; red lines: in the absence of MeOH. (a) CW X-band EPR. The Y_0 , centered about $g \sim 2$, was removed for clarity of presentation. Experimental parameters: microwave frequencies: 9.4 GHz; microwave power: 20 mW; modulation amplitude: 25 G; time constant: 80 ms, temperature: 8.6 K. (b) Q-band pulse ^{55}Mn -Davies ENDOR. The *T. elongatus* spectrum presented was smoothed using a 5 point moving average. Experimental parameters: microwave frequencies: 34.05 GHz (*T. elongatus*), 33.85 GHz (spinach); magnetic field: $B_0 = 1260$ mT; shot repetition rate: 5 ms; microwave pulse length (τ): 80 ns, τ_r : 440 ns, RF pulse (τ_{RF}): 3.5 μs .

^{55}Mn ENDOR spectrum is broader and more structured (~ 115 MHz width) spanning 65–180 MHz [69,76]. The same behavior is not observed for *T. elongatus*. The addition of MeOH does not alter the CW EPR line shape of the S_2 multiline signal. Consistent with this earlier result, it is observed that the ^{55}Mn ENDOR spectrum also does not change significantly when MeOH is added to the sample. Only subtle changes are observed in the positions of peaks 4 and 6, both shifting to slightly lower radio-frequencies when MeOH is added. The *T. elongatus* spectra shown in Fig. 3 are similar to those reported in a previous study of Pudollek et al. [108]; the total ENDOR signal spans approximately the same width but there are differences in the intensities of the individual lines.

4. Discussion

4.1. General remarks

Refined crystal structure models obtained from thermophilic cyanobacteria form the basis for all current models of the OEC. However much of the spectroscopic data in the literature were obtained using PS II from plants rather than *T. elongatus*. As mentioned

in the introduction, although the PS II from the two species behave similarly, some differences are observed. The results presented here demonstrate that the OEC of the two species are highly similar but not identical. The small differences that are observed are interpreted within a framework in which the spin manifold/energy ladder of the higher plant system is intrinsically more variable than the cyanobacterial system, with the former being more strongly affected by the addition of MeOH. The difference between the action of MeOH in the two species can be explained in two alternative ways. (i) Solvent access to the Mn cluster in the plant vs. cyanobacterial OEC may be different such that MeOH is unable to directly interact with the OEC in the *T. elongatus*. Earlier ESEEM measurements have already shown that MeOH binds to the plant OEC [64,66]. This may reflect changes close to the active site or properties of the more peripheral subunits (which are known to be different between plants and cyanobacteria) and related channels [21,25,86,87]. (ii) Alternatively, the nature of the interaction between MeOH and OEC (e.g. its binding site, the type of binding, or the result of its binding) must somehow differ in the two species. We consider the latter option more reasonable. The change in the electronic structure, as inferred from T_1 relaxation measurements when MeOH is added is similar (an increase in Δ) and only differs by a factor of two in magnitude for both species (~ 10 cm^{-1} for *T. elongatus* vs. 20 cm^{-1} for spinach). As such, the work presented here suggests that some degree of flexibility can be accommodated within the 1st or 2nd coordination sphere of the $\text{Mn}_4\text{O}_x\text{Ca}$ cluster without impairing water-splitting function. This is in line with a number of mutant studies that show that several mutations in the first coordination sphere do not impair water-splitting [88] or the shape of the S_2 multiline signal [89].

4.2. OEC models consistent with higher plant spinach EPR/ENDOR data

In an earlier article [39] we examined the effect of $\text{Ca}^{2+}/\text{Sr}^{2+}$ substitution on the X- and Q-band EPR and Q-band ^{55}Mn -ENDOR spectra of the S_2 multiline signal of *T. elongatus* (with MeOH). These results were then used to discriminate between current literature models of the OEC. As stated in the introduction, there are currently six types of DFT models for the OEC. Of those for which we had the coordinates at the time of the study, we demonstrated that only one coupling scheme, based on the Siegbahn core [4,37,38], is consistent with all EPR/ENDOR data. It is noted that the Siegbahn structure in our study was slightly modified (as compared to the structure reported in [4]) to confer it a ground state of spin $S_T = 1/2$, see Pantazis et al. [36]. This model was selected as it: (i) reproduces the correct ground state spin multiplicity ($S_T = 1/2$); (ii) the correct ground to first excited state energy difference (to within a factor of 2–3); (iii) yields a spin projection coefficient of $|\rho| \sim 1$ for all four Mn ions, consistent with the EPR/ENDOR data; and (iv) gave reasonable estimates for the on-site zero-field splitting (ZFS) of the Mn^{III} i.e. within the range seen for model complexes and the zero-field splitting was affected by Sr^{2+} substitution in a way that is consistent with the changes seen in polarized EXAFS and DFT calculations.

It does not immediately follow that the Siegbahn model is also consistent for the higher plant spinach S_2 state (with MeOH); this must be tested. It is noted that criteria (i), (ii) and (iii) apply equally well to both the S_2 states of spinach and *T. elongatus*. Both require the ground state to be $S_T = 1/2$, spin projection coefficients for all four Mn of approximately 1 and a similar ground to first excited state energy difference, in MeOH treated samples. The only question that remains is whether the Siegbahn model also gives sensible estimates for the on-site ZFS (d) of the Mn^{III} for the spinach OEC (criterion iv). As d is reflected by the fitted hyperfine anisotropy, which is shown above to change between higher plant spinach and *T. elongatus* (see Table 1), its contribution to the energy levels of the system for the two species must differ.

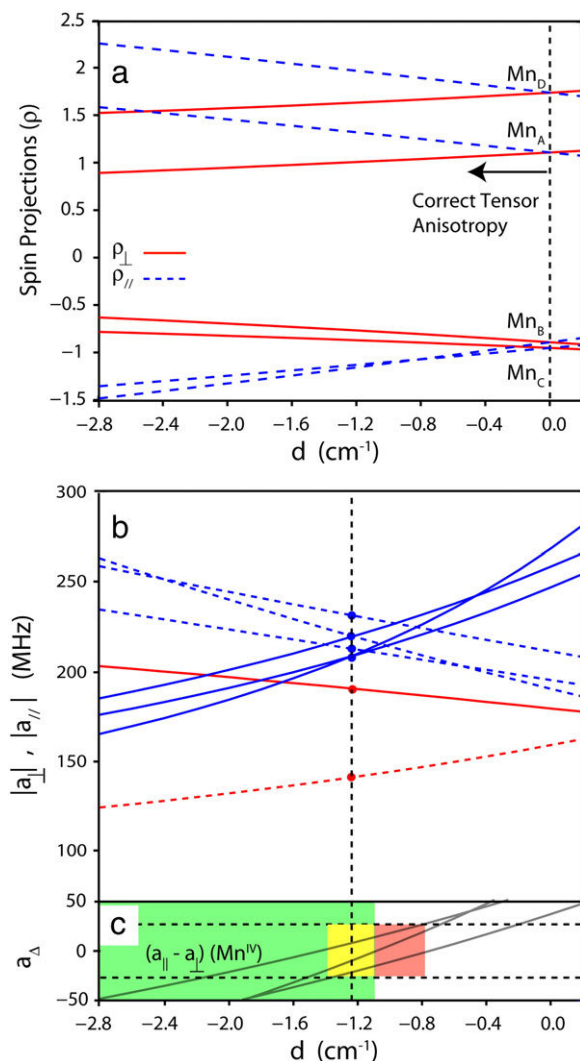


Fig. 4. (a) The dependence of the spin projection factors (ρ_{\perp} , ρ_{\parallel}) on the zero-field splitting parameter (d) of the Mn^{III} ion assuming the exchange coupling model for the Siegbahn core (scheme Fig. 5A). (b) The dependence of the on-site hyperfine tensor components (a_{\perp} , a_{\parallel}) of the spinach $\text{Mn}_4\text{O}_x\text{Ca}$ cluster in the presence of methanol for each of the four manganese ions on the zero-field splitting parameter (d) of the Mn^{III} ion. The bottom panel (c) shows the difference (a_{Δ}) between the parallel (a_{\parallel}) and perpendicular (a_{\perp}) hyperfine components of the three Mn^{IV} ions. The green shaded region represents the range of ZFS values for the Mn^{III} seen in model complexes (when $d < 0$). The red shaded region represents the range of acceptable ZFS values for the Mn^{III} which are consistent with the electronic coupling model, i.e. the range over which the intrinsic hyperfine anisotropy of the Mn^{IV} ions is within the range seen for model complexes. The intersection of the green and red regions is shown by the yellow shaded region. Table 3 lists the intrinsic hyperfine tensor components for all four Mn ions calculated at the midpoint of the range of consistent d values, i.e. the midpoint of the yellow shaded region.

A description of how the on-site ZFS of the Mn^{III} can be estimated from fitted effective Spin Hamiltonian parameters (i.e. A_1, A_2, A_3, A_4) can be found in an earlier article [39]. A brief summary is given below. The effect of the on-site ZFS of the Mn^{III} ion can be taken into account in the calculation of the spin projection coefficients. The spin projection coefficients provide a means to scale the effective Spin Hamiltonian parameters to the on-site (intrinsic) parameters of the individual Mn ions. It is the on-site (intrinsic) parameters that can be compared to literature values. The inclusion of the on-site ZFS of the Mn^{III} requires that the spin projections for all four Mn ions must be considered as tensors as opposed to scalar quantities; that is to say that their magnitude is now orientationally dependent. Fig. 4a displays the dependence of the parallel and perpendicular components of the spin projection tensor of each of the four Mn ions (A, B, C, D) as a function of the ZFS of the Mn^{III} ion. When $d = 0$, the two components are necessarily equal. It can be readily observed that the correct anisotropy of the effective hyperfine tensors of the Mn^{IV} ions can only be reproduced if the d value is negative. This yields a larger parallel as opposed to perpendicular spin projection component, as seen for the effective Mn^{IV} hyperfine tensors (A_2 – A_4). The on-site/intrinsic parallel and perpendicular hyperfine tensor components (a_{\parallel} , a_{\perp}) can then be calculated from the ratio of the fitted effective hyperfine tensor components (A_{\parallel} , A_{\perp}) and the spin projection components seen in panel a (ρ_{\parallel} , ρ_{\perp}). Their dependence on the choice of d is shown in Fig. 4b. An estimate for the ZFS of the Mn^{III} ion can be made using panel c. It shows the anisotropy of the three Mn^{IV} ions i.e. the difference between a_{\parallel} , a_{\perp} , shown in panel b. It is expected that the intrinsic anisotropy of the three Mn^{IV} ions is small, less than 30 MHz (for a full discussion see Cox et al. [39]). The values of d that are consistent with this range are shown by the red shaded region. Literature values for d as measured in monomeric Mn^{III} model complexes provide a second constraint. This range is shown by the green shaded region. The intersection of the red and green shaded regions, colored yellow, then gives the allowed range of d for the Mn^{III} of the OEC. The on-site hyperfine parameters for all four Mn ions calculated at the midpoint of this acceptable range are given in Table 3.

The inferred on-site ZFS of the Mn^{III} ion for the plant OEC is $\sim -1.2 \text{ cm}^{-1}$ (see Fig. 4, caption). A d value of -1.2 cm^{-1} is small for a Mn^{III} ion, falling just inside the range of d values seen in model complexes i.e. $1 < |d| < 5 \text{ cm}^{-1}$, see [39]. The d value is negative and the intrinsic parameters for the Mn^{III} are: $a_{\text{iso}} \sim 174 \text{ MHz}$, $a_{\perp} \sim 190 \text{ MHz}$, $a_{\parallel} \sim 141 \text{ MHz}$, $a_{\text{aniso}} \sim 49 \text{ MHz}$. These values are consistent with a Mn^{III} ion with a 5 coordinate square-pyramidal or 6 coordinate tetragonally elongated ligand field. These are approximately the same values as determined for the *T. elongatus* (see Table 3 and [39]). Importantly, the inferred geometry of the Mn^{III} is consistent with the Siegbahn model; the Mn^{III} in the Siegbahn structure has a square-pyramidal ligand field. Thus, this model is consistent with the EPR/ENDOR data for the S_2 states of both *T. elongatus* and spinach. We note that the small difference inferred between the d values for the *T. elongatus* and spinach PS II may be real or an indirect consequence of the above

Table 3

Calculated spin projection tensor components (ρ_{\perp} , ρ_{\parallel}) and hyperfine tensor components (a_{\perp} , a_{\parallel}) for the 4 Mn ions of PS II in the S_2 state.

		ρ_{\perp}	ρ_{\parallel}	a_{\perp}	a_{\parallel}	a_{iso}	a_{aniso}
<i>T. elongatus</i>	Mn_A (Mn^{IV})	1.01	1.33	235.2	209.6	226.6	−25.6 (−8.5)
	d (Mn^{III}) = -1.32 to -1.26 cm^{-1}	−0.77	−1.16	201.7	226.7	210.0	25.0 (8.3)
	$d_{\text{midpt}} = -1.29 \text{ cm}^{-1}$	−0.87	−1.12	221.6	213.5	218.9	−8.0 (−2.7)
	Mn_D (Mn^{III})	1.62	1.96	203.3	140.5	182.4	−62.8 (−20.9)
Spinach	Mn_A (Mn^{IV})	1.02	1.32	231.0	209.1	223.7	−21.9 (−7.3)
	d (Mn^{III}) = -1.34 to -1.1 cm^{-1}	−0.77	−1.15	219.0	209.4	216.1	−10.0 (−3.3)
	$d_{\text{midpt}} = -1.22 \text{ cm}^{-1}$	−0.87	−1.11	212.5	219.9	224.9	7.4 (2.4)
	Mn_D (Mn^{III})	1.62	1.95	190.4	141.3	174.0	−49.0 (−16.3)

The isotropic a_i values are defined as: $a_{i,\text{iso}} = (2a_{i,\perp} + a_{i,\parallel})/3$. The anisotropy $a_{i,\text{aniso}}$ is expressed as the difference between the parallel and perpendicular component of the tensor. For direct comparison to the work of Pelouquin et al. [70] the anisotropy is also expressed as the difference divided by three (see value in brackets).

described, small changes in the electronic structure of the $\text{Mn}_4\text{O}_x\text{Ca}$ cluster i.e. as the Δ is slightly different for plant and *T. elongatus* samples with MeOH, their electronic structure (exchange coupling topology) must be slightly different. The important result is that the d value is similar for the two species and consistent with literature benchmarks (see [39], supporting information Table S3). The Siegbahn model as presented here is in agreement with the experimental results of Teutloff et al. [109]. These authors performed an EPR/ENDOR study on PS II single crystals. The comparison of these results to the crystal structure of Guskov et al. [22], allowed a tentative assignment of the position of the Mn^{III} . Its preferred location was within bonding distance to the Asp342 residue. Here it was assumed that the Mn-Asp342 bond defines the Jahn-Teller axis of the Mn^{III} ion.

4.3. Decoupling of the OEC

A uniquely determined experimental solution for the ladder of spin states of the $\text{Mn}_4\text{O}_x\text{Ca}$ cluster can not be obtained. If only pairwise interactions are considered between the four Mn ions, six exchange couplings are required to describe the energy ladder of the system. Experimentally though, only one observable is measured, the ground to the first excited state energy-level difference (Δ). As a consequence, a simpler model is often invoked for interpreting EPR data, in which the energy levels of the system are described in terms of an effective coupling constant, J_{eff} ($\Delta = 3/2J_{\text{eff}}$, for the S_2 multiline). Here, the four-spin system is described in terms of a two-spin system as shown in Fig. 5b and c, respectively. The electronic coupling component of the Spin Hamiltonian for this simplified system takes the form:

$$H = -J_{\text{eff}}S_1 \cdot S_2 \quad (3)$$

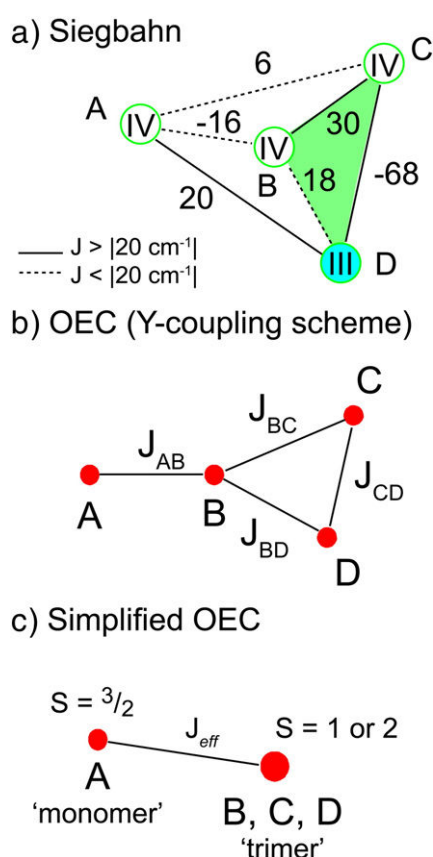


Fig. 5. Current models for the electronic structure of the OEC. (a) The J coupling scheme for the Siegbahn structure [4,36]; (b) Y-coupling scheme developed from EPR/ENDOR [69]; (c) a simplified OEC coupling scheme in which the Y-scheme is approximated by two spins.

where S_1 and S_2 describe the two fragments of the tetramer: a monomeric Mn^{IV} ($S = 3/2$) and a coupled trimer ($\text{Mn}^{\text{IV}})_2\text{Mn}^{\text{III}}$ of total spin $S = 1$ or 2 , and J_{eff} , the coupling between them [40]. The spin state ladder for this system is $E_s = J_{\text{eff}}/2S(S + 1)$. Within this simple model, solvent-induced effects are easily rationalized. MeOH somehow modulates the electronic coupling of the monomeric Mn to the trimer (i.e. J). MeOH binding causes J to increase by approximately 4- to 10-fold in spinach and ~ 2 fold for *T. elongatus* in the S_2 state.

It is useful to consider how the simple model described above maps onto the Siegbahn model (Fig. 5a). The Siegbahn model broadly fits with the Y-coupling scheme topology [36,39] (Fig. 5b), which was developed on the basis of $(3 + 1)$ coupling schemes first proposed by Peloquin et al. [70]. Mn_B , Mn_C and Mn_D couple together to form the trimer fragment with a total ground state spin of $S = 1$. To this fragment the Mn_A monomer fragment is coupled. The effective coupling J_{eff} in the simple model above includes contributions from the J_{AB} , J_{AC} , J_{AD} exchange pathways. In the work of Pantazis et al. [36] it was noted that the ground to first excited state energy difference in this model was dependent on the magnitude of the coupling between Mn_A and the trimer unit and that the net sign of this interaction also defined the spin multiplicity of the ground state. Thus, even within this more complicated electronic coupling scheme, a mechanism seems reasonable in which solvents such as MeOH modulate the electronic coupling of the monomeric Mn to the trimer.

This simple description of the action of small organic solvent molecules on the electronic structure of the OEC also provides a rationale for the changes observed in the width and line shape of both the EPR and ENDOR data. The line shape of the EPR and ENDOR spectra changes because the contribution of the on-site ZFS of the Mn^{III} changes. This is because the relative contribution of the on-site ZFS of the Mn^{III} ion to the energy levels of the cluster is dependent on Δ . For large Δ , the on-site ZFS can be considered a small perturbation of the electronic structure. Within this regime, variation in Δ should not significantly change the spin projection coefficients; the perpendicular and parallel components (ρ_{\perp} , ρ_{\parallel}) of the spin projection tensor are approximately equal. If however Δ is of the same size as the on-site ZFS of the Mn^{III} , relatively small changes in Δ can lead to large changes in the spin projection coefficients and thus large changes in the effective hyperfine tensors. For the OEC, Δ is small, being at most an order of magnitude larger than the on-site ZFS of the Mn^{III} and thus the second regime holds (Fig. 6).

It was shown above that in plant PS II, there is a large change of Δ induced by MeOH. This should then lead to a large change in the spin projection coefficients of the OEC and as a consequence, a large change in the effective hyperfine tensors. Compared to the MeOH treated system (the system that was simulated), it is expected that in the absence of MeOH the perpendicular and parallel components (A_{\perp} , A_{\parallel}) of the effective hyperfine tensors should diverge, leading to an increase in the width of both the EPR and ^{55}Mn -ENDOR spectrum. This is exactly what is observed experimentally. Similarly, as the MeOH-induced change in Δ is much smaller in the cyanobacteria, no large change in the spin projection coefficients is expected and thus no change should be seen in the EPR and ENDOR spectra.

It can be shown that the Siegbahn model is at least semi-quantitatively consistent with the mechanism described above. This is shown in Fig. 7. Here the coupling between Mn_A and the trimer is varied to demonstrate how the energy gap and spin projections change as a function of this coupling. The coupling is varied in a simple way; the three exchange couplings that connect Mn_A to the trimer (J_{AB} , J_{AC} , J_{AD}) are simply multiplied by a factor c . As such, the factor c represents an average increase/decrease in the connectivity of the two OEC fragments, the $S = 3/2$ (Mn_A) and the $S = 1$ (Mn_B , Mn_C , Mn_D). The on-site ZFS of the Mn^{III} was fixed to the value determined in section 4.2, i.e. $d = -1.2 \text{ cm}^{-1}$. As expected, over the range of energy gap values determined for *T. elongatus* ($\Delta = 22.4\text{--}13.5 \text{ cm}^{-1}$) only small changes should occur for the spin projection coefficients

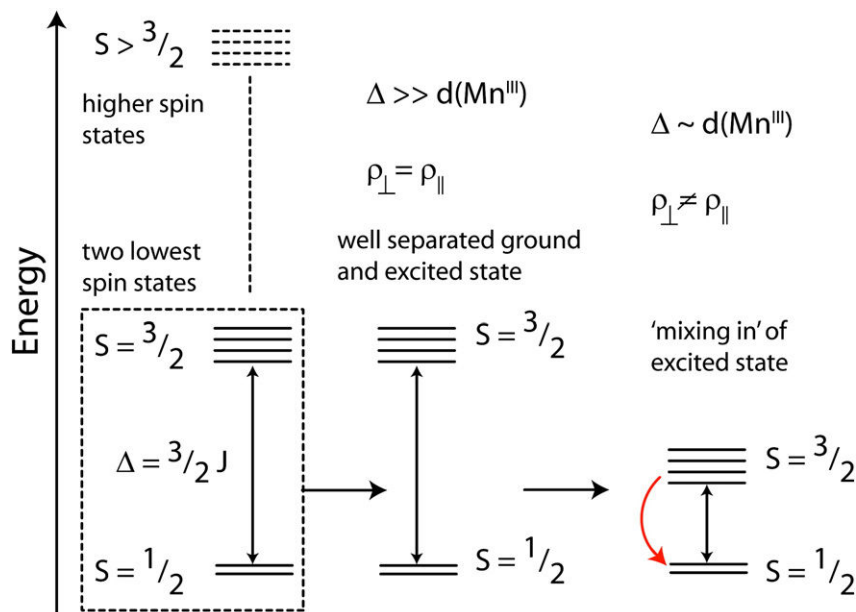


Fig. 6. The energy levels of the OEC. In the limit where energy separation between ground and first excited state (Δ) is large compared to the on-site ZFS (d) of the Mn^{III} ion, the perpendicular and parallel components of spin projection tensor ($\rho_{\perp}, \rho_{\parallel}$) are approximately equal. In the limit where Δ is of the same magnitude as the on-site ZFS of the Mn^{III} , a large difference (anisotropy) in the perpendicular and parallel components of the spin projection tensor ($\rho_{\perp}, \rho_{\parallel}$) is expected.

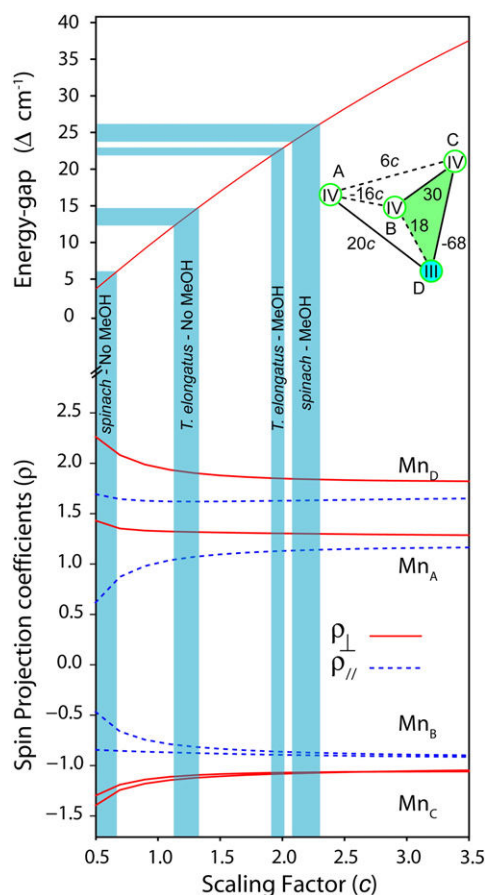


Fig. 7. Top: The dependence of the ground to first excited state energy difference on the coupling of Mn_A to the trimer unit. The extent of coupling between Mn_A and the trimer is given in terms of the factor c . The factor c is applied to all three exchange couplings that connect Mn_A to the trimer (J_{AB}, J_{AC}, J_{AD}), and thus represents an average increase/decrease in the coupling of the two OEC fragments. Bottom: The dependence of the spin projection factors ($\rho_{\perp}, \rho_{\parallel}$) on the factor c , described above. The zero-field splitting parameter (d) of the Mn^{III} ion was fixed to the value determined in section 4.3 i.e. $d = -1.2 \text{ cm}^{-1}$. $c = 1$ gives the original Siegbahn coupling scheme.

(<10%). As such, no change in the EPR/ENDOR spectra is expected, as observed. The range of energy gap values observed for spinach is much larger ($\Delta = 25\text{--}35 \text{ cm}^{-1}$ to $2\text{--}6 \text{ cm}^{-1}$), and as a consequence a more significant change in the spin projection coefficients is expected. Importantly, the spinach PS II sample in the absence of MeOH has an energy gap of only $2\text{--}6 \text{ cm}^{-1}$. In this regime large deviations are observed for the spin projection coefficients as the spin $1/2$ model for the ground state breaks down. Note that: $c = 1$ gives the original coupling scheme of the Siegbahn model. This gives an energy gap of $\sim 10 \text{ cm}^{-1}$, approximately that seen for *T. elongatus* without MeOH.

The above arguments bring into question the simulations of Charlot et al. [68] performed on the broad S_2 multiline signal of plant PS II in the absence of MeOH. The broad multiline signal in this earlier study refers to the component of the multiline signal that is sensitive to NIR light (see introduction). In this earlier study the multiline signal was assumed to arise from a well isolated spin $1/2$ ground state. The above results demonstrate that this is not the case. In the absence of MeOH, the energy spacing (Δ) in spinach PS II is of the order of the on-site zero-field splitting/fine structure of the Mn^{III} . As such, it is unclear whether a spin $1/2$ model for this system is appropriate as it does not explicitly include the Spin Hamiltonian terms that describe the on-site zero-field splitting of the Mn^{III} . In this circumstance it is expected that a more complicated two- or four-spin model should be used that does include these terms.

Table 4

Theoretical interspin distances between the methyl deuterons of the CD_3OH and Mn_A/Mn_D using the point dipole model.

	^2H (MHz)	Theoretical distance (\AA)					
		\AA	$\text{Mn}_A\text{-Asp170}$ ($\rho = 1.33$)	$\text{Mn}_A\text{-OH}$ ($\rho = 1.01$)	$\text{Mn}_D\text{-Glu189}$ ($\rho = 1.62$)	$\text{Mn}_D\text{-open}$ ($\rho = 1.96$)	
a	CD_3	0.448	3.00	3.30	3.01	3.51	3.76
		0.209	3.91	4.29	3.92	4.59	4.89
		0.177	4.10	4.51	4.11	4.81	5.13
b	CD_3	0.64	2.67	2.93	2.68	3.13	3.34
		0.38	3.15	3.46	3.16	3.70	3.94
		0.38	3.15	3.46	3.16	3.70	3.94

^aExp. data of Force et al. [64]. ^bExp. data of Åhrling et al. [66].

4.4. Methanol–OEC interaction in plant and cyanobacterial PS II

^2H -ESEEM measurements performed on the S_2 state of plant PS II demonstrated that one MeOH molecule interacts with the OEC, i.e. it coordinates one of the Mn ions [64,66]. Similar data has yet to be reported for *T. elongatus* PS II. In the studies reported in the literature, ^2H couplings were reported in the range of 0.2–0.6 MHz. In both studies, best fits were obtained using two inequivalent nuclei for the deuterons of the methyl group, i.e. one more strongly coupled deuteron and two approximately identical more weakly coupled deuterons. Curiously, the two reports give contradictory results; ^2H couplings were approximately 1.5- to 2-fold larger in the second study. We offer no assessment of which experimental data set and subsequent analysis is correct. We note though that in the second study this discrepancy was accounted for by invoking sample heterogeneity [66]. Here it was stated that in the original study of Force et al. the S_2 state was generated by low temperature illumination leading to a mixture of S_2 (multiline) states that represent both the MeOH bound and non-bound OEC. In contrast, the study of Åhrling et al. used room temperature laser flash advancement, yielding a more homogeneous S_2 state i.e. uniformly MeOH bound. As multiline heterogeneity in spinach PS II has been well documented in the literature, this explanation seems reasonable [55,90,91].

Within the Siegbahn model, there are four good Mn–ligand/residue candidates for MeOH displacement: the two Mn_A –OH ligands, the Mn_A –Asp170 ligand and the Mn_D –Glu189. Using the anisotropic spin projection values determined in the discussion section 4.2, theoretical estimates can be made for the expected MeOH bound Mn– ^2H interspin distances (See Table 4). Here we employ the point dipole model for the Mn– ^2H interspin distance. This should give reasonably good estimates for the Mn– ^2H interspin distance for ligands bound to Mn_A (the ‘external’ Mn), and poorer estimates for the Mn of the trimer unit (Mn_B , Mn_C , Mn_D). This simple approach was used due to the uncertainty of the binding mode of the MeOH at each of the four sites identified. This forms ongoing work in our laboratory.

Each ESEEM data set, Force [64] or Åhrling [66], is consistent with one binding position using the Siegbahn model [4]. The results of Force et al. [64] favor displacement of one of the OH ligands on Mn_A . The theoretical Mn– ^2H distances for this site match those seen for $\text{Mn}^{\text{III}}\text{Mn}^{\text{IV}}$ model complexes where MeOH is bound to the Mn^{III} [92]. In contrast, the results of Åhrling et al. [66] give very short Mn– ^2H distances for Mn_A either displacing the OH or Asp170, outside the range seen for model complexes and as such binding at Mn_A can be excluded assuming this data set is correct. This data set instead favors binding at Mn_D displacing the Glu189. It is again reiterated though that a more complete multipole treatment of the dipolar coupling interaction is required to precisely assign the position of MeOH binding.

It is noted that MeOH could also potentially bind at the open coordination site on Mn_D . This would give reasonable values for Mn– ^2H distances using the coupling values of Åhrling et al. [66] However, if MeOH does bind at this open site, a significant rearrangement of the core geometry is required as a MeOH molecule can otherwise not fit into this site. Indeed the site itself is too small to bind even a water molecule, as has been previously discussed in the literature [4] (Fig. 8). A structural change of the OEC of this magnitude should lead to a large change of the electronic structure that would seem inconsistent with the data presented in this manuscript and as such, this binding mode is not favored.

As stated in section 4.3, we consider that the mechanism for MeOH action is to somehow modulate the electronic coupling between Mn_A and the trimer unit (Mn_B , Mn_C , Mn_D). This action could potentially be rationalized for the two binding models, ‘Force’ and ‘Åhrling’, discussed above. In the Force model, the replacement of either of the negatively charged OH ligands around Mn_A with MeOH would affect the distribution of electron density in the OEC core, directly

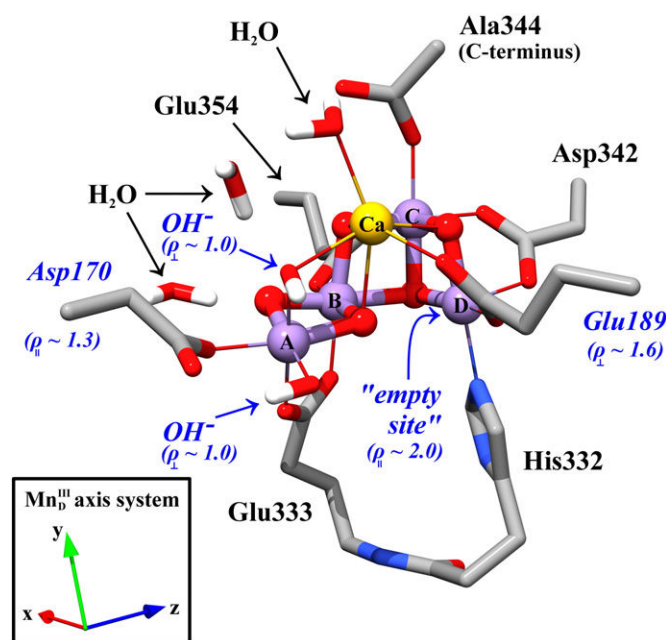


Fig. 8. Potential sites for MeOH binding for the Siegbahn model [4]. Ligands that can be substituted for MeOH and that are consistent with the ESEEM studies of either Force et al. [64] or Åhrling et al. [66] are labelled in blue italic. The Arg357 as well as backbone H-atoms are not included in the figure for clarity. The orientation of the spin projection coefficients is defined by the axis system of the Mn^{III} ion shown in the inset.

changing the nature of the Mn_A – Mn_B interaction. This might lead to a larger Mn_A – Mn_B anti-ferromagnetic coupling and as such, a modification of the spin ladder of the system consistent with the data presented. The species-dependent effect of MeOH could describe a change in ligand mobility. While the same ligand is likely to be substituted in either the plant or cyanobacterial OEC, the 2nd coordination sphere interaction between the MeOH and the surrounding protein pocket could differ, thus changing the binding mode of the MeOH molecule, its H-bonding interactions and thus its effect on the electronic coupling within the OEC. In an analogous way, direct substitution of the Glu189 ligand to Mn_D (Åhrling model) could also explain the change in the electronic coupling between the Mn_A and the trimer unit (Mn_B , Mn_C , Mn_D). Direct substitution of Glu189 with MeOH would have an effect similar to that of ligand substitution on Mn_A , but within the Mn_B , Mn_C , Mn_D subunit, again possibly giving rise to a stronger Mn_A –trimer exchange interaction through a propagation of the localized electron and spin density rearrangement of the trimer subunit. Here, as with direct substitution of Asp170 on Mn_A the species-dependent effect of MeOH could be rationalized in the context of the facility of protein ligand displacement being dependent on differences between the proteins from spinach and *T. elongatus* further away from the OEC core itself. Indeed differences in rigidity – or lack of rigidity – of the Glu189 amino acid within the two species could play an important role in its possible direct substitution by MeOH.

4.5. Structural flexibility of the $\text{Mn}_4\text{O}_x\text{Ca}$ cluster

S_0 state dependent structural changes were proposed both from biochemical and spectroscopic studies of the OEC. A structural rearrangement during the $S_2 \rightarrow S_3$ transition was demonstrated by Boussac et al. [93,94] and Messinger et al. [95]. Here it was shown that: (i) the protein has a lower affinity for Ca in S_3 ; (ii) that the S_3 state has a much slower reactivity towards NH_2OH and NH_2NH_2 ; and (iii) a slower rate of NH_3 binding in S_3 . Similarly, temperature

dependent measurements of the reduction kinetics of Y_2^{ox} provided evidence for a high reorganization energy for the $S_2 \rightarrow S_3$ transition [96,97]. Subsequently, EXAFS measurements [98–103] provided strong spectroscopic evidence for structural changes during the $S_2 \rightarrow S_3$, and also the $S_0 \rightarrow S_1$ transitions, and also FTIR experiments [104,105] suggest significant alterations in carboxylic acid vibrations during the $S_2 \rightarrow S_3$ transition. It can therefore be proposed that the structural flexibility of the $\text{Mn}_4\text{O}_x\text{Ca}$ cluster is a key feature for its high water-oxidation rates [2,3,103,106]. This hypothesis is supported by the recent work of Siegbahn on modeling the reaction pathway for water-splitting [4] (for similar proposals see also [2,69,107]). The facility for structural rearrangement has been identified as a key feature in this theoretical water-splitting pathway. Without this flexibility the OEC would not be able to oxidize water. Similarly, structural flexibility within a given oxidation state (S_n state) of the $\text{Mn}_4\text{O}_x\text{Ca}$ cluster has been proposed based on mechanistic considerations, EPR simulations and DFT calculations [32,34,106]. It should be noted that the effect of these rearrangements, in the context of this work, would be to alter the coupling between the Mn centers, changing the effective spin ladder. Upon the addition of MeOH, one conformation, or possibly a subset of conformations, is stabilized over the remaining conformations, giving rise to the homogeneous multiline signal observed.

Conclusion

The electronic properties of the $\text{Mn}_4\text{O}_x\text{Ca}$ cluster in the S_2 state of the OEC of the thermophilic cyanobacterium *T. elongatus* and higher plants (spinach) were shown to be very similar. The data presented here show that both OEC types can be explained using the same electronic coupling scheme, namely a coupling scheme based on the structural model of Siegbahn [4,36]. The small spectral changes observed between the two species are interpreted within a model in which the contribution of the on-site ZFS of the only Mn^{III} of the S_2 to the total ZFS of the cluster changes. An analogous argument is invoked to explain the spectral differences seen in the presence and absence of MeOH. Potential sites for MeOH binding are discussed within the context of the Siegbahn model, which are consistent with the earlier ESEEM studies of Force et al. [64] and Åhrling et al. [66].

Acknowledgment

Financial support was provided by the DFG (Me1629/2-4), the Max Planck Gesellschaft, the EU SOLAR-H2 (FP7 contract 212508), the Wallenberg and Kempe foundations and VR (J.M.), National Natural Science Foundation of China (31070211) and Initial Funding of University of Science and Technology of China (ZC9850290071) (J.S.). L.R. is a fellow of North Rhine-Westphalia (NRW) Research School BioStruct program.

References

- [1] W. Lubitz, E.J. Reijerse, J. Messinger, Solar water-splitting into H_2 and O_2 : design principles of photosystem II and hydrogenases, *Energy Environ. Sci.* 1 (2008) 15–31.
- [2] J. Messinger, G. Renger, Photosynthetic water splitting, in: G. Renger (Ed.), Primary processes of photosynthesis—part 2: basic principles and apparatus, Royal Society of Chemistry, Cambridge, 2008, pp. 291–349.
- [3] W. Hillier, J. Messinger, Mechanism of photosynthetic oxygen production, Springer, 2005.
- [4] P.E.M. Siegbahn, Structures and energetics for O_2 formation in photosystem II, *Acc. Chem. Res.* 42 (2009) 1871–1880.
- [5] H. Dau, I. Zaharieva, Principles, efficiency, and blueprint character of solar-energy conversion in photosynthetic water oxidation, *Accounts Chem. Res.* 42 (2009) 1861–1870.
- [6] J.P. McEvoy, G.W. Brudvig, Water-splitting chemistry of photosystem II, *Chem. Rev.* 106 (2006) 4455–4483.
- [7] K. Åhrling, R.J. Pace, M.C.W. Evans, The catalytic manganese cluster: implications from spectroscopy, Springer, 2005.
- [8] N. Nelson, C.F. Yocum, Structure and function of photosystems I and II, *Annu. Rev. Plant Biol.* 57 (2006) 521–565.
- [9] G. Renger, T. Renger, Photosystem II: the machinery of photosynthetic water splitting, *Photosynth. Res.* 98 (2008) 53–80.
- [10] J. Yano, J. Kern, K. Sauer, M.J. Latimer, Y. Pushkar, J. Biesiadka, B. Loll, W. Saenger, J. Messinger, A. Zouni, V.K. Yachandra, Where water is oxidized to dioxygen: structure of the photosynthetic Mn_4Ca cluster, *Science* 314 (2006) 821–825.
- [11] B. Kok, B. Forbush, M. McGloin, Cooperation of charges in photosynthetic O_2 evolution-1. A linear four step mechanism, *Photochem. Photobiol.* 11 (1970).
- [12] M. Haumann, P. Liebisch, C. Müller, M. Barra, M. Grabolle, H. Dau, Photosynthetic O_2 formation tracked by time-resolved X-ray experiments, *Science* 310 (2005) 1019–1021.
- [13] H. Dau, A. Grundmeier, P. Loja, M. Haumann, On the structure of the manganese complex of photosystem II: extended-range EXAFS data and specific atomic-resolution models for the four S-states, *Phil. Trans. R. Soc. B* 363 (2008) 1237–1244.
- [14] J. Clausen, W. Junge, Detection of an intermediate of photosynthetic water oxidation, *Nature* 430 (2004) 480–483.
- [15] D.R.J. Kolling, T.S. Brown, G. Ananyev, G.C. Dismukes, Photosynthetic oxygen evolution is not reversed at high oxygen pressures: mechanistic consequences for the water-oxidizing complex, *Biochemistry* 48 (2009).
- [16] D. Shevela, K. Beckmann, C. Clausen, W. Junge, J. Messinger, Membrane-inlet-mass spectrometry reveals a high driving force for oxygen-production by photosystem II, *Proc. Natl. Acad. Sci. USA* 108 (9) (2011) 3602–3607.
- [17] S. Styring, A.W. Rutherford, In the oxygen-evolving complex of photosystem II the S_0 state is oxidized to the S_1 state by D^+ (signal I_{slow}), *Biochemistry* 26 (1987) 2401–2405.
- [18] W.F.J. Vermaas, G. Renger, G. Dohnt, The reduction of the oxygen-evolving system in chloroplasts by thylakoid components, *Biochim. Biophys. Acta* 764 (1984) 194–202.
- [19] A. Zouni, H.T. Witt, J. Kern, P. Fromme, N. Krauss, W. Saenger, P. Orth, Crystal structure of photosystem II from *Synechococcus elongatus* at 3.8 Å resolution, *Nature* 409 (2001) 739–743.
- [20] N. Kamiya, J.R. Shen, Crystal structure of oxygen-evolving photosystem II from *Thermosynechococcus vulcanus* at 3.7-Å resolution, *Proc. Natl. Acad. Sci. USA* 100 (2003) 98–103.
- [21] K.N. Ferreira, T.M. Iverson, K. Maghlaoui, J. Barber, S. Iwata, Architecture of the photosynthetic oxygen-evolving center, *Science* 303 (2004) 1831–1838.
- [22] A. Guskov, A. Gabdulkhakov, M. Broser, C. Glöckner, J. Hellmich, J. Kern, J. Frank, F. Müh, W. Saenger, A. Zouni, Recent progress in the crystallographic studies of photosystem II, *ChemPhysChem* 11 (2010) 1160–1171.
- [23] B. Loll, J. Kern, W. Saenger, A. Zouni, J. Biesiadka, Towards complete cofactor arrangement in the 3.0 Å resolution structure of photosystem II, *Nature* 438 (2005) 1040–1044.
- [24] A new crystal structure was recently disclosed by Jian-Ren Shen (Okayama University, Japan) at the 15th International Congress of Photosynthesis. This new structure has yet to be published and as such, is not explicitly considered in this manuscript. It is noted that the structure of the OEC reported is most similar to the Siegbahn structure.
- [25] A. Guskov, J. Kern, A. Gabdulkhakov, M. Broser, A. Zouni, W. Saenger, Cyanobacterial photosystem II at 2.9-Å resolution and the role of quinones, lipids, channels and chloride, *Nat. Struct. Mol. Biol.* 16 (2009) 334–342.
- [26] J. Kargul, K. Maghlaoui, J.W. Murray, Z. Deak, A. Boussac, A.W. Rutherford, I. Vass, J. Barber, Purification, crystallization and X-ray diffraction analyses of the *T. elongatus* PSII core dimer with strontium replacing calcium in the oxygen-evolving complex, *Biochim. Biophys. Acta* 1767 (2007) 404–413.
- [27] Y. Pushkar, J. Yano, P. Glatzel, J. Messinger, A. Lewis, K. Sauer, U. Bergmann, V.K. Yachandra, Structure and orientation of the Mn_4Ca cluster in plant photosystem II membranes studied by polarized range-extended x-ray absorption spectroscopy, *J. Biol. Chem.* 282 (2007) 7198–7208.
- [28] R.M. Cinco, J.H. Robblee, J. Messinger, C. Fernandez, K.L.M. Holman, K. Sauer, V.K. Yachandra, Orientation of calcium in the $\text{Mn}_4\text{O}_x\text{Ca}$ of the oxygen-evolving complex determined using polarized strontium EXAFS of photosystem II membranes, *Biochemistry* 43 (2004) 13271–13282.
- [29] E.M. Sproviero, J.A. Gascón, J.P. McEvoy, G.W. Brudvig, V.S. Batista, QM/MM models of the O_2 -evolving complex of photosystem II, *J. Chem. Theory Comput.* 2 (2006) 1119–1134.
- [30] E.M. Sproviero, J.A. Gascón, J.P. McEvoy, G.W. Brudvig, V.S. Batista, A model of the oxygen-evolving center of photosystem II predicted by Structural refinement based on EXAFS simulations, *J. Am. Chem. Soc.* 130 (2008) 6728–6730.
- [31] E.M. Sproviero, J.A. Gascón, J.P. McEvoy, G.W. Brudvig, V.S. Batista, Quantum mechanics/molecular mechanics structural models of the oxygen-evolving complex of photosystem II, *Curr. Opin. Struct. Biol.* 17 (2007) 173–180.
- [32] S. Petrie, R. Stranger, P. Gatt, Ron J. Pace, Bridge over troubled water: resolving the competing photosystem II crystal structures, *Chem. Eur. J.* 13 (2007) 5082–5089.
- [33] S. Petrie, R. Stranger, R.J. Pace, Structural, magnetic coupling and oxidation state trends in models of the CaMn_4 cluster in photosystem II, *Chem. Eur. J.* 14 (2008) 5482–5494.
- [34] M. Kusunoki, Mono-manganese mechanism of the photosystem II water splitting reaction by a unique Mn_4Ca cluster, *Biochim. Biophys. Acta* 1767 (2007) 484–492.
- [35] H. Dau, M. Haumann, The manganese complex of photosystem II in its reaction cycle—basic framework and possible realization at the atomic level, *Coord. Chem. Rev.* 252 (2008) 273–295.
- [36] D.A. Pantazis, M. Orto, T. Petrenko, S. Zein, W. Lubitz, J. Messinger, F. Neese, Structure of the oxygen-evolving complex of photosystem II: information on the S_2 state through quantum chemical calculation of its magnetic properties, *Phys. Chem. Chem. Phys.* 11 (2009) 6788–6798.

- [37] P.E.M. Siegbahn, A structure-consistent mechanism for dioxygen formation in photosystem II, *Chem. Eur. J.* 14 (2008) 8290–8302.
- [38] P.E.M. Siegbahn, An energetic comparison of different models for the oxygen evolving complex of photosystem II, *J. Am. Chem. Soc.* 131 (2009) 18238–18239.
- [39] N. Cox, L. Rapatskiy, J.-H. Su, D.A. Pantazis, M. Sugiura, L. Kulik, P. Dorlet, A.W. Rutherford, F. Neese, A. Boussac, W. Lubitz, J. Messinger, The effect of $\text{Ca}^{2+}/\text{Sr}^{2+}$ substitution on the electronic structure of the oxygen-evolving complex of photosystem II: a combined multi-frequency EPR, ^{55}Mn -ENDOR and DFT study of the S_2 state, *J. Am. Chem. Soc.* 133 (10) (2011) 3635–3648.
- [40] G.C. Dismukes, Y. Siderer, Intermediates of a polynuclear manganese center involved in photosynthetic oxidation of water, *Proc. Natl. Acad. Sci. USA* 78 (1981) 274–278.
- [41] H. Levanon, K. Möbius, Advanced EPR spectroscopy on electron transfer processes in photosynthesis and biomimetic model systems, *Annu. Rev. Biophys. Biomol.* 26 (1997) 495–540.
- [42] R.D. Britt, J.M. Peloquin, K.A. Campbell, Pulsed and parallel-polarization EPR characterization of the photosystem II oxygen-evolving complex, *Annu. Rev. Biophys. Biomol.* 29 (2000) 463–495.
- [43] A. Haddy, EPR spectroscopy of the manganese cluster of photosystem II, *Photosynth. Res.* 92 (2007) 357–368.
- [44] K.A. Campbell, D.A. Force, P.J. Nixon, F. Dole, B.A. Diner, R.D. Britt, Dual-mode EPR detects the initial intermediate in photoassembly of the photosystem II Mn cluster: the influence of amino acid residue 170 of the D1 polypeptide on Mn coordination, *J. Am. Chem. Soc.* 122 (2000) 3754–3761.
- [45] S.L. Dexheimer, M.P. Klein, Detection of a paramagnetic intermediate in the S_1 state of the photosynthetic oxygen-evolving complex, *J. Am. Chem. Soc.* 114 (1992) 2821–2826.
- [46] T. Yamauchi, H. Mino, T. Matsukawa, A. Kawamori, T. Ono, Parallel polarization electron paramagnetic resonance studies of the S_1 -state manganese cluster in the photosynthetic oxygen-evolving system, *Biochemistry* 36 (1997) 7520–7526.
- [47] A. Boussac, M. Sugiura, A.W. Rutherford, P. Dorlet, Complete EPR spectrum of the S_3 -state of the oxygen-evolving photosystem II, *J. Am. Chem. Soc.* 131 (2009) 5050.
- [48] K.A. Åhring, S. Peterson, S. Styring, The S_0 state EPR signal from the Mn cluster in photosystem II arises from an isolated $S = 1/2$ ground state, *Biochemistry* 37 (1998) 8115–8120.
- [49] J. Messinger, J.H.A. Nugent, M.C.W. Evans, Detection of an EPR multiline signal for the S_0^* state in photosystem II, *Biochemistry* 36 (1997) 11055–11060.
- [50] J. Messinger, J.H. Robblee, W.O. Yu, K. Sauer, V.K. Yachandra, M.P. Klein, The S_0 state of the oxygen-evolving complex in photosystem II is paramagnetic: detection of an EPR multiline signal, *J. Am. Chem. Soc.* 119 (1997) 11349–11350.
- [51] O. Horner, E. Rivière, G. Blondin, S. Un, A.W. Rutherford, J.-J. Girerd, A. Boussac, SQUID Magnetization Study of the Infrared-Induced Spin Transition in the S_2 State of Photosystem II: Spin Value Associated with the $g = 4.1$ EPR Signal, *J. Am. Chem. Soc.* 120 (1998) 7924–7928.
- [52] A. Boussac, A.W. Rutherford, Comparative study of the $g = 4.1$ EPR signals in the S_2 -state of photosystem II, *Biochim. Biophys. Acta* 1457 (2000) 145–156.
- [53] A. Boussac, J.J. Girerd, A.W. Rutherford, Conversion of the spin state of the manganese complex in photosystem II induced by near-infrared light, *Biochemistry* 35 (1996) 6984–6989.
- [54] R.J. Pace, P.J. Smith, R. Bramley, D. Stehlik, EPR saturation and temperature dependence studies on signals from the oxygen-evolving centre of photosystem II, *Biochim. Biophys. Acta* 1058 (1991) 161–170.
- [55] A. Boussac, Inhomogeneity of the EPR multiline signal from the S_2 -state of the photosystem II oxygen evolving enzyme, *J. Biol. Inorg. Chem.* 2 (1997) 580–585.
- [56] P. Geijer, S. Peterson, K.A. Åhring, Z. Deak, S. Styring, Comparative studies of the S_0 and S_2 multiline electron paramagnetic resonance signals from the manganese cluster in photosystem II, *Biochim. Biophys. Acta* 1503 (2001) 83–95.
- [57] Z. Deak, S. Peterson, P. Geijer, K.A. Åhring, S. Styring, Methanol modification of the electron paramagnetic resonance signals from the S_0 and S_2 states of the water-oxidizing complex of photosystem II, *Biochim. Biophys. Acta* 1412 (1999) 240–249.
- [58] K.A. Åhring, S. Peterson, S. Styring, An oscillating manganese electron paramagnetic resonance signal from the S_0 state of the oxygen evolving complex in photosystem II, *Biochemistry* 36 (1997) 13148–13152.
- [59] T. Matsukawa, H. Mino, D. Yoneda, A. Kawamori, Dual-mode EPR study of new signals from the S_3 -state of oxygen-evolving complex in photosystem II, *Biochemistry* 38 (1999) 4072–4077.
- [60] J.H. Su, K.G.V. Havelius, F. Mamedov, F.M. Ho, S. Styring, Split EPR signals from photosystem II are modified by methanol, reflecting S state-dependent binding and alterations in the magnetic coupling in the CaMn_4 cluster, *Biochemistry* 45 (2006) 7617–7627.
- [61] N. Cox, F.M. Ho, N. Pevnim, R. Steffen, P.J. Smith, K.G.V. Havelius, J.L. Hughes, L. Debono, S. Styring, E. Krausz, R.J. Pace, The S_1 split signal of photosystem II; a tyrosine-manganese coupled interaction, *Biochim. Biophys. Acta* 1787 (2009) 882–889.
- [62] A. Boussac, H. Kuhl, S. Un, M. Rögner, A.W. Rutherford, Effect of near-infrared light on the S_2 -state of the manganese complex of photosystem II from *Synechococcus elongatus*, *Biochemistry* 37 (1998) 8995–9000.
- [63] A. Boussac, H. Kuhl, E. Ghibaudi, M. Rögner, A.W. Rutherford, Detection of an electron paramagnetic resonance signal in the S_0 state of the manganese complex of photosystem II from *Synechococcus elongatus*, *Biochemistry* 38 (1999) 11942–11948.
- [64] D.A. Force, D.W. Randall, G.A. Lorigan, K.L. Clemens, R.D. Britt, ESEEM studies of alcohol binding to the manganese cluster of the oxygen evolving cluster of photosystem II, *J. Am. Chem. Soc.* 120 (1998) 13321–13333.
- [65] R.D. Britt, K.A. Campbell, J.M. Peloquin, M.L. Gilchrist, C.P. Aznar, M.M. Dicus, J. Robblee, J. Messinger, Recent pulsed EPR studies of the photosystem II oxygen-evolving complex: implications as to water oxidation mechanisms, *Biochim. Biophys. Acta* 1655 (2004) 158–171.
- [66] K.A. Åhring, M.C.W. Evans, J.H.A. Nugent, R.J. Ball, R.J. Pace, ESEEM studies of substrate water and small alcohol binding to the oxygen-evolving complex of photosystem II during functional turnover, *Biochemistry* 45 (2006) 7069–7082.
- [67] B. Nöring, D. Shevela, G. Renger, J. Messinger, Effects of methanol on the S_2 -state transitions in photosynthetic water-splitting, *Photosynth. Res.* 98 (2008) 251–260.
- [68] M.-F. Charlot, A. Boussac, G. Blondin, Towards a spin coupling model for the Mn_4 cluster in photosystem II, *Biochim. Biophys. Acta* 1708 (2005) 120–132.
- [69] L.V. Kulik, B. Epel, W. Lubitz, J. Messinger, Electronic structure of the $\text{Mn}_4\text{O}_3\text{Ca}$ cluster in the S_0 and S_2 states of the oxygen-evolving complex of photosystem II based on pulse ^{55}Mn ENDOR and EPR Spectroscopy, *J. Am. Chem. Soc.* 129 (2007) 13421–13435.
- [70] J.M. Peloquin, K.A. Campbell, D.W. Randall, M.A. Evanchik, V.L. Pecoraro, W.H. Armstrong, R.D. Britt, ^{55}Mn ENDOR of the S_2 -state multiline EPR signal of photosystem II: implications on the structure of the tetranuclear Mn cluster, *J. Am. Chem. Soc.* 122 (2000) 10926–10942.
- [71] D.A. Berthold, G.T. Babcock, C.F. Yocum, A highly resolved, oxygen-evolving photosystem-II preparation from spinach thylakoid membranes—electron-paramagnetic-res and electron-transport properties, *FEBS Lett.* 134 (1981) 231–234.
- [72] M. Sugiura, A. Boussac, T. Noguchi, F. Rappaport, Influence of histidine-198 of the D1 subunit on the properties of the primary electron donor, P680, of photosystem II in *Thermosynechococcus elongatus*, *Biochim. Biophys. Acta* 1777 (2008) 331–342.
- [73] A. Boussac, F. Rappaport, P. Carrier, J.M. Verbavatz, R. Gobin, D. Kirilovsky, A.W. Rutherford, M. Sugiura, Biosynthetic $\text{Ca}^{2+}/\text{Sr}^{2+}$ exchange in the photosystem II oxygen-evolving enzyme of *Thermosynechococcus elongatus*, *J. Biol. Chem.* 279 (2004) 22809–22819.
- [74] N. Ishida, M. Sugiura, F. Rappaport, T.L. Lai, A.W. Rutherford, A. Boussac, Biosynthetic exchange of bromide for chloride and strontium for calcium in the photosystem II oxygen-evolving enzymes, *J. Biol. Chem.* 283 (2008) 13330–13340.
- [75] L. Kulik, B. Epel, J. Messinger, W. Lubitz, Pulse EPR, ^{55}Mn ENDOR and ELDOR-detected NMR of the S_2 -state of the oxygen evolving complex in photosystem II, *Photosynth. Res.* 84 (2005) 347–353.
- [76] L.V. Kulik, B. Epel, W. Lubitz, J. Messinger, ^{55}Mn pulse ENDOR at 34 GHz of the S_0 and S_2 states of the oxygen-evolving complex in photosystem II, *J. Am. Chem. Soc.* 127 (2005) 2392–2393.
- [77] B. Epel, I. Gromov, S. Stoll, A. Schweiger, D. Goldfarb, Spectrometer manager: a versatile control software for pulse EPR spectrometers, *Concepts Magn. Res. B* 26B (2005) 36–45.
- [78] C. Teutloff, S. Kessen, J. Kern, A. Zouni, R. Bittl, High-field (94-GHz) EPR spectroscopy on the S_2 multiline signal of photosystem II, *FEBS Lett.* 580 (2006) 3605–3609.
- [79] D.W. Randall, B.E. Sturgeon, J.A. Ball, G.A. Lorigan, M.K. Chan, M.P. Klein, W.H. Armstrong, R.D. Britt, ^{55}Mn ESE-ENDOR of a mixed valence Mn(III)Mn(IV) complex: comparison with the Mn cluster of the photosynthetic oxygen-evolving complex, *J. Am. Chem. Soc.* 117 (1995) 11780–11789.
- [80] K.O. Schäfer, R. Bittl, W. Zweggart, F. Lendzian, G. Haselhorst, T. Weyhermüller, K. Wieghardt, W. Lubitz, Electronic structure of antiferromagnetically coupled dinuclear manganese ($\text{Mn}^{\text{III}}\text{Mn}^{\text{IV}}$) complexes studied by magnetic resonance techniques, *J. Am. Chem. Soc.* 120 (1998) 13104–13120.
- [81] M. Zheng, G.C. Dismukes, Orbital configuration of the valence electrons, ligand field symmetry, and manganese oxidation states of the photosynthetic water oxidizing complex: analysis of the S_2 state multiline EPR signals, *Inorg. Chem.* 35 (1996) 3307–3319.
- [82] M. Zheng, S.V. Khangulov, G.C. Dismukes, V.V. Barynin, Electronic structure of dimanganese(II, III) and dimanganese(III, IV) complexes and dimanganese catalase enzyme: a general EPR spectral simulation approach, *Inorg. Chem.* 33 (1994) 382–387.
- [83] R. Orbach, Spin-lattice relaxation in rare-earth salts, *Proc. R. Soc. Lon. Ser-A* 264 (1961) 458–484.
- [84] A. Schweiger, G. Jeschke, Principles of pulse electron paramagnetic resonance, Oxford University Press, Oxford, 2001.
- [85] G.A. Lorigan, R.D. Britt, Temperature-dependent pulsed electron-paramagnetic-resonance studies of the S_2 state multiline signal of the photosynthetic oxygen-evolving complex, *Biochemistry* 33 (1994) 12072–12076.
- [86] J.W. Murray, J. Barber, Structural characteristics of channels and pathways in photosystem II including the identification of an oxygen channel, 3rd International Conference on Structure, Dynamics and Function of Proteins in Biological Membranes, vol. 159, J. Struc. Biol., Mt Verita, Switzerland, 2006, pp. 228–237.
- [87] F.M. Ho, S. Styring, Access channels and methanol binding site to the CaMn_4 cluster in photosystem II based on solvent accessibility simulations, with implications for substrate water access, *Biochim. Biophys. Acta* 1777 (2008) 140–153.
- [88] R.J. Debus, Protein ligation of the photosynthetic oxygen-evolving center, *Coord. Chem. Rev.* 252 (2008) 244–258.
- [89] M. Sugiura, F. Rappaport, W. Hillier, P. Dorlet, Y. Ohno, H. Hayashi, A. Boussac, Evidence that D1-His332 in photosystem II from *Thermosynechococcus elongatus* interacts with the S_3 -state and not with the S_2 -state, *Biochemistry* 48 (2009) 7856–7866.
- [90] A. Boussac, J.-J. Girerd, A. Rutherford, Conversion of the spin state of the manganese cluster in photosystem II induced by near-infrared light, *Biochemistry* 35 (1996) 6984–6989.

- [91] K.A. Åhrling, M.C.W. Evans, J.H.A. Nugent, R.J. Pace, The two forms of the S_2 state multiline signal in photosystem II: effect of methanol and ethanol, *Biochim. Biophys. Acta* 1656 (2004) 66–77.
- [92] D.W. Randall, A. Gelasco, M.T. Caudle, V.L. Pecoraro, R.D. Britt, ESE-ENDOR and ESEEM characterization of water and methanol ligation to a dinuclear Mn(III)Mn(IV) complex, *J. Am. Chem. Soc.* 119 (1997) 4481–4491.
- [93] A. Boussac, A.W. Rutherford, Ca^{2+} binding to the oxygen evolving enzyme varies with the redox state of the Mn cluster, *FEBS Lett.* 236 (1988) 432–436.
- [94] A. Boussac, A.W. Rutherford, S. Styring, Interaction of ammonia with the water splitting enzyme of photosystem II, *Biochemistry* 29 (1990) 24–32.
- [95] J. Messinger, U. Wacker, G. Renger, Unusual low reactivity of the water oxidase in redox state S_3 toward exogenous reductants. Analysis of the NH_2OH - and NH_2NH_2 -induced modifications of flash-induced oxygen evolution in isolated spinach thylakoids, *Biochemistry* 30 (1991) 7852–7862.
- [96] H. Koike, B. Hanssum, Y. Inoue, G. Renger, Temperature dependence of S-state transition in a thermophilic cyanobacterium, *Synechococcus vulcanus* Copeland measured by absorption changes in the ultraviolet region, *Biochim. Biophys. Acta* 893 (1987) 524–533.
- [97] G. Renger, B. Hanssum, Studies on the reaction coordinates of the water oxidase in PS II membrane fragments from spinach, *FEBS Lett.* 299 (1992) 28–32.
- [98] R.D. Guiles, J.L. Zimmermann, A.E. McDermott, V.K. Yachandra, J.L. Cole, S.L. Dexheimer, R.D. Britt, K. Wieghardt, U. Bossek, The S_3 state of photosystem II: differences between the structure of the manganese complex in the S_2 and S_3 states determined by x-ray absorption spectroscopy, *Biochemistry-Us* 29 (1990) 471–485.
- [99] W. Liang, T.A. Roelofs, R.M. Cinco, A. Rompel, M.J. Latimer, W.O. Yu, K. Sauer, M.P. Klein, V.K. Yachandra, Structural change of the Mn cluster during the $S_2 \rightarrow S_3$ state transition of the oxygen-evolving complex of photosystem II. Does it reflect the onset of water/substrate oxidation? Determination by Mn X-ray absorption spectroscopy, *J. Am. Chem. Soc.* 122 (2000) 3399–3412.
- [100] H. Dau, L. Iuzzolino, J. Dittmer, The tetra-manganese complex of photosystem II during its redox cycle—X-ray absorption results and mechanistic implications, *Biochim. Biophys. Acta* 1503 (2001) 24–39.
- [101] J.H. Robblee, J. Messinger, R.M. Cinco, K.L. McFarlane, C. Fernandez, S.A. Pizarro, K. Sauer, V.K. Yachandra, The Mn cluster in the S_0 state of the oxygen-evolving complex of photosystem II studied by EXAFS spectroscopy: are there three di- μ -oxo-bridged Mn_2 moieties in the tetranuclear Mn complex? *J. Am. Chem. Soc.* 124 (2002) 7459–7471.
- [102] M. Haumann, C. Müller, P. Liebisch, L. Iuzzolino, J. Dittmer, M. Grabolle, T. Neisius, W. Meyer-Klaucke, H. Dau, Structural and oxidation state changes of the photosystem II manganese complex in four transitions of the water oxidation cycle ($S_0 \rightarrow S_1$, $S_1 \rightarrow S_2$, $S_2 \rightarrow S_3$, and $S_3 \rightarrow S_0$) characterized by x-ray absorption spectroscopy at 20 K and room temperature, *Biochemistry* 44 (2005) 1894–1908.
- [103] Y.L. Pushkar, J. Yano, K. Sauer, A. Boussac, V.K. Yachandra, Structural changes in the Mn_4Ca cluster and the mechanism of photosynthetic water splitting, *Proc. Natl. Acad. Sci. USA* 105 (2008) 1879–1884.
- [104] W. Hillier, G.T. Babcock, S-state dependent fourier transform infrared difference spectra for the photosystem II oxygen evolving complex, *Biochemistry* 40 (2001) 1503–1509.
- [105] T. Noguchi, M. Sugiura, Flash-induced fourier transform infrared detection of the structural changes during the S-state cycle of the oxygen-evolving complex in photosystem II, *Biochemistry* 40 (2001) 1497–1502.
- [106] G. Renger, Coupling of electron and proton transfer in oxidative water cleavage in photosynthesis, *Biochim. Biophys. Acta* 1655 (2004) 195–204.
- [107] J. Messinger, Evaluation of different mechanistic proposals for water oxidation in photosynthesis on the basis of Mn_4O_xCa structures for the catalytic site and spectroscopic data, *Phys. Chem. Chem. Phys.* 6 (2004) 4764–4771.
- [108] S. Pudollek, F. Lenzian, R. Bittl, ^{55}Mn -ENDOR of the S_2 -state multiline signal of Photosystem II from *Thermosynechococcus elongatus*, *Biochem. Soc. Trans.* 36 (2008) 1001–1004.
- [109] C. Teutloff, S. Pudollek, S. Keßen, M. Broser, A. Zouni, R. Bittl, Electronic structure of the tyrosine D radical and the water-splitting complex from pulsed ENDOR spectroscopy on photosystem II single crystals, *Phys. Chem. Chem. Phys.* 11 (2009) 6715–6726.

**Electronic structure of a weakly antiferromagnetically coupled
Mn^{II}Mn^{III} model relevant to manganese proteins: a combined EPR,
⁵⁵Mn-ENDOR, and DFT study**

*Nicholas Cox, William Ames, Boris Epel, Leonid V. Kulik, Leonid Rapatskiy, Frank Neese, Johannes Messinger, Karl
Wieghardt, and Wolfgang Lubitz*

Electronic Structure of a Weakly Antiferromagnetically Coupled Mn^{II}Mn^{III} Model Relevant to Manganese Proteins: A Combined EPR, ⁵⁵Mn-ENDOR, and DFT Study

Nicholas Cox,^{*,†} William Ames,^{†,‡} Boris Epel,[†] Leonid V. Kulik,[§] Leonid Rapatskiy,[†] Frank Neese,^{†,‡} Johannes Messinger,^{||} Karl Wieghardt,[†] and Wolfgang Lubitz^{*,†}

[†]Max-Planck-Institut für Bioorganische Chemie, Stiftstrasse 34-36, D-45470 Mülheim an der Ruhr, Germany

[‡]Lehrstuhl für Theoretische Chemie, Institut für Physikalische und Theoretische Chemie, Universität Bonn, Wegelerstrasse 12, D-53115 Bonn, Germany

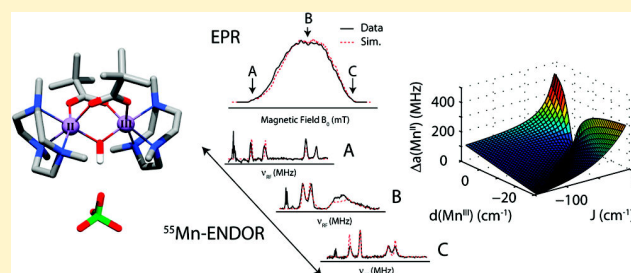
[§]Institute of Chemical Kinetics and Combustion, Institutskaya 3, 630090 Novosibirsk, Russia

^{||}Department of Chemistry, Kemiskt Biologiskt Centrum (KBC), Umeå University, S-90187 Umeå, Sweden

S Supporting Information

ABSTRACT: An analysis of the electronic structure of the [Mn^{II}Mn^{III}(μ -OH)-(μ -piv)₂(Me₃tacn)₂](ClO₄)₂ (**PivOH**) complex is reported. It displays features that include: (i) a ground 1/2 spin state; (ii) a small exchange (J) coupling between the two Mn ions; (iii) a mono- μ -hydroxo bridge, bis- μ -carboxylato motif; and (iv) a strongly coupled, terminally bound N ligand to the Mn^{III}. All of these features are observed in structural models of the oxygen evolving complex (OEC). Multifrequency electron paramagnetic resonance (EPR) and electron nuclear double resonance (ENDOR) measurements

were performed on this complex, and the resultant spectra simulated using the Spin Hamiltonian formalism. The strong field dependence of the ⁵⁵Mn-ENDOR constrains the ⁵⁵Mn hyperfine tensors such that a unique solution for the electronic structure can be deduced. Large hyperfine anisotropy is required to reproduce the EPR/ENDOR spectra for both the Mn^{II} and Mn^{III} ions. The large effective hyperfine tensor anisotropy of the Mn^{II}, a d⁵ ion which usually exhibits small anisotropy, is interpreted within a formalism in which the fine structure tensor of the Mn^{III} ion strongly perturbs the zero-field energy levels of the Mn^{II}Mn^{III} complex. An estimate of the fine structure parameter (d) for the Mn^{III} of -4 cm^{-1} was made, by assuming the intrinsic anisotropy of the Mn^{II} ion is small. The magnitude of the fine structure and intrinsic (onsite) hyperfine tensor of the Mn^{III} is consistent with the known coordination environment of the Mn^{III} ion as seen from its crystal structure. Broken symmetry density functional theory (DFT) calculations were performed on the crystal structure geometry. DFT values for both the isotropic and the anisotropic components of the onsite (intrinsic) hyperfine tensors match those inferred from the EPR/ENDOR simulations described above, to within 5%. This study demonstrates that DFT calculations provide reliable estimates for spectroscopic observables of mixed valence Mn complexes, even in the limit where the description of a well isolated $S = 1/2$ ground state begins to break down.



1. INTRODUCTION

Several μ -oxo/hydroxo bridged Mn cofactors have been found in biological enzymes. Important examples include (a) the dimanganese catalase,^{1,2} which catalyzes the dismutation of H₂O₂ to H₂O and O₂; (b) the recently identified Mn containing class Ib ribonucleotide reductase;^{3,4} and (c) the tetra-manganese oxygen evolving complex (OEC) of reference PSII which performs the multistep oxidation of H₂O to O₂. To understand the chemistry these complexes perform it is important to resolve, in detail, their geometric and electronic structures. Synthetic complexes play a crucial part in this exercise, allowing specific features to be examined separately. In multielectron-reactions such as water-splitting the catalysts must cycle through several different oxidation states, many of which are paramagnetic. As such, electron paramagnetic resonance (EPR) spectroscopy is

an invaluable tool for the elucidation of the properties of these complexes. Mixed valence complexes such as Mn^{II}Mn^{III} and Mn^{III}Mn^{IV}, typically exhibit antiferromagnetic coupling leading to the ground state configuration of total electron spin (S_T) of 1/2. The $S_T = 1/2$ state manifests itself in CW-EPR as a characteristic multiline signal centered at $g \sim 2$. The large number of spectral lines observed arises from the coupling of the two ⁵⁵Mn nuclei to the total unpaired electronic spin. In principle, the electronic structures can be derived from these measurements. However, the analysis of EPR spectra of exchange-coupled systems is often complicated by the presence of multiple terms of similar energetic importance in the spin Hamiltonian. In

Received: April 13, 2011

Published: August 11, 2011

general it is impossible to obtain unique parameters for the Hamiltonian from a single EPR spectrum. One solution to this problem is to measure the EPR spectrum at multiple frequencies (X-, Q-, and W-band). As the different components of the Spin Hamiltonian have different magnetic field dependence, this allows the relative contributions to be resolved.^{5,6} An important complementary approach is electron nuclear double resonance (ENDOR) spectroscopy.^{7,8} ⁵⁵Mn-ENDOR spectra are usually much simpler to analyze because of the lower number of overlapping transitions and its insensitivity to the exact geometry of the hyperfine tensors relative to each other. As a consequence, reliable information on the hyperfine couplings, and, to a lesser extent, nuclear quadrupole couplings of the ⁵⁵Mn ($I = 5/2$) nuclei can be readily obtained using such measurements. In studies on mixed valence Mn^{III}Mn^{IV} complexes the combination of both multifrequency-EPR and ⁵⁵Mn-ENDOR has allowed not only a determination of the effective G and hyperfine tensors (A_1, A_2) but also their relative orientations. While there are multiple EPR/⁵⁵Mn-ENDOR studies on synthetic and biological Mn^{III}Mn^{IV} complexes^{5,6,9–14} all efforts, including our own, to obtain such measurements for Mn^{II}Mn^{III} complexes have failed thus far. The reason for this is the very fast T_1 relaxation in such complexes.¹⁵ As such only CW-EPR studies have yet been reported for Mn^{II}Mn^{III} model complexes.^{5,16–19} Here we demonstrate for the first time that pulsed ⁵⁵Mn ENDOR measurements at Q-band frequency can be successfully employed for deriving the electronic structure of an exchange coupled Mn^{II}Mn^{III} complex. The complex used is the well characterized [Mn^{II}Mn^{III}(μ -OH)(μ -piv)₂(Me₃tacn)₂](ClO₄)₂ (PivOH) complex previously reported by Bossek et al.²⁰ This complex contains a μ -hydroxo (μ -OH) and two μ -carboxylato (μ -piv) bridges between the two Mn ions (see Figure 5). The oxidation states of the two Mn ions could be identified from the crystal structure because of the elongation of the Mn(2)–N(5) and Mn(2)–O(3) bonds. This elongation represents the Jahn–Teller axis of the Mn^{III}.

Static magnetization measurements have estimated the exchange coupling between the two Mn ions as antiferromagnetic $J = -8.5 \text{ cm}^{-1}$ with an unusually large on-site zero-field splitting for the Mn^{III} ion, $|d^{\text{III}}| = 8 \text{ cm}^{-1}$ (see ref 21). Subsequent pulse EPR measurements on frozen solution samples agree with this result; J was found to lie within -9.3 to -8.2 cm^{-1} , see ref 15. Thus this complex represents a system where the J coupling alone does not describe well the energy-levels of the system. A demonstration of how additional terms in the Spin Hamiltonian contribute to the total zero-field splitting of the complex and the experimental manifestation of these effects are discussed.

2. MATERIALS AND METHODS

2.1. Magnetic Susceptibility Measurements. Measurements were performed on powder samples of solid material in the temperature range 2–300 K by using a SQUID susceptometer with a field of 1.0 T (MPMS-7, Quantum Design, calibrated with standard a palladium reference sample, error <2%). Multiple-field variable-temperature magnetization measurements were done at 1 T, 4 T, and 7 T also in the range 2–300 K with the magnetization equidistantly sampled on a $1/T$ temperature scale. The experimental data were corrected for underlying diamagnetism by use of tabulated Pascal's constants,^{22,23} as well as for temperature-independent paramagnetism. The susceptibility and magnetization data were simulated with the program *JulX* for exchange coupled systems.²⁴ Simulations presented are based on the Spin

Hamilton formalism (see Theory section 3). The magnetic moments were obtained from the eigenfunctions ψ_i of the appropriate Spin Hamiltonian (\hat{H}) by using the Hellman–Feynman theorem $\mu_i(\vec{B}) = -\langle \psi_i | d\hat{H}/d\vec{B} | \psi_i \rangle$ where \vec{B} denotes the applied magnetic field. Powder summations were done by using a 16-point Lebedev grid.^{25,26} Intermolecular interactions were considered by using a Weiss temperature, Θ_w , as perturbation of the temperature scale, $kT' = k(T - \Theta_w)$ for the calculation.

2.2. EPR Measurements. Q-band CW-EPR measurements were performed using a Bruker ESR 200D spectrometer equipped with an Oxford Instruments ESR 935 cryostat and ITC4 temperature controller. For data acquisition and spectrometer control a computer was used running a lab-written control program. The microwave frequency and magnetic field strength were monitored using a Hewlett-Packard 5352B frequency counter and a Bruker ER035M NMR gaussmeter, respectively.

Q-band pulse EPR and ⁵⁵Mn-Davies ENDOR measurements were performed at 4.2 K using a Bruker ELEXSYS E580 Q-band pulse EPR spectrometer equipped with an Oxford-CF935 liquid helium cryostat and an ITC-503 temperature controller. Electron spin echo-detected (ESE) field-swept spectra were measured using the pulse sequence: $\pi/2 - \tau - \pi - \tau - \text{echo}$, where $\pi = 80 \text{ ns}$ and $\tau = 440 \text{ ns}$. ⁵⁵Mn-Davies ENDOR spectra were collected using the pulse sequence: $\pi - \pi_{\text{RF}} - T - \pi/2 - \tau - \pi - \tau - \text{echo}$, where $\pi = 80 \text{ ns}$, $\tau = 440 \text{ ns}$, π_{RF} (RF pulse, radio frequency) = $3.5 \mu\text{s}$ and a delay of $T = 600 \text{ ns}$. To measure hyperfine couplings larger than 150 MHz, an external home-built computer console (SpecMan4EPR control software^{12,27,28}) was used with the ELEXSYS E580 Q-band pulse EPR spectrometer, coupled to a external RF generator (SMT02 signal generator) and RF amplifier (ENI 5100 L). A shot repetition rate of $\sim 300 \text{ Hz}$ was used for all measurements. Mn-ENDOR experiments were performed using the random (stochastic) acquisition technique as described in Epel et al.²⁹ Usual sequential acquisition in this ENDOR experiment with the PivOH complex resulted in a severe distortion of the Mn-ENDOR spectrum caused by “heating artifacts”. This is described in more details in Kulik et al.⁸

2.3. CW-EPR/⁵⁵Mn-ENDOR Simulations. CW-EPR/⁵⁵Mn-ENDOR spectra were simultaneously fit assuming an effective spin $S = 1/2$ ground state (see Theory section 3.2). The same Spin Hamiltonian was used for both CW-EPR and ⁵⁵Mn-ENDOR spectra. The electron Zeeman term was treated exactly. The nuclear Zeeman, hyperfine, and quadrupole terms were treated using second order perturbation theory. Spectral simulations were performed numerically using Scilab-4.4.1, an open source vector-based linear algebra package (www.scilab.org) and the EasySpin package³⁰ in MATLAB. Linewidths (fwhm) used for the simulations presented in Figures 1 and 2 are CW-EPR 6.5 MHz; Pulse-EPR 2.7 MHz; Pulse-ENDOR 5.0 MHz. An anisotropic line broadening was included in simulations with principal values [320 163 112] MHz. A Gaussian profile was used to describe the excitation line width, with a fwhm of 20 MHz.

2.4. Computational Details. **2.4.1. Geometry Optimizations.** Geometry optimizations used the BP86 density functional^{31,32} along with the 2010 DFT dispersion corrections from Grimme et al.³³ and the zero-order regular approximation (ZORA) to account for relativistic effects.^{34–36} The segmented all-electron relativistically contracted (SARC) def2-SVP basis sets were used for the hydrogen and carbon atoms while the SARC def2-TZVP(-f) basis sets were used for all other atoms.³⁷ Optimizations took advantage of the RI approximation with the decontracted auxiliary def2-TZVP/J Coulomb fitting basis sets³⁸ as implemented in ORCA.³⁹ Increased integration grids (Grid4 in ORCA convention) and tight SCF convergence criteria were used throughout.

2.4.2. EPR Parameter Calculations. The exchange coupling constant (J), hyperfine tensors, and nuclear quadrupole tensors were calculated for the manganese ions and nitrogen atoms in each model of PivOH using

the broken-symmetry density functional theory (DFT) methodology (BS-DFT).^{40–43} The hybrid meta-GGA TPSSh functional⁴⁴ was used with the chain-of-spheres (RIJCOSX) approximation to exact exchange.⁴⁵ Scalar relativistic effects were included with ZORA paired with the SARC def2-TZVP(-f) basis sets and the decontracted def2-TZVP/J Coulomb fitting basis sets for all atoms. Increased integration grids (Grid4 and GridX4 in ORCA convention) and tight SCF convergence criteria were used in the calculation of all EPR parameters. For the calculation of the manganese hyperfine and quadrupole tensors specially constructed basis sets, based on SARC def2-TZVP, were used for the Mn, N, and O atoms. These basis sets contain fully decontracted s-shells with three additional steep primitives added to the core (details are presented in the Supporting Information S7). This construction is similar to that used previously in the Core Properties (CP) basis set,⁴⁶ with the benefit of being consistent with the ZORA method used. The integration grids were increased to an integration accuracy of 11 and 9 (ORCA convention) for Mn and N/O, respectively. Picture change effects were applied for the calculation of the ⁵⁵Mn hyperfine and quadrupole tensors. The application of the BS-DFT approach and the performance of the TPSSh functional for the calculation of exchange coupling constants and hyperfine coupling constants in manganese systems has been extensively discussed, benchmarked and calibrated in previous studies of manganese dimers,^{47–49} trimers,⁵⁰ and tetramers.^{51,52}

3. THEORY

3.1. The Spin Hamiltonian Formalism. Here we consider an antiferromagnetically exchange coupled Mn^{II}Mn^{III} dimer. A basis set that describes the Mn-dimer spin manifold can be built from the product of the eigenstates of the two interacting spins:

$$|S_1 S_2 M_1 M_2 I_1 I_2 m_1 m_2\rangle \quad (1)$$

Here S_i refers to the electronic spin state of Mn_{*i*}, M_i refers to the electronic magnetic sublevel of Mn_{*i*}, I_i refers to the nuclear spin state of Mn_{*i*}, and m_i refers to the nuclear magnetic sublevel of Mn_{*i*}. S_i takes the value $5/2$ for Mn^{II} and 2 for Mn^{III}; M_i takes the values: $S_i, S_i-1, \dots, 1-S_i, -S_i$; I_i takes the value $5/2$ for ⁵⁵Mn (100% natural abundance) and; m_i takes the values $-I_i, 1-I_i, \dots, I_i-1, I_i$. The Spin Hamiltonian that describes the spin manifold of the Mn dimer is

$$\hat{H} = \sum_i \beta_e \vec{B}_0 \cdot \hat{g}_i \cdot \vec{S}_i - \sum_i g_n \beta_n \vec{B}_0 \cdot \vec{I}_i + \sum_i \vec{S}_i \cdot \hat{a}_i \vec{I}_i + \sum_i \vec{I}_i \cdot \hat{p}_i \cdot \vec{I}_i + \sum_i \vec{S}_i \cdot \hat{d}_i \cdot \vec{S}_i - 2\vec{S}_1 \cdot \vec{J} \cdot \vec{S}_2 \quad (2)$$

It contains (i) an electronic Zeeman term for each Mn ion; (ii) a nuclear Zeeman term for each ⁵⁵Mn nucleus; (iii) an electron–nuclear hyperfine term for each ⁵⁵Mn nucleus; (iv) a nuclear quadrupole term for each ⁵⁵Mn nucleus; (v) a fine structure term for each Mn ion; and (vi) a electron spin coupling term for the Mn–Mn interaction.

3.2. Effective Spin 1/2 Ground State. The electronic coupling between the two Mn ions in mixed valence Mn dimers is usually dominated by the through bond exchange interaction and sufficiently large that the spin manifold can be treated within the strong exchange limit. In this instance the exchange interaction between the two Mn ions is significantly larger than any other term of the Spin Hamiltonian. The resultant electronic spin states of the manifold are then adequately described by a single quantum number, the total spin (S_T). The “multiline” EPR signal observed for the PivOH complex is derived from only one total spin state, the ground state of the spin manifold with total spin

$S_T = 1/2$. The basis set that describes this subspace takes the form

$$\left| \frac{1}{2} \quad M \quad m_1 \quad m_2 \right\rangle \quad (3)$$

Where M takes all half-integer values $-1/2 \leq M \leq 1/2$; and m_i (where $i = 1-2$) takes all half integer values $-5/2 \leq m_i \leq 5/2$. The effective Spin Hamiltonian that describes the ground state of the spin manifold ($S_T = 1/2$) is

$$\hat{H} = \beta_e \vec{B}_0 \cdot \hat{G} \cdot \vec{S} + \sum_i (g_n \beta_n \vec{B}_0 \cdot \vec{I}_i + \vec{S} \cdot \hat{A}_i \cdot \vec{I}_i + \vec{I}_i \cdot \hat{P}_i \cdot \vec{I}_i) \quad (4)$$

It contains (i) the electronic Zeeman term for the total electronic spin; (ii) nuclear Zeeman terms for each ⁵⁵Mn nucleus; (iii) electron–nuclear hyperfine terms for each ⁵⁵Mn nucleus, and (iv) nuclear quadrupole terms for each ⁵⁵Mn nucleus.

3.3. Isotropic Spin Projections. A mapping of the spin subspace in section 3.2 onto the original basis set as described in section 3.1 can be made. This was first described by Sage et al.⁵³ in relation to the dimeric iron cofactor of purple acid phosphatase and extended to mixed valence manganese complexes by Zheng et al.¹⁹ and Peloquin et al.¹¹ This allows the intrinsic g and hyperfine tensors of the four Mn ions (g_i, a_i see eq 2) to be calculated from the effective G and hyperfine tensors (A_i , see eq 4). For an exchanged coupled Mn^{II}Mn^{III} complex the effective g -factor G , hyperfine tensors A_i , and quadrupole tensors P_i are related to the parameters of the complete spin Hamiltonian of the exchange-coupled system^{53,54} by the spin-projection coefficients, where the isotropic spin projection coefficients (ρ_1, ρ_2) are defined as:

$$\rho_1(\text{Mn}^{\text{II}}) = \frac{S_1(S_1 + 1) - S_2(S_2 + 1) + S(S + 1)}{2S(S + 1)}$$

$$\rho_2(\text{Mn}^{\text{III}}) = \frac{S_2(S_2 + 1) - S_1(S_1 + 1) + S(S + 1)}{2S(S + 1)} \quad (5)$$

and effective G and hyperfine values (A_i), assuming all g_i and a_i are isotropic:

$$G = \rho_1 g_1 + \rho_2 g_2 + \frac{\rho_1 \rho_2}{S J} (g_1 - g_2) [(3\rho_1 + 1)d_1 - (3\rho_2 + 1)d_2]$$

$$A_1 = \rho_1 a_1 - a_1 \frac{\rho_1 \rho_2}{S J} [(3\rho_1 + 1)d_1 - (3\rho_2 + 1)d_2]$$

$$A_2 = \rho_2 a_2 + a_2 \frac{\rho_1 \rho_2}{S J} [(3\rho_1 + 1)d_1 - (3\rho_2 + 1)d_2]$$

$$P_1 = p_1$$

$$P_2 = p_2 \quad (6)$$

For an Mn^{II}Mn^{III} dimer, $S_1(\text{Mn}^{\text{II}}) = 5/2$; and $S_2(\text{Mn}^{\text{III}}) = 2$ which gives isotropic spin projection values of $\rho_1 = 7/3$ and $\rho_2 = -4/3$, respectively. In the limit where exchange coupling J is large, the above relations are approximately: $G = 7/3g^{\text{II}} - 4/3g^{\text{III}}$, $A^{\text{II}} = 7/3a^{\text{II}}$, $A^{\text{III}} = -4/3a^{\text{III}}$, $P^{\text{II}} = p^{\text{II}}$, $P^{\text{III}} = p^{\text{III}}$.^{13,55}

3.4. Anisotropic Spin Projections. It is noted that the expressions above derived from first order perturbation theory break down in systems where J is not large. In systems that have a pseudo-well isolated ground state it is often more convenient to describe the spin projections ρ_i as a tensor as opposed to a scalar quantity, that is, the correction to the projected g /hyperfine tensor (second/third terms of eq 6) is subsumed into the spin projection coefficient itself. This formalism can also be readily generalized to

the large spin systems. Here the Mn ion fine structure terms are included in the Spin Hamiltonian that describes the spin manifold (total zero-field splitting) of the complex.

$$\hat{H} = -2J\vec{S}_1 \cdot \vec{S}_2 + \vec{S}_1 \cdot \hat{d}_1 \cdot \vec{S}_1 + \vec{S}_2 \cdot \hat{d}_2 \cdot \vec{S}_2 \quad (7)$$

The fine structure tensors are traceless and as such be expressed in terms of two parameters $d_{1,2}$ and $e_{1,2}$:

$$\hat{d}_i = \begin{bmatrix} -\frac{1}{3}(d_i - 3e_i) & 0 & 0 \\ 0 & -\frac{1}{3}(d_i + 3e_i) & 0 \\ 0 & 0 & \frac{2}{3}d_i \end{bmatrix} \quad (8)$$

The projection of the total spin onto the individual Mn centers is defined as the ratio of the on-site spin expectation value $\langle S_z^i \rangle$ of the i -th Mn to the “total spin” S_T or equally $\langle S_z \rangle$:⁵¹

$$\rho_i = \frac{\langle S_z^i \rangle}{\langle S_z \rangle} \quad \text{or} \quad \rho_i = \frac{\langle S_z^i \rangle}{S_T} \quad (9)$$

For the $S_T = 1/2$ electronic spin-manifold the expectation value of the spin operator $\langle S_z \rangle$ is $1/2$ and thus eq 6 can be re-expressed as

$$\rho_i = 2 \cdot \langle S_z^i \rangle \quad (10)$$

The effective \hat{G} and hyperfine tensors (\hat{A}_i) are a weighted, linear sum of the intrinsic g and hyperfine tensors (a_i) of the individual Mn ions.

$$\begin{aligned} \hat{G} &= \hat{\rho}_1 \hat{g} + \hat{\rho}_2 \hat{g} \\ \hat{A}_1 &= \hat{\rho}_1 \hat{a}_1 \\ \hat{A}_2 &= \hat{\rho}_2 \hat{a}_2 \\ \hat{P}_1 &= \hat{p}_1 \\ \hat{P}_2 &= \hat{p}_2 \end{aligned} \quad (11)$$

3.5. Calculation of Mn–Mn Exchange Couplings Using Broken Symmetry (BS) DFT. The calculation of the exchange coupling (J) was performed assuming the “isotropic” Heisenberg Hamiltonian shown below, that is, the same as eq 7 but excluding the fine structure terms.

$$\hat{H} = -2J\vec{S}_1 \cdot \vec{S}_2 \quad (12)$$

Within the formalism of BS-DFT the exchange coupling constant (J) can be calculated in a number of ways. Here the method of Yamaguchi was used (eq 13), which has been shown to correctly estimate exchange couplings over the entire range of coupling regimes, that is, from the weak to strong coupling limit.^{55,56}

$$J = -\frac{E_{\text{HS}} - E_{\text{BS}}}{\langle S^2 \rangle_{\text{HS}} - \langle S^2 \rangle_{\text{BS}}} \quad (13)$$

The calculation of the exchange coupling constants can be performed using either an adiabatic or a single geometry approach. For the adiabatic approximation of J , the energies and $\langle S^2 \rangle$ values from both the optimized high-spin and broken-symmetry geometries are entered into eq 13. The more common approach is to simply use the high-spin and broken-symmetry energies and $\langle S^2 \rangle$ values for a single geometry, usually optimized in the high-spin state. The adiabatic approximation is the better

representation of the measured exchange coupling as the experiments are inherently adiabatic.

3.6. Hyperfine Couplings from Broken-Symmetry DFT. A technique which allows for the extraction of hyperfine coupling constants from BS-DFT calculations was developed recently.⁵¹ The approach was shown to give calculated ⁵⁵Mn hyperfine couplings that can be meaningfully compared with experimental values of manganese dimers,^{47–49} trimers,⁵⁰ and tetramers.^{51,52} The main concepts of the method will be highlighted here, for more detailed descriptions of the method see refs 51,52.

For a system composed of metal-centered subsystems, in this case subsystems centered on the Mn^{II} and Mn^{III} ions, the general equation linking the isotropic BS calculated hyperfine coupling constants to experiment is given below for a nucleus j within subsystem i .

$$A_{\text{iso}}^{(i,j)} = A_{\text{iso,site}}^{(i,j)} \frac{\langle S_z^{(j)} \rangle}{S_T} \quad (14)$$

where S_T is the effective total spin ($1/2$), $\langle S_z^{(j)} \rangle$ is the on-site spin expectation value, and $A_{\text{iso,site}}^{(i,j)}$ is the site isotropic coupling constant defined as follows:

$$A_{\text{iso,site}}^{(i,j)} = A_{\text{iso,BS}}^{(j)} \frac{\langle S_z \rangle_{\text{BS}}}{S_i} \quad (15)$$

Here S_i is the site-spin of subsystem i and is positive or negative depending on whether the subsystem carries majority or minority spin. $\langle S_z \rangle_{\text{BS}}$ is the total M_S of the BS wave function and $A_{\text{iso,BS}}^{(j)}$ is the “raw” hyperfine coupling constant calculated directly from the BS calculation. The final projection of the site isotropic coupling constant into the correct effective hyperfine coupling constant is possible through the use of the isotropic spin projection coefficients, $7/3$ and $-4/3$ for Mn^{II} and Mn^{III}, or alternatively, the anisotropic spin-projection coefficients as described in the previous section. It has been previously established that calculations of hyperfine components of Mn are underestimated with the BS-DFT method and require an empirically determined scaling factor.^{47,48,51,52} As the methodology used here differs from previous reports we redetermined the scaling factor to be 1.50 for the basis set and density functional used here. See the Supporting Information S8 for more information on the determination of the scaling factor.

4. RESULTS

4.1. Magnetic Susceptibility. Pure samples of the Mn^{II}Mn^{III} PIVO complex used in this study were synthesized as described in ref 20. In the Supporting Information S1 the temperature dependence of the magnetic susceptibility of a powder sample of the PivOH complex recorded at an applied field of $B_0 = 1$ T (plotted as χT vs T) is shown. A small offset on the y -axis (χT) is inferred and is assigned to a paramagnetic impurity. This impurity presumably represents the fraction of complexes which have decomposed to a monomeric Mn²⁺ species (see section 4.2.1). The data could be readily modeled using the Spin Hamiltonian given in the Theory section 3.1 (eq 2). In these simulations only the electronic terms are considered. The nuclear terms (hyperfine, quadrupole) are sufficiently small, of the order of MHz, that they form no significant contribution to the total zero-field splitting of the complex, which is of the order of cm^{-1} . The simulation strongly depends on the signed magnitude of the exchange coupling J , estimated to be -8.6 cm^{-1} . In contrast,

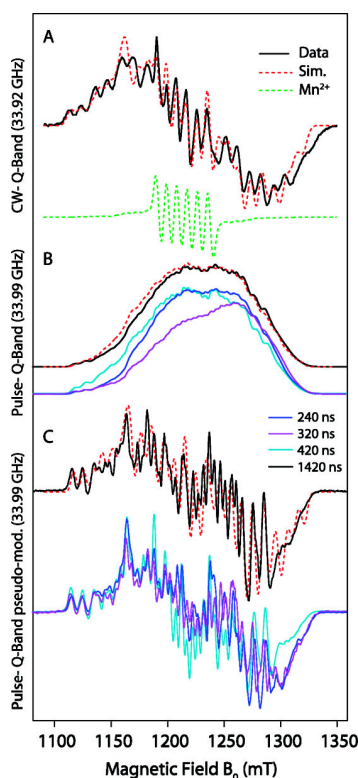


Figure 1. CW and pulsed Q-band EPR spectra of the $\text{Mn}^{\text{II}}\text{Mn}^{\text{III}}$ PivOH complex. (A) CW-Q-band. Experimental parameters: microwave frequency: 33.92 GHz; microwave power: 8 mW; modulation amplitude: 0.2 mT, 1.5 kHz; temperature: 10 K. (B) Q-band pulse EPR, ESE-detected field sweep. Experimental parameters: microwave frequencies: 33.69 GHz; shot repetition rate: 5 μs ; microwave pulse length (τ): 80 ns, τ : 240 ns, 320 ns, 420 and 1420 ns, temperature: 4.2 K. (C) Corresponding pseudomodulated 'CW like' EPR lineshapes for the absorption spectra presented in panel B. These spectra were generated by convoluting the original absorption spectra with a Bessel function of the 1st kind. The peak-to-peak field modulation used was 3 mT. Solid lines represent the experimental data. The red dashed lines superimposing each data trace represent a least-squares fitting to the whole data set (see Figures 1 and 2) using a model based on the Spin Hamiltonian formalism (see Theory eq 4). It is noted that the CW-Q-band EPR spectrum contains a small contribution of free Mn^{2+} . In solution Mn^{2+} usually appears as a narrow EPR signal centered at $g \sim 2$, with 6 sharp peaks with peak-to-peak separation of 8–10 mT. The contribution of the Mn^{2+} signal is shown by the green dashed traces and is included in the simulation profile shown by the red dashed traces. All fitting parameters are given in Table 1.

the fine structure parameters of both Mn ions (d_1 , d_2) are not well-defined. This is plausible because the ground state is a doublet, without zero-field splitting and the splitting in the excited manifolds should barely affect the values of χT . An error correlation diagram for the exchange coupling constant J and the fine structure parameter d_2 of Mn(III) as shown in the Supporting Information S1 which shows this feature of the static magnetic measurements.

4.2. EPR Spectroscopy. **4.2.1. CW EPR.** The CW-Q-band EPR frozen solution spectrum of the $\text{Mn}^{\text{II}}\text{Mn}^{\text{III}}$ PivOH complex is shown in Figure 1A. The samples were dissolved in a mixture of purified dry CH_3CN and CH_2Cl_2 (1:3 v/v) at a concentration of ~ 1 mM. This solvent combination was previously seen to impart

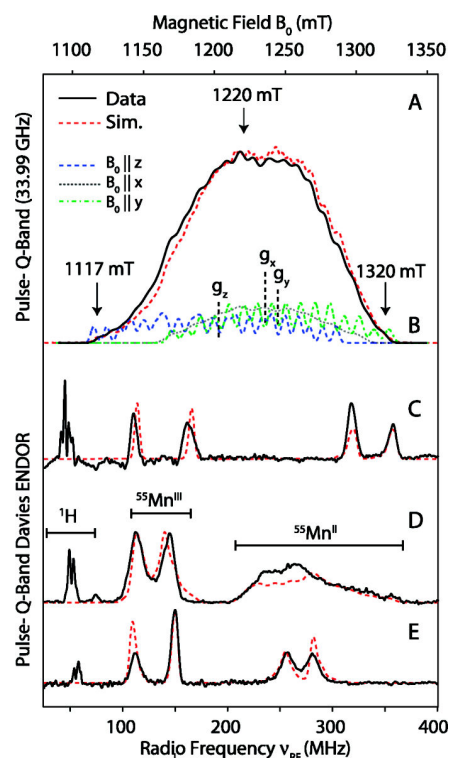


Figure 2. Pulsed Q-band EPR and ENDOR spectra of the $\text{Mn}^{\text{II}}\text{Mn}^{\text{III}}$ PivOH complex. (A) Q-band pulse EPR, ESE-detected field sweep (as shown in Figure 1B). (B) A decomposition of the EPR simulation along the three principal axes, x , y , and z . (C, D, and E) ^{55}Mn -ENDOR spectra collected at three field positions within the EPR absorption profile: 1117 mT, 1220 mT, and 1320 mT, respectively. The black, solid line represents the experimental data. The red dashed lines superimposing each data trace represent a least-squares fitting to the whole data set (see Figures 1 and 2) using a model based on the Spin Hamiltonian formalism (see Theory eq 4). The optimized parameter sets are given in Table 1. The contribution of the Mn^{II} and Mn^{III} ions to the ^{55}Mn -ENDOR spectra is shown by the black bars.

good relaxation properties (T_1 , T_2). The spectrum is centered at $g \sim 1.97$, and it contains at least 23 spectral lines spread over a field range of 220 mT. The hyperfine line spacing is of the order of 10–12 mT, as estimated from the spectral lines at the low and high field edges of the spectrum. The center of the hyperfine pattern has a slightly different hyperfine spacing suggesting a small contamination from a monomeric Mn^{2+} species. Monomeric Mn^{2+} typically manifests itself as a "six line" EPR signal, centered at $g \sim 2.0$, with hyperfine line spacing of ~ 9 mT. The estimated contribution of the Mn^{2+} species is shown by the green dashed line (Figure 1A).

The spectral pattern observed for the $\text{Mn}^{\text{II}}\text{Mn}^{\text{III}}$ PivOH complex is typical of antiferromagnetically coupled, mixed valence manganese dimers ($\text{Mn}^{\text{III}}\text{Mn}^{\text{II}}/\text{Mn}^{\text{III}}\text{Mn}^{\text{IV}}$). The coupled Mn dimer can be treated as an effective spin 1/2 state, where the inhomogeneous line width of the spectrum (the total spectral breadth) is defined by the ^{55}Mn hyperfine couplings of the two Mn nuclei to the fictitious electron spin $S_T = 1/2$. The G -tensor anisotropy of such systems is typically small and not resolved at low microwave frequencies (X , Q-band); that is to say the G -anisotropy is smaller than the line-broadening/line-splitting due to the hyperfine interaction. Regardless, an estimate can

be made of the G -anisotropy by comparing the total spectral breadth of the spectrum measured at both X and Q-band frequencies. The CW-X-band EPR spectrum of the $\text{Mn}^{\text{II}}\text{Mn}^{\text{III}}$ PivOH complex was previously reported in refs 5,57 with total spectral breadth of ~ 180 mT. This is approximately 40 mT narrower than that measured at Q-band. As the G -tensor is the only term of the effective Spin Hamiltonian (eq 4) that is dependent on the magnetic field, the increase in the total spectral breadth of the signal measured at the Q-band is a direct measure of the G -anisotropy. Thus a ΔG of ~ 0.1 is inferred, where ΔG represents the difference between the largest and smallest component of the G -tensor, as seen for previous $\text{Mn}^{\text{II}}\text{Mn}^{\text{III}}$ model complex studies.^{5,19,57}

Pulse-Q-band EPR spectra of the $\text{Mn}^{\text{II}}\text{Mn}^{\text{III}}$ PivOH complex are shown in Figure 1B. These spectra were detected using a Hahn-echo detection sequence ($\pi/2$ - τ - π - τ -echo) with varying pulse spacing of $\tau = 240$ ns, 320 ns, 420 and 1420 ns. At each of these pulse spacings (τ) a different absorption line shape is observed. This is due to the large ^{14}N hyperfine couplings of the Mn ligands (see Figure 5), which modulate the detected Hahn-echo as the magnetic field is swept (see ref 58 and references therein). This effect can be partially suppressed by using longer τ values. Importantly, the total spectral breadth for all pulse spectra is the same and approximately that seen using CW-EPR. It is noted that the exact frequency of the CW-Q-band spectrum was calibrated such that the edges of the spectral envelope matched in the CW and pulse experiments. The corresponding pseudomodulated "CW-like" spectra are shown in Figure 1C. These spectra were generated by convoluting the original pulse (absorption) spectra with a Bessel function of the first kind. The hyperfine pattern observed is similar, but not identical to the CW spectrum. This appears to be mainly due to a difference in the line width. Spectral simulations are described in section 4.2.3.

The absorption lineshapes for pulse Q-band spectra regardless of the values of τ (Figure 1B) are not Gaussian, but instead are skewed such that the spectra are elongated on their low field edge. This observation is consistent with a pseudo axial G -tensor of large anisotropy, as described above, and suggests the unique axis (z -component) of the G -tensor (G_z) is larger than that the other two components (G_x and G_y). This result is expected for $\text{Mn}^{\text{II}}\text{Mn}^{\text{III}}$ complexes and has been previously inferred from spectral simulations of CW-EPR data (see section 4.2.4). It is pointed out that this feature of the PivOH complex can be demonstrated simply by using a higher frequency pulse-EPR experiment without the need to perform any spectral simulation. It should be noted that the inverse is seen for $\text{Mn}^{\text{III}}\text{Mn}^{\text{IV}}$ complexes; the unique axis, G_z , is always smallest in these systems.^{5,6,9–14}

4.2.2. ^{55}Mn -ENDOR. Pulsed-Q-band Davies ^{55}Mn -ENDOR spectra of the $\text{Mn}^{\text{II}}\text{Mn}^{\text{III}}$ PivOH complex are shown in Figure 2. Spectra were recorded at the center of the absorption envelope (powder position) and at the low and high field edges of the absorption envelope (single crystal orientations). ENDOR signals assigned to the two ^{55}Mn nuclei are observed over the 100–380 MHz range. Additional signals are seen in the region of 40–70 MHz. These are assigned to ^1H nuclei associated with the $\text{Mn}^{\text{II}}\text{Mn}^{\text{III}}$ PivOH complex, for example the μ -hydroxo proton, see Figure 5.

Mn^{II} , Mn^{III} , and Mn^{IV} complexes typically resolve ENDOR signals across a large radio frequency range. At all obtainable microwave frequencies available (X, Q, W-band etc), the hyperfine coupling of the ^{55}Mn nuclei is significantly larger than that of the ^{55}Mn Larmor frequency. As such, ^{55}Mn -ENDOR spectral

lines appear at about half the hyperfine coupling ($a/2$) split by the nuclear Zeeman interaction.⁵⁹ The magnitude of the ^{55}Mn quadrupole couplings is 2 orders of magnitude smaller than the hyperfine coupling and as such has only a small effect on the ^{55}Mn -ENDOR spectrum. Onsite ^{55}Mn hyperfine couplings (a) for Mn^{II} , Mn^{III} , and Mn^{IV} monomeric, dimeric, and tetrameric complexes in the current literature all fall within the range 140–260 MHz, and as such ^{55}Mn -ENDOR signals are expected for the $\text{Mn}^{\text{II}}\text{Mn}^{\text{III}}$ PivOH complex between 70 and 130 MHz, that is, $a/2$. It can be clearly observed in Figure 2 that this is not the case; experimentally ^{55}Mn -ENDOR signals extend to 380 MHz. The reason for this is that the effective hyperfine parameters of the coupled cluster measured in the EPR experiment represent scaled versions of the onsite (or intrinsic) hyperfine parameters of the two Mn ions. These scaling factors or spin projections (see Theory section 3.3-3.4) result in a spreading of the ^{55}Mn -ENDOR spectrum across a larger frequency range. It is noted that the isotropic spin projections for the Mn^{II} and Mn^{III} ions ($7/3$ and $-4/3$, respectively) are sufficiently different such that the ^{55}Mn -ENDOR signals arising from the Mn^{II} and Mn^{III} nuclei are spectrally resolved. This is shown by the black bars in Figure 2D. This same basic phenomenology has been observed for mixed valence $\text{Mn}^{\text{III}}\text{Mn}^{\text{IV}}$ complexes, see refs 5,6,9–14. Spectrum D represents the powder position. Here all orientations contribute approximately equally to the ^{55}Mn -ENDOR signal. The spectral breadth of the Mn^{III} ENDOR signal is approximately 3 times smaller than that of the Mn^{II} ENDOR signal. An increase in the spectral breadth of the Mn^{II} ion is expected as it carries the larger spin projection, and this increase can be estimated by taking the ratio of the two isotropic spin projections, that is, $7/3:4/3 = 1^3/4$. This is approximately 2 times smaller than that seen experimentally suggesting the effective hyperfine tensor associated with the Mn^{II} ion is intrinsically more anisotropic than that of the Mn^{III} . This surprising result is discussed further in section 4.1.4.

The magnitude of the effective hyperfine tensor components along the three principal axes (x, y, z) for the Mn^{II} and Mn^{III} ions can be deduced from the ^{55}Mn -ENDOR spectra (C and E) collected at the low and high field edge of the absorption envelope respectively. The low field edge, which here is defined by G_z , displays the largest hyperfine tensor component (A_z) for the effective hyperfine tensor associated with Mn^{II} and is estimated as ~ 670 MHz; twice the midpoint of the doublet that appears between 320 and 360 MHz. Similarly, the Mn^{III} A_z component is estimated to be 270 MHz. In contrast, the high field edge which is here defined by G_y , that appears to define the middle component of the Mn^{II} hyperfine tensor, is estimated to be ~ 540 MHz. The corresponding Mn^{III} hyperfine component is ~ 260 MHz. The Mn^{II} hyperfine tensor component along G_x can thus be deduced from the powder pattern spectrum. It must be of the order of ~ 450 MHz to explain the low-frequency edge of the Mn^{II} -ENDOR signal, not seen at either of the single crystal orientations. The corresponding Mn^{III} hyperfine component is ~ 260 MHz.

Radio-frequency nutation curves for three positions within the ^{55}Mn -ENDOR spectrum are shown in Figure 3. It is readily observed across the 100–400 MHz radio frequency range, that the optimal τ_{rf} pulse length for the ^{55}Mn -ENDOR experiment varies. From these results the effective B_2 (rf) field was estimated throughout the ^{55}Mn -ENDOR signal envelope. As expected the B_2 field falls off at high frequencies, leading to a partial suppression of ^{55}Mn signals above 250 MHz. More unexpectedly, the B_2

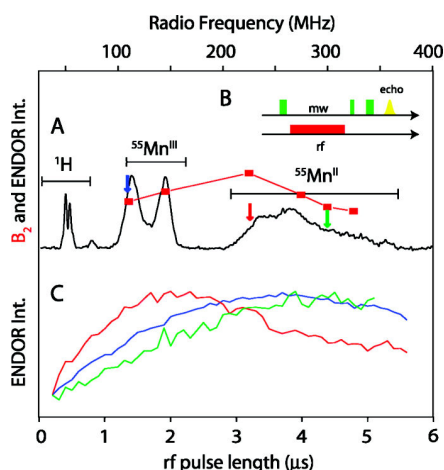


Figure 3. ^{55}Mn -ENDOR intensity profile of the $\text{Mn}^{\text{II}}\text{Mn}^{\text{III}}$ PivOH complex. (A) Q-band pulse ^{55}Mn -ENDOR spectrum collected at the central field position 1220 mT of the EPR absorption profile. The superimposed red squares show the effective B_2 (rf) field. (B) The Davies ENDOR microwave and radiowave pulse sequence. (C) Radio-frequency nutation curves for the three ^{55}Mn -ENDOR positions marked with the colored arrows. The contribution of the Mn^{II} and Mn^{III} ions to the ^{55}Mn -ENDOR spectra is shown by the black bars.

field also drops at low frequency, a consequence of the decrease in the hyperfine enhancement factor. The net consequence of this is that the relative line-intensities of ^{55}Mn -ENDOR signals reported are only an approximation of the real line-intensities as they in part reflect the response of the instrument. It is noted though that although the ENDOR signals are dampened at either end of the radiofrequency range probed, none of the signal envelope is completely suppressed.

4.2.3. Spectral Simulations. Spectral simulations of the entire data set were performed using the Spin Hamiltonian formalism described in the Theory section. Simulations of the data are shown in Figures 1 and 2, see red-dashed lines. All simulation parameters are given in Table 1. More emphasis was placed on reproducing the pseudomodulated derivative spectrum than the corresponding CW-line shape as the pulse spectra resolved more hyperfine structure and was free from Mn^{2+} artifacts. The isotropic line width used for the pulse and CW simulations differed by a factor of 2. An anisotropic line width broadening was included in the simulation that presumably accounts for unresolved hyperfine couplings (^{14}N etc), see Materials Methods 2.2.

The semiquantitative estimates of the Spin Hamiltonian parameters given in sections 4.2.1–4.2.2 all approximately agree with the fitted values. Single crystal orientation EPR simulations, solved for B_0 aligned along the three principal axes (x , y , z) are shown in Figure 2B. As expected, the single crystal orientation for which B_0 coincides with the molecular z -axis, is the broadest, spanning 1116–1285 mT and defines the low-field of the spectral envelope. Similarly, the single crystal orientation where B_0 coincides with the molecular y -axis, is narrower, spanning 1171–1322 mT and defines the high-field edge of the spectrum. The single crystal orientation where B_0 coincides with the molecular x -axis, is narrower still and is located in the center of the spectral envelope, 1170–1300 mT. This requires $G_z > G_x > G_y$, and the Mn^{II} hyperfine tensor components to be $|A_z| > |A_y| > |A_x|$.

Table 1. Principal Values of the Effective G and ^{55}Mn Hyperfine Tensors for the Simulations of the $\text{Mn}^{\text{II}}\text{Mn}^{\text{III}}$ PivOH Complex^a

	spin hamiltonian parameters						
	G	hyperfine (MHz)				quadrupole (P_ρ , MHz)	
		projected (A_i)		intrinsic (a_i)		Mn^{II}	Mn^{III}
	Mn^{II}	Mn^{III}	Mn^{II}	Mn^{III}	Mn^{II}	Mn^{III}	
x	1.964	−453	255	−240	−287	−3.24	1.50
y	1.947	−544	279	−239	−218	2.80	3.00
z	2.022	−696	260	−240	−137	0.44	−4.00
iso (P)	1.978	−564	264	−240	−214	−1.62	−2.00
aniso (η)	0.066	−207	−7	−1	116	0.73	0.38

^aThe isotropic G_{iso} and $A_{i, \text{iso}}$ ($i = 1-2$) values are the average of the individual values: $G_{\text{iso}} = (G_x + G_y + G_z)/3$ and $A_{i, \text{iso}} = (A_{i,x} + A_{i,y} + A_{i,z})/3$. The perpendicular and parallel G and A_i values are defined as $G_\perp = (G_x + G_y)/2$, $G_\parallel = G_z$ and $A_{i,\perp} = (A_{i,x} + A_{i,y})/2$, $A_{i,\parallel} = A_{i,z}$. The anisotropy in the \hat{G} and \hat{A}_i values is expressed as the difference between the parallel and perpendicular component of the tensor. The nuclear quadrupole coupling constant P is defined as: $P = (e^2qQ)/(4hI(2I - 1)) = (P_3/2)$ and $\eta = (P_1 - P_2)/(P_3)$. P_1 , P_2 , and P_3 are defined such that $|P_1| \leq |P_2| < |P_3|$. As a consequence, the axis system for the quadrupole tensors of the Mn^{II} and Mn^{III} ions are different. Their principal axes are rotated 90° relative to each other. The intrinsic hyperfine tensor components (a_i) are equal to the projected hyperfine tensor components (A_i) divided by the spin projection coefficients ρ_i as defined in the Theory section. The spin projection coefficients $[\rho_x, \rho_y, \rho_z]$ for the Mn^{II} and Mn^{III} ion are $\text{Mn}^{\text{II}} = [1.90 \ 2.28 \ 2.89]$ and $\text{Mn}^{\text{III}} = [-0.90 \ -1.28 \ -1.89]$.

The simultaneous fitting of both the EPR and ENDOR data did not require an axis rotation of the $\text{Mn}^{\text{II}}/\text{Mn}^{\text{III}}$ hyperfine tensors relative to the G -tensor. The simulations shown in the text assume the G tensor, hyperfine tensors A_1 and A_2 and quadrupole tensors Q_1 and Q_2 are collinear. It can be seen in Figure 5 that there is no structural requirement for this to be the case, the ligand sphere of the two metal ions is such that all components of the onsite axis system of the Mn^{III} do not coincide with the Mn^{II} ion. A three Euler angle rotation ($\alpha = 53^\circ$, $\beta = 81^\circ$, $\gamma = 48^\circ$) is required to map the onsite axis system of the Mn^{III} to the Mn^{II} . This is a unique feature of the PivOH complex. All current EPR/ENDOR studies of mixed valence Mn dimers have been performed on complexes which contain a bridging network that enforces a common onsite axis system, such as the bis- μ -oxo bridge template.^{6,9,11,57,60} Simulations that included an axis rotation are shown in the Supporting Information S3. In contrast to the hyperfine tensors, it was found that to reproduce the high frequency (250–400 MHz) ^{55}Mn ENDOR, a rotation of the Mn^{II} quadrupole tensor was required. This rotation consisted of a permutation of the principal values of the tensor, that is, corresponded to a 90° rotation of the quadrupole tensor. The same rotation was not required for the Mn^{III} ion. Both of these observations can be readily explained and stem from the effective Spin Hamiltonian description used to model the system.

4.2.4. Calculation of the Onsite (Intrinsic) Spin Hamiltonian Parameters. A mapping of the effective (fitted) Spin Hamiltonian parameters described in section 4.2.3 to the onsite (intrinsic) Spin Hamiltonian parameter can be made for the $\text{Mn}^{\text{II}}\text{Mn}^{\text{III}}$ PivOH complex as described in the Theory section 3.3–3.4.

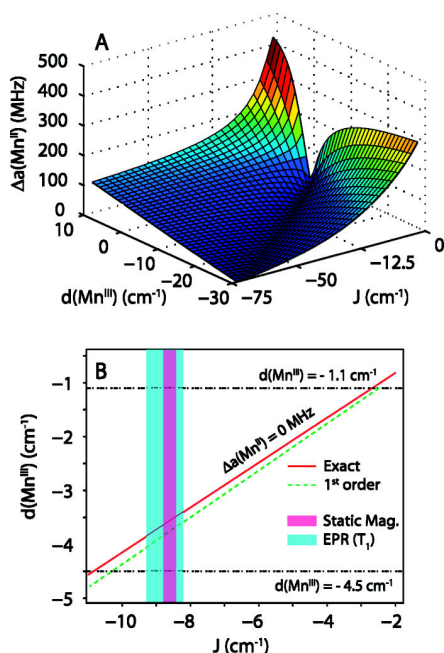


Figure 4. (A) Surface of the anisotropy of the onsite Mn^{II} hyperfine tensor (Δa_{aniso}) as a function of both the Mn^{II} – Mn^{III} exchange interaction (J) and the onsite fine structure parameter of the Mn^{III} ion $d(\text{Mn}^{\text{III}})$. (B) The projection of the surface shown in panel A, where the $\Delta a_{\text{aniso}}(\text{Mn}^{\text{II}})$ is approximately zero. The trend is linear over the range -2 to -10 cm^{-1} , consistent with the eq 6. The onsite fine structure tensor for the Mn^{II} ion was assumed to be 0 cm^{-1} for all calculations.

The procedure described here is similar to that reported earlier.^{11,19,53,60} This mapping requires knowledge of all contributions to the zero-field splitting of the coupled dimer, namely, an estimate of the exchange coupling between the two Mn ions and an estimate of the fine structure tensors for both Mn ions. As stated in the Introduction, good estimates exist for the exchange coupling between the two Mn ions. Static magnetization measurements reported earlier in Bossek et al.²⁰ and repeated here (see Section 4.1) yield a value of -8.6 cm^{-1} consistent with that previously reported by Kulik et al.,¹⁵ as estimated from the temperature dependence of the T_1 relaxation time using pulse-EPR experiments.¹⁵ Similar reliable estimates do not exist for the fine structure tensors of the two Mn ions and as such, a unique mapping of the effective parameter space to the intrinsic parameter space can not be made without further restrictions. Here we use two key assumptions that pertain to the nature of Mn^{II} which is a $d^5, ^6S$ ion ($S = 5/2$). As all of the d-orbitals on Mn^{II} are half filled it can be expected that the valence electron shell is approximately spherically symmetric. This electronic configuration typically engenders small fine structure and hyperfine tensor anisotropy.⁶¹ Literature values for the anisotropy of the fine structure and hyperfine tensors of Mn^{II} complexes are of the order of 1000 MHz. Of particular relevance are the dimeric equivalent $\text{Mn}^{\text{II}}\text{Mn}^{\text{II}}$ complexes which contain a similar bridging template as seen for the **PivOH** complex. For these model systems small values have been reported for the effective zero-field splitting tensors of the $S_T = 1$ and $S_T = 2$ spin manifolds, consistent with the dipolar interaction between the two Mn^{II} ions dominantly defining the zero-field splitting within these manifolds,⁶² that is, the

contribution of the onsite Mn^{II} fine structures to the zero field splitting is small. Thus it is expected that the contribution of the fine structure tensor of the Mn^{II} ion to the zero-field splitting of the **PivOH** complex is negligible^{63–65} and that the anisotropy of its onsite hyperfine tensor should be small. It is these two properties that can be used as constraints to solve the remaining Spin Hamiltonian parameters, namely, the onsite fine structure and hyperfine tensors for the Mn^{III} ion.

The calculation of the onsite (intrinsic) Spin Hamiltonian parameters amounts to determining the spin projection coefficients for the two Mn ions. The spin projection coefficients are described in detail in the theory section. They can be thought of simply as scaling factors which take into account the effect of the exchange coupling (J) and the fine structure tensors (d_1 and d_2) in the coupled basis. Spin projection coefficients were calculated numerically (see Theory eqs 7–11). The anisotropy of the exchange interaction was considered to be small and was thus not included in the calculations. The dipole–dipole coupling between the two manganese centers is of the order of 1200 MHz (0.04 cm^{-1}).

The solution space for the onsite anisotropy ($\Delta a_{\text{aniso}} = a_{\parallel} - a_{\perp}$) of the Mn^{II} ion as function of both the exchange coupling and the onsite fine structure parameter (d) of the Mn^{III} ion is shown in Figure 4A. Each point on the surface represents a different estimate for the spin projections of the two Mn ions and thus a different estimate for the onsite $\text{Mn}^{\text{II}}/\text{Mn}^{\text{III}}$ hyperfine tensor. This figure was generated by assuming the fine structure parameter d for the Mn^{II} ion was zero and by approximating the effective (fitted) hyperfine tensor of the Mn^{II} as axial. This approximation is simply used to conveniently display the onsite anisotropy surface. An estimate of the rhombicity of the fine structure tensor was also made.

It is observed that there is no unique solution as no global minimum can be identified (Figure 4A). Instead, a trough is observed, such that for every choice of J there is a value for $d(\text{Mn}^{\text{III}})$ that is consistent with a virtually isotropic onsite Mn^{II} hyperfine tensor. The 2D projection of this solution is shown in Figure 4B. There is a clear linear dependence of $d(\text{Mn}^{\text{III}})$ on the value of J over the range -10 to -2 cm^{-1} range. This behavior is the same as predicted by the analytical expressions (eq 6) given in the theory section that has been derived from first order perturbation theory (see Supporting Information S2). The first order solution is also shown in Figure 4B (green dashed line). It is slightly offset from the numerical solution (red line), overestimating the magnitude of $d(\text{Mn}^{\text{III}})$. This offset presumably describes the contribution of higher order terms to the total zero-field splitting of the complex. As J for the **PivOH** complex has already been determined,¹⁵ an estimate of $d(\text{Mn}^{\text{III}})$ can be made. The EPR experimental range of J (-8.2 to -9.3 cm^{-1}) is shown in Figure 4B by the cyan shaded area and corresponds to $d(\text{Mn}^{\text{III}})$ of -3.49 to -3.95 cm^{-1} .

Table 1 also lists the calculated onsite hyperfine parameters for Mn^{II} and Mn^{III} at the midpoint of the allowed range of J , that is, $J = -8.78 \text{ cm}^{-1}$, $d(\text{Mn}^{\text{III}}) = -3.72 \text{ cm}^{-1}$, $e/d(\text{Mn}^{\text{III}}) = 0.315$. By design, this point yields an isotropic Mn^{II} hyperfine tensor with isotropic component ($a_{\text{iso}}(\text{Mn}^{\text{II}})$) of -239 MHz , typical of Mn^{II} complexes. Similarly, the isotropic component of the onsite Mn^{III} hyperfine tensor ($a_{\text{iso}}(\text{Mn}^{\text{III}})$) is -213 MHz and is within the range seen for model complexes (-165 to -225 MHz). Unlike the Mn^{II} onsite hyperfine tensor, the Mn^{III} hyperfine tensor is highly anisotropic, as expected. Furthermore, the anisotropy as defined by the difference between the parallel and the perpendicular components of the hyperfine tensor is positive, consistent with the sign of the inferred fine structure

tensor, that is, $d(\text{Mn}^{\text{III}})$. Thus the anisotropy of the two Mn ions in the coupled representation (section 4.2.3) is reversed when mapped to the original basis. A similar “transfer of anisotropy” has been previously observed in ^{55}Mn -ENDOR studies of $\text{Mn}^{\text{III}}\text{Mn}^{\text{IV}}$ complexes^{11,60} albeit somewhat smaller and was inferred from simulations in the cw-EPR study of $\text{Mn}^{\text{II}}\text{Mn}^{\text{III}}/\text{Mn}^{\text{III}}\text{Mn}^{\text{IV}}$ complexes by Zheng et al.¹⁹

The sign of the fine structure tensor parameter $d(\text{Mn}^{\text{III}})$ accurately describes the coordination sphere of the Mn^{III} ion. Mn^{III} ($S = 2$) is a d^4 ion, which does not usually exhibit Kramers degeneracy at zero-field.^{19,61,66,67} The inherent asymmetry of the valence electron configuration leads to a large Jahn–Teller distortion. Spin–orbit coupling removes the degeneracy of the $^5\text{E}_g$ energy-levels, which gives rise to either a $^5\text{A}_{1g}$ or a $^5\text{B}_{1g}$ ground state.^{66,68} It was demonstrated in refs 68 and 69 that (i) a $^5\text{A}_{1g}$ ground state is obtained for a trigonal bipyramidal (5 coordinate) or a tetragonally compressed octahedral (6 coordinate) ligand geometry with a vacant electron d_{z^2} orbital. Spectroscopically this manifests itself as both a positive fine structure parameter ($d(\text{Mn}^{\text{III}})$) and yields a negative hyperfine tensor anisotropy ($\Delta a_{\text{aniso}} = a_{\parallel} - a_{\perp}$, see above); (ii) a $^5\text{B}_{1g}$ ground state is obtained for a square-pyramidal (5 coordinate) or tetragonally elongated (6 coordinate) ligand geometry. In this case the vacant electron orbital is now the $d_{x^2 - y^2}$ orbital. Spectroscopically this manifests itself as both a negative fine structure parameter ($d(\text{Mn}^{\text{III}})$) and yields a positive hyperfine tensor anisotropy. This behavior was observed for monomeric Mn^{III} model complexes and mixed valence $\text{Mn}^{\text{II}}\text{Mn}^{\text{III}}$ and $\text{Mn}^{\text{III}}\text{Mn}^{\text{IV}}$ dimers. The only exception known is the complex *trans*- $[\text{Mn}(\text{cyclam})\text{I}_2]\text{I}$,⁷⁰ which is thought to have unique, low-lying charge transfer states which strongly perturb the ground state multiplet. As the Mn^{III} ion of the **PivOH** complex displays a negative fine structure parameter ($d(\text{Mn}^{\text{III}})$) and the anisotropy of its hyperfine tensor is positive, its ground state is expected to be $^5\text{B}_{1g}$. This is consistent with the X-ray crystal structure of the **PivOH** complex which demonstrates the Mn^{III} ion has a tetragonally elongated (6 coordinate) ligand field. Thus all onsite parameters calculated using the method described above are consistent with literature benchmarks.

The large anisotropy of the effective G -tensor noted in section 4.2.1 can be explained using the calculated anisotropic spin projections described above. It is again expected that the onsite g -anisotropy of the Mn^{II} ion is small and thus the fitted anisotropy is a consequence of the onsite g -anisotropy of the Mn^{III} ion. This anisotropy is enhanced in the coupled basis as the parallel and perpendicular spin projections are significantly different; that is to say the G -anisotropy is large because the exchange coupling between the two Mn ions is small. Again it is the onsite fine structure tensor of the Mn^{III} ion that maps into the effective G -tensor as described above for the $\text{Mn}^{\text{II}}/\text{Mn}^{\text{III}}$ hyperfine tensors. The onsite g -anisotropy of the Mn^{III} ion must be such that the parallel component of the g -tensor (g_z) is smaller than the equatorial components of the g -tensor (g_x, g_y). This is consistent within the set of mixed valence Mn dimers ($\text{Mn}^{\text{III}}\text{Mn}^{\text{IV}}$ and $\text{Mn}^{\text{II}}\text{Mn}^{\text{III}}$). Note that the same g -anisotropy for the Mn^{III} ion in $\text{Mn}^{\text{III}}\text{Mn}^{\text{IV}}$ complexes results in the opposite G -anisotropy as seen in $\text{Mn}^{\text{II}}\text{Mn}^{\text{III}}$ complexes since in the former the Mn^{III} carries the larger (positive) spin projection as opposed to the latter where it carries the smaller (negative) spin projection.

4.3. DFT. Calculations of EPR parameters using DFT were performed to further refine and support the analysis of the

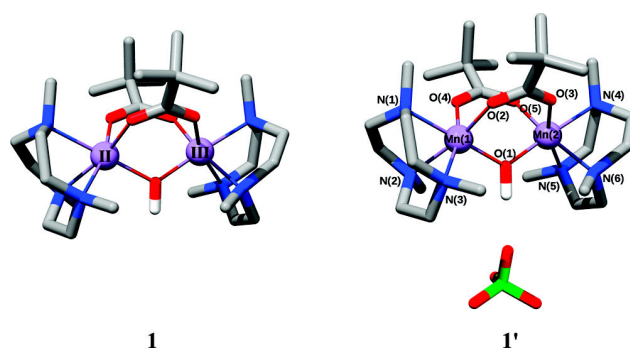


Figure 5. Geometries for models **1** and **1'** based on XRD crystal structure coordinates. All but the bridging hydroxo hydrogen atoms are omitted for clarity. Mn, C, N, O, H, Cl are colored purple, gray, blue, red, white, and green, respectively.

experimental EPR data. The calculated values, including the tensor orientations, are consistent with the presented interpretation of the experimentally recorded EPR spectra. The implications of the calculated results on future computational studies of more complex but related systems, such as the OEC, are discussed.

4.3.1. Model Complex Geometries. Six models were considered in the calculations. Models **1**, **1'**, **2**, **2'**, **3**, and **3'** were generated from the X-ray crystal structure published previously.²⁰ Model **1** was constrained to the previously determined X-ray crystal structure coordinates²⁰ while optimizing the positions of the hydrogen atoms. Model **2** represents the high-spin geometry optimization ($S = 9/2$) while model **3** represents the optimized geometry obtained using the broken-symmetry formalism with an effective spin of $S_T = 1/2$. Additional models (**1'**, **2'**, and **3'**), which include the ClO_4^- counterion located near the bridging $\mu\text{-OH}$ seen in the X-ray crystal structure were also examined and optimized in exactly the same way. Figure 5 shows the geometries for models **1** and **1'** and the oxidation states for each Mn.

In the Supporting Information S4 selected geometric parameters for each model of the **PivOH** complex are given. The crystal structure (models **1** and **1'**) contains two well separated Mn transition metal centers with a largely uniform octahedral ligand environment around the Mn^{II} ion and a Mn^{III} ion in a tetragonally elongated octahedral ligand field, with the Jahn–Teller axis located along the $\text{Mn}^{\text{III}}\text{-N}(5)$ bond (see Figure 5). The optimized geometries of the **PivOH** complex (models **3** and **3'**) using the broken-symmetry approach lead to similar geometric features with shorter Mn–Mn distances and longer, on average, Mn–N bond lengths. Significantly, the broken-symmetry optimized geometry without the counterion, **3**, shows an out of plane bend of the hydrogen on the $\mu\text{-OH}$ bridge with respect to the plane formed by the two Mn ions and the oxygen atom of the bridge, see the Supporting Information S4. This is inconsistent with the other models where the proton of the $\mu\text{-OH}$ bridge is coplanar with the Mn ions and the oxygen atom of the bridge, as depicted in Figure 5. It should be noted that the geometries optimized in the high-spin state, the current preferred methodology for Mn dimers^{47,48} have symmetric Mn centers, indicating a delocalization of the unpaired electrons between the two transition metal centers. This interpretation is further supported by an analysis of the calculated Mulliken spin populations, presented in Supporting Information S5. In the high-spin state, $S = 9/2$, model geometries **1**, **1'**, **3**, and **3'** show well-defined spin populations near 5.0 and 4.0 for the Mn^{II} and Mn^{III} , respectively. For the models **2** and **2'**, optimized in the high-spin

Table 2. Calculated Intrinsic ^{55}Mn Hyperfine Coupling Constants (MHz)^a

	onsite ^{55}Mn hyperfine tensors (MHz)										
	Mn^{II}					Mn^{III}					rmsd
	a_x	a_y	a_z	a_{iso}	a_{aniso}	a_x	a_y	a_z	a_{iso}	a_{aniso}	
1	-226.8	-225.7	-234.1	-228.9	-7.8	-273.9	-234.3	-127.2	-211.8	126.9	12.2
1'	-227.5	-226.7	-234.2	-229.5	-7.1	-280.1	-227.0	-129.3	-212.1	124.2	9.2
2	-219.2	-216.0	-228.9	-221.4	-11.2	-262.7	-254.3	-121.0	-212.7	137.5	23.1
2'	-212.8	-211.1	-227.4	-217.1	-15.4	-284.7	-218.1	-117.5	-206.8	133.9	18.4
3	-228.7	-228.2	-234.2	-230.4	-5.7	-261.9	-221.0	-119.0	-200.6	122.4	14.1
3'	-227.2	-225.8	-232.9	-228.7	-6.4	-260.8	-208.4	-110.1	-193.1	124.5	17.5
exp.	-239.7	-238.8	-240.0	-239.5	-0.7	-286.6	-218.1	-136.6	-213.8	115.8	

^a Calculated values scaled by a factor of 1.50, see the Supporting Information S8. The a values are the average of the individual value: $a_{\text{iso}} = (a_x + a_y + a_z)/3$. The perpendicular and parallel a values are defined as: $a_{\perp} = (a_x + a_y)/2$, $a_{\parallel} = a_z$. The anisotropy of a_i is expressed as the difference between the parallel and perpendicular component of the tensor. Calculated tensor components were re-oriented to the experimental.

state, each Mn center shows a spin population of approximately 4.5 indicating a delocalization of electron spin between the two metal centers. Application of the broken symmetry approach leads to a localization of spin of approximately 5.0 and -4.0 for the Mn^{II} and Mn^{III} , respectively.

4.3.2. Heisenberg Exchange Coupling Constants. The exchange coupling constant for the **PivOH** complex has been determined experimentally to be antiferromagnetic and small, on the order of -10 cm^{-1} . In our previous BS-DFT study of Mn dimers, exchange coupling constants calculated using the single geometry approach described in Theory section 3.5 gave a variation between experiment and theory of 27.1 cm^{-1} (rmsd), see Orio et al.,⁴⁸ three times greater than the experimental exchange coupling for **PivOH**. Given the relatively large error found in this previous study the extent to which the single geometry approach can produce reliable estimates for exchange constant (J) for the **PivOH** complex is marginal at best.

Calculated "single geometry" exchange coupling constants for each model complex are given in the Supporting Information S6. Models 1, 1', 2, and 2' indicate ferromagnetic behavior for the **PivOH** complex, contrary to experiment. Models 2 and 2' have strongly ferromagnetic calculated values near 140 cm^{-1} , indicative of spin delocalization as discussed above. Only models 3 and 3' show the correct antiferromagnetic behavior. For these models, 3 and 3', the calculated couplings deviate from the experimental value determined from EPR measurements by 9.65 cm^{-1} and 4.47 cm^{-1} respectively, both of which can be considered well within the expected error seen in the previous study.⁴⁸ The better estimation for the exchange coupling in model 3' over 3 can be attributed to the presence of the ClO_4^- counterion. As stated above, model 3, without the counterion, shows an out of plane bend of the $\mu\text{-OH}$ bridge proton with respect to the plane formed by the two Mn ions and the bridging oxygen atom (see the Supporting Information S4). The effect of this subtle change in geometry, which presumably describes some change in the superexchange pathway between the two Mn ions, leads to an increase in the energy gap between the calculated high-spin and the broken-symmetry states giving a larger calculated antiferromagnetic coupling for model 3 than for model 3'.

The methodology for the calculation of exchange coupling constants as described by Orio et al.⁴⁸ can be improved by using the adiabatic energy difference as seen for calculations on a

$\text{Mn}^{\text{III}}\text{Mn}^{\text{IV}}$ DTNE model complex and models of dimanganese catalase.^{47,71} The calculated adiabatic exchange coupling constant, using eq 13 (see Theory section 3.5), includes respective terms from the high-spin and broken-symmetry geometries. From a theoretical perspective this treatment for calculating the exchange coupling constants is preferred, as the experiments are adiabatic in nature. For a more complete discussion of the adiabatic approach see ref 40. For the models presented here, extremely good agreement, with an error of 4.9 cm^{-1} , is achieved between theory and experiment using the adiabatic energy difference for models 2' and 3'. A further improvement in the calculated exchange coupling constant can be made through the application of a van der Waals (VDW) correction,³³ accounting for weak interactions within each model structure which are different for the high-spin and broken symmetry geometries. For exchange coupling constants using a "single geometry" approach the VDW DFT dispersion correction does not contribute because of cancelation, see eq 13. This is because the VDW correction gives an energy correction related to the geometry and density functional used, but is not related to the spin state of the system being studied. As such both the high-spin and broken symmetry states for a single geometry have the same correction applied. Using both the adiabatic approximation and the VDW correction, the adiabatic energy difference for models 2' and 3' gives an error of only 2.6 cm^{-1} . However, similar agreement is lacking for the calculated exchange using models 2 and 3. Again, this is due to the aforementioned out of plane bend of the $\mu\text{-OH}$ bridge proton which leads to a significant stabilization of the broken-symmetry geometry over that of the high-spin geometry.

4.3.3. ^{55}Mn Hyperfine Tensors. The calculated intrinsic site ^{55}Mn hyperfine values are shown in Table 2 as compared to the experimental determination discussed above. Comparison of intrinsic site values was chosen over the more conventional spin projected comparison, because of the largely anisotropic spin projection tensors determined from the analysis of the on-site fine structure parameter of the Mn^{III} . Within the framework of BS-DFT it is currently not possible to account for the on-site fine structure parameters of individual ions in complexes of effective ground state spins of $S_T = 1/2$, such as **PivOH**. However, as is shown in Table 2 the intrinsic site hyperfine couplings for transition metal ions within such systems can be calculated to a high degree of accuracy. Excellent agreement (within 5%) is seen between the experimental values reported in section 4.2.4

Table 3. Calculated ^{55}Mn Nuclear Quadrupole Coupling Constants^a

	nuclear quadrupole couplings (p_i)			
	Mn^{II}		Mn^{III}	
	p	η	p	η
1	-1.83	0.661	2.49	0.838
1'	-0.74	0.783	-3.52	0.262
2	-1.84	0.446	2.18	0.787
2'	-0.76	0.749	-2.72	0.614
3	-1.86	0.614	2.14	0.908
3'	-0.72	0.460	-2.23	0.439
exp.	-1.62	0.73	-2.00	0.38

^aThe nuclear quadrupole coupling constant p is defined as: $p = (e^2qQ)/(4\hbar I(2I - 1)) = (p_3/2)$ and $\eta = (p_1 - p_2)/(p_3)$. p_1 , p_2 , and p_3 are defined such that $|p_1| \leq |p_2| < |p_3|$.

(Table 1) and the calculations presented here. It is noted that a comparison of experimental (the fitted or effective Spin Hamiltonian parameters) and the projected DFT values, using the standard method of scalar, isotropic spin-projections still yields a reasonably good agreement (within 10%) of the experimentally determined A_{iso} values; however, the agreement of the calculated anisotropy is, as expected, much poorer.

As has been discussed earlier, the anisotropy of the Mn transition metal centers in the coupled basis is inverted from the anticipated solution, that is, that of a largely isotropic Mn^{II} and an anisotropic Mn^{III} . In section 4.2.4, this was explained by the inclusion of the fine structure tensor of the Mn^{III} ion. It was shown that if this term is included, the intrinsic hyperfine parameters for both Mn ions match expectations derived from monomer studies. The DFT calculations presented here support this analysis (Table 2 and Supporting Information S9). The calculated intrinsic site values reproduce the tensor anisotropies seen for the experiment, namely, an isotropic Mn^{II} ($a_{\text{aniso}} < 10$ MHz) and a highly anisotropic Mn^{III} ion ($a_{\text{aniso}} \sim 100$ MHz) and thus support the notion that the projected anisotropies of the Mn centers cannot be explained without the use of tensor spin-projections. The best agreement with experiment is given by model 1' with models 1, 3, and 3' giving slightly larger errors. The models optimized in the high spin state, 2 and 2', show larger anisotropies for the Mn^{II} , symptomatic of the symmetric geometry observed in these models. It should be noted that the high spin models, 2 and 2', still show remarkable agreement with experiment with maximal errors of 17% and 14% in the tensor components with respect to the experimentally determined values, respectively. Indeed errors for the isotropic component of the intrinsic site hyperfine tensors is less than 10% and as low as 0.5% for the high spin models, although this level of agreement is achieved through a convenient cancelation of errors. For more complete agreement between the calculated and experimentally determined values the models based on either the crystal structure geometry or the broken-symmetry optimized geometries are needed.

4.3.4. ^{55}Mn Nuclear Quadrupole Tensors. The calculated nuclear quadrupole couplings for each ^{55}Mn nucleus are shown in Table 3. The best agreement with experiment is found in models without the ClO_4^- counterion, although the electric field gradient of the Mn^{III} for all models is calculated as much too

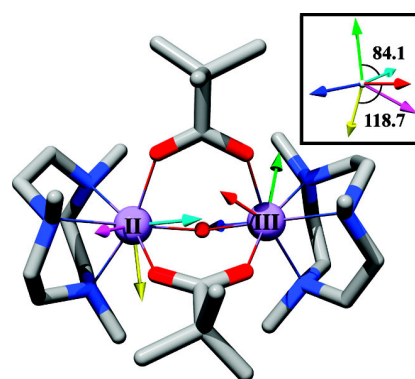


Figure 6. Relative orientation of calculated electric field gradient components in model 1 following the standard convention: $|p_1| \leq |p_2| < |p_3|$. Red, green, and blue arrows represent the orientation for p_1 , p_2 , and p_3 on Mn^{III} , respectively. Yellow, magenta, and cyan arrows represent the orientation for p_1 , p_2 , and p_3 on Mn^{II} . All other models without the ClO_4^- counterion show similar electric field gradient component orientations, see Supporting Information S10.

rhombic. In the presence of the counterion, model 1' gives good values with the exception of the magnitude of the Mn^{II} nuclear quadrupole coupling $p(\text{Mn}^{\text{II}})$, which is calculated as approximately 1 MHz too small. The significant differences seen between models 1 (2, 3), and 1' (2', 3') indicate the sensitivity of the calculated electric field gradient to the presence of the counterion even though it is more than 5 Å away from either Mn. A similar situation has previously been encountered for Fe complexes.⁷² It is possible that the inclusion of additional counterions, seen in the crystal structure,²⁰ would improve the calculated results of the electric field gradient at the Mn.

The orientation of the quadrupole components were analyzed previously in the context of fitting the experimental spectrum. Figure 6 shows a representative depiction of the calculated relative orientations of the electric field gradient components for Mn^{II} and Mn^{III} . The calculated orientations for all three models broadly agree with the experimentally determined orientations, that is, through fitting of the experimental spectra, namely, that the components are roughly collinear but transposed (see also Supporting Information S10).

DISCUSSION

5.1. Comparison of EPR/ENDOR Data with BS-DFT Calculations. The BS-DFT calculations presented above for the PivOH complex demonstrate the increasing utility of DFT theory with regard to spectral analysis of complicated exchange coupled systems. Here it is shown that even for a complex with a small exchange coupling, that is to say only a small energetic separation between the effective ground spin 1/2 state and the first excited state, robust estimates for all EPR observables can be made. In these systems though, care must be taken when comparing spectroscopic observables to onsite properties. Spectroscopic observables ($^{55}\text{Mn}/^1\text{H}/^{14}\text{N}$ -hyperfine couplings) as deduced from the simulation of EPR/ENDOR data solved in the coupled basis represent effective values that must be correctly mapped to the uncoupled basis to yield the onsite values of the individual Mn ion. It is only then that these measurements provide meaningful results; they provide a window into the coordination sphere of Mn ions and their individual electronic

structure. The mapping requires a complete understanding of the zero-field splitting of the complex including the onsite contribution of each Mn. For this complex, which contains an isotropic spin center (Mn^{II}), this can be achieved.

As demonstrated above, the appropriately mapped experimental EPR/ENDOR data and the onsite properties as estimated from DFT essentially match. All ^{55}Mn hyperfine tensor components agree to within 10%. Thus, the EPR/ENDOR analysis, DFT calculations, and crystallographic data all arrive at the same result. All three correctly assign the nature of the Mn^{III} ion, its ground electronic state, and its coordination sphere and in doing so have the potential to accurately predict the chemistry the complex can perform.

5.2. Implications for Further BS-DFT Studies on Mn Systems. Current techniques for the calculation of ^{55}Mn EPR parameters using BS-DFT focus largely on the calculation of the high-spin geometry. Importantly, it has been shown that for Mn^{III} and Mn^{IV} ions and related dimeric complexes, the calculated high-spin geometry yields a good representation of the real geometry of the complex as assessed by comparison to crystallographic data. The same is not seen here for the **PivOH** complex, a weakly coupled Mn-dimer which contains a Mn^{II} ion. The calculated high-spin geometry is significantly different from that of the crystal structure. The high spin geometry contains a unique electron delocalization and a bias toward ferromagnetic coupling, in contrast to all existing data seen in mixed valence Mn complexes studied so far. As such, particular care should be taken when applying BS-DFT methods to weakly coupled systems and those that contain low Mn oxidation states for the calculation of EPR parameters.

The inclusion of the ClO_4^- counterion had a non-negligible impact on the calculated EPR parameters presented in this work. Specifically the calculated electric field gradient of both Mn ions was remarkably sensitive to this distant counterion ($\sim 5 \text{ \AA}$). This observation is of importance for studies on metal cofactors in proteins. DFT models of these metal sites must be constructed in such a way that the influence of remote ions is considered, including counterions such as calcium or chloride and charged amino acid residues such as arginine or lysine. Without the inclusion of these charged groups, DFT estimates of charge sensitive properties, such as the nuclear quadrupole coupling constants, are limited.

5.3. Implications for Current Studies of the OEC. The combined experimental (EPR/ENDOR) and theoretical analysis (DFT) presented above validates a recent study performed in our laboratory on the tetramanganese ($\text{Mn}^{\text{III}}\text{Mn}^{\text{IV}}_3$) cluster that comprises the OEC. In our earlier work we investigated the effect of the replacement of the Ca^{2+} ion with Sr^{2+} .⁷³ Ca^{2+} is an essential cofactor of the OEC that is structurally coupled to the Mn ions via μ -oxo or μ -hydroxo bridges. It was shown that this replacement does not significantly alter the overall electronic structure of the OEC. The changes that were observed were interpreted as evidence of a small modification of the fine structure tensor of the only Mn^{III} ion and was deduced using the same procedure as described here. It was further suggested that the sign of the fine structure parameters d of the Mn^{III} ion ($d(\text{Mn}^{\text{III}})$) must be negative to reproduce the fitted Spin Hamiltonian parameters, which requires the Mn^{III} ion to have a 5 coordinate square-bipyramidal or 6 coordinate tetragonally elongated ligand field. This result is of importance as it potentially identifies one of the sites of substrate water binding. The only DFT structural model of the OEC in the current literature

consistent with the Ca^{2+} replacement study described above is the Siegbahn model.⁷⁴ As in models proposed by EXAFS spectroscopy⁷⁵ it contains three short Mn–Mn distances, and one long (3.3 Å) Mn–Mn distance. The long Mn–Mn distance is inside a distorted cuboidal structure and forms its open site. The missing “corner oxygen” leads to a 5 coordinate square-pyramidal ligation for the $\text{Mn}_{\text{D}}^{\text{III}}$ ion in the S_2 state. It is to this open coordination site that one of the substrate “waters” (H_2O , OH^-) could bind during the $S_2 \rightarrow S_3$ transition (either from bulk water, or water bound to Ca^{2+}). The 3.3 Å Mn–Mn distance within the distorted cuboid could then provide an ideal geometry for low energy barrier O–O bond formation during the $S_3 \rightarrow S_4 \rightarrow S_0$ transition.^{74,76–78}

The results and analyses presented here are equally applicable to the lower oxidation states of the OEC including the S_0 and S_{-2} states. S_0 , the lowest oxidation state obtained by the OEC during the catalytic cycle, most probably contains three Mn^{III} ions and one Mn^{IV} (see refs 13,79). The S_{-2} state is instead a reduced form of the OEC. It is generated by the addition of exogenous chemical reductants such as NH_2OH , NH_2NH_2 , or NO .^{80–83} It is thought that this state may represent an assembly intermediate with net oxidation state $(\text{Mn}^{\text{III}})_3\text{Mn}^{\text{II}}$.^{84,85} These states both represent weakly antiferromagnetically coupled systems where an intrinsically isotropic spin (Mn^{II} , octahedral Mn^{IV}) is coupled to an intrinsically anisotropic spin (Mn^{III}), the same situation seen for the **PivOH** complex.

6. CONCLUSIONS

The $\text{Mn}^{\text{II}}\text{Mn}^{\text{III}}$ **PivOH** and related dimeric complexes represent robust structural mimics of several metal cofactors of biological enzymes. The relevance of the **PivOH** complex for the OEC of Photosystem II was discussed above, but a comparison can be equally made for (i) the dimanganese catalase,^{1,2} which catalyzes the dismutation of H_2O_2 to H_2O and O_2 ; or (ii) the recently identified Mn containing class Ib/Ic ribonucleotide reductases,^{3,4,86–88} to name but two examples. The experimental and theoretical methodologies developed for the **PivOH** complex described above should be directly applicable to these biological systems. Similarly, this model provides important empirical benchmarks for all spectroscopic observables.

The EPR/ENDOR measurements and DFT calculations presented here serve as a demonstration that these methods, when used in tandem can provide a complete picture of the electronic structure of highly complicated metal systems. In the circumstance where X-ray crystallography is unattainable or at very least compromised, the combined EPR/ENDOR and DFT approach described here is the obvious recourse as it essentially provides complementary information. This is of particular relevance to metal cofactors in proteins, which cannot often be measured using crystallographic techniques, especially when poised in catalytically relevant higher oxidation states.

Future studies on manganese containing enzymes such as these systems require a shift in scope. From the results presented here, BS-DFT can provide reliable estimates for nearly all magnetic spectroscopic parameters when appropriately optimized for the system of interest. This includes the hyperfine tensor anisotropy, which is often disregarded in the discussion of BS-DFT results. It is this feature that will provide important information with regard to the ligand geometry of metal ions of multivalent active sites and the subsequent elucidation of their reaction mechanisms.

■ ASSOCIATED CONTENT

S Supporting Information. Additional material detailing (1) magnetic susceptibility data and error plots; (2) derivation of Mn^{III} fine structure constant from 1st-order perturbation theory; (3) fitting of EPR/ENDOR spectra using noncollinear tensors; (4) geometric parameters for model complexes; (5) manganese Mulliken spin populations; (6) BS-DFT calculated exchange coupling constants; (7) basis sets used for EPR parameter calculations; (8) determination of the ^{55}Mn hyperfine scaling factor for use with broken-symmetry DFT; (9) calculated ^{55}Mn hyperfine orientations; (10) calculated ^{55}Mn quadrupole/electric field gradient orientations; (11) sample input files for DFT calculations. This material is available free of charge via the Internet at <http://pubs.acs.org>.

■ AUTHOR INFORMATION

Corresponding Author

*Phone: +49-208-306-3552 (N.C.), +49-208-306-3614 (W.L.).
E-mail: cox@mpi-muelheim.mpg.de (N.C.), wolfgang.lubitz@mpi-mail.mpg.de (W.L.).

■ ACKNOWLEDGMENT

The authors acknowledge Dr. T. Weyhermüller and Dr. E. Bill for their assistance with the collection of experimental data and its interpretation and their help in the preparation of the manuscript. Financial support was provided by the DFG (Me1629/2-4), the Max Planck Society, the EU SOLAR-H2 (FP7 contract 212508), and the Wallenberg and Kempe foundations (J.M.). L.R. is a fellow of the North Rhine-Westphalia (NRW) Research School BioStruct program.

■ REFERENCES

- Barynin, V. V.; Whittaker, M. M.; Antonyuk, S. V.; Lamzin, S. V.; Harrison, P. M.; Artymiuik, A. J.; Whittaker, J. M. *Structure* **2001**, *9*, 725–738.
- Dismukes, G. C. *Chem. Rev.* **1996**, *96*, 2909–2926.
- Cox, N.; Ogata, H.; Stolle, P.; Reijerse, E.; Auling, G.; Lubitz, W. *J. Am. Chem. Soc.* **2010**, *132*, 11197–11213.
- Cotruvo, J. A.; Stubbe, J. *Biochemistry* **2010**, *49*, 1297–1309.
- Teutloff, C.; Schäfer, K.-O.; Sinnecker, S.; Barynin, V.; Bittl, R.; Wieghardt, K.; Lendzian, F.; Lubitz, W. *Magn. Reson. Chem.* **2005**, *43*, S51–S64.
- Schäfer, K. O.; Bittl, R.; Lendzian, F.; Barynin, V. V.; Weyhermüller, T.; Wieghardt, K.; Lubitz, W. *J. Phys. Chem. B* **2003**, *107*, 1242–1250.
- Schweiger, A.; Jeschke, G. *Principles of Pulsed Electron Paramagnetic Resonance*; Oxford University Press: Oxford, 2001.
- Kulik, L. V.; Lubitz, W. *Photosynth. Res.* **2009**, *102*, 391–401.
- Randall, D. W.; Sturgeon, B. E.; Ball, J. A.; Lorigan, G. A.; Chan, M. K.; Klein, M. P.; Armstrong, W. H.; Britt, R. D. *J. Am. Chem. Soc.* **1995**, *117*, 11780–11789.
- Randall, D. W.; Chan, M. K.; Armstrong, W. H.; Britt, R. D. *Mol. Phys.* **1998**, *95*, 1283–1294.
- Peloquin, J. M.; Campbell, K. A.; Randall, D. W.; Evanchik, M. A.; Pecoraro, V. L.; Armstrong, W. H.; Britt, R. D. *J. Am. Chem. Soc.* **2000**, *122*, 10926–10942.
- Kulik, L.; Epel, B.; Messinger, J.; Lubitz, W. *Photosynth. Res.* **2005**, *84*, 347–353.
- Kulik, L. V.; Epel, B.; Lubitz, W.; Messinger, J. *J. Am. Chem. Soc.* **2007**, *129*, 13421–13435.
- Zweygart, W.; Bittl, R.; Wieghardt, K.; Lubitz, W. *Chem. Phys. Lett.* **1996**, *261*, 272–276.
- Kulik, L. V.; Lubitz, W.; Messinger, J. *Biochemistry* **2005**, *44*, 9368–9374.
- Larson, E.; Haddy, A.; Kirk, M. L.; Sands, R. H.; Hatfield, W. E.; Pecoraro, V. L. *J. Am. Chem. Soc.* **1992**, *114*, 6263–6265.
- Diril, H.; Chang, H. R.; Zhang, X.; Larsen, S. K.; Potenza, J. A.; Pierpont, C. G.; Schugar, H. J.; Isied, S. S.; Hendrickson, D. N. *J. Am. Chem. Soc.* **1987**, *109*, 6207–6208.
- Chang, H. R.; Larsen, S. K.; Boyd, P. D. W.; Pierpont, C. G.; Hendrickson, D. N. *J. Am. Chem. Soc.* **1988**, *110*, 4565–4576.
- Zheng, M.; Khangulov, S. V.; Dismukes, G. C.; Barynin, V. V. *Inorg. Chem.* **1994**, *33*, 382–387.
- Bossek, U.; Hummel, H.; Weyhermüller, T.; Wieghardt, K.; Russell, S.; van der Wolf, L.; Kolb, U. *Angew. Chem.* **1996**, *108*, 1653–1656.
- Using the $H = -2J\mathbf{S}_1 \cdot \mathbf{S}_2$ as opposed to $H = -J\mathbf{S}_1 \cdot \mathbf{S}_2$ convention.
- O'Connor, C. J. *Prog. Inorg. Chem.* **1982**, *29*, 203–283.
- Weast, R. C.; Astle, M. J. *CRC Handbook of Chemistry and Physics*; CRC Press Inc.: Boca Raton, FL, 1979.
- Bill, E. *JulX*, version 1.41; Max-Planck-Institut: Muelheim an der Ruhr, Germany, 2008; http://ewww.mpi-muelheim.mpg.de/bac/logins/bill/julX_en.php.
- Lebedev, V. I.; Laikov, D. N. *Doklady Math.* **1999**, *59*, 477.
- Wang 2003, <http://server.ccl.net/cca/software/SOURCES/>
- Epel, B.; Gromov, I.; Stoll, S.; Schweiger, A.; Goldfarb, D. *Concepts Magn. Res. B* **2005**, *26B*, 36–45.
- Kulik, L. V.; Epel, B.; Lubitz, W.; Messinger, J. *J. Am. Chem. Soc.* **2005**, *127*, 2392–2393.
- Epel, B.; Arieli, D.; Baute, D.; Goldfarb, D. *J. Magn. Reson.* **2003**, *164*, 78–83.
- Stoll, S.; Schweiger, A. *J. Magn. Reson.* **2006**, *178*, 42–55.
- Becke, A. D. *Phys. Rev. A* **1988**, *38*, 3098–3100.
- Perdew, J. P. *Phys. Rev. B* **1986**, *33*, 8822–8824.
- Grimme, S.; Antony, J.; Ehrlich, S.; Krieg, H. *J. Chem. Phys.* **2010**, *132*, 154104.
- van Wüllen, C. *J. Chem. Phys.* **1998**, *109*, 392–399.
- van Lenthe, E.; Baerends, E. J.; Snijders, J. G. *J. Chem. Phys.* **1993**, *99*, 4597–4610.
- van Lenthe, E.; Ehlers, A.; Baerends, E.-J. *J. Chem. Phys.* **1999**, *110*, 8943–8953.
- Pantazis, D. A.; Chen, X. Y.; Landis, C. R.; Neese, F. *J. Chem. Theory Comput.* **2008**, *4*, 908–919.
- Weigend, F. *Phys. Chem. Chem. Phys.* **2006**, *8*, 1057–1065.
- Neese, F. *ORCA—an ab initio, Density Functional and Semiempirical Program Package*, v. 2.6-35; University of Bonn: Bonn, Germany, 2007.
- Neese, F. *Coord. Chem. Rev.* **2009**, *253*, 526–563.
- Noodleman, L. *J. Chem. Phys.* **1981**, *74*, 5737–5743.
- Noodleman, L.; Case, D. A. *Adv. Inorg. Chem.* **1992**, *38*, 423–470.
- Noodleman, L.; Davidson, E. R. *Chem. Phys.* **1986**, *109*, 131–143.
- Staroverov, V. N.; Scuseria, G. E.; Tao, J.; Perdew, J. P. *J. Chem. Phys.* **2003**, *119*, 12129–12137.
- Neese, F.; Wennmohs, F.; Hansen, A.; Becker, U. *Chem. Phys.* **2009**, *356*, 98–109.
- Neese, F. *Inorg. Chim. Acta* **2002**, *337*, 181–192.
- Sinnecker, S.; Neese, F.; Noodleman, L.; Lubitz, W. *J. Am. Chem. Soc.* **2004**, *126*, 2613–2622.
- Orio, M.; Pantazis, D. A.; Petrenko, T.; Neese, F. *Inorg. Chem.* **2009**, *48*, 7251–7260.
- Pantazis, D. A.; Krewald, V.; Orio, M.; Neese, F. *Dalton Trans.* **2010**, *39*, 4959–4967.
- Baffert, C.; Orio, M.; Pantazis, D. A.; Duboc, C.; Blackman, A. G.; Blondin, G.; Neese, F.; Deronzier, A.; Collomb, M.-N. *Inorg. Chem.* **2009**, *48*, 10281–10288.
- Pantazis, D. A.; Orio, M.; Petrenko, T.; Zein, S.; Bill, E.; Lubitz, W.; Messinger, J.; Neese, F. *Chem.—Eur. J.* **2009**, *15*, 5108–5123.

- (52) Pantazis, D. A.; Orio, M.; Petrenko, T.; Zein, S.; Lubitz, W.; Messinger, J.; Neese, F. *Phys. Chem. Chem. Phys.* **2009**, *11*, 6788–6798.
- (53) Sage, J. T.; Xia, Y. M.; Debrunner, P. G.; Keough, D. T.; de Jersey, J.; Zerner, B. *J. Am. Chem. Soc.* **1989**, *111*, 7239–7247.
- (54) Bencini, A.; Gatteschi, D. *EPR of Exchange Coupled Systems*; Springer-Verlag: Berlin, Germany, 1990.
- (55) Yamaguchi, K.; Takahara, Y.; Fueno, T. *Applied Quantum Chemistry*; Springer: New York, 1986; p 155.
- (56) Yamanaka, S.; Kawakami, T.; Nagao, H.; Yamaguchi, K. *Chem. Phys. Lett.* **1994**, *231*, 25–33.
- (57) Schäfer, K. O. Exchange Coupled Manganese Complexes: Model Systems for the Active Centres of Redoxproteins Investigated with EPR Techniques. Doctoral Thesis, Technische Universität, Berlin, Germany, 2002.
- (58) Schweiger, A.; Jeschke, G. *Principles of pulse electron paramagnetic resonance*, Oxford University Press: Oxford, England, 2001; Vol. 1.
- (59) Monomeric Mn^{II}, Mn^{III}, and Mn^{IV} complexes all have $S > 1/2$. As such, multiple sets of spectral lines are observed. For example Mn^{II} exhibits spectral lines centered at $a/2$, $3a/2$, and $5a/2$.
- (60) Schäfer, K. O.; Bittl, R.; Zweggart, W.; Lendzian, F.; Haselhorst, G.; Weyhermüller, T.; Wieghardt, K.; Lubitz, W. *J. Am. Chem. Soc.* **1998**, *120*, 13104–13120.
- (61) Abragam, A.; Bleaney, B. *Electron Paramagnetic Resonance of Transition Metal Ions*; Clarendon Press: Oxford, England, 1970.
- (62) Blanchard, S.; Rivière, G. B.; Nierlich, M.; Girerd, J.-J. *Inorg. Chem.* **2003**, *42*, 4568–4578.
- (63) Duboc, C.; Astier-Perret, V.; Chen, H.; Pécaut, J.; Crabtree, R. H.; Brudvig, G. W.; Collomb, M.-N. *Inorg. Chim. Acta* **2006**, *359*, 1541–1548.
- (64) Duboc, C.; Collomb, M.-N.; Pécaut, J.; Deronzier, A.; Neese, F. *Chem.—Eur. J.* **2008**, *14*, 6498–6509.
- (65) Duboc, C.; Phoeung, T.; Jouvenot, D.; Blackman, A. G.; McClintock, L. F.; Pécaut, J.; Collomb, M.-N.; Deronzier, A. *Polyhedron* **2007**, *26*, 5243–5249.
- (66) Griffith, J. S. *The theory of Transition-Metal Ions*; Cambridge University Press: London, England, 1971.
- (67) Carrington, A.; McLachlan, A. D. *Introduction to Magnetic Resonance*, 1st ed.; Harper and Row: New York, 1967.
- (68) Gerritsen, H. J.; Sabisky, E. S. *Phys. Rev.* **1963**, *132*, 1507–1512.
- (69) Campbell, K. A.; Force, D. A.; Nixon, P. J.; Dole, F.; Diner, B. A.; Britt, R. D. *J. Am. Chem. Soc.* **2000**, *122*, 3754–3761.
- (70) Mossin, S.; Weihe, H.; Barra, A.-L. *J. Am. Chem. Soc.* **2002**, *124*, 8764–8765.
- (71) Sinnecker, S.; Neese, F.; Lubitz, W. *J. Biol. Inorg. Chem.* **2005**, *10*, 231–238.
- (72) Ray, K.; Begum, A.; Weyhermüller, T.; Piligkos, S.; van Slagereen, J.; Neese, F.; Wieghardt, K. *J. Am. Chem. Soc.* **2005**, *127*, 4403–4415.
- (73) Cox, N.; Rapatskiy, L.; Su, J.-H.; Pantazis, D. A.; Sugiura, M.; Kulik, L.; Dorlet, P.; Rutherford, A. W.; Neese, F.; Boussac, A.; Lubitz, W.; Messinger, J. *J. Am. Chem. Soc.* **2011**, *133*, 3635–3648.
- (74) Siegbahn, P. E. M. *Acc. Chem. Res.* **2009**, *42*, 1871–1880.
- (75) Yano, J.; Kern, J.; Sauer, K.; Latimer, M. J.; Pushkar, Y.; Biesiadka, J.; Loll, B.; Saenger, W.; Messinger, J.; Zouni, A.; Yachandra, V. K. *Science* **2006**, *314*, 821–825.
- (76) Messinger, J. *Phys. Chem. Chem. Phys.* **2004**, *6*, 4764–4771.
- (77) Zein, S.; Kulik, L. V.; Yano, J.; Kern, J.; Pushkar, Y.; Zouni, A.; Yachandra, V. K.; Lubitz, W.; Neese, F.; Messinger, J. *Phil. Trans. R. Soc.* **2008**, *363*, 1167–1177.
- (78) Petrie, S.; Stranger, R.; Pace, R. J. *Angew. Chem.* **2010**, *122*, 4329–4332.
- (79) Yachandra, V. K.; Sauer, K.; Klein, M. P. *Chem. Rev.* **1996**, *96*, 2927–2950.
- (80) Messinger, J.; Renger, G. *FEBS Lett.* **1990**, *277*, 141–146.
- (81) Hanley, J.; Sarrou, J.; Petrouleas, V. *Biochemistry* **2000**, *39*, 15441–15445.
- (82) Ioannidis, N.; Sarrou, J.; Schansker, G.; Petrouleas, V. *Biochemistry* **1998**, *37*, 16445–16451.
- (83) Sarrou, J.; Isgandarova, S.; Kern, J.; Zouni, A.; Renger, G.; Lubitz, W.; Messinger, J. *Biochemistry* **2003**, *42*, 1016–1023.
- (84) Tamura, N.; Cheniae, G. *Biochim. Biophys. Acta* **1987**, *890*, 179–194.
- (85) Ono, T. *Biochim. Biophys. Acta* **2001**, *1503*, 40–51.
- (86) Jiang, W.; Yun, D.; Saleh, L.; Barr, E. W.; Xing, G.; Hoffart, L. M.; Maslak, M.-A.; Krebs, C.; Bollinger, J. M. *Science* **2007**, *316*, 1188–1191.
- (87) Jiang, W.; Yun, D.; Saleh, L.; Bollinger, J. M.; Krebs, C. *Biochemistry* **2008**, *47*, 13736–13744.
- (88) Voevodskaya, N.; Lendzian, F.; Ehrenberg, A.; Gräslund, A. *FEBS Lett.* **2007**, *581*, 3351–3355.

Detection of water binding sites in the oxygen-evolving complex of photosystem II poised in the S₂ state using high field (94 GHz) ¹⁷O-ELDOR-detected NMR spectroscopy

Leonid Rapatskiy, Nicholas Cox, Anton Savitsky, William Ames, Julia Sander, Mark Nowaczyk, Matthias Rögner, Alain Boussac, Frank Neese, Johannes Messinger and Wolfgang Lubitz

Detection of the water binding sites of the oxygen-evolving complex of Photosystem II using W-band ^{17}O -ELDOR detected NMR spectroscopy

Leonid Rapatskiy¹, Nicholas Cox^{1}, Anton Savitsky¹, William M. Ames¹, Julia Sander², Marc. M. Nowaczyk², Matthias Rögnér², Alain Boussac³, Frank Neese¹, Johannes Messinger⁴ and Wolfgang Lubitz^{1*}*

¹Max-Planck-Institut für Bioanorganische Chemie, Stiftstrasse 34-36, D-45470 Mülheim an der Ruhr, Germany; ² Plant Biochemistry, Ruhr University Bochum, Universitätsstrasse 150, D-44780 Bochum, Germany; ³iBiTec-S, URA UMR 8221, CEA Saclay, 91191 Gif-sur-Yvette, France; ⁴Department of Chemistry, Chemical Biological Centre (KBC), Umeå University, S-90187 Umeå, Sweden

AUTHOR EMAIL ADDRESS: rapatskiy@mpi-muelheim.mpg.de, nicholas.cox@mpi-muelheim.mpg.de, ames@mpi-muelheim.mpg.de, savistky@mpi-muelheim.mpg.de, Julia.Sander@rub.de, marc.m.nowaczyk@rub.de, matthias.roegner@rub.de, alain.boussac@cea.fr, frank.neese@mpi-mail.mpg.de, johannes.messinger@chem.umu.se, wolfgang.lubitz@mpi-mail.mpg.de

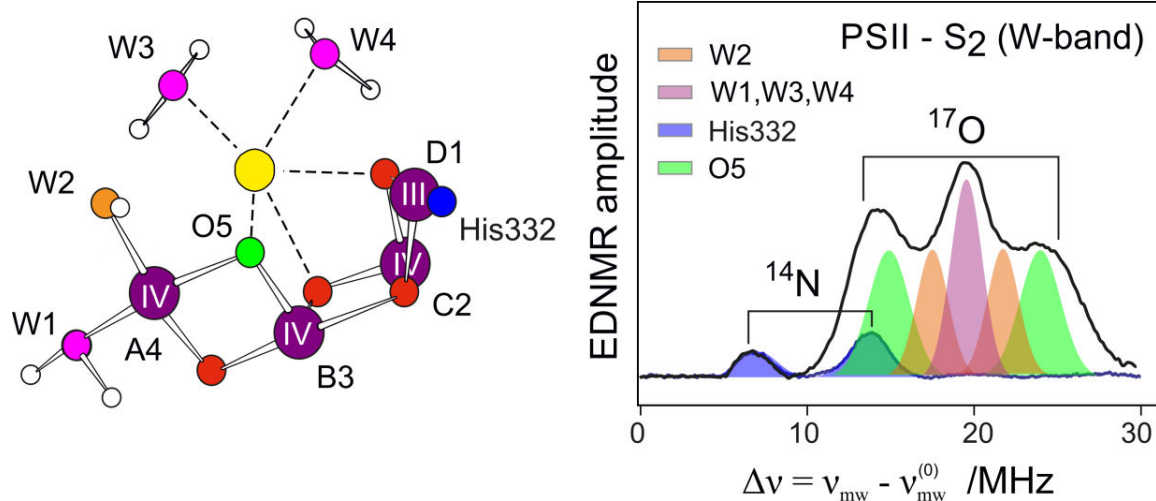
RECEIVED DATE (to be automatically inserted after your manuscript is accepted if required according to the journal that you are submitting your paper to)

TITLE RUNNING HEAD: Water binding sites in the OEC.

CORRESPONDING AUTHOR FOOTNOTE: Nicholas Cox, Telephone: +49-208-306-3552; Email: Nicholas.Cox@mpi-mail.mpg.de, Wolfgang Lubitz, Telephone: +49-208-306-3614; Email: Wolfgang.Lubitz@mpi-mail.mpg.de

ABSTRACT. Water binding to the $\text{Mn}_4\text{O}_5\text{Ca}$ cluster of the Oxygen Evolving Complex (OEC) of Photosystem II (PSII) was studied via H_2^{17}O and $^2\text{H}_2\text{O}$ labelling and high-field EPR spectroscopy. Hyperfine couplings of coordinating ^{17}O ($I = 5/2$) nuclei were detected using W-band (94 GHz) ELDOR (electron-electron double resonance) detected NMR and Davies/Mims ENDOR (electron-nuclear double resonance) techniques. Universal ^{15}N ($I = 1/2$) labeling was employed to clearly discriminate the ^{17}O hyperfine couplings which overlap with ^{14}N ($I = 1$) signals from the D1-His332 ligand of the OEC [Stich, T. et al. *Biochemistry* **2011** 50 (34), 7390-7404]. Three classes of ^{17}O nuclei were identified: i) one μ -oxo bridge; ii) a terminal Mn-OH/ OH_2 ligand; and iii) Mn/Ca- H_2O ligand(s). These assignments are based on ^{17}O model complex data, on comparison to the recent 1.9 Å resolution PS II crystal structure [Umena, Y. et al **2011**, *Nature*, 473:55-60], on NH_3 perturbation of the ^{17}O signal envelope and density functional theory calculations. The relative orientation of the putative ^{17}O μ -oxo bridge hyperfine tensor to the ^{14}N (^{15}N) hyperfine tensor of the D1-His332 ligand, suggests that the exchangeable μ -oxo bridge links the outer Mn to the $\text{Mn}_3\text{O}_3\text{Ca}$ open-cuboidal unit (O4 and O5 in the Umena et al. structure). Comparison to literature data favors the Ca-linked O5 oxygen over the alternative assignment to O4. All ^{17}O signals were seen even after very short (≤ 15 second) incubations in H_2^{17}O suggesting that all exchange sites identified could represent bound substrate in the S_1 state including the μ -oxo bridge. $^1\text{H}/^2\text{H}$ ($I = 1/2, 1$) ENDOR data performed at Q- (34 GHz) and W-bands complement the above findings. The relatively small $^1\text{H}/^2\text{H}$ couplings observed requires that all the μ -oxo bridges of the $\text{Mn}_4\text{O}_5\text{Ca}$ cluster are deprotonated in the S_2 state. Together, these results further limit the possible substrate water binding sites and modes within the OEC. This information restricts the number of possible reaction pathways for O-O bond formation, supporting an oxo/oxyl coupling mechanism in S_4 .

TOC FIGURE



INTRODUCTION

In oxygenic photosynthesis light-driven water-splitting is catalyzed by the oxygen-evolving complex (OEC) of Photosystem II (PSII). The OEC consists of an inorganic Mn₄O₅Ca cluster and its surrounding protein matrix.¹⁻⁸ The functionally important protein matrix includes the redox-active tyrosine residue Y_Z (D1-Y₁₆₁). Y_Z couples electron transfer from the Mn₄O₅Ca cluster to P₆₈₀^{•+} and is involved in proton transfer reactions.⁹ P₆₈₀/P₆₈₀^{•+} and Pheo/Pheo^{•-} form the primary component of the photoactive reaction centre of PSII, which energetically drives water-splitting by four sequential light-induced charge separations, for reviews see refs.^{5-8,10,11} During water-splitting, the Mn₄O₅Ca cluster steps through a reaction cycle comprising five distinct redox intermediates. These are known as the S_n states, where the subscript indicates the number of stored oxidizing equivalents (n = 0-4).¹² Once formed the S₃Y_Z[•] state rapidly decays to the S₀ state with the concomitant release of molecular triplet oxygen and the rebinding of at least one substrate water molecule.¹⁰ A S₄ state, different from the S₃Y_Z[•] state, has not yet been spectroscopically identified.

The structure of PSII, including the OEC was recently determined at a resolution of 1.9 Å by Umena et al.¹ The position of all four Mn ions of the OEC and the network of five bridging μ-oxo ligands

connecting the metal ions were resolved. The proposed structure bears similarities to earlier literature models,² including those derived from (polarized) EXAFS measurements^{4,13} and to the computational models of Kusunoki,¹⁴ Siegbahn⁶ and Dau.^{7,15} The Umena model has a distorted chair-like structure where the base is formed by a μ -oxo-bridged cuboidal $\text{Mn}_3\text{O}_4\text{Ca}$ unit (**Figure 1A**). The fourth ‘outer’ manganese, $\text{Mn}_{\text{A}4}$ (this nomenclature combines the numbering based on polarised EXAFS⁴ models with that of Umena et al.¹), is attached to this core structure via a μ -oxo-bridged ligation (O4) and by one hydroxo bridge (O5) to the central manganese, $\text{Mn}_{\text{B}3}$. Compared to the experimental EXAFS data the Mn-Mn, Mn-Ca and Mn-O/N distances determined from the crystal structure are all elongated, suggesting that the cluster underwent some degree of radiation-induced reduction during data collection and thus may represent a ‘super-reduced’ S-state (S_{-1} , S_{-2} , S_{-3})¹⁶ which can also be generated via chemical reduction (NH_2OH , NH_2NH_2) of the cluster.¹⁷ Nevertheless, the general pattern of three short and one long Mn-Mn distances and four Mn-Ca distances as observed in EXAFS measurements is preserved.^{4,13,18}

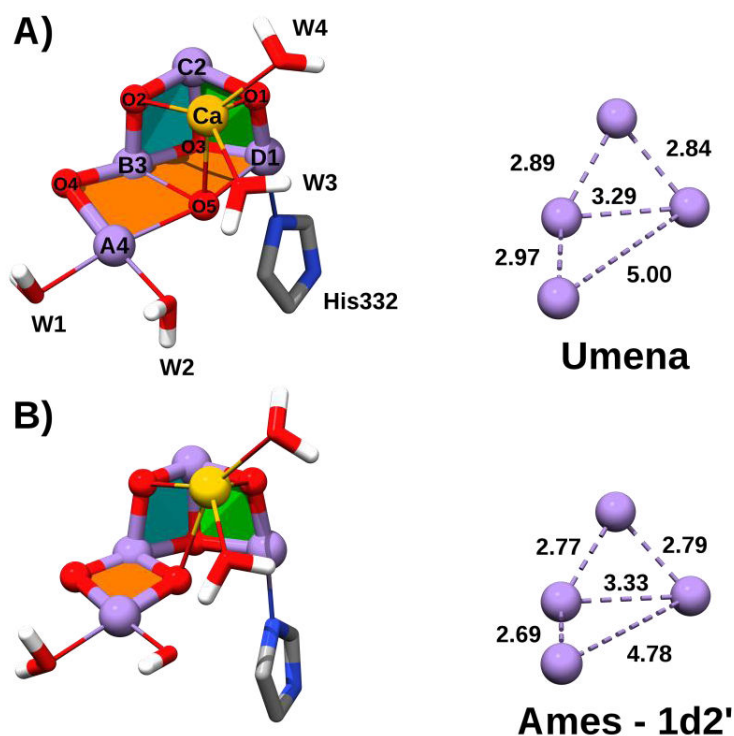


Figure 1. The topography of the $\text{Mn}_4\text{O}_5\text{Ca}$ cluster of the OEC. **A)** The crystal structure model of Umena et al.¹ **B)** A recent representative computational model of Ames et al.¹⁹ The right-hand side structures show the five Mn-Mn distances of the cluster. Atom numbering combines the polarized EXAFS⁴ nomenclature (Mn_A , Mn_B etc) with that of Umena et al.¹ (Mn_1 , Mn_2 etc). Atom coloring is as follows: Mn - purple; Ca - yellow; O - red; N - blue; H - white. W1-W4 stand for water molecules/hydroxo groups identified in the crystal structure.¹ The three Mn-(μO)₂-Mn planes of the μ -oxo bridge subunits of the OEC are colored orange, green and turquoise.

In the Umena structure the central O5 has unusually long bonds to three Mn ions and to the Ca ion. It was suggested that it represents a hydroxo group or a water molecule and is potentially one of the substrate ‘waters’ (the term substrate water does not distinguish between the three possible protonation states, water/hydroxo/oxo). In contrast, in polarized EXAFS models and in most computational models, O5 is a μ -oxo bridge between Mn_{A4} and Mn_{B3} in the S_1 and S_2 states, rendering this unit bis- μ -oxo bridged, and Mn_{D1} as five coordinate.^{6,19,20} One such computational model, proposed in the recent

density functional theory study performed by our laboratory¹⁹ is shown in **Figure 1B**. A μ -oxo bridged linkage between Mn_{A4} and Mn_{B3} was found to be energetically favourable and engendered Mn-Mn distances and magnetic properties consistent with EXAFS and EPR/ENDOR data.

To elucidate the mechanism of water-oxidation to molecular oxygen it is crucial to identify which of the water-derived ligands represent the two substrate molecules. Time-resolved $H_2^{16}O/H_2^{18}O$ exchange membrane-inlet mass spectrometry experiments have shown that at least one substrate water (the slowly exchanging, W_s) is bound in all S-states and that its exchange kinetics are significantly affected by replacement of the Ca ion with Sr.^{21,22} The second, faster exchanging substrate water (W_f) has been shown to bind in the S_3 state and possibly already in the S_2 state.²²⁻²⁴ FTIR measurements provide independent information about the binding site and mode of water molecules in the various S_n states.^{25,26} These data indicate that one water molecule, possibly W_f , binds during the $S_2 \rightarrow S_3$ transition. The binding of W_f in this transition is a key feature in the oxo/oxyl coupling mechanism of water oxidation proposed by Siegbahn based on DFT calculations.^{6,27}

EPR spectroscopy is a powerful tool for determining the identity ($H_2O/OH/O^{2-}$) and location of water-derived species bound in the vicinity of the Mn_4O_5Ca cluster. In the paramagnetic S_2 and S_0 states water-exchangeable protons can be identified via the disappearance of signals originating from the hyperfine couplings of 1H nuclei ($I = 1/2$) to the net electronic spin ($S_T = 1/2$) of the Mn_4O_5Ca cluster after $^1H_2O/2H_2O$ exchange. Kawamori et al.²⁸ were the first to report 1H couplings to the OEC obtained from spinach, poised in the S_2 state using X-band (continuous wave) cw-ENDOR. The measured 1H envelope extended out from the 1H -nuclear Larmor frequency by ± 2 MHz and disappeared after resuspension of the PSII in buffer made in 2H_2O . These results were interpreted as evidence for water molecule(s) directly coordinating to one or more Mn ions (1H at a distance of 2-3 Å from a Mn). The first attempt at a quantitative fitting of the 1H envelope was performed in the pulse 1H -ENDOR and 2H ESEEM (electron spin echo envelope modulation) studies of Britt et al.^{29,30} Here a four shell model (inclusive of ambient water) was developed with electron-nuclear dipolar hyperfine couplings (A_{dip}) similar to those seen in earlier studies.^{28,31} As before, these results were interpreted as evidence for a direct Mn-water

interaction, fixing the number of protonated coordinating water molecules to two. Similar hyperfine couplings were estimated for the S_0 state and approximately the same number of Mn-proton interactions were inferred.³⁰ A subsequent X-band ^2H -ESEEM study by Åhrling et al.³² reached a similar conclusion albeit with an increase of the A_{dip} of the largest hyperfine tensor which was also seen in the recent X-band HYSCORE studies of Martínez et al.³³

A more direct probe for water derived ligands is via the direct detection of oxygen using ^{17}O labeling. One particular advantage is that the fully deprotonated substrate state e.g. the incorporation of a water into a Mn- μ -oxo bridge, can be identified. Only a small number of publications describing ^{17}O couplings of metallocofactors and related model complexes have been published to date (see refs³⁴⁻³⁸ for examples and the supporting information **S2**). This is due to a combination of factors, including the low natural abundance (0.038%) of ^{17}O and as a consequence the high costs for enrichment, the large nuclear spin ($I = 5/2$) and small nuclear g-factor (-0.7575) of ^{17}O , and significant quadrupole coupling value ($\frac{e^2Qq}{h} \sim 6$ MHz).³⁹ The first ^{17}O labeling X-band cw-EPR study reported in PSII attempted to resolve line-broadening of the individual lines of the S_2 multiline spectrum due to the coupling of the Mn ions to an ^{17}O nucleus.⁴⁰ This was followed by the X-band ESEEM study of Nugent/Evans laboratory.^{41,42} The authors clearly identified only a matrix ^{17}O signal, but also speculated that a second species may be observed which gives rise to a larger hyperfine coupling of about 5 MHz. However, owing to the large number of overlapping background ^{14}N signals (see below), this latter assignment was considered tentative. The next ^{17}O study used X-band HYSCORE to characterize substrate binding.⁴³ Two sharp peaks were observed centered about the Larmor frequency of ^{17}O and were assigned to the coupling of a ^{17}O nucleus to the Mn complex. It has been recently demonstrated that this assignment is incorrect⁴⁴ and that these signals should be attributed to couplings of ^{14}N to the cytochrome b559.⁴⁵ Finally, a broad Q-band ^{17}O -ENDOR signal at about 15 MHz has very recently been observed in higher plant PSII.⁴⁶ This signal was assigned to a μ -oxo bridge based on its similarity to a broad, structureless signal seen for the labeled $\text{Mn}^{\text{III}}-(\mu\text{O})_2\text{-Mn}^{\text{IV}}$ BIPY complex.⁴⁷ The μ -oxo bridge species observed was considered to

exchange on a timescale of the order of 10^4 - 10^5 s and as a consequence represents a slowly exchanging structural site as opposed to a substrate of the catalyst.⁴⁸

In this work we present an EPR investigation of water binding to the $\text{Mn}_4\text{O}_5\text{Ca}$ cluster via measurement of ^{17}O hyperfine couplings. In order to obtain complete ^{17}O -hyperfine patterns and discriminate these from those of ^{14}N nuclei, the EPR experiments were performed at W-band using the ELDOR-detected NMR technique (EDNMR).⁴⁹ While this technique was reported over 20 years ago, it has been little utilized for the study of low γ nuclei,^{50,51} such as ^{17}O .⁵² As a consequence, model systems were examined first to better gauge the advantages and limitations of this technique. The enhanced nuclear frequency resolution at high magnetic fields of about 3.4 T (W-band) in conjunction with the superior sensitivity of EDNMR as compared to ENDOR, allows clear assignments of water derived ligands of the $\text{Mn}_4\text{O}_5\text{Ca}$ cluster, which were resolved in the recent 1.9 Å structure of PSII.¹ In addition, time-resolved water-exchange experiments also provide direct comparison to kinetics of substrate binding as determined earlier by time-resolved membrane inlet mass spectrometry experiments.²²

2. MATERIALS AND METHODS

2.1 PSII sample preparation. PSII core complex preparations from WT* *T. elongatus*⁵³ were isolated as described earlier.⁵⁴⁻⁵⁶ Universal ^{15}N -labelling of the PSII preparation was achieved by growing the cyanobacteria in modified BG11 media that contained $^{15}\text{NH}_4\text{Cl}$ as the sole nitrogen source.⁵⁷ Samples were stored at -80°C until use. Dark-adapted samples were placed in Q-band (1.6 mm I.D.) and W-band (0.6 mm I.D.) quartz tubes. The sample concentration was 3.0-4.0 mg(Chl)/mL for both Q- and W-band samples. The S_2 -state was generated by short, white light illumination (5 s) with a tungsten lamp at 200 K using a dry-ice/ethanol bath.

Resuspension of the PSII samples in labelled H_2^{17}O (90%) and $^2\text{H}_2\text{O}$ (99%) buffer was achieved as follows. The H_2^{17}O and $^2\text{H}_2\text{O}$ buffers were composed of: 20 mM MES (2-(N-morpholino)ethanesulfonic acid); 10 mM MgCl_2 ; 10 mM NaCl; 0.03% DDM (dodecyl maltoside) and 50 mM mannitol. For the H_2^{17}O buffer, the buffer ingredients were first dissolved at 10 fold higher

concentrations in unlabelled water. This stock solution was then added to clean H₂¹⁷O (1:10 v/v) to make the labelled buffer. As a final step the buffers were poised at a pH of 6.5 (MES/NaOH) and pD 6.5 (MES/NaOD). The PSII sample was diluted by 50% in the isotopically labeled buffer and reconcentrated to the initial concentration using Millipore microcentrifuge filters (Amicon Ultra - 0.5 mL, 100 kDa). This isotope enrichment procedure was repeated 3 times. The final enrichment of ¹⁷O was estimated to be greater than 70%.

“Rapid dilution” experiments were also performed for PSII W-band samples. In these experiments, the PSII sample was not resuspended into the labelled H₂¹⁷O buffer but instead simply diluted by the H₂¹⁷O (90%). In this way, the total exchange time could be reduced to the seconds timescale. In these experiments H₂¹⁷O water (1-1.5 μL) was placed at the bottom of the W-band sample tube. The unlabeled PSII sample (1-1.5 μL) was then added to the tube 5-10 mm above the level of the water. Capillary action prevented the mixing of the two components. The W-band tube was then placed in a bench top centrifuge (Fischer Scientific, model 3722L) and spun for approximately 2 seconds. The sample was then rapidly frozen in liquid nitrogen. The entire procedure took less than 15 seconds from the start of the spin cycle to the freezing of the sample. High isotope enriched H₂¹⁷O (90%) was used to maximize sample labelling, which theoretically cannot exceed 45% in these samples.

2.2 Q-band EPR measurements. Q-band pulse EPR and ¹H and ²H ENDOR measurements were performed at 4.8 K using a Bruker ELEXSYS E580 Q-band pulse EPR spectrometer equipped with home-build TE₀₁₁ microwave cavity,⁵⁸ Oxford-CF935 liquid helium cryostat. Electron spin echo-detected (ESE) field-swept spectra were measured using the pulse sequence: $t_p - \tau - 2t_p - \tau - \text{echo}$. The length of the $\pi/2$ microwave pulse was generally set to $t_p = 12$ ns. The interpulse distance was varied in the range $\tau = 200$ -500 ns. ¹H ENDOR spectra were acquired using the Davies-type pulse sequence: $t_{inv} - t_{RF} - T - t_p - \tau - 2t_p - \tau - \text{echo}$ using an inversion microwave pulse of length $t_{inv} = 128$ ns, and a radio frequency π pulse of length $t_{RF} = 20$ μs. The length of the $\pi/2$ microwave pulse in the detection sequence

was generally set to $t_p = 64$ ns and the interpulse delays to $T = 1.5$ μ s and $\tau = 468$ ns. The RF frequency was swept 20 MHz around the ^1H -Larmor frequency of about 53 MHz (1.2 T) in 50 kHz steps. ^2H ENDOR spectra were collected using the Mims-type pulse sequence: $t_p - \tau - t_p - t_{\text{RF}} - T - t_p - \tau - \text{echo}$, with $t_p = 16$ ns, $t_{\text{RF}} = 40$ μ s, $\tau = 300$ -500 ns and $T = 2$ μ s. The RF frequency was swept 2 MHz around the ^2H -Larmor frequency of about 8 MHz (1.2 T) in 6.67 kHz steps.

2.3 W-band EPR measurements. High-field EPR experiments were performed at 4.8 K using a W-band EPR spectrometer (Bruker ELEXSYS E680) operating at about 94 GHz. All experiments were carried out using a homebuilt ENDOR microwave cavity, which contained a solenoid of Teflon coated silver wire integrated in to commercial W-band ENDOR probehead (Bruker). The RF coil contains 20 turns for optimized RF performance at low RF frequencies (< 100 MHz, optimum performance at 20 MHz). To ensure the broadband microwave excitation and minimize the distortions caused by high-power RF excitation, the loaded quality factor, Q_L , was lowered to 700 to obtain a microwave frequency bandwidth of 130 MHz.

Electron spin echo-detected (ESE) field-swept spectra were measured using the pulse sequence: $t_p - \tau - 2t_p - \tau - \text{echo}$ with $t_p = 24$ ns and $\tau = 200$ -500 ns. ^{17}O -Davies ENDOR spectra were collected using the pulse sequence: $t_{\text{inv}} - t_{\text{RF}} - T - t_p - \tau - 2t_p - \tau - \text{echo}$ with $t_{\text{inv}} = 128$ ns, $t_p = 24$ ns, $t_{\text{RF}} = 15$ μ s, $T = 1$ μ s and $\tau = 348$ ns. ^{17}O -Mims ENDOR spectra were collected using the pulse sequence: $t_p - \tau - t_p - t_{\text{RF}} - T - t_p - \tau - \text{echo}$, with $t_p = 24$ ns, $t_{\text{RF}} = 15$ μ s, $\tau = 300$ -500 ns and $T = 1$ μ s. In both ENDOR experiments the RF frequency was swept 6.4 MHz around the ^{17}O -Larmor frequency of about 19.7 MHz (3.4 T) in 43 kHz steps.

ELDOR-detected NMR (EDNMR) measurements were done using the pulse sequence: $t_{\text{HTA}} - T - t_p - \tau - 2t_p - \tau - \text{echo}$. The high turning angle (HTA) microwave pulse was applied at microwave frequency ν_{mw} . The detection Hahn echo pulse sequence $t_p - \tau - 2t_p - \tau - \text{echo}$ at microwave frequency $\nu_{\text{mw}}^{(0)}$, matched to the cavity resonance, was set 6 μ s after the HTA pulse to ensure near-complete decay of the electron

spin coherencies. The pulse length used for detection $\pi/2$ was $t_p = 100$ ns and an interpulse pulse separation of $\tau = 500$ ns was generally used. The echo was integrated 600 ns around its maximum. The spectra were acquired via continuously sweeping the HTA frequency ν_{mw} at fixed B_0 in steps of 68.4 kHz. A low-power HTA microwave pulse of $t_{HTA} = 8-14$ μ s length and amplitude of $\omega_1 = 4-6 \times 10^6$ $\text{rad}\cdot\text{s}^{-1}$ was used to minimize the width of the central blind spot (see **section 2.5**) to allow resolution of the low frequency $^{14}\text{N}(^{15}\text{N})$ spectral lines. The microwave settings of the EDNMR experiment do not represent the optimal conditions for the resolution of ^{17}O hyperfine couplings but instead are a compromise that allows simultaneous detection of both ^{14}N and ^{17}O responses from both single and double quantum transitions, minimally perturbed by the central blind spot (see **section 2.5**).

2.4 Spectral simulations. Spectra were simultaneously fit assuming an effective spin $S = 1/2$ ground state (for details see supporting information **S3 and S4**). The basis set that describes the $^{17}\text{O}/^{14}\text{N}$ -Mn-tetramer spin manifold can be built from the product of the eigenstates of the interacting spins:

$$\left| \frac{1}{2} \quad M \quad I \quad m \right\rangle \quad (\text{Eq. 1})$$

Here M_i refers to the electronic magnetic sub-level, $\pm 1/2$; I takes the value $5/2$ for ^{17}O , 1 for ^{14}N and $1/2$ for ^{15}N ; m_i takes the values $-I_i, 1-I_i, \dots, I_i-1, I_i$.

The Spin Hamiltonian that describes the single nucleus-electron spin manifold is:

$$\hat{H} = \beta_e \vec{B}_0 \cdot \hat{G} \cdot \vec{S} + g_o \beta_n \vec{B} \cdot \vec{I} + \vec{S} \cdot \hat{A} \cdot \vec{I} \quad (\text{Eq. 2})$$

It contains: i) the Zeeman term for the total electronic spin; ii) the Zeeman term for the $^{17}\text{O}/^{14}\text{N}/^{15}\text{N}$ nucleus; iii) the hyperfine term for the $^{17}\text{O}/^{14}\text{N}/^{15}\text{N}$ nucleus. This Hamiltonian was used to simulate all spectra. The electron Zeeman term was treated exactly. The nuclear Zeeman and hyperfine terms were treated using second order perturbation theory. The nuclear quadrupole coupling was not explicitly

considered. Spectral simulations were performed numerically using Scilab-4.4.1, an open source vector-based linear algebra package (www.scilab.org) and the EasySpin package⁵⁹ in MATLAB.

2.5 EPR techniques for measuring nuclear transition frequencies. There are several pulsed EPR techniques which are capable of probing nuclear transition frequencies of paramagnetic compounds: ESEEM-based techniques, ENDOR and ELDOR-detected NMR.⁶⁰ ESEEM is a so-called *coherence-transfer* technique in which the nuclear frequencies are obtained from the analysis of time-dependent electron spin-echo modulation caused by the oscillation between allowed and forbidden electron coherences or by the evolution of nuclear coherencies. ESEEM is particularly sensitive for the detection of nuclear frequencies in the low-frequency range (below 20 MHz), relatively narrow NMR lines and moderate spin relaxation rates. In the case of broad NMR lines the ESEEM techniques suffers from the long dead times of the EPR spectrometer and the finite bandwidth of microwave excitation. In a *polarization-transfer* pulsed EPR experiment, such as ENDOR and EDNMR, the nuclear frequencies are detected by manipulating the polarizations of electron and nuclear levels. The principal difference between ENDOR and EDNMR is the way in which the population of the nuclear levels is changed. In pulse ENDOR the nuclear polarization is inverted by driving the allowed NMR transition ($\Delta m_S=0$, $\Delta m_I=\pm 1$, **Figure 2A**) with a radio-frequency (RF) π -pulse. In contrast, in EDNMR, the nuclear transitions of the spin manifold are probed indirectly by using a second high-turning-angle (HTA) microwave pulse, which drives forbidden electron transitions, i.e., the transitions where both the electron and nuclear spin change their projection direction (**Figure 2A**). The pump pulse is swept around the resonance frequency, $\nu_{mw}^{(0)}$ of the detection Hahn-echo pulse sequence. At microwave frequencies, where the HTA pulse coincides with the forbidden electron transitions ($\Delta m_S=\pm 1$, $\Delta m_I=\pm 1$) of the spin manifold ($\nu_{mw}^{(1)}$, $\nu_{mw}^{(2)}$, **Figure 2A**), the observed primary echo signal decreases due to population transfer via forbidden transitions. These ν_{mw} dependent signal changes are detected as spectral lines, which correspond to the nuclear transitions of the spin manifold. In addition, the HTA

pulse excites the allowed transitions of the spin manifold ($\nu_{mw}^{(0)}$). This results in a decrease of the observed primary echo across the entire swept region. For a rectangular pump pulse the response profile (central blind spot) is Lorentzian centered at $\nu_{mw}^{(0)}$ with $\Delta\nu_{1/2} = \omega_1^{\text{HTA}} / \pi$, where ω_1^{HTA} is the amplitude of the HTA microwave pulse. For an inhomogeneously broadened EPR line, where the EPR linewidth is larger than that of the nuclear coupling of interest, the nuclear spectral lines appear symmetrically about the central frequency, $\nu_{mw}^{(0)}$.

At high magnetic field (W-band EPR), the nuclear Larmor frequency of many low- γ nuclei (^2H , ^{14}N , ^{17}O , etc...) is sufficiently large so that the signals from these nuclei can be resolved from the central blind spot, especially for the case in which the hyperfine coupling of the nuclei to the electronic spin is weak, i.e., less than twice the Larmor frequency. The W-band EDNMR spectrum of a complex containing both ^{14}N and ^{17}O ligands in the weak-coupling limit is shown as a diagram in **Figure 2B**. The lines associated with a particular nucleus are centered around the Larmor frequency of the nucleus of interest, split by the hyperfine (and quadrupole) coupling (see supporting information **S7**). Importantly, at high magnetic fields the Larmor frequency of ^{17}O [$\nu_{\text{N}}(^{17}\text{O}) = 19.6$ MHz at 3.4T] is significantly different from that of ^{14}N [$\nu_{\text{N}}(^{14}\text{N}) = 10.4$ MHz at 3.4 T], thus allowing both components to be readily resolved. For nuclei which have a nuclear spin greater than $1/2$, multiple quantum transitions ($\Delta m_{\text{S}} = \pm 1$, $\Delta m_{\text{I}} = \pm 2$, ...) can be observed. These are centered around multiples of the Larmor frequency split by the same multiple i.e. in the case of double quantum transitions ($\Delta m_{\text{S}} = \pm 1$, $\Delta m_{\text{I}} = \pm 2$), these are now centered about twice the Larmor frequency split by twice the hyperfine coupling (see supporting information **S7**).

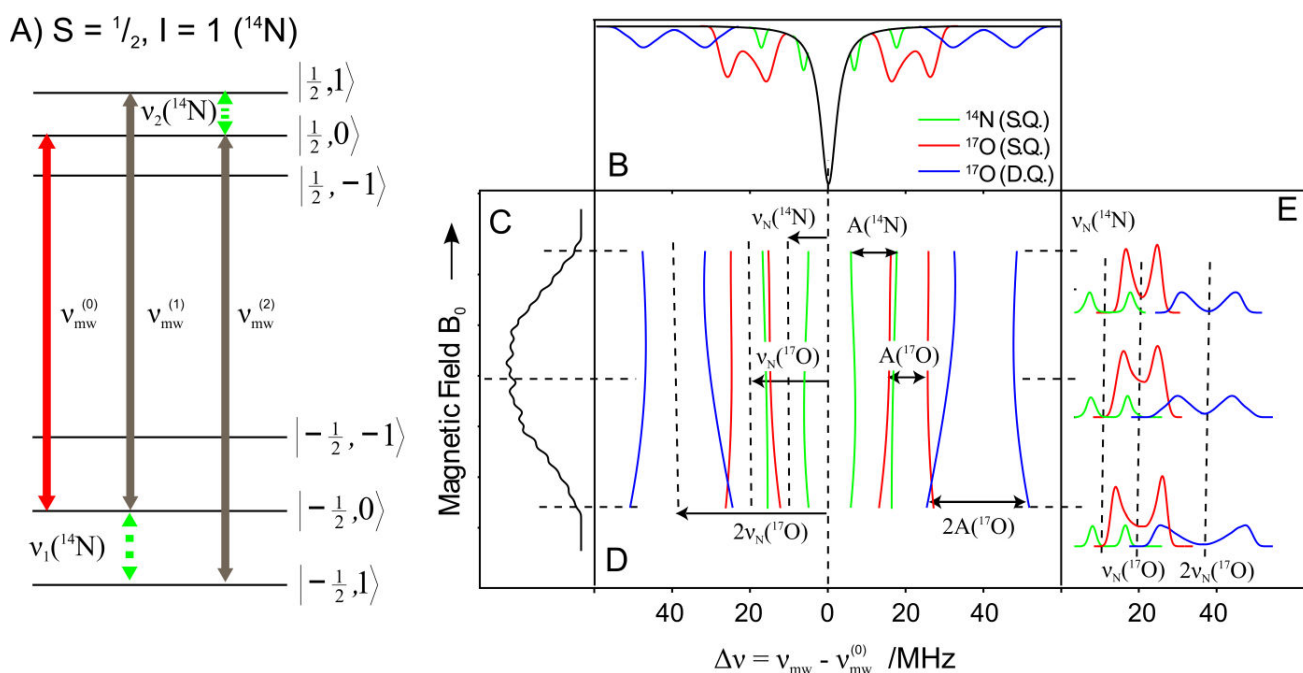


Figure 2. Simulated W-band EDNMR spectra of a mixed-valence Mn-dimer complex ($S = 1/2$) containing weakly anisotropically coupled low- γ nuclei (^{17}O , ^{14}N). **A)** The energy-levels of an $S = 1/2, I = 1$ spin manifold showing the allowed (EPR, $\nu_{mw}^{(0)}$, red) and forbidden (ELDOR, $\nu_{mw}^{(1)}$, $\nu_{mw}^{(2)}$, grey) transitions of the manifold. **B)** The EDNMR spectrum measured at the center of the multiline spectrum. S.Q. and D.Q. refer to single and double quantum transition, respectively. **C)** The EPR multiline spectrum of the complex in field sweep mode. **D)** The 2D EDNMR surface representation of **B)**. **E)** The baseline corrected EDNMR spectrum at three selected field positions within **C)**: the center field and the low and high field edge. Only half the EDNMR spectrum is shown and inverted for clarity of presentation. Simulation parameters used for the EPR lineshape are approximately those fitted for the mixed valence $\text{Mn}^{\text{III}}\text{Mn}^{\text{IV}}$ BIPY complex⁶¹, see **Table 1**.

In the 2D experiment, an EDNMR spectrum is taken at a series of magnetic field positions across the EPR spectrum (**Figure 2C**). A 2D EDNMR surface is shown in **Figure 2D**. As the nuclear Larmor frequency is linearly field dependent, the mean peak positions of the nuclear lines linearly increases with respect to the central frequency ($\nu_{mw}^{(0)}$) as the magnetic field increases. As a consequence, not only the

position but also the rate of change of the peak shift is characteristic of a particular nucleus and as such can be used as a marker for the identity of the nucleus. It is noted that double-quantum transitions must have a field dependence twice that of the corresponding single-quantum transitions.

Compared to ENDOR, high-field EDNMR presents several advantages for the investigation of low- γ nuclei coupled to the electron spin of metalloproteins. EDNMR is more robust against fast electron spin-lattice relaxation, T_1 and spectral diffusion than ENDOR. This robustness is because no preparation of the electron spin system prior to the HTA pulse is required, and short HTA pulses can be realized with the available microwave power. This results in high sensitivity and allows one to record 2D-EDNMR spectra with a sufficient signal-to-noise ratio rapidly. Moreover, the recorded EDNMR spectrum is not distorted either by blind spots around the nuclear Larmor frequencies or by a possible frequency dependence of the RF excitation amplitude. These advantages are demonstrated using a simple model system, $\text{Mn}^{\text{II}}(\text{H}_2^{17}\text{O})_6$ (**Figure 3**). The study of Baute and Goldfarb³⁹ showed that the ^{17}O signals arising from the hyperfine splitting of the ^{17}O nucleus within the $m_s = \pm 1/2$ and $m_s = \pm 3/2$ sublevels of the Mn^{II} electron spin manifold could be readily detected at W-band using Davies ENDOR. The corresponding EDNMR of the $\text{Mn}^{\text{II}}(\text{H}_2^{17}\text{O})_6$ complex is also shown in **Figure 3 (red traces)**. At the three field positions selected, both the Davies ENDOR and EDNMR spectra yield virtually the same lineshape for the single quantum transitions; the only difference is that EDNMR also resolves a sharp signal centered at the Larmor frequency of ^{17}O , corresponding to weakly coupled (second shell) water molecules associated with the Mn^{II} ion (see asterisks).

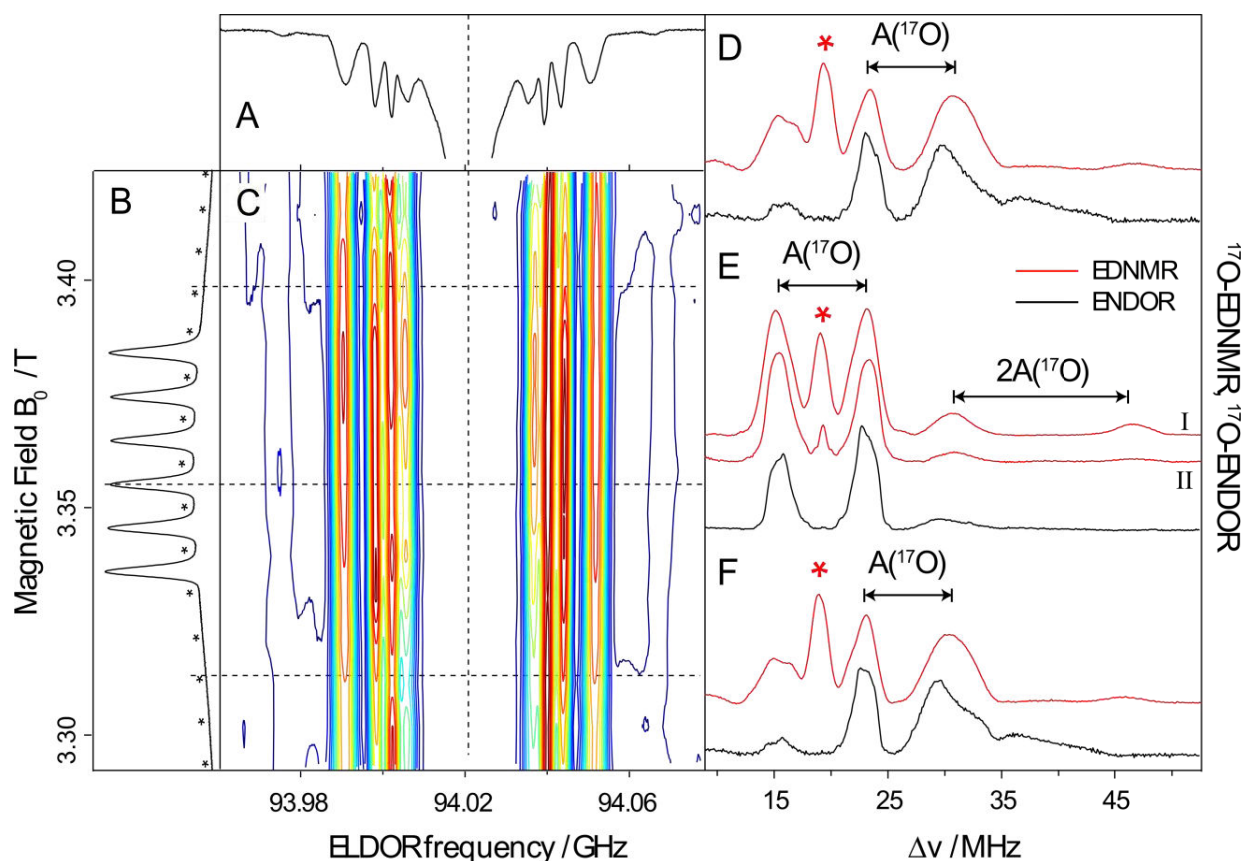


Figure 3 Comparison of W-band ^{17}O Davies ENDOR and EDNMR of $\text{Mn}^{\text{II}}(\text{H}_2^{17}\text{O})_6$. **A**) the EDNMR spectrum measured at the center field; **B**) The EPR multiline spectrum of the complex. **C**) 2D EDNMR surface. **D, E, F**) a comparison of the EDNMR signal to the Davies ENDOR signal seen at three field positions, the low field edge 3.320 T (**D**), the third central line 3.355 T (**E**) and the high field edge 3.400 T (**F**). For (**C**) the EDNMR traces were measured with HTA pulses that varied amplitude (ω_1) **I**) $\omega_1^{\text{HTA}} = 1.8 \times 10^6$, vs. **II**) $\omega_2^{\text{HTA}} = 0.8 \times 10^6 \text{ rad.s}^{-1}$.

This weakly coupled water signal is suppressed in the Davies ENDOR experiment due to blind spotting, but can be readily observed in the corresponding Mims ENDOR experiment. All traces shown in panels **D, E** and **F** were collected for the same time period, with approximately the same frequency step, yielding a sensitivity of EDNMR for this system 20 fold higher than for Davies ENDOR. As the ^{17}O signals for metalloproteins such as the OEC are expected to be much weaker than in model compounds, recourse to the EDNMR technique for these systems may be necessary, especially for orientation

selectivity measurements. These measurements require data collection on the edges of the signal profile (i.e., S_2 multiline signal), where signal intensities are often vanishingly small. As a final note, it is seen that the intensity of the ^{17}O matrix and double quantum lines in the EDNMR experiment can be enhanced by varying the amplitude (ω_1) of the HTA pulse, see **Figure 3E, I**: $\omega_1 = 1.8 \times 10^6$, vs. **II**: $\omega_1 = 0.8 \times 10^6 \text{ rad.s}^{-1}$.

4 RESULTS

4.1 ^{17}O EDNMR of μ -oxo bridges in a model system. Mixed valence Mn dimer complexes have been historically used to calibrate measurements performed on the OEC of PSII. These complexes are considered ‘good’ spectroscopic models as they typically display the same electronic ground state ($S = \frac{1}{2}$) and thus their multiline EPR spectrum is comparable to that seen for the half-integer paramagnetic states of the OEC, i.e. S_0 and S_2 .⁶¹⁻⁷⁰ In this way, a magnetic fingerprint of different Mn ligand motifs can be developed. The approach of using Mn dimer complexes as electronic structure mimics has been previously employed for benchmarking ^{55}Mn -ENDOR,⁶⁶⁻⁷⁰ ^{14}N -ESEEM⁷¹⁻⁷³ and ^{13}C ENDOR⁷⁴ studies on the OEC. One particular binding motif, the μ -oxo bridge, has been little studied.⁴⁷ The section below briefly demonstrates the capabilities of ^{17}O -EDNMR as applied to the model complex $[\text{Mn}^{\text{III}}\text{Mn}^{\text{IV}}(\mu\text{-O})_2\text{BIPY}_4]\text{ClO}_4$ ⁷⁵⁻⁷⁷, BIPY = bipyridine, which was previously studied by Usov et al.⁴⁷ using ^{17}O -ENDOR. It is shown that this technique allows a complete characterization of the μ -oxo bridge motif and the structural factors that influence it.

The EDNMR surface of the ^{17}O labeled mixed valent planar $\text{Mn}^{\text{III}}(\mu\text{-O})_2\text{-Mn}^{\text{IV}}$ BIPY complex⁷⁵⁻⁷⁷ is shown in **Figure 4**. The ^{17}O label was incorporated via isotope exchange with ^{17}O labelled water. The final complex contained approximately 75% ^{17}O bridges, i.e. in the majority of complexes both μ -oxo bridges were exchanged. The control ^{16}O BIPY complex data are shown **black** in **Figure 4** panels **D, E** and **F**, resolving signals attributable to a ^{14}N ligand. Both single and double quantum transitions are observed. The single quantum transitions are centered about the Larmor frequency of ^{14}N [$\nu_{\text{N}}(^{14}\text{N}) = 10.4 \text{ MHz}$], split by the hyperfine coupling and (full arrow in panels **D, E, F**), while double quantum ^{14}N

transitions are centered at twice the Larmor frequency of ^{14}N [$\nu_{\text{N}}(^{14}\text{N}) = 20.8$ MHz] and split by twice the hyperfine coupling (dashed arrows in panels **D**, **E**, **F**). The ^{14}N peaks are narrow with peak widths of FWHM 3 MHz. This signal represents the strongly coupled ^{14}N axial ligand of the Mn^{III} ion which sits along its Jahn-Teller axis.⁶¹ The remaining equatorial ^{14}N ligands of the Mn^{III} and all ^{14}N ligands of the Mn^{IV} are only weakly coupled and appear as a ‘matrix’ line centered at the ^{14}N Larmor frequency. A further splitting of the high frequency 1.2 MHz ^{14}N line is observed which is best resolved on the high field edge. This splitting is tentatively assigned to a quadrupole coupling of 2 MHz.

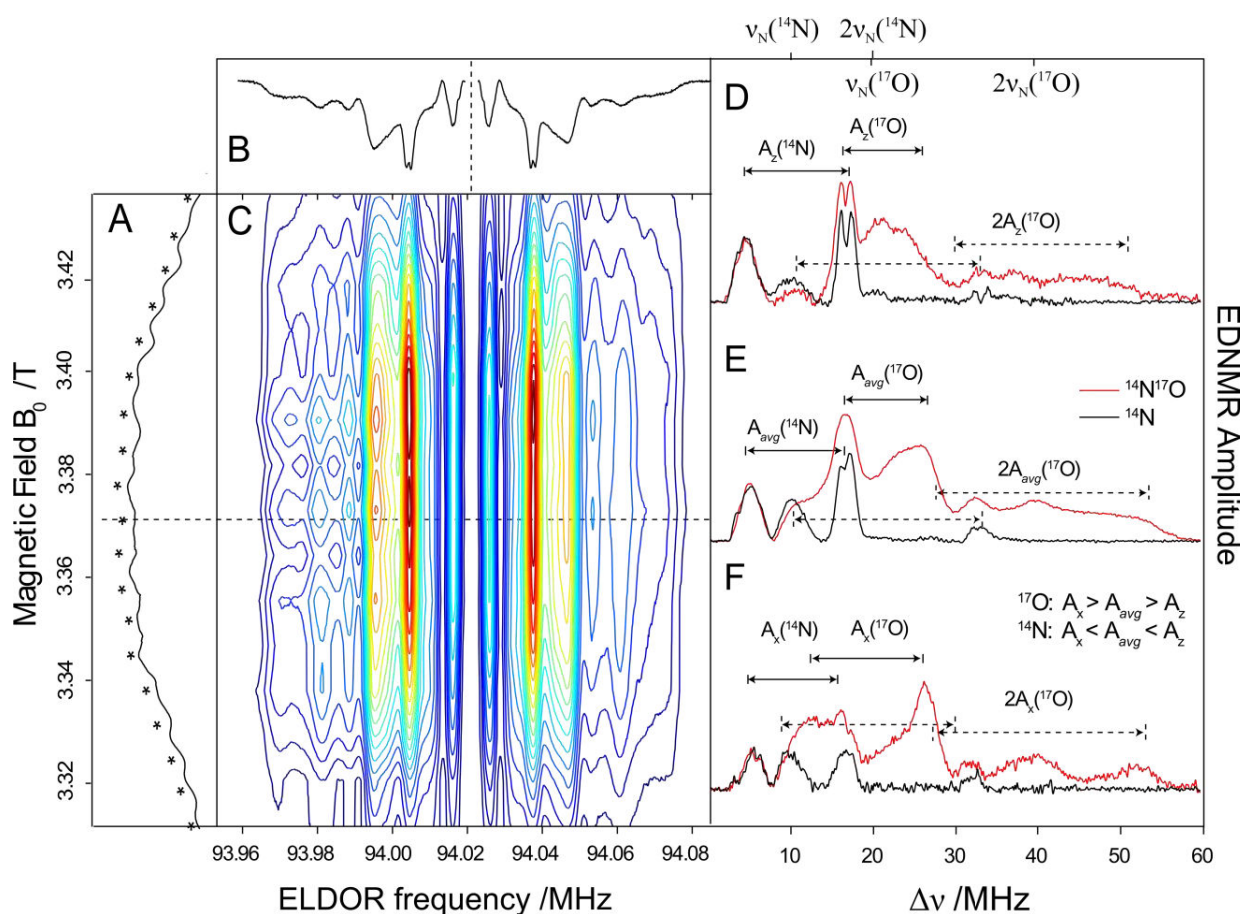


Figure 4. W-band EDNMR spectra of ^{17}O labeled $\text{Mn}^{\text{III}}-(\mu\text{O})_2\text{-Mn}^{\text{IV}}$ BIPY complex. **A**) The EPR spectrum of the complex; **B**) The EDNMR signal; **C**) 2D EDNMR surface; **D**, **E**, **F**) the EDNMR signals seen for the ^{17}O labeled complex at three field positions (**red** lines) compared to those of unlabeled complex (**black** lines) collected at: **D**) the high field edge 3.44 T; **E**) the central field 3.37 T; **F**) the low field edge 3.30 T.

The corresponding ^{17}O labeled BIPY complex data are shown **red** in **Figure 4** panels **D**, **E** and **F**. The single quantum ^{17}O transitions appear as a broad doublet centered about the Larmor frequency of ^{17}O [$\nu_{\text{N}}(^{17}\text{O}) = 19.5$ MHz]. The two peak of this broad envelope are best resolved when the EDNMR spectrum is measured on the low field edge (**Figure 4F**). When measured on the high field edge (**Figure 4D**), the two ^{17}O peaks strongly overlap. The center field EDNMR spectrum represents an average of the two edge spectra (**Figure 4E**). The ^{14}N and ^{17}O signals were simulated using the Spin Hamiltonian formalism, see supporting information **S7**. The large difference seen between the low, high and center field spectra of the ^{17}O signal suggests that the hyperfine tensor is not axial but rather has a high degree of rhombicity. The fitted parameters show that the hyperfine anisotropy is of the same order as the isotropic hyperfine coupling ($A_{\text{iso}} \sim 8$ MHz, $A_{\text{dip}} \sim 5$ MHz). These parameters serve as a preliminary magnetic fingerprint for a Mn μ -oxo bridge: namely that the ^{17}O hyperfine tensor of the bridge should display: i) a large isotropic coupling ~ 8 MHz and; ii) a hyperfine anisotropy that is large and highly rhombic.

4.2 ^{17}O -EDNMR based detection of water-exchangeable ligands of the $\text{Mn}_4\text{O}_5\text{Ca}$ cluster. EDNMR presents the same advantages seen in model complexes for detection of ^{17}O coupling to the OEC. As seen for the BIPY model complex, the OEC is expected to exhibit at least one nitrogen signal from a coordinating Histidine residue (D1-His332), seen in the X-ray crystal structure. As such, it is important to carefully characterize this ^{14}N species prior to performing the ^{17}O labeling experiment. It will be shown later that this nitrogen signal also serves as a basis for assigning ^{17}O signals, as its geometric position within the OEC is known. As a final note, it is important to perform the ^{17}O labeling experiments on approximately the same timescale as observed for substrate exchange. Long incubations in labeled water can lead to exchange of structural oxygens; oxygen ligands of the manganese cluster that are not substrate sites. This last point is detailed in **section 4.4**.

4.2.1 The EDNMR nitrogen signal of the D1-His332 ligand of the $\text{Mn}_4\text{O}_5\text{Ca}$ cluster. W-band EDNMR spectra of ^{14}N -PSII and universally labeled ^{15}N -PSII, resuspended in unlabelled water and poised in the S_2 state are shown in **Figure 5**. The EDNMR spectrum of ^{14}N -PSII (**Figure 5A, black trace**) resolves a doublet centered about the Larmor frequency of ^{14}N [$\nu_{\text{N}}(^{14}\text{N}) = 10.46$ MHz, 3.4 T] with peak spacing of 7.0 MHz and peak width FWHM 2.5 MHz. A corresponding doublet is seen of ^{15}N -PSII (**Figure 5C, black trace**), but shifted to higher frequency, now centered about the Larmor frequency of ^{15}N [$\nu_{\text{N}}(^{15}\text{N}) = 14.68$ MHz, 3.4 T] with peak-to-peak spacing of 9.7 MHz and peak width FWHM 2.5 MHz. These signals were absent in spectra in the S_1 state recorded using the same conditions. In contrast to the BIPY data (**Figure 4**), no quadrupole splitting was observed in the ^{14}N -PSII spectra. Double quantum transitions for the ^{14}N -PSII sample were also observed. These were best visualized by increasing the length of the HTA pulse by an order of magnitude. This also enhances the matrix line, centered at the ^{14}N Larmor frequency (**Figure 5A, lower black trace, II**). A nitrogen species of approximately the same coupling (~ 7 MHz) was previously observed using Q-band ESEEM, in samples prepared from higher plant and cyanobacterial (*Synechocystis*) PSII by the Britt laboratory.^{72,73,78} It was assigned to the D1-His332, the only nitrogen ligand that directly coordinates a Mn of the OEC (Mn_{D1}), see **Figure 1**.

4.2.2 Exchangeable water-derived ligands of the $\text{Mn}_4\text{O}_5\text{Ca}$ cluster. W-band EDNMR spectra of ^{14}N -PSII and universally labeled ^{15}N -PSII, resuspended in H_2^{17}O and poised in the S_2 state are also shown in **Figure 5A and 5C (red traces)**. In these samples an additional signal is observed centered at the Larmor frequency of ^{17}O [$\nu_{\text{N}}(^{17}\text{O}) = 19.63$ MHz, 3.4 T].

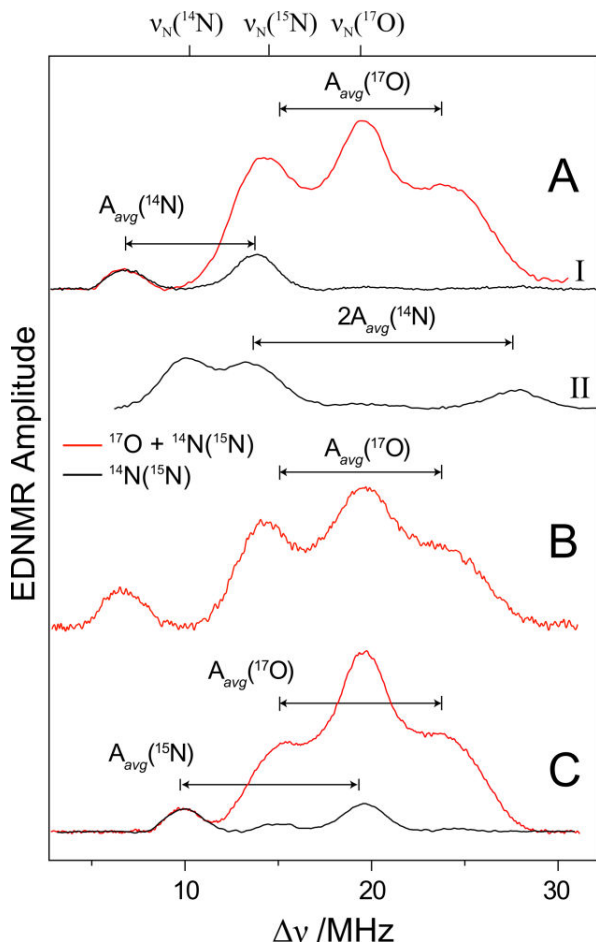


Figure 5. W-band EDNMR spectra of $^{14}\text{N}(^{15}\text{N})$ -PSII poised in the S_2 state measured at the center of the multiline spectrum ($B_0 = 3.40$ T). **A)** ^{14}N -PSII resuspended in unlabelled water (**black**) / H_2^{17}O (**red**). **B)** ^{14}N -PSII rapidly diluted (15 s) in H_2^{17}O ; **C)** ^{15}N -PSII resuspended in unlabelled water (**black**) / H_2^{17}O (**red**). For **(A)**, the EDNMR traces (**black**) were measured with using HTA pulses optimal for **I)** single quantum ^{14}N ; and **II)** double quantum ^{14}N signals. For further sample information and all instrumentation parameters see **Section 2 Materials and Methods**.

The new signal observed upon ^{17}O enrichment, consists of three peaks, a central line centered at $\nu_{\text{N}}(^{17}\text{O})$ and two satellite lines appearing symmetrically about this position. The central line represents weakly coupled (matrix) exchangeable ^{17}O species associated with the OEC whereas the two satellite lines represent one or more exchangeable Mn-O ligands. The peak positions of the signal do not change between the ^{14}N and ^{15}N labeled samples but the line intensities do vary. This is due to the different

contributions of $^{14}\text{N}(^{15}\text{N})$ signal described above. Subtraction of the $^{14}\text{N}(^{15}\text{N})$ signal results approximately in the same lineshape for the two sample types. The corresponding ^{17}O -Davies ENDOR spectrum was also recorded and is shown in the supporting information **S8**. Double quantum transitions are also observed for the ^{17}O signal envelope, centered about twice the Larmor frequency of ^{17}O (see **Figure 7A**). The structure of the double quantum envelope suggests there is at least two exchangeable oxygen nuclei coupled to the OEC. This second oxygen, which has an intermediate hyperfine coupling, is not resolved in the single quantum envelope due to spectral congestion. Further experiments (NH_3 addition, magnetic field dependence) shown below (**section 4.2.4**) demonstrate this is indeed the case. The ^{17}O signal profile seen in PSII is of approximately the same width as the ^{17}O signal profile observed for the BIPY model complex described above (see **Figure 4E**).

Corresponding S_2 state field-sweep W-band EPR spectra of the OEC of ^{14}N -PSII and universally labeled ^{15}N -PSII, resuspended in buffer solutions made with either unlabelled water or H_2^{17}O are shown in the supporting information **S5**. They displayed the typical unstructured S_2 multiline signal centered at $g \sim 1.976$, of width (FWHM) 90 mT.⁷⁹

4.2.3 Protonation state of oxo-bridges of the $\text{Mn}_4\text{O}_5\text{Ca}$ cluster. The protonation state of the exchangeable water ligands identified above can be probed using $^1\text{H}/^2\text{H}$ -ENDOR spectroscopy. **Figure 6** shows the ^1H Davies and corresponding ^2H -Mims ENDOR spectra of the OEC of *T. elongatus* poised in both the S_1 and S_2 states. The spectra were symmetrised about the Larmor frequency of the $^1\text{H}/^2\text{H}$ nucleus [$\nu_{\text{N}}(^1\text{H}) = 51.94$ MHz, $\nu_{\text{N}}(^2\text{H}) = 7.97$ MHz at $B_0 = 1.22$ T]. All raw data is given in the supporting information **S6**. The width of the $^1\text{H}/^2\text{H}$ envelope is essentially the same as reported in earlier studies of higher plants. The magnitude of the hyperfine couplings observed are consistent with coordinating terminal water/hydroxyl ligands but are too small to represent a hydroxo bridge species. This is demonstrated in the supporting information using the Umena et al.¹ crystal structure coordinates and the current electronic model for the OEC.^{20,80} Electron-nuclear dipolar hyperfine coupling estimates (dipolar) for the ^1H nuclei for all ‘water’ molecules identified in within 5 Å of the OEC are listed in

supporting information **S9 and S10**, along with a simulation of the $^1\text{H}/^2\text{H}$ envelope using these calculated values, see **S11**.

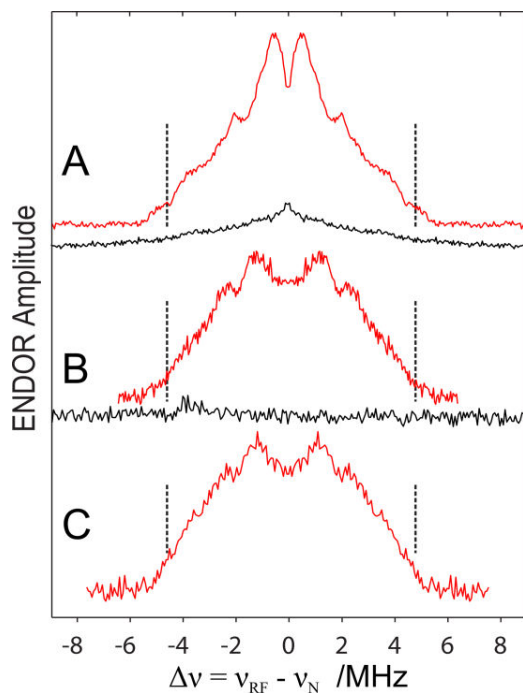


Figure 6. Proton/Deuteron ENDOR spectra of ^{14}N -PSII of *T. elongatus* poised in the S_2 state measured at the center of the multiline spectrum (1.2 T). **A)** Q-band ^1H Davies-ENDOR, S_2 (red), S_1 (black); **B)** Q-band ^2H Mims-ENDOR, S_2 (red), S_1 (black); **C)** W-band ^2H Mims-ENDOR, S_2 (red). All signals are centered at the appropriate $^1\text{H}/^2\text{H}$ Larmor frequency. The frequency axis of the ^2H data sets are scaled to the ^1H frequency axis for easy comparison.

4.2.4 Experimental verification of three classes of exchangeable water-Mn couplings. Beck et al.⁸¹ demonstrated that NH_3 modifies the electronic structure of the Mn cluster poised in the S_2 state. Britt et al.⁷¹ subsequently showed using ESEEM that NH_3 binds to the OEC, in samples prepared from higher plants, poised in the S_2 state ($A_{\text{iso}} = 2.29$ MHz). Curiously, NH_3 does not bind to the OEC in the S_1 state. Similar results have been observed in thermophilic cyanobacteria,⁸² the PSII material used in this study. While it remains unclear what the exact action of NH_3 is, and how many binding sites it has at/near the $\text{Mn}_4\text{O}_5\text{Ca}$ cluster, one role proposed for this water-analog is that it displaces or modifies a manganese bound water substrate.

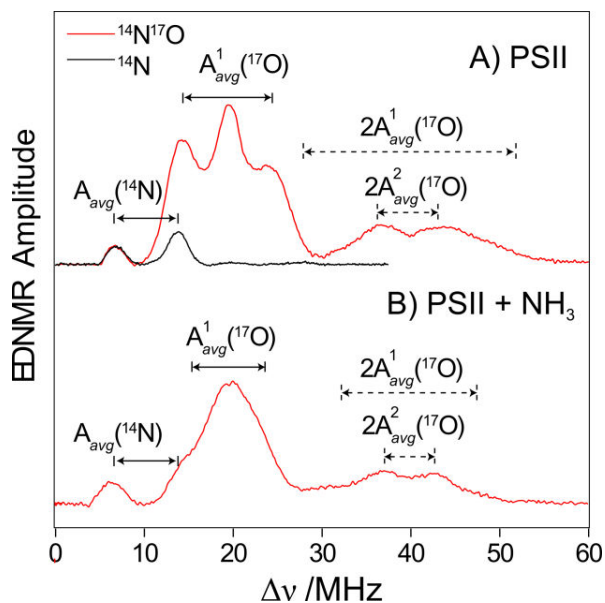


Figure 7. W-band EDNMR spectra of PSII poised in the S_2 state measured at the center of the corresponding EPR spectrum. **A)** ^{14}N -PSII resuspended in unlabelled water (**black**) and H_2^{17}O (**red**); **B)** ^{14}N -PSII + NH_3 , resuspended in H_2^{17}O (**red**). Experimental/instrument parameters are listed in the **Materials and Methods** section.

Here we have tested this proposal by addition of ammonia to dark adapted, i.e. S_1 , H_2^{17}O exchanged PSII samples. Upon illumination at temperatures below 190 K,⁸³ the typical S_2 state EPR multiline signal was seen in control samples using Q-band EPR. In addition, W-band EDNMR measurements resolve the same ^{17}O signal profile, demonstrating NH_3 does not bind to or modify the S_1 state. As shown previously by Boussac et al.⁸³, subsequent annealing of the sample to 250 K allows NH_3 to interact with the S_2 state of the OEC (**Figure 7B**). In the EDNMR experiments reported here, annealing led to a narrowing of the ^{17}O signal envelope (single quantum), with the two satellite lines seen at 14.2 and 23.8 MHz shifting toward the ^{17}O Larmor frequency. The remaining single quantum envelope was only ~6 MHz broad. The change observed for the double quantum envelope is more complicated. Consistent with the narrowing seen for the ^{17}O single quantum envelope, the broad edges do contract by ~6 MHz (i.e. twice the contraction seen for the single quantum satellites). In contrast however, the

structural peaks observed at about twice the ^{17}O Larmor frequency are retained, and only slightly narrow ($\sim 1\text{-}2$ MHz). This differential behavior demonstrates that the observed ^{17}O signal envelope must be comprised of at least three components. It contains: i) a strongly coupled species, with ^{17}O hyperfine coupling of ~ 10 MHz, representing a Mn-bound ^{17}O species; ii) an intermediately coupled species, with ^{17}O hyperfine coupling of ~ 5 MHz, representing a second Mn-bound ^{17}O species, which is hidden in the single quantum envelope due to spectral congestion; and iii) more weakly coupled matrix water molecules of unresolved hyperfine coupling, which manifest as the central line observed at the Larmor frequency.

The magnetic field dependence of the EDNMR signals can provide further information about the identity of exchangeable water ligands, as seen for the model complex in **section 4.1**. The ^{17}O signal profile seen for the OEC also exhibits a small, but observable magnetic field dependence (2-3 MHz, **Figure 8 and 9**). The exact peak separation of the single quantum satellite peaks (14.2 and 23.8 MHz) increases as the magnetic field increases. This is best resolved at the high frequency edge as this feature does not overlap with the ^{14}N signal. As before, the behavior of the double quantum signal is more complicated. The edges of the double quantum envelope are not well resolved across the whole EDNMR surface but do appear to follow the trend seen for the single quantum envelope. This is in contrast to the narrow component. The splitting of its peaks (37.0 and 43.5 MHz) instead decreases measured across the multiline spectrum. This is further evidence that the ^{17}O EDNMR signal envelope contains two ^{17}O couplings (>4 MHz), consistent with the NH_3 experiment described above. It is noted that the $^{14}\text{N}(^{15}\text{N})$ signal also displayed a weak magnetic field dependence (~ 1.5 MHz), with the hyperfine splitting smallest for the EDNMR spectrum measured on the low field edge of the EPR signal. The same field dependence is observed for the ^{14}N double quantum signal at 26-28 MHz (see **Figure 9**).

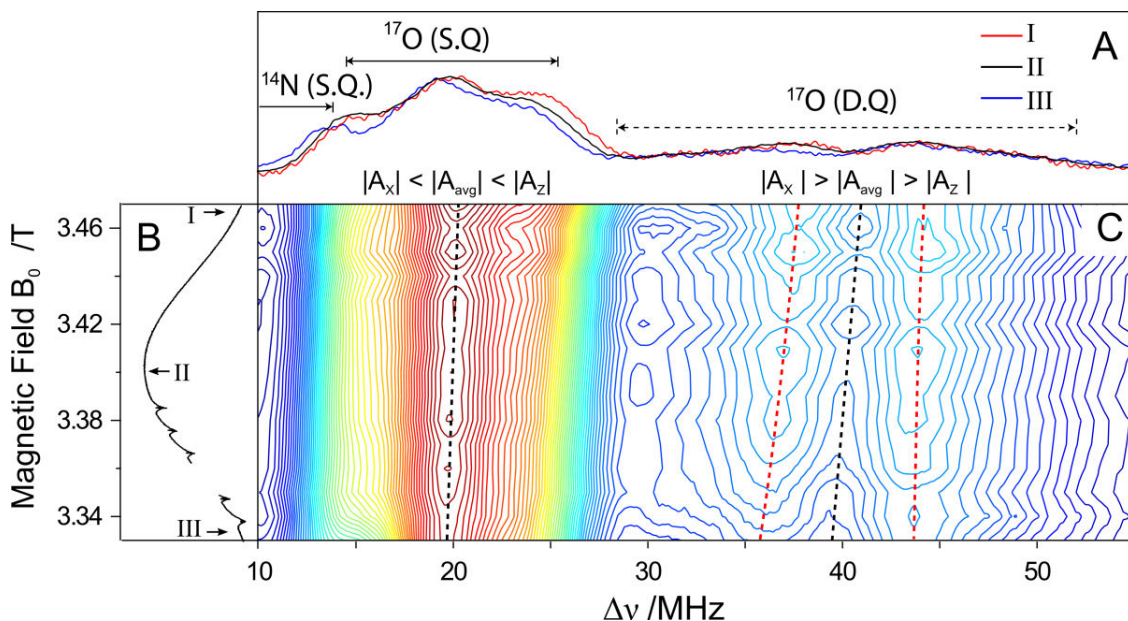


Figure 8. W-band 2D-EDNMR surface of ^{14}N -PSII poised in the S_2 state, resuspended in H_2^{17}O in the S_1 state. **A)** EDNMR spectra measured at the high field (**I**: 3.47 T, **red**), center (**II**: 3.40 T, **black**) and low field (**III**: 3.43 T, **blue**) edge of the multiline spectrum. **B)** The EPR multiline spectrum. **C)** The 2D EDNMR representation of **A**. The black dashed lines show the magnetic field dependence of the single quantum and double quantum ^{17}O Larmor frequency. Lines locating the average peak separation of the narrow component of the double quantum envelope are also shown (**red dashed line**). Experimental/instrument parameters are listed in the **Materials and Methods** section.

4.3 Assignment of ^{17}O EDNMR signals - Spin Hamiltonian Simulations. Spectral simulations of the ^{17}O signal envelope inclusive of both single and double quantum transitions were performed using the Spin Hamiltonian formalism, for details see **section 2.5** and the supporting information **S7**. Spectral simulations of the ^{17}O EDNMR signal envelope measured for the ^{14}N -PSII are shown in **Figure 9**. Simulation of the EDNMR surface ensured that correct estimates were made for both the isotropic and anisotropic components of the ^{17}O hyperfine tensors.

A simulation of the ^{14}N using similar Spin Hamiltonian parameters as reported by Stich et al.⁷² is shown in **Figure 9**. A small decrease in the A_{iso} of 10% and consequently an increase in A_{dip} was required to reproduce the field dependence, see **Table 1**. The simulation places the principal axis of the

^{14}N hyperfine tensor approximately along g_x , i.e. it coincides with powder pattern orientations that define the low field edge of the EPR (multiline) spectrum. The best fit to the data included a 30° rotation of the hyperfine tensor in the g_x/g_z frame, see supporting information **S12**.

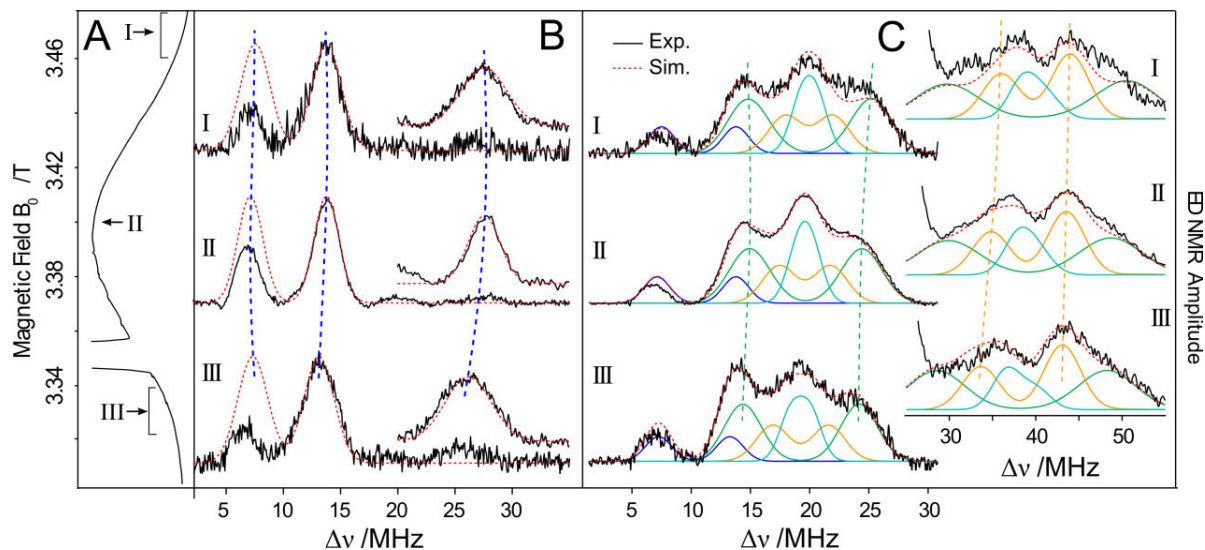


Figure 9. Spin Hamiltonian simulations of the ^{14}N and ^{17}O signals seen for the OEC. **A:** A representative S_2 multiline spectrum. **B/C:** simulation of the single (**left**) and double quantum (**right**) $^{14}\text{N}/^{17}\text{O}$ -EDNMR signal envelopes at three field positions: **I**) the high field edge (3.46-3.47 T); **II**) the center (3.40 T); and **III**) the low field edge (3.33-3.34 T). Spin Hamiltonian parameters are listed in **Table 1**. Dashed lines show the field dependence of the respective EDNMR peaks.

As described in the previous section, the fitted ^{17}O signal envelope requires three oxygen species, one strongly coupled oxygen species, one intermediately coupled oxygen species and weakly coupled ‘matrix’ oxygen species. All Spin Hamiltonian parameters are given in **Table 1**. Assignments for the three ^{17}O oxygens are as follows:

- 1) *A Mn μ -oxo bridge.* The fitted hyperfine tensor of the 1st species has an isotropic hyperfine coupling of $A_{\text{iso}} = 9.7$ MHz and anisotropic coupling of $A_{\text{dip}} = 2.2$ MHz of large rhombicity $\eta \sim 0.6$. These parameters broadly match those seen for the μ -oxo bridges of the $\text{Mn}^{\text{III}}-(\mu\text{O})_2\text{-Mn}^{\text{IV}}$ model complex shown in the Results **section 4.1** and thus this oxygen is assigned to a μ -oxo bridge. A rationale for the apparent decrease in hyperfine anisotropy is given in the discussion and in part

serves to identify the μ -oxo bridge (see discussion). This component of the ^{17}O signal envelope is broadly consistent with the signal seen in the study of McConnel et al.⁴⁶, which was also assigned to a μ -oxo bridge.

- 2) *A terminal Mn-water/hydroxo ligand.* The fitted hyperfine tensor of the 2nd species has an isotropic hyperfine coupling of $A_{\text{iso}} = 4.5$ MHz and an anisotropic coupling of $A_{\text{dip}} = 0.6$ MHz with rhombicity $\eta \sim 0.1$. These parameters do not match well with those determined for the μ -oxo bridges of the $\text{Mn}^{\text{III}}-(\mu\text{O})_2-\text{Mn}^{\text{IV}}$ model complex, shown in Results **section 4.1**; both the isotropic and anisotropic hyperfine components are significantly smaller. However, these parameters do match ^{14}N hyperfine couplings seen for terminal nitrogen Mn^{IV} and equatorial Mn^{III} ligands in mixed valance model complexes,^{71,84} (see the BIPY complex above). As such, the 2nd species is assigned to one or both of the terminal water/hydroxo ligands of $\text{Mn}_{\text{A}4}$. The more axial nature of the hyperfine tensor associated with this oxygen is consistent with this assignment.
- 3) *Matrix water.* The ‘3rd oxygen’, or rather collection of oxygen species, which defines the central line describes weakly coupled ‘matrix’ water. The fitted isotropic hyperfine coupling is $A_{\text{iso}} \sim 1-2$ MHz which suggests one component of the matrix line describes a ligand to a manganese i.e. $\text{Mn}-\text{OH}_2$. Very weak couplings within this envelope can be extracted using an alternative technique, W-band Mims-ENDOR (supporting information **S8**). The Mims-ENDOR signal has a near Lorentzian lineshape with a splitting of 0.5 MHz. Similar lineshapes albeit of enhanced resolution have been identified previously in ^{17}O model systems e.g. weakly coupled $^1\text{H}_2^{17}\text{O}$ coordinating Gd^{3+} complexes.⁸⁵ The Mims ENDOR envelope is assigned to the Ca bound waters W3 and W4, (see supporting information **S8**).

Table 1. ^{14}N and ^{17}O hyperfine spin Hamiltonian parameters, comparison to calculated parameters for the **1d2'** model of Ames et al. (**Figure 1B**).

		Spin Hamiltonian Parameters (MHz)					DFT (MHz)		
		A_x	A_y	A_z	A_{iso}	A_{dip}	$A(\eta)$	A_{iso}	Site
BIPY	N (JT)	10.8	11.3	12.5	11.5	0.5	0.50	-	-
	μO	18.0	-0.8	6.8	8.0	5.0	0.75	-	-
D1-His332	^{14}N	3.8	7.7	6.2	5.9	0.9	0.71	-5.2	His332
^{17}O Envelope	<i>strong</i>	10.7	5.2	13.1	9.7	2.2	0.55	-	-
	<i>interm.</i>	5.0	5.1	3.3	4.5	0.6	0.08	-4.7	W2
	<i>matrix</i>	2.1	0.2	2.0	1.4	0.6	0.06	-1.5	W1

A_{iso} is defined as the average of the principal components of the hyperfine tensor: $A_{iso} = (A_x + A_y + A_z)/3$. A_{dip} is defined in terms of T_1 , T_2 and T_3 as: $A_{dip} = \frac{T_1 + T_2}{2} = -\frac{T_3}{2}$ and the rhombicity is as defined by: $\eta = \frac{T_1 - T_2}{T_3}$. T_1 , T_2 and T_3 represent the three principal components of the hyperfine tensor minus A_{iso} , and labeled such that $|T_1| \leq |T_2| \leq |T_3|$

DFT calculations were performed to validate the above assignment of the ^{17}O EDNMR envelope (see supporting information **S13**). Currently, Broken symmetry (BS)-DFT estimates for the isotropic hyperfine coupling of the five μ -oxo bridges of the $\text{Mn}_4\text{O}_5\text{Ca}$ cluster cannot be made. Thus only estimates for the terminal Mn-OH/OH₂ ligands and more distant Ca-OH₂ ligands are reported. The structural model used was the previously published **1d2'** model of Ames et al. (see **Figure 1B**). DFT calculated hyperfine values for W1-W4 are all less than 5 MHz (**Table 1**), significantly smaller than the largest measured hyperfine coupling (10 MHz), suggesting this large coupling does indeed arise for another Mn-O ligand motif i.e. a μ -oxo bridge of the Mn_4O_5 core complex. In addition, the DFT hyperfine values for W2 and W1 appear to correlate with the experimental *intermediate* and *weak*

coupling components of the fitted EDNMR signal envelope: W2, a terminal hydroxide ligand coordinated to Mn_{A4} in the **1d2'** model, has a calculated hyperfine coupling of 4.7 MHz and W1, a terminal water ligand coordinated to Mn_{A4} in the **1d2'**, has a calculated hyperfine coupling of 1.5 MHz. The remaining waters W3/W4, water ligands to the Ca, are all predicted to display small hyperfine couplings (~0.1 MHz). This is consistent with the Mims-ENDOR signal envelope observed (see supporting information **S8**).

4.4 Water exchange rates. To test whether the ¹⁷O signal(s) described in the previous section are potential candidates for the substrate bound in the S₁/S₂ state, further experiments were performed in which the PSII core complexes poised in the S₁ state were rapidly diluted into ¹H₂¹⁷O buffer (see **Materials and Methods**). The PSII sample was diluted by 50% with H₂¹⁷O water and frozen to 77 K. and then illuminated with white light for 5 s at 200 K to generate the S₂ state. The time resolution of the experiment i.e. the minimum mixing and incubation time of the PSII sample in ¹H₂¹⁷O buffer prior to freezing, was less than 15 seconds. The exchange rate of the slowly exchanging substrate molecule has been measured by membrane-inlet mass spectrometry to be in the order of 0.066 s⁻¹ (t_{1/2} = 15 s) at 20 °C, thus this period of time should be sufficient to significantly exchange substrate water molecules in the S₁ state.²²⁻²⁴ **Figure 5B (red trace)** shows the ¹⁷O-EDNMR signal seen in the samples prepared using this protocol. It is readily seen that approximately the same ¹⁷O signal envelope is observed as in **Figure 5A**. As expected the intensity of the entire signal, relative to the ¹⁴N (D1-His332) signal, is lower than in the resuspended sample as the final ¹⁷O enrichment is lower, max. 45% vs. >70%. Thus all detected ¹⁷O signal(s) exchange within 15 s, i.e. on the same time scale as substrate water. A more robust exchange procedure with enhanced time-resolution is currently being developed in our laboratory to provide a quantitative estimate of the exchange rate(s) of the three exchangeable oxygen species.

5. DISCUSSION

5.1 General remarks. In this study, an attempt has been made to develop a new experimental approach to solve one of the most important remaining question regarding the function of the OEC, substrate water binding. The two-step program described above, where both model complexes and the OEC were studied, places new important constraints on the structure and function of the OEC. Multiple ^{17}O signals are resolved, demonstrating the complex interplay of the OEC with the solvent background, which uniquely also forms the substrate for the catalyst. Furthermore, all spectroscopic parameters measured for the $^1\text{H}/^{14}\text{N}$ nuclei associated with the OEC are consistent with current literature models for the electronic structure of the OEC,^{20,66,80} a tetramer, where all four Mn are coupled and contribute approximately equally to the ground electronic state. In the following discussion, preliminary assignments are proposed for the ^{17}O signals observed.

5.2 μ -oxo- ^{17}O model complex data. Only one study exists in the current literature which describes a ^{17}O nucleus coupled to a high valent (Mn^{III} , Mn^{IV}) model complex, namely the BIPY complex, the same as studied here.⁴⁷ In this earlier work a broad, structureless ^{17}O signal was seen using Q-band ENDOR centered at ~ 12 MHz. An estimate of the isotropic coupling was made from the center of the peak of the signal (+ branch) of ~ 13 MHz, which was shown to be consistent with the observed line-broadening seen in the cw-EPR experiments. No estimate was reported for either the hyperfine anisotropy or quadrupole splitting. An isotropic coupling estimate of $A_{\text{iso}} \sim 13$ MHz is somewhat larger than the value reported here, $A_{\text{iso}} \sim 8$ MHz. The difference is suspected to arise from an experimental feature of the experiment. Q-band ENDOR is often not particularly sensitive at very low frequencies where much of the ^{17}O signal envelope is expected when measured at 34 GHz. Thus the signal peak observed does not represent a true average coupling, but is instead skewed toward higher frequencies, overestimating the isotropic coupling. The same problem is not encountered using W-band EDNMR.

The key advantage, however, of W-band EDNMR for ^{17}O -model complexes of this type is that it allows hyperfine anisotropy to be estimated, thus allowing a characteristic fingerprint of the μ -oxo bridge to be developed. As noted in the results **section 4.1**, the strong field dependence of the width of

the ^{17}O signal, where the low, high and center field spectra all have a different width, suggest the hyperfine anisotropy is large and that the tensor is not axial but rather has a high degree of rhombicity. Spectral simulations (shown in the supporting information **S7**), using the Spin Hamiltonian formalism, are consistent with this description ($A_{\text{iso}} \sim 8$ MHz, $A_{\text{dip}} \sim 5$ MHz). The hyperfine tensor is aligned such that the largest and smallest components of the hyperfine tensor (in terms of signed magnitude) are aligned along g_x and g_y (or at least are orientated in the g_x/g_y plane) whereas the middle component is aligned along g_z . This result can be well understood within the current model for strongly antiferromagnetically coupled $\text{Mn}^{\text{III}}\text{Mn}^{\text{IV}}$ dimers ($J < -100$ cm^{-1}). In these systems the Jahn-Teller axis of the Mn^{III} ion defines the unique axis (g_z -axis) of the system.⁸⁶ It is aligned along the $\text{Mn}^{\text{III}}\text{-N}$ bond perpendicular to the plane defined by the $\text{Mn}-(\mu\text{O})_2\text{-Mn}$ atoms. The large hyperfine anisotropy of the ^{17}O bridge (5 MHz) comes about from the through space (dipolar) interaction between the ligand and the two Mn ions; the electron-nuclear dipolar hyperfine coupling estimate for the μ -oxo bridge is 4.5 MHz. The measured (projected) ^{17}O hyperfine interaction is a weighted sum of the two onsite ^{17}O hyperfine tensors which describe the interaction of the ^{17}O nucleus with either the Mn^{III} or Mn^{IV} . The relative contribution of each onsite ^{17}O hyperfine tensor depends upon the contribution of the Mn^{III} and Mn^{IV} ions to the electronic state of the complex, which is often described in terms of a spin projection coefficient, see refs.^{87,88} For the antiferromagnetically coupled $\text{Mn}^{\text{III}}\text{Mn}^{\text{IV}}$ dimer, $S_{1(\text{Mn}^{\text{III}})} = 2$, and $S_{2(\text{Mn}^{\text{IV}})} = 3/2$ the spin projection values are $\rho_1 = 2$ and $\rho_2 = -1$, respectively. The tensor sum is shown as a diagram in **Figure 10**.

The two onsite hyperfine tensors, which are expected to be approximately axial, yield a projected ^{17}O hyperfine tensor that has about rhombic symmetry. The unique principal axis should be parallel to a plane that is defined by the $\text{Mn}-(\mu\text{O})_2\text{-Mn}$ bridging motif, whereas, the middle component (in signed magnitude) must be perpendicular to the $\text{Mn}-(\mu\text{O})_2\text{-Mn}$ bridging motif. This is exactly the behavior observed experimentally. The largest component (unique axis) of the ^{17}O hyperfine tensor coincides with g_x/g_y , i.e. the plane defined by the $\text{Mn}-(\mu\text{O})_2\text{-Mn}$ bridging motif, whereas the middle component of

the ^{17}O hyperfine tensor coincides with g_z i.e. perpendicular to the plane defined by the $\text{Mn}-(\mu\text{O})_2\text{-Mn}$ bridging motif.

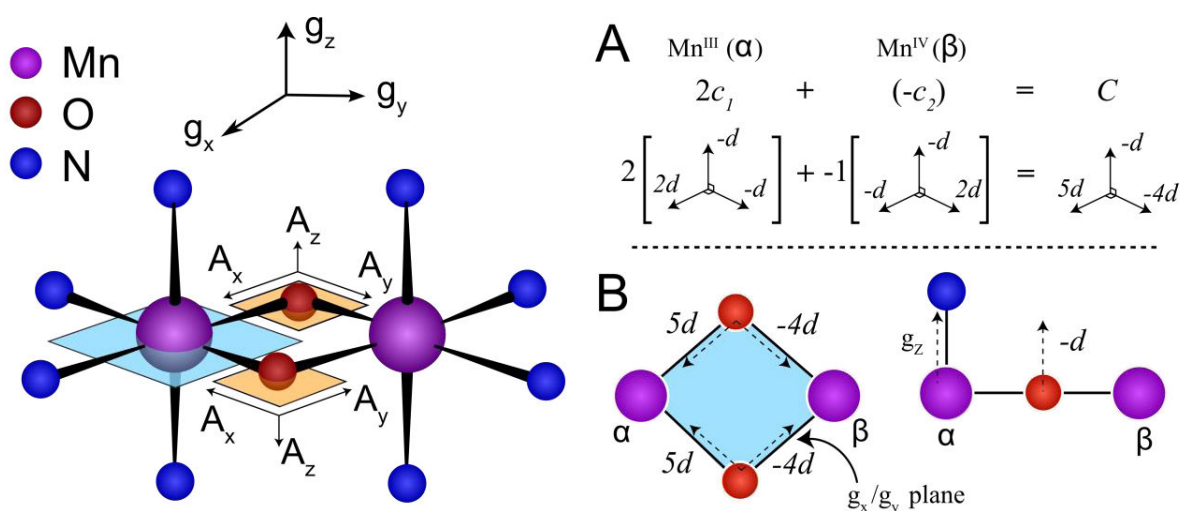


Figure 10. The dipolar hyperfine tensor of the μ -oxo bridge of an antiferromagnetically coupled $\text{Mn}^{III}\text{Mn}^{IV}$ dimer. **A)** onsite (individual) dipolar hyperfine tensor components in the Mn-O-Mn plane and perpendicular to the Mn-O-Mn plane. **B)** orientation of projected (experimental) hyperfine tensor.

5.3. Assignment of the μ - ^{17}O bridge in the $\text{Mn}_4\text{O}_5\text{Ca}$ cluster. The model system described above provides a basis for the assignment of the exchangeable μ - ^{17}O bridge. Two parameters can be used: i) the magnitude of the hyperfine anisotropy; and ii) the orientation of the hyperfine tensor with respect to the three planes that describe the $\text{Mn}-(\mu\text{O})_2\text{-Mn}$ bridge network (see **Figure 1**).

As described above, the hyperfine anisotropy of Mn complexes is predominately due to a through space coupling mechanism and as such can be readily calculated for the oxo-bridges of the OEC. These calculations, termed multipole calculations, have been described in a number of papers e.g. ref.⁸⁹ Its implementation here is described in the supporting information **S9** and **S10**. The results are summarized in **Table 2**. Here all Mn- ^{17}O distances and ^{17}O electron-nuclear dipolar hyperfine coupling estimates are provided for the five μ -oxo bridges for the Umena et al.¹ structure and for a representative computational model of the recent DFT study of Ames et al.¹⁹

It is readily seen that the hyperfine anisotropy of all the μ -oxo bridges of the OEC is systematically lower than that of model complexes. This result is unsurprising as the spin projection coefficients for the four Mn ions are all smaller, falling in the range of 0.9-1.6, as now the electron spin is distributed across more Mn ions. The bridges that consist of a mixed valence pair of Mn ions (O1 and O3), those that best resemble the BIPY complex, have anisotropies approaching that of the model system. In contrast, the μ -oxo bridges between equivalent Mn ions (O2 and O4) have smaller anisotropies, between 50 to 75% of that seen for the model system. O5, which can equally be considered an elongated μ -oxo bridge between either Mn_{A4} and Mn_{B3} or Mn_{B3} and Mn_{D1} in the Umena crystal structure, more closely resembles the O2 and O4 (equivalent limit) than O1 and O3 (mixed valence limit). It should be noted though that in optimized DFT structures, the position of O5 shifts such that it becomes a genuine μ -oxo bridge between Mn_{A4} and Mn_{B3}.¹⁹ As the estimated hyperfine anisotropy of the μ -oxo bridge is small (2.2 MHz), the μ -oxo bridges between the equivalent Mn are the best candidates i.e. O2 and especially O4 and O5 (**Figure 1**).

The orientation of the μ -oxo bridge hyperfine tensor can then be used to refine the assignment of the μ -oxo bridge signal. This can be mapped to the three dimensional structure of the OEC using the D1-His332 signal. It is seen from the EDNMR simulations that the unique principal axis of the μ -oxo bridge ¹⁷O hyperfine tensor coincides with powder pattern orientations that define the center of the multiline spectrum (aligned along g_y). This is in contrast to the D1-His332 signal. Its unique principal axis instead coincides with powder pattern orientations that define the low field edge of the multiline spectrum (approximately aligned along g_x). Thus the two hyperfine tensors must be rotated by 90° to each other. The orientation of the unique principal axis of the ¹⁴N(¹⁵N) D1-His332 should lie along the Mn_{D1}-N bond as the magnitude of its hyperfine anisotropy is consistent with the through space (dipolar) interaction. The orientation of the unique principal axis for each of the μ -oxo bridges can be determined from the multipole calculations and is given in the supporting information **S12 (Tables S12.1-Table S12.4)**. Importantly, it was found that their unique principal axes for all μ -oxo bridges lie in the respective Mn_X-(O)₂-Mn_Y plane (see **Figure 1**), as seen in model complexes. The only exception is the

unique principal axis of O2. It is rotated out of the $\text{Mn}_{\text{B3}}\text{-O-Mn}_{\text{C2}}$ plane, that is to say it is perpendicular to the $\text{Mn}_{\text{B3}}\text{-Mn}_{\text{C2}}$ interspin vector. This is not surprising as the $\text{Mn}_{\text{B3}}\text{-O-Mn}_{\text{C2}}$ couple is unlike the BIPY model systems; it has been determined from calculations that the exchange pathway between Mn_{B3} and Mn_{C2} is ferromagnetic.^{19,80,90}

Table 2: ^{17}O -Mn distances and electron-nuclear dipolar hyperfine couplings for the μ -oxo bridges of the Umena et al.¹ structure and a recent representative computational model of Ames et al.¹⁹ (**1d2'**, numbers in brackets, see **Figure 1**) using the isotropic spin projections for the model of Siegbahn (model 11) reported in Pantazis et al.⁸⁰

	Mn-O distances (Å)				
	$\text{Mn}_{\text{A4}}\text{-O-Mn}_{\text{B3}}$		$\text{Mn}_{\text{B3}}\text{-O-Mn}_{\text{C2}}$	$\text{Mn}_{\text{C2}}\text{-O-Mn}_{\text{D1}}$	
	O4	O5	O2	O1	O3
Mn_{A4}	2.1 (1.8)	2.5 (1.8)	3.8 (3.7)	5.2 (5.0)	4.7 (4.3)
Mn_{B3}	2.1 (1.8)	2.4 (1.9)	1.9 (1.8)	3.5 (3.4)	2.1 (2.0)
Mn_{C2}	4.5 (4.4)	3.8 (3.6)	2.1 (1.8)	2.1 (1.8)	2.1 (1.9)
Mn_{D1}	5.2 (5.0)	2.6 (3.0)	3.7 (3.6)	1.9 (1.8)	1.8 (1.9)
Projected ^{17}O Hyperfine Tensors (MHz)					
$A_{\text{dip}}(^{17}\text{O})^{\text{a}}$	1.8 (2.0)	2.0 (3.2)	1.2 (1.6)	3.5 (3.8)	4.0 (3.6)
$\eta(^{17}\text{O})^{\text{b}}$	0.8 (0.9)	0.5 (0.7)	0.6 (0.4)	0.5 (0.7)	0.1 (0.2)

^{a)} principal value for the ^{17}O hyperfine tensor: $A_{\text{dip}}(^{17}\text{O}) = \frac{T_1 + T_2}{2} = -\frac{T_3}{2}; |T_1| \leq |T_2| \leq |T_3|$

^{b)} rhombicity of the ^{17}O hyperfine tensor as defined by: $\eta(^{17}\text{O}) = \frac{T_1 - T_2}{T_3}; |T_1| \leq |T_2| \leq |T_3|$

From inspection of **Figure 1**, it can be seen that the unique principal axis direction for bridges O2, O3, O4 and O5 are all approximately perpendicular to the unique principal axis direction of the D1-His332. This is explicitly demonstrated in the supporting information **S12**. A better restriction is to consider what component of the ^{17}O hyperfine tensor is aligned (parallel) to the unique principal axis of the D1-His332 hyperfine tensor i.e. the $\text{Mn}_{\text{D1}}\text{-N}$ bond. In the simulations it was found that the middle

component of the ^{17}O hyperfine tensor coincides with powder pattern orientations that define the high field edge of the multiline spectrum. In **Figure 10** it can be seen that the middle component of the ^{17}O hyperfine tensor is normal to the $\text{Mn}-(\mu\text{O})_2\text{-Mn}$ plane for an antiferromagnetically coupled dimer. Again from inspection of **Figure 1**, it can be readily seen that only the $\text{Mn}-(\mu\text{O})_2\text{-Mn}$ plane whose normal is approximately parallel with the $\text{Mn}_{\text{D1}}\text{-N}$ bond is the one containing O4 and O5 (**orange plane**) and thus must contain the exchangeable μ -oxo bridge (see supporting information **S12**). No further restriction can be made as O4 and O5 are arranged in a similar fashion relative to the $\text{Mn}_{\text{D1}}\text{-N}$ bond. It is also noted that the $\text{Mn}_{\text{D1}}\text{-His332}$ ^{14}N signal^{72,73} is not significantly perturbed by the binding of ammonia suggesting ammonia does not affect the ligand environment of the Mn_{D1} ion. This further supports the assignment of the exchangeable μ -oxo bridge to either O4 or O5 as these are the only bridges (along with O2) that are not ligands of Mn_{D1} .

5.4 Literature evidence for an exchangeable μ -oxo bridge – FTIR spectroscopy and mass spectrometry. Low frequency FTIR spectroscopy supports the above hypothesis that the OEC contains an exchangeable μ -oxo bridge. In the higher plant study of Chu et al.⁹¹ a Mn-O mode was identified in the S_2/S_1 difference spectrum, downshifting from 625 cm^{-1} to 606 cm^{-1} . This mode also showed an isotope labeling effect, shifting 10 cm^{-1} in samples suspended in H_2^{18}O .⁹¹ Similar results were also obtained for *T. elongatus* core preparations by Kimura et al.⁹² Recently, it was demonstrated that this exchangeable μ -oxo bridge signal is not observed in NH_3 treated samples.⁹³ Unfortunately, as the FTIR experiments require long incubation times to reach thermal equilibrium, this signal could not be straightforwardly assigned to a potential substrate. Our rapid dilution exchange EDNMR experiments (**Figure 5B**) support such an assignment. By comparison of these PSII FTIR signals to data obtained with Mn (di- μ -oxo) and related Mn/Fe compounds - both in terms of the frequency of the vibrational mode and the magnitude of the isotope effect - this signal was assigned to a $\nu_{\text{sym}}(\text{Mn}-\mu\text{O}-\text{Mn})$ bridge or potentially a μ_2 -oxo, μ_3 -oxo bridge. Interestingly, this mode was sensitive to Sr^{2+} substitution (upshift by 12 cm^{-1}), but insensitive to ^{44}Ca substitution.⁹¹ Chu et al. used this finding to favor that the Sr-

induced shift is due to an indirect structural change and not to a direct ligation of this μ -oxo bridge to Ca/Sr. However, EXAFS data by Pushkar et al.¹⁸ and our recent EPR/ENDOR data (Cox et al.²⁰, Lohmiller et al.⁹⁴) show that no significant structural change is imparted to the Mn_4O_5 cluster by Ca/Sr substitution or even Ca depletion. It is therefore suggested, that the above FTIR data indeed provide direct evidence for Ca/Sr ligation of the exchangeable bridge and that the significantly smaller vibrational shift to be expected from $^{40}\text{Ca}/^{44}\text{Ca}$ exchange was lost within the S/N of the FTIR experiments. It is noted that of the two bridging ligands that are considered candidates for an exchangeable μ -oxo bridge, only O5 is a μ -oxo linkage of the Mn_4O_5 cluster to the Ca^{2+} ion and thus the observed shift induced by Sr^{2+} favors O5 as the exchangeable μ -oxo bridge. This assignment also seems to fit best with the exchange kinetics of the slowly exchanging substrate water (W_s) as determined by fast membrane inlet mass spectrometry.⁴⁸ The rate of exchange is significantly increased by replacement of the Ca ion with Sr,^{21,22} favoring the Mn/Ca-bridging O5 as opposed to the non-Ca ion bridging O4 ligand.

5.5. A fast exchanging μ -oxo bridge. The demonstration that a Mn μ -oxo bridge of the OEC can exchange on a timescale similar to that of the substrate is novel. Similar fast exchange rates have yet to be observed in model systems⁹⁵ including a recent report for the superoxidized Mn catalase metallocofactor.⁴⁶ For synthetic complexes, dissolved in organic solvents, this difference in μ -oxo bridge exchange rates is perhaps unsurprising. These models lack several features of the OEC, such as nearby acid/base derivatives that presumably couple oxygen inclusion with proton release/uptake. The same rationale cannot be applied to the slow exchange seen for the Mn catalase model as it contains many of these features. As such it is unclear why the measured exchange rate of the μ -oxo bridge in this system is so slow. It should be noted though, that the state characterized was the superoxidized state ($\text{Mn}^{\text{III}}\text{Mn}^{\text{IV}}$) which is not physiological. Similarly, the physiological states ($\text{Mn}^{\text{II}}\text{Mn}^{\text{II}}/\text{Mn}^{\text{III}}\text{Mn}^{\text{III}}$) of the cofactor do require the bridge to be exchangeable as one of the bridges represents the first substrate (HOOH) of the dismutation reaction. In addition, in the di-Mn catalase the oxo-bridge is not connected

to a $\text{Ca}^{2+}/\text{Sr}^{2+}$ ion with terminal water-ligands, and the hydration sphere of the Mn^{III} is smaller; it has one water ligand as opposed to two (see **Figure 1**, Mn_{A4}), and this water is located in a hydrophobic pocket. It has also been suggested that internal oxygen-exchange between terminal water-ligands to Ca (or Mn) may allow the fast exchange observed for O5 (W_S).^{95,96}

In the same study on the Mn catalase, water/ μ -oxo bridge exchange in the S_1 state of the OEC was examined. It was found that long incubations in H_2^{17}O water were required to exchange a putative μ -oxo bridge signal; likely the same species observed in the present study. In addition, no fast exchanging signals attributable to terminal bound Mn_{A4} -water/OH were reported. Both of these results do not agree with the findings presented in this manuscript. The latter observation is especially curious as in all model systems terminal water ligands exchange rapidly. At this point we cannot offer a concrete explanation for this discrepancy.

5.6 Consequences for the mechanism of water oxidation. The question of what catalytic reaction pathway the OEC employs to generate an O-O bond is essentially two-fold. It requires both the identification of the two substrate sites and an understanding of the chemical mechanism via which these adjacent substrates couple together. Importantly, these two considerations are not mutually exclusive. The position of the substrate site(s) limits the chemistry that can occur and *visa versa*.

The chemical mechanism via which the two oxygen atoms couple together can be broadly grouped into two classes: I) mechanisms that involve nucleophilic attack between two substrate oxygen atoms and II) oxo/oxyl radical coupling of two Mn oxygen ligands (**Figure 11**). The nucleophilic attack mechanism has the advantage that it has been previously observed in Mn model systems that perform O-O bond formation. However, these systems display turnover rates orders of magnitude slower than that of the OEC.^{97,98} In contrast, the radical coupling mechanism has no precedence in Mn model chemistry but is often the energetically favorable pathway for efficient O-O bond formation in 2nd row transition metal catalysts such as the ruthenium blue dimer (for a recent review see ref⁹⁹). Within these considerations a number of pathways for O-O bond formation have been proposed in the literature^{6,14,15,23,48,70,100-104} (for

a more complete discussion on mechanisms proposed for the OEC see Refs.^{8,10,11,48,96} and the citations therein).

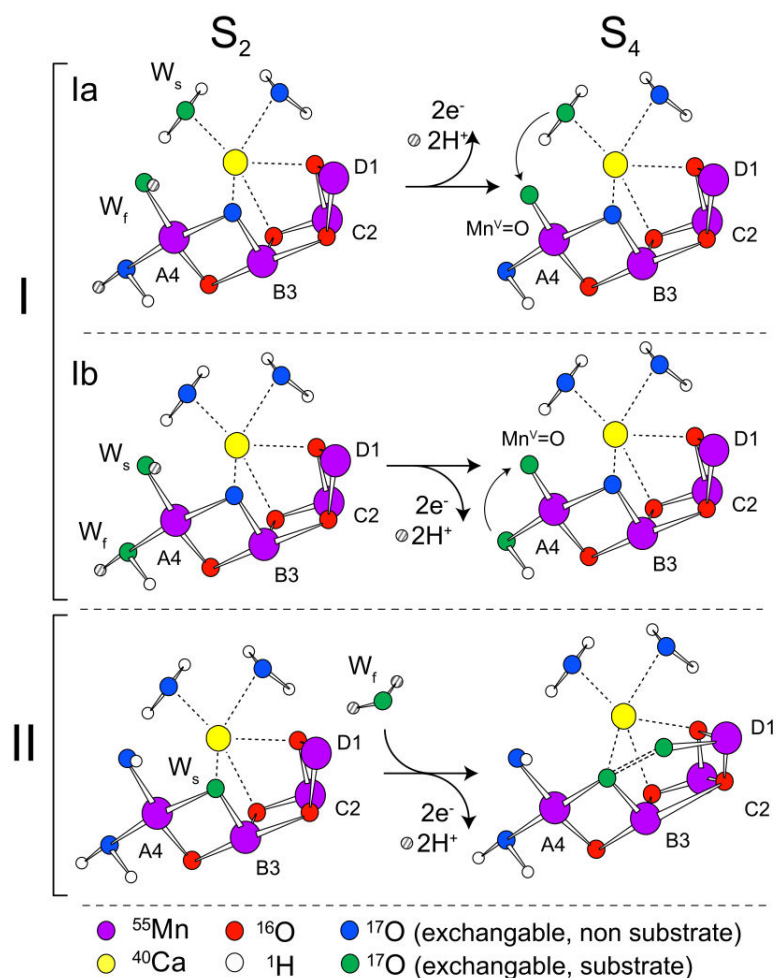


Figure 11. Possible catalytic pathways of O-O bond formation consistent with the recent crystal structure of Umena et al.¹ and the substrate exchange data presented here. Both class I (nucleophilic attack) and class II (oxo/oxyl radical coupling) are shown. The left hand side structure represents the S_2 state probed by EPR/EDNMR. The right hand side structure represents the inferred S_4 structure prior to O-O bond formation and release. The $\text{Mn}_{\text{A4}}(\text{V})=\text{O}$ may equally be considered a $\text{Mn}(\text{IV})\equiv\text{O}^+$ or $\text{Mn}(\text{IV})-\text{O}^\bullet$ species.

There are a number of class I type nucleophilic attack mechanisms proposed in the literature that differ in the locations of the substrate oxygen atoms within the Kok cycle and thus where O-O bond formation

occurs. Here we limit our discussion of reaction mechanisms to those broadly consistent with current crystallographic data. Specifically the two substrates are thought to be:

Ia) a Ca^{2+} bound water/hydroxo and a Mn^{IV} -oxyl or Mn^{V} -oxo species, presumably W3 and W1.^{23,101,104} In some proposals the Ca^{2+} bound water/hydroxo is considered to be the slow exchanging substrate.¹⁰¹

Ib) two terminal water/hydroxo ligands (W1 and W2) on Mn_{A4} .¹⁴

Ic) a μ -oxo/hydroxo bridge between Mn_{C2} and Mn_{D1} (O1) and the Ca^{2+} bound W4.^{100,105} The Mn μ -oxo /hydroxo is considered to be the slow exchanging substrate.

Id) O5 (which is a water molecule in S_1) and an as yet unidentified water.¹⁰²

Suggestion Id is unique in that it assumes a low-oxidation state model for the OEC Kok cycle ($\text{S}_1 = \text{Mn}_4(\text{II,III,III,IV})$), in contrast to the other models, which favor the high-oxidation state model ($\text{S}_1 = \text{Mn}_4(\text{III,III,IV,IV})$).¹⁰²

There is also a number of class II type radical coupling mechanisms in the literature, for reviews see Refs.^{8,10,11,48,70,96} Here we limit our discussion to the most detailed and rigorous proposal at present, the mechanism proposed by Siegbahn.⁶ In his catalytic cycle, the slow exchanging substrate is considered to be the O5 μ -oxo bridge between Mn_{A4} and Mn_{B3} . The fast substrate binds then at the open coordination site on the Mn_{D1} as water/hydroxo in S_2/S_3 , forming an oxyl radical in S_4 (see **Figure 11**).⁶ As detailed above, the ^{17}O EDNMR data presented here suggests that one of the exchangeable-substrate oxygen atoms in S_1 (and S_2) is a μ -oxo bridge, most likely O5 (see **Figure 11**). This location and protonation state (in the S_1 state) for this putative substrate position is only consistent with the class II mechanism of Siegbahn. However, the nucleophilic attack mechanisms Ia and Ib can potentially be modified to include this requirement. In the modified Ia' (equally Ic') type reaction, the two oxygens that form the O-O bound would be instead the Ca^{2+} bound water/hydroxo (W3) and bridging μ -oxo (O5).¹⁰³ Similarly, in a modified Ib' type reaction, the two Mn_{A4} oxygens that form the O-O bound would be a terminal water/hydroxo (W2) and bridging μ -oxo (O5).¹⁰³ In contrast, mechanism 1d cannot be readily modified as it requires O5 to be a water ligand in S_1/S_2 , which is inconsistent with $^1\text{H}/^2\text{H}$ -ENDOR data shown

above. The type II (Siegbahn) mechanism allows for the possibility that O-O bond formation can occur in the S_3 state, i.e. the WOC contains a complexed peroxide in the S_3 state which presumably is in redox equilibrium with various other forms of S_3 , that may include an oxygen radical and/or a formal $Mn_4(IV,IV,IV,IV)$ state. Upon formation of the S_3YZ^\bullet state, only centers which contain the complexed peroxide configuration are able to donate an electron to YZ^\bullet and liberate O_2 . Thus the rate of the $S_3 \rightarrow S_4$ transition reflects the equilibrium constants between the different S_3 redox states, and would follow directly the time course of YZ^\bullet reduction as observed experimentally.⁹⁶

For the definitive assignment of the exchangeable μ -oxo bridge observed here by ^{17}O EDNMR data to the slowly exchanging substrate W_S the matching of the exchange rates needs to be demonstrated. Since sufficient time resolution has not currently been achieved for the EDNMR experiments, our present data do not yet definitively assign this μ -oxo as a substrate. As such, mechanisms Ia and Ib as currently proposed are still potential pathways for catalytic O-O bond formation, but not Ic as it requires an exchangeable O1 which is inconsistent with the ^{17}O -EDNMR data shown above. However, it should be noted that class I type nucleophilic attack mechanisms have been historically favored as they do not involve μ -oxo bridges, which were previously considered to be slow exchanging and thus catalytically irrelevant. As this is not the case, a concerted tetramer mechanism, such as that proposed by Siegbahn,⁶ which uses the unique geometry of the Mn_4O_5Ca cluster to bind and position the two substrates, presents a more appealing pathway than that of monomeric Mn chemistry.

6. CONCLUSIONS

In this article the nature of the substrate bound to the OEC poised in the S_1 state has been addressed. It is shown that one of the five μ -oxo bridges and at least one of the two terminal water ligands of Mn_{A4} , identified in the recent X-ray structure of Umena et al.¹ contribute to the measured ^{17}O EDNMR signal as seen using W-band EPR spectroscopy. Furthermore, it is shown that all 'waters' exchange within 15 s, consistent with substrate exchange as assessed using time resolved mass spectrometry. The identity of

the exchangeable μ -oxo bridge was resolved using model complex data. In these models it is shown that the μ -oxo bridge motif is well characterized by the hyperfine tensor anisotropy. The hyperfine tensor anisotropy and orientation observed for the exchangeable μ -oxo bridge of the OEC constrain its position to either O4 or O5, i.e. the μ -oxo bridges that connects the outer Mn to the $\text{Mn}_3\text{O}_3\text{Ca}$ open-cuboidal unit.

The observation that a μ -oxo bridge can exchange on timescales similar to that of the substrate and that the bridge is fully deprotonated in S_2 both support the mechanism of O-O bond formation put forward by Siegbahn.⁶ Here the reaction pathway proceeds via an oxo/oxyl coupling mechanism in S_4 . Interestingly, this model for water oxidation excludes the binding of both substrates in the resting states (S_0 , S_1) of the catalyst. This feature may in part explain the high selectivity of the OEC towards O_2 formation disfavoring ‘catalase like’ two-electron chemistry. While the structural change that would allow a second substrate (W_f) to bind at the open coordination site of the Mn_{D1} remains unclear, a growing body of evidence from both EPR and FTIR studies suggest that binding is associated with S_3 formation.

ACKNOWLEDGMENT. The authors acknowledge B. Swoboda and Dr. T. Weyhermüller (MPI-Mülheim) for the synthesis of the BIPY model complex and subsequent ^{17}O labelling and the assistance of M. Pérez Navarro and J. Martínez (CSIC-U. Zaragoza) for the characterization of the ammonia treated PSII preparation. Financial support was provided by: the Max Planck Gesellschaft, the JSPS and CNRS under the Japan-France Research Cooperative Program, the EU SOLAR-H2 (FP7 contract 212508), Vetenskapsrådet, Strong Research Environment Solar Fuels (Umeå University), The Artificial Leaf Project (K&A Wallenberg foundation), German Research Foundation (DFG, SFB 480, project C1) and the Kempe foundation. LR is a fellow of the North Rhine-Westphalia (NRW) Research School BioStruct program.

SUPPORTING INFORMATION. This contains additional material detailing: S1) ^1H hyperfine coupling data for the S-states (OEC); S2) Literature ^{17}O hyperfine/quadrupole couplings for metallocofactors/model complexes; S3) Spin Hamiltonian formalism for the Mn model system; S4) Spin Hamiltonian formalism of the Mn tetramer system; S5) Control ESE detected field sweep W- and Q-band EPR of the OEC; S6) EDMR/ENDOR data processing; S7) Spin Hamiltonian simulations of the ^{17}O EDNMR spectra; S8) W-band ^{17}O -ENDOR of $^{14}\text{N}(^{15}\text{N})$ -PSII; S9) Material describing the multipole coupling model; S10) $^1\text{H}/^{17}\text{O}$ multipole coupling estimates for all O/H within 5 Å of the OEC (Umena et al.); S11) Simulations of $^1\text{H}/^{17}\text{O}$ -ENDOR data; S12) ^{17}O hyperfine tensor orientations for all coordinating oxygen ligands of the OEC.; S13) Theoretical EPR Parameters calculations from BS-DFT; S14) References. The material is available free of charge via the Web at <http://pubs.acs.org>

7. REFERENCE LIST

- (1) Umena, Y.; Kawakami, K.; Shen, J.-R.; Kamiya, N. *Nature* **2011**, *473*, 55-60.
- (2) Ferreira, K. N.; Iverson, T. M.; Maghlaoui, K.; Barber, J.; Iwata, S. *Science* **2004**, *303*, 1831-1838.
- (3) Loll, B.; Kern, J.; Saenger, W.; Zouni, A.; Biesiadka, J. *Nature* **2005**, *438*, 1040-1044.
- (4) Yano, J.; Kern, J.; Sauer, K.; Latimer, M. J.; Pushkar, Y.; Biesiadka, J.; Loll, B.; Saenger, W.; Messinger, J.; Zouni, A.; Yachandra, V. K. *Science* **2006**, *314*, 821-825.
- (5) Lubitz, W.; Reijerse, E. J.; Messinger, J. *Energy Environ. Sci.* **2008**, *1*, 15 - 31.
- (6) Siegbahn, P. E. M. *Acc. Chem. Res.* **2009**, *42*, 1871-1880.
- (7) Dau, H.; Zaharieva, I. *Acc. Chem. Res.* **2009**, *42*, 1861-1870.
- (8) McEvoy, J. P.; Brudvig, G. W. *Chem. Rev.* **2006**, *106*, 4455-4483.
- (9) Tommos, C.; Babcock, G. T. *Acc. Chem. Res.* **1998**, *31*, 18-25.
- (10) Hillier, W.; Messinger, J. *Mechanism of photosynthetic oxygen production*; Springer, 2005; Vol. 1.

- (11) Messinger, J.; Noguchi, T.; Yano, J. In *Molecular Solar Fuels* Wydrzynski, T., Hillier, W., Eds.; RSC: 2012.
- (12) Kok, B.; Forbush, B.; McGloin, M. *Photochem. Photobiol.* **1970**, *11*, 457-467.
- (13) Yano, J.; Yachandra, V. K. *Inorg. Chem.* **2008**, *47*, 1711-1726.
- (14) Kusunoki, M. *Biochim. Biophys. Acta* **2007**, *1767*, 484-492.
- (15) Dau, H.; Grundmeier, A.; Loja, P.; Haumann, M. *Phil. Trans. R. Soc. B* **2008**, *363*, 1237-1244.
- (16) Yano, J.; Kern, J.; Irrgang, K.-D.; Latimer, M. J.; Bergmann, U.; Glatzel, P.; Pushkar, Y.; Biesiadka, J.; Loll, B.; Sauer, K.; Messinger, J.; Zouni, A.; Yachandra, V. K. *Proc. Nat. Acad. Sci.* **2005**, *102*, 12047-12052.
- (17) Messinger, J.; Seaton, G.; Wydrzynski, T.; Wacker, U.; Renger, G. *Biochemistry* **1997**, *36*, 6862-6873.
- (18) Pushkar, Y. L.; Yano, J.; Sauer, K.; Boussac, A.; Yachandra, V. K. *Proc. Natl. Acad. Sci. USA* **2008**, *105*, 1879-1884.
- (19) Ames, W.; Pantazis, D. A.; Krewald, V.; Cox, N.; Lubitz, W.; Neese, F. *J. Am. Chem. Soc.* **2011**, *133*, 19743-19757.
- (20) Cox, N.; Rapatskiy, L.; Su, J.-H.; Pantazis, D. A.; Sugiura, M.; Kulik, L.; Dorlet, P.; Rutherford, A. W.; Neese, F.; Boussac, A.; Lubitz, W.; Messinger, J. *J. Am. Chem. Soc.* **2011**, *133*, 3635-3648.
- (21) Hendry, G.; Wydrzynski, T. *Biochemistry* **2003**, *42*, 6209-6217.
- (22) Hillier, W.; Wydrzynski, T. *Coord. Chem. Rev.* **2008**, *252*, 306-317.
- (23) Messinger, J.; Badger, M.; Wydrzynski, T. *Proc. Natl. Acad. Sci. USA* **1995**, *92*, 3209-3213.
- (24) Hillier, W.; Messinger, J.; Wydrzynski, T. *Biochemistry* **1998**, *37*, 16908-16914.
- (25) Noguchi, T. *Phil. Trans. R. Soc. B* **2008**, *363*, 1189-1195.
- (26) Noguchi, T.; Sugiura, M. *Biochemistry* **2002**, *41*, 15706-15712.

- (27) Siegbahn, Per E. M. *Chem. Eur. J.* **2008**, *14*, 8290-8302.
- (28) Kawamori, A.; Inui, T.; Ono, T.; Inoue, Y. *FEBS Lett.* **1989**, *254*, 219-224.
- (29) Aznar, C. P.; Britt, R. D. *Phil. Trans. R. Soc. B* **2002**, *357*, 1359-1366.
- (30) Britt, R. D.; Campbell, K. A.; Peloquin, J. M.; Gilchrist, M. L.; Aznar, C. P.; Dicus, M. M.; Robblee, J.; Messinger, J. *Biochim. Biophys. Acta* **2004**, *1655*, 158-171.
- (31) Fiege, R.; Zweggart, W.; Bittl, R.; Adir, N.; Renger, G.; Lubitz, W. *Photosynth. Res.* **1996**, *48*, 227-237.
- (32) Ahrling, K. A.; Evans, M. C. W.; Nugent, J. H. A.; Ball, R. J.; Pace, R. J. *Biochemistry* **2006**, *45*, 7069-7082.
- (33) Martínez, J. I.; Yruela, I.; Picorel, R.; Alonso, P. J. *J. Phys. Chem. B* **2010**, *114*, 15345-15353.
- (34) Thomann, H.; Bernardo, M.; Goldfarb, D.; Kroneck, P. M. H.; Ullrich, V. *J. Am. Chem. Soc.* **1995**, *117*, 8243-8251.
- (35) Burdi, D.; Willems, J.-P.; Riggs-Gelasco, P.; Antholine, W. E.; Stubbe, J.; Hoffman, B. M. *J. Am. Chem. Soc.* **1998**, *120*, 12910-12919.
- (36) Carepo, M.; Tierney, D. L.; Brondino, C. D.; Yang, T. C.; Pamplona, A.; Telser, J.; Moura, I.; Moura, J. J. G.; Hoffman, B. M. *J. Am. Chem. Soc.* **2001**, *124*, 281-286.
- (37) Astashkin, A. V.; Feng; Raitsimring, A. M.; Enemark, J. H. *J. Am. Chem. Soc.* **2004**, *127*, 502-503.
- (38) Enemark, J. H.; Raitsimring, A. M.; Astashkin, A. V.; Klein, E. L. *Faraday Discuss.* **2011**, *148*, 249-267.
- (39) Baute, D.; Goldfarb, D. *J. Phys. Chem. A* **2005**, *109*, 7865-7871.
- (40) Hansson, Ö.; Andréasson, L.-E.; Vänngård, T. *FEBS Lett.* **1986**, *195*, 151-154.
- (41) Turconi, S.; MacLachlan, D. J.; Bratt, P. J.; Nugent, J. H. A.; Evans, M. C. W. *Biochemistry* **1997**, *36*, 879-885.

- (42) Evans, M. C. W.; Nugent, J. H. A.; Ball, R. J.; Muhiuddin, I.; Pace, R. J. *Biochemistry* **2004**, *43*, 989-994.
- (43) Su, J.-H.; Lubitz, W.; Messinger, J. *J. Am. Chem. Soc.* **2007**, *130*, 786-787.
- (44) Su, J.-H.; Lubitz, W.; Messinger, J. *J. Am. Chem. Soc.* **2011**, *133*, 12317-12317.
- (45) García-Rubio, I.; Martínez, J. I.; Picorel, R.; Yruela, I.; Alonso, P. J. *J. Am. Chem. Soc.* **2003**, *125*, 15846-15854.
- (46) McConnell, I. L.; Grigoryants, V. M.; Scholes, C. P.; Myers, W. K.; Chen, P. P. Y.; Whittaker, J. W.; Brudvig, G. W. *J. Am. Chem. Soc.* **Just Accepted**.
- (47) Usov, O. M.; Grigoryants, V. M.; Tagore, R.; Brudvig, G. W.; Scholes, C. P. *J. Am. Chem. Soc.* **2007**, *129*, 11886-11887.
- (48) Messinger, J. *Phys. Chem. Chem. Phys.* **2004**, *6*, 4764-4771.
- (49) Schosseler, P.; Wacker, T.; Schweiger, A. *Chem. Phys. Lett.* **1994**, *224*, 319-324.
- (50) Vinck, E.; Van Doorslaer, S.; Dewilde, S.; Mitrikas, G.; Schweiger, A.; Moens, L. *J. Biol. Inorg. Chem.* **2006**, *11*, 467-475.
- (51) Florent, M.; Kaminker, I.; Nagarajan, V.; Goldfarb, D. *J. Magn. Res.* **2011**, *210*, 192-199.
- (52) Klein, E. L.; Raitsimring, A. M.; Astashkin, A. V.; Rajapakshe, A.; Johnson-Winters, K.; Arnold, A. R.; Potapov, A.; Goldfarb, D.; Enemark, J. H. *Inorg. Chem.* **2012**, *51*, 1408-1418.
- (53) Sugiura, M.; Boussac, A.; Noguchi, T.; Rappaport, F. *Biochim. Biophys. Acta* **2008**, *1777*, 331-342.
- (54) Boussac, A.; Rappaport, F.; Carrier, P.; Verbavatz, J. M.; Gobin, R.; Kirilovsky, D.; Rutherford, A. W.; Sugiura, M. *J. Biol. Chem.* **2004**, *279*, 22809-22819.
- (55) Ishida, N.; Sugiura, M.; Rappaport, F.; Lai, T. L.; Rutherford, A. W.; Boussac, A. *J. Biol. Chem.* **2008**, *283*, 13330-13340.
- (56) Sander, J.; Nowaczyk, M.; Buchta, J.; Dau, H.; Vass, I.; Deak, Z.; Dorogi, M.; Iwai, M.; Roegner, M. *J. Biol. Chem.* **2010**, *285*, 29851-29856.

- (57) Nowaczyk, M. M.; Krause, K.; Mieseler, M.; Sczibilanski, A.; Ikeuchi, M.; Roegner, M. *Biochim. Biophys. Acta* **2011**.
- (58) Reijerse, E.; Lendzian, F.; Isaacson, R.; Lubitz, W. *J. Magn. Res.* **2012**, *214*, 237-243.
- (59) Stoll, S.; Schweiger, A. *J. Magn. Res.* **2006**, *178*, 42-55.
- (60) Schweiger, A.; Jeschke, G. *Principles of Pulse Electron Paramagnetic Resonance*; Oxford University Press: Oxford, 2001.
- (61) Schäfer, K. O.; Bittl, R.; Zweggart, W.; Lendzian, F.; Haselhorst, G.; Weyhermuller, T.; Wieghardt, K.; Lubitz, W. *J. Am. Chem. Soc.* **1998**, *120*, 13104-13120.
- (62) Cooper, S. R.; Dismukes, G. C.; Klein, M. P.; Calvin, M. *J. Am. Chem. Soc.* **1978**, *100*, 7248-7252.
- (63) Dismukes, G. C.; Siderer, Y. *Proc. Natl. Acad. Sci. USA* **1981**, *78*, 274-278.
- (64) Åhrling, K. A.; Peterson, S.; Styring, S. *Biochemistry* **1997**, *36*, 13148-13152.
- (65) Messinger, J.; Robblee, J. H.; Yu, W. O.; Sauer, K.; Yachandra, V. K.; Klein, M. P. *J. Am. Chem. Soc.* **1997**, *119*, 11349-11350.
- (66) Peloquin, J. M.; Campbell, K. A.; Randall, D. W.; Evanchik, M. A.; Pecoraro, V. L.; Armstrong, W. H.; Britt, R. D. *J. Am. Chem. Soc.* **2000**, *122*, 10926-10942.
- (67) Randall, D. W.; Chan, M. K.; Armstrong, W. H.; Britt, R. D. *Mol. Phys.* **1998**, *95*, 1283 - 1294.
- (68) Randall, D. W.; Sturgeon, B. E.; Ball, J. A.; Lorigan, G. A.; Chan, M. K.; Klein, M. P.; Armstrong, W. H.; Britt, R. D. *J. Am. Chem. Soc.* **1995**, *117*, 11780-11789.
- (69) Kulik, L. V.; Epel, B.; Lubitz, W.; Messinger, J. *J. Am. Chem. Soc.* **2005**, *127*, 2392-2393.
- (70) Kulik, L. V.; Epel, B.; Lubitz, W.; Messinger, J. *J. Am. Chem. Soc.* **2007**, *129*, 13421-13435.
- (71) Britt, R. D.; Zimmermann, J. L.; Sauer, K.; Klein, M. P. *J. Am. Chem. Soc.* **1989**, *111*, 3522-3532.

- (72) Stich, T. A.; Yeagle, G. J.; Service, R. J.; Debus, R. J.; Britt, R. D. *Biochemistry* **2011**, *50*, 7390-7404.
- (73) Yeagle, G. J.; Gilchrist, M. L.; Walker, L. M.; Debus, R. J.; Britt, R. D. *Phil. Trans. R. Soc. B* **2008**, *363*, 1157-1166.
- (74) Stull, J. A.; Stich, T. A.; Service, R. J.; Debus, R. J.; Mandal, S. K.; Armstrong, W. H.; Britt, R. D. *J. Am. Chem. Soc.* **2009**, *132*, 446-447.
- (75) Plaksin, P. M.; Stoufer, R. C.; Mathew, M.; Palenik, G. J. *J. Am. Chem. Soc.* **1972**, *94*, 2121-2122.
- (76) Cooper, S. R.; Calvin, M. *J. Am. Chem. Soc.* **1977**, *99*, 6623-6630.
- (77) Jensen, A. F.; Su, Z.; Hansen, N. K.; Larsen, F. K. *Inorg. Chem.* **1995**, *34*, 4244-4252.
- (78) Debus, R. J.; Campbell, K. A.; Gregor, W.; Li, Z.-L.; Burnap, R. L.; Britt, R. D. *Biochemistry* **2001**, *40*, 3690-3699.
- (79) Teutloff, C.; Kessen, S.; Kern, J.; Zouni, A.; Bittl, R. *FEBS Lett.* **2006**, *580*, 3605-3609.
- (80) Pantazis, D. A.; Orio, M.; Petrenko, T.; Zein, S.; Lubitz, W.; Messinger, J.; Neese, F. *Phys. Chem. Chem. Phys.* **2009**, *11*, 6788-6798.
- (81) Beck, W. F.; De Paula, J. C.; Brudvig, G. W. *J. Am. Chem. Soc.* **1986**, *108*, 4018-4022.
- (82) Boussac, A.; Sugiura, M.; Inoue, Y.; Rutherford, A. W. *Biochemistry* **2000**, *39*, 13788-13799.
- (83) Boussac, A.; Rutherford, A. W.; Styring, S. *Biochemistry* **1990**, *29*, 24-32.
- (84) Stich, T. A.; Whittaker, J. W.; Britt, R. D. *J. Phys. Chem. B* **2010**, *114*, 14178-14188.
- (85) Raitsimring, A. M.; Astashkin, A. V.; Baute, D.; Goldfarb, D.; Caravan, P. *J. Phys. Chem. A* **2004**, *108*, 7318-7323.
- (86) Schäfer, K. O. Doctoral Thesis, Technische Universität, 2002.
- (87) Sage, J. T.; Xia, Y. M.; Debrunner, P. G.; Keough, D. T.; De Jersey, J.; Zerner, B. *J. Am. Chem. Soc.* **1989**, *111*, 7239-7247.

- (88) Bencini, A.; Gatteschi, D. *EPR of Exchange Coupled Systems*; Springer-Verlag: Berlin, 1990.
- (89) Force, D. A.; Randall, D. W.; Lorigan, G. A.; Clemens, K. L.; Britt, R. D. *J. Am. Chem. Soc.* **1998**, *120*, 13321-13333.
- (90) Schinzel, S.; Schraut, J.; Arbuznikov, A.; Siegbahn, P.; Kaupp, M. *Chem. Eur. J.* **2010**, *16*, 10424-10438.
- (91) Chu, H.-A.; Sackett, H.; Babcock, G. T. *Biochemistry* **2000**, *39*, 14371-14376.
- (92) Kimura, Y.; Ishii, A.; Yamanari, T.; Ono, T.-a. *Biochemistry* **2005**, *44*, 7613-7622.
- (93) Hou, L.-H.; Wu, C.-M.; Huang, H.-H.; Chu, H.-A. *Biochemistry* **2011**, *50*, 9248-9254.
- (94) Lohmiller, T.; Cox, N.; Su, J.-H.; Messinger, J.; Lubitz, W. *J. Biol. Chem.* **2012**, *In Press*.
- (95) Tagore, R.; Crabtree, R. H.; Brudvig, G. W. *Inorg. Chem.* **2007**, *46*, 2193-2203.
- (96) Messinger, J.; Renger, G. In *Primary Processes of Photosynthesis - Part 2: Basic Principles and Apparatus*; Renger, G., Ed.; Royal Society of Chemistry: Cambridge, 2008, p 291-349.
- (97) Gao, Y.; Åkermark, T. r.; Liu, J.; Sun, L.; Åkermark, B. r. *J. Am. Chem. Soc.* **2009**, *131*, 8726-8727.
- (98) Privalov, T.; Sun, L.; Åkermark, B.; Liu, J.; Gao, Y.; Wang, M. *Inorg. Chem.* **2007**, *46*, 7075-7086.
- (99) Liu, F.; Concepcion, J. J.; Jurss, J. W.; Cardolaccia, T.; Templeton, J. L.; Meyer, T. J. *Inorg. Chem.* **2008**, *47*, 1727-1752.
- (100) Dau, H.; Haumann, M. *Biochim. Biophys. Acta* **2007**, *1767*, 472-483.
- (101) Sproviero, E. M.; Gascon, J. A.; McEvoy, J. P.; Brudvig, G. W.; Batista, V. S. *J. Am. Chem. Soc.* **2008**, *130*, 3428-3442.
- (102) Jaszewski, A. R.; Petrie, S.; Pace, R. J.; Stranger, R. *Chem. Eur. J.* **2011**, *17*, 5699-5713.
- (103) Yamanaka, S.; Isobe, H.; Kanda, K.; Saito, T.; Umena, Y.; Kawakami, K.; Shen, J. R.; Kamiya, N.; Okumura, M.; Nakamura, H.; Yamaguchi, K. *Chem. Phys. Lett.* **2011**, *511*, 138-145.

- (104) Barber, J.; Ferreira, K.; Maghlaoui, K.; Iwata, S. *Phys. Chem. Chem. Phys.* **2004**, *6*, 4737-4742.
- (105) Dau, H.; Haumann, M. *Coord. Chem. Rev.* **2008**, *252*, 273-295.

Characterization of μ -oxo bridge of Mn model complexes using high field (94 GHz) ^{17}O -HYSCORE and ^{17}O -ELDOR detected NMR spectroscopy

Leonid Rapatskiy, William Ames, Anton Savitsky, Thomas Weyhermüller, Frank Neese, Wolfgang Lubitz, Nicholas Cox

Characterization of the μ -oxo bridge of Mn model
complexes using high field (94 GHz) ^{17}O -HYSCORE
and ^{17}O -ELDOR detected NMR spectroscopy

*Leonid Rapatskiy¹, William Ames¹, Anton Savitsky¹, Thomas Weyhermüller,¹ Frank Neese¹, Wolfgang
Lubitz¹, Nicholas Cox^{1*}*

¹Max-Planck-Institut für Bioanorganische Chemie, Stiftstrasse 34-36, D-45470 Mülheim an der Ruhr,
Germany

AUTHOR EMAIL ADDRESS: rapatskiy@mpi-muelheim.mpg.de; ames@mpi-muelheim.mpg.de;
savitsky@mpi-muelheim.mpg.de; Franl.Neese@mpi-mail.mpg.de; weyhermueller@mpi-muelheim.mpg.de;
Wolfgang.Lubitz@mpi-mail.mpg.de; Nicholas.Cox@mpi-mail.mpg.de.

**RECEIVED DATE (to be automatically inserted after your manuscript is accepted if required
according to the journal that you are submitting your paper to)**

TITLE RUNNING HEAD ^{17}O couplings of mixed valence, μ -oxo bridged $\text{Mn}^{\text{III}}\text{Mn}^{\text{IV}}$ model complex

CORRESPONDING AUTHOR FOOTNOTE Nicholas Cox (+49-208-306-3552)

ABSTRACT. A multi-frequency pulsed EPR study of the electronic structure of the μ -oxo bridge for high valence manganese ($\text{Mn}^{\text{III}}/\text{Mn}^{\text{IV}}$) is reported via magnetically labeling the oxygen atom of the bridge with ^{17}O isotope ($I = 5/2$, natural abundance 0.038%). Two complexes are examined: the planer bis- μ -oxo bridged BIPY complex ($[\text{Mn}^{\text{III}}\text{Mn}^{\text{IV}}(\mu\text{-O})_2\text{bipy}_4]\text{ClO}_4$, BIPY = bipyridine) and the bent, bis- μ -oxo- μ -carboxylato bridge DTNE complex ($[\text{Mn}^{\text{III}}\text{Mn}^{\text{IV}}(\mu\text{-O})_2(\mu\text{-O}_2\text{CCH}_3)\text{DTNE}]\text{BPh}_4$, DTNE = 1,2-di-(1,4,7-triazacyclononyl)-ethane. These complexes are structurally similar to metallocofactors seen in biological enzymes including: (i) the di-manganese catalase, which catalyzes the dismutation of H_2O_2 to H_2O and O_2 ; (ii) the recently identified di-manganese cofactor of class Ib ribonucleotide reductase and; (iii) the tetra-manganese oxygen evolving complex (OEC) of Photosystem II, which performs the multi-step oxidation of H_2O to O_2 . CW and pulse X/Q and W-band EPR measurements of the DTNE complex reveal line-broadenings (~ 10 MHz) in the ^{17}O labeled complex relative to their ^{18}O labeled counterpart, prepared in exactly the same way. Consistent with this observation, signals readily attributable to the ^{17}O nucleus were observed high field (W-band) using ESEEM (HYSCORE) and EDNMR spectroscopy. Spectral simulations of the entire data set using the Spin Hamiltonian formalism reveal a ^{17}O isotropic hyperfine coupling of $A_{\text{iso}} \sim 7\text{-}8$ MHz. The ^{17}O hyperfine tensor is highly anisotropic (5 MHz) and rhombic, consistent with the hyperfine anisotropy being through space (dipolar) in origin. Estimates are also made for the quadrupole tensor. Similar results were obtained for the BIPY complex. BS-DFT calculations are shown to be in agreement with experimental values. The isotropic hyperfine coupling seen here for the μ -oxo bridge is significantly smaller than previously reported for corresponding Fe complexes, presumably because $\text{Fe}^{\text{II/III}}$ delocalizes its valence d-electrons across its ligands to a greater extent than $\text{Mn}^{\text{III/IV}}$. The trend seen for the isotropic hyperfine couplings of ligands to $\text{Mn}^{\text{III/IV}}$ complexes is: all terminal Mn^{IV} ligands and terminal Mn^{III} equatorial ligands have small couplings (2-4 MHz), bridging ligands have intermediate couplings (7 MHz) and the axial ligands of Mn^{III} (which lie along the Jahn-Teller axis) have large couplings, in excess of 10 MHz. It is hypothesized that the magnitude of the

isotropic hyperfine coupling, along with hyperfine anisotropy, can be used as a fingerprint for ligand identity for Mn metallocofactor systems.

1. INTRODUCTION

The development of synthetic catalysts for a diverse number of chemical problems is increasingly turning to nature for inspiration as biological systems use cheap, abundant materials to do complex multielectron chemistry. Of particular interest is the oxygen evolving complex (OEC) of the Photosystem II enzyme, which performs the four-electron, four-proton water-splitting reaction. Recent crystallographic data at atomic resolution has resolved the basic topology of the manganese tetramer that comprises the OEC.¹ Five μ -oxo bonds provide the network of bridges linking the four manganese together. This μ -oxo/hydroxo motif is common structural feature of homo and heteronuclear metal clusters and governs the electronic (exchange) coupling between the metal ions. Examples of manganese containing metallocofactors include: the di-manganese catalase^{2,3}, b) the recently identified Mn containing class Ib and 1c ribonucleotide reductases⁴⁻⁶; c) the purple acid phosphatases.⁷

Electron paramagnetic resonance (EPR) and complementary techniques, such as ESEEM and ENDOR, are ideal methods to specifically probe the electronic nature of the μ -oxo bridge via isotopic labeling with the paramagnetic ¹⁷O nucleus. The low natural abundance (0.038%) of the oxygen isotope (¹⁷O) together with its less than ideal magnetic properties including i) a large nuclear spin $I = 5/2$, ii) small nuclear g-factor and iii) non-trivial nuclear quadrupole moment $Q = -2.558 \text{ fm}^2$, have resulted in a relatively small number of examples presented in the literature. These magnetic characteristics generally yield in a large number of spectral splittings, which are often difficult to disentangle from spectral lines of other nuclei including ²H and ¹⁴N/¹⁵N, especially at low microwave frequencies.

¹⁷O labeling has been successfully employed to characterize the μ -oxo bridge of two Fe containing metallocofactors: the mixed Fe^{II}Ni^{III} ($S = 1/2$)⁸ the active site of a class of Hydrogenase enzymes and

non-mixed $\text{Fe}^{\text{III}}\text{Fe}^{\text{IV}}$ ($S = 1/2$)⁹ of the small subunit of class 1 ribonucleotide reductase. Both of these studies used low-frequency (X, Q band) ENDOR to characterize the ^{17}O in μ -oxo bridges. The measured hyperfine couplings were in the range of 10-15 MHz. The large hyperfine anisotropy (14-23 MHz), which arises dominantly from the through space dipolar interaction of the ^{17}O nucleus and the electronic spin, together with the large quadrupole splitting (3-11 MHz), a consequence of the large electric field gradient experienced by coordinating ligands, resulted in very broad ENDOR transitions. As such, a constrained fitting of these data sets was only achieved by resorting to 2D techniques, where the magnetic field dependence of the ENDOR signals was mapped out. The large g-anisotropy of these two systems ensured a high level of orientation selectivity.

In investigating the μ -oxo bridge of Mn complex a good starting point is the mixed valence complexes such as $\text{Mn}^{\text{II}}\text{Mn}^{\text{III}}$ and $\text{Mn}^{\text{III}}\text{Mn}^{\text{IV}}$. These typically exhibit antiferromagnetic coupling leading to the ground state configuration of total electron spin (S_{T}) of $1/2$ ¹⁰⁻¹³. The $S_{\text{T}} = 1/2$ state manifests itself in CW-EPR as a characteristic multiline signal centered at $g \sim 2$. The large number of spectral lines observed arises from the coupling of the two ^{55}Mn nuclei to the total unpaired electronic spin, i.e. the inhomogeneous linewidth is defined by the ^{55}Mn hyperfine; the intrinsic g-anisotropy is small. This in contrast to the Ni-Fe and Fe-Fe systems discussed above,^{8,9} both of which have large g-anisotropy which defines the width of the signal. Thus there is virtually no disadvantage (in terms of increased orientation selectivity) with mixed valence Mn systems upon shifting to higher frequency, since the inhomogeneous linewidth of the EPR signal is virtually invariant when measured at X, Q and W band.

To date, there is only one report of a Mn-O-Mn bridge motif.¹⁴ Brudvig and coworkers reported a structureless ^{17}O signal using Q-band ENDOR (i.e. as used in Fe-Fe, Fe=Ni studies) centered at 12.8 MHz. This signal was assigned to the $\nu^+(^{17}\text{O})$ branch of the nuclear manifold. The $\nu(^{17}\text{O})$ branch was unobserved, presumably appearing at ~ 0 MHz. An estimate of the isotropic coupling was made taken from the peak of the envelope. No estimates were reported for either the hyperfine anisotropy or quadrupole coupling.

Recently, high field EPR (95 GHz) has been shown to be ideal for the study of nuclei with low nuclear g-values i.e. ^{14}N , ^{17}O . At these high frequencies, the nuclear Zeeman term is now the leading term of the Spin Hamiltonian, and thus, the hyperfine and quadrupole terms can be treated to 1st order. Goldfarb and coworkers have demonstrated at this frequency the number and scope of pulse EPR experiments open up. They have successfully resolved the solvation of Ga complexes using Mims ENDOR.¹⁵ Similarly, they have demonstrated ESEEM techniques such as HYSCORE are readily applicable to ^{17}O nucleus.

Here we demonstrate that high field pulsed EPR/ENDOR/ESEEM/EDNMR can be successfully employed for deriving the complete electronic structure of the Mn- μ -O-Mn motif. The two complexes used are the well-characterized $[\text{Mn}^{\text{III}}\text{Mn}^{\text{IV}}(\mu\text{-O})-(\mu\text{-piv})_2(\text{Me}_3\text{tacn})_2](\text{ClO}_4)_2$ (**DTNE**) complex previously reported by Weyhermüller et al.¹⁶ and the $[\text{Mn}^{\text{III}}\text{Mn}^{\text{IV}}(\mu\text{-O})_2\text{bipy}_4]\text{ClO}_4$, (**BIPY**). Both complexes contain a bis- μ -oxo bridging template (see Figure **1**). The DTNE complex has an additional μ -carboxylato (μ -piv) bridges between the two Mn ions (see Figure **1B**). Because of this additional bridge, the DTNE complex is considered a better structural mimic of Mn metallocofactors seen in several enzymes. The oxidation states of the two Mn ions for both complexes can be identified from the crystal structure due to the elongation of the Mn(1)–N(5) and Mn(1)–N(5) bonds in the **BIPY** structure and the elongation of the Mn(1)–N(5) and Mn(1)–O(3) bonds in the **DTNE** structure. This elongation represents the Jahn-Teller axis of the Mn^{III} . The use of three microwave frequencies and multiple spectroscopic techniques tightly constrains all Spin Hamiltonian terms. It is seen that two complexes are highly similar in terms of the electronic structure of the μ -oxo bridge. BS-DFT calculations further refine out understanding of the Mn- μ -O-Mn motif, providing a rationale for the trends seen in the isotropic hyperfine, hyperfine anisotropy and quadrupole couplings observed in these two model systems.

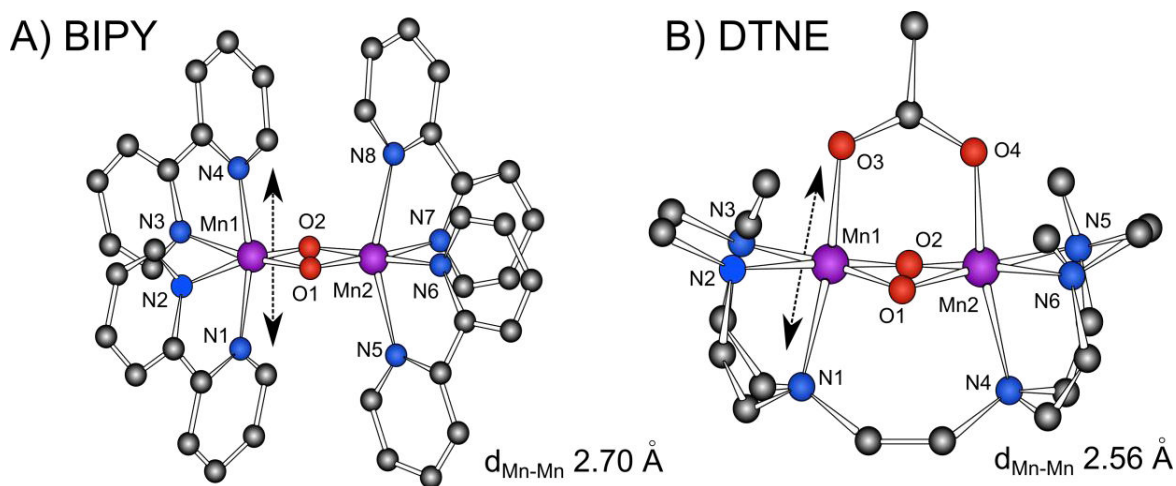


Figure 1. ^{17}O -labeled manganese dimer model complexes. **A)** planer $\text{Mn}^{\text{III}}-\mu\text{O}_2-\text{Mn}^{\text{IV}}$ BIPY complex¹⁷⁻¹⁹; $[\text{Mn}^{\text{III}}\text{Mn}^{\text{IV}}(\mu\text{-O})_2\text{bipy}_4]\text{ClO}_4$, BIPY = bipyridine. **B)** bent $\text{Mn}^{\text{III}}-\mu\text{O}_2-\text{Mn}^{\text{IV}}$ DTNE complex, $[\text{Mn}^{\text{III}}\text{Mn}^{\text{IV}}(\mu\text{-O})_2(\mu\text{-O}_2\text{CCH}_3)\text{DTNE}]\text{BPh}_4$, DTNE = 1,2-di-(1,4,7-triazacyclononyl)-ethane.^{13,20} The bridging oxygens of the BIPY complex have an identical chemical environment. In contrast, the bridging oxygens of the DTNE complex are not strictly identical due to the additional bridge (-N(CH₂)₂N-) that connects the two ligand adducts. The dashed line indicates the Jahn-Teller axis of the Mn^{III} ion.

2. MATERIALS AND METHODS

2.1 Low frequency (X, Q) EPR measurements. X-Band pulse EPR measurements were performed at 40 K using a Bruker ESR 200D spectrometer, equipped with an Oxford Instruments ESR 935 cryostat and ITC4 temperature controller. Q-band pulse EPR measurements were performed at 40 K using a Bruker ELEXSYS E580 Q-band pulse EPR spectrometer, equipped with homebuilt TE₀₁₁ microwave cavity,²¹ Oxford-CF935 liquid helium cryostat and an ITC-503 temperature controller. All ENDOR data was collected using an external home-built computer console (SpecMan4EPR control software²²⁻²⁴) with the ELEXSYS E580 X-band pulse EPR spectrometer, coupled to a external RF generator (SMT02 signal generator) and RF amplifier (ENI 5100L). Electron spin echo-detected (ESE) field-swept spectra were measured using the pulse sequence: $t_p-\tau-2t_p-\tau$ -echo. The length of $\pi/2$ microwave pulse was generally

set to $t_p = 8$ ns (X-band), 24 ns (Q-band). The interpulse distance was varied in the range $\tau = 200$ -500 ns (X-band), 200-500 ns (Q-band). ^{17}O ENDOR spectra were acquired using the Davies-type pulse sequence: $t_{inv} - t_{RF} - T - t_p - \tau - 2t_p - \tau - \text{echo}$ using the length of inversion microwave π pulse of $t_{inv} = 128$ ns, radio frequency π pulse length of $t_{RF} = 6$ μs . The length of $\pi/2$ microwave pulse in the detection sequence was generally set to $t_p = 64$ ns and the interpulse delays to $T = 1.5$ μs and $\tau = 468$ ns. ^{17}O ENDOR spectra were collected using the Mims-type pulse sequence: $t_p - \tau - t_p - t_{RF} - T - t_p - \tau - \text{echo}$, with $t_p = 8$ ns, $t_{RF} = 6$ μs , $\tau = 300$ -500 ns and $T = 2$ μs . The RF frequency was swept 20 MHz around ^{17}O -larmor frequency of about 3 MHz (3.4 T) in 50 kHz steps. All ENDOR measurements were performed using the random(stochastic) acquisition technique as described in Epel et al.²². Usual sequential acquisition resulted in a severe distortion the ENDOR spectrum caused by "heating artifacts", for details see Kulik et al.²³ A shot repetition rate of ~ 300 Hz was used for all measurements.

2.2 W-band EPR measurements. The high-field EPR experiments were performed at 40 K using W-band EPR spectrometer (Bruker Elexsys E680) operating at about 94 GHz. All experiments were carried out using homebuilt ENDOR microwave cavity manufactured in form of solenoid from Teflon coated silver wire and integrated in to commercial W-band ENDOR probehead (Bruker). The RF coil contains 20 wire turns for the optimized RF performance at low RF frequencies (< 100 MHz, optimum performance at 20 MHz). To ensure the broadband microwave excitation and minimize the distortions caused by high-power RF excitation, the loaded quality factor, Q_L , was lowered to 700 to obtain the microwave frequency bandwidth of 130 MHz.

Electron spin echo-detected (ESE) field-swept spectra were measured using the pulse sequence: $t_p - \tau - 2t_p - \tau - \text{echo}$ with $t_p = 26$ ns and $\tau = 200$ -500 ns. ^{17}O -Davies ENDOR spectra were collected using the pulse sequence: $t_{inv} - t_{RF} - T - t_p - \tau - 2t_p - \tau - \text{echo}$ with $t_{inv} = 128$ ns, $t_p = 24$ ns, $t_{RF} = 15$ μs , $T = 1$ μs and $\tau = 348$ ns. ^{17}O -Mims ENDOR spectra were collected using the pulse sequence: $t_p - \tau - t_p - t_{RF} - T - t_p - \tau - \text{echo}$, with $t_p = 24$ ns, $t_{RF} = 15$ μs , $\tau = 300$ -500 ns and $T = 1$ μs . In both ENDOR

experiments the RF frequency was swept 6.4 MHz around ^{17}O -larmor frequency of about 19.7 MHz (3.4 T) in 43 kHz steps.

ELDOR-detected NMR (EDNMR) measurements were done using the pulse sequence: $t_{\text{HTA}} - T - t_p - \tau - 2t_p - \tau - \text{echo}$. The high tuning angle (HTA) microwave pulse was applied at microwave frequency ν_{mw} . The detection Hahn echo pulse sequence $t_p - \tau - 2t_p - \tau - \text{echo}$ at microwave frequency $\nu_{\text{mw}}^{(0)}$ matched to the cavity resonance was set 2 μs post HTA pulse to ensure the decay of the electron spin coherencies. The pulse length for a detection $\pi/2$ pulse $t_p = 100$ ns and the pulse separation $\tau = 500$ ns were generally set. The echo was integrated 700 ns around its maximum. The spectra were acquired continuously sweeping the HTA frequency ν_{mw} at fixed B_0 in steps of 127 kHz. A low-power HTA microwave pulse of $t_{\text{HTA}} = 8\text{-}14\mu\text{s}$ length was used to minimize the width of the central hole (see supporting information) to allow resolution of the low frequency $^{14}\text{N}/^{15}\text{N}$ spectral lines. The microwave settings of EDNMR experiment do not represent the optimal conditions for the resolution of ^{17}O hyperfine couplings but instead are a compromise that allows simultaneous detection of both ^{14}N and ^{17}O responses from both single and double quantum transitions, minimally perturbed by the central hole.

2.3 CW-EPR/ ^{55}Mn -ENDOR simulations. EPR/ENDOR/HYSCORE/EDNMR spectra were simultaneously fit assuming an effective spin $S = 1/2$ ground state (see Theory section 3.2). The electron Zeeman term was treated exactly. The nuclear Zeeman, hyperfine and quadrupole terms were treated using second order perturbation theory. Spectral simulations were performed numerically using Scilab-4.4.1, an open source vector-based linear algebra package (www.scilab.org) and the EasySpin package²⁵ in MATLAB.

2.4. Geometry optimizations and EPR parameter calculations using BS-DFT. The $\text{Mn}^{\text{III}}\text{Mn}^{\text{IV}}$ BIPY and DTNE models were optimized in the high spin state ($S=7/2$) using the B3LYP hybrid density functional^{26,27} along with the most recent DFT dispersion corrections from Grimme²⁸ and the zero-order regular approximation (ZORA) to account for relativistic effects²⁹⁻³¹ The segmented all-electron

relativistically contracted (SARC) SV(P) basis sets³² were used for all light elements (H, C, N and O) while the SARC TZVPP basis set was used for the Mn atoms³². Optimizations took advantage of the chain-of-spheres RIJCOX approximation³³ with the decontracted auxiliary TZVP/J Coulomb fitting basis sets as implemented in ORCA.³⁴ Increased integration grids (Grid4 in ORCA convention) and tight SCF convergence criteria were used throughout. Hyperfine tensors for the N, O and Mn atoms were calculated from the broken symmetry solution using the same methodology as published previously for a model Mn^{II}Mn^{III} PivOH S=1/2 complex.³⁵ Solvation effects were modeled using the conductor-like screening model (COSMO) with the dielectric constant of acetonitrile ($\epsilon = 36.6$) for all calculations.^{36,37}

3. THEORY

3.1 The Spin Hamiltonian Formalism. Here we consider an antiferromagnetically exchange coupled Mn^{III}-O₂-Mn^{IV} dimer. A basis set that describes the Mn-dimer spin manifold can be built from the product of the eigenstates of the interacting spins:

$$|S_1 S_2 M_1 M_2 I_1 I_2 m_1 m_2 L_1 L_2 l_1 l_2\rangle, \quad (\text{Eq. 1})$$

Here S_i refers to the electronic spin state of Mn_i, M_i refers to the electronic magnetic sub-level of Mn_i, I_i refers to the nuclear spin state of Mn_i, m_i refers to the nuclear magnetic sub-level of Mn_i, L_i refers to the nuclear spin state of O_i, and k_i refers to the nuclear magnetic sub-level of O_i. S_i takes the value 2 for Mn^{III} and 3/2 for Mn^{IV}; M_i takes the values: $S_i, S_i-1, \dots, 1-S_i, -S_i$; I_i takes the value 5/2 for ⁵⁵Mn (100% natural abundance); m_i takes the values $-I_i, 1-I_i, \dots, I_i-1, I_i$; L_i takes the values 5/2 for ¹⁷O; and l_i takes the values $-L_i, 1-L_i, \dots, L_i-1, L_i$.

The Spin Hamiltonian that describes the spin manifold of the ¹⁷O labeled Mn dimer is:

$$\begin{aligned} \hat{H} = & \sum_i \beta_e \vec{B}_0 \cdot \hat{g}_i \cdot \vec{S}_i - \sum_i g_{Mn} \beta_n \vec{B}_0 \cdot \vec{I}_i - \sum_i g_O \beta_n \vec{B}_0 \cdot \vec{L}_i + \sum_i \vec{S}_i \cdot \hat{a}_{Mn,i} \vec{I}_i \\ & + \sum_i \sum_j \vec{S}_i \cdot \hat{a}_{O,ij} \vec{L}_j + \sum_i \vec{I}_i \cdot \hat{p}_{Mn,i} \cdot \vec{I}_i + \sum_i \vec{L}_i \cdot \hat{p}_{O,i} \cdot \vec{L}_i + \sum_i \vec{S}_i \cdot \hat{d}_i \cdot \vec{S}_i - 2\vec{S}_1 \cdot J \cdot \vec{S}_2 \end{aligned} \quad (\text{Eq. 2})$$

It contains: i) an electronic Zeeman term for each Mn ion ; ii) a nuclear Zeeman term for each ^{55}Mn and ^{17}O nucleus; iii) an electron-nuclear hyperfine term for each ^{55}Mn and ^{17}O nucleus; iv) an nuclear quadrupole term for each ^{55}Mn and ^{17}O nucleus; v) a fine structure term for each Mn ion; and vi) a electron spin coupling term for the Mn-Mn interaction.

3.2 An Effective Spin $\frac{1}{2}$ Ground State. The electronic coupling between the two Mn ions in mixed valence Mn dimers is usually dominated by the through bond exchange interaction and sufficiently large that the spin manifold can be treated within the strong exchange limit. In this instance the exchange interaction between the two Mn ions is significantly larger than any other term of the Spin Hamiltonian. The resultant electronic spin states of the manifold are then adequately described by a single quantum number, the total spin (S_T). The ‘multiline’ EPR signal observed for the **DTNE** complex is derived from only one total spin state, the ground state of the spin manifold with total spin $S_T = \frac{1}{2}$. The basis set that describes this subspace takes the form

$$\left| \frac{1}{2} \ M \ m_1 \ m_2 \ L_1 \ L_2 \ l_1 \ l_2 \right\rangle \quad (\text{Eq. 3})$$

Where M takes all half-integer values: $-\frac{1}{2} \leq M \leq \frac{1}{2}$; m_i (where $i = 1-2$) takes all half integer values: $-\frac{5}{2} \leq m_i \leq \frac{5}{2}$; L_i takes the value 5/2 and k_i talks all half integer values $-\frac{5}{2} \leq l_i \leq \frac{5}{2}$. The effective Spin Hamiltonian that describes the ground state of the spin manifold ($S_T = \frac{1}{2}$) is:

$$\begin{aligned} \hat{H} = & \beta_e \vec{B}_0 \cdot \hat{G} \cdot \vec{S} + \sum_i \left(g_{Mn} \beta_n \vec{B}_0 \cdot \vec{I}_i + \vec{S} \cdot \hat{A}_{Mn,i} \cdot \vec{I}_i + \vec{I}_i \cdot \hat{P}_{Mni} \cdot \vec{I}_i \right) \\ & + \sum_i \left(g_o \beta_n \vec{B}_0 \cdot \vec{L}_i + \vec{S} \cdot \hat{A}_{O_i} \cdot \vec{L}_i + \vec{L}_i \cdot \hat{P}_{O_i} \cdot \vec{L}_i \right) \end{aligned} \quad (\text{Eq. 4})$$

It contains: i) the electronic Zeeman term for the total electronic spin; ii) nuclear Zeeman terms for each ^{55}Mn and ^{17}O nucleus; iii) electron-nuclear hyperfine terms for each ^{55}Mn and ^{17}O nucleus and; iv) nuclear quadrupole terms for each ^{55}Mn and ^{17}O nucleus.

3.3 Isotropic Spin Projections. A mapping of the spin subspace in section 3.2 onto the original basis set as described in section 3.1 can be made. This allows the intrinsic g and hyperfine tensors of the two Mn ions and the two ^{17}O nuclei (g_i, a_i , see eq. 2) to be calculated from the effective G and hyperfine tensors (G, A_i , see eq. 4). For an exchanged coupled $\text{Mn}^{\text{II}}\text{Mn}^{\text{III}}$ complex the effective g -factor G , hyperfine tensors A_i and quadrupole tensors p_i are related to the parameters of the complete spin Hamiltonian of the exchange-coupled system^{38,39} by the spin-projection coefficients, where the isotropic spin projection coefficients (ρ_1, ρ_2) are defined as :

$$\begin{aligned}\rho_1(\text{Mn}^{\text{III}}) &= \frac{S_1(S_1 + 1) - S_2(S_2 + 1) + S(S + 1)}{2S(S + 1)} \\ \rho_2(\text{Mn}^{\text{IV}}) &= \frac{S_2(S_2 + 1) - S_1(S_1 + 1) + S(S + 1)}{2S(S + 1)}\end{aligned}\quad (\text{Eq. 5})$$

and effective G and hyperfine values (A_i), assuming all g_i and a_i are isotropic and the exchange coupling J is large:

$$\begin{aligned}G &= \rho_1 g_1 + \rho_2 g_2 & P_{\text{Mn},1} &= p_{\text{Mn},1} \\ A_{\text{Mn},1} &= \rho_1 a_{\text{Mn},1} & P_{\text{Mn},2} &= p_{\text{Mn},2} \\ A_{\text{Mn},2} &= \rho_2 a_{\text{Mn},2} & P_{\text{O},1} &= p_{\text{O},1} \\ A_{\text{O},1} &= \rho_1 a_{\text{O},11} + \rho_2 a_{\text{O},12} & P_{\text{O},2} &= p_{\text{O},2} \\ A_{\text{O},2} &= \rho_1 a_{\text{O},21} + \rho_2 a_{\text{O},22}\end{aligned}\quad (\text{Eq. 6})$$

For an $\text{Mn}^{\text{III}}\text{Mn}^{\text{IV}}$ dimer, $S_{I(\text{MnIII})} = 2$; and $S_{2(\text{MnIV})} = 3/2$ which gives isotopic spin projection values of $\rho_1 = 2$ and $\rho_2 = -1$, respectively. The above relations are thus approximately: $G = 2g_1 - g_2$, $A_{\text{Mn},1} = 2a_{\text{Mn},1}$, $A_{\text{Mn},2} = -a_{\text{Mn},2}$, $A_{\text{O},1} = 2a_{\text{O},11} - a_{\text{O},12}$; $A_{\text{O},2} = 2a_{\text{O},12} - a_{\text{O},22}$; $P_{\text{Mn},1} = p_{\text{Mn},1}$, $P_{\text{Mn},2} = p_{\text{Mn},2}$;

$P_{O,1} = p_{O,1}, P_{O,2} = p_{O,2}$.^{38,40} Note that for terminal ligands such as ^{14}N , the same projections apply as for the individual Mn nuclei.

4. RESULTS AND DISCUSSION

4.1 EPR Spectroscopy

4.1.1 Multi-frequency CW/pulse EPR data. CW and pulse EPR data of the $\text{Mn}^{\text{III}}\text{Mn}^{\text{IV}}$ **DTNE** complex dissolved in butyronitrile (5 mM) are presented in Fig. 2. Pulse EPR data were collected using the Hahn echo sequence. A standard 16 line EPR pattern typical of mixed valence $\text{Mn}^{\text{III}}\text{Mn}^{\text{IV}}$ was observed at all frequencies. The X-band CW-EPR lineshape of the ^{16}O -**DTNE** complex matched those of an earlier study of Schäfer et al. Similarly the pseudo-modulated pulse X, Q and W band spectra of the ^{16}O -**DNTE** complex are very similar to this previous study; the observed line positions are unchanged, but specific line intensities do differ by up to ~10%. Optimal reproduction of the CW-EPR lineshape using pulse EPR was achieved using τ values in excess of 380 ns. Using either FID detection or Hahn echo sequence did not significantly change the measured pulse spectrum. The relatively slow T_1 relaxation time observed for this complex required the measurement temperature to be above 30 K for efficient data collection (shot rep rates of 1000 μs). Similar results were obtained for the ^{16}O labeled **BIPY** complex dissolved in 1:3 acetonitrile:dichloromethane.

Typical for these type of manganese complexes, the total spectral breadth (the inhomogeneous linewidth) of the EPR signal is approximately the same at all frequencies used in this study; the g -anisotropy of the complex is small. The intrinsic (homogeneous) EPR linewidth of the major 16 lines is very narrow when using the solvent butyronitrile (FWHM 30 G – X-band) and additional side lines are resolved throughout the EPR spectrum. This fine structure is more readily observed at X-band, suggesting g -strain contributes to the EPR linewidth at higher frequency.

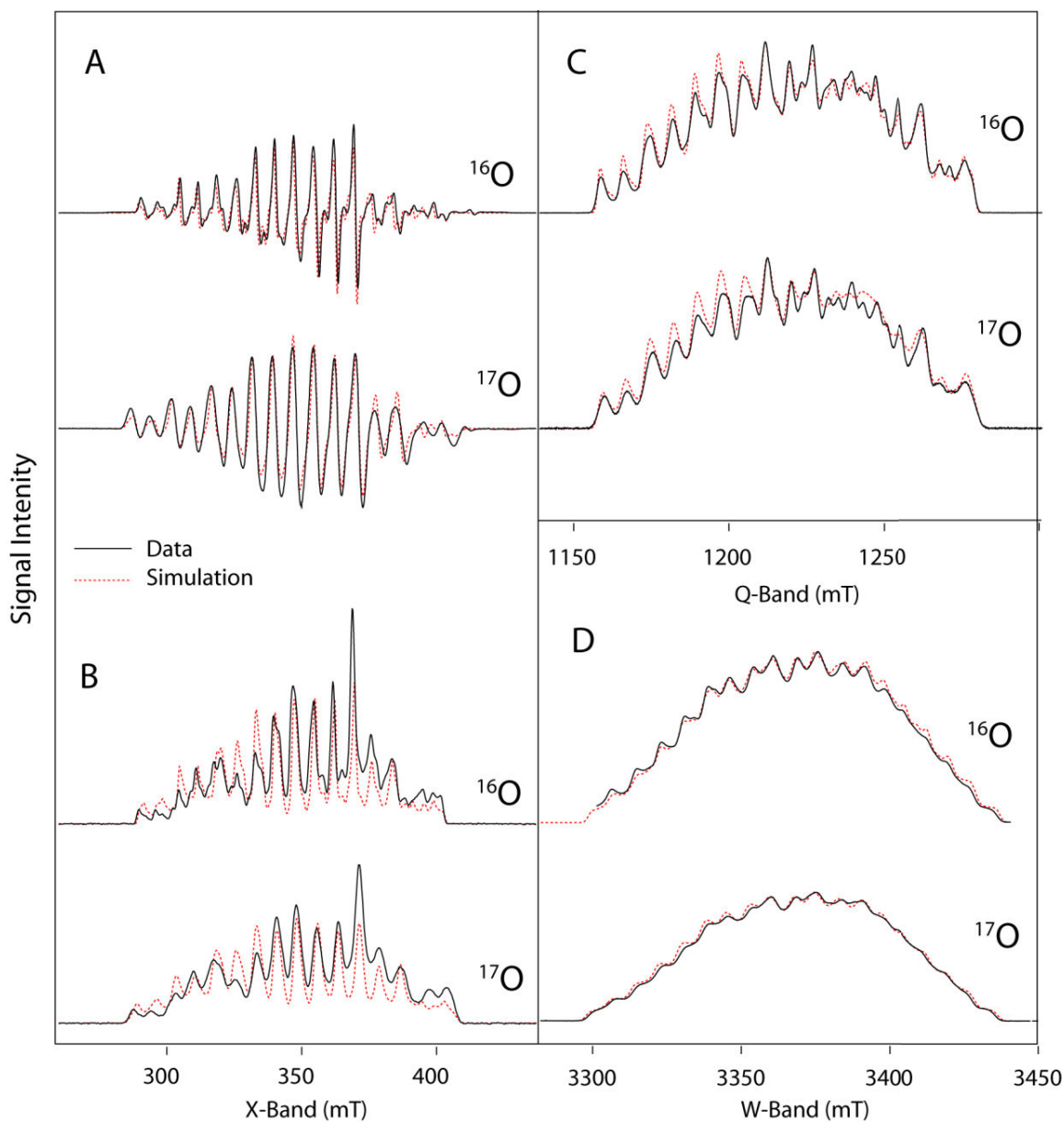


Figure 2. CW and pulse EPR data of the $\text{Mn}^{\text{III}}\text{Mn}^{\text{IV}}$ DTNE complex dissolved in butyronitrile (5 mM). The data is shown in black lines. A simulation of the data using the Spin Hamiltonian formalism is shown by the red dashed lines superimposing the data. The simulations are described below. All EPR parameters are given in the materials and methods section.

The ^{17}O label was incorporated via isotope exchange with ^{17}O labelled water. The final complex contained approximately 1:3 ratio of ^{16}O to ^{17}O bridges. Labelling of the DTNE complex with ^{17}O led to a significant increase in the homogeneous EPR linewidth. Line broadening (FWHM 40 MHz, X-

band) was observed at all frequency, but again, was most readily observed at X-band. Here, the fine structure of the spectrum is lost such that only 16 lines are observed. The same labelling procedure was repeated with ^{18}O labelled water. The ^{18}O labelled **DTNE** complex is identical to the standard ^{16}O **DTNE** complex (data not shown). Exactly the same spectral lines are reproduced of identical linewidth. Similarly, the additional side line structure seen in the ^{16}O **DNTE** complex is preserved in the ^{18}O complex.

Similar results were obtained for the **BIPY** complex (data not shown). Importantly, the same magnitude in linebroadening was observed for the ^{17}O -**BIPY** complex as compared to the ^{16}O -**BIPY** complex.

4.1.2 Pulse Mims/Davies ^{17}O -ENDOR measured at low frequency (X-band). Mims/Davies ENDOR was performed on both the ^{17}O and ^{18}O labeled **DTNE** complex described above. In the ^{16}O labeled sample two sharp lines at 5.5 MHz and 7.5 MHz were observed using Mims ENDOR, split by ~ 2 MHz. The doublet had a pronounced dependence on the magnetic field used, with the center of the doublet shifting 0.5-1.0 MHz to higher frequency when comparing the ENDOR spectrum, collected at the high and low edge of the EPR signal. This doublet is consistent with its assignment to the double-quantum transitions of a ^{14}N ligand ($A \sim 1$ MHz). The signals were not observed in the corresponding Davies ENDOR experiment.

In ^{17}O labeled **DTNE** complexes a new, broad signal was observed using both Mims and Davies ENDOR. The new signal appears at ~ 6 MHz. Unlike the background ^{14}N doublet, the frequency position of this new signal had only a weak dependence on the magnetic field used. This behavior is consistent with the assignment of this signal to a strongly coupled ($A > 2\nu(^{17}\text{O})$) ^{17}O Mn ligand. It is suspected that this turning point only represents half of the ^{17}O -ENDOR signal, specifically the plus (+) branch, see sections **4.1.5 and 4.1.7**. Assuming the hyperfine coupling is isotropic and quadrupole splitting is ignored, the position of the ^{17}O -ENDOR signal is given by the equation

$\nu^+(^{17}\text{O}) = \left| \frac{A}{2} + \nu(^{17}\text{O}) \right|$, where A is the isotropic hyperfine coupling and $\nu(^{17}\text{O})$ the Larmor frequency of the ^{17}O nucleus at a given magnetic field (350 mT, $\nu(^{17}\text{O}) = 2.02$). Thus the estimated ^{17}O hyperfine coupling is ~ 8 MHz. It is emphasized though that this is only a rough estimate and that a Spin Hamiltonian simulation of the entire lineshape, inclusive of hyperfine anisotropy and quadrupole splitting is required to give an exact estimate.

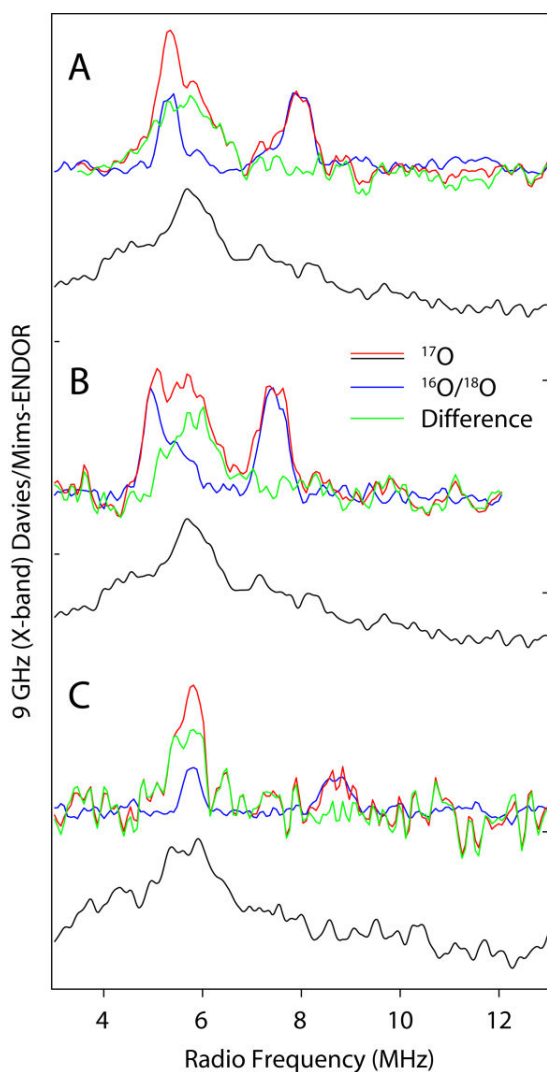


Figure 3. X-Band ^{17}O -ENDOR using the Davies and Mims pulse sequence of $\text{Mn}^{\text{III}}\text{Mn}^{\text{IV}}$ DTNE complex dissolved in butyronitrile (5 mM). The colored traces represent Mims ENDOR spectra of the ^{17}O labeled (**red**) and ^{16}O labeled (**blue**) DTNE complex. The difference is show in **green**. The offset black trace represents corresponding Davies ENDOR spectra of the ^{17}O labeled complex. Panels **A**, **B**, **C**

correspond to three field (B_0) positions measured: the low field edge 317 mT (**C**), the center field 347 mT (**B**) and the high field edge 371 mT (**C**). All EPR parameters are given in the materials and methods section.

4.1.3 High Field (W-band) ^{17}O -HYSCORE. W-band HYSCORE was performed on both the ^{16}O and ^{17}O labeled **DTNE** complex described above (**Figure 4A**). In the unlabelled ^{16}O **DTNE** sample two discrete cross peaks were observed in the ++ quadrant, centered about the Larmor frequency of ^{14}N [$\nu(^{14}\text{N}) \sim 10.4$ MHz]. They both have crescent structure with the maxima appearing at [5 15, 15 5] MHz. These cross peaks are consistent with a dominantly isotropic hyperfine coupling of ~ 10 MHz.

In the corresponding ^{17}O labeled **DTNE** complex, two new signals are observed: a structured correlation ridge centered about the Larmor frequency of ^{17}O [$\nu(^{17}\text{O}) \sim 19.5$ MHz] and a second ridge which appears about 1.5 times the Larmor frequency (~ 29.3 MHz). The latter ridge is distorted due to the limited bandwidth. When measured at single τ values, the 1st correlation ridge resolves approximately 6 peaks spaced by about 2 MHz. These represent blind spot artifacts that are partially suppressed by averaging spectra at a series of τ values. The spectrum shown in **Figure 4A** is an average of three τ values (396, 408 and 420 nm).

The two structured ridges observed for the ^{17}O **DTNE** complex are derived from the single-single quantum transition and single-double quantum transition correlations within the ^{17}O sub-manifold (**Figure 4C**). Importantly, as two ridges are observed, a rough estimate of the A_{iso} and A_{aniso} terms can be made by inspection. This is shown in **Figure 4D**. A_{aniso} must clearly be large as there is no separation of the two correlation ridges that make up the structured signal centered about the Larmor frequency of ^{17}O ; for comparison see the ^{14}N signal. However, A_{iso} must still be large to account for the overlap of the second ridge about the diagonal, while still reproducing the spread of the 1st ridge signal. In which A_{iso} is zero, the magnitude of A_{aniso} required to observe this overlap for the single-double correlation ridge yields a single-single correlation ridge which is significantly too broad. Thus, A_{iso} and

A_{aniso} must be of approximately the same size to reproduce the pattern. As a final comment it is noted that the width of the 1st structured ridge along the diagonal gives the quadrupole splitting, which must be of the order of 3-4 MHz

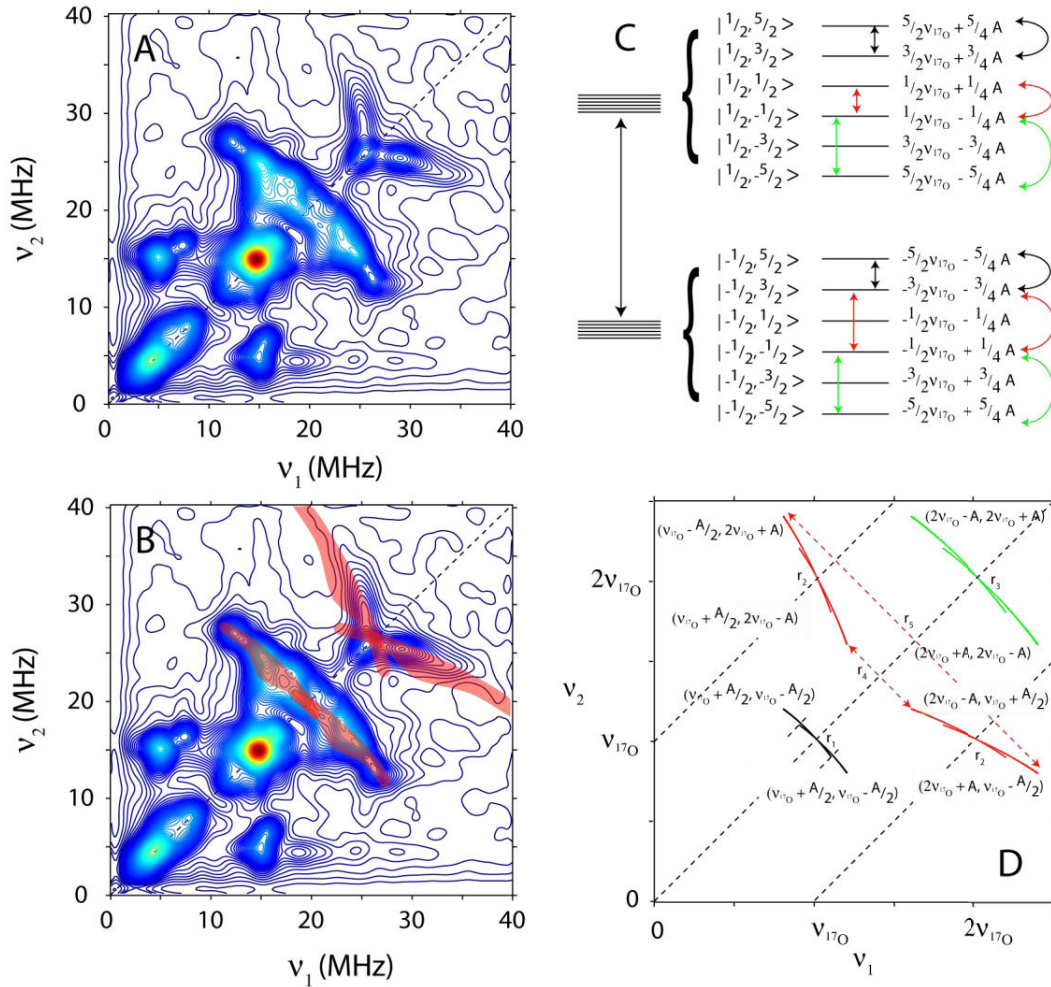


Figure 4. W-Band ^{17}O -HYSCORE $\text{Mn}^{\text{III}}\text{Mn}^{\text{IV}}$ DTNE complex dissolved in butyronitrile (5 mM) measured at the center field 3372 mT. **A)** The colored traces represent Mims ENDOR spectra of the ^{17}O labeled (red) and ^{16}O labeled (blue) DTNE complex. The difference is shown in green. The offset black trace represents corresponding Davies ENDOR spectra of the ^{17}O labeled complex. Panels **A**, **B**, **C** correspond to three field (B_0) positions measured: the low field edge 317 mT (**C**), the center field 347 mT (**B**) and the high field edge 371 mT (**C**). All EPR parameters are given in the materials and methods section.

4.1.4 High Field (W-band) ^{17}O -EDNMR. An alternative method detection of ^{17}O hyperfine couplings to correlation techniques such as ESEEM/HYSCORE is to directly drive transitions within the nuclear manifold, i.e. ENDOR. Unfortunately for the two model complexes measured here, no ENDOR signal could be obtained. An alternative to ENDOR is ELDOR detected NMR (EDNMR).^{41,42} Both are an example of a polarization transfer experiment, but EDNMR is still more closely related to ESEEM. In the EDNMR experiment, nuclear transitions of the spin manifold are probed indirectly using a second microwave pulse, which pumps spin forbidden electron transitions, i.e. transition where both the electron and nuclear spin change (**Figure 5I and II**). The pump pulse is swept around the resonance frequency ($\nu_{\text{mw}}^{(0)}$). At microwave frequencies where the pump pulse coincides with the forbidden electron transitions of the spin manifold, the observed primary echo signal decreases, leading to apparent side-holes, which correspond to the nuclear transitions of the spin manifold. In addition, the pump pulse excites the allowed transitions of the spin manifold ($\nu_{\text{mw}}^{(0)}$). These results in a decrease in the observed primary echo across the entire region swept. For the experiments shown here the response profile is Lorentzian and as the pump pulse is rectangular. This profile is termed here the central hole. Side holes appear symmetrically about the resonance frequency ($\nu_{\text{mw}}^{(0)}$), for an inhomogeneously broadened EPR line where the EPR linewidth is larger than that of the nuclear coupling of interest (see **Figure 5III**).

At high field (W-band) though, the Larmor frequency of many low γ nuclei (^{14}N , ^{17}O) is now sufficiently large that signals from these nuclei can be resolved from the central hole even for the circumstance where the coupling of the nuclei to the electronic spin is weak (i.e. less than twice the Larmor frequency). For the model complexes described here the W-band EDNMR, the spectra contain both ^{14}N and ^{17}O ligands in weak coupling limit; i.e. the lines associated with a particular nucleus are centered at the Larmor frequency of the nucleus of interest, split by the hyperfine (and quadrupole) coupling (see **Figures 6 and 7**). Importantly, at high field the Larmor frequency of ^{17}O [$\nu(^{17}\text{O}) \sim 20$ MHz] is significantly different from that of ^{14}N [$\nu(^{14}\text{N}) \sim 10$ MHz], thus allowing both components to be readily identified. For nuclei which have a nuclear spin greater than $\frac{1}{2}$, multiple quanta transitions are observed. These are centered about scalar multiples of the Larmor frequency split by the same scalar

multiple i.e. in the case of double quantum transitions, these are now centered about twice the Larmor frequency split by twice the hyperfine coupling.

A cartoon of the multiple contributions to the EDNMR spectrum is shown in **Figure 5**.

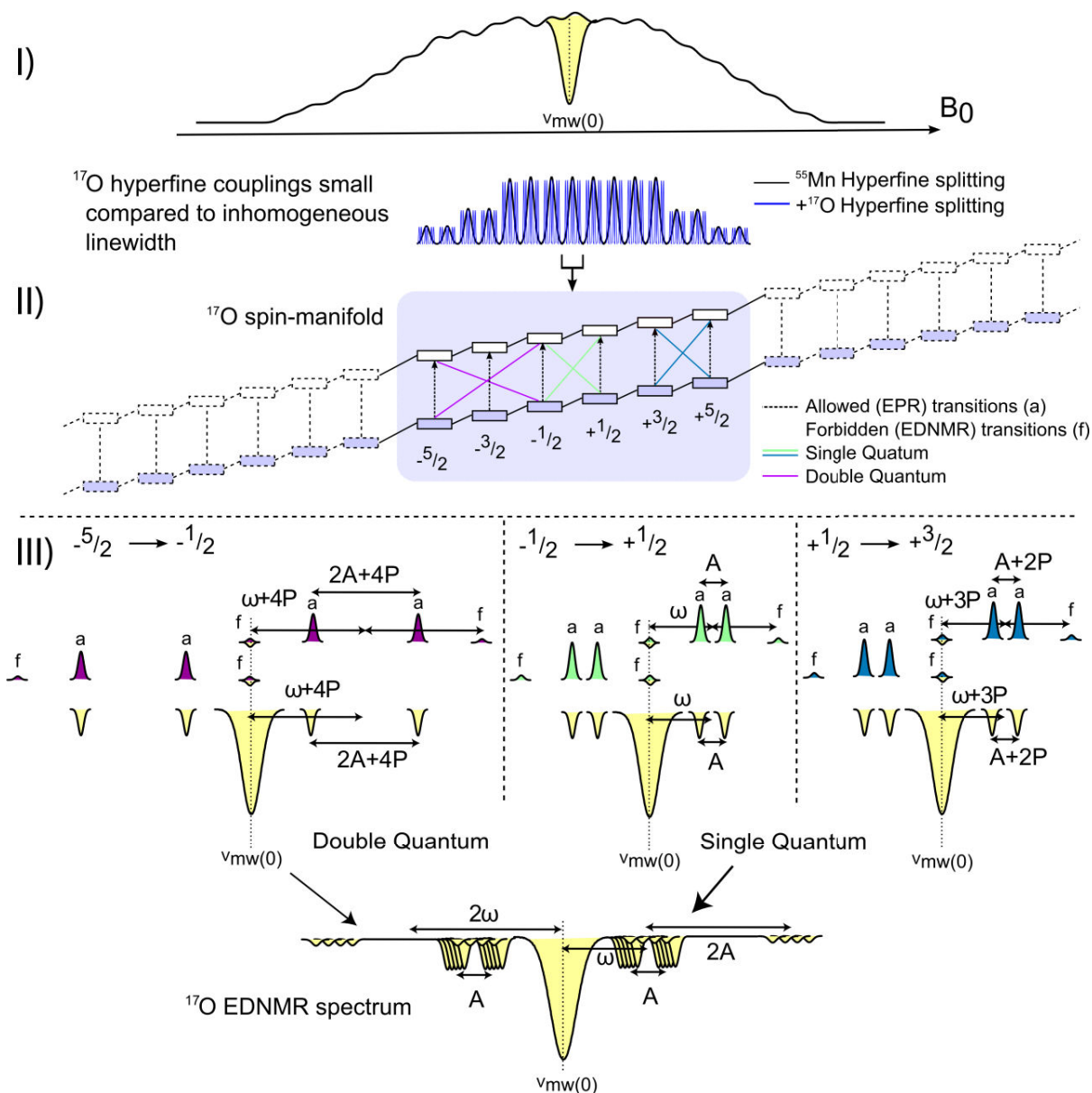


Figure 5. I) Typical EPR multiline spectrum seen for the exchange coupled Mn dimer systems presented here. The ^{17}O hyperfine couplings of O ligands bound to the Mn are smaller or of the same order of magnitude of the linewidth of the EPR spectrum. II) Cartoon of the ^{17}O -spin submanifold at the marked field position showing a selection of single and double quantum transitions. III) EDNMR spectra of individual single (green/blue) and quanta double (purple) transitions within the ^{17}O -spin

submanifold. Also shown is the net EDNMR spectrum for the ^{17}O -spin submanifold including only single and quanta double transition. The energy-level scheme/EDNMR spectrum assumes the weak coupling limit i.e. $|\omega| > \left| \frac{A}{2} \right|$.

4.1.1 ^{17}O -EDNMR of the bent $\text{Mn}^{\text{III}}-(\mu\text{-O})_2\text{-Mn}^{\text{IV}}$ DTNE complex. The 2D EDNMR surface of the ^{17}O labeled mixed-valent $\text{Mn}^{\text{III}}-\mu\text{O}_2\text{-Mn}^{\text{IV}}$ DTNE complex. In the 2D experiment, an EDNMR spectrum is taken at a series of magnetic field positions across the EPR spectrum, forming a pictorial 2D EDNMR surface (**Figure 6C**). As the Larmor frequency is linearly field dependent, the mean peak positions of the side-holes linearly increases with respect to the central hole ($\nu_{\text{mw}}^{(0)}$) as the magnetic field increases. As a consequence, not only the position but also the rate of change of the peak shift is characteristic of a particular nucleus and as such can be used as a marker for the nucleus identity. It is noted that double quantum transitions must have a field dependence twice that of the corresponding single quantum transitions. The control ^{16}O DTNE complex data are shown **black** in **Figure 5** panels **D**, **E** and **F**, resolving signals attributable to a ^{14}N ligand. Both single and double quantum transitions are observed. The single quantum transitions are centered about the Larmor frequency of ^{14}N [$\nu(^{14}\text{N}) \sim 10.4$ MHz], split by the hyperfine coupling and (full arrow in panels D, E, F), while double quantum ^{14}N transitions are centered at twice the Larmor frequency of ^{14}N [$\nu(^{14}\text{N}) \sim 20.8$ MHz] and split by twice the hyperfine coupling (dashed arrows in panels D,E,F). The ^{14}N peaks are characteristically narrow with peak widths of FWHM 3 MHz. This signal represents the strongly coupled ^{14}N axial ligand of the Mn^{III} ion which sits along its Jahn-Teller axis. The remaining equatorial ^{14}N ligands of the Mn^{III} and all ^{14}N ligands of the Mn^{IV} are only weakly coupled and appear as a ‘matrix’ line centered at the ^{14}N Larmor frequency. A further splitting of the high frequency 1.2 MHz ^{14}N ligand is observed which is best resolved on the high field edge. This splitting is tentatively assigned to a quadrupole coupling of 2 MHz.

The corresponding ^{17}O labeled DTNE complex data are shown **red** in **Figure 5** panels **D**, **E** and **F**. The ^{17}O signal observed is significantly different from that of the background ^{14}N signal. It is much

broader and does not resolve any structure. The single quantum ^{17}O transitions does not appear as a doublet centered about the Larmor frequency of ^{17}O [$\nu(^{17}\text{O}) \sim 19.5$ MHz]. It instead is a broad envelope, where a two peak structure is only observed for the EDNMR spectrum, measured on the low field edge (**Figure 5F**). An apparent splitting is all but lost for the spectrum, measured on the high field edge (**Figure 5D**) and the spectrum in the center represents an average of the two edge spectra (**Figure 5E**). While a discrete peak structure is absent for the ^{17}O signal, the total width of the envelope still provides a complete description of the ^{17}O hyperfine tensor. The anisotropy of the ^{17}O hyperfine tensor is significantly larger than that seen for the ^{14}N signal and of the same order as the isotropic ^{17}O hyperfine coupling as seen in the HYSCORE spectrum. The large difference seen between the low, high and center field spectra suggests that the hyperfine tensor is not axial but rather has a high degree of rhombicity.

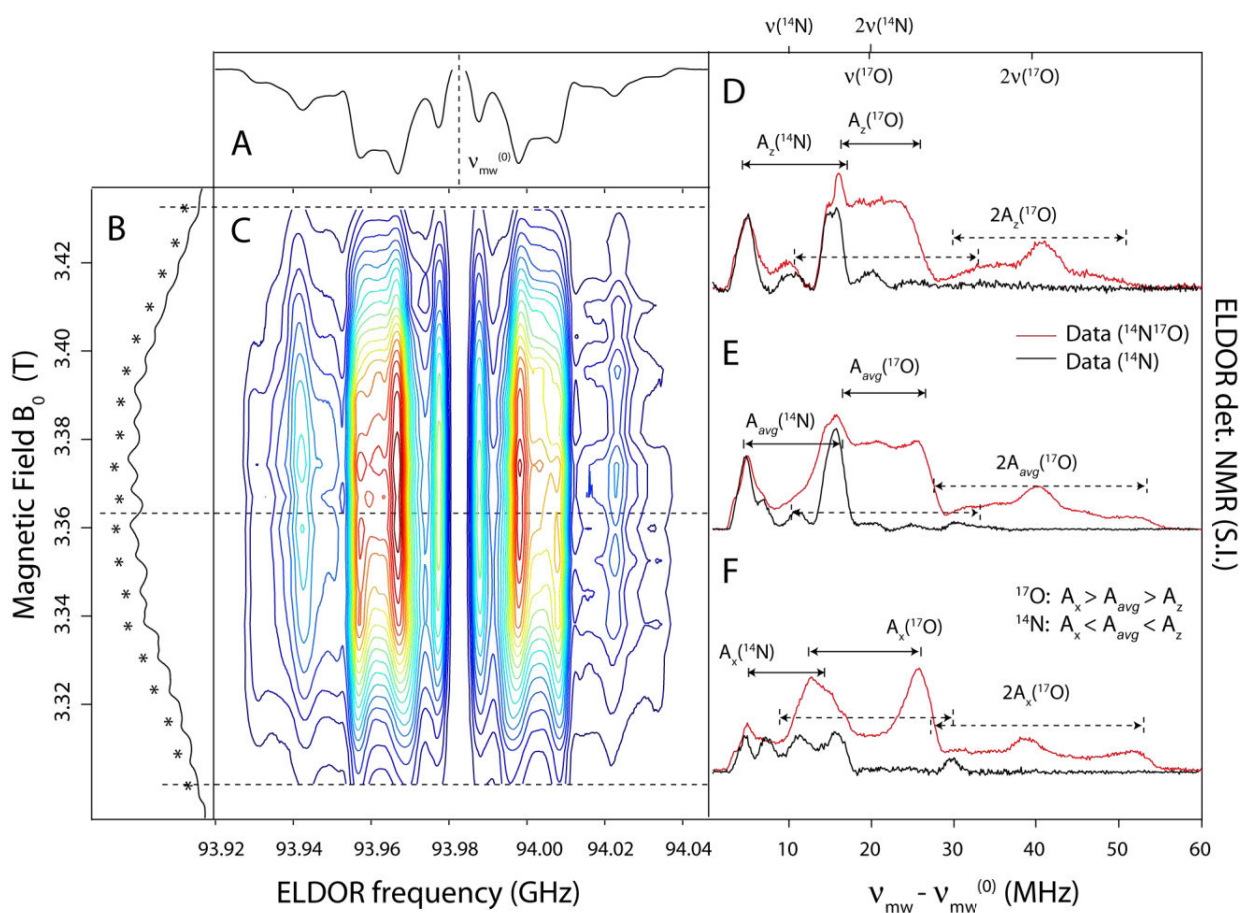


Figure 6. 94 GHz (W-band) EDNMR spectra of a ^{17}O labeled mixed valence $\text{Mn}^{\text{III}}-\mu\text{O}_2-\text{Mn}^{\text{IV}}$ DTNE complex. **A:** the projection of ELDOR detected NMR surface averaged over all field positions; **B** a two dimensional representation (contour map) of the field dependence EDNMR signal; **C, D, E** a comparison of the EDNMR signal seen for the ^{17}O labeled complex (**red** lines) compared to unlabeled complex (**black** lines) at three field positions, the low field edge 3302 mT (**C**), the third central line 3372 mT (**D**) and the high field edge 3432 mT (**E**).

4.1.1 ^{17}O -EDNMR of the planer $\text{Mn}^{\text{III}}-(\mu\text{-O})_2-\text{Mn}^{\text{IV}}$ BIPY complex. The EDNMR surface of the ^{17}O labeled mixed-valent complex is shown in **Figure 7**. Interestingly, the ^{17}O -EDNMR spectra of the **BIPY** complex is essentially the same as the **DTNE** complex; the width of the ^{17}O signal profile and its dependence on the magnetic field of the **DTNE** complex is approximately that of the **BIPY** complex. The **BIPY** complex is though systematically broader by about ~ 2 MHz (for the single quantum transitions).

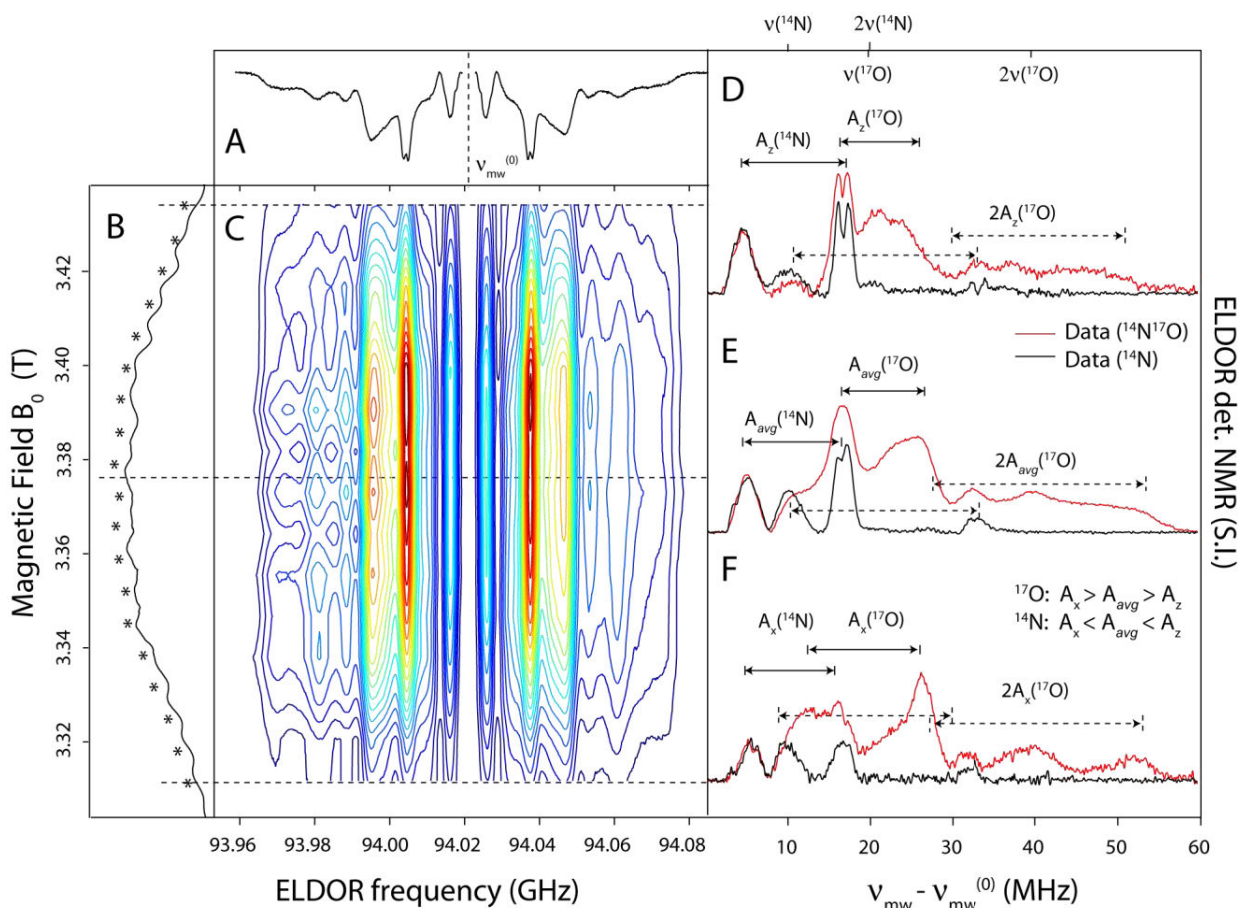


Figure 7. 94 GHz (W-band) EDNMR spectra of ^{17}O labeled $\text{Mn}^{\text{III}}\text{-}\mu\text{O}_2\text{-Mn}^{\text{IV}}$ BIPY complex. **A)** the EDNMR surface averaged over all field positions; **B)** The EPR multiline spectrum of the complex in field sweep mode. **C)** a two dimensional representation (contour map) of the field dependence EDNMR signal; **D, E, F)** a comparison of the EDNMR signals seen for the ^{17}O labeled complex at three field positions (**red** lines) compared to those of unlabeled complex (**black** lines): **D)** the low field edge 3.303 T; **E)** the central field 3.373 T; **F)** the high field edge 3.443 T.

4.1.5 Spin Hamiltonian Simulations. The spectral profile of the ^{17}O EDNMR signal at all field positions could be simulated using the Spin Hamiltonian formalism described in the theory section. Table 1 lists all Spin Hamiltonian parameters. These preliminary simulations required only one a strongly coupled ^{17}O nucleus as the two labelled μ -oxo bridges are symmetrically related and a weakly

coupled ^{17}O nucleus representing a more distant matrix water molecule. The simulations are described in the Theory section.

Simulations of the multi-frequency EPR spectra along with the W-band HYSORE measurements using the parameters fit to the EDNMR are shown in red (dashed lines/shaded area) in **Figure 2 and 4**. It is readily seen that the simulations reproduce the spectral width and overall lineshape of the all the ^{17}O signal seen.

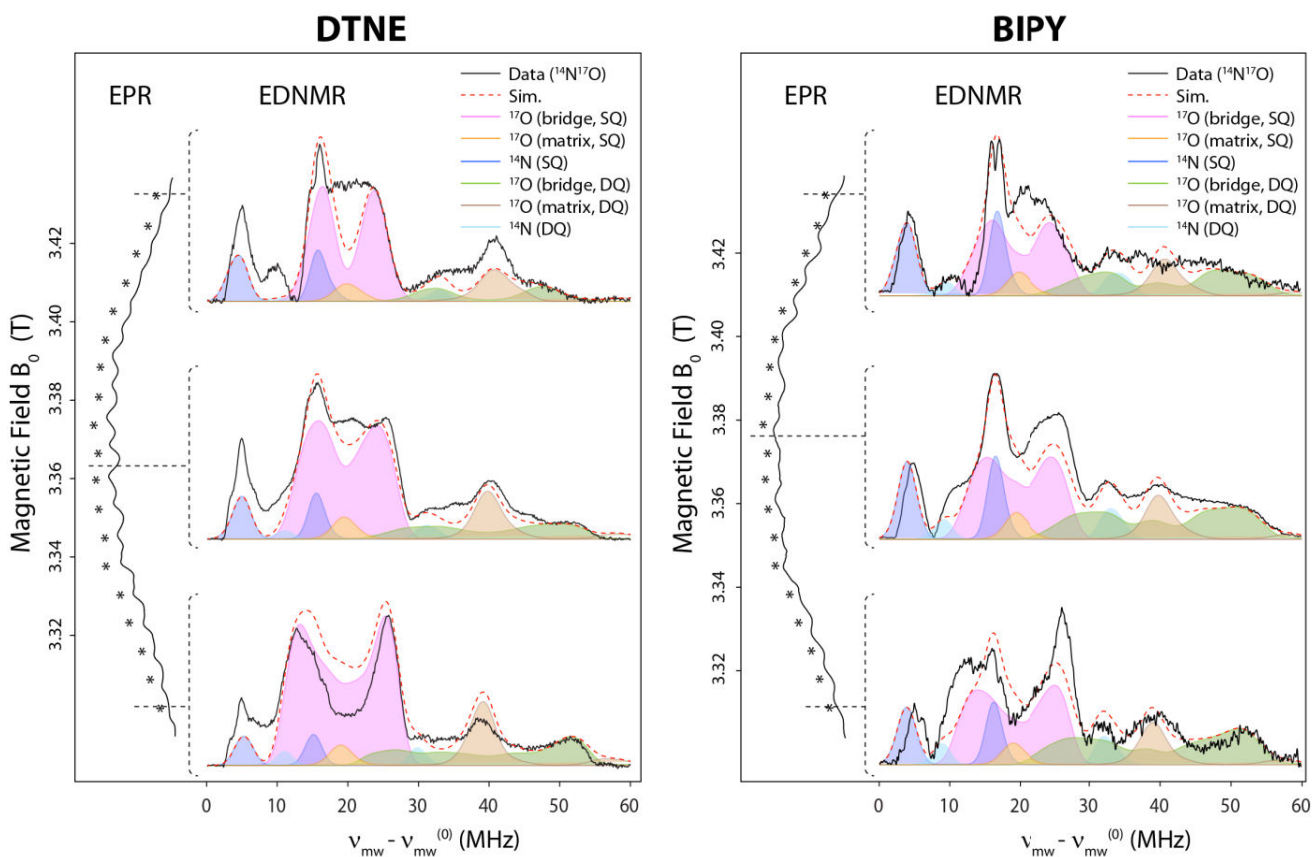


Figure 8. Simulations of the EDNMR data presented in **Figures 6 and 7** spectra using the Spin Hamiltonian formalism. The black lines represent the data, the red dashed lines represent the simulation. The different components of the simulation are shown by transparent colored traces. All Spin Hamiltonian parameters can be found in **Table 1**

Table 1. The principal values of the effective ^{14}N and ^{17}O hyperfine and quadrupole tensors for the simulations of the BIPY and DTNE data

		Spin Hamiltonian Parameters (MHz)							
		A_x	A_y	A_z	A_{iso}	A_{aniso}	$A(\eta)$	Q	$Q(\eta)$
DTNE	N (JT)	9.0	9.0	13.5	10.5	1.5	0.0	2.0	0.0
	N (w.c.)	~1	~1	~1	~1	0	0.0	-	-
	μ -oxo	16.0	-2	7.0	7.0	4.5	1.0	3.0	1.0
	H ₂ O	-2.0	4	-2.0	0.0	-2	0.0	10.0	1.0
BIPY	N (JT)	11.0	11.0	-15.5	12.5	1.5	0.0	2.0	0.0
	μ -oxo	17.5	0.0	7.5	7.5	5.0	1.0	4.0	1.0
	H ₂ O	-2.0	4.0	2.0	0.0	-2.0	0.0	10.0	1.0

A_{iso} is defined the average of the principal components of the hyperfine tensor: $A_{iso} = (A_x + A_y + A_z)/3$.

A_{aniso} is defined in terms of A_1 , A_2 and A_3 as: $A_{aniso} = \frac{A_1 + A_2}{2} = -\frac{A_3}{2}$ and the rhombicity is as defined

by: $\eta = \frac{A_1 - A_2}{A_3}$. A_1 , A_2 and A_3 represent the three principal components of the hyperfine tensor minus

A_{iso} . and labeled such that $|A_1| \leq |A_2| \leq |A_3|$

4.1.7 A fingerprint of the μ -oxo- ^{17}O bridge motif. The strong similarity of the two complexes shown provides a basis for a magnetic fingerprint for a Mn μ -oxo bridge. For table 1 it can be seen that the ^{17}O hyperfine tensor of the bridge should display: i) a large isotropic coupling ~ 7 -8 MHz and; ii) a hyperfine anisotropy. The requirement of large hyperfine anisotropy is immediate from the strong field dependence of the width of the ^{17}O signal, where the low, high and center field spectra all have a different width, suggest further suggests the hyperfine tensor is not axial but rather has a high degree of rhombicity. In the simulations the hyperfine tensor is aligned such that the largest and smallest components of the hyperfine tensor (in terms of signed magnitude) are aligned along g_x and g_y (or at least are orientated in the g_x/g_y plane) whereas the middle component is aligned along g_z .

The orientation of the μo_2 bridge hyperfine tensor can be understood within the current model for the electronic structure of strongly antiferromagnetically coupled $\text{Mn}^{\text{III}}\text{Mn}^{\text{IV}}$ dimers ($J < -100 \text{ cm}^{-1}$). In these complexes the anisotropies of the effective G and ^{55}Mn hyperfine tensors are dominantly derived from the Mn^{III} ion ($S = 2, d^4$ ion).^{13,43} The Mn^{IV} ($S = 3/2, d^3$ ion) has a half filled ${}^2T_{2g}$ level which results in a relatively isotropic ion. Thus the Jahn-Teller axis of the Mn^{III} ion defined the unique axis (z -axis) of the system. For both the **BIPY** and **DTNE** complexes the z -axis can be identified in the crystal structure.^{20,44} It is aligned along the $\text{Mn}^{\text{III}}\text{-N}$ bond perpendicular to the plane defined by the $\text{Mn}-\mu\text{O}_2\text{-Mn}$ atoms (see **Figure 1**). Spin Hamiltonian parameters ($g/^{55}\text{Mn}$ hyperfine tensors) for both the BIPY and DTNE have been previously determined using multifrequency EPR and ^{55}Mn -ENDOR.¹³ The unique component for the molecular g tensor, which must be parallel to the Jahn-Teller axis of the Mn^{III} ion is defined by g_z and is smallest in magnitude and as a consequence defines the high field edge of the EPR spectrum. Within this framework the ^{17}O hyperfine tensor components can be mapped to the molecular structure. The middle component of the ^{17}O hyperfine tensor, as it is coincided with g_z , is perpendicular to the $\text{Mn}-\mu\text{O}_2\text{-Mn}$ plane and the largest and smallest component lie in the $\text{Mn}-\mu\text{O}_2\text{-Mn}$ plane, in signed magnitude.

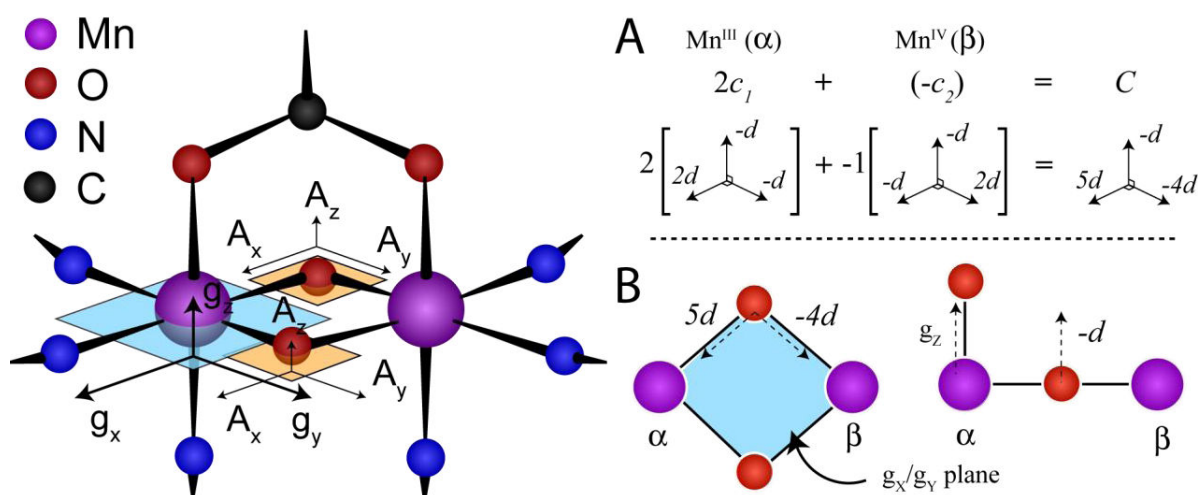


Figure 9. The hyperfine tensor of the μ -oxo bridge of an antiferromagnetically coupled $\text{Mn}^{\text{III}}\text{Mn}^{\text{IV}}$ dimer. **A:** onsite (individual) hyperfine tensor components in the Mn-O-Mn plane and perpendicular to the Mn-O-Mn plane. **B:** orientation of projected (experimental) hyperfine tensor.

From this basis geometric considerations then allow us to map the onsite hyperfine interaction between to the O bridges and the two Mn ions to the measured the hyperfine tensor. The experimental G, ^{55}Mn and ^{17}O hyperfine tensors are described by the Spin Hamiltonian in the coupled representation. Here the two Mn ions are treated as a single fictitious spin ($S = 1/2$) and it is to this electronic state that the nuclear spins of the system are coupled to. Thus, the ^{17}O hyperfine tensor measured consists of contributions from the hyperfine coupling of the ^{17}O nucleus to both the Mn^{III} ion and Mn^{IV} ion; that is to say the measured (or projected) ^{17}O hyperfine tensor is a weighted sum of the two onsite ^{17}O hyperfine tensors which describe the interaction of the ^{17}O nucleus with either the Mn^{III} or Mn^{IV} . The relative contribution of each onsite ^{17}O hyperfine tensor to the projected ^{17}O hyperfine tensor depends upon the contribution of the Mn^{III} and Mn^{IV} ions to the electronic state. The contribution of the individual ions in a coupled complex to a particular electronic state of the system can be described in terms of a spin projection coefficient, (for a full description see ref.³⁹). For the antiferromagnetically coupled $\text{Mn}^{\text{III}}\text{Mn}^{\text{IV}}$ dimer, $S_{1(\text{Mn}^{\text{III}})} = 2$; and $S_{2(\text{Mn}^{\text{IV}})} = 3/2$ which gives isotopic spin projection values of $\rho_1 = 2$ and $\rho_2 = -1$, respectively. Thus the hyperfine coupling of the ^{17}O nucleus to the Mn^{III} ion has twice the contribution to the projected (or experimentally measured) ^{17}O hyperfine tensor than the coupling of the ^{17}O nucleus to the Mn^{IV} ion. In addition, the two contributions must differ in sign as the complex is antiferromagnetically coupled; the electron spins of the Mn^{III} ion pair with the oppositely signed spins of the Mn^{IV} ion.

The hyperfine interaction of the ^{17}O nucleus with each individual Mn ion will have both a through bond (Fermi contact term) and through space components. A reasonable starting assumption is that the through bond interaction is isotropic and that the through space interaction is dipolar in nature. Thus the unique (principal) axis of the onsite hyperfine should lie along the Mn-O bond. Summing the two onsite

hyperfine tensors yields a projected ^{17}O hyperfine tensor that has approximately rhombic symmetry. This is shown in **Figure 9**. The principal (unique) axis should be parallel to a plane that is defined by the Mn-O₂-Mn bridging motif. The middle component (in signed magnitude) must be perpendicular to the Mn-O₂-Mn bridging motif. This is exactly the behavior observed experimentally. The largest component of the ^{17}O hyperfine tensor coincides with g_x/g_y , i.e. the plane defined by the Mn-O₂-Mn bridging motif, whereas the middle component of the ^{17}O hyperfine tensor coincides with g_z i.e. perpendicular to the plane defined by the Mn-O₂-Mn bridging motif.

Table 2: ^{17}O -Mn distances and theoretical ^{17}O couplings for the μ -oxo substrate positions of the Umena et al.¹ structure and recent representative computational model of Ames et al.⁴⁵ (**1d2'**, see **Figure 1**) using the isotropic spin projections for the model of Siegbahn (model 11) reported in Pantazis et al.⁴⁶

			$d_{\text{Mn-L}} (\text{\AA})$		Hyperfine (MHz)	
			Mn _A	Mn _B	A	η
DTNE	O1	μ -oxo	1.83	1.78	4.46	0.64
	O2	μ -oxo	1.83	1.78	4.44	0.64
	O3	Mn ^{III} carboxo	2.14	3.16	2.19	0.16
	O4	Mn ^{IV} carboxo	3.14	1.97	1.13	0.52
	N2-N3	Mn ^{III} - (eq.)	2.07	4.34	-1.22	0.01
	N1	Mn ^{III} - (ax.)	2.21	3.74	-1.03	0.07
	N5-N6	Mn ^{IV} - (eq.)	4.33	2.07	0.53	0.07
	N4	Mn ^{IV} - (ax.)	3.65	2.09	0.58	0.34
BIPY	O1	μ -oxo	1.88	1.77	4.20	0.68
	O2	μ -oxo	1.88	1.77	4.17	0.69
	N2, N3	Mn ^{III} - (eq.)	2.13	4.44	-1.14	0.02
	N1, N5	Mn ^{III} - (ax.)	2.27	3.80	-0.96	0.09
	N26 N7	Mn ^{IV} - (eq.)	4.45	2.10	0.53	0.08
	N5, N8	Mn ^{IV} - (ax.)	3.55	2.02	0.69	0.37

^{a)} principal value for the hyperfine/quadrupole tensor: $A = \frac{A_1 + A_2}{2} = -\frac{A_3}{2}; |A_1| \leq |A_2| \leq |A_3|$

b) rhombicity of the hyperfine/quadrupole tensor as defined by: $\eta = \frac{A_1 - A_2}{A_3}; |A_1| \leq |A_2| \leq |A_3|$

For the above rationale to be correct the magnitude of the magnitude of the measured anisotropy of the ^{17}O hyperfine tensor should be consistent with a through space dipolar mechanism. The dipolar coupling of the ligands of each complex can be readily calculated using the crystal structure coordinates. Calculated values are given in **Table 2**. It is readily observed that the estimated dipolar coupling matches the fitted A_{aniso} values.

4.1.8 μ -oxo- ^{17}O model complex data, comparison to literature. There currently exists in the literature only a limited number of studies where the ^{17}O hyperfine coupling of a bridge of a high valent (Mn^{III} , Mn^{IV}) complexes has been measured. In the study of Usov et al. ¹⁴, the ^{17}O couplings of the μ oxo bridges of the BIPY complex, one of the complexes measured here, were detected using Q-band ENDOR. They observed a broad, structureless ^{17}O signal centered at ~ 13 MHz. An estimate of the isotropic coupling was made from the center of the peak of the signal ($\nu^+(^{17}\text{O})$ branch) of ~ 13 MHz, which was shown to be consistent with the observed line-broadening seen in the cw EPR experiments. No estimate was reported for either the hyperfine anisotropy or quadrupole splitting. An isotropic coupling estimate of $A_{\text{iso}} \sim 13$ MHz approximately for the μ oxo bridges is twice that seen in this study, $A_{\text{iso}} \sim 8$ MHz. The difference between these two studies is suspected to arise from an experimental feature of the Q-band ENDOR experiment. This method is often not particularly sensitive at low frequency where much of the ^{17}O signal envelope is expected when measured at 34 GHz. Thus the signal peak observed at Q-band does not represent a true average coupling, but is instead skewed to higher frequency, overestimating the isotropic coupling (**Figure 10, panel B**). The same problem is not encountered using high field EPR spectroscopy, namely 94 GHz EDNMR (**Figure 10, panel A**) and thus more accurate hyperfine coupling estimates can be made. This is chiefly because the as compared

to the Q-band envelope, all ^{17}O signal are shifted 10 MHz to higher frequency and thus the entire envelope can now be resolved.

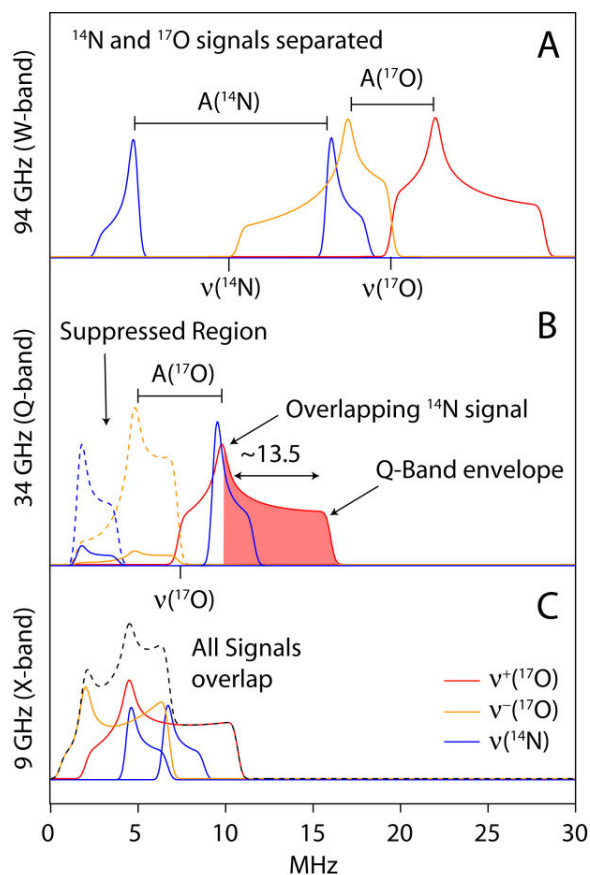


Figure 10. A pictorial representation the ^{17}O ($\mu\text{o xo}$) and ^{14}N (J.T. axis Mn^{III}) ENDOR signals seen for the BIPY complex measured at three microwave frequencies: **A**) 9 (X-band); **B**) 34 (Q-band); and **C**) 94 GHz (W-band).

A pictorial demonstration of the how the ^{17}O Q-band signal envelope is distorted is shown in **Figure 10, panel B**. Signals below 7 MHz, the $\nu^-(^{17}\text{O})$ and $\nu^-(^{14}\text{N})$ branches (dashed line) are strongly suppressed, presumably due to non-linearity of the B_2 (RF) field. The Q-band ^{17}O signal that is resolved, a broad featureless line extending to 15 MHz (**Figure 10B**, shaded red region) thus does not represent the real spectral envelope. Resolution of its exact shape is further compounded by an overlapping ^{14}N signal which is suspected to coincide with one of the major turning points of the $\nu^+(^{17}\text{O})$ signal branch. From comparison to our 94 GHz data (**Figure 10, panel A**), the Q-band ^{17}O signal

envelope should instead be assigned to the A_x component of the hyperfine tensor i.e. the largest component of the hyperfine tensor. It can also be seen in **Figure 10C** that at frequencies lower than Q-band (X-band), all spectral components strongly overlap making any interpretation difficult.

As a final note, it is suspected that the same observations made above for the Q-band BIPY study of Usov et al. also apply for the later Q-band study the same authors conducted on the super-oxidized state of the Mn-catalase. The superoxidized state represents a bis- μ -oxo, μ -carboxylato $Mn^{III}Mn^{IV}$ complex structurally similar to the **DTNE** complex. As seen for the BIPY complex, the superoxidized Mn-catalase also resolves a broad structureless ^{17}O signal at Q-band centered at ~ 13 MHz. It is likely this signal again represents the largest hyperfine splitting. Thus the isotropic hyperfine coupling (A_{iso}) of the μ -oxo bridge will be of the order of 7-8 MHz, as the anisotropic hyperfine (dipolar) coupling is approximately invariant.

4.2 DFT Calculations

4.2.1 Broken Symmetry-DFT Calculated ^{17}O and ^{14}N Hyperfine Coupling Constants. The projection of the hyperfine coupling constants calculated using broken symmetry DFT (BS-DFT) for the ^{14}N atoms directly coordinated to the ^{55}Mn spin centers has been discussed previously in the literature.⁴⁷ In short, each nitrogen atom (k) is assigned to a particular spin center (A) and the resulting projection from the as-calculated “raw” broken symmetry values is the same as that of the projection for the ^{55}Mn spin centers as shown by **Equation 7**.

$$A_{iso}^{(k;A)} = \pm A_{iso,BS}^{(k)} \frac{\langle S_z \rangle_{BS}}{S_A} \frac{\langle S_z^{(A)} \rangle}{S_t} \quad (\text{Eq. 7})$$

Where $A_{iso,BS}^{(k)}$ is the as-calculated “raw” BS-DFT value and $\langle S_z^{(A)} \rangle$ is the on-site spin expectation value. $\langle S_z \rangle_{BS}$, S_A , and S_t are the M_S for the broken symmetry wave-function, ^{55}Mn site-spin, and effective total spin for the complex, respectively. The formalism shown in **Equation 7** generalizes for all components

of the hyperfine tensor. For more information on the projection of calculated BS-DFT values for comparison with experiment we refer the reader to refs.⁴⁷⁻⁵⁰

Bridging μ -oxo ligands, however, cannot be assigned to any single ^{55}Mn spin-centered system. Here we propose to use the direct sum of the interactions from each spin system to project the calculated BS-DFT values for the comparison with experimentally determined values. The subsequent formalism is shown in **Equation 8**.

$$A_{iso}^{(k;A,B)} = \pm A_{iso,BS}^{(k)} \frac{\langle S_z \rangle_{BS} \langle S_z^{(A)} \rangle}{S_A S_t} \mp A_{iso,BS}^{(k)} \frac{\langle S_z \rangle_{BS} \langle S_z^{(B)} \rangle}{S_B S_t} \quad (\text{Eq. 8})$$

Equation 8 can be rewritten into the more standard form of:

$$A_{iso}^{(k;A,B)} = \rho_A A_{iso,site}^{(k,A)} + \rho_B A_{iso,site}^{(k,B)}$$

such that, ρ_i is the spin-projection value for site A or B and $A_{iso,site}^{(k,i)}$ is the on-site hyperfine coupling constant with respect to either site A or B. For a $\text{Mn}^{\text{III}}\text{Mn}^{\text{IV}}$ dimer equation 8 simply reduces to $\frac{5}{6} A_{iso,BS}^{(k)}$. Table 3 shows the projected isotropic ^{17}O and ^{14}N BS-DFT hyperfine values calculated for the **DTNE** and **BIPY** complexes using **Equations 7 and 8** for the terminal and bridging ligands respectively.

Table 3. Calculated isotropic BS-DFT hyperfine coupling constants (MHz).*

Model	Nuclei	Coordination	Spin System	
			Mn^{III}	Mn^{IV}
DTNE	^{14}N	Axial	11.5	1.8
	^{14}N	Equatorial	-2.8	1.6
	^{17}O	Bridge	5.7	
BIPY	^{14}N	Axial	14.4	1.8
	^{14}N	Equatorial	-0.6	2.1

* Average contribution of pseudo-symmetric sites reported.

From the calculated values shown in **Table 3** it is clear that the isotropic hyperfine coupling constants fall into three categories such that the axial ligands for Mn^{III} have the largest hyperfine coupling constants while terminal equatorial ligands and ligands coordinated to Mn^{IV} have small hyperfine coupling constants. Such observations have been made, both experimentally and computationally, for Mn^{III}Mn^{IV} dimer systems before.^{13,47,50,51} The values calculated for the μ-oxo bridges, however, show intermediate hyperfine coupling constants even though they are also equatorial ligands. Here the calculations are in agreement with the experimental data.

It can be deduced from **Equation 8** that the intermediate magnitude of the isotropic ¹⁷O hyperfine coupling constants for the μ-oxo bridges is a direct result of an overall additive on-site spin contribution from each Mn ion. For example the contributions from Mn^{III} and Mn^{IV} are 4.8 and 3.2 MHz in the BIPY model, respectively. Understandably the spin center with the largest number of unpaired electrons, Mn^{III}, contributes the most to the calculated hyperfine coupling constant. Additionally while the resultant contributions are approximately two times the values calculated for the ¹⁴N equatorial ligands it can be shown that this is a result of the larger P_N proportionality factor of ¹⁷O vs. that of ¹⁴N. Isotropic hyperfines are calculated using the following formula when using either DFT or *ab initio* methods.

$$A_{iso} = \frac{4}{3} \pi (S_z)^{-1} P_N \rho(\vec{R}_N)$$

In equation GG (S_z) is the z-component of the expectation value for the total spin and $\rho(\vec{R}_N)$ is the spin density at the nucleus. P_N is a proportionality factor equal to the product of the electron and nuclear g-factors and magnetons, $P_N = g_e g_N \beta_e \beta_N$. The ratios of the proportionality factors for ¹⁷O and ¹⁴N is -1.88 ie. ¹⁷O has a proportionality factor twice that of ¹⁴N. Thus, as a back of the envelope calculation, assuming an equivalent spin density for a bridging ¹⁴N in place of the μ-oxo bridge the expected

contributions from Mn^{III} and Mn^{IV} would be -2.5 and -1.7 MHz. Both values are within the absolute range shown on Table ZZ for nitrogen ligands coordinated to Mn^{III} or Mn^{IV} spin centers.

The calculated quadrupole coupling constants (**Table 4**) show trends that, similar to the hyperfine coupling constants, are in agreement with the experimental data. With respect to the magnitude of the calculated quadrupole coupling constants it is clear that the ^{17}O quadrupole cannot be resolved experimentally in these model systems as they are approximately an order of magnitude smaller than those of the ^{14}N nuclei. The relative magnitudes of the quadrupole coupling constants for the ^{14}N nuclei coordinated to Mn^{III} or Mn^{IV} can be, in part, explained based on geometric considerations. The observed reduction of the free uncoordinated ligand nitrogen quadrupole coupling constant upon metal coordination is attributed to a transfer of electron density from the lone pair of the nitrogen atom to bonding orbitals of the Mn transition metal center.^{51,52} As such, the subsequently longer Mn-N bonds for the axially coordinated nitrogen atom on Mn^{III} engender a smaller reduction in the nuclear quadrupole coupling constant of the coordinating ^{14}N . **Figure 11** shows the geometric relationship between the Mn-N bond length and the calculated quadrupole coupling constants of the **DTNE** and **BIPY** models. The plot shows a mostly linear relationship for the calculated quadrupole coupling constants with respect to the Mn-N distances. An inspection of the calculated values indicates that the coordinating nitrogen atoms of the DTNE model transfer less lone pair electron density to the Mn metal centers than the nitrogen atoms in the BIPY complex, resulting in larger absolute magnitudes of the quadrupole coupling constants for similar Mn-N distances. Prior experimental determinations for the quadrupole coupling constants of the axial nitrogen coordinated to Mn^{III} for a number of $\text{Mn}^{\text{III}}\text{Mn}^{\text{IV}}$ show an opposite trend with sp^3 and sp^2 hybridized nitrogen ligands having quadrupole coupling constants of approximately 0.55 and 0.73 MHz, respectively.^{13,51} This is interesting as the calculated isotropic ^{14}N hyperfine coupling constants follow the experimental trend; whereby A_{iso} for the axially coordinated nitrogen atom on Mn^{III} is larger for sp^2 vs. sp^3 hybridized nitrogen ligands.^{13,51}

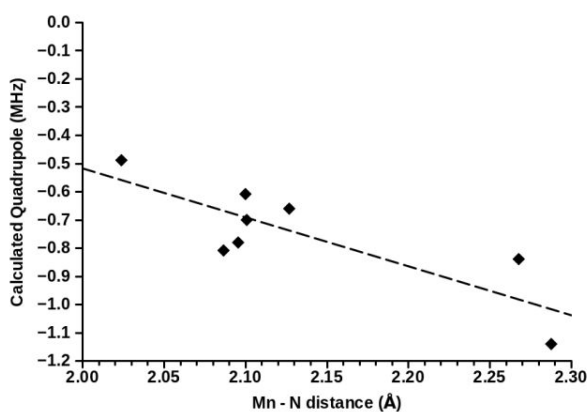


Figure 11. Calculated quadrupole coupling constants vs. the Mn-N distances for the DTNE and BIPY models. The dashed line indicates the linear trend.

It has been shown previously that the magnitude of the asymmetry parameter, η , can be correlated to the accessibility of the nitrogen nuclei to the surrounding solvent.^{53,54} From **Table 4** it can be seen that the equatorial ligands of DTNE, both the ^{14}N and ^{17}O , have more solvent accessibility than the axial ^{14}N ligands. This can be easily rationalized by a quick inspection of the structure of **DTNE** (see **Figure 1**) whereby it can be seen that the axial nitrogen ligands are tertiary amines and thus due to the coordination to the Mn transition metal centers are not solvent accessible and have near zero asymmetry values. The equatorially ligated nitrogen atoms of **DTNE**, however, are secondary amines and can interact weakly with a solvent, which is reflected in their much larger η values of approximately 0.30. The most accessible ligands for both complexes (**DTNE** and **BIPY**) are the μ -oxo bridges having asymmetry parameters much closer to unity. For the **BIPY** complex the pyridine, sp^2 hybridized, nitrogen atoms directly coordinated to the Mn metal centers have small asymmetry parameters as the primary solvent accessible site is blocked via metal ligation similar to the case of the remote nitrogen of 4-methyl imidazole complexes.^{53,54} The slightly larger η value calculated for the **BIPY** axial ligands can be in part explained due to both the longer axial Mn-N bond for Mn^{III} and the π - π stacking of the bipyridine ligands at the axial interface.⁵⁵

Table 4. Calculated Nuclear Quadrupole Coupling Constants $e^2qQ/(4hI(2I-1))$ (MHz).^{a,b}

Model	Nuclei	Coordination	Spin System	
			Mn ^{III}	Mn ^{IV}
DTNE	¹⁴ N	Axial	-1.14 [0.01]	-0.70 [0.05]
	¹⁴ N	Equatorial	-0.81 [0.29]	-0.78 [0.31]
	¹⁷ O	Bridge	0.08 [0.63]	
BIPY	¹⁴ N	Axial	-0.84 [0.15]	-0.49 [0.18]
	¹⁴ N	Equatorial	-0.66 [0.02]	-0.61 [0.08]
	¹⁷ O	Bridge	0.07 [0.73]	

^a Average contribution of pseudo-symmetric sites reported.

^b Quadrupole anisotropy term, η , in brackets ($\eta = \frac{q_1 - q_2}{q_3}$).

4.2.2 BS-DFT Hyperfine and Quadrupole Coupling Constant Orientation. The orientation of the calculated hyperfine coupling constants for the μ -oxo bridges as well as the axial ¹⁴N ligand of the Mn^{III} for both DTNE and BIPY are shown in **Figure 12**. Of particular note is the orientation of the “unique” axis (blue vectors) of the axial nitrogen ligands vs. that of the μ -oxo bridges. The calculations show that the unique axis of the bridge(s) is orthogonal to that of the unique axis for the axial nitrogen, in agreement with the experimental observations and has been shown to be a necessary condition for the experimental interpretation (see **Figure 9, Results 4.1.7**). It is also shown from the calculations that the remaining two components of the axial nitrogen ligands coordinated to Mn^{III} (red and green arrows in **Figure 12**) are oriented along the Mn-Mn and O-O interatomic vectors while the unique component is oriented along the Mn-N bond. A different situation arises with the μ -oxo bridges and it can also be seen in **Figure 12** that the **DTNE** and **BIPY** models have different orientations for the non-unique components of the hyperfine tensor. For **DTNE** the smallest component is calculated to be orthogonal to the Mn-oxo plane, while the medium and unique component are oriented along Mn-oxo bonds. In the case of the **BIPY** model the unique axis is oriented similarly as in the **DTNE** complex, ie. along Mn-

oxo bonds, while the other components are both shown to be pointing about 45° out of the Mn-oxo plane. This out of plane distortion of the non-unique components of the μ -oxo hyperfine tensor can presumably be attributed to an overlap contribution from the π orbitals of the bipyridine ligands with the p_z orbital on the oxo bridge.

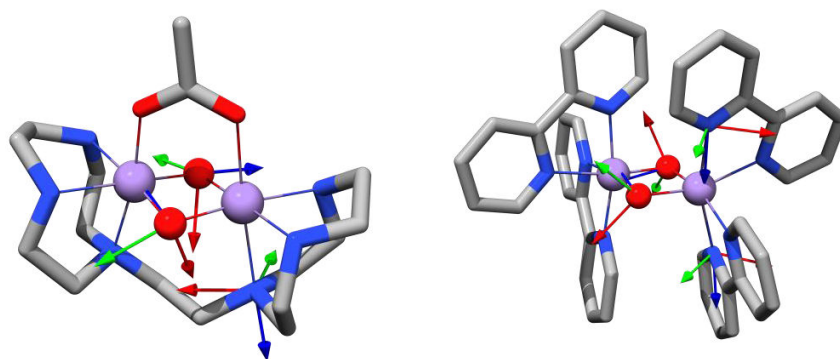


Figure 12. Calculated orientations of the hyperfine coupling constants for the (left) **DTNE** and (right) **BIPY** models. Red, green and blue vectors are the A_1 , A_2 and A_3 components of the hyperfine tensor. The blue vectors represent the “unique” axis of the hyperfine tensors for the μ -oxo bridges as well as the axial nitrogen ligand of the Mn^{III} . The components have been ordered in terms of absolute magnitude, such that $A_1 \leq A_2 < A_3$.

Of similar importance as the orientation of the hyperfine tensor is the orientation of the quadrupole tensor. **Figure 13** shows the calculated orientations of the quadrupole tensors for the **DTNE** and **BIPY** complexes. Here the largest component of the quadrupole tensor, q_3 , for both the bridge(s) and the axial nitrogen on Mn^{III} are shown to be collinear, along the Jahn-Teller axis of Mn^{III} . For both complexes (**DTNE** and **BIPY**) the small and medium quadrupole components are oriented along the O-O and Mn-Mn interatomic vectors, respectively. The small and medium components for the axial nitrogen of Mn^{III} are oriented with an approximate 45° rotation with respect to the μ -oxo small and medium components. Here this aligns the small and medium components for the axial nitrogen roughly along the N-C bonds

for **DTNE** and as in and out of plane vectors for the **BIPY** complex. These orientations result in an approximate 45° rotation with respect to the orientations of the calculated ^{14}N hyperfine tensor.

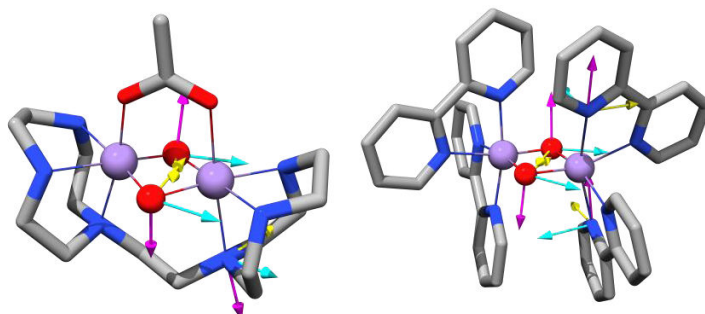


Figure 13. Calculated orientations of the quadrupole tensor for the (left) **DTNE** and (right) **BIPY** models. The yellow, cyan and magenta vectors represent the q_1 , q_2 and q_3 components, respectively.

Here the standard definition is used where $|q_1| < |q_2| < |q_3|$ and $\eta = \frac{q_1 - q_2}{q_3}$.

CONCLUSIONS

The strong similarity of the two complexes shown provides a basis for a magnetic fingerprint for a Mn μ -oxo bridge, which includes two main properties of the ^{17}O hyperfine tensor: i) a large isotropic coupling $\sim 7\text{-}8$ MHz and; ii) hyperfine tensor anisotropy. The strong field dependence of the width of the ^{17}O signal required the hyperfine anisotropy to be large (of the same order of isotropic coupling). This fingerprint provides a means of monitoring the μ -oxo bridges of a metallocofactor throughout its catalytic cycle. This is critical for understanding the chemistry that Mn metallocofactors perform, as they often locate substrates for the reaction they catalyze as bridging species, e.g. the Mn catalase takes up a HOOH as a μ -oxo during the dismutation reaction.

ACKNOWLEDGMENT

Financial supported was provided by, the Max Planck Gesellschaft, the JSPS and CNRS under the Japan-France Research Cooperative Program, the EU SOLAR-H2 (FP7 contract 212508). LR is a fellow of North Rhine-Westphalia (NRW) Research School BioStruct program.

REFERENCES

- (1) Umena, Y.; Kawakami, K.; Shen, J.-R.; Kamiya, N. *Nature* **2011**, *473*, 55-60.
- (2) Barynin, V. V.; Whittaker, M. M.; Antonyuk, S. V.; Lamzin, S. V.; Harrison, P. M.; Artymiuk, A. J.; Whittaker, J. M. *Structure* **2001**, *9*, 725-738.
- (3) Dismukes, G. C. *Chem. Rev.* **1996**, *96*, 2909-2926.
- (4) Cotruvo, J. A.; Stubbe, J. *Biochemistry* **2010**, *49*, 1297-1309.
- (5) Cox, N.; Ogata, H.; Stolle, P.; Reijerse, E.; Auling, G.; Lubitz, W. *J. Am. Chem. Soc.* **2010**, *132*, 11197-11213.
- (6) Jiang, W.; Yun, D.; Saleh, L.; Barr, E. W.; Xing, G.; Hoffart, L. M.; Maslak, M.-A.; Krebs, C.; Bollinger, J. M., Jr. *Science* **2007**, *316*, 1188-1191.
- (7) Schenk, G.; Boutchard, C. L.; Carrington, L. E.; Noble, C. J.; Moubaraki, B.; Murray, K. S.; de Jersey, J.; Hanson, G. R.; Hamilton, S. *J. Biol. Chem.* **2001**, *276*, 19084-19088.
- (8) Carepo, M.; Tierney, D. L.; Brondino, C. D.; Yang, T. C.; Pamplona, A.; Telser, J.; Moura, I.; Moura, J. J. G.; Hoffman, B. M. *J. Am. Chem. Soc.* **2001**, *124*, 281-286.
- (9) Burdi, D.; Willems, J.-P.; Riggs-Gelasco, P.; Antholine, W. E.; Stubbe, J.; Hoffman, B. M. *J. Am. Chem. Soc.* **1998**, *120*, 12910-12919.
- (10) Cooper, S. R.; Dismukes, G. C.; Klein, M. P.; Calvin, M. *J. Am. Chem. Soc.* **1978**, *100*, 7248-7252.
- (11) Randall, D. W.; Sturgeon, B. E.; Ball, J. A.; Lorigan, G. A.; Chan, M. K.; Klein, M. P.; Armstrong, W. H.; Britt, R. D. *J. Am. Chem. Soc.* **1995**, *117*, 11780-11789.
- (12) Schäfer, K. O.; Bittl, R.; Lenzian, F.; Barynin, V. V.; Weyhermuller, T.; Wieghardt, K.; Lubitz, W. *J. Phys. Chem. B* **2003**, *107*, 1242-1250.
- (13) Schäfer, K. O.; Bittl, R.; Zweggart, W.; Lenzian, F.; Haselhorst, G.; Weyhermuller, T.; Wieghardt, K.; Lubitz, W. *J. Am. Chem. Soc.* **1998**, *120*, 13104-13120.

- (14) Usov, O. M.; Grigoryants, V. M.; Tagore, R.; Brudvig, G. W.; Scholes, C. P. *J. Am. Chem. Soc.* **2007**, *129*, 11886-11887.
- (15) Raitsimring, A. M.; Astashkin, A. V.; Baute, D.; Goldfarb, D.; Caravan, P. *J. Phys. Chem. A* **2004**, *108*, 7318-7323.
- (16) Bossek, U.; Hummel, H.; Weyhermüller, T.; Wieghardt, K.; Russell, S.; van der Wolf, L.; Kolb, U. *Angew. Chem.* **1996**, *108*, 1653-1656.
- (17) Plaksin, P. M.; Stoufer, R. C.; Mathew, M.; Palenik, G. J. *J. Am. Chem. Soc.* **1972**, *94*, 2121-2122.
- (18) Cooper, S. R.; Calvin, M. *J. Am. Chem. Soc.* **1977**, *99*, 6623-6630.
- (19) Jensen, A. F.; Su, Z.; Hansen, N. K.; Larsen, F. K. *Inorg. Chem.* **1995**, *34*, 4244-4252.
- (20) Weyhermüller, T., Ruhr universität, 1994.
- (21) Reijerse, E.; Lendzian, F.; Isaacson, R.; Lubitz, W. *J. Magn. Res.* **2012**, *214*, 237-243.
- (22) Epel, B.; Gromov, I.; Stoll, S.; Schweiger, A.; Goldfarb, D. *Concepts Magn. Res. B* **2005**, *26B*, 36-45.
- (23) Kulik, L.; Epel, B.; Messinger, J.; Lubitz, W. *Photosynth. Res.* **2005**, *84*, 347-353.
- (24) Kulik, L. V.; Epel, B.; Lubitz, W.; Messinger, J. *J. Am. Chem. Soc.* **2005**, *127*, 2392-2393.
- (25) Stoll, S.; Schweiger, A. *J. Magn. Res.* **2006**, *178*, 42-55.
- (26) Becke, A. D. *Phys. Rev. A* **1988**, *38*, 3098-3100.
- (27) Lee, C.; Yang, W.; Parr, R. G. *Phys. Rev. B* **1988**, *37*, 785.
- (28) Grimme, S.; Antony, J.; Ehrlich, S.; Krieg, H. *J. Chem. Phys.* **2010**, *132*, 154104
- (29) Lenthe, E. v.; Baerends, E. J.; Snijders, J. G. *J. Chem. Phys.* **1993**, *99*, 4597-4610.
- (30) Lenthe, E. v.; Ehlers, A.; Baerends, E.-J. *J. Chem. Phys.* **1999**, *110*, 8943-8953.
- (31) van Wüllen, C. *J. Chem. Phys.* **1998**, *109*, 392-399.
- (32) Pantazis, D. A.; Chen, X. Y.; Landis, C. R.; Neese, F. *J. Chem. Theory Comp.* **2008**, *4*, 908-919.
- (33) Neese, F.; Wennmohs, F.; Hansen, A.; Becker, U. *Chem. Phys.* **2009**, *356*, 98-109.
- (34)
- (35) Cox, N.; Ames, W.; Epel, B.; Kulik, L. V.; Rapatskiy, L.; Neese, F.; Messinger, J.; Wieghardt, K.; Lubitz, W. *Inorg. Chem.* **2011**, *50*, 8238-8251.
- (36) Klamt, A.; Schuurman, D. *J. Chem. Soc., Perkin Trans. 2* **1993**, 799-805.
- (37) Sinnecker, S.; Rajendran, A.; Klamt, A.; Diedenhofen, M.; Neese, F. *J. Phys. Chem. A* **2006**, *110*, 2235-2245.

- (38) Sage, J. T.; Xia, Y. M.; Debrunner, P. G.; Keough, D. T.; De Jersey, J.; Zerner, B. *J. Am. Chem. Soc.* **1989**, *111*, 7239-7247.
- (39) Bencini, A.; Gatteschi, D. *EPR of Exchange Coupled Systems*; Springer-Verlag: Berlin, 1990.
- (40) Kulik, L. V.; Epel, B.; Lubitz, W.; Messinger, J. *J. Am. Chem. Soc.* **2007**, *129*, 13421-13435.
- (41) Schosseler, P.; Wacker, T.; Schweiger, A. *Chem. Phys. Lett.* **1994**, *224*, 319-324.
- (42) Schweiger, A.; Jeschke, G. *Principles of Pulse Electron Paramagnetic Resonance*; Oxford University Press: Oxford, 2001.
- (43) Peloquin, J. M.; Campbell, K. A.; Randall, D. W.; Evanchik, M. A.; Pecoraro, V. L.; Armstrong, W. H.; Britt, R. D. *J. Am. Chem. Soc.* **2000**, *122*, 10926-10942.
- (44) Schäfer, K. O. Doctoral Thesis, Technische Universität, 2002.
- (45) Ames, W.; Pantazis, D. A.; Krewald, V.; Cox, N.; Lubitz, W.; Neese, F. *J. Am. Chem. Soc.* **2011**, *133*, 19743-19757.
- (46) Pantazis, D. A.; Orio, M.; Petrenko, T.; Zein, S.; Lubitz, W.; Messinger, J.; Neese, F. *Phys. Chem. Chem. Phys.* **2009**, *11*, 6788-6798.
- (47) Sinnecker, S.; Neese, F.; Noodleman, L.; Lubitz, W. *J. Am. Chem. Soc.* **2004**, *126*, 2613-2622.
- (48) Pantazis, D. A.; Orio, M.; Petrenko, T.; Zein, S.; Bill, E.; Lubitz, W.; Messinger, J.; Neese, F. *Chem. Euro. J.* **2009**, *15*, 5108-5123.
- (49) Orio, M.; Pantazis, D. A.; Petrenko, T.; Neese, F. *Inorg. Chem.* **2009**, *48*, 7251-7260.
- (50) Schinzel, S.; Kaupp, M. *Can. J. Chem.* **2009**, *87*, 1521-1539.
- (51) Tan, X. L.; Gultneh, Y.; Sarneski, J. E.; Scholes, C. P. *J. Am. Chem. Soc.* **1991**, *113*, 7853-7858.
- (52) Lucken, E. A. *Nuclear Quadrupole Coupling Constants*; Academic Press: New York, 1969.
- (53) Ames, W. M.; Larsen, S. C. *Phys. Chem. Chem. Phys.* **2009**, *11*, 8266-8274.
- (54) Jiang, F.; McCracken, J.; Peisach, J. *J. Am. Chem. Soc.* **1990**, *112*, 9035-9044.
- (55) Singh, N.; Stephenson, D. *Hyperfine Interactions* **2010**, *197*, 309-315.

APPENDIX

This part includes supporting information for three of the journal articles used in this work.

The effect of $\text{Ca}^{2+}/\text{Sr}^{2+}$ substitution on the electronic structure of the oxygen-evolving complex of photosystem II: A combined pulse ^{55}Mn -ENDOR, multi-frequency EPR and DFT study of the S_2 state

Nicholas Cox, Leonid Rapatskiy, Ji-Hu Su, Dimitrios A. Pantazis, Miwa Sugiura, Leonid Kulik, Pierre Dorlet, A. William Rutherford, Frank Neese, Alain Boussac, Wolfgang Lubitz and Johannes Messinger

SUPPORTING INFORMATION

TITLE: The effect of Ca/Sr substitution on the electronic structure of the oxygen-evolving complex of photosystem II: A combined multifrequency EPR, ^{55}Mn -ENDOR and DFT study of the S_2 state

AUTHORS: Nicholas Cox*, Leonid Rapatskiy, Ji-Hu Su, Dimitrios A. Pantazis, Miwa Sugiura, Leonid Kulik, Pierre Dorlet, A. William Rutherford, Frank Neese, Alain Boussac, Wolfgang Lubitz* and Johannes Messinger*

CORRESPONDING AUTHOR: Nicholas Cox, email: cox@mpi-muelheim.mpg.de, telephone: (+49)-208-306-3865; Wolfgang Lubitz, email: lubitz@mpi-muelheim.mpg.de, telephone: (+49)-208-306-3611; Johannes Messinger, email: johannes.messinger@chem.umu.se, telephone: (+46)-90-7865933.

SUPPORTING INFORMATION S1 – ADDITIONAL THEORY (SECTION 3)

S1.1 The spin manifold. A mapping of the spin subspace in section 3.2 to the original basis set as described in section 3.1 can be made. This allows the intrinsic g and hyperfine tensors of the four Mn ions (g_i, a_i , see eq. 2) to be calculated from the effective \mathbf{G} and hyperfine tensors (\mathbf{A} , see eq. 4). Here we consider only the electronic component of the basis functions. We adopted the coupling scheme: $|S_1 S_2 S_{12} S_3 S_4 S_{34} S M\rangle$, or more succinctly $|S_{12} S_{34} S M\rangle$, where $|S_1 - S_2| \leq S_{12} \leq |S_1 + S_2|$, $|S_3 - S_4| \leq S_{34} \leq |S_3 + S_4|$, and $|S_{12} - S_{34}| \leq S \leq |S_{12} + S_{34}|$. It can be readily shown that the $S = 1/2$ doublet has contributions from up to seven basis states of total spin $S = 1/2$, listed in the appendix, if only an isotropic exchange interaction between the four Mn is considered.

The contribution of each basis state to the ground state doublet is dependent on the coupling scheme. Here we consider that the electronic exchange term of the Spin Hamiltonian takes the form of a series of pair-wise interactions i.e.

$$H = - \sum_{i < j} J_{ij} S_i \cdot S_j \quad (\text{Eq. S1})$$

Expressions for all matrix elements of the Spin Hamiltonian are given in the supporting information S1. The matrix elements are given in generalized operator notation. The matrix is block diagonal. States of the same total spin appear in the same block.

Scaling factors can be calculated that describe the contribution of each of the Mn ions to a particular total spin state. These scaling factors are called spin projections. The projection of the total spin onto the individual Mn centers is defined as the ratio of the on-site spin expectation value $\langle S_Z^i \rangle$ of the i^{th} Mn to the ‘total spin’ $\langle S_Z \rangle$ ^{1,2}:

$$\rho_i = \frac{\langle S_Z^i \rangle}{\langle S_Z \rangle} \quad (\text{Eq. S2})$$

For the $S = 1/2$ electronic spin-manifold the expectation value of the spin operator $\langle S_Z \rangle$ is $1/2$ and thus

Eq. 6 can re-expressed as:

$$\rho_i = 2 \cdot \langle S_Z^i \rangle \quad (\text{Eq. S3})$$

Analytical expressions for the spin projections ρ_i can be calculated using generalized operator notation as per the methodology outlined in chapter 3 of Bencini and Gatteschi³. These are given in the supporting information S2. The spin projections (ρ_i) now allow us to relate the effective isotropic G and hyperfine values to the intrinsic isotropic g and hyperfine values of the individual four Mn ions. It can be shown that the effective isotropic G and hyperfine values are a weighted linear sum of the intrinsic hyperfine values of the individual Mn ions (Eq. S4).

$$\begin{aligned} G &= \rho_1 g_1 + \rho_2 g_2 + \rho_3 g_3 + \rho_4 g_4 \\ A_1 &= \rho_1 a_1 \\ A_2 &= \rho_2 a_2 \\ A_3 &= \rho_3 a_3 \\ A_4 &= \rho_4 a_4 \end{aligned} \quad (\text{Eq. S4})$$

Where the weighting factor (ρ_i), corresponds to the projection of the total spin onto Mn_i .

S.1.2 Inclusion of the Zero-field Splitting (ZFS) of Mn^{III} . The spin projections calculated above can be corrected for the zero-field splitting (ZFS) of the only Mn^{III} ion of the Mn_4O_xCa cluster in the S_2 state.

$$H = - \sum_{i < j} J_{ij} S_i \cdot S_j + S_j \cdot d_j \cdot S_j \quad (\text{Eq. S5})$$

Where the j^{th} spin operator (S_j) refers to the Mn^{III} ion and d_j , is its corresponding fine structure tensor. The fine structure tensor is assumed to be axial and can thus be expressed in terms of a single parameter

(d):

$$d_j = \begin{bmatrix} -\frac{1}{3}d & 0 & 0 \\ 0 & -\frac{1}{3}d & 0 \\ 0 & 0 & \frac{2}{3}d \end{bmatrix} \quad (\text{Eq. S6})$$

The inclusion of the ZFS of the Mn^{III} requires the spin projections (ρ_i) to be expressed as a tensor as opposed to a scalar quantity. As we assume that all pair-wise exchange couplings (J_{ij}) are isotropic and that the fine structure tensor of the Mn^{III} is axial, the spin projection tensor of the i^{th} Mn can be expressed as a diagonal matrix of the form:

$$\rho_i = \begin{bmatrix} \rho_{\perp_i} & 0 & 0 \\ 0 & \rho_{\perp_i} & 0 \\ 0 & 0 & \rho_{\parallel_i} \end{bmatrix} \quad (\text{Eq. S7})$$

The effective \mathbf{G} and hyperfine tensors (\mathbf{A}_i) are a weighted, linear sum of the intrinsic \mathbf{g} and hyperfine tensors (\mathbf{a}_i) of the individual Mn ions as described above, (see Eq. S4).

S.1.3 Hyperfine couplings from broken-symmetry DFT. A quantum chemical approach that allows the extraction of hyperfine coupling constants (HFCs) from BS-DFT calculations of oligonuclear exchange-coupled clusters was developed recently⁴ and has been already applied to candidate models of the OEC.² The approach was shown to lead to predicted ^{55}Mn HFCs that can be meaningfully compared with experimental values and that can be used to distinguish between different cluster topologies and ligand environments of the Mn centers. Since the methodology has been previously described in detail,⁴ here we will only highlight the main concepts. Considering the system under study as composed of metal-centered subsystems, with nucleus K belonging to subsystem A, the general equation that directly connects the BS calculation to the observable HFC is

$$A_{\text{iso}}^{(\text{K})} = A_{\text{iso,site}}^{(\text{K})} \left(\frac{\langle S_z^{(\text{A})} \rangle}{S_t} \right) \quad (\text{Eq. S8})$$

where S_t is the effective total spin (1/2), $\langle S_z^{(\text{A})} \rangle$ is the on-site spin expectation value and $A_{\text{iso,site}}^{(\text{K})}$ is the site isotropic coupling constant

$$A_{\text{iso,site}}^{(\text{A})} = \pm A_{\text{iso,BS}}^{(\text{A})} \left(\frac{\langle S_z \rangle_{\text{BS}}}{S_A} \right) \quad (\text{Eq. S9})$$

S_A is the site-spin of subsystem A and the positive or negative sign depends on whether the fragment carries majority or minority spin. $\langle S_z \rangle_{\text{BS}}$ is the total M_S of the BS wavefunction and $A_{\text{iso,BS}}^{(\text{K})}$ the “raw” hyperfine coupling constant calculated directly from the BS calculation. The final projection of the site isotropic coupling constant into the correct effective HFC requires the determination of the site spin expectation value $\langle S_z^{(\text{A})} \rangle$, which for a given subsystem A is given by

$$\langle S_z^{(\text{A})} \rangle = \sum_{S_A M_{S_A} \dots S_N M_{S_N}} \left| C_I^{S_A M_{S_A} \dots S_N M_{S_N}} \right|^2 M_{S_A} \quad (\text{Eq. S10})$$

where $\left| C_I^{S_A M_{S_A} \dots S_N M_{S_N}} \right|^2$ is the weight of the basis state $\left| S_A M_{S_A}, \dots, S_N M_{S_N} \right\rangle$ in the ground-state eigenfunction describing the lowest-energy Kramers doublet. The TPSSh functional is also used in the calculation of effective ^{55}Mn HFCs for the models considered in the present study, following previous applications that established the reliability of the approach and the necessary scaling factors for the isotropic couplings.^{2,4,5} To ensure the accuracy of the results, the size of the integration grid was increased to “7” (ORCA convention) for the manganese atoms.

SUPPORTING INFORMATION S2 – SPIN PROJECTIONS

Spin projections were calculated as per the methodology outlined in chapter 3 of Bencini and Gatteschi³. We adopted the coupling scheme: $|S_1 S_2 S_{12} S_3 S_4 S_{34} S M\rangle$, or more succinctly $|S_{12} S_{34} S M\rangle$, where $|S_1 - S_2| \leq S_{12} \leq |S_1 + S_2|$, $|S_3 - S_4| \leq S_{34} \leq |S_3 + S_4|$, and $|S_{12} - S_{34}| \leq S \leq |S_{12} + S_{34}|$

The resultant basis set, for the subset where $S = \frac{1}{2}$ and assuming (S_1, S_2, S_3, S_4) is $(\frac{3}{2}, \frac{3}{2}, \frac{3}{2}, 2)$ or $(\frac{3}{2}, \frac{3}{2}, 2, \frac{3}{2})$ is:

$$\begin{array}{lll} |0 \frac{1}{2} \frac{1}{2} M\rangle & |2 \frac{3}{2} \frac{1}{2} M\rangle & |3 \frac{7}{2} \frac{1}{2} M\rangle \\ |1 \frac{1}{2} \frac{1}{2} M\rangle & |2 \frac{5}{2} \frac{1}{2} M\rangle & \\ |1 \frac{3}{2} \frac{1}{2} M\rangle & |3 \frac{5}{2} \frac{1}{2} M\rangle & \end{array}$$

Where M takes all half-integer values: $-\frac{1}{2} \leq M \leq \frac{1}{2}$

The complete set of basis vectors can be found in Table S1:

Table S2.1. Table of eigenstates $|S_{12} S_{34} S M\rangle$. M takes all half-integer values: $-S \leq M \leq S$, for each entry.

S		S ₁₂			
		0	1	2	3
S ₃₄	$\frac{1}{2}$	$\frac{1}{2}$	$\frac{1}{2}, \frac{3}{2}$	$\frac{3}{2}, \frac{5}{2}$	$\frac{5}{2}, \frac{7}{2}$
	$\frac{3}{2}$	$\frac{3}{2}$	$\frac{1}{2}, \frac{3}{2}, \frac{5}{2}$	$\frac{1}{2}, \frac{3}{2}, \frac{5}{2}, \frac{7}{2}$	$\frac{3}{2}, \frac{5}{2}, \frac{7}{2}, \frac{9}{2}$
	$\frac{5}{2}$	$\frac{5}{2}$	$\frac{3}{2}, \frac{5}{2}, \frac{7}{2}$	$\frac{1}{2}, \frac{3}{2}, \frac{5}{2}, \frac{7}{2}, \frac{9}{2}$	$\frac{1}{2}, \frac{3}{2}, \frac{5}{2}, \frac{7}{2}, \frac{9}{2}, \frac{11}{2}$
	$\frac{7}{2}$	$\frac{7}{2}$	$\frac{5}{2}, \frac{7}{2}, \frac{9}{2}$	$\frac{3}{2}, \frac{5}{2}, \frac{7}{2}, \frac{9}{2}, \frac{11}{2}$	$\frac{1}{2}, \frac{3}{2}, \frac{5}{2}, \frac{7}{2}, \frac{9}{2}, \frac{11}{2}, \frac{13}{2}$

The Spin Hamiltonian for the system takes the form of a series of pairwise interactions i.e.

$$H = \sum_{i < j} J_{ij} S_i \cdot S_j$$

Which can be re-expressed in generalized operator form:

$$H = \sum_k \sqrt{2k+1} \cdot O_k(k_1 \ k_2 \ k_{12} \ k_3 \ k_4 \ k_{34} \ k) \cdot \left\{ \{T_{k1}(S_1) \otimes T_{k2}(S_2)\}_{k_{12}} \otimes \{T_{k3}(S_3) \otimes T_{k4}(S_4)\}_{k_{34}} \right\}_k \\ = \sum_k \sqrt{2k+1} \cdot O_k(k_1 \ k_2 \ k_{12} \ k_3 \ k_4 \ k_{34} \ k) \cdot X_k(k_1 \ k_2 \ k_{12} \ k_3 \ k_4 \ k_{34} \ k)$$

Where O_k corresponds to the scalar exchange coupling term J i.e.

$$O_k(k_1 \ k_2 \ k_{12} \ k_3 \ k_4 \ k_{34} \ k) = -\sqrt{3} J_{ij};$$

$$\text{i.e. } O_0(1100000) = -\sqrt{3} J_{12}, O_0(1011010) = -\sqrt{3} J_{12} \text{ etc}$$

And the matrix elements X_k correspond to:

$$\langle S_1 S_2 S_{12} S_3 S_{34} S M | X_k | S_1 S_2 S'_{12} S_3 S'_{34} S M \rangle = (-1)^{S-M} \begin{pmatrix} S & k & S \\ -M & q & M \end{pmatrix} \cdot \langle S_1 S_2 S_{12} S_3 S_{34} S | X_k | S_1 S_2 S'_{12} S_3 S'_{34} S \rangle$$

The reduced matrix elements can be calculated using:

$$\langle S_1 S_2 S_{12} S_3 S_{34} S | X_k | S_1 S_2 S'_{12} S_3 S'_{34} S \rangle = (2S+1) \sqrt{(2k_{12}+1)(2S_{12}+1)(2S'_{12}+1)(2k_{34}+1)(2S_{34}+1)(2S'_{34}+1)} \\ \cdot \begin{Bmatrix} S_{12} & S'_{12} & k_{12} \\ S_{34} & S'_{34} & k_{34} \\ S & S & k \end{Bmatrix} \cdot \begin{Bmatrix} S_1 & S_1 & k_1 \\ S_2 & S_2 & k_2 \\ S_{12} & S'_{12} & k_{12} \end{Bmatrix} \cdot \begin{Bmatrix} S_3 & S_3 & k_3 \\ S_4 & S_4 & k_4 \\ S_{34} & S'_{34} & k_{34} \end{Bmatrix} \\ \cdot \langle S_1 | T_{k1} | S_1 \rangle \cdot \langle S_2 | T_{k2} | S_2 \rangle \cdot \langle S_3 | T_{k3} | S_3 \rangle \cdot \langle S_4 | T_{k4} | S_4 \rangle$$

The six reduced matrix elements corresponding to the six pair-wise interactions, that the form:

$$\langle S_1 S_2 S_{12} S_3 S_{34} S \| X_0(1100000) \| S_1 S_2 S'_{12} S_3 S'_{34} S \rangle = \frac{\delta_{S_{12} S'_{12}} \delta_{S_{34} S'_{34}}}{2} \sqrt{\frac{(2S+1)}{3}} [S_1(S_1+1) + S_2(S_2+1) - S_{12}(S_{12}+1)]$$

$$\langle S_1 S_2 S_{12} S_3 S_{34} S \| X_0(1011010) \| S_1 S_2 S'_{12} S_3 S'_{34} S \rangle = \frac{(-1)^{3(S_1+S_2+S_3+S_4+S_{34})+2(S_{12}+S'_{12})+S'_{34}+S}}{\sqrt{3}} \sqrt{(2S+1)(2S_{12}+1)(2S'_{12}+1)(2S_{34}+1)(2S'_{34}+1)} \cdot \sqrt{(2S_1+1)S_1(S_1+1)(2S_3+1)S_3(S_3+1)} \cdot \begin{Bmatrix} S_{12} & S'_{12} & 1 \\ S_{34} & S'_{34} & S \end{Bmatrix} \cdot \begin{Bmatrix} S_1 & S_1 & 1 \\ S'_{12} & S_{12} & S_2 \end{Bmatrix} \cdot \begin{Bmatrix} S_3 & S_3 & 1 \\ S'_{34} & S_{34} & S_4 \end{Bmatrix}$$

$$\langle S_1 S_2 S_{12} S_3 S_{34} S \| X_0(1010110) \| S_1 S_2 S'_{12} S_3 S'_{34} S \rangle = \frac{(-1)^{3(S_1+S_2+S_3+S_4)+2(S_{12}+S'_{12}+S_{34}+S'_{34})+S}}{\sqrt{3}} \sqrt{(2S+1)(2S_{12}+1)(2S'_{12}+1)(2S_{34}+1)(2S'_{34}+1)} \cdot \sqrt{(2S_1+1)S_1(S_1+1)(2S_4+1)S_4(S_4+1)} \cdot \begin{Bmatrix} S_{12} & S'_{12} & 1 \\ S_{34} & S'_{34} & S \end{Bmatrix} \cdot \begin{Bmatrix} S_1 & S_1 & 1 \\ S'_{12} & S_{12} & S_2 \end{Bmatrix} \cdot \begin{Bmatrix} S_4 & S_4 & 1 \\ S'_{34} & S_{34} & S_3 \end{Bmatrix}$$

$$\langle S_1 S_2 S_{12} S_3 S_{34} S \| X_0(0111010) \| S_1 S_2 S'_{12} S_3 S'_{34} S \rangle = \frac{(-1)^{3(S_1+S_2+S_3+S_4+S_{12}+S'_{34})+S'_{12}+S_{34}+S}}{\sqrt{3}} \sqrt{(2S+1)(2S_{12}+1)(2S'_{12}+1)(2S_{34}+1)(2S'_{34}+1)} \cdot \sqrt{(2S_2+1)S_2(S_2+1)(2S_3+1)S_3(S_3+1)} \cdot \begin{Bmatrix} S_{12} & S'_{12} & 1 \\ S_{34} & S'_{34} & S \end{Bmatrix} \cdot \begin{Bmatrix} S_2 & S_2 & 1 \\ S'_{12} & S_{12} & S_1 \end{Bmatrix} \cdot \begin{Bmatrix} S_3 & S_3 & 1 \\ S'_{34} & S_{34} & S_4 \end{Bmatrix}$$

$$\langle S_1 S_2 S_{12} S_3 S_{34} S \| X_0(0111010) \| S_1 S_2 S'_{12} S_3 S'_{34} S \rangle = \frac{(-1)^{3(S_1+S_2+S_3+S_4+S_{12}+S'_{34})+S'_{12}+S_{34}+S}}{\sqrt{3}} \sqrt{(2S+1)(2S_{12}+1)(2S'_{12}+1)(2S_{34}+1)(2S'_{34}+1)} \cdot \sqrt{(2S_2+1)S_2(S_2+1)(2S_4+1)S_4(S_4+1)} \cdot \begin{Bmatrix} S_{12} & S'_{12} & 1 \\ S_{34} & S'_{34} & S \end{Bmatrix} \cdot \begin{Bmatrix} S_2 & S_2 & 1 \\ S'_{12} & S_{12} & S_1 \end{Bmatrix} \cdot \begin{Bmatrix} S_3 & S_3 & 1 \\ S'_{34} & S_{34} & S_4 \end{Bmatrix}$$

$$\langle S_1 S_2 S_{12} S_3 S_{34} S \| X_0(0001100) \| S_1 S_2 S'_{12} S_3 S'_{34} S \rangle = \frac{\delta_{S_{12} S'_{12}} \delta_{S_{34} S'_{34}}}{2} \sqrt{\frac{(2S+1)}{3}} [S_3(S_3+1) + S_4(S_4+1) - S_{34}(S_{34}+1)]$$

The resulting matrix is block diagonal; only terms with the same total spin mix.

The projection of the total spin onto the individual Mn ions can be calculated in a similar manner using the Wigner Echart Theorem. This reduced to calculating the matrix elements X_k , where X_k now refers to the spin operators S_x ($x = 1, 2, 3$ or 4). For instance, for $X_k = T_1(S_1)$:

$$\langle S_1 S_2 S_{12} S_3 S_{34} S \| T_1(S_1) \| S_1 S_2 S'_{12} S_3 S'_{34} S \rangle = (-1)^{(S_1+S_2+S_{12}+S'_{12}+S_{34}+S)} \delta_{S_{34} S'_{34}} (2S+1) \sqrt{(2S_{12}+1)(2S'_{12}+1)(2S_1+1)S_1(S_1+1)} \cdot \begin{Bmatrix} S_{12} & S'_{12} & 1 \\ S & S & S_{34} \end{Bmatrix} \cdot \begin{Bmatrix} S_1 & S_1 & 1 \\ S'_{12} & S_{12} & S_2 \end{Bmatrix}$$

The ratio of the matrix element $\langle \dots \| X_k \| \dots \rangle$ to the expectation value of the total spin $\langle \dots \| S \| \dots \rangle$ then yields the spin projection number (c_k) for each Mn center.

$$c_1 = \frac{\langle S_1 S_2 S_{12} S_3 S_{34} S \| T_1(S_1) \| S_1 S_2 S'_{12} S_3 S'_{34} S \rangle}{\langle S_1 S_2 S_{12} S_3 S_{34} S \| T_1(S) \| S_1 S_2 S'_{12} S_3 S'_{34} S \rangle} = (-1)^{(S_1+S_2+S_{12}+S'_{12}+S_{34}+S)} \delta_{S_{34} S'_{34}} \frac{\sqrt{(2S+1)(2S_{12}+1)(2S'_{12}+1)(2S_1+1)S_1(S_1+1)}}{\sqrt{S(S+1)}} \cdot \begin{Bmatrix} S_{12} & S'_{12} & 1 \\ S & S & S_{34} \end{Bmatrix} \cdot \begin{Bmatrix} S_1 & S_1 & 1 \\ S'_{12} & S_{12} & S_2 \end{Bmatrix}$$

$$c_2 = \frac{\langle S_1 S_2 S_{12} S_3 S_{34} S \| T_1(S_2) \| S_1 S_2 S'_{12} S_3 S'_{34} S \rangle}{\langle S_1 S_2 S_{12} S_3 S_{34} S \| T_1(S) \| S_1 S_2 S'_{12} S_3 S'_{34} S \rangle} = (-1)^{(S_1 + S_2 + 2S_{12} + 2S'_{12} + S_{34} + S)}$$

$$\delta_{S_{34} S'_{34}} \frac{\sqrt{(2S+1)(2S_{12}+1)(2S'_{12}+1)(2S_2+1)S_2(S_2+1)}}{\sqrt{S(S+1)}} \begin{Bmatrix} S_{12} & S'_{12} & 1 \\ S & S & S_{34} \end{Bmatrix} \cdot \begin{Bmatrix} S_2 & S_2 & 1 \\ S'_{12} & S_{12} & S_1 \end{Bmatrix}$$

$$c_3 = \frac{\langle S_1 S_2 S_{12} S_3 S_{34} S \| T_1(S_3) \| S_1 S_2 S'_{12} S_3 S'_{34} S \rangle}{\langle S_1 S_2 S_{12} S_3 S_{34} S \| T_1(S) \| S_1 S_2 S'_{12} S_3 S'_{34} S \rangle} = (-1)^{(S_3 + S_4 + S_{12} + 2S'_{34} + 2S_{34} + S)}$$

$$\delta_{S_{12} S'_{12}} \frac{\sqrt{(2S+1)(2S_{34}+1)(2S'_{34}+1)(2S_3+1)S_3(S_3+1)}}{\sqrt{S(S+1)}} \begin{Bmatrix} S_{34} & S'_{34} & 1 \\ S & S & S_{12} \end{Bmatrix} \cdot \begin{Bmatrix} S_3 & S_3 & 1 \\ S'_{34} & S_{34} & S_4 \end{Bmatrix}$$

$$c_4 = \frac{\langle S_1 S_2 S_{12} S_3 S_{34} S \| T_1(S_4) \| S_1 S_2 S'_{12} S_3 S'_{34} S \rangle}{\langle S_1 S_2 S_{12} S_3 S_{34} S \| T_1(S) \| S_1 S_2 S'_{12} S_3 S'_{34} S \rangle} = (-1)^{(S_3 + S_4 + S_{12} + 2S'_{34} + S_{34} + S)}$$

$$\delta_{S_{12} S'_{12}} \frac{\sqrt{(2S+1)(2S_{34}+1)(2S'_{34}+1)(2S_4+1)S_4(S_4+1)}}{\sqrt{S(S+1)}} \begin{Bmatrix} S_{34} & S'_{34} & 1 \\ S & S & S_{12} \end{Bmatrix} \cdot \begin{Bmatrix} S_4 & S_4 & 1 \\ S'_{34} & S_{34} & S_3 \end{Bmatrix}$$

For an arbitrary coupling scheme, the basis eigenstates take the form:

$$\Psi_a = \sum_{S_{12}} \sum_{S_{34}} C_{S_{12} S_{34}} |S_1 S_2 S_{12} S_3 S_{34} S\rangle$$

Thus, the calculation of the spin projection value requires the weighted sum over all matrix elements:

$$c_k = \sum_{S_{12}} \sum_{S_{34}} C_{S_{12} S_{34}} C_{S'_{12} S'_{34}} \frac{\langle S_1 S_2 S'_{12} S_3 S'_{34} S \| X_k \| S_1 S_2 S_{12} S_3 S_{34} S \rangle}{\langle S_1 S_2 S'_{12} S_3 S'_{34} S \| S \| S_1 S_2 S_{12} S_3 S_{34} S \rangle}$$

SUPPORTING INFORMATION S3: The magnetic field dependence of the ^{55}Mn -ENDOR spectra of the free Mn^{2+} artifact.

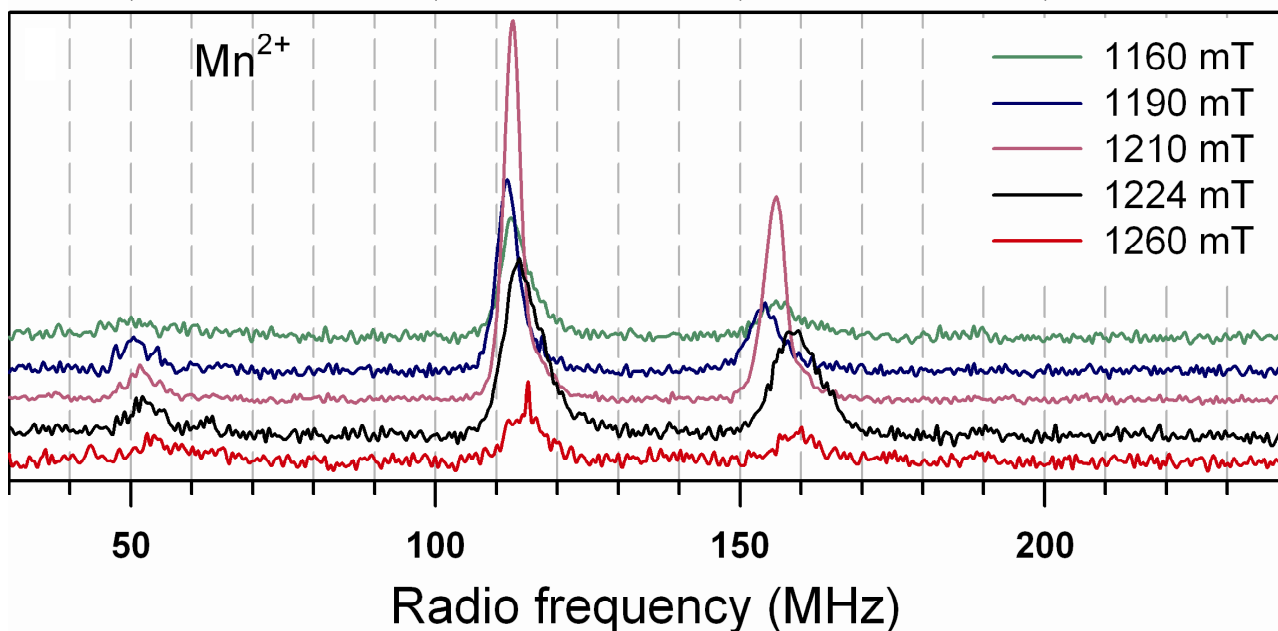


Figure S3. The field dependence of Q-band pulse ^{55}Mn Davies ENDOR of denatured (heat treatment) spinach PSII sample. The EPR settings are the same as described in the main text. Mn^{2+} has two characteristic peaks located the RF of ~ 114 MHz, ~ 158 MHz and at 375 MHz (not shown) under these experimental conditions described in Figure caption 2, see also ref⁶⁻⁸.

Mn^{2+} fitting parameters (Fig. 2 dashed green line)

$$g_{\text{iso}} = 1.996$$

$$[A_x A_y A_z] = 92.0 \text{ G}$$

$$D = -669 \text{ MHz}, E/D = 0.212$$

Supporting Information S4 – Monomeric Mn^{III} data

Mn ^{III}		g _⊥		g _∥	D	E	a _⊥	a _∥	a _{iso}	a _{aniso}
		g _x	g _y	g _z						
Mn ^{III} in rutile (TiO ₂) ⁹		2.00		1.99	-3.4	0.116	256	158	233	-98 (-33)
Mn(H ₂ O) ₆ ³⁺¹⁰		2.000		1.984	-4.514	-0.162	261	159	197	-102 (-34)
[Mn(dbm) ₃] elongated ¹¹	Octahedral/ tetrahedral	1.99		1.87	-4.35	0.26	-		-	
[(terpy)Mn ^{III} (N ₃) ₃] elongated ¹²	Octahedral/ tetrahedral	2.00	1.98	2.01	-3.29	0.51	-		-	
[Mn(cyclam)I ₂]I elongated ¹³	Octahedral/ tetrahedral	2.00		1.99	0.604	0.034	-		-	
[Mn(bpia)(OAc)-(OCH ₃)]PF ₃ tetragonally compressed ¹⁴	Octahedral/ tetrahedral	1.981	1.952	1.978	3.526	0.589	-		-	
Mn ^{III} -Porphyrins 15-17	Mn(TPP)Cl	2.005		1.982	-2.29	0.00	-		-	
	MnPcCl	2.005		2.00	-2.31	0.00	-		-	
	Mn(ODMAP _Z)Cl	-		1.984	-2.33	~0	-		-	
	Mn(ODMAP _Z)DTC	-		1.983	-2.61	~0	-		-	
	Mn(DP-IX_DME)Cl	-		-	-2.53	~0	-		-	
	Mn(DPDME)Cl	2		2	-2.53	~0.01	-		-	
	Mn(DPDME)Br	2		2	-1.1	~0	-		-	
Mn ^{III} -Corrole ^{18,19}	(tpfc)Mn(OPPh ₃)	1.994		1.980	2.69	0.03	-		-	
	Mn ^{III} C ³⁻	2.002		-	-2.66 - - 2.78	0.13 - 0.15	-		-	
Mn-Salen ^{20,21}	+ NMO (CH ₂ Cl ₂)	2.0		1.98	-2.5	0.269	190	126	167	-64 (-21)
	+ 4-PPNO (CH ₂ Cl ₂)	2.0		1.98	-2.5	0.249	190	119	166	-71 (-24)
	HFEPR (CH ₂ Cl ₂ /toluene 3:2 v/v)	2.00		-	-2.47	0.17	-		-	
PS II Mn ^{III} bound to the high affinity site ²²		2.0		1.98	-2.5	0.269	190	123	168	-67 (-22)
MnSOD Trigonal-bipyramidal ²³		2.00	1.99	1.98	2.10	0.243	283	280	282	-2 (-1)

Monomeric Mn^{IV} data

Mn ^{IV}		g _⊥		g _∥	D	E (E/D)	a _⊥		a _∥	a _{iso}	a _{aniso}
		g _x	g _y	g _z			a _x	a _y	a _z		
Mn ^{IV} in MgO (Octahedral) ²⁴		1.994			-	-	212		212	-	
Mn ^{IV} in MgO (Tetragonal) ²⁴		1.9940		1.993 1	0.5287	-	213		213	-	
Mn ^{IV} in Al ₂ O ₃ (tetragonal distorted) ²⁵		1.993		-	-0.1957	-	209		211	210	2 (1)
Mn ^{IV} in SnO ₂ /TiO ₂ (octahedral, rhomically distorted) ^{26,27}		1.98 79	1.98 70	1.987 0	0.8818	0.2635	252	209	226	229	-26 (-1.5)
K ₂ MnCl ₆ (perfect octahedron) ²⁸		~2.00			0	0	-		-	-	
[Mn(MePH) ₃]PF ₆ ²⁹		~2.00			<<0.31	-	266		-	-	
Mn ^{IV} tridentate ONO ligands ³⁰	[Mn ^{IV} (azpSS) ₂] ⁴⁻	2.01			0.0115	-	272		-	-	
	[Mn ^{IV} (□mps) ₂] ⁴⁻	2.00			0.0116	-	272		-	-	
	[Mn ^{IV} (azpSa) ₂] ⁴⁻	2.03			0.0117	-	263		-	-	
	[Mn ^{IV} (azpSb) ₂] ⁴⁻	2.02			0.0117	-	272		-	-	
Schiff base (N ₂ O ₂ coordination environment) ³¹⁻³³	Mn(SALAHE) ₂ .2H ₂ O	g _{eff} 5.45			>>0.31	(0.32)	-		-	-	
	Mn(SALAHF) ₂ .3H ₂ O	g _{eff} 5.91			>>0.31	(0.07)	216		216	-	
	Mn(SALAHF) ₂ .2DMF	g _{eff} 5.15, 4.38, 1.96			>>0.31	(0.22)	-		-	-	
	Mn(SALATHM) ₂ .H ₂ O	g _{eff} 4.32			>>0.31	(0.06)	-		-	-	
	Mn(SALAPDH) ₂ .DMF	g _{eff} 4.98			>>0.31	(0.19)	-		-	-	
	Mn(L) ₂ .2THF (2 phenolic O)	g _{eff} ~ 4.0			>>0.31	~0	-		-	-	
	Mn(als) ₂ (carbox ligand)	g _{eff} ~ 3.86, 2.02			>>0.31	~0	a _{av} ~ 216		216	-	
Mn(salen) ³⁴		g _{eff} ~ 5.02			>>0.31	-	210		210	-	
[Mn ^{IV} H ₃ burea(O)] ⁻ (terminal oxo) ³⁵		g _{eff} ~ 5.15, 2.44, 1.63			3.0	(0.26)	190		190	-	
Mn ^{IV} (dbpip) ₂ (N ₂ O ₂ coordination environment) ³⁶		~2.00			<<0.31		-		-	-	
[Mn ^{IV} (HIB) ₃] ²⁻ (hydroxyl acid ligands) ³⁷		g _{eff} ~ 3.9 (crossover)			>>0.31	0.05	198		198	-	
[Mn ^{IV} Br(T _{piv} PP)] (Mn-porphyrins) ³⁸		g _{eff} ~ 4.0			>>0.31	~0	-		-	-	

Mn^{III}Mn^{IV} mixed valance complexes

Mn ^{III} Mn ^{IV} complexes		g _⊥		g _∥	a _⊥		a _∥	a _{iso}	a _{aniso}
		g _x	g _y	g _z	a _x	a _y	a _z		
[(phen) ₂ Mn ^{III} O ₂ -Mn ^{IV} (phen) ₂](ClO ₄) ₃ (J = -150 cm ⁻¹) ³⁹	Mn ^{III}	-	-	-	245		189	227	-56 (-18.6)
	Mn ^{IV}	-	-	-	-	-	-	-	-
[Mn ^{III} Mn ^{IV} O ₂ (OAc)(HB(pz) ₃) ₂] (J < -150 cm ⁻¹) ³⁹	Mn ^{III}				228		163	206	65 (-21.7)
	Mn ^{IV}	-	-	-	-	-	-	-	-
[(phen) ₂ Mn ^{III} O ₂ -Mn ^{IV} (phen) ₂](ClO ₄) ₃ (J = -150 cm ⁻¹) ^{40a}	Mn ^{III}	-	-	-	237 to 249		178 to 187	220	-59 (-19.7) to -62 (-20.7)
	Mn ^{IV}	-	-	-	208 to 229		226 to 249	218	18 (6) to 20 (7)
Mn ^{III} Mn ^{IV} -[2-OH-3,5-Cl ₂ -salpn] ₂ (THF)(ClO ₄) (J = -10 cm ⁻¹) ^{40a}	Mn ^{III}	-	-	-	-	-	-	170-180	60 (20) to 30 (10)
	Mn ^{IV}	-	-	-	-	-	-	200-210	15 (5) to -27 (-9)
[Mn ^{III} Mn ^{IV} (μ-O) ₂ bipy ₄](ClO ₄) (BIPY) (J = -144 to -150 cm ⁻¹) ^{41,42b}	Mn ^{III}	1.991	1.988	1.984	253	242	183	226	-70 (-21.5)
	Mn ^{IV}	1.988	1.987	1.991	214	219	223	219	9 (2.2)
[Mn ^{III} Mn ^{IV} (μ-O) ₂ (μ-OAc)tacn ₂]BPh ₄ (TACN) (J = -110 cm ⁻¹) ^{41,42b}	Mn ^{III}	1.995	1.994	1.988	209	233	143	195	-90 (-26.0)
	Mn ^{IV}	1.988	1.987	1.991	227	198	213	213	15 (0.2)
[Mn ^{III} Mn ^{IV} (μ-O) ₂ (μ-OAc)dtne]BPh ₄ (DTNE) (J = -110 cm ⁻¹) ^{41,42b}	Mn ^{III}	1.995	1.992	1.987	212	238	144	198	-94 (-27.0)
	Mn ^{IV}	1.988	1.987	1.991	227	199	201	209	-26 (-4.0)
[Mn ^{III} Mn ^{IV} (μ-O) ₂ (μ-OAc)Me ₄ dtne]BPh ₄ (MDTN) (J = -130 cm ⁻¹) ^{41,42b}	Mn ^{III}	1.995	1.992	1.987	212	244	153	203	-51 (-25.0)
	Mn ^{IV}	1.988	1.987	1.991	226	198	206	210	-20 (-2)
MnCat 1 (J < -175 cm ⁻¹) ³⁹	Mn ^{III}	-	-	-	245		157	192	-88 (-29.3)
	Mn ^{IV}	-	-	-	-	-	-	-	-
MnCat 2 (J < -175 cm ⁻¹) ^{41,42b}	Mn ^{III}	1.996	1.995	1.989	215	208	147	190	-68 (21.5)
	Mn ^{IV}	1.988	1.987	1.991	228	237	245	237	17 (4.2)

^aUsing the range of acceptable D values (see Peloquin et al.⁴⁰ Fig. 4); ^bUsing the literature D values of Gerristen et al.⁹ and From et al.²⁷ (see table 4.4 Schäfer doctoral thesis⁴¹)

SUPPORTING INFORMATION S5

Table S5.1. Pair-wise exchange coupling constants J (cm^{-1}) for the literature coupling schemes referred to in the text (assuming $-JS_iS_j$ convention).

	J_{AB}	J_{AC}	J_{AD}	J_{BC}	J_{BD}	J_{CD}
Kulik (1) ⁴³	-180	0	0	-52	-5	-42
Kulik (3) ⁴³	-117	0	0	-40	-12	-32
Peloquin (3) ⁴⁰	-115	0	0	-150	0	-15
Peloquin (4) ⁴⁰	-150	0	0	-150	0	-16
Pantazis (1) – EXAFS I ²	-94	10	-2	-18	24	-86
Pantazis (2) – EXAFS II ²	-2	6	-2	-16	24	2
Pantazis (3) – EXAFS IIb ²	0	6	0	-12	22	-36
Pantazis (4) – EXAFS III ²	-20	0	-2	14	-16	-74
Pantazis (5) – EXAFS III ²	-6	0	-4	-6	-16	-54
Pantazis (10) – EXAFS III ²	-4	-2	-8	10	-52	28
Pantazis (11) – Siegbahn ²	-16	6	20	30	18	-68

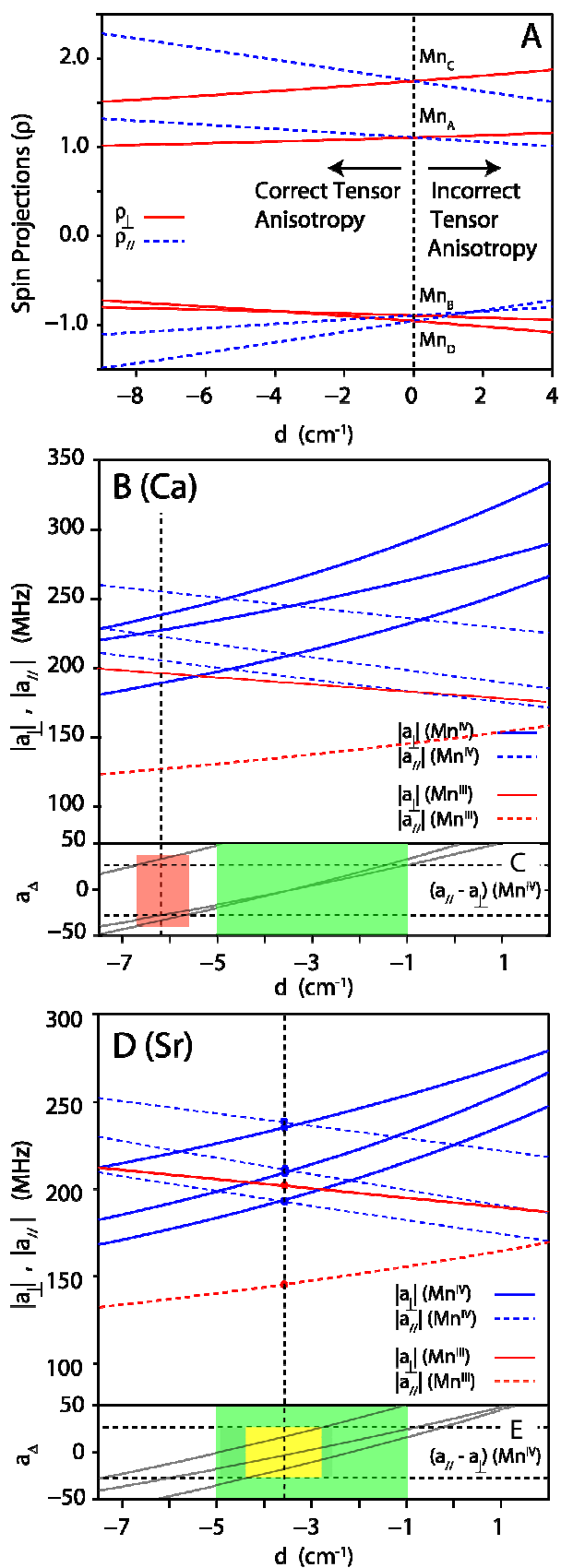


Figure S5. Panel A: The dependence of the spin projection (ρ_{\perp} , ρ_{\parallel}) on the zero-field splitting parameter (d) of the Mn^{III} ion assuming the EXAFS I core exchange coupling (scheme Fig. 1F). Tile B: The dependence of the on-site hyperfine tensor components (a_{\perp} , a_{\parallel}) of the $\text{Mn}_4\text{O}_x\text{Ca}$ cluster for each of the four manganese ions on the zero-field splitting parameter (d) of the Mn^{III} ion (see text). The bottom panel (C) shows the difference (a_{Δ}) between the parallel (a_{\parallel} or a_z) and perpendicular (a_{\perp} or a_x , a_y) hyperfine components of the three Mn^{IV} ions. The green shaded region represents the range of ZFS values for the Mn^{III} seen in model complexes (when $d < 0$). The red shaded region represents the range of acceptable ZFS values for the Mn^{III} which are consistent with the electronic model i.e. the range over which the intrinsic hyperfine anisotropy of the Mn^{IV} ions are within the range seen for model complexes. Their intersection is shown by the orange shaded region. Panels D and E are exactly the same as tiles B and C, except that here the Sr containing OEC was examined. Table 5 lists the intrinsic hyperfine tensor components for all four Mn ions calculated at the mid-point of the range of consistent d values i.e. the yellow shaded region.

REFERENCE LIST

- (1) Charlot, M.-F.; Boussac, A.; Blondin, G. *Biochim. Biophys. Acta* **2005**, *1708*, 120-132.
- (2) Pantazis, D. A.; Orio, M.; Petrenko, T.; Zein, S.; Lubitz, W.; Messinger, J.; Neese, F. *Phys. Chem. Chem. Phys.* **2009**, *11*, 6788-6798.
- (3) Bencini, A.; Gatteschi, D. *EPR of Exchange Coupled Systems*; Springer-Verlag: Berlin, 1990.
- (4) Pantazis, D. A.; Orio, M.; Petrenko, T.; Zein, S.; Bill, E.; Lubitz, W.; Messinger, J.; Neese, F. *Chem.-Eur. J.* **2009**, *15*, 5108-5123.
- (5) Orio, M.; Pantazis, D. A.; Petrenko, T.; Neese, F. *Inorg. Chem.* **2009**, *48*, 7251-7260.
- (6) Sturgeon, B. E.; Ball, J. A.; Randall, D. W.; Britt, R. D. *J. Phys. Chem.* **1994**, *98*, 12871-12883.
- (7) Goldfarb, D.; Narasimhulu, K. V.; Carmieli, R. *Magn. Reson. Chem.* **2005**, *43*, S40-S50.
- (8) Narasimhulu, K. V.; Carmieli, R.; Goldfarb, D. *J. Am. Chem. Soc.* **2007**, *129*, 5391-5402.
- (9) Gerritsen, H. J.; Sabisky, E. S. *Phys. Rev* **1963**, *132*.
- (10) Krivokapic, I.; Noble, C.; Klitgaard, S.; Tregenna-Piggott, P.; Weihe, H.; Barra, A.-L. *Angew. Chem. Int. Ed.* **2005**, *44*, 3613-3616.
- (11) Barra, A.-L.; Gatteschi, D.; Sessoli, R.; Abbati, G. L.; Cornia, A.; Fabretti, A. C.; Uytterhoeven, M. G. *Angew. Chem. Int. Ed.* **1997**, *36*, 2329-2331.
- (12) Limburg, J.; Vrettos, J. S.; Crabtree, R. H.; Brudvig, G. W.; de Paula, J. C.; Hassan, A.; Barra, A.-L.; Duboc-Toia, C.; Collomb, M.-N. *Inorg. Chem.* **2001**, *40*, 1698-1703.
- (13) Mossin, S.; Weihe, H.; Barra, A.-L. *J. Am. Chem. Soc.* **2002**, *124*, 8764-8765.
- (14) Scheifele, Q.; Riplinger, C.; Neese, F.; Weihe, H.; Barra, A.-L.; Juranyi, F.; Podlesnyak, A.; Tregenna-Piggott, P. L. W. *Inorg. Chem.* **2007**, *47*, 439-447.
- (15) Goldberg, D. P.; Telsler, J.; Krzystek, J.; Montalban, A. G.; Brunel, L.-C.; Barrett, A. G.

M.; Hoffman, B. M. *J. Am. Chem. Soc.* **1997**, *119*, 8722-8723.

(16) Krzystek, J.; Telsler, J.; Pardi, L. A.; Goldberg, D. P.; Hoffman, B. M.; Brunel, L.-C. *Inorg. Chem.* **1999**, *38*, 6121-6129.

(17) Brackett, G. C.; Richards, P. L.; Caughey, W. S. *J. Chem. Phys.* **1971**, *54*, 4383-4401.

(18) Bendix, J.; Gray, H. B.; Golubkov, G.; Gross, Z. *Chem. Commun.* **2000**, 1957-1958.

(19) Krzystek, J.; Telsler, J.; Hoffman, B. M.; Brunel, L.-C.; Licoccia, S. *J. Am. Chem. Soc.* **2001**, *123*, 7890-7897.

(20) Campbell, K. A.; Lashley, M. R.; Wyatt, J. K.; Nantz, M. H.; Britt, R. D. *J. Am. Chem. Soc.* **2001**, *123*, 5710-5719.

(21) Krzystek, J.; Telsler, J. *J. Magn. Reson.* **2003**, *162*, 454-465.

(22) Campbell, K. A.; Force, D. A.; Nixon, P. J.; Dole, F.; Diner, B. A.; Britt, R. D. *J. Am. Chem. Soc.* **2000**, *122*, 3754-3761.

(23) Campbell, K. A.; Yikilmaz, E.; Grant, C. V.; Gregor, W.; Miller, A.-F.; Britt, R. D. *J. Am. Chem. Soc.* **1999**, *121*, 4714-4715.

(24) Davies, J. J.; Smith, S. R. P.; Wertz, J. E. *Phys. Rev.* **1969**, *178*, 608.

(25) Laurance, N.; Lambe, J. *Phys. Rev.* **1963**, *132*, 1029.

(26) Andresen, H. G. *Phys. Rev.* **1960**, *120*, 1606.

(27) From, W. H.; Dorain, P. B.; Kikuchi, C. *Phys. Rev.* **1964**, *135*, A710.

(28) Richens, D. T.; Sawyer, D. T. *J. Am. Chem. Soc.* **1979**, *101*, 3681-3683.

(29) Pal, S.; Ghosh, P.; Chakravorty, A. *Inorg. Chem.* **1985**, *24*, 3704-3706.

(30) Dutta, S.; Chakravorty, A. *Polyhedron* **1994**, *13*, 1811-1816.

(31) Chandra, S. K.; Basu, P.; Ray, D.; Pal, S.; Chakravorty, A. *Inorg. Chem.* **1990**, *29*, 2423-2428.

(32) Kessissoglou, D. P.; Li, X.; Butler, W. M.; Pecoraro, V. L. *Inorg. Chem.* **1987**, *26*, 2487-2492.

- (33) Mikuriya, M.; Shigematsu, S.; Kawano, K.; Tokii, T.; Oshio, H. *Chem. Lett.* **1990**, *19*, 729-732.
- (34) Bryliakov, K. P.; Kholdeeva, O. A.; Vanina, M. P.; Talsi, E. P. *J. Mol. Cat. A* **2002**, *178*, 47-53.
- (35) Parsell, T. H.; Behan, R. K.; Green, M. T.; Hendrich, M. P.; Borovik, A. S. *J. Am. Chem. Soc.* **2006**, *128*, 8728-8729.
- (36) Rajendiran, T. M.; Kampf, J. W.; Pecoraro, V. L. *Inorg. Chim. Acta* **2002**, *339*, 497-502.
- (37) Saadeh, S. M.; Lah, M. S.; Pecoraro, V. L. *Inorg. Chem.* **1991**, *30*, 8-15.
- (38) Ayougou, K.; Bill, E.; Charnock, J. M.; Garner, C. D.; Mandon, D.; Trautwein, A. X.; Weiss, R.; Winkler, H. *Angew. Chem.* **1995**, *107*, 370-373.
- (39) Zheng, M.; Khangulov, S. V.; Dismukes, G. C.; Barynin, V. V. *Inorg. Chem.* **1994**, *33*, 382-387.
- (40) Peloquin, J. M.; Campbell, K. A.; Randall, D. W.; Evanchik, M. A.; Pecoraro, V. L.; Armstrong, W. H.; Britt, R. D. *J. Am. Chem. Soc.* **2000**, *122*, 10926-10942.
- (41) Schäfer, K. O., Technischen Universität, Berlin, 2002.
- (42) Schäfer, K. O.; Bittl, R.; Zweggart, W.; Lendzian, F.; Haselhorst, G.; Weyhermuller, T.; Wieghardt, K.; Lubitz, W. *J. Am. Chem. Soc.* **1998**, *120*, 13104-13120.
- (43) Kulik, L. V.; Epel, B.; Lubitz, W.; Messinger, J. *J. Am. Chem. Soc.* **2007**, *129*, 13421-13435.

**Electronic structure of a weakly antiferromagnetically coupled
Mn^{II}Mn^{III} model relevant to manganese proteins: a combined EPR,
⁵⁵Mn-ENDOR, and DFT study**

*Nicholas Cox, William Ames, Boris Epel, Leonid V. Kulik, Leonid Rapatskiy, Frank Neese, Johannes Messinger, Karl
Wieghardt, and Wolfgang Lubitz*

Supporting Information for:

The electronic structure of a weakly antiferromagnetically coupled Mn^{II}Mn^{III} model relevant to manganese proteins: A combined EPR, ⁵⁵Mn-ENDOR and DFT study

Nicholas Cox, William Ames, Boris Epel, Leonid V. Kulik, Leonid Rapatskiy, Frank Neese, Johannes Messinger, Karl Wieghardt, Wolfgang Lubitz

CONTENTS.

- 1) Magnetic susceptibility plots.
- 2) Derivation of Mn^{III} fine structure constant from 1st-order perturbation theory.
- 3) Fitting of EPR/ENDOR spectra using non-collinear tensors.
- 4) Geometric parameters for model complexes.
- 5) Manganese Mulliken spin populations.
- 6) BS-DFT calculated exchange coupling constants.
- 7) Basis sets used for EPR parameter calculations.
- 8) Determination of the ⁵⁵Mn hyperfine scaling factor for use with broken-symmetry DFT.
- 9) Calculated ⁵⁵Mn hyperfine orientations.
- 10) Calculated ⁵⁵Mn quadrupole/electric field gradient orientations.
- 11) Sample input files for DFT calculations.
- 12) Selected references.

Magnetic Properties of solid PivOH

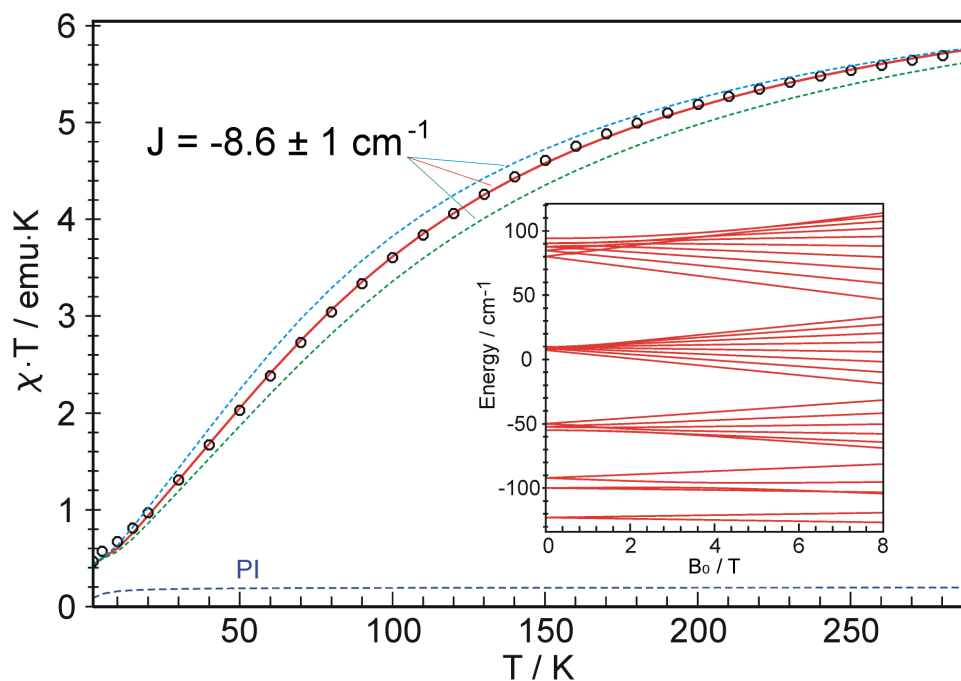


Figure S1: Temperature dependence of the magnetic susceptibility of the PivOH complex recorded with a powder sample and an applied field of $B = 1$ T (plotted as χT vs. T). The solid red line is a spin Hamiltonian simulation for an exchange coupled dimer of Mn^{II} , $S_1 = 5/2$ and Mn^{III} , $S_2 = 2$ with exchange coupling constant $J = -8.6 \text{ cm}^{-1}$, $g_1 = 2$, $d_1 = 0$, $g_2 = 1.98$, $d_2 = -3.5 \text{ cm}^{-1}$, $e_2/d_2 = 0.31$. The dashed green and light blue lines mark an error range of $\pm 1 \text{ cm}^{-1}$ for J . The dotted line (PI) is the contribution of a paramagnetic impurity of 3.5% with assumed spin $S = 5/2$ (Mn^{2+}). The inset shows the energy spectrum (spin ladder) of the coupled system as a function of a field applied along the z-axis.

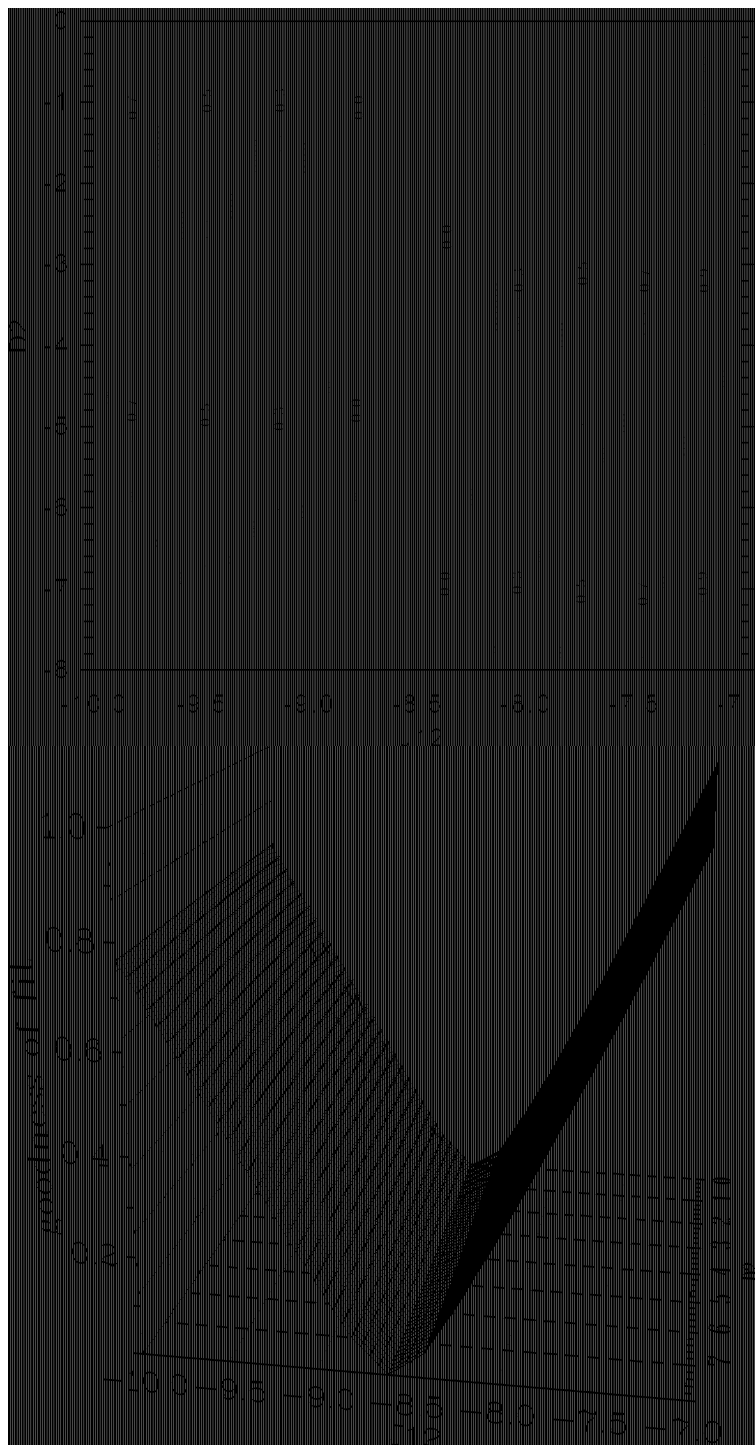


Figure S2: Error contour plot and error surface for the correlation of the exchange coupling constant J_{12} and the axial zfs parameter D_2 of Mn(III) of the exchange coupled dimer PivOH as derived from the magnetic susceptibility data described in the text (with $g_1 = 2$, $D_1 = 0$, $g_2 = 1.98$, $D_2 = -3.5 \text{ cm}^{-1}$, $E/D_2 = 0.31$).

Mn^{III} Fine Structure Constant from 1st-order Perturbation Theory.

The effective A value for Mn^{II} is given by the following:

$$A_1 = \rho_1 a_1 - \frac{\rho_1 \rho_2 a_1}{5J} (b_1 d_1 - b_2 d_2) ; \quad b_1 = 3\rho_1 + 1 \quad \& \quad b_2 = 3\rho_2 + 1$$

Solving for a_1 gives:

$$a_1 = \frac{A_1}{\rho_1 - \frac{\rho_1 \rho_2}{5J} (b_1 d_1 - b_2 d_2)}$$

For Mn^{II} $\Delta a = a_{\perp} - a_{\parallel} = 0$ and $d_1 = 0$.

which implies that; $d_{\parallel} = \frac{2}{3}d_2$ and $d_{\perp} = -\frac{1}{3}d_2$ giving the following relation:

$$\frac{A_{\parallel}}{\rho_1 + \frac{2\rho_1 \rho_2 d_2}{15J}} = \frac{A_{\perp}}{\rho_1 - \frac{\rho_1 \rho_2 d_2}{15J}}$$

or

$$A_{\parallel} \left(\rho_1 - \frac{\rho_1 \rho_2 d_2}{15J} \right) = A_{\perp} \left(\rho_1 + \frac{2\rho_1 \rho_2 d_2}{15J} \right)$$

Solving for d_2 gives the resultant formula which is a function of J , shown below.

$$d_2 = \frac{15(A_{\parallel} - A_{\perp})}{\rho_2(A_{\parallel} + 2A_{\perp})} J$$

The 1st-order linear solution is plotted in Figure 5 in the text.

Fitting Using Rotated G, Hyperfine, and Quadrupole Tensors.

Figures S3 and S4 show fittings of the experimental spectra using non-collinear tensors. The fittings using this method show similar ^{55}Mn HFC, shown in table S1, as the collinear tensors used in the analysis described in the text. Most importantly, the addition of extra degrees of freedom in the fitting procedure still require a highly anisotropic Mn^{II} and isotropic Mn^{III} validating the approach presented in the text.

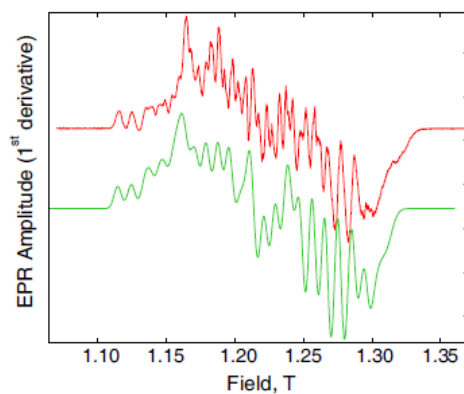


Figure S3: CW-like Q-band spectrum of PivOH (red), obtained from the experimental two-pulse spin echo Q-band EPR spectra by pseudomodulation (1 mT modulation amplitude). The simulation (green trace) was obtained with the parameters displayed in Table 1.

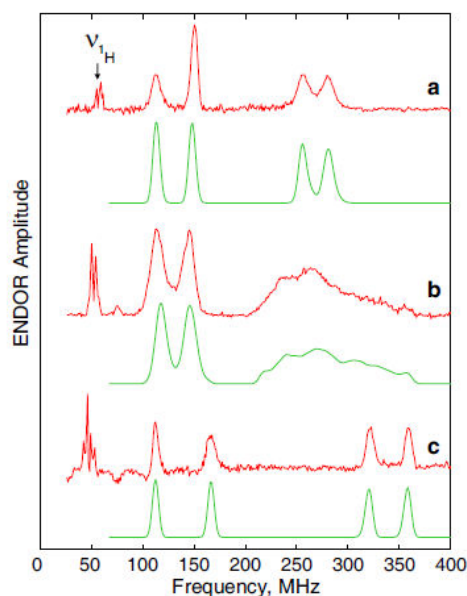


Figure S4: The experimental Q-band ^{55}Mn ENDOR spectra (red) recorded at different magnetic field positions as described in the text. The corresponding simulations are shown (green) with the parameters given in Table 1.

Table S1. Spin Hamiltonian Parameters for Simulation of Q-band EPR and ENDOR spectra for PivOH. EPR line width W_{EPR} ; ENDOR line width $W_{\text{ENDOR}} = 7$ MHz.

g factor	1.97	1.950	2.02
W_{EPR} , MHz	50	250	30
	Mn^{II}	Mn^{III}	
A, MHz	-465, -518, -699	264, 252, 285	
angles	0, (+)10, (-)25	0, (+)10, (-)25	
P, MHz	-2.6, -1.2, 1.4	3.0, 0.8, -3.8	
angles	0,0,0	0,0,0	

Model Complex Geometries.

Table S2. Selected Geometric Parameters for Model Complexes. Mn-X (X = Mn, O, N) interatomic distances (Å) and angles (in degrees).

	Mn ^{II} -Mn ^{III}	Mn ^{II/III} -μOH	Mn ^{II} -N(1/2/3)	Mn ^{III} -N(4/5/6)	Mn-μOH-Mn
1/1'	3.45	2.06/1.93	2.27/2.26/2.26	2.30/2.17/2.17	119.3
2	3.48	2.03/2.02	2.30/2.21/2.22	2.31/2.21/2.20	118.8
2'	3.42	1.96/1.96	2.28/2.22/2.23	2.30/2.23/2.21	121.5
3	3.42	2.14/1.91	2.28/2.26/2.33	2.36/2.12/2.16	121.5
3'	3.35	2.04/1.85	2.28/2.31/2.31	2.34/2.14/2.15	118.4

Selected Spin Populations.

Table S3. Manganese Mulliken Spin Populations.

	1	1'	2	2'	3	3'
Mn ^{II} (HS)	4.73	4.74	4.54	4.52	4.87	4.82
Mn ^{III} (HS)	4.29	4.28	4.51	4.52	4.11	4.14
Mn ^{II} (BS)	4.84	4.85	4.77	4.74	4.88	4.85
Mn ^{III} (BS)	-3.95	-3.95	-3.93	-3.86	-3.97	-3.91

Exchange Coupling Constants from BS-DFT Calculations.

Table S4. Calculated Exchange Coupling Constants J (cm⁻¹)

J	1	1'	2	2'	3	3'	2:3^a	2:3^b	2':3'^a	2':3'^b	Exp. (Stat.)	Exp. (EPR)
	36.3	37.1	141.5	139.6	-18.4	-13.3	-35.1	-22.6	-3.9	-11.4	-8.6	-8.8

^a Calculated using adiabatic approximation, see Theory section. ^b Calculated using adiabatic approximation and additional Van der Waals corrections from the different high-spin and broken-symmetry optimized geometries.

EPR Parameter Basis Sets:

Basis sets for the calculation of EPR parameters were constructed, using the procedure of F. Neese for the “core properties” (CP) basis sets,^[1] as follows:

- 1) A full decontraction of the S shell for the SARC def2-TZVP basis sets
- 2) Three additional steep primitives were added with exponents 2.5, 6.25 and 15.625 times the largest S primitive.

These basis sets were applied for the Mn, N and O atoms of the PivOH models. The added primitives are shown below. The full basis sets used are shown in the example input file for EPR parameter calculations starting on page 11.

NewGTO Mn

```
S 1
  1 4331015.6489062500 1.0000000000
S 1
  1 1732406.2595625000 1.0000000000
S 1
  1 692962.5038250000 1.0000000000
```

...

NewGTO N

```
S 1
  1 308293.7601093750 1.0000000000
S 1
  1 123317.5040437500 1.0000000000
S 1
  1 49327.0016175000 1.0000000000
```

...

NewGTO O

```
S 1
  1 422380.9786093750 1.0000000000
S 1
  1 168952.3914437500 1.0000000000
S 1
  1 67580.9565775000 1.0000000000
```

...

Determination of ^{55}Mn HFC Scaling Factor:

The empirical scaling factor for the ^{55}Mn hyperfine coupling constants was determined through the calculation of ^{55}Mn HFCC for well studied model complexes. In this work the model complexes used were: $[\text{Mn}^{\text{III}}\text{Mn}^{\text{IV}}(\mu\text{-O})_2(\text{bipy})_4]^{3+}$, $[\text{Mn}^{\text{III}}\text{Mn}^{\text{IV}}(\mu\text{-O})_2(\text{bispiMe}_2\text{en})_2]^{3+}$, $[\text{Mn}^{\text{III}}\text{Mn}^{\text{IV}}(\mu\text{-O})_2(\text{tren})_2]^{3+}$, $[\text{Mn}^{\text{III}}\text{Mn}^{\text{IV}}(\mu\text{-O})_2(\mu\text{-OAc})(\text{dtne})]^{2+}$ and $[\text{Mn}^{\text{II}}(\text{H}_2\text{O})_6]^{2+}$. The $\text{Mn}^{\text{III}}\text{Mn}^{\text{IV}}$ models have been previously studied in detail by Orio et al.^[2] All calculations for EPR parameters and optimizations were done at the same level of theory as for the PivOH complexes.

Table S5: Ratio, f_{iso} , of calculated to experimental hyperfine couplings for selected model complexes. Experimental and calculated A_{iso} values shown in MHz.

redox state	complex	$A_{\text{iso}}(\text{calc})$	$A_{\text{iso}}(\text{exp})$	f_{iso}	Ref.
Mn^{III}	$[\text{Mn}^{\text{III}}\text{Mn}^{\text{IV}}(\mu\text{-O})_2(\text{bipy})_4]^{3+}$	-298	-452	1.52	3, 6
Mn^{IV}	$[\text{Mn}^{\text{III}}\text{Mn}^{\text{IV}}(\mu\text{-O})_2(\text{bipy})_4]^{3+}$	-142	-219	1.54	3, 6
Mn^{III}	$[\text{Mn}^{\text{III}}\text{Mn}^{\text{IV}}(\mu\text{-O})_2(\text{bispiMe}_2\text{en})_2]^{3+}$	-290	-408	1.41	4
Mn^{IV}	$[\text{Mn}^{\text{III}}\text{Mn}^{\text{IV}}(\mu\text{-O})_2(\text{bispiMe}_2\text{en})_2]^{3+}$	-141	-230	1.63	4
Mn^{III}	$[\text{Mn}^{\text{III}}\text{Mn}^{\text{IV}}(\mu\text{-O})_2(\text{tren})_2]^{3+}$	-275	-428	1.56	5
Mn^{IV}	$[\text{Mn}^{\text{III}}\text{Mn}^{\text{IV}}(\mu\text{-O})_2(\text{tren})_2]^{3+}$	-138	-207	1.50	5
Mn^{III}	$[\text{Mn}^{\text{III}}\text{Mn}^{\text{IV}}(\mu\text{-O})_2(\mu\text{-OAc})(\text{dtne})]^{2+}$	-266	-391	1.47	6
Mn^{IV}	$[\text{Mn}^{\text{III}}\text{Mn}^{\text{IV}}(\mu\text{-O})_2(\mu\text{-OAc})(\text{dtne})]^{2+}$	-140	-209	1.49	6
Mn^{II}	$[\text{Mn}^{\text{II}}(\text{H}_2\text{O})_6]^{2+}$	-191	-264	1.38	7
				Ave. f_{iso}	1.50

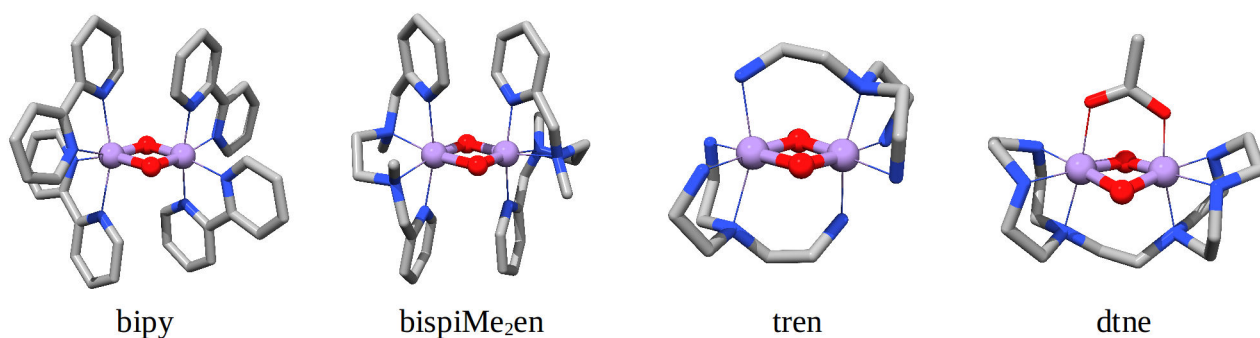
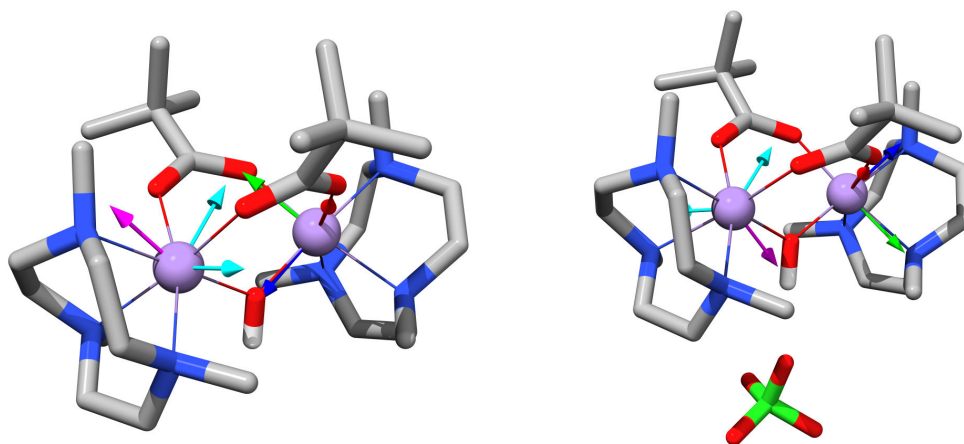


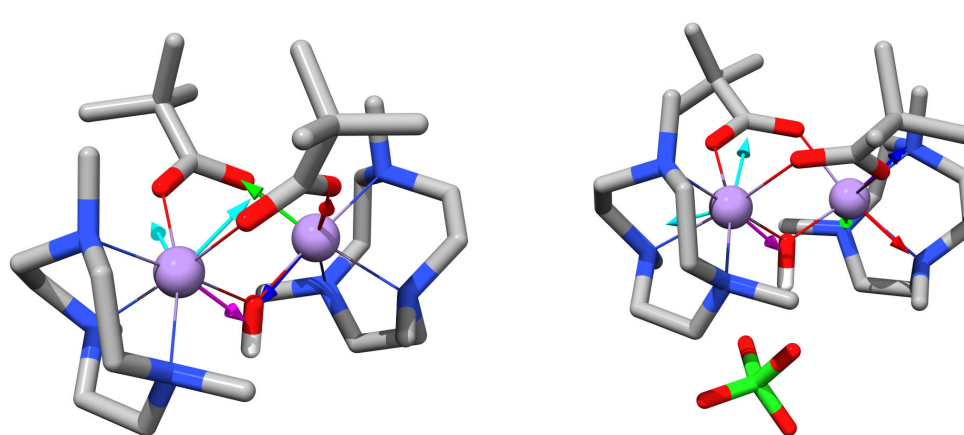
Figure S5: Optimized geometries for selected models used in determination of the ^{55}Mn HFC scaling factor.

⁵⁵Mn HFC tensor orientations:

1 & 1'



2 & 2'



3 & 3'

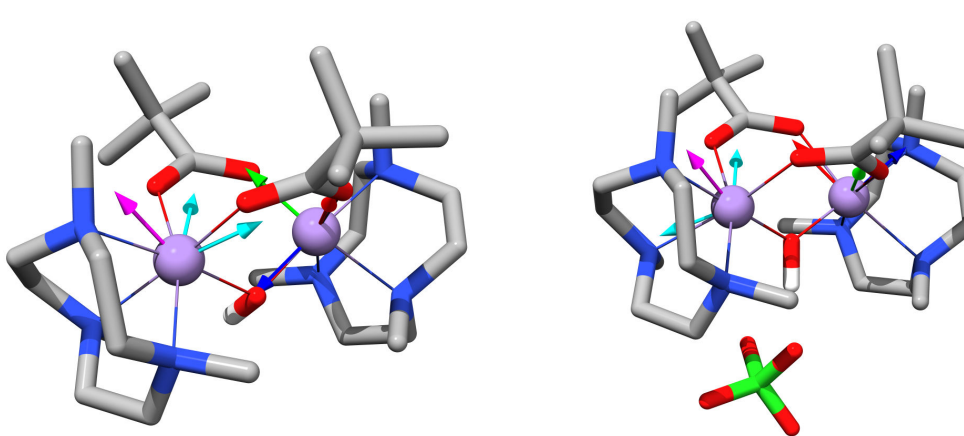


Figure S6: Orientations of the calculated Mn hyperfine tensors. Blue, green and red arrows correspond to a_x , a_y and a_z components on Mn^{III} . The a_z component is always facing along the Jahn-Teller axis of Mn^{III} . Cyan and magenta arrows depict the perpendicular, a_{\perp} , and parallel, a_{\parallel} , components on Mn^{II} .

Mn Quadrupole Tensor Orientations:

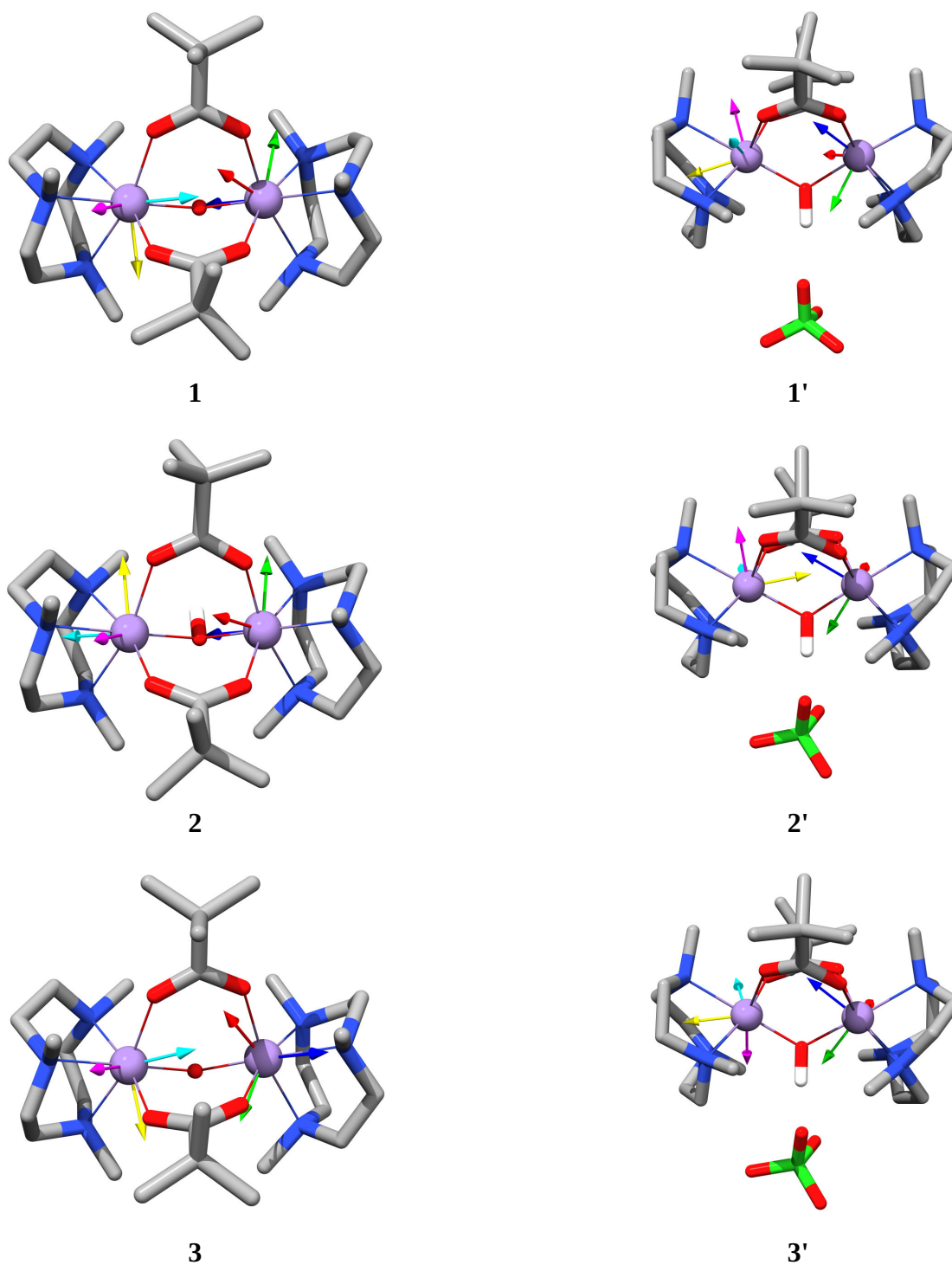


Figure S7: Relative orientations of the EFG tensors of Mn^{III} and Mn^{II} . Following the standard convention, $|q_x| \leq |q_y| \leq |q_z|$. The red, q_x , green, q_y , and blue, q_z , arrows correspond to components on Mn^{III} ; while cyan, q_x , yellow, q_y , and magenta, q_z , correspond to components on Mn^{II} .

Sample ORCA input files:

a) Crystal structure proton position optimization.

```
! uks bp def2-tzvp(-f) def2-tzvp/j zora decontractaux
! tightscf grid4 nofinalgrid
! vdw10 pmodel opt slowconv

%basis newgto H "svp" end
      newgto C "svp" end
end

%geom optimizehydrogens true
end

* xyzfile 1 10 myxyzfile.xyz
```

b) High-spin geometry optimization.

```
! uks bp def2-tzvp(-f) def2-tzvp/j zora decontractaux
! tightscf grid4 nofinalgrid
! vdw10 pmodel opt slowconv

%basis newgto H "svp" end
      newgto C "svp" end
end

* xyzfile 1 10 myxyzfile.xyz
```

c) Broken symmetry single point.

```
! uks tpssh def2-tzvp(-f) def2-tzvp/j zora decontractaux
! tightscf grid4 nofinalgrid rijcosx gridx4
! pmodel veryslowconv

%scf flipspin 1
      finalms 0.5
      maxiter 300
end

* xyzfile 1 10 myxyzfile.xyz
```

d) Broken symmetry geometry optimization.

```
! uks bp def2-tzvp(-f) def2-tzvp/j zora decontractaux
! tightscf grid4 nofinalgrid
! vdw10 moread opt slowconv

%moinp "BS-SinglePoint.gbw"

%basis newgto H "svp" end
      newgto C "svp" end
end

%scf maxiter 300
end

* xyzfile 1 2 myxyzfile.xyz
```

e) EPR parameter calculation.

```
! uks tpssh def2-tzvp(-f) def2-tzvp/j zora decontractaux  
! tightscf grid4 nfinalgrid rijcosx gridx4  
! moread slowconv
```

```
%moinp "BS-SinglePoint.gbw"
```

```
%scf maxiter 300 end
```

```
%basis
```

```
# CP Basis set for element : N
```

```
NewGTO N
```

```
S 1  
 1 308293.7601093750 1.0000000000  
S 1  
 1 123317.5040437500 1.0000000000  
S 1  
 1 49327.0016175000 1.0000000000  
S 1  
 1 19730.8006470000 1.0000000000  
S 1  
 1 2957.8958745000 1.0000000000  
S 1  
 1 673.2213359500 1.0000000000  
S 1  
 1 190.6824949400 1.0000000000  
S 1  
 1 62.2954419000 1.0000000000  
S 1  
 1 22.6541611800 1.0000000000  
S 1  
 1 8.9791477400 1.0000000000  
S 1  
 1 3.6863002400 1.0000000000  
S 1  
 1 0.8466007700 1.0000000000  
S 1  
 1 0.3364713400 1.0000000000  
S 1  
 1 0.1364765400 1.0000000000  
P 4  
 1 49.2003805100 0.0115131336  
 2 11.3467905400 0.0785386070  
 3 3.4273972400 0.3081978103  
 4 1.1785525100 0.7201896814  
P 1  
 1 0.4164220500 1.0000000000  
P 1  
 1 0.1426082600 1.0000000000  
D 1  
 1 1.6540000000 1.0000000000  
D 1  
 1 0.4690000000 1.0000000000  
end;
```

```
# CP Basis set for element : O
```

```
NewGTO O
```

```
S 1  
 1 422380.9786093750 1.0000000000  
S 1  
 1 168952.3914437500 1.0000000000  
S 1  
 1 67580.9565775000 1.0000000000
```

S	1		
1	27032.3826310000	1.0000000000	
S	1		
1	4052.3871392000	1.0000000000	
S	1		
1	922.3272271000	1.0000000000	
S	1		
1	261.2407098900	1.0000000000	
S	1		
1	85.3546413500	1.0000000000	
S	1		
1	31.0350352400	1.0000000000	
S	1		
1	12.2608607300	1.0000000000	
S	1		
1	4.9987076000	1.0000000000	
S	1		
1	1.1703108200	1.0000000000	
S	1		
1	0.4647474100	1.0000000000	
S	1		
1	0.1850453600	1.0000000000	
P	4		
1	63.2749548000	0.0121096626	
2	14.6270493800	0.0831734399	
3	4.4501223500	0.3200012219	
4	1.5275799600	0.7069790865	
P	1		
1	0.5293511800	1.0000000000	
P	1		
1	0.1747842100	1.0000000000	
D	1		
1	2.3140000000	1.0000000000	
D	1		
1	0.6450000000	1.0000000000	

end;

CP Basis set for element : Mn

NewGTO Mn

S	1		
1	4331015.6489062500	1.0000000000	
S	1		
1	1732406.2595625000	1.0000000000	
S	1		
1	692962.5038250000	1.0000000000	
S	1		
1	277185.0015300000	1.0000000000	
S	1		
1	41550.7698900000	1.0000000000	
S	1		
1	9455.9700152000	1.0000000000	
S	1		
1	2676.5206482000	1.0000000000	
S	1		
1	871.4668753000	1.0000000000	
S	1		
1	312.9830642000	1.0000000000	
S	1		
1	121.4445405100	1.0000000000	
S	1		
1	47.9225988300	1.0000000000	
S	1		
1	303.6672316300	1.0000000000	
S	1		
1	93.8814031900	1.0000000000	

```

S 1
 1      14.8794212100      1.0000000000
S 1
 1      6.2865200700      1.0000000000
S 1
 1      9.4858591300      1.0000000000
S 1
 1      1.5698706200      1.0000000000
S 1
 1      0.6590321400      1.0000000000
S 1
 1      0.1068629200      1.0000000000
S 1
 1      0.0392674400      1.0000000000
P 6
 1      1444.7978182000     0.0032493630
 2      342.0655119700     0.0237346473
 3      109.5840089100     0.1067232634
 4      40.7479881700      0.3007617717
 5      16.1886265700     0.4790147038
 6      6.5484506000      0.2708283465
P 1
 1      25.3570864400     -1.0000000000
P 1
 1      3.4830168800      1.0000000000
P 1
 1      1.3858800900      1.0000000000
P 1
 1      0.5255509500     -1.0000000000
D 4
 1      56.5631891200     0.0192444440
 2      16.2787347100     0.1161060412
 3      5.6964273900     0.3706567953
 4      2.1411147900     0.6570040408
D 1
 1      0.7829180200      1.0000000000
D 1
 1      0.2595231100      1.0000000000
P 1
 1      0.1276500000      1.0000000000
D 1
 1      0.0860000000      1.0000000000
F 1
 1      1.3260000000      1.0000000000
end;
end

%method specialgridatoms 25,8,7
      specialgridintacc 11,9,9
end

%rel soctype 3
      socflags 1,3,3,1
      picturechange true
end

* xyzfile 2 2 myxyzfile.xyz

%eprnmr nuclei = all Mn { aiso, adip, aorb, fgrad }
      nuclei = all N { aiso, adip, aorb, fgrad }
      nuclei = all O { aiso, adip, aorb, fgrad }
end

```

References:

- [1] Neese, F. *Inorg. Chim. Acta.* **2002**, 337, 181-192.
- [2] Orio, M.; Pantazis, D. A.; Petrenko, T.; Neese, F. *Inorg. Chem.* **2009**, 48, 7251-7260.
- [3] Jensen, A. F.; Su, Z.; Hansen, N. K.; Larsen, F. K. *Inorg. Chem.* **1995**, 34, 4244-4252.
- [4] Hureau, C.; Blondin, G.; Cesario, M.; Un, S. *J. Am. Chem. Soc.* **2003**, 125, 11637-11645.
- [5] a) Horner, O.; Charlot, M.-F.; Boussac, A.; Anxolabehere-Mallart, E.; Tchertanov, L.; Guilhem, J.; Girerd, J. J. *Eur. J. Inorg. Chem.* **1998**, 1998, 721-727. b) Hagen, K. S.; Armstrong, W. H.; Hope, H. *Inorg. Chem.* **1988**, 27, 967-969.
- [6] Schäfer, K. O.; Bittl, R.; Zweggart, W.; Lenzian, F.; Haselhorst, G.; Weyhermüller, T.; Wieghardt, K.; Lubitz, W. *J. Am. Chem. Soc.* **1998**, 120, 13104-13120.
- [7] Luckhurst, G. R.; Pedulli, G. F. *Mol. Phys.* **1971**, 22, 931-935.

Detection of water binding sites in the oxygen-evolving complex of photosystem II poised in the S₂ state using high field (94 GHz) ¹⁷O-ELDOR-detected NMR spectroscopy

Leonid Rapatskiy, Nicholas Cox, Anton Savitsky, William Ames, Julia Sander, Mark Nowaczyk, Matthias Rögner, Alain Boussac, Frank Neese, Johannes Messinger and Wolfgang Lubitz

SUPPORTING INFORMATION

TITLE: Detection of the water binding sites of the oxygen-evolving complex of Photosystem II using W-band ^{17}O -ELDOR detected NMR spectroscopy

AUTHORS: Leonid Rapatskiy, Nicholas Cox*, Anton Savitsky, William M. Ames, Julia Sander, Marc. M. Nowaczyk, Matthias Rögner, Alain Boussac, Frank Neese, Johannes Messinger and Wolfgang Lubitz¹

CORRESPONDING AUTHOR: Nicholas Cox, email: Nicholas.Cox@mpi-mail.mpg.de, telephone: (+49)-208-306-3552; Wolfgang Lubitz, email: Wolfgang.Lubitz@mpi-mail.mpg.de, telephone: (+49)-208-306-3614.

The material is available free of charge via the Web at <http://pubs.acs.org>

TABLE OF CONTENTS

- S1) Literature ^1H coupling data for the OEC poised in the S_0 and S_2 states
- S2) Literature ^{17}O hyperfine and quadrupole couplings of metallocofactors and related model complexes
- S3) Material describing the Spin Hamiltonian Formalism of the Mn model systems
- S4) Material describing the Spin Hamiltonian Formalism of the Mn tetramer
- S5) Control ESE detected field sweep W and Q-band EPR of the OEC poised in the S_1 and S_2 states
- S6) ^{17}O -EDNMR/ $^1\text{H}/^2\text{H}$ -ENDOR data processing
- S7) Spin Hamiltonian Simulations of the ^{17}O EDNMR spectra of PSII and of the Mn model complex
- S8) W-band ^{17}O Davies and Mims ENDOR of ^{14}N -PSII *T. elongatus* poised in the S_2 state
- S9) Material describing the multipole coupling model
- S10) $^1\text{H}/^{17}\text{O}$ multipole coupling estimates for all O/H within 5 Å of the OEC as based on the crystal structure coordinates of Umena et al.
- S11) Simulations of $^1\text{H}/^{17}\text{O}$ ENDOR of ^{14}N -PSII of *T. elongatus* poised in the S_2 state using the multipole coupling estimates in S11
- S12) ^{17}O hyperfine tensor orientations for all coordinating oxygen ligands of the OEC based on the crystal structure coordinates of Umena et al.
- S13) Theoretical EPR Parameters calculations from Broken Symmetry DFT
- S14) References

S1. Literature ^1H coupling data for the OEC poised in the S_0 and S_2 states. CW-ENDOR spectroscopy provided the first information on water-derived species bound in the vicinity of the $\text{Mn}_4\text{O}_5\text{Ca}$ cluster. In the paramagnetic S_2 and S_0 states water-exchangeable protons can be identified via the disappearance of signals originating from the hyperfine coupling of the ^1H nucleus ($I = \frac{1}{2}$) to the net electronic spin ($S_T = \frac{1}{2}$) of the $\text{Mn}_4\text{O}_5\text{Ca}$ cluster after $^1\text{H}_2\text{O}/^2\text{H}_2\text{O}$ exchange. Kawamori et al.¹ were the first to report ^1H couplings to the OEC obtained from spinach, poised in the S_2 state.

Table S1.1: ^1H -couplings measured by Kawamori et al.¹ and Fiege et al.² for the OEC poised in the S_2 .

^1H coupling (MHz) (A_{\perp})		
	Kawamori et al.	Fiege et al.
1	4.016	4.0-4.2
2	2.011 – 2.412	2.3
3	1.407 – 1.441	
4	1.067 – 1.190	1.1
5	0.693 – 0.761	0.6
6	0.370 – 0.531	

The measured ^1H envelope extended out from the ^1H -nuclear Larmor frequency by ± 2 MHz and disappeared after resuspension of the PSII in buffer made in $^2\text{H}_2\text{O}$. The peaks of this envelope were interpreted as the overlap of a series of individual ^1H species. The magnitude of the hyperfine splittings was considered to be electron-nuclear dipolar in origin. A point dipole model was assumed, i.e. the envelope was considered to be a sum of pake patterns. A Pake pattern can be described in terms of two hyperfine parameters, A_{\parallel} and A_{\perp} . A_{\parallel} defines the hyperfine interaction for powder pattern orientation where the axis of magnetization (B_0) coincides with the spin-spin interaction vector (maximum interaction), whereas A_{\perp} defines the hyperfine splitting of powder pattern orientations where B_0 is perpendicular to the spin-spin interaction vector (minimum interaction). As A_{\parallel} effectively defines only

one powder pattern orientation, the pake spectrum is dominated by the A_{\perp} splitting. As such, the hyperfine splittings identified by Kawamori et al. were interpreted as corresponding to A_{\perp} . The magnitude of at least one A_{\perp} was consistent with a water molecule(s) directly coordinating to one or more Mn ions (^1H at a distance of 2-3 Å from a Mn). Similar results were observed in the subsequent study of Fiege et al.² which employed a more sophisticated electron-nuclear dipole model for the interpretation of their data.

The first attempt at a quantitative fitting of the ^1H envelope was performed in the pulse ^1H -ENDOR and ^2H ESEEM (electron spin echo envelope modulation) study of Aznar et al.^{3,4} Here a four shell model (inclusive of ambient water) was developed with electron-nuclear dipolar hyperfine couplings (A_{dip}) similar to those seen in the Kawamori and Fiege studies. As before, these results were interpreted as evidence for a direct Mn-water interaction, fixing the number of protonated coordinating water molecules to two. Similar hyperfine couplings were estimated for the S_0 state and approximately the same number of Mn-proton interactions were inferred.⁴ A subsequent X-band ^2H -ESEEM study by Åhrling et al.⁵ reached a similar conclusion albeit with an increase of the A_{dip} of the largest hyperfine tensor which was also seen in the recent X-band HYSCORE studies of Martínez et al.⁶

Table S1.2: $^1\text{H}/^2\text{H}$ -couplings measured by Anzar et al.^{3,4} and Åhrling et al.⁵ for the OEC poised in the S_0 and S_2 states. ^2H data are scaled to the ^1H Larmor frequency for easy comparison.

Anzar et al. 2002, Britt et al. 2004						
$^1\text{H}/^2\text{H}$ Coupling (MHz)						
	S_2			S_0		
	No. ^1H	A_{iso}	A_{dip}	No. ^1H	A_{iso}	A_{dip}
1	2	2.93	4.17	2	2.61	5.54
2	2	0.00	3.97	1	1.95	4.89
3	2	0.00	1.95	2	0.00	4.56
4	-	-	-	2	0.00	2.61
ambient water	-	0.00	≤ 1.24	-	0.00	≤ 1.24

Åhrling et al. 2006						
A Coupling (MHz)						
	S_2			S_0		
	No. ^1H	A_{iso}	A_{dip}	No. ^1H	A_{iso}	A_{dip}
1	1	2.08	6.32	1	1.76	5.86
2	1	1.76	4.23	1	1.37	3.78
3	0-10	0.39	2.87	5-8	0.33	2.74
4	4	0.32	1.63	4	0.33	1.63

S2. Literature ^{17}O hyperfine and quadrupole couplings for metallofactors and related model complexes. ^{17}O labeling has only been successfully employed to characterize a handful of metallofactors and corresponding model complexes. Of particular relevance to the study presented here are the two Fe containing metallofactors characterized by the Hoffman group: the mixed $\text{Fe}^{\text{II}}\text{Ni}^{\text{III}}$ ($S = 1/2$)⁷ active site of a class of Hydrogenase enzymes and non-mixed $\text{Fe}^{\text{III}}\text{Fe}^{\text{IV}}$ state ($S = 1/2$)⁸ of the small subunit of class 1 ribonucleotide reductase (see **Table S2.1**). Both of these studies used low-frequency (X, Q band) ENDOR to characterize the ^{17}O in μ -oxo bridges. The measured hyperfine couplings were in the range of 10-15 MHz. The large hyperfine anisotropy (14-23 MHz) of which the through space dipolar interaction contributes significantly, together with the large quadrupole splitting resulting (3-11 MHz), a consequence of the large electric field gradient experienced by coordinating ligands, resulted in very broad ENDOR transitions. These characteristics (large hyperfine anisotropy, broad lines) match well the results reported in this manuscript for the BIPY complex. Literature ^{17}O data are given in Table S2.1.

Table S2.1: ^{17}O hyperfine and quadrupole couplings for metallocofactors and related model complexes

Species		Hyperfine Coupling (MHz)					Quadrupole Coupling (MHz)						
		a_{\perp}		a_{\parallel}	a_{iso}	a_{aniso}	α, β, γ	p_{\perp}		p_{\parallel}	$\frac{e^2qQ}{h}$	η	α, β, γ
		a_x	a_y	a_z				p_x	p_y	p_z			
$\text{Mn}^{\text{II}}\text{-OH}_2$ ($\text{Mn}^{\text{II}}(\text{H}_2\text{O})_6$) ref ⁹⁻¹¹	1	-6.3		-10.0	-7.5	1.2	0,0,0	-0.33	0.37	-0.04	7.4	0.78	180,90,90
	2	-6.5		-9.6	-7.5	1.0	0,0,0	-	-	-	6.0	1	0,0,0
	3	-6.0		-9.6	-7.4	0.8	0,0,0	-	-	-	7.4	1	30,30,0
	4	-9.6	-10.8	-13.5		3.3	90,0,0	-	-	-	10.5	0.62	0,90,0
$\text{Mn}^{\text{III}}\text{-O-Mn}^{\text{IV}}$ (BIPY) ref ¹²		12.8			12.8	-	-	-	-	-	-	-	-
$\text{Fe}^{\text{III}}\text{-O}^c$ ref ¹³ (Cyt. P450cam)	1				[2.6]	[0.3]	-	-	-	-	[6.6]	0.95	0,90,50
	2				[0.4]	[1.8]	-	-	-	-	[6.6]	0.95	0,90,50
RNR 1a ref ⁸	$\text{Fe}^{\text{III}}\text{-O-Fe}^{\text{IV}}$	0	23.5	22.5	15.3	23.0	40,0,0	-0.60	-0.80	1.4	11.2	0.14	25,45,0
	$\text{Fe}^{\text{III}}\text{-OH}_2$	34.0	20.5	17	28.3	15.3	0,20,0	-0.05	-0.25	0.30	2.4	0.67	90,45,90
$\text{Fe}^{\text{II}}\text{-OH-Ni}^{\text{III}}$ (Hydrogenase) ref ⁷		7	5	20	10.7	14	90,45,0	-0.075	-0.075	0.15	3.0	0.0	90,45,0
$\text{Mo}^{\text{V}}\text{-O}$ ref ^{14,15}	Mo				4-7								
	Mo=O				30	<10							
$\text{Ga}^{\text{III}}\text{-OH}_2$ ref ¹⁶					0.75 ^a	0.69	0,0,0	-	-	-	7±0.5	≥0.8	0,35,0
VO (H_2O) ₅ ref ⁹	$\text{V}^{\text{IV}}\text{-OH}_2$ eq.	8.0	6.3	7.2	7.2	1.3	x,0,0	-	-	-	10.7	0.52	0,0,0
		5.7	6.3	7.2	6.4	1.2	x,0,0	-	-	-	10.7	0.52	0,0,0
	$\text{V}^{\text{IV}}\text{-OH}_2$ (ax)	-1.1	-0.9	-3.8	-1.9	1.8	0,0,0	-	-	-	10.7	0.59	90,90,0
	$\text{V}^{\text{IV}}\text{=O}$	16.0		-6.9	8.4	9.0	0,0,0	-	-	-	3.3	0.14	0,0,0
		16.5	16.4	-6.9	8.7	9.5	0,0,0	-	-	-	3.3	0.14	0,0,0

a) center of Gaussian distribution of width $\Delta a_{iso} = 0.3$ MHz

b) aquo/single H_2O ligand.

c) two possible solution, not resolvable which is correct.

Spin Hamiltonian Formalism – Mn^{III}-(μO)₂-Mn^{IV} dimer

S3.1 The Spin Hamiltonian Formalism. Here we consider an antiferromagnetically exchange coupled Mn^{III}-(μO)₂-Mn^{IV} dimer. A basis set that describes the Mn-dimer spin manifold can be built from the product of the eigenstates of the interacting spins:

$$|S_1 S_2 M_1 M_2 I_1 I_2 m_1 m_2 K_1 K_2 k_1 k_2\rangle, \quad (\text{Eq. S3.1})$$

Here S_i refers to the electronic spin state of Mn_i, M_i refers to the electronic magnetic sub-level of Mn_i, I_i refers to the nuclear spin state of Mn_i, m_i refers to the nuclear magnetic sub-level of Mn_i, L_i refers to the nuclear spin state of O_i, and k_i refers to the nuclear magnetic sub-level of O_i. S_i takes the value 2 for Mn^{III} and 3/2 for Mn^{IV}; M_i takes the values: $S_i, S_i-1, \dots, 1-S_i, -S_i$; I_i takes the value 5/2 for ⁵⁵Mn (100% natural abundance); m_i takes the values $-I_i, 1-I_i, \dots, I_i-1, I_i$; K_i takes the values 5/2 for ¹⁷O; and k_i takes the values $-K_i, 1-K_i, \dots, K_i-1, K_i$.

The Spin Hamiltonian that describes the spin manifold of the ¹⁷O labeled Mn dimer is:

$$\begin{aligned} \hat{H} = & \sum_i \beta_e \vec{B}_0 \cdot \hat{g}_i \cdot \vec{S}_i - \sum_i g_{Mn} \beta_n \vec{B}_0 \cdot \vec{I}_i - \sum_i g_o \beta_n \vec{B}_0 \cdot \vec{K}_i + \sum_i \vec{S}_i \cdot \hat{a}_{Mn,i} \vec{I}_i \\ & + \sum_i \sum_j \vec{S}_i \cdot \hat{a}_{O,ij} \vec{K}_j + \sum_i \vec{I}_i \cdot \hat{p}_{Mn,i} \cdot \vec{I}_i + \sum_i \vec{K}_i \cdot \hat{p}_{O,i} \cdot \vec{K}_i + \sum_i \vec{S}_i \cdot \hat{d}_i \cdot \vec{S}_i - 2\vec{S}_1 \cdot \hat{J} \cdot \vec{S}_2 \end{aligned} \quad (\text{Eq. S3.2})$$

It contains: i) an electronic Zeeman term for each Mn ion ; ii) a nuclear Zeeman term for each ⁵⁵Mn and ¹⁷O nucleus; iii) an electron-nuclear hyperfine term for each ⁵⁵Mn and ¹⁷O nucleus; iv) an nuclear quadrupole term for each ⁵⁵Mn and ¹⁷O nucleus; v) a fine structure term for each Mn ion; and vi) a electron spin coupling term for the Mn-Mn interaction.

S3.2 An Effective Spin ½ Ground State. The electronic coupling between the two Mn ions in mixed valence Mn dimers is usually dominated by the through bond exchange interaction and sufficiently large that the spin manifold can be treated within the strong exchange limit. In this instance the exchange interaction between the two Mn ions is significantly larger than any other term of the Spin Hamiltonian.

The resultant electronic spin states of the manifold are then adequately described by a single quantum number, the total spin (S_T). The ‘multiline’ EPR signal observed for the **BIPY** complex is derived from only one total spin state, the ground state of the spin manifold with total spin $S_T = 1/2$. The basis set that describes this subspace takes the form

$$\left| \frac{1}{2} \quad M \quad m_1 \quad m_2 \quad K_1 \quad K_2 \quad k_1 \quad k_2 \right\rangle \quad (\text{Eq. S3.3})$$

Where M takes all half-integer values: $-\frac{1}{2} \leq M \leq \frac{1}{2}$; m_i (where $i = 1-2$) takes all half integer values: $-\frac{5}{2} \leq m_i \leq \frac{5}{2}$; K_i takes the value $5/2$ and k_i takes all half integer values $-\frac{5}{2} \leq k_i \leq \frac{5}{2}$. The effective Spin Hamiltonian that describes the ground state of the spin manifold ($S_T = 1/2$) is:

$$\begin{aligned} \hat{H} = & \beta_e \vec{B}_0 \cdot \hat{G} \cdot \vec{S} + \sum_i \left(-g_{Mn} \beta_n \vec{B}_0 \cdot \vec{I}_i + \vec{S} \cdot \hat{A}_{Mn,i} \cdot \vec{I}_i + \vec{I}_i \cdot \hat{P}_{Mn,i} \cdot \vec{I}_i \right) \\ & + \sum_i \left(-g_o \beta_n \vec{B}_0 \cdot \vec{K}_i + \vec{S} \cdot \hat{A}_{O,i} \cdot \vec{K}_i + \vec{K}_i \cdot \hat{P}_{O,i} \cdot \vec{K}_i \right) \end{aligned} \quad (\text{Eq. S3.4})$$

It contains: i) the electronic Zeeman term for the total electronic spin; ii) nuclear Zeeman terms for each ^{55}Mn and ^{17}O nucleus; iii) electron-nuclear hyperfine terms for each ^{55}Mn and ^{17}O nucleus and; iv) nuclear quadrupole terms for each ^{55}Mn and ^{17}O nucleus.

S3.3 Isotropic Spin Projections. A mapping of the spin subspace in section S3.2 onto the original basis set as described in section 3.1 can be made. This allows the intrinsic g and hyperfine tensors of the two Mn ions and the two ^{17}O nuclei (g_i, a_i , see eq. 2) to be calculated from the effective G and hyperfine tensors (G, A_i , see eq. 4). For an exchanged coupled $\text{Mn}^{\text{II}}\text{Mn}^{\text{III}}$ complex the effective g -factor G , hyperfine tensors A_i and quadrupole tensors p_i are related to the parameters of the complete spin Hamiltonian of the exchange-coupled system^{17,18} by the spin-projection coefficients, where the isotropic

spin projection coefficients (ρ_1, ρ_2) are defined as :

$$\begin{aligned}\rho_1(Mn^{III}) &= \frac{S_1(S_1+1) - S_2(S_2+1) + S(S+1)}{2S(S+1)} \\ \rho_2(Mn^{IV}) &= \frac{S_2(S_2+1) - S_1(S_1+1) + S(S+1)}{2S(S+1)}\end{aligned}\quad (\text{Eq. S3.5})$$

and effective G and hyperfine values (A_i), assuming all g_i and a_i are isotropic and the exchange coupling J is large:

$$\begin{aligned}G &= \rho_1 g_1 + \rho_2 g_2 & P_{Mn,1} &= p_{Mn,1} \\ A_{Mn,1} &= \rho_1 a_{Mn,1} & P_{Mn,2} &= p_{Mn,2} \\ A_{Mn,2} &= \rho_2 a_{Mn,2} & P_{O,1} &= p_{O,1} \\ A_{O,1} &= \rho_1 a_{O,11} + \rho_2 a_{O,12} & P_{O,2} &= p_{O,2} \\ A_{O,2} &= \rho_1 a_{O,21} + \rho_2 a_{O,22}\end{aligned}\quad (\text{Eq. S3.6})$$

For an $Mn^{III}Mn^{IV}$ dimer, $S_{I(Mn^{III})} = 2$; and $S_{2(Mn^{IV})} = 3/2$ which gives isotropic spin projection values of $\rho_1 = 2$ and $\rho_2 = -1$, respectively. The above relations are thus approximately: $G = 2g_1 - g_2$, $A_{Mn,1} = 2a_{Mn,1}$, $A_{Mn,2} = -a_{Mn,2}$, $A_{O,1} = 2a_{O,11} - a_{O,12}$; $A_{O,2} = 2a_{O,12} - a_{O,22}$; $P_{Mn,1} = p_{Mn,1}$, $P_{Mn,2} = p_{Mn,2}$; $P_{O,1} = p_{O,1}$, $P_{O,2} = p_{O,2}$.^{17,19} Note that for terminal ligands such as ^{14}N , the same projections apply as for the individual Mn nuclei.

S4. Spin Hamiltonian Formalism – Mn tetramer

S4.1 The Spin Hamiltonian Formalism. Here we consider a single ^{17}O nucleus magnetically interacting with an exchange coupled Mn tetramer. The current assignment for the oxidation states of the four Mn ions when poised in the S_2 state is $\text{Mn}^{\text{III}}\text{Mn}^{\text{IV}}\text{Mn}^{\text{IV}}\text{Mn}^{\text{IV}}$ refs.¹⁹⁻²² This net oxidation state is assumed throughout the text. A basis set that describes the ^{17}O -Mn-tetramer spin manifold can be built from the product of the eigenstates of the interacting spins:

$$|S_1 S_2 S_3 S_4 M_1 M_2 M_3 M_4 I_1 I_2 I_3 I_4 m_1 m_2 m_3 m_4 K k\rangle, \quad \text{Eq. S4.1}$$

Here S_i refers to the electronic spin state of Mn_i , M_i refers to the electronic magnetic sub-level of Mn_i , I_i refers to the nuclear spin state of Mn_i , and m_i refers to the nuclear magnetic sub-level of Mn_i . S_i takes the value 2 for Mn^{III} and 3/2 for Mn^{IV} ; M_i takes the values: $S_i, S_i-1, \dots, 1-S_i, -S_i$; I_i takes the value 5/2 for ^{55}Mn (100% natural abundance); m_i takes the values $-I_i, 1-I_i, \dots, I_i-1, I_i$. K takes the values 5/2 for ^{17}O (0.038% natural abundance); and k takes the values $-K, 1-K, \dots, K-1, K$.

The Spin Hamiltonian that describes the spin manifold of the ^{17}O -Mn tetramer is:

$$\begin{aligned} \hat{H} = & \sum_i \beta_e \vec{B}_0 \cdot \hat{g}_i \cdot \vec{S}_i - \sum_i g_n \beta_n \vec{B}_0 \cdot \vec{I}_i + \sum_i \vec{S}_i \cdot \hat{a}_{\text{Mn}_i} \cdot \vec{I}_i + \sum_i \vec{I}_i \cdot \hat{p}_{\text{Mn}_i} \cdot \vec{I}_i \\ & + \sum_i \vec{S}_i \cdot \hat{d}_i \cdot \vec{S}_i - \sum_{i<j} \vec{S}_i \cdot \hat{J}_{ij} \cdot \vec{S}_j - g_o \beta_n \vec{B}_0 \cdot \vec{K} + \sum_i \vec{S}_i \cdot \hat{a}_{\text{O}_i} \cdot \vec{K} + \vec{K} \cdot \hat{p}_{\text{O}} \cdot \vec{K} \end{aligned} \quad \text{Eq. S4.2}$$

It contains: i) an electronic Zeeman term for each Mn (g_i) ion ; ii) a nuclear Zeeman term for each ^{55}Mn (g_n) and ^{17}O (g_o) nucleus; iii) an electron-nuclear hyperfine term for each ^{55}Mn (a_{Mn}) and ^{17}O (a_o) nucleus; iv) an nuclear quadrupole term for each ^{55}Mn (p_{Mn}) and ^{17}O (p_o) nucleus; v) a fine structure term for each Mn (d_i) ion; and vi) pair-wise exchange terms for each Mn-Mn (J_{ij}) interaction .

S4.2 An Effective Spin $\frac{1}{2}$ Ground State. The tetranuclear-manganese cluster of the OEC ($\text{Mn}_4\text{O}_5\text{Ca}$), is usually considered within the strong exchange limit. In this instance the exchange interactions between the Mn ions are significantly larger than any other term of the Spin Hamiltonian.

The resultant electronic spin states of the manifold are then adequately described by a single quantum number, the total spin (S_T). The ‘multiline’ EPR signal observed for the S_2 state of the OEC is derived from only one total spin state, the ground state of the spin manifold with total spin $S_T = 1/2$. The basis set that describes this subspace requires only 15552 vectors which represent the coupling of the effective electronic spin ($S_T = 1/2$) to the nuclear spin of each ^{55}Mn ($I = 5/2$) and ^{17}O ($I = 5/2$) nucleus.

$$\left| \frac{1}{2} \quad M \quad m_1 \quad m_2 \quad m_3 \quad m_4 \quad K \quad k \right\rangle \quad \text{Eq. S4.3}$$

Where M takes all half-integer values: $-\frac{1}{2} \leq M \leq \frac{1}{2}$; m_i (where $i = 1-4$) takes all half integer values: $-\frac{5}{2} \leq m_i \leq \frac{5}{2}$; and k takes all half integer values: $-\frac{5}{2} \leq k \leq \frac{5}{2}$.

The effective Spin Hamiltonian that describes the ground state of the spin manifold ($S_T = 1/2$) is:

$$\hat{H} = \beta_e \vec{B}_0 \cdot \hat{G} \cdot \vec{S} + \sum_i \left(-g_n \beta_n \vec{B}_0 \cdot \vec{I}_i + \vec{S} \cdot \hat{A}_{Mni} \cdot \vec{I}_i \right) - g_o \beta_o \vec{B}_0 \cdot \vec{K} + \vec{S} \cdot \hat{A}_o \cdot \vec{K} + \vec{K} \cdot \hat{P}_o \cdot \vec{K} \quad \text{Eq. S4.4}$$

It contains: i) the Zeeman term for the total electronic spin; ii) Zeeman terms for each ^{55}Mn nucleus and the ^{17}O nucleus; iii) hyperfine terms for each ^{55}Mn nucleus and the ^{17}O nucleus and iv) a quadrupole term for the ^{17}O nucleus. Quadrupole terms are neglected for the ^{55}Mn nuclei as they are considered to only have a small contribution to the energy levels/ eigenstates of the system.

S4.3 ^{17}O Electron Nuclear Double Resonance (ENDOR) spectroscopy. The simulation of ^{17}O EPR/ENDOR spectra of the OEC can be further simplified. As the ^{17}O couplings are small, they do not significantly contribute to the inhomogeneous linewidth of the S_2 EPR spectrum. Thus for simulation of the EPR spectrum, the terms in Eq. 10 relating to the ^{17}O nucleus can be excluded (Eq. S4.5).

$$\hat{H}_{EPR} = \beta_e \vec{B}_0 \cdot \hat{G} \cdot \vec{S} + \sum_i \left(-g_n \beta_n \vec{B}_0 \cdot \vec{I}_i + \vec{S} \cdot \hat{A}_{Mni} \cdot \vec{I}_i \right) \quad \text{Eq. S4.5}$$

Similarly, a simplified effective Spin Hamiltonian can be used for the simulation of ENDOR spectra associated with the ^{17}O nucleus. As the ^{17}O nuclei does not significantly couple to the four ^{55}Mn nuclei, terms in Eq. S4.4 associated with the ^{55}Mn nuclei can be excluded (Eq. S4.6).

$$\hat{H}_{ENDOR} = \beta_e \vec{B}_0 \cdot \hat{G} \cdot \vec{S} - g_o \beta_o \vec{B}_0 \cdot \vec{K} + \vec{S} \cdot \hat{A}_o \cdot \vec{K} + \vec{K} \cdot \hat{P}_o \cdot \vec{K} \quad \text{Eq. S4.6}$$

In practice however, the above Spin Hamiltonian (Eq. S4.6) is only valid when the ^{17}O ENDOR spectrum is collected at the center field of the S_2 multiline spectrum as at this position all powder pattern orientations are sampled uniformly. ^{17}O ENDOR spectra collected on the high and low field edges of the multiline spectrum must also take into account the sampling of the powder pattern orientations, which for the OEC is defined by the hyperfine coupling of the ^{55}Mn nuclei along with the g-tensor. Eq. S4.6 can still be used (i.e. terms associated with the ^{55}Mn nuclei can be excluded) but each orientation must include a weighting derived from simulation of the EPR lineshape.

S5.1 Control ESE detected field sweep W- and Q-band EPR

S5.1. ESE detected field sweep W band EPR. Field sweep W-band spectra of the OEC of *T. elongatus* grown in $^{14}\text{NH}_4$ and $^{15}\text{NH}_4$ media, poised in the S_1 and S_2 states, resuspended in buffer solutions made with $^1\text{H}_2^{16}\text{O}$ and $^1\text{H}_2^{17}\text{O}$ were collected and are shown in **Figure S5.1**. A broad species that spans the entire spectral range collected is observed in the background S_1 spectra, assigned to the oxidized cyt.b559/cyt.c550. A small amount of Mn^{II} is also observed, centered at $g\sim 2$. At W-band the six-line structure of this species is readily observed: it is made up of two contaminant species, a cavity signal seen with an empty sample tube and a $\text{Mn}^{\text{II}}(\text{H}_2\text{O})_6$. Care was taken to minimize the second component. A third, narrow species is seen at $g\sim 2$, assigned to the stable tyrosine D (Y_D) radical. This signal served as a reference for the quality of the resonator such that the optimal $\pi/2$ pulse seen in the Y_D microwave nutation experiment was subsequently used for the S_2 state, typically varying between 20-28 ns. All these species are partially saturated and in the case of Mn^{II} , partially suppressed under the experimental conditions used to collect the S_2 spectra.

The S_2 spectra observed for both buffering regimes all display the multiline signal centered at $g = 1.976$. The hyperfine structure is less resolved at high field presumably due to an increase in the g /hyperfine strain. The envelope is broader than that observed at Q-band suggesting that while the g -tensor components are still unresolved, the g -anisotropy significantly contributes to the width of the signal. The spectrum is nominally the same as observed in the studies by Teutloff et al.²³ A simulation of the EPR lineshape was performed using the ^{55}Mn hyperfine tensors measured for *T. elongatus*. The fitted G-tensor was found to be [1.997, 1.973, 1.963], similar to that previously reported by Teutloff et al.²³ In these simulations the hyperfine tensors and their relative orientations to the G-tensor were fixed as per the publication of Cox et al.²⁴

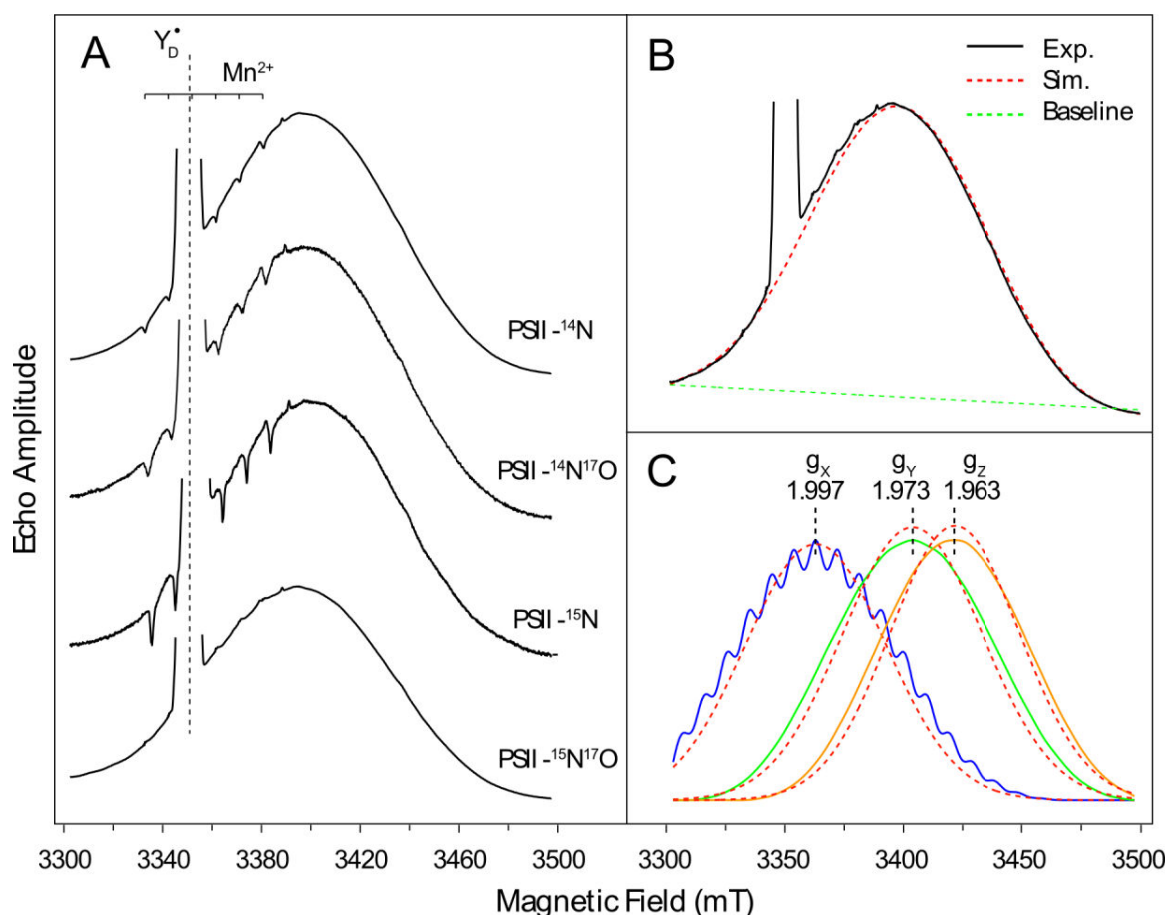


Figure S5.1 A: W-band Echo-detected field-sweep spectra of ^{14}N -PSII and ^{15}N -PSII of *T. elongatus* poised in the S_2 state (200 K white light), exchanged into H_2^{16}O and H_2^{17}O buffer in the S_1 state. **B:** A simulation of the S_2 spectrum of ^{15}N -PSII exchanged in H_2^{17}O buffer using the Spin Hamiltonian formalism, black line – data, red dashed line – simulation; green dashed lined - baseline; **C** A decomposition of the EPR simulation along the three principal axes, x (blue), y (green) and z (red).

S5.2. ESE detected field sweep Q band EPR. Figure S5.2 shows the Hahn-echo detected field sweep Q-band spectra of the OEC of *T. elongatus* poised in the S_1 and S_2 states, resuspended in buffer solutions made with unlabelled water, $^2\text{H}_2\text{O}$ and $^1\text{H}_2^{17}\text{O}$. The top panel displays the raw spectra, whereas the bottom panel represents the pseudo-modulated, ‘cw like’, spectra. A broad species that spans the entire spectral range is observed in the background S_1 spectra, assigned to the oxidized cyt.b559/cyt.c550. A similar broad species assigned to a small amount of $\text{Mn}^{\text{II}}(\text{H}_2\text{O})_6$ is also observed,

centered at $g \sim 2$. A third, narrow species is seen at $g \sim 2$, assigned to the stable tyrosine D (Y_D) radical. All these species are partially saturated and in the case of Mn^{II} , partially suppressed under the experimental conditions used.

The S_2 spectra observed for the three buffering regimes all display the typical 20-24 line multiline signal. The three spectra are essentially invariant and identical to a previous report from our laboratory. The absence of line-broadening for the sample resuspended in $^1H_2^{17}O$ suggest the magnetic coupling of exchangeable O (water/hydroxo/oxo) groups to the OEC is smaller than the intrinsic EPR linewidth, i.e. <20 MHz. A similar upper bound can be placed on the 1H coupling to the OEC, as the EPR linewidth does not narrow upon exchange into the 2H_2O buffer.

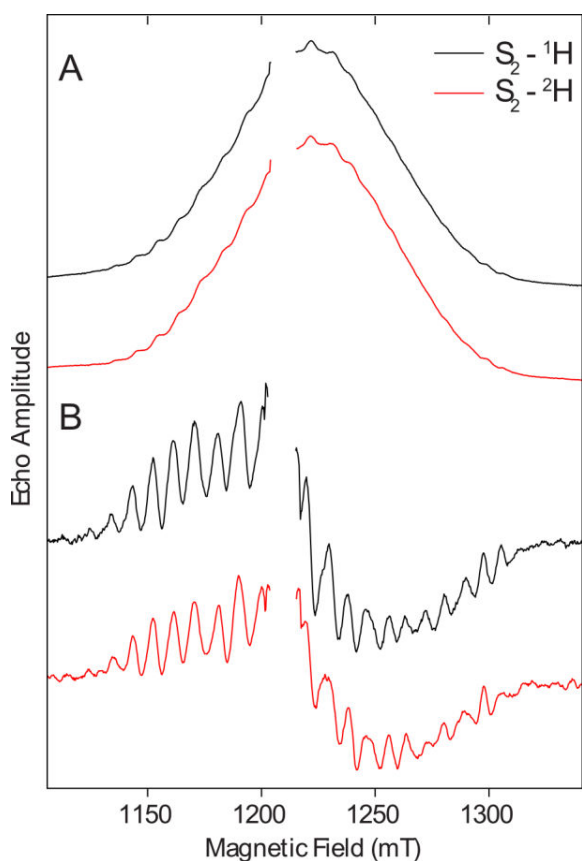


Figure S5.2 A: Q-band Echo-Detected Field sweep spectra of ^{14}N -PSII *T. elongatus* poised in the S_2 state (200 K white light), exchanged into unlabelled water (black) and 2H_2O (red) buffer in the S_1 state. **B:** Corresponding pseudo-modulated EPR lineshapes for the absorption spectra presented in panel A. These spectra were generated by convoluting the original absorption spectra with a Bessel function of the 1st kind. The peak-to-peak field modulation used was 3 mT.

S6.1 ^{17}O -ELDOR detected NMR/ $^1\text{H}/^2\text{H}$ -ENDOR data processing. EDNMR spectra presented throughout the manuscript were processed as follows. The central blind spot, a Lorentzian like line centered at the fixed microwave frequency ($\nu_{\text{mw}}^{(0)}$) was subtracted from the spectrum. As the blind spot was not symmetric about $\nu_{\text{mw}}^{(0)}$ the baseline was approximated by a cubic spline. The two halves of the EDNMR were then inverted, overlaid and averaged to give an ENDOR like spectrum shown in the text, see **Figures 3, 4, 5, 6, 7, 8 and 7**. The x-axis gives the difference of the spectral line positions relative to the central hole in MHz. The overlaid halves of the EDNMR spectrum served as an internal check with regard to the baseline subtraction as the two halves should be essentially the same in terms of both line positions and intensities.

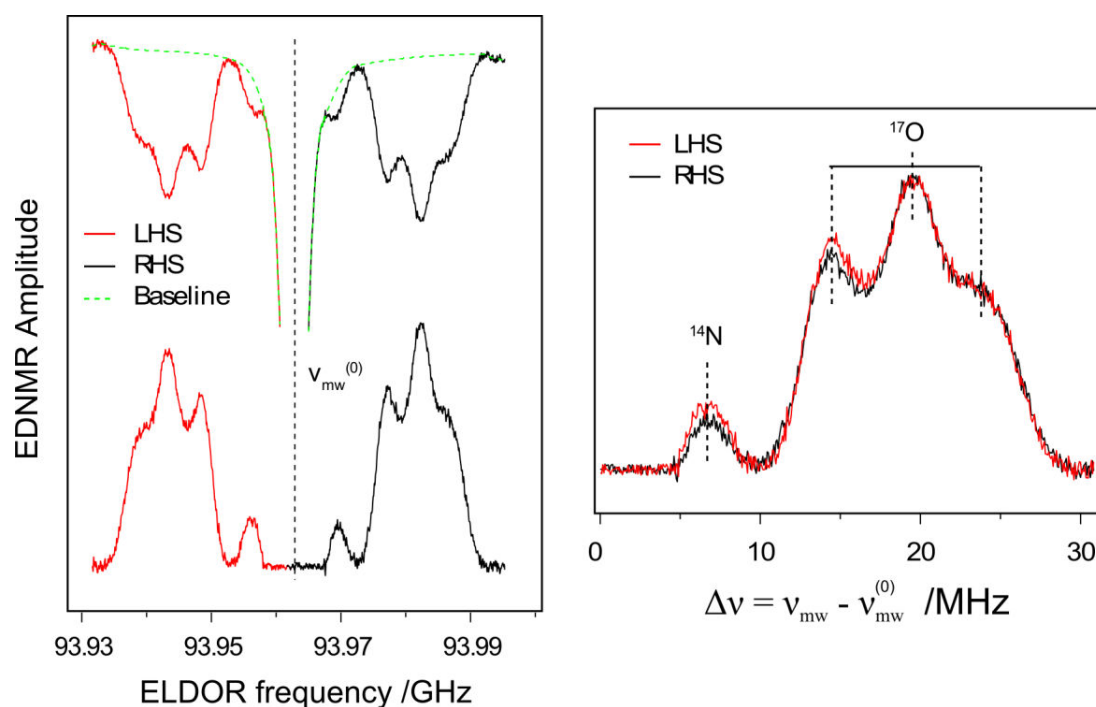


Figure S6.1 Baseline correction procedure used for processing of 94 GHz EDNMR data. **LHS panel:** raw EDNMR data (red/black line) fitted to an cubic spline (green dashed line); **RHS panel:** The two halves of the baseline corrected EDNMR spectrum overlaid.

A similar procedure was used to symmetrise the $^1\text{H}/^2\text{H}$ ENDOR data presented in **Figure 6**.

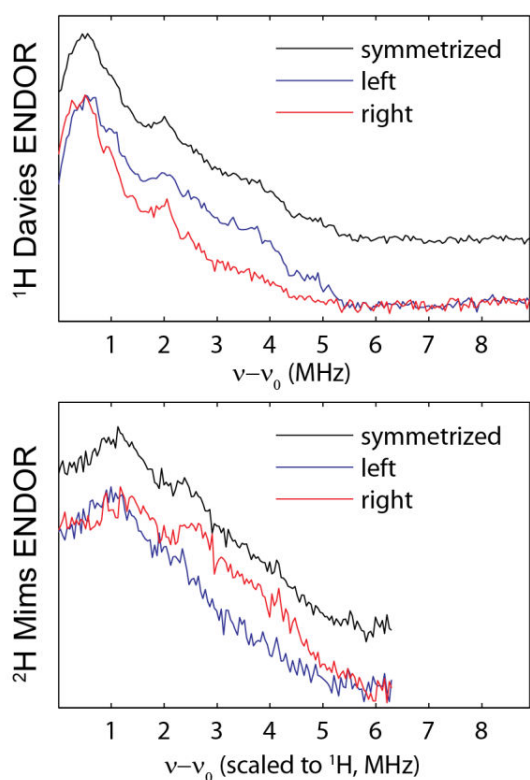


Figure S6.2. Symmetrization procedure for $^1\text{H}/^2\text{H}$ -ENDOR spectra. Left ($\nu < \nu_0$) and right ($\nu > \nu_0$) parts of spectrum were compared and mirrored against the Larmor frequency of the respective nucleus (ν_0). ^2H -ENDOR spectra were scaled to ^1H . Simulations were performed on the averaged spectra.

S7.1 Spin Hamiltonian Simulations of the ^{17}O EDNMR

S7.1. The $S = 1/2$, $I = 5/2$ (^{17}O) Spin manifold. The $S = 1/2$, $I = 5/2$ (^{17}O) spin sub-manifold for the ^{17}O labeled mixed-valence $\text{Mn}^{\text{III}}\text{Mn}^{\text{IV}}$ complexes (and the ^{17}O labeled PSII poised in the S_2 state) is shown in **Figure S7.1** at a position within the inhomogeneous linewidth of the EPR multiline signal, with effective g value g_{eff} . The inhomogeneous linewidth of the EPR signal is defined by the coupling of the unpaired electronic spin ($S = 1/2$) with the two ^{55}Mn hyperfine tensors. As the hyperfine couplings are significantly larger than the g -anisotropy and relatively isotropic, for most positions within the spectral envelope all powder pattern orientations are equally sampled. This however is not the case for the high and low field edges of the spectral envelope. Here only a fraction of the powder pattern orientations are sampled and thus the resulting $^{55}\text{Mn}/^{17}\text{O}$ ENDOR/EDNMR spectra show small but measureable orientation selectivity. As the interaction between the ^{55}Mn and ^{17}O nuclei is small, they can be treated separately as described in the Theory section.

The energy-level scheme of the ^{17}O spin sub-manifold assumes the weak coupling limit i.e. $|v| > \left| \frac{A}{2} \right|$.

The red arrows indicate the allowed (single quantum) NMR transitions of the manifold however as the spin sub-manifold now contains multiple levels, multiple quantum transitions can occur (not shown).

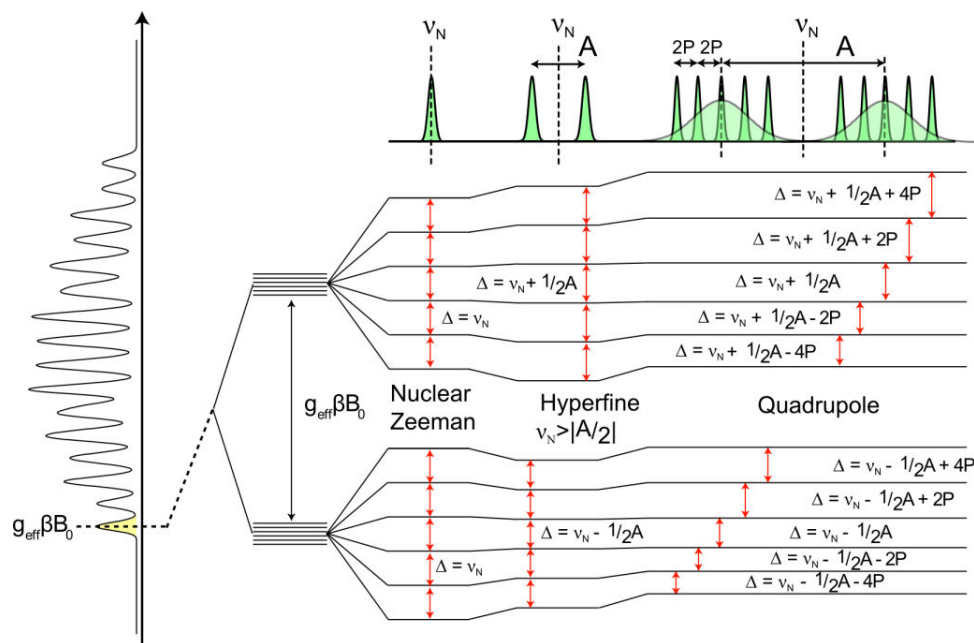


Figure S7.1. ^{17}O -spin submanifold of the effective $S = \frac{1}{2}$ spin system that described the exchange coupled Mn dimer/tetramer systems presented here. The ^{17}O splitting (spin manifold) shown are unresolved in the EPR spectrum (**LHS trace**) but can be probed using pulse EPR techniques ENDOR/EDNMR (**Top trace**). The energy-level scheme/ENDOR spectrum assumes the weak coupling limit i.e. $|v_N| > \left| \frac{A}{2} \right|$.

S7.2. EDNMR as compared to ENDOR, the four level system. ELDOR-detected NMR (EDNMR) and Davies ENDOR are both polarization transfer experiments. They essentially generate the same magnetization state but via two different routes. This can be seen in the four level system i.e. $S = \frac{1}{2}$, $I = \frac{1}{2}$. In Davies ENDOR, the initial/preparatory inversion pulse selectively inverts one pair of electronic sublevels i.e. $\psi_1 \rightarrow \psi_3$, where $\psi_1 = \left| \frac{1}{2} \quad \frac{1}{2} \right\rangle$ and $\psi_3 = \left| -\frac{1}{2} \quad \frac{1}{2} \right\rangle$. A subsequent radiofrequency pulse then induces a transition between the nuclear sublevels i.e. $\psi_3 \rightarrow \psi_4$ resulting in the non-thermal

equilibrium population shown in **Figure S7.2A**. The same state is achieved in the EDNMR experiment by direct excitation of the spin forbidden transition $\psi_1 \rightarrow \psi_4$ using a second (pump) microwave pulse, which is swept about the resonance frequency. Thus both methods give the same nuclear transition.

The two techniques though differ in the detection of nuclear transitions. In the Davies experiment, the nuclear transition is observed via the recovery (loss of inversion) of the inverted primary echo, analogous to CW-ENDOR where nuclear transitions are detected via desaturation of the pumped EPR transition. In contrast in the EDNMR experiment, the same nuclear transition is measured via the loss of the primary echo. Thus both techniques are dependent on the initial intensity of the primary echo i.e. transition probability of the allowed EPR transition. However, in the weak coupling limit where the hyperfine coupling is small relative to the Larmor frequency ($A \ll 2\nu$), both allowed EPR transitions i.e. $\psi_1 \rightarrow \psi_3, \psi_2 \rightarrow \psi_4$, will have a transition probability of approximately 1. As a consequence this component of the intensity calculation does not need to be explicitly included.

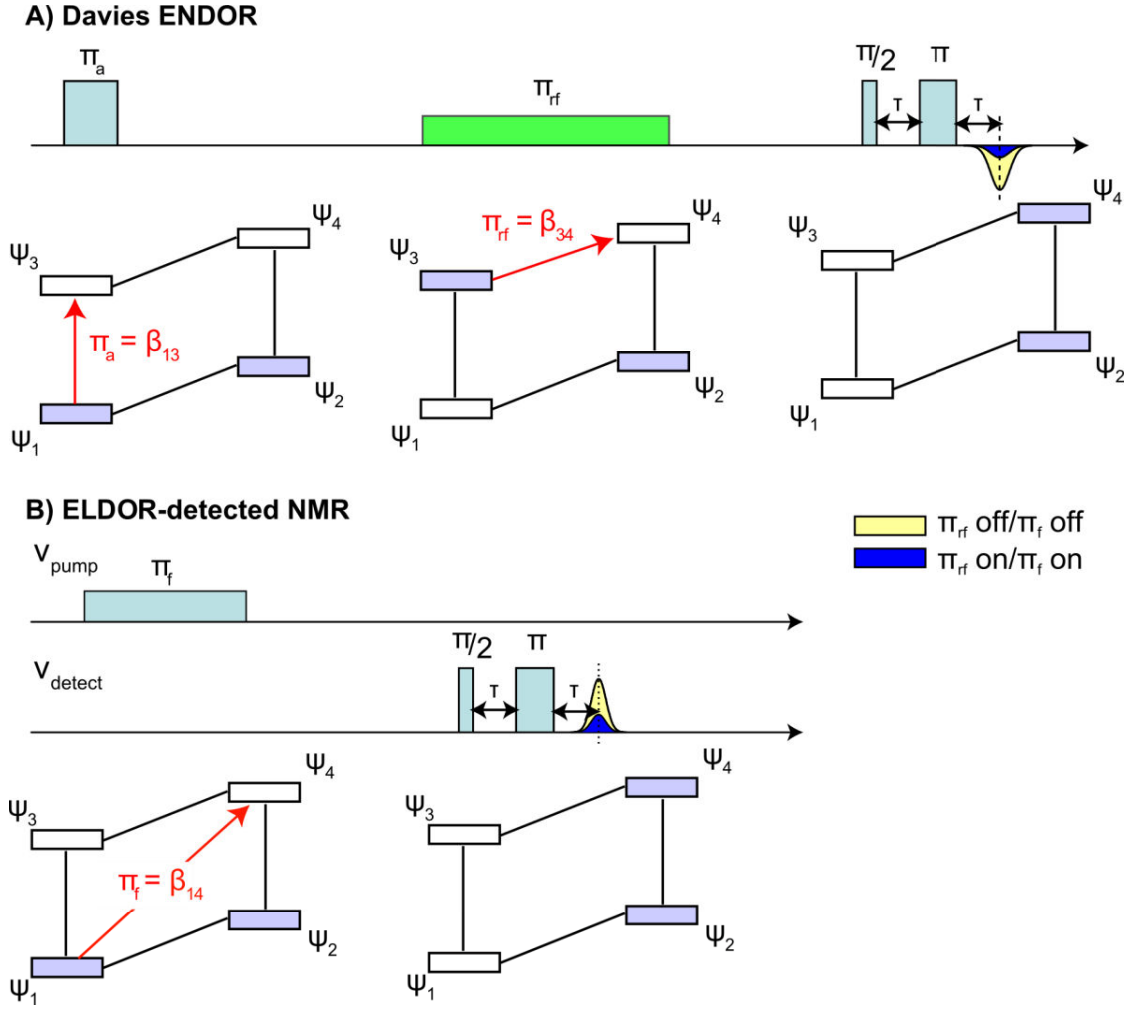


Figure S7.2. The population evolution for the four level system generated using A) Davies ENDOR sequence; B) ELDOR-detected NMR sequence. The 1st microwave pulse must be selective. It should only excite one transition of the Spin manifold: A) $\psi_1 \rightarrow \psi_3$, B) $\psi_1 \rightarrow \psi_4$.

The transition probabilities of the EDNMR experiment can be expressed in terms of effective flip angles:

$$\beta_{14} = \beta_0 \sqrt{P_{14}} \quad \text{Eq. S7.2} \quad P_{14} = \left| \langle \psi_4 | \hat{H}_1 | \psi_1 \rangle \right|^2 \quad \text{Eq. S7.1}$$

Where: β_0 is the nominal flip angle (for an allowed electronic transition) and \hat{H}_1 is given by:

$$\hat{H}_1 = \beta \vec{B}_1 \cdot \hat{g} \cdot \vec{S} - \beta_n g_n \vec{B}_1 \cdot \vec{I} \quad \text{Eq. S7.2}$$

This gives the approximate transition intensities for the nuclear transition of interest in the weak coupling limit:²⁵

$$I_{EDNMR} \approx 1 - \cos(\beta_{14}) \approx 1 - \left(1 - \frac{(\beta_{14})^2}{2} + \dots \right) \propto P_{14} \quad \text{Eq. S7.3}$$

As a final point, it should be noted that β_0 is not constant but instead is dependent on the microwave frequency of the HTA pulse. As the pump frequency (ν_{MW}) shifts away from the resonator frequency (ν_{MW}^0) the HTA pulse must increase in amplitude to compensate for the effective decrease in the B_1 field.

$$I_{EDNMR} \approx 1 - \cos(\beta_{14}) \approx 1 - \left(1 - \frac{(\beta_{14})^2}{2} + \dots \right) \propto \beta_0(\nu_{MW}) \cdot P_{14} \quad \text{Eq. S7.4}$$

Where $\beta_0(\nu_{MW})$ is the functional representation of the resonator response profile which should be approximately Lorentzian, centered at the resonator frequency (ν_{MW}^0). Thus an EDNMR signal spread over a large frequency range will be susceptible to a predictable line-intensity modification. If however the EDNMR signal is narrow (<10 MHz) as seen for the $^{17}\text{O}/^{14}\text{N}$ single quantum signals reported here, this effect does not need to be explicitly included in Spin Hamiltonian simulations to reproduce the spectral profile. This is not the case though for the double quantum envelope and as such the optimal HTA pulse for the low and high frequency edges is not the same, leading to enhancement/suppression of the edges of the envelope relative to each other. It is noted that similar line-intensity artifacts are seen in pulse ENDOR due to non-linearity in the B_2 field.

S7.3. The $S = 1/2$, $I = 5/2$ (^{17}O) EDNMR spectrum. A cartoon of the multiple contributions to the EDNMR spectrum is shown in **Figure S7.3**. This figure essentially shows the same information as

Figure S7.1, but uses the same layout shown in **Figure S7.2**. In this way the positions of the spin allowed and forbidden transitions of the manifold for any pair of states within the ^{17}O -submanifold can be identified.

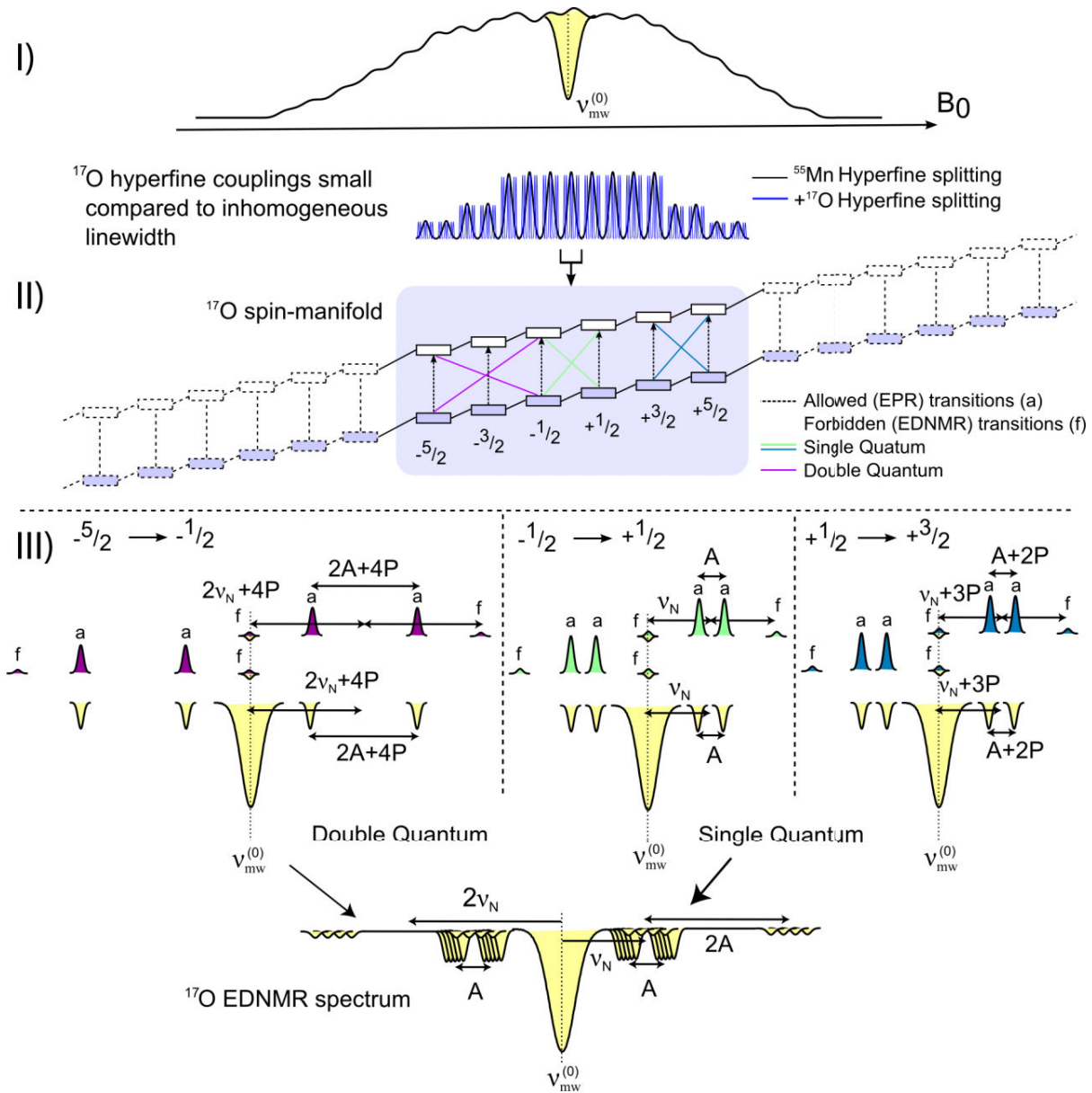


Figure S7.3. I) Typical EPR multiline spectrum seen for the exchange coupled Mn dimer/tetramer systems presented here. The ^{17}O hyperfine couplings of O ligands bound to the Mn are smaller or of the same order of magnitude as the linewidth of the EPR spectrum. II) Cartoon of the ^{17}O -spin submanifold (see **Figure S7.1**) at the marked field position showing a selection of single and double quantum transitions. III) EDNMR spectra of individual single (green/blue) and double (purple) transitions.

within the ^{17}O -spin submanifold. Also shown is the net EDNMR spectrum for the ^{17}O -spin submanifold including only single and double quantum transitions. The energy-level scheme/EDNMR spectrum assumes the weak coupling limit i.e. $|v| > \left| \frac{A}{2} \right|$.

S7.4. ^{17}O EDNMR Spin Hamiltonian Simulations. The preliminary EDNMR Spin Hamilton simulation shown in the text take into account the features described in the previous sections. EDNMR line intensities were calculated as per equation S7.7. The contribution of the three ^{17}O species was scaled to the component of largest hyperfine coupling i.e. the μ -oxo bridge. The experimental parameters of the EDNMR experiment were optimized to visualize this species and as such the HTA pulse used represents a π pulse for this species. The two more weakly coupled species are under rotated by this HTA pulse (as the transition intensity scales with the size of A_{dip}) and are thus partially suppressed under these conditions. Scaling factors used were: $^{17}\text{O}(\text{strong}) = 1$; $^{17}\text{O}(\text{intermediate}) = 0.62$; $^{17}\text{O}(\text{matrix}) = 0.46$. The same scaling factors were used for all data traces collected across the ^{17}O EDNMR surface. The same scaling factors reproduced the ^{17}O EDNMR data collected in ^{15}N -PSII (not shown).

The intensity of the double quantum ^{17}O signal envelope relative to the single quantum envelope is significantly larger than expected for both the BIPY model and PSII. It is hypothesized that this is primarily due to the large unresolved quadrupole coupling. Test simulations show that inclusion of the quadrupole coupling can increase the magnitude of the double quantum envelope to approximately the same magnitude as seen in the experiment i.e. $\sim 20\%$ of the single quantum envelope. It is also noted that quadrupole coupling also appears to modify the intensity profile of the EDNMR double quantum transitions and can lead to significant asymmetry, especially for the more weakly coupled species where the quadrupole coupling is of the same order as the hyperfine coupling. As the quadrupole coupling was not explicitly included in our simulations three corrections were included:

- a. The intensity profile of the double quantum envelope was fitted independently from the single quantum envelope.
- b. The relative intensities of the (+) and (-) branches for the fitted double quantum signals were allowed to vary by up to 50%.
- c. The double quantum lines were allowed to broaden as compared to the single quantum lines as the quadrupole splitting should be larger for the double quantum envelope (see **Figure S7.3**).

Simulations that explicitly include quadrupole coupling form part of ongoing work of our laboratory.

S7.5 ^{17}O EDNMR Spin Hamiltonian Simulations of the BIPY complex. The spectral profile of the ^{17}O EDNMR signal at all field positions could be simulated using the Spin Hamiltonian formalism described in the theory section. Table 1 lists all Spin Hamiltonian parameters. These preliminary simulations required only one strongly coupled ^{17}O nucleus as the two labelled μ -oxo bridges are symmetrically related and a weakly coupled ^{17}O nucleus representing a more distant matrix water molecule. The simulations are described in the Theory section. It is readily seen that the simulations reproduce the spectral width and overall lineshape of all the ^{17}O signal seen.

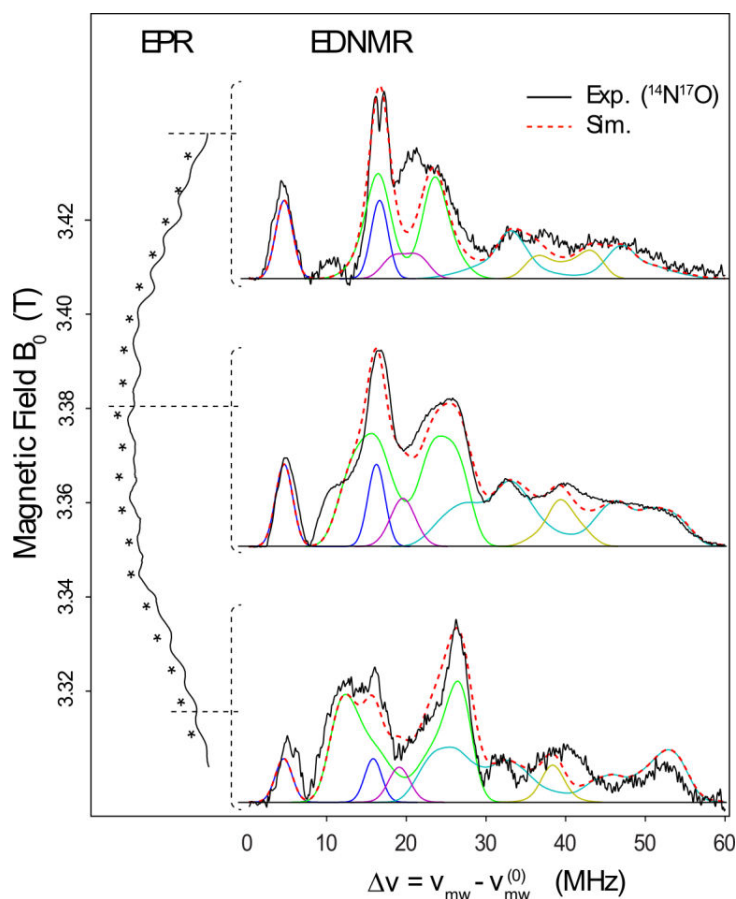


Figure S7.4. Simulations of the EDNMR data presented in **Figures 4** spectra using the Spin Hamiltonian formalism. The black lines represent the data, the red dashed lines represent the simulation. The different components of the simulation are shown by transparent coloured traces: $^{14}\text{N}(\text{S.Q})$ blue, $^{17}\text{O}(\mu\text{oxo-S.Q})$ green; $^{17}\text{O}(\mu\text{oxo-D.Q})$ cyan; $^{17}\text{O}(\text{matrix-S.Q})$ purple; $^{17}\text{O}(\text{matrix-D.Q})$ yellow. Spin Hamiltonian parameters can be found in **Table 1** of the main text.

S.8 W-band ^{17}O ENDOR ^{14}N -PSII *T. elongatus* poised in the S_2 state (200 K white light)

S.8.1 ^{17}O Davies ENDOR of the OEC poised in the S_2 State. The most strongly coupled ^{17}O signal seen using EDNMR assigned to a μ -oxo bridge can also be observed using Davies-ENDOR. 94 GHz EDNMR spectra of ^{14}N -PSII and universally labeled ^{15}N -PSII, resuspended in H_2^{17}O and poised in the S_2 state compared to Davies ENDOR are shown in **Figure S8.1**. In all samples the same signal is observed centered at the Larmor frequency of ^{17}O [$\nu(^{17}\text{O}) \sim 19.6$ MHz]. This weakly coupled component of the signal is suppressed in the Davies ENDOR experiment due to blind spotting, as seen for the Mn^{II} complex, see main text **Figure 3**.

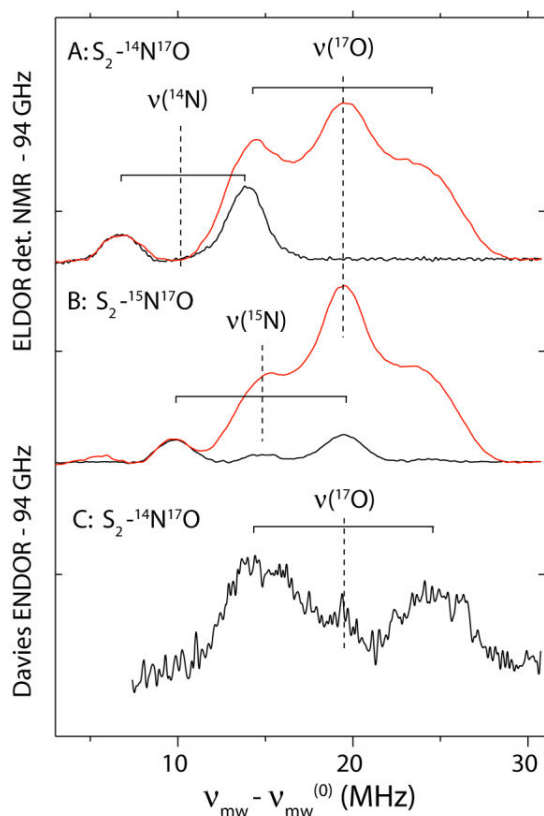


Figure S8.1 W-band EDNMR spectra of ^{14}N -PSII and ^{15}N -PSII of *T. elongatus* poised in the S_2 state (200 K white light), exchanged into unlabelled water and H_2^{17}O buffer in the S_1 state, measured at the center of the multiline spectrum (3.4 T). **A**: ^{14}N -PSII in unlabelled water (black) and resuspended in H_2^{17}O (red); **B** ^{15}N -PSII in unlabelled water (black) and resuspended in H_2^{17}O (red); **C** Davies ENDOR spectrum of ^{14}N -PSII resuspended in H_2^{17}O (after 12 hours of accumulation)

S.8.2 Weakly coupled ‘Matrix’ water - W-band ^{17}O -Mims ENDOR. The matrix component of the envelope is best visualized not by using EDNMR but instead by using Mims ENDOR. 94 GHz EDNMR spectra of ^{14}N -PSII and universally labeled ^{15}N -PSII, resuspended in H_2^{17}O and poised in the S_2 state are shown in **Figure S8.2A and B (black solid lines)**. In both samples the same signal is observed centered at the Larmor frequency of ^{17}O [$\nu(^{17}\text{O}) \sim 19.6$ MHz]. The signal has FWHM < 1 MHz and a near Lorentzian lineshape, with a resolved splitting of 0.5 MHz. Similar lineshapes albeit of enhanced resolution have been identified previously in ^{17}O model complex systems e.g. weakly coupled $^1\text{H}_2^{17}\text{O}$ coordinating Gd^{3+} complexes. The characteristic Lorentzian lineshapes arise due to the relatively large quadrupole interaction relative to the hyperfine term.¹⁶

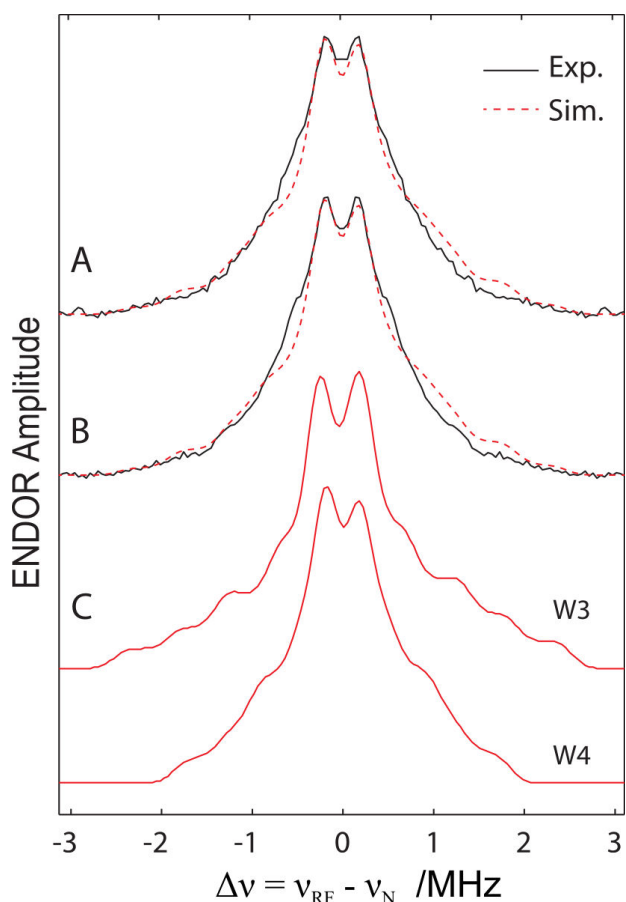


Figure S8.2 W-band ^{17}O -Mims ENDOR spectra of ^{14}N -PSII and ^{15}N -PSII of *T. elongatus* poised in the S_2 state (200 K white light), resuspended into H_2^{17}O buffer in the S_1 state, measured at the center of the multiline spectrum (3.4 T). Simulations are shown red (dashed line). Simulation parameters are expressed in the form:

$$A_L = A_{iso} + A_{aniso} = A_{iso} + [A_X \quad A_Y \quad A_Z],$$

$$P_L = [Q \quad \eta] \text{ Simulation parameters:}$$

$$A(W3) = 0.25 + [0.07 \quad -0.28 \quad -0.35],$$

$$A(W4) = 0.25 + [0.01 \quad -0.23 \quad 0.24] \text{ and}$$

$$Q(W3/W4) = [7.4 \quad 0.25], \text{ see S11.}$$

S9. Multipole coupling model. The through-space coupling estimates for the ^1H and ^{17}O nuclei associated with the OEC were calculated numerically using the same approach adopted in Randall et al.²⁶ and references therein. Here the contribution of all four Mn are included in the calculation of the through space interaction. The effective through space interaction for a given nucleus is made up of a weighted linear sum of the individual dipolar interaction of said nucleus with each Mn ion. The contribution (weight) of each Mn interaction is given by its corresponding spin projection coefficient. For the calculations reported here the values of model 11 (Siegbahn model) Cox et al.²⁷ /Pantazis et al.²⁸ are used. The effective through space interaction takes the form:

$$\hat{A} = \sum_i \rho_i \hat{a}_i \tag{Eq. S9.1}$$

Where \hat{a}_i defines the $\text{Mn}_i\text{-}^1\text{H}/^{17}\text{O}$ dipole interaction and ρ_i is the spin projection coefficient for Mn_i .

The dipole tensor \hat{a}_i takes the form:

$$\hat{a}_i = \frac{g_e g_n \beta \beta_n}{r_i^5} \begin{bmatrix} r_i^2 - 3x^2 & -3xy & -3xz \\ -3xy & r_i^2 - 3y^2 & -3yz \\ -3xz & -3yz & r_i^2 - 3z^2 \end{bmatrix} \quad \text{Eq. S9.2}$$

Where r_i is the distance between the nucleus and Mn_i .

$$r_i = \sqrt{(x - x_{\text{Mn},i})^2 + (y - y_{\text{Mn},i})^2 + (z - z_{\text{Mn},i})^2} \quad \text{Eq. S9.3}$$

The solution of the eigenvalue problem:

$$\hat{A}\phi = \hat{\lambda}\phi \quad \text{Eq. S9.4}$$

yields the principal values of the hyperfine tensor $[\lambda_1, \lambda_2, \lambda_3]$ – the hyperfine tensor expressed in a coordinate system such that the tensor is diagonal – and eigenvectors ϕ_1, ϕ_2, ϕ_3 , which define the orientations of the principal components of the hyperfine tensor expressed in the original coordinate system. The rotated hyperfine tensor ($\hat{\lambda}$) takes the form:

$$\hat{\lambda} = \begin{bmatrix} \lambda_1 & 0 & 0 \\ 0 & \lambda_2 & 0 \\ 0 & 0 & \lambda_3 \end{bmatrix} = \delta \cdot \begin{bmatrix} 1 - \eta & 0 & 0 \\ 0 & 1 + \eta & 0 \\ 0 & 0 & -2 \end{bmatrix} \quad \delta = \frac{\lambda_3}{2}; \eta = \frac{\lambda_1 - \lambda_2}{\lambda_3}; \quad \text{Eq. S9.5}$$

$$|\lambda_1| \leq |\lambda_2| \leq |\lambda_3|$$

It can be re-expressed in terms of two parameters δ and η ; where δ defines the magnitude of the hyperfine coupling and η the deviation of the hyperfine tensor from axial symmetry, $\eta = 0$ (axial), $\eta = 1$ (rhombic). These values are tabulated in the in the next section (**S10**) for all $^1\text{H}/^{17}\text{O}$ nuclei within 5 Å of the OEC as identified in the Umena et al.²⁹ structure.

S10. $^1\text{H}/^2\text{H}/^{17}\text{O}$ coupling estimates based on the coordinates of Umena et al.²⁹

Mn(IV): A4, B3, C2

Mn(III): D1

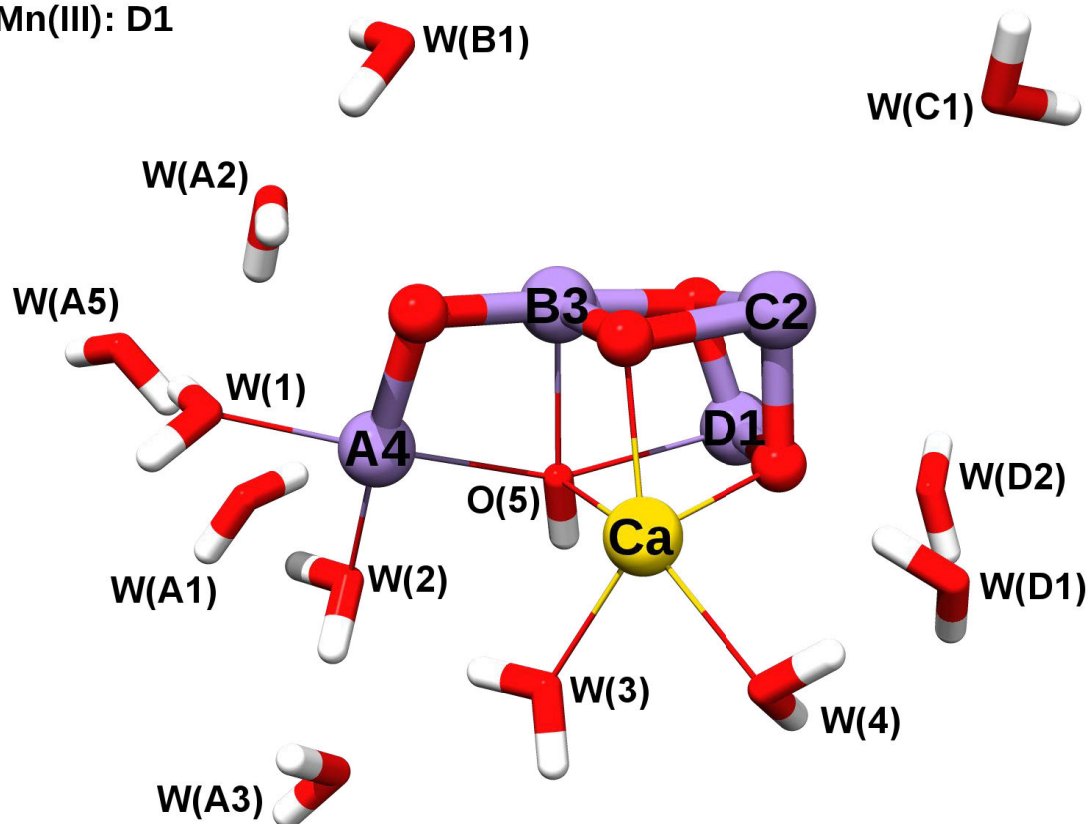


Figure S10.1: The positions of the potential (exchangeable) substrate ($\text{H}_2\text{O}/\text{HO}^-/\text{O}^{2-}$) in the structure of Umena et al.²⁹

Using the approach outlined in the previous section, supporting information S9, through-space (dipolar) coupling estimates for the ^1H and ^{17}O nuclei associated the OEC, out to a radius of 5 Å. The contribution of all four Mn were included in the calculation of the net through space interaction. The effective through space interaction for a given nucleus is made up of a weighted linear sum of the individual dipolar interaction of said nucleus with each Mn ion. The contribution (weight) of each Mn interaction is given by its corresponding spin projection coefficient. For the calculations reported here the values of model 11 (Siegbahn model) Cox et al.²⁷ /Pantazis et al.²⁸ are used.

Table S10.1: ^{17}O -Mn distances and theoretical ^{17}O couplings for the μ -oxo substrate positions in the Umena et al.²⁹ structure using the isotropic spin projections for the model of Siegbahn (model 11) reported in Pantazis et al.²⁸

	Mn-O distances (Å)				
	Mn _{A4} -O-Mn _{B3}		Mn _{B3} -O-Mn _{C2}	Mn _{C2} -O-Mn _{D1}	
	O4	O5	O2	O1	O3
Mn _{A4}	2.107	2.504	3.778	5.172	4.704
Mn _{B3}	2.089	2.379	1.873	3.517	2.126
Mn _{C2}	4.524	3.840	2.131	2.062	2.103
Mn _{D1}	5.163	2.602	3.730	1.871	1.810
Projected ^{17}O hyperfine Tensors (MHz)					
$A_{dip}(^{17}\text{O})^a$	2.041	1.750	1.229	3.476	3.972
$\eta(^{17}\text{O})^b$	0.513	0.842	0.589	0.526	0.140

a) principal value for anisotropic component of the ^{17}O hyperfine tensor:

$$A_{dip}(^{17}\text{O}) = \frac{T_1 + T_2}{2} = -\frac{T_3}{2}; |T_1| \leq |T_2| \leq |T_3|$$

b) rhombicity of the ^{17}O hyperfine tensor as defined by: $\eta(^{17}\text{O}) = \frac{T_1 - T_2}{T_3}; |T_1| \leq |T_2| \leq |T_3|$

Table S10.2: ^{17}O -Mn distances and theoretical ^{17}O couplings for the remaining (protonated) substrate positions in the Umena et al.²⁹ structure using the isotropic spin projections for the model of Siegbahn (model 11) reported in Pantazis et al.²⁸

	Mn-O distances (Å)			
	Mn _{A4} -OH		Ca-OH ₂	
	W(2)	W(1)	W(3)	W(4)
Mn _{A4}	2.082	2.220	3.775	6.046
Mn _{B3}	4.639	4.689	4.925	5.826
Mn _{C2}	6.777	7.357	5.598	4.883
Mn _{D1}	5.551	7.143	4.726	4.927
Projected ^{17}O Hyperfine Tensors (MHz)				
$A_{dip}(^{17}\text{O})^a$	1.187 ^b	1.032	-0.177	0.119
$\eta(^{17}\text{O})^b$	0.070 ^c	0.040	0.614	0.945

Table S10.3: ^{17}O -Mn distances and theoretical ^{17}O couplings for the additional waters in the Umena et al.²⁹ structure using the isotropic spin projections for the model of Siegbahn (model 11) reported in Pantazis et al.²⁸

	Mn-O distances (Å)							
	Near Mn _{A4}			Near Mn _{D1}		Near Mn _{B3}	Near Mn _{C2}	
	W(A3)	W(A4)	W(A1)	W(A2)	W(D2)	W(D1)	W(B1)	W(C1)
Mn _{A4}	4.169	4.708	3.909	3.984	8.729	7.550	5.227	9.080
Mn _{B3}	6.627	6.523	5.972	4.366	7.187	6.173	3.982	6.319
Mn _{C2}	8.131	9.381	8.521	6.567	6.084	4.107	5.810	3.922
Mn _{D1}	7.109	8.492	6.978	7.601	3.992	3.967	7.099	6.334
Projected ^{17}O Hyperfine Tensors (MHz)								
$A_{dip}(^{17}\text{O})$	0.140 ^a	0.098	0.168	0.185	0.254	0.270	-0.124	-0.130
$\eta(^{17}\text{O})^b$	0.215 ^b	0.172	0.213	0.554	0.039	0.549	0.454	0.147

Table S10.4: ^1H -Mn distances and theoretical ^1H couplings for the μ -oxo substrate positions in the Umena et al.²⁹ structure using the isotropic spin projections for the model of Siegbahn (model 11) reported in Pantazis et al.²⁸

	Mn-O distances (Å)								
	Mn _{B3} -OH O5	Mn _{A4} -OH ₂			Ca-OH ₂				
		W(2)	W(1)	W(3)	W(4)	W(5)	W(6)	W(7)	W(8)
Mn _{A4}	3.043	2.769	2.590	2.703	2.896	3.173	4.638	6.336	6.641
Mn _{B3}	3.324	5.381	5.140	5.008	5.527	4.820	5.890	6.086	6.031
Mn _{C2}	4.533	7.321	7.469	7.802	8.092	5.975	6.403	5.096	4.632
Mn _{D1}	2.712	6.131	6.117	7.369	7.890	4.909	5.431	4.650	5.099
Projected ^1H Hyperfine Tensors (MHz)									
$A_{dip}(^1\text{H})^a$	-7.827 ^c	-3.607	-4.455	-4.139	-3.350	-2.055	0.708	-1.062	0.839
$\eta(^1\text{H})^b$	0.070 ^d	0.119	0.098	0.067	0.028	0.627	0.943	0.617	0.952

Table S10.5: ^1H -Mn distances and theoretical ^1H couplings for the additional waters near Mn_{A4} in the Umena et al.²⁹ structure using the isotropic spin projections for the model of Siegbahn (model 11) reported in Pantazis et al.²⁸

	Mn-O distances (Å)							
	W(A3)		W(A4)		W(A1)		W(A2)	
Mn_{A4}	3.147	4.282	5.608	4.180	4.683	4.245	4.182	4.843
Mn_{B3}	4.098	4.765	7.420	6.138	6.896	5.861	6.740	7.418
Mn_{C2}	6.539	6.689	10.260	8.933	9.379	8.308	8.307	9.022
Mn_{D1}	7.219	7.909	9.236	7.833	7.725	6.563	7.601	7.828
Projected ^1H Hyperfine Tensors (MHz)								
$A_{\text{dip}}(^1\text{H})^{\text{a}}$	-2.806 ^a	-1.064	-0.421	-1.039	-0.727	-0.915	-1.050	-0.670
$\eta(^1\text{H})^{\text{b}}$	0.333 ^b	0.519	0.174	0.166	0.198	0.394	0.155	0.190

Table S10.6: ^1H -Mn distances and theoretical ^1H couplings for the additional waters near $\text{Mn}_{\text{B}}/\text{Mn}_{\text{C}}/\text{Mn}_{\text{D}}$ in the Umena et al.²⁹ structure using the isotropic spin projections for the model of Siegbahn (model 11) reported in Pantazis et al.²⁸

	Mn-O distances (Å)							
	Near Mn_{B3}		Near Mn_{C2}		Near Mn_{D1}			
	W(B1)		W(C1)		W(D2)		W(D1)	
Mn_{A4}	4.605	5.325	9.263	9.236	7.742	6.640	9.727	9.695
Mn_{B3}	3.875	4.260	7.611	7.922	6.562	5.203	6.978	6.910
Mn_{C2}	5.926	6.331	6.594	6.856	4.756	3.274	4.766	4.363
Mn_{D1}	7.132	7.285	4.569	4.672	4.001	3.114	7.261	6.479
Projected ^1H Hyperfine Tensors (MHz)								
$A_{\text{dip}}(^1\text{H})^{\text{a}}$	1.104 ^a	0.725	-1.207	-1.127	-1.857	-4.710	0.484	0.664
$\eta(^1\text{H})^{\text{b}}$	0.760 ^b	0.537	0.045	0.031	0.314	0.574	0.144	0.262

S11 Simulations of $^1\text{H}/^{17}\text{O}$ ENDOR data using the multipole estimates for the Umena et al. structure listed in S10.

S11.1 Simulations of the ^{17}O Mims ENDOR signal based on the coordinates of Umena et al. A simulation of the matrix signal is also shown in **Figure S8.2A and B (red dashed lines)**. These simulations were generated by assuming this signal arises from W3 and W4, the waters bound to the Ca^{2+} ion (see **Figure 1, main text**). As W3 and W4 do not directly ligate the Mn tetramer, their hyperfine interaction is expected to be dominantly through space (dipolar) and thus theoretical ^{17}O hyperfine coupling estimates can be made. These calculations, which assume a multipole model and the crystal structure coordinates of Umena et al. are described in the supporting information **S10**. In addition, a quadrupole coupling of ~ 7 MHz was assumed, as seen for water coordinating Mn^{2+} . Simulations, using these values reproduced the Lorentzian lineshape of the signal but not the 0.5 MHz splitting. This required the inclusion of a small isotropic coupling of 0.25 MHz. The lineshape of W3 and W4 are also shown separately in red solid line **Figure S8.2C**.

It is noted that 2nd shell waters in the vicinity of Mn_{D1} also have surprisingly large through space couplings, due to their interaction with the only Mn^{III} ion in S_2 and may also contribute to the splitting observed for the matrix line, see supporting information **S10, Tables S10.2 and S10.3**. In principle these two coupling sites (Ca-OH_2 and Mn_{D1} waters) should be differentiable in a 2D-ESSEM experiment such as HYSORE as they should have very different hyperfine tensor geometries; the Ca-OH_2 ^{17}O hyperfine tensors should appear rhombic the ^{17}O nucleus is located midway between two/three Mn whereas the ^{17}O nucleus of waters surrounding Mn_{D1} should instead appear axial. Extraction of these two species forms part of our ongoing experimental work.

S11.2 Simulations of the ^1H Davies/Mims ENDOR based on the coordinates of Umena et al. The $^1\text{H}/^2\text{H}$ data shown in the main text (**Figure 9**) clearly resolves the absolute edges of the $^1\text{H}/^2\text{H}$ ENDOR profile. The overall envelope is slightly larger than previously reported by Aznar et al.³ measured in

higher plant PSII but is nominally consistent with more recent ESEEM data.^{5,6} The magnitude of the couplings suggests that the $^1\text{H}/^2\text{H}$ species observed are coordinating water/hydroxyl ligands. Using the Umena et al.²⁹ crystal structure, dressed with protons using standard molecular modeling techniques, and the current electronic model for the OEC,^{27,28} estimates can be made for the minimum (dipolar) ^1H couplings for all ‘water’ molecules identified in the crystal structure. These multipole calculations, discussed above in reference to ^{17}O couplings, along with dipolar coupling estimates for all $^1\text{H}/^2\text{H}$ substrate positions are described in the supporting information **S10**. A simulation of the edges of the ^1H ENDOR profile is displayed as the 1st derivative using the dipolar coupling estimates described above is shown in **Figure S11.1**. The blue trace shows the expected ^1H ENDOR profile of a protonated O5 ligand, as proposed in the Umena et al. crystal structure. It is readily observed that the edges of the simulated profile are significantly broader (~6 MHz) than those observed experimentally. This suggests that O5 (and for that matter no μ -oxo bridge) is protonated in S_2 . The width of the experimental profile is however consistent with either of the largest proton coupling of W1 or W2 (**Figure S11.1 C, D**: red and green traces respectively), the two water/hydroxyl ligands of Mn_{A4} . To reproduce the line position exactly a small isotropic coupling of 2 MHz needs to be included (**Figure S11.1 E, F**: red and green traces respectively).

A similar simulation was made of the ^1H Mims ENDOR signal, **Figure S11.2**. In these simulations, all protons from water within 8 Å of the OEC were included, see **Figure S10.1**. The 2nd shell ‘water’ protons are seen to reproduce the structure of the ^1H Mims ENDOR envelope (solid blue line). However, to reproduce the intensity profile a matrix line needs to be added, presumably describing protein residue protons.

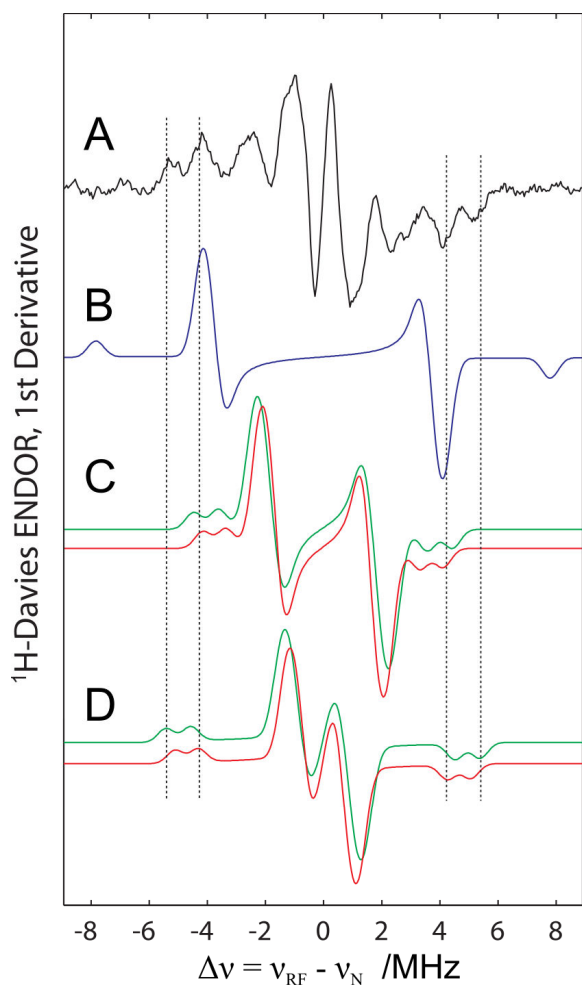


Figure S11.1. Analysis of the Proton/Deuteron ENDOR spectra. **A** 34 GHz (Q-band) ^1H Davies-ENDOR, displayed as the first derivative; **B** ^1H -ENDOR Simulation for the protonated (hydroxo) O5 bridge (blue); **C, D** ^1H -ENDOR Simulation for the terminal $\text{Mn}_{\text{A4}}\text{-OH}_2$ W1 (red), W2 (green); **E, F** ^1H -ENDOR Simulation for the terminal $\text{Mn}_{\text{A4}}\text{-OH}_2$ W1, W2 that includes a isotropic hyperfine coupling of 2 MHz (as used in Aznar et al.³), $\text{Mn}_{\text{A4}}\text{-OH}_2$ W1 (red), W2 (green).

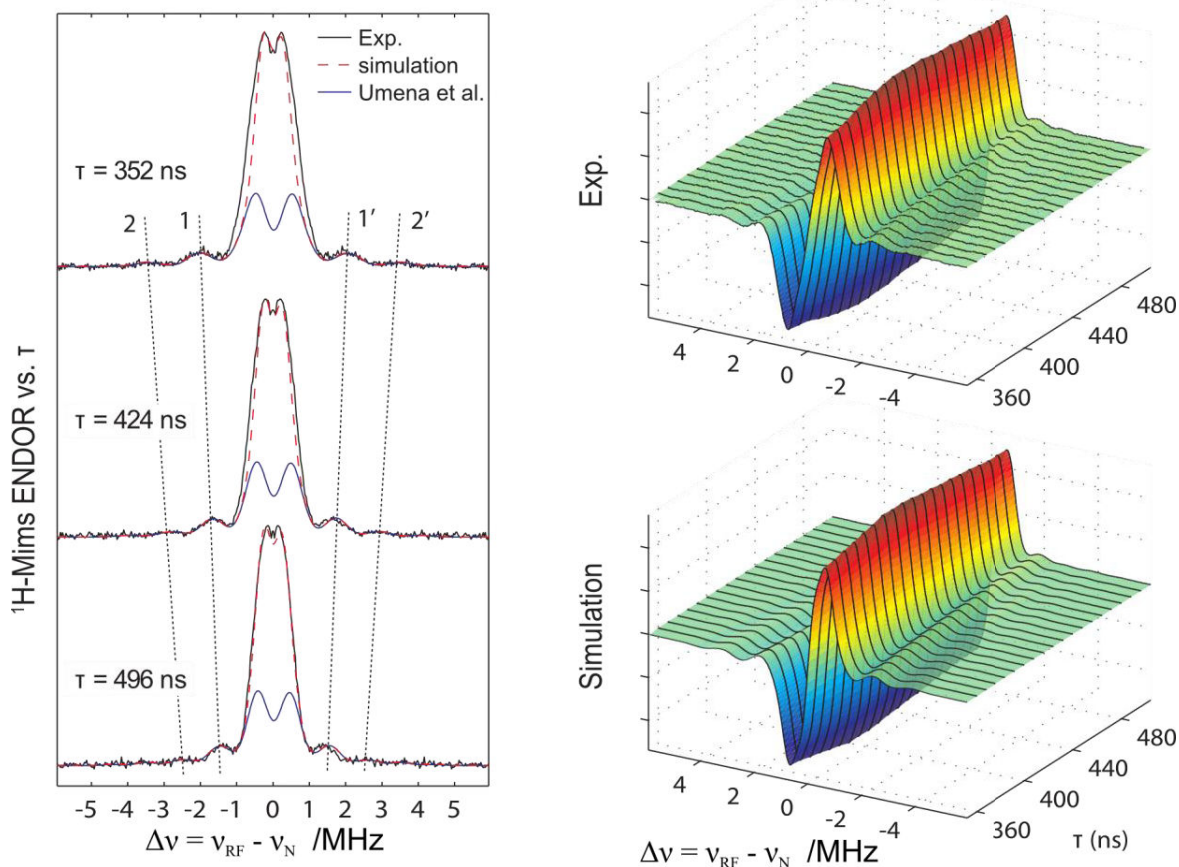


Figure S11.2 Q-band ^1H -Mims ENDOR vs. τ spectra of ^{14}N -PSII and ^{15}N -PSII of *T. elongatus* poised in the S_2 state (200 K white light), measured at the center of the multiline spectrum (1.22 T). **Left-hand panel:** ^1H -Mims ENDOR measured at $\tau = 352, 424$ and 496 ns. The superimposed simulation of ^1H -Mims ENDOR uses theoretical estimations of hyperfine couplings based on the crystal structure of Umena et al. (blue lines) excluding a protonated O(5) bridge and with an additional ‘matrix’ line (dashed red lines), introduced in simulations as additional number of protons with isotropic hyperfine coupling of 0.25 MHz; **Right-hand panel:** A derivative representation of ^1H -Mims ENDOR surface data and corresponding simulation.

S12 ^{17}O hyperfine tensor orientations based on the coordinates of Umena et al.²⁹ The orientation of the anisotropic component of the μ -oxo bridge hyperfine tensor can be used to refine the assignment of the μ -oxo bridge signal. This can be mapped to the three dimension structure of the OEC using the D1-His332 signal. The Mn-Mn interspin vectors are given in **Table S12.1**. By taking the vector product of the Mn-Mn interspin vector and the calculated ^{17}O hyperfine tensors (see **S9 and S10**) the orientation of the hyperfine tensor can be ascertained. It is seen that the unique principal axes of the ^{17}O hyperfine tensor for the μ -oxo bridges lie in the respective $\text{Mn}_X\text{-O}_2\text{-Mn}_Y$ plane (see **Table S12.2 and Figure S12.1**). The only exception is O2. It is rotated out of the $\text{Mn}_{\text{B3}}\text{-O-Mn}_{\text{C2}}$ plane, that is to say it is perpendicular to the $\text{Mn}_{\text{B3}}\text{-Mn}_{\text{C2}}$ interspin vector. This is not surprising as the $\text{Mn}_{\text{B3}}\text{-O-Mn}_{\text{C2}}$ couple is unlike the BIPY model system; the exchange pathway between Mn_{B3} and Mn_{C2} is ferromagnetic.

The orientation of the $\text{Mn}_{\text{D1}}\text{-}^{14}\text{N}$ (His332) hyperfine tensor to the Mn-Mn interspin vectors can be calculated in the same way. The orientation of the unique principal axis of the $^{14}\text{N}/^{15}\text{N}$ D1-His332 lies approximately along the $\text{Mn}_{\text{D1}}\text{-N}$ bond. It is approximately perpendicular to both the $\text{Mn}_{\text{B3}}\text{-Mn}_{\text{C2}}$ and $\text{Mn}_{\text{A4}}\text{-Mn}_{\text{B3}}$ interspin vectors and at 45° to the $\text{Mn}_{\text{C2}}\text{-Mn}_{\text{D1}}$ interspin vector as expected; it is an equatorial ligand to Mn_{D1} and thus is in the same plane as the $\text{Mn}_{\text{C2}}\text{-O}_2\text{-Mn}_{\text{D1}}$ bridge motif.

A similar procedure can be performed to ascertain the orientation of each of the ^{17}O hyperfine tensor to the $\text{Mn}_{\text{D1}}\text{-}^{14}\text{N}$ (His332) hyperfine tensor. As a starting point, the angle between the unique principal axis of each μ -oxo bridge hyperfine tensor relative to the unique principal axis of the D1-His332 hyperfine can be calculated, see **Table S12.4**, column 1. Interestingly the unique principal axis direction for bridges O2, O3, O4 and O5 are all perpendicular to the unique principal axis direction of the D1-His332. In addition, the angle between of the other two components of each μ -oxo bridge hyperfine tensor relative to the principal axis of the D1-His332 hyperfine can also be calculated.

The spin Hamiltonian simulations presented in the manuscript require the exchangeable μ -oxo bridge to display two properties:

1. The unique principal axis of the ^{17}O hyperfine tensor (\hat{y}_1) must be approximately perpendicular to the unique principal axis of the D1-His332 hyperfine tensor (\hat{x}_1).
2. The axis which defines the middle component of the ^{17}O hyperfine tensor (\hat{y}_2) must be approximately parallel to the unique principal axis of the D1-His332 hyperfine tensor (\hat{x}_1).

It is readily seen from inspection of **Table S12.4 (column 4, $\hat{x}_1 \cdot \hat{y}_2$)** that both of these criteria only hold for the bridges O4 and O5; they are approximately parallel with the $\text{Mn}_{\text{D1}}\text{-N}$ bond, 26° and 169° (i.e. 11°) respectively. Thus are the most likely candidates for the μ -oxo bridge.

The intermediate ^{17}O coupling provides an internal check as to whether the approach described above is valid for assigning the position of the μ -oxo bridge species. The intermediate coupling is assigned to W1/W2 (most likely W2), the terminal ligands of Mn_{A4} . The unique principal axis for both the terminal ^{17}O waters and for the ^{14}N of the D1-His332 should lie approximately along the Mn-Ligand bond. Taking the crystal structure coordinates and performing the same multipole calculation as above, it can be shown that the angles between the $\text{Mn}_{\text{A4}}\text{-W1/W2}$ metal-ligand bonds and that of the $\text{Mn}_{\text{D1}}\text{-}^{14}\text{N}$ (D1-His332) are 105° and 97° respectively, i.e. their principal axes are approximately perpendicular. The same as observed in the simulations of the EDNMR surface; the unique principal axis of the intermediate ^{17}O coupling (aligned along g_z) is approximately perpendicular to the principal axis of the D1-His332 ligand, thus the μ -oxo bridge assignment is reasonable.

Table S12.1: Mn-Mn vectors using the coordinates of Umena et al.²⁹

	\tilde{i}	\tilde{j}	\tilde{k}
Mn _{C2} -Mn _{D1}	0.85	-0.11	-0.52
Mn _{B3} -Mn _{C2}	-0.05	-0.68	0.73
Mn _{A4} -Mn _{B3}	0.12	-0.01	0.99

The Mn_{C2}-Mn_{D1} vector is roughly perpendicular to the Mn_{B3}-Mn_{C2} vector (69.7°) and Mn_{A4}-Mn_{B3} vector (65.7°).

Table S12.2: The angle in degrees between the Mn-Mn vectors vs. the three vectors $\hat{x}_1, \hat{x}_2, \hat{x}_3$ which define the directions of the principal components of each Mn-O-Mn hyperfine tensor using the coordinates of Umena et al.²⁹ and the isotropic spin projections for the model of Siegbahn (model 11) reported in Pantazis et al.²⁸

	Angle (°)		
	$(\hat{x}_{Mn-Mn} \cdot \hat{x}_1)$	$(\hat{x}_{Mn-Mn} \cdot \hat{x}_2)$	$(\hat{x}_{Mn-Mn} \cdot \hat{x}_3)$
O1 (Mn _{C2} -O-Mn _{D1})	133.6	93.4	136.1
O2 (Mn _{B3} -O-Mn _{C2})	90.0	48.7	41.4
O3 (Mn _{C2} -O-Mn _{D1})	131.3	94.0	41.4
O4 (Mn _{A4} -O-Mn _{B3})	133.6	90.0	43.9
O5 (Mn _{A4} -O-Mn _{B3})	38.7	89.4	129.1

The signed magnitude of the three principal components of each ¹⁷O hyperfine tensor is such that the largest component lies along \hat{x}_1 , the middle component along \hat{x}_2 and the smallest along \hat{x}_3 . For Mn-O-Mn bridges where the sign of the spin projections of the two Mn is opposite (antiferromagnetic coupling) the middle component is always perpendicular to the Mn-Mn interspin vector. In contrast for Mn-O-Mn bridges where the sign of the spin projections of the two Mn is the same (ferromagnetic coupling) the largest component is now perpendicular to the Mn-Mn interspin vector.

Table S12.3: The angle in degrees between the Mn-Mn interspin vectors vs. three vectors $\hat{x}_1, \hat{x}_2, \hat{x}_3$ which define the directions of the principal components the $\text{Mn}_{\text{D1}}\text{-N}(\text{His332})$ hyperfine tensor using the coordinates of Umena et al.²⁹ and the isotropic spin projections for the model of Siegbahn (model 11) reported in Pantazis et al.²⁸

	Angle ($^\circ$)		
	$(\hat{x}_{\text{Mn-Mn}} \cdot \hat{x}_1)$	$(\hat{x}_{\text{Mn-Mn}} \cdot \hat{x}_2)$	$(\hat{x}_{\text{Mn-Mn}} \cdot \hat{x}_3)$
$\text{Mn}_{\text{C2}}\text{-Mn}_{\text{D1}}$	48.7	108.1	46.4
$\text{Mn}_{\text{B3}}\text{-Mn}_{\text{C2}}$	118.7	144.1	70.7
$\text{Mn}_{\text{A4}}\text{-Mn}_{\text{B3}}$	88.6	10.6	100.5

The signed magnitude of the three principal components of $\text{Mn}_{\text{D1}}\text{-N}(\text{His332})$ hyperfine tensor $[-1.96 \ 0.91 \ 1.05]$ is such that the largest component (negative) lies along \hat{x}_1 , the middle component along \hat{x}_2 and the smallest along \hat{x}_3 . The largest component (\hat{x}_1) is aligned along the $\text{Mn}_{\text{D1}}\text{-N}(\text{His332})$ interspin vector.

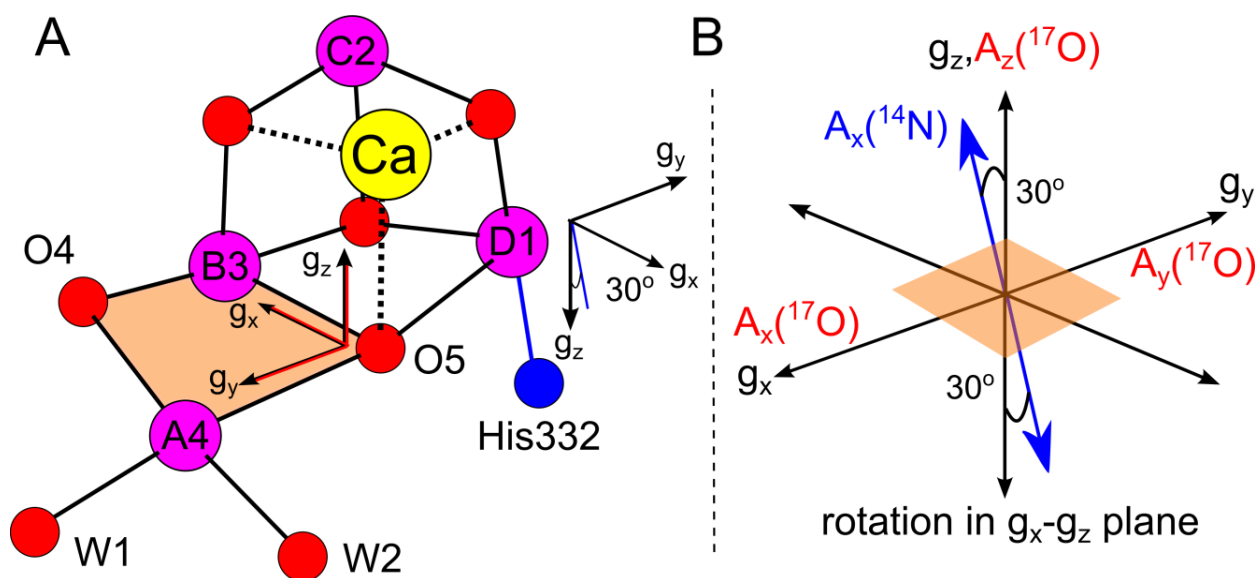


Figure S12.1 The orientations of the molecular g tensor as compared to the ^{14}N (His332) and ^{17}O (O5) hyperfine tensor.

Table S12.4: The angle in degrees between the three vectors $\hat{x}_1, \hat{x}_2, \hat{x}_3$ which define the directions of the principal components the $\text{Mn}_{\text{D1-N(D1-His332)}}$ hyperfine tensor and the three vectors $\hat{y}_1, \hat{y}_2, \hat{y}_3$ which define the directions of the principal components the μ -oxo bridges using the coordinates of Umena et al.²⁹

	Angle in degrees ($\arccos(\hat{x}_i \cdot \hat{y}_j)$)			
	$\hat{x}_1 \cdot \hat{y}_1$	$\hat{x}_2 \cdot \hat{y}_2$	$\hat{x}_3 \cdot \hat{y}_3$	$\hat{x}_1 \cdot \hat{y}_2$
<i>O1 · His332</i>	177.4	160.4	160.4	90.6
<i>O2 · His332</i>	82.9	25.3	77.2	70.5
<i>O3 · His332</i>	83.5	14.8	85.0	84.1
<i>O4 · His332</i>	72.3	95.8	61.4	26.3
<i>O5 · His332</i>	81.7	86.1	29.7	168.9

S11 Theoretical EPR Parameter Calculations from Broken Symmetry DFT. The model geometries used for EPR parameter calculations were taken from Ames et al.²⁴ Isotropic hyperfine couplings A_{iso} were calculated for the terminal ^{17}O ligands (^{55}Mn and ^{14}N couplings were reported in Ames et al.) For the calculation of EPR parameters the same methods were used (ZORA-TPSSh) as for the single-point calculations described above. Picture-change effects were applied to the calculation of hyperfine coupling constants. The integration grids were increased to 9 (ORCA convention) for the ^{17}O centers. The theoretical approach follows previously established protocols that define a transformation of the “raw” value obtained from BS-DFT for a given nucleus K , $A_{\text{iso,BS}}^{(K)}$, to values that can be compared to observable isotropic hyperfine couplings according to:²⁸

$$A_{\text{iso}}^{(K)} = \pm A_{\text{iso,BS}}^{(K)} \left(\frac{\langle S_z \rangle_{\text{BS}}}{S_A} \right) \left(\frac{\langle S_z^{(A)} \rangle}{S_t} \right) \quad \text{Eq. S13.1}$$

In the above equation S_t is the total spin (1/2 in our case) and $\langle S_z \rangle_{\text{BS}}$ is simply the total M_S of the BS wavefunction, therefore the projection consists of adjusting $A_{\text{iso,BS}}^{(K)}$ according to the ratio of the on-site

spin expectation value $\langle S_z^{(A)} \rangle$ and the formal site spin S_A . The positive or negative sign refers to the majority (α) or minority (β) spin carried by the fragment. The on-site spin expectation value $\langle S_z^{(A)} \rangle$ that represents the coupling of the local spin of site A into the complicated multiconfigurational ground state wavefunction is the most critical quantity for the procedure, and is obtained as

$$\langle S_z^{(A)} \rangle = \sum_{S_A M_{S_A} \dots S_N M_{S_N}} \left| C_I^{S_A M_{S_A} \dots S_N M_{S_N}} \right|^2 M_{S_A} \quad \text{Eq. S13.2}$$

where $|C_I^{S_A M_{S_A} \dots S_N M_{S_N}}|^2$ represents the weight of basis state I , $|S_A M_{S_A}, \dots, S_N M_{S_N}\rangle$, in the ground state eigenfunction of the Hisenberg-Diac-van-Velck Hamiltonian $|S_A S_B \dots S_{N-1} S_N S M_S\rangle$ with $M_S = S$. We refer the reader to the recent literature for a more detailed theoretical treatment.³⁰

S12 References

- (1) Kawamori, A.; Inui, T.; Ono, T.; Inoue, Y. *FEBS Lett.* **1989**, *254*, 219-224.
- (2) Fiege, R.; Zwegart, W.; Bittl, R.; Adir, N.; Renger, G.; Lubitz, W. *Photosynth. Res.* **1996**, *48*, 227-237.
- (3) Aznar, C. P.; Britt, R. D. *Phil. Trans. R. Soc. B* **2002**, *357*, 1359-1366.
- (4) Britt, R. D.; Campbell, K. A.; Peloquin, J. M.; Gilchrist, M. L.; Aznar, C. P.; Dicus, M. M.; Robblee, J.; Messinger, J. *Biochim. Biophys. Acta* **2004**, *1655*, 158-171.
- (5) Ahrling, K. A.; Evans, M. C. W.; Nugent, J. H. A.; Ball, R. J.; Pace, R. J. *Biochemistry* **2006**, *45*, 7069-7082.
- (6) Martínez, J. I.; Yruela, I.; Picorel, R.; Alonso, P. J. *J. Phys. Chem. B* **2010**, *114*, 15345-15353.
- (7) Carepo, M.; Tierney, D. L.; Brondino, C. D.; Yang, T. C.; Pamplona, A.; Telser, J.; Moura, I.; Moura, J. J. G.; Hoffman, B. M. *J. Am. Chem. Soc.* **2001**, *124*, 281-286.

- (8) Burdi, D.; Willems, J.-P.; Riggs-Gelasco, P.; Antholine, W. E.; Stubbe, J.; Hoffman, B. *M. J. Am. Chem. Soc.* **1998**, *120*, 12910-12919.
- (9) Baute, D.; Goldfarb, D. *J. Phys. Chem. A* **2005**, *109*, 7865-7871.
- (10) Tan, X.; Bernardo, M.; Thomann, H.; Scholes, C. P. *J. Phys. Chem. A* **1995**, *102*, 2675-2691.
- (11) Glotfelty, H. W., University of Kansas, 1978.
- (12) Usov, O. M.; Grigoryants, V. M.; Tagore, R.; Brudvig, G. W.; Scholes, C. P. *J. Am. Chem. Soc.* **2007**, *129*, 11886-11887.
- (13) Thomann, H.; Bernardo, M.; Goldfarb, D.; Kroneck, P. M. H.; Ullrich, V. *J. Am. Chem. Soc.* **1995**, *117*, 8243-8251.
- (14) Astashkin, A. V.; Feng; Raitsimring, A. M.; Enemark, J. H. *J. Am. Chem. Soc.* **2004**, *127*, 502-503.
- (15) Wilson, G. L.; Kony, M.; Tiekink, E. R. T.; Pilbrow, J. R.; Spence, J. T.; Wedd, A. G. *J. Am. Chem. Soc.* **1988**, *110*, 6923-6925.
- (16) Raitsimring, A. M.; Astashkin, A. V.; Baute, D.; Goldfarb, D.; Caravan, P. *J. Phys. Chem. A* **2004**, *108*, 7318-7323.
- (17) Sage, J. T.; Xia, Y. M.; Debrunner, P. G.; Keough, D. T.; De Jersey, J.; Zerner, B. *J. Am. Chem. Soc.* **1989**, *111*, 7239-7247.
- (18) Bencini, A.; Gatteschi, D. *EPR of Exchange Coupled Systems*; Springer-Verlag: Berlin, 1990.
- (19) Kulik, L. V.; Epel, B.; Lubitz, W.; Messinger, J. *J. Am. Chem. Soc.* **2007**, *129*, 13421-13435.
- (20) Messinger, J.; Robblee, J. H.; Bergmann, U.; Fernandez, C.; Glatzel, P.; Visser, H.; Cinco, R. M.; McFarlane, K. L.; Bellacchio, E.; Pizarro, S. A.; Cramer, S. P.; Sauer, K.; Klein, M. P.; Yachandra, V. K. *J. Am. Chem. Soc.* **2001**, *123*, 7804-7820.

- (21) Haumann, M.; Müller, C.; Liebisch, P.; Iuzzolino, L.; Dittmer, J.; Grabolle, M.; Neisius, T.; Meyer-Klaucke, W.; Dau, H. *Biochemistry* **2005**, *44*, 1894-1908.
- (22) Yachandra, V. K.; Sauer, K.; Klein, M. P. *Chem. Rev.* **1996**, *96*, 2927-2950.
- (23) Teutloff, C.; Kessen, S.; Kern, J.; Zouni, A.; Bittl, R. *FEBS Lett.* **2006**, *580*, 3605-3609.
- (24) Ames, W.; Pantazis, D. A.; Krewald, V.; Cox, N.; Lubitz, W.; Neese, F. *J. Am. Chem. Soc.* **2011**, *133*, 19743-19757.
- (25) Schosseler, P.; Wacker, T.; Schweiger, A. *Chem. Phys. Lett.* **1994**, *224*, 319-324.
- (26) Randall, D. W.; Sturgeon, B. E.; Ball, J. A.; Lorigan, G. A.; Chan, M. K.; Klein, M. P.; Armstrong, W. H.; Britt, R. D. *J. Am. Chem. Soc.* **1995**, *117*, 11780-11789.
- (27) Cox, N.; Rapatskiy, L.; Su, J.-H.; Pantazis, D. A.; Sugiura, M.; Kulik, L.; Dorlet, P.; Rutherford, A. W.; Neese, F.; Boussac, A.; Lubitz, W.; Messinger, J. *J. Am. Chem. Soc.* **2011**, *133*, 3635-3648.
- (28) Pantazis, D. A.; Orio, M.; Petrenko, T.; Zein, S.; Lubitz, W.; Messinger, J.; Neese, F. *Phys. Chem. Chem. Phys.* **2009**, *11*, 6788-6798.
- (29) Umena, Y.; Kawakami, K.; Shen, J.-R.; Kamiya, N. *Nature* **2011**, *473*, 55-60.
- (30) Pantazis, D. A.; Orio, M.; Petrenko, T.; Zein, S.; Bill, E.; Lubitz, W.; Messinger, J.; Neese, F. *Chemistry-a European Journal* **2009**, *15*, 5108-5123.